Université de Valenciennes et du Hainaut-Cambrésis

Thèse de doctorat

Pour obtenir le grade de Docteur de l'Université de

VALENCIENNES ET DU HAINAUT-CAMBRESIS

Discipline, spécialité selon la liste des spécialités pour lesquelles l'Ecole Doctorale est accréditée :
Mécanique

Présentée et soutenue par Thomas VANNESTE.

Le 04/07/2013, à Lille

Ecole doctorale :
Sciences Pour l'Ingénieur (SPI)

Equipe de recherche, Laboratoire :
Institut d'Electronique, de Micro-Electronique et de Nanotechnologie/Département d'Opto-Acousto-Electronique (IEMN/DOAE)

Développement d'un outil de modélisation aéroélastique du vol battu de l'insecte appliqué à la conception d'un nano-drone résonant

JURY

Président du jury
- Thomas, Olivier. Professeur. ENSAM, Lille.

Rapporteurs
- Knowles, Kevin. Professeur. Cranfield University, Shrivenham.
- Dufour, Régis. Professeur. INSA, Lyon.

Examinateurs

- Chapin, Vincent. Professeur Associé. ISAE, Toulouse.
- Chassaing, Jean-Camille. HDR. UPMC, Paris.

Directeur de thèse

- Cattan, Eric. Professeur. IEMN, Valenciennes.

Co-directeur de thèse :

- Grondel, Sébastien. Professeur. IEMN, Valenciennes.

Co-encadrant :

- Paquet, Jean-Bernard. Ingénieur-docteur. ONERA, Lille.

Engagez-vous qu'ils disaient...

Légionnaire romain

Acknowledgments

Voici une page délicate à écrire afin de remercier toutes les personnes qui ont contribué, directement ou indirectement, à clore ce travail. Cette page n'est évidemment pas exhaustive et plutôt professionnelle, mais les absents et les amis se reconnaîtront. *Mea Culpa*.

Je voudrais tout d'abord remercier M. Bruno Mialon qui a accepté de m'accueillir au sein de l'équipe MMHD à l'ONERA Lille mais qui a également veillé à ce que je puisse bénéficier de toutes les conditions matérielles et formations nécessaires à la réalisation de cette thèse mais également à sa promotion.

Cette thèse n'aurait pas pu être terminée correctement sans les membres du jury et je tiens à les remercier sincèrement d'avoir accepté de juger ce travail. A cet égard, j'exprime toute ma reconnaissance aux rapporteurs, MM. Kevin Knowles et Régis Dufour, qui ont accepté cette tâche de relecture intensive, parfois ingrate. Ma gratitude s'étend bien naturellement aux examinateurs, MM. Vincent Chapin, Jean-Camille Chassaing et Olivier Thomas.

Je souhaite ensuite remercier vivement les encadrants de cette thèse, MM. Eric Cattan, Sébastien Grondel et Jean-Bernard Paquet, de m'avoir accorder leur confiance en me laissant une grande autonomie, mais également en tempérant et canalisant ma fougue pour que ma thèse avance du mieux possible malgré les soubresauts administratifs. J'ai parfois poussé le bouchon un peu trop loin, je m'en excuse et vous remercie de vos indulgences. Eric, merci d'avoir pu financer l'extension des quelques mois nécessaires à la réalisation de la campagne expérimentale, mais également le congrès AIAA qui m'a ouvert les yeux sur la portée de mes travaux, d'avoir été à l'écoute de ma créativité parfois débordante, d'avoir prêter main forte pour résoudre mes problèmes de vide et d'avoir toujours essayer de positiver. Sébastien, merci d'avoir suivi mes travaux en plus grande profondeur et d'avoir su guider ma réflexion lorsqu'un souci se présentait en synthétisant mes avancées et en positivant tout cela, même perdu dans les montagnes. Je vous remercie tous les deux aussi pour notre discussion dans le hall de l'hôtel, à Denver, qui m'a permis de faire un grand bond en avant à ce travail. Jean-Bernard, merci d'avoir été là pour répondre à mes questions aérodynamiques/structures, parfois redondantes, même si je ne sais toujours pas répondre aux questions plus théoriques que vous souleviez, et d'avoir été force de propositions pour chercher des explications cohérentes, mais également d'être fin diplomate.

Je souhaite ensuite remercier mes collègues à l'ONERA. D'abord ceux de MMHD qui ont apporté leurs aides à différents niveaux : Brigitte pour avoir tenté de me guider dans les méandres administratifs ; Jean-Paul pour m'avoir prêté main-forte pour monter et réaliser les manips mais aussi pour m'avoir montré l'étendue des essais que l'on pouvait faire en aéro, je t'ai aidé avec un grand plaisir, et d'égayer les journées avec des phrases comme: "Les spécialistes, il y en a plein les cimetières" ; Jean-Michel pour m'avoir expliqué l'optique en 2 *min* et ses applications en aéro autour de mousses australiennes. Ensuite, mes collègues des essais à CRD et des ateliers à DERM qui sont toujours sources de bons conseils et de discussions intéressantes, aussi bien professionnellement qu'humainement, mais également de joies et de bonne humeur: j'aurais aimé pouvoir travailler encore davantage avec vous.

Je tiens également à remercier mes collègues doctorants/stagiaires et d'équipes MSG. Benjamin, pour m'avoir tenu la tête hors de l'eau pendant les deux premières années et plus de la thèse, mais également pour assouvir notre soif de bières du Nord et d'Allemagne. Stéphane, pour s'être tenu les coudes pendant cette thèse notamment en y partageant, pour le meilleur et pour le pire, le même bureau et ma programmation

Deezer/Youtube éclectique mais aussi pour t'inquiéter quand je souhaite dormir dans les bois, et surtout d'être toujours dispo. Alex, pour m'avoir montré qu'un laboratoire pouvait être un lieu dynamique et d'échanges mais également pour m'avoir fabriqué mes protos et apporter du positif dans nos essais.

Enfin, un grand et sincère merci à ma famille pour leur soutien indéfectible tout au long de mon cursus et de cette dernière étape, ainsi qu'à Malika pour avoir veillé sur la dernière ligne droite de rédaction et sur ma azizen tout ce temps.

Un immense merci à Sadia, pour avoir toujours été là, dans les mauvais comme les bons moments, avec ses sourires et ses paroles. Merci du fond du coeur.

Contents

List of Figures

List of Tables

Nomenclature

Variables

$\mathbf{C}$	Damping matrix in a finite element formulation	
C_D	Drag coefficient	–
C_L	Lift coefficient	–
C_N	Normal coefficient	–
C_{blade}	Mean chord of a blade	m
C_{rot}	Rotational force coefficient	–
ΔC	Shift from the blade mid-chord to the blade rotation axis	m
$\Delta \hat{C}$	Non-dimensial location of the blade rotation axis	–
E	Young modulus	MPa
I_b	Bending moment of inertia	m^4
I_t	Torsional moment of inertia	m^4
J	Objective function in a optimization problem	–
$\mathbf{K}$	Stiffness matrix in a finite element formulation	
Kn	Knudsen number	–
$\mathbf{M}$	Mass matrix in a finite element formulation	
$N_{FE_{Chord}}$	Number of finite element in the chordwise direction	–
$N_{FE_{Span}}$	Number of finite element in the spanwise direction	–
N_{Steps}	Number of time steps per period	–
$N_{Substeps}$	Number of substeps of iteration between two consecutive time steps steps	–
$\mathbf{Rot_X}$	Rotation matrix around the ζ-axis	
$\mathbf{Rot_Y}$	Rotation matrix around the y-axis	
$\mathbf{Rot_Z}$	Rotation matrix around the Z-axis	
Re	Reynolds number	–
S	Projected airfoil surface	m^2

Sr	Strouhal number	–
Ut	Translational wing tip velocity	$m.s^{-1}$
V_{inf}	Free-stream velocity	$m.s^{-1}$
N_{FE}	Number of chordwise element in a blade	–
$\bar{c}$	Airfoil mean chord	m
$\bar{c}_i$	Finite element mean chord	m
$\hat{c}$	Non-dimensional chord length	–
f	Resonant frequency	Hz
q	Displacement vector of the structure	
$\hat{r}$	Non-dimensional radial position	–
$\hat{r_2}^2(S)$	Non-dimensional second moment of wing area	–
s	Airfoil span	m
s_i	Finite element span	m
s_{blade}	Span of a blade	m
α	Airfoil morphological angle of attack	$^\circ$
α	Rayleigh mass matrix coefficient	–
α'	Airfoil effective angle of attack	$^\circ$
β	Rayleigh stiffness matrix coefficient	–
$\ddot{\eta}$	Normal acceleration of a wing finite-element	$m.s^{-2}$
$\lambda_{\eta,i}$	Added-mass coefficient	kg
ν	Poisson's ratio	–
ω	Pulsation	$rad.s^{-1}$
ϕ	Flapping angle in Sane and Dickinson [2002]	rad
ϕ	Pitch angle around the ζ-axis	rad
ψ	Roll angle around the Z-axis	rad
ρ	Air density	$kg.m^{-3}$
θ	Yaw angle around the y-axis	rad
ζ	Damping ratio of a cantilever –)	(

Abbreviations

AOA	Angle of attack
CFD	Computational fluid dynamics

DOF	Degree of freedom
FE	Finite Element
FEM	Finite Element Method
FFT	Fast Fourier transform
FPV	First-person view
FW	Flapping-wing
$FWMAV$	Flapping-wing micro air vehicle
$FWNAV$	Flapping-wing nano air vehicle
GA	Genetic algorithm
GTW	Gross takeoff weight
LA	Large actuation
LD	Large deflection hypothesis for the FE i.e. its large displacement capability turned on
LEV	Leading edge vortex
MAV	Micro air vehicle
NAV	Nano air vehicle
$OVMI$	Object volant mimant l'insecte (French for Flying Object Mimicking the Insect
PIV	Particle image velocimetry
SA	Small actuation
SD	Small deflection hypothesis for the FE i.e. its large displacement capability turned off
UAV	Unmanned air vehicles

Indices

eta	Norman to an airfoil element
ξ	Tangent to an airfoil element
b	Air
b	Bending
c	Cantilever
exp	Experimental value
f	Balance foil
i	Local value on the finite element or incremental index
exp	Numerical value
t	Torsion
t	Vacuum

General introduction

Unmanned air vehicles (UAV) are today very common in the field of remote sensing and information gathering both in military and civilian applications. A strong international effort is made to deploy them in a wide variety of operation theaters. Initiated by the DARPA (Defense Advanced Research Projects Agency) in the 1990s (McMichael and Francis [1997]), the concept of micro air vehicles (MAV) was depicted so as to provide local situational awareness, such as "over the hill" reconnaissance mission, right down to the platoon level with on demand local reconnaissance or other sensor information. There a MAV was defined as having its largest linear dimension below $15cm$, a range of about $10km$, an endurance of 20-60min with $20g$ payload and with a peak velocity between 10-20$m.s^{-1}$. Consequently, a large variety of fixed-, rotary- and flapping-wing concepts emerged meeting these requirements and getting in service both in the military and in the civil. In 2005, DARPA tackles down these specifications for even more constrained areas, such as indoor and urban environment, by launching the Nano Air Vehicle (NAV) program (DARPA and DSO [2005]). The aim is to develop fully functional and integrated UAV with a maximal linear dimension below $7.5cm$, a gross takeoff weight (GTW) below $10g$, an endurance of $20min$, a range of $1km$ with a peak velocity of $10m.s^{-1}$ and a hovering capability.

With these drastic requirements, nature provides an obvious source of inspiration with insects and some birds falling typically into these dimensions. Through thousand years of evolution and adaptation, flying insects have developed and perfected their flight towards amazing flight capabilities, agility and maneuverability while responding each time to their specific environmental constraints with success. Therefore flapping-wing concepts are preferentially considered to meet the NAV requirements strengthened by the availability of already fully functional flapping-wing MAV (FWMAV). Thus several flapping-wing NAVs (FWNAV) are currently under development aiming at mimicking the insect flight using mostly MEMS technologies and various actuation concepts. Among them, the Robobee from the Harvard university has shown sustained flight (Wood [2007a,b]) crediting further the feasibility of FWNAVs while announcing other prototypes. Two categories of FWNAVs are yet arising: one driving the wing to its desired motion through an appropriate transmission system and the second exploiting the wing mode shape to generate the appropriate motion. The OVMI (French for Flying Object Mimicking the Insect) FWNAV, developed currently at the IEMN (Vanneste et al. [2010]; Bontemps et al. [2013]), belongs to the latter and is the backbone of this work and of its applications.

One of the major issues faced by designers is the definition of both the wing actuation strategy, i.e. how the wing should be actuated, and of the wing geometry so that the wing motion is compatible with lift generation and eventually with energy-efficiency. These challenges are essential for the designers as they define or affect subsequently all systems on board. Given the very limited GTW of FWNAVs, an integrated design approach is here crucial to release an efficient FWNAV and maximize its operational potential.

When starting the design of a FWNAV from scratch, there is *a priori* a broad design space ahead, as outlined by the number of flying insects found in nature, and designers have to crawl through it before finding the correct combination of parameters meeting their requirements. This is even more true, when novel technology choices are introduced and no know-how is available to pave the way. The usual method,

used then, is experimental trial and error which might be quite time-consuming and discouraging. Therefore to assist the designers navigating through the preliminary design stage of their FWNAV and to alleviate the experimental hiccup, a numerical model of the insect flight is here essential.

The success of insect flight is notably due to two key-features: a specific wing stroke motion, combining translational and rotational motions, and a low-Reynolds number unsteady aerodynamics with phenomena such as leading-edge vortices or wing-wake interaction occurring. Accordingly, structural forces, due to the wing stroke, and aerodynamic forces, which are determined by the wing motion and shape, are acting simultaneously on the wing. Given its flexibility, the insect wing can not be considered as indeformable and defines thus an aeroelastic problem.

These phenomena, or at least the most critical, have to be accounted for and implemented in a framework so as to escort designers in their preliminary design choices. To comply with the requisites of such preliminary design tool, the aeroelastic framework has to swarm around and evaluate quickly and accurately enough a broad design space of wing geometries, material and actuation strategies. This requires a robust, efficient and modular framework whose development, validation and applications are the subjects of this thesis.

Given that the framework will, *in fine*, be used to assist the sizing of the OVMI mode shape, strong consideration should be given to handle correctly the flexibility of the wing, both in the spanwise and in the chordwise direction, and its effects on the aerodynamics. As suggested by Combes and Daniel [2003a] in their conclusion and to avoid, at least at the preliminary design stage, time-consuming computational fluids dynamics (CFD), a dedicated aerodynamic model of the insect flight coupled to a finite element method (FEM) based structural solver is an appropriate setup to tackle down preliminary design tasks. Similar conclusions are also issued by Zbikowski [2002] and Blair et al. [2007]. The definition and development of such aeroelastic framework constitutes the first part of this work.

However as any numerical tool, the framework has to be validated against experimental or literature data before being released. Given the very flexible high-frequency wing typical of the OVMI, literature data are already scarce and moreover do not meet the specificity of the OVMI in terms of material and actuation for example. Therefore a complete experimental database has to be generated covering the validation of each aspect of the aeroelastic framework along with the definition of the appropriate equipment and methodologies. These tasks constitute the second part of this work along with the validation itself.

Once the design tool validated, several preliminary design tasks may be undertaken to hasten the development of novel FWNAVs. As mentioned earlier, among the first challenges faced by designers are the definition of an appropriate actuation strategy and foremost of an aerodynamic potentially interesting wing. While the first task can be solved by comparing computations of various actuation concepts, the second one is quite time-consuming in the absence of know-how being much more like looking for a needle in a haystack given the broad design space found in nature. As a requirement of the design tool is its evaluation speed and autonomy, an optimization strategy, calling iteratively the aeroelastic framework, can be initiated to assist the designer in choosing and refining gradually its wing design. Such applications on the OVMI constitute the third and final part of this thesis.

Keeping in mind the aim of the present work, developing a preliminary design tool of FWNAVs, the layout of this dissertation has been thought in such a way that each subject results as the development of the previous one and is organized around 6 chapters as follow:

- Chapter 1 introduces briefly the concept of FWNAV and the specificity of the OVMI before outlining the current understanding of insect flight and reviewing experimental and numerical works performed towards the design of FWNAV,

- Chapter 2 defines an aerodynamic model of insect flight accounting for the wing deformation in both the spanwise and in the chordwise direction along with a chordwise averaged model derived from Sane

and Dickinson [2002],

- Chapter 3 focuses on the development of an aeroelastic framework of insect flight and the integration of the aerodynamic models within the FEM based structural solver as well as the overall computation process,
- Chapter 4 investigates, through several numerical studies, the performance of the aeroelastic framework and delivers computational and practical guidelines for designers,
- Chapter 5 exhibits the validation of the framework using experimental data, acquired on a dedicated test bench with a tailor-made methodology for high-frequency resonant wings under large deflection, and discusses several points aimed at improving the framework accuracy,
- Chapter 6 demonstrates the capabilities of using the aeroelastic framework at the preliminary design stage of a FWNAV with applications on the OVMI case.

At last, the dissertation is concluded by stating the main achievements of this work and by providing recommendations for future studies.

Chapter 1

State of the art and literature review

Contents

As explained UAVs are deployed, nowadays, worldwide to accomplish a broad variety of missions both in military and civilian applications. As initiated by the DARPA, the trends is to deliver smaller and smaller vehicles fulfilling technological and application niches as depicted by the launch of the MAV projects quickly followed by the NAV initiative. There, the flapping-wing concept seems to be legitimate and appropriate to beat down the drastic requirement set by the DARPA as nature provides thousands of successful examples. However the development of such vehicles is not straightforward and faces a series of challenges, the main ones being the insect flight and its reverse engineering towards airborne FWNAVs, which is the aim, to some extents, of the preliminary design tool envisioned in this work.

Before heading straight to its development, it is essential to put this work into context and foremost review the past and current research works on FWNAV so as to draw a proper course for this work.

1.1 Flapping-wing for nano air vehicles

With the requirements of UAVs shifting gradually to a hover capability, an increased maneuverability for more and more constrained areas such as indoor and urban environment, and a decreased overall size, to

comply with the dimension requirement of the MAV (max. $15cm$) or NAV (max. $7.5cm$) categories, nature is an obvious source of inspiration for designers as birds and insects are typically falling within this range as highlighted by the figure 1.1.

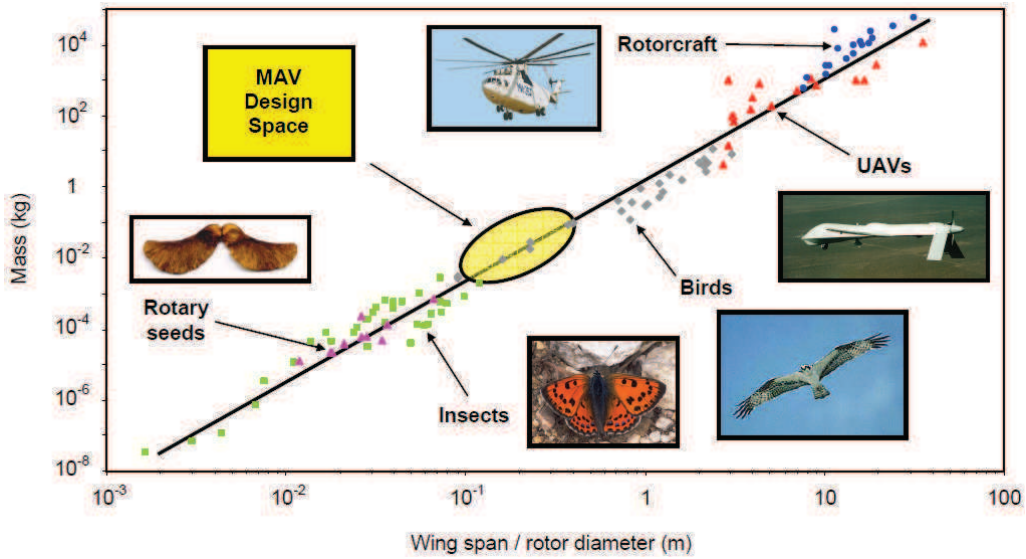

Figure 1.1: Size of various flying objects (Source: Singh [2006]).

Therefore flapping-wing concepts are considered for meeting the MAV and NAV specifications while competing also with the more traditional fixed- and rotary-wing concepts in this challenge.

1.1.1 Flapping-wing vs fixed-/rotary-wing

Current MAVs/NAVs are based either on fixed-, rotary-, or flapping-wing concepts. While fixed- and rotary-wing systems benefit from more than a century of continuous understanding, development, and most of all of off-the-shelf technology, flapping-wing systems are fundamentally different, lacking well-established know-how and are just at the beginning of their era.

1.1.1.1 Fixed wing system

Due to the decoupling between the thrust and lift generating systems and its simplicity, fixed wing system has been chosen at first (Grasmeyer and Keennon [2001]; Wood et al. [2005]; Zufferey et al. [2006]; Kovac et al. [2007]) for MAV applications. They benefit also from relative simple flight control and available framework for the optimization of their performance. By definition, fixed wing designs are incapable of hovering flight and suffer thus from a limited maneuverability in confined space, where good low-speed performance is essential. To minimize these disadvantages, novel approaches are currently being developed with vehicles capable of flexible wing (Ifju et al. [2002]; Johnson et al. [2007]), morphing wing (Abdulrahim et al. [2004]), transition flight (Moschetta et al. [2008]; Green and Oh [2009]; Carr et al. [2010]). Some examples of fixed wing MAVs or slightly larger systems are depicted in the figure 1.2.

However no true fixed-wing NAV has been, to our knowledge, yet developed. The need for more hover- and indoor-capable systems has triggered instead the development of rotary-wing systems.

1.1.1.2 Rotary-wing systems

Inspired by the larger UAVs available, current rotary-wing MAVs/NAVs are based on a multi-rotor approach (Kroo et al. [2001]; Bitcraze AB [2012]; KMel Robotics LLC [2012]), on a contra-rotating

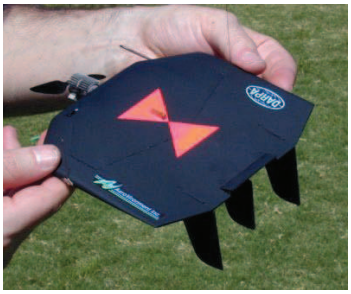

(a) *AV* Black Widow

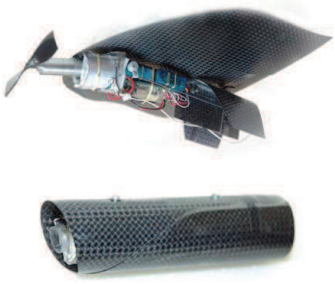

(b) Bendable-wing endurance MAV

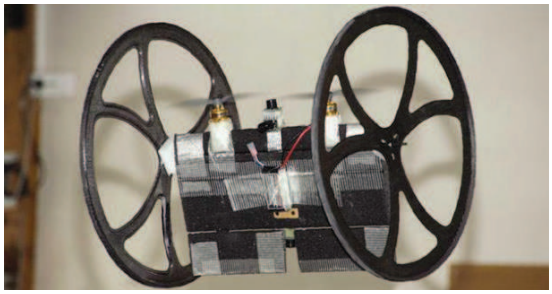

(c) MAVion Roll & Fly

Figure 1.2: Examples of fixed wing MAVs, taken from Grasmeyer and Keennon [2001], Johnson et al. [2007] and Baritou [2013] respectively. The *AV* Black Widow is a 15.2cm wingspan MAV able to fly for 30min and weighting 80g offering first-person view (FPV) capability to the operator. The bendable-wing endurance MAV highlights the potential of such MAVs to be stored in a minimal volume while released and made operational quickly. The reported prototype with a wingspan of 15.25cm and a length of 14.0cm fits within a cylindrical container measuring 2.54cm in diameter and 11.4cm in length and fly autonomously over 15min while sending video feedback. The MAVion Roll & Fly is an hybrid MAV with a 36cm wingspan and 100g payload able to flight for 30min offering a hover capability and a compatibility with indoor operations through the wheels that protect the propellers and enable rolling on walls.

coaxial-rotor approach (Bohorquez et al. [2003]; Muren [2005]; Samuel et al. [2005]; Roussel et al. [2012]) and on the traditional combination of a main and a tail rotors (Prox Dynamics [2013]). Some rotary-wing systems are even exploring novel approaches based on MEMS technologies (Miki and Shimoyama [2000]; Chabak [2008]) to reduce drastically the characteristic size. Unlike the fixed wing systems, rotary-wing systems have proof to match both the MAV and the NAV requirements but MAV systems are mostly preferred due to an higher payload capacity. Some examples of rotary-wing MAVs and NAVs are depicted in the figures 1.3 and 1.4.

As mentioned relatively few rotary-wing systems are currently able to fly while offering any operational sensor. Their performance at low scale are poor due to the hover efficiency, also known as the Figure of Merit, decreasing from 0.7-0.8 for full-scale rotors to 0.45-0.55 for existing rotary-wing MAVs (Leishman [2006]; Pines and Bohorquez [2006]; Ramasamy et al. [2008]). Those are the consequences of low Reynolds number (Re)[1] and higher relative viscous effects which produce long laminar separation bubbles on the blades, thicker boundary layers, and the possibilities of flow separation at relatively low angles of attack. These flow characteristics result in low values of maximum lift coefficient and lower overall values of lift-to-drag ratio: all of which substantially decrease the overall operating efficiency of the rotor system (Pines and Bohorquez [2006]; Ramasamy et al. [2008]). Additionally, the induced power[2] is relatively higher and combined with higher rotational and turbulent losses in the wakes downstream of the rotating blades (Ramasamy et al. [2008]). Furthermore, the power requirements of MAV-scale rotors are also generally higher due to a higher wing loading (Lasek et al. [2006]; Pines and Bohorquez [2006]; Ramasamy et al. [2008]) which reduces the maneuverability. Finally, the noise signature of both fixed and rotary-wing systems is quite significant due to the single actuation frequency of their propellers or rotors and a quieter solution might be an advantageous feature for indoor operations.

[1] The Reynolds number is a dimensionless number defined as the ratio of inertial forces to viscous forces and is computed as $Re = \frac{vL}{\nu}$ where v is the mean velocity of the object relative to the fluid, ν is the dynamic viscosity of the fluid and L is a characteristic linear dimension usually the chord for wing.

[2] The induced power is the power required to maintain enough lift to overcome the force of gravity.

(a) CrazyFlie (b) Black Hornet (c) GLMAV

Figure 1.3: Examples of rotary-wing NAVs, taken from Bitcraze AB [2012], Prox Dynamics [2013] and Roussel et al. [2012] respectively. The CrazyFlie is a $19g$ quadcopter flying up to $7min$ with a 5-$10g$ payload and about $90mm$ from motor to motor which is available as an opensource development platform offering eventually FPV capability. The Black Hornet is a $16g$ helicopter with a $120mm$ diameter rotor flying up to $25min$ at a maximum speed of $10m.s^{-1}$ that is currently in service within international units featuring FPV and GPS navigation. The GLMAV (Gun Launched MAV) is a $250mm$ contra-rotating coaxial rotor in development offering GPS navigation and real-time observations, currently weighting $1.1kg$, that will be launched as a subsonic projectile from a dedicated tube and deployed once over the target maximizing its use on site.

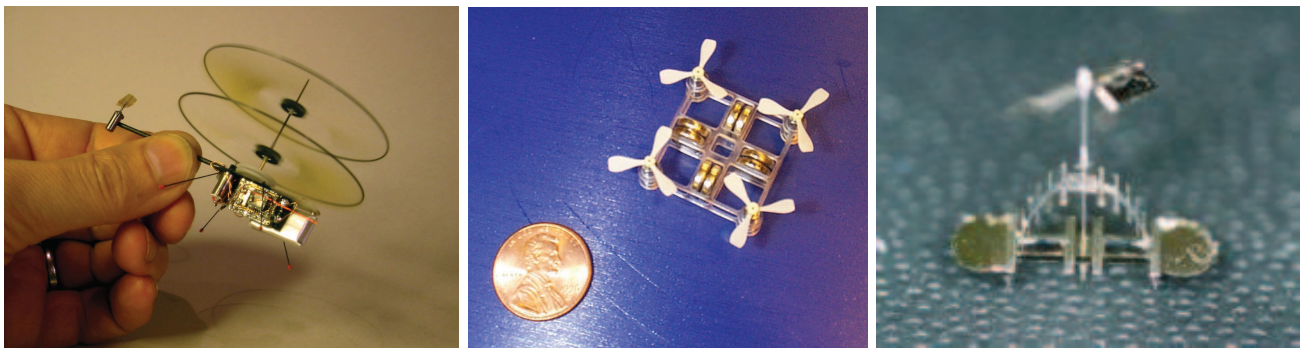

(a) Picoflyer (b) Mesicopter (c) Microflight Mechanism

Figure 1.4: Examples of rotary-wing NAVs, taken from Kroo et al. [2001], Muren [2005] and Miki and Shimoyama [2000] respectively. The Picoflyer is the world's smallest RC helicopter, weighting only $3.3g$ and flying for $30s$ in continue, based on two $60mm$ diameter contra-rotating coaxial-rotors. Although being passively stable, it requires an experienced pilot for operations and is not fitted with any sensors. The Mesicopter is $3g$ quadrotor NAV launched as a feasibility study for very small-scale rotorcraft. Using $1.5cm$ diameter rotors and an external power source, the prototype exhibits a hover capability when constrained to a test bench. However it can not sustain real flight as the battery are too heavy and control electronics are missing. The Microflight Mechanism is composed of a $2.5mm$ diameter magnetic rotor weighting $3.5mg$. The prototype has succeeded in flying under an alternating magnetic field.

Even if the best NAV strategy is still under discussion (Liu and Moschetta [2009]; Lentink et al. [2010]), unconventional design strategies are mandatory for the design of an efficient hover-capable and quiet NAV such as flapping-wing systems.

1.1.1.3 Flapping-wing systems

Bird and insect, as exceptional flyers at small scale and low Re, are an obvious source of inspiration for researchers interested in the design of flapping-wing MAV (FWMAV) or NAV (FWNAV). Biological flappers differ from conventional propulsion solution with a constantly accelerating and decelerating airfoil.

In one hand, bird-like flapping, named ornithopter, uses in regular flight a nearly vertical flapping plane with small change in the wing pitch during a flapping cycle. The propulsion is primarily due to the wing flapping, while lift is generated by a combination of forward speed and wing flapping. Therefore ornithopter-based FWMAVs (Jones et al. [2001]; Pornsin-Sirirak et al. [2001]; Gerdes et al. [2012]; Tan et al. [2012] lacks intrinsically the hover capability.

On the other hand, insect-like flapping uses a nearly horizontal flapping-wing with relative large changes in the wing pitch to produce sufficient lift even in hovering. Propulsion is achieved by tilting forward or backward the flapping plane while high maneuverability is performed by slightly breaking the wing symmetry in their flapping cycle. Hummingbird also hovers by adopting a wing motion similar to the insect. Various engineering studies and researches are currently being done to develop viable bio-inspired devices fulfilling the MAV requirements in terms of dimensions and operations (Luc-Bouhali [2006]; de Croon et al. [2009]; Bolsman et al. [2009]; Gerdes et al. [2012]; Keennon [2012]; Nagai et al. [2012]; Tan et al. [2012]) or NAV (Steltz et al. [2007]; Wood [2007a]; Dargent et al. [2009]; Coleman [2009]; Chi et al. [2011]; Meng et al. [2011]). Some examples of insect-like flapping-wing MAVs and NAVs are depicted in the figure 1.5 and 1.6 respectively.

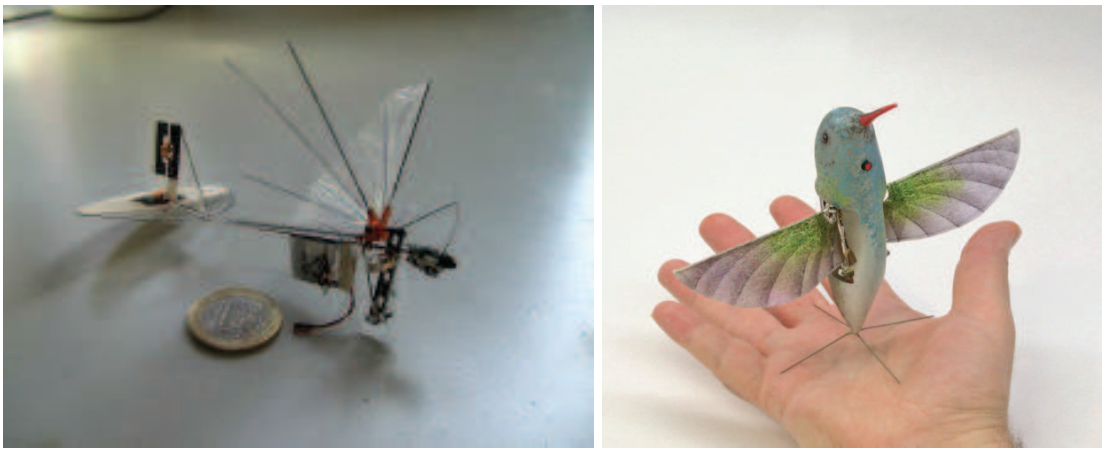

(a) DelFly Micro (b) *AV* Hummingbird

Figure 1.5: Examples of insect-like FWMAV, taken from de Croon et al. [2009] and Keennon [2012] respectively. The DelFly Micro is a $3.07g$ and $10cm$ ornithopter able to fly for $3min$ with video transmission. Larger version exists offering higher performance and broader field of applications. The *AV* Hummingbird is a $19g$ and $16.5cm$ MAV able to fly 4-$11min$ with video transmission exhibiting impressive agility both in indoor and in outdoor flight with light wind.

When compared to FWMAV, FWNAVs are facing a major issue as their GTW is even more limited which directly bounds the energy supply as well as the electronics, for sensing and controlling, available on

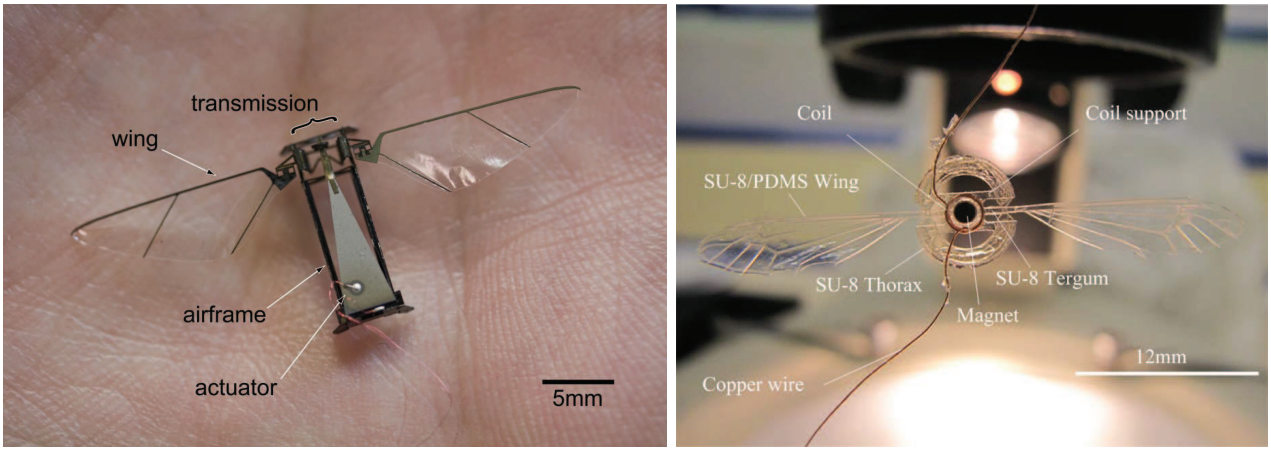

(a) Robobee (b) OVMI

Figure 1.6: Examples of insect-like FWNAV. The Robobee is a $60mg$ and $3cm$ NAV able to fly when run on an external power source even if the flight is quite unstable[3](Wood [2007b]; Wood et al. [2012]). However a new version has been demonstrated recently[4]showing impressive maneuverability but with each wing having its own actuation and relying on external flight control and power. The OVMI is a $22mg$ and $3.5cm$ NAV not yet able to fly which is introduced more extensively in the section 1.1.3.

board. Thus any design choice is significant as it might impact the overall system efficiency and viability. For example, the actuation choice has a direct consequence on the weight, due to the numbers of links and electronics implied by this choice, and on the overall efficiency, as any system induces its own energy losses. Thus a FWNAV has to be inherently efficient in terms of energy, weight and aerodynamic forces.

Another issue with a FWNAV is the design of its wings so that, when actuated, the appropriate aerodynamic forces are generated enabling its flight. Given the very broad design space outlined by nature, partially shown in the figure 1.7, the task might be quite challenging and time-consuming in absence of know-how before finding the proper wing geometry matching the FWNAV requirements.

These issues are especially relevant for insect-like FWNAVs which are, in this work, under focus. However the success of the Robobee credits the feasibility of insect-like FWNAV and paves the way for other designs. Two distinct categories of FWMAVs/FWNAVS are currently emerging: the one driving the wing to its desired motion through a transmission system and the other relying on the wing resonance to generate the appropriate motion. Both approaches have their pros and cons. Unless otherwise stated, the term flapping-wing (FW) will now always refer to the insect-like flapping-wing.

1.1.2 Wing resonant and non-resonant flapping-wing systems

When reviewing the choices made by nature in terms of wing actuation, two configurations appear for insect flight: the direct and the indirect actuation as depicted in the figure 1.8.

Given the simplicity of the direct actuation from an engineering point of view, designer of FW-MAVs have mainly chosen this approach as highlighted by the *AV* Hummingbird. Constrained by the very limited GTW of FWNAVs, the indirect actuation is more attractive as it reduces naturally the inertial cost of wing movement due to its continuous acceleration and deceleration. From this observation, two

[3] http://youtu.be/GgR-mH6X5VU
[4] http://youtu.be/b9FDkJZCMuE

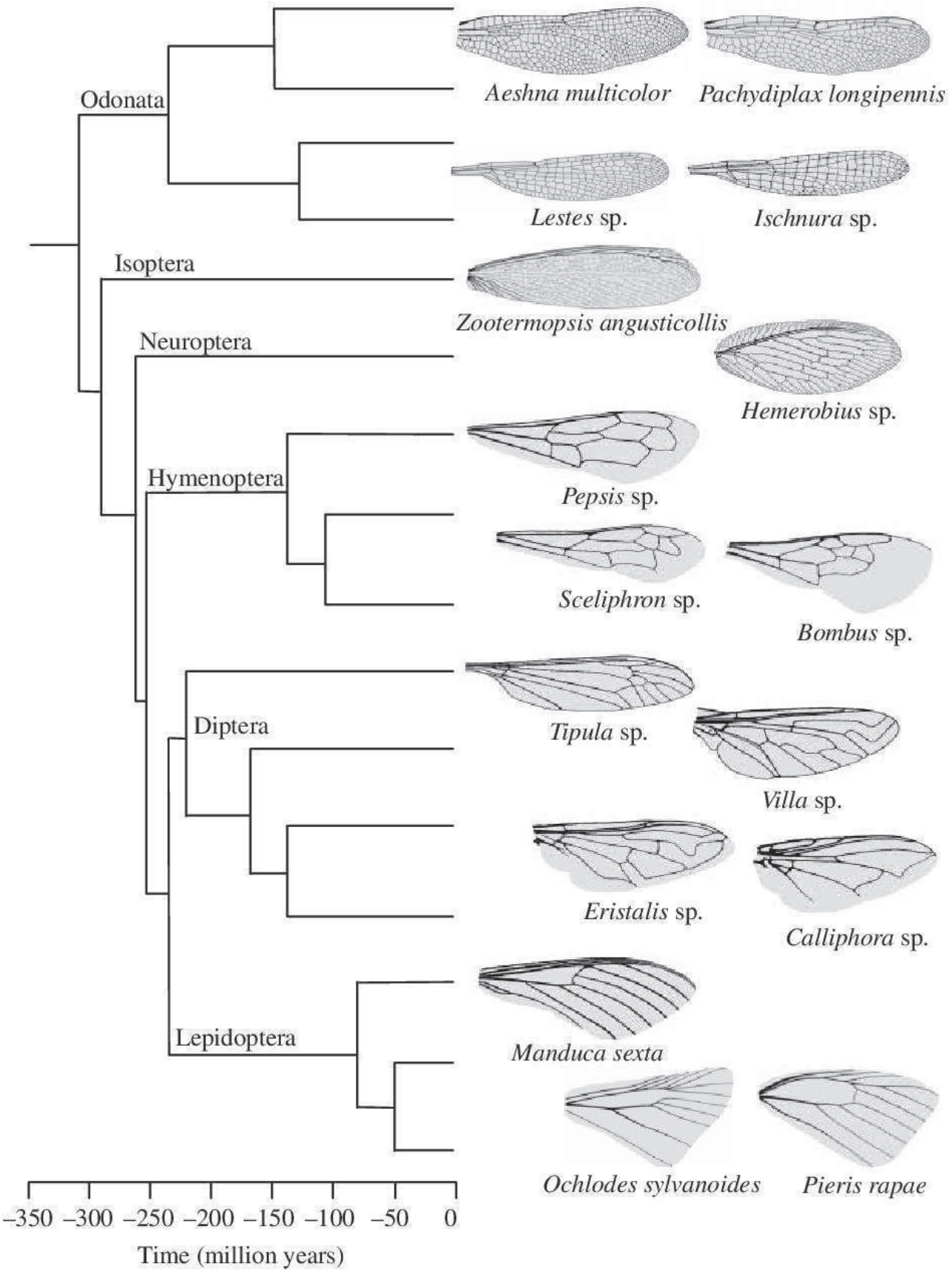

Figure 1.7: Various wing design achieved by nature throughout the years (Source: Combes and Daniel [2003b]). The wing span tends to decrease over time and refinement of the insect flight which is not coherent with classical airplane aerodynamics which would favor slender and longer wing.

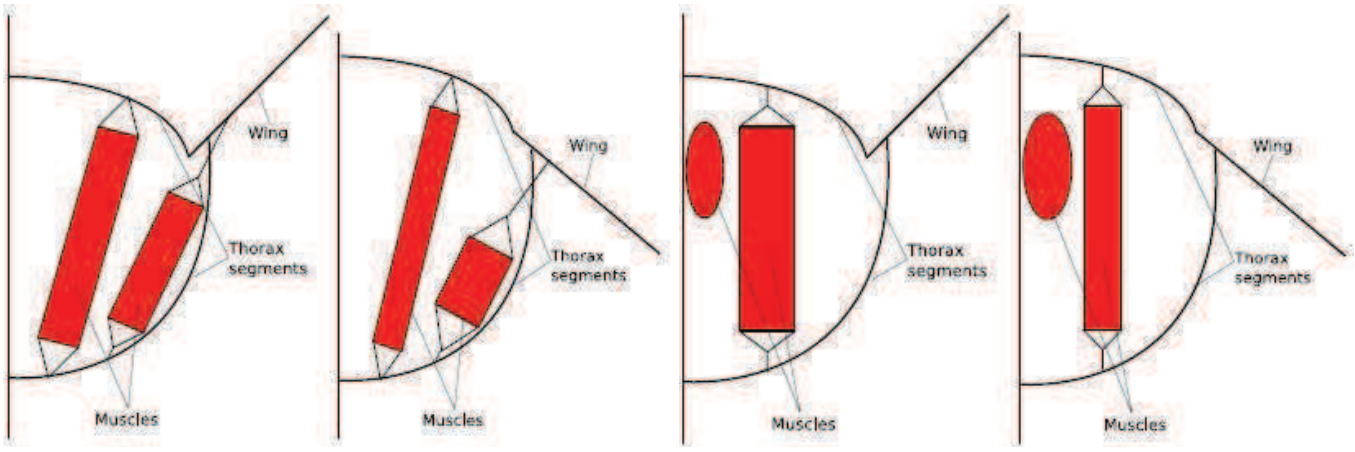

(a) Direct actuation (b) Indirect actuation

Figure 1.8: Schematic representation of the cross-section of the two main insect thorax types. With the direct actuation, the muscles are connected directly to the wing and controlled on a wingbeat-to-wingbeat basis. With the indirect actuation, the muscles are connected directly to the thorax and controlled to maintain its resonance while driving passively the wing motion (Source: Bolsman et al. [2007]).

consequences for the sizing of FWNAV can be drawn. First, the actuator can be sized for a smaller duty cycle saving thus some weight. Second, the power consumption might also be reduced given that the system has just to maintain its resonance which requires much less energy than continuously actuating a wing. Therefore almost all FWNAVs, developed until now, are inspired by this indirect actuation and are using a resonant thorax or a similar concept.

However, as it will be described in the section 1.2.1, the insect flight requires large wing stroke, especially when hovering, but also a specific kinematics pattern based on a combination of wing translation and rotation. Given the limited number of actuation solution compatible with the NAV requirements, both in term of size and of power density, the actuator motion (linear or rotational) has to be amplified in somehow to generate the appropriate wing motion. To generate this motion and as mentioned earlier, two categories of FWNAVs are emerging: the one driving the wing to its desired motion through a transmission system, referred to non-resonant wing system, and the other relying on the wing resonance, referred to resonant wing system.

The first category amplifies the actuator motion through a transmission system, typically transforming a small linear actuator actuation to a large rotation of the wing root (Luc-Bouhali [2006]; Steltz et al. [2007]; Wood [2007b]; Bolsman et al. [2009]; Meng et al. [2011]; Keennon [2012]). This approach is the simplest engineering solution for the wing kinematics problematic and has proved to be quite successful with the Robobee (Wood [2007b]; Wood et al. [2012]). However the design and fabrication of the link requires special attention in order to generate the proper amplification and motion while minimizing the energy-loss and the risk of jamming. In addition to that, the aerodynamic damping are with such system accounted mainly as losses even if some saving can be made using flexible wing, as it will be outlined later.

The second category uses the resonance of the wing so that the mode shape once actuated generates the appropriate kinematics (Dargent et al. [2009]; Chi et al. [2011]; Nagai et al. [2012]). Thanks to the resonance phenomenon, the small actuation amplitude at the root is amplified naturally and generates high amplitude bending and twisting of the wing. Thus no transmission system is needed which simplifies the design of such FWNAV and also increases implicitly the robustness of the overall system and suppresses the associated energy losses. Furthermore by using resonant wing, the energy losses are minimized from the actuation to the wing tip as the aerodynamic damping is part of the resonance phenomenon enabling

bigger savings when compared to the other approach. This approach has proved to be quite successful as demonstrated by the FWMAV developed by Nagai et al. [2012] that flies. However the design of the mode shape is a pretty challenging task as it requires a fine distribution of the rigidity and density of the wing which is *a priori* unknown. Unfortunately from a design and engineering points of view, this approach is slightly more complex and not so intuitive when compared to the first one, but the game might be worth it.

The OVMI project, initiated in Dargent et al. [2009] and backed by the IEMN, belongs to the second category. The purpose of this work being to assist the design of the OVMI, its specifications and highlights are now presented.

1.1.3 Presentation of OVMI

The main motive of the OVMI (French for Flying Object Mimicking the Insect) is to design a robust, autonomous and efficient FWNAV relying on MEMS technologies and on resonant actuation with a minimum of links and actuators.

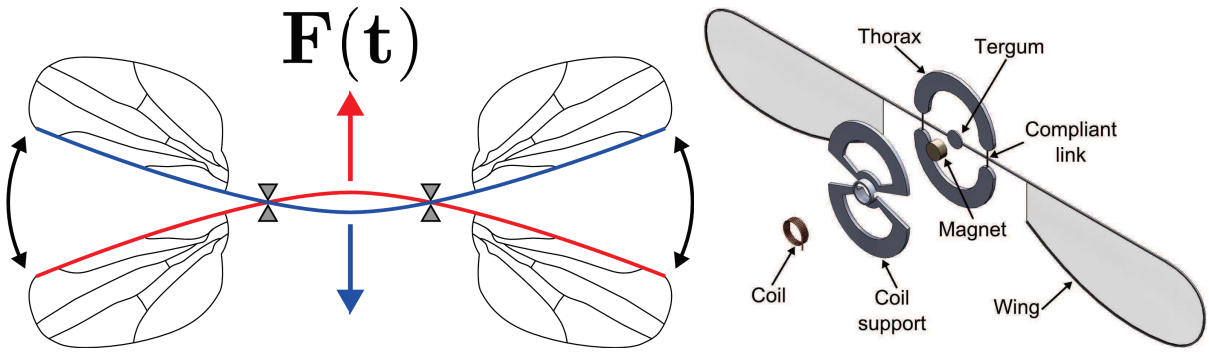

(a) Active bending and passive twisting actuation concept.

(b) CAD view of the TWT structure embedded on the OVMI

Figure 1.9: Actuation concept of the OVMI taking shape into the bio-inspired TWT-structure. Bending is actively sought unlike the twisting which is expected through the off-center masses.

To do so, the OVMI uses the wing resonant actuation concept in combination with a resonant-like thorax. Indeed one of its notable feature is that the tergum and the wing are forming just one piece, as illustrated in the figure 1.9(b), rotating at resonance around two nodes serving as rotation axis as depicted by the figure 1.9(a). The mode shape is tuned so as to obtain a spanwise active bending, through the leading-edge, and a chordwise passive twisting, due to the wing masses off the leading-edge. This mode shape has proved to be quite similar to the flapping motion of insect (Dargent et al. [2009]). With such an actuation concept, the actuator has just to initiate and maintain the resonance, synonymous of an increase of the overall efficiency. Furthermore forced oscillations keep the wing kinematics safe through any slight disturbances which might be quite helpful when flying.

The tergum-wing-thorax (TWT) structure, illustrated in figure 1.9(b), materializes this concept. An actuator, here the magnet, is positioned on the tergum which crosses the thorax, here the two horseshoe arches bonded to the coil support, using a compliant link to actuate the wing (Bontemps et al. [2013]). Using these nodes as a rotation axis, a flapping actuation of the wing is made possible without interfering with the resonant state of the tergum and of the wing. Given the reduced number of parts at stake, the overall robustness of the OVMI is increased, limiting the risk of failure or jamming, while reducing dramatically the source of energy losses (Bontemps et al. [2013]). Among the other advantages of the compliant link are also an ease of fabrication and of assembly. To actuate the wing, an electromagnet is currently used due to its availability and practicability. However electroactive polymer is also envisioned (Khaldi et al. [2011])

which will strongly reduce the weight of the OVMI and simplify further its design.

Great progress in MEMS micromachining has enabled the development of complex micro-structures for various applications with the necessary reliability, repeatability and size control to carry out biomimetic structures such as the OVMI (Bao et al. [2011b]; Bao and Cattan [2011]) or other FWNAVs (Tanaka et al. [2007, 2008]; Tanaka and Wood [2010]). Thus, the choice of the appropriate material and fabrication techniques was made among the one commonly available in MEMS. More details about the material choice and the fabrication of the OVMI are given in appendix A. To sum up, the epoxy-based negative photoresist resin SU-8 is used preferentially given its good agreement with insect wing structural performance and its compatibility with spin-coating and lithography techniques. Thus the OVMI might be fabricated easily and a typical prototype assembly is shown in the figure 1.10.

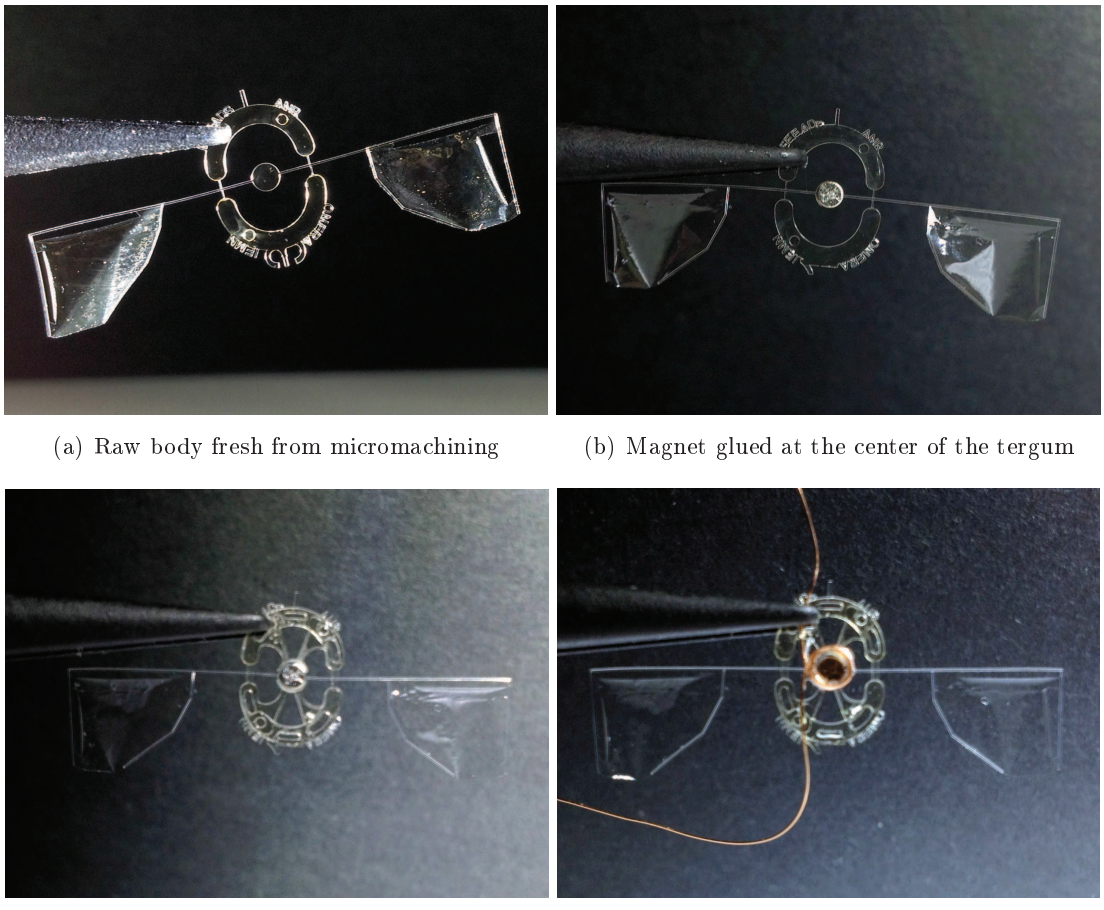

(a) Raw body fresh from micromachining

(b) Magnet glued at the center of the tergum

(c) A coil support is added stiffening the thorax and enabling a precise positionning of the coil

(d) Fixation of the coil on its support

Figure 1.10: Assembly procedure of an OVMI prototype in 4 steps using a simple binocular and some glue. The assembly process is thus quite simple and a prototype is rapidly assembled and tested.

The current prototype OVMI weights $22mg$ and flaps at about $30Hz$, but higher actuation frequencies are actively sought. Even if unable to fly yet, the OVMI performance are rather encouraging in terms of wing kinematics and of lift generation (see the appendix C.4.1). However a stronger understanding of the phenomena on its wing is mandatory to accelerate its development and get it airborne at first and optimize its performance at second. This is what drives this work: developing a numerical model able to assist engineers and scientists in sizing their FWNAVs at the preliminary design stage. But before developing such a design tool, a good understanding of the insect flight specificity is mandatory.

1.2 Understanding the insect flight

Through thousand years of evolution and adaptation, flying insects have developed and perfected their flight enabling amazing flight capabilities, agility and maneuverability yet unbeaten at their scale. The success of their flight is mainly due to two key features unseen in other flying creatures or machines, except for the hummingbird, the wing kinematics and its induced aerodynamic forces.

1.2.1 Insect wing kinematics

With the advances in high speed photography, the description of the wing kinematics has taken a big step forward and is now relatively good described (Weis-Fogh [1973]; Ellington [1984c]; Ennos [1989]). It is, today, even more precise with the availability of high speed camera providing close and continuous insight of the wing kinematics. Flying insects can be broadly divided among two categories either the one having one pair of wings (fly, bee, etc.) or the one having two (locust, dragonfly, etc.). The OVMI and most FWNAVs being inspired by the former, only the kinematics of the former group is here described. Typical flapping frequencies for those insects are in the range of 5-500Hz (Dudley [2002]) with the frequency decreasing with increasing insect size and weight (Ellington [1999]).

The overall wing motion is a periodic cycle seen as a combination of four basic motions: the downstroke, the supination, the upstroke, and finally the pronation. As illustrated in the figure 1.11, the half-strokes (down or upstroke) are primarily translational motions along the stroke plane, unlike the pronation/supination which are rotational motions along the pitch axis. During a half-stroke, the wing accelerates to an almost constant velocity around the first half of the half-stroke, before slowing down to rest for the second half. The wing reversal follows with the wing rapidly rotating, reversing direction and preparing the next half-stroke. Typical stroke lengths are of the order of 3-5 wing chords. Also, the wing pitch i.e. the angle of attack (AOA) changes continuously within a half-stroke and along the chord, increasing gradually, to achieve on average about 35 $^\circ$ at 70%-span (Ansari et al. [2006c]). During a flapping wing cycle, the wing tip describes a banana-like or a figure-eight motion in the stroke plane, as shown in the figure 1.11.

By tilting this stroke plane back or forth and by shifting slightly the symmetry between its half-strokes, the insect can thus fly forward, backward or stationary. For example at the hovering station, most insects use a horizontal stroke plane along with symmetrical half-strokes. On forward flight, the stroke plane is tilted forward and the half-stroke symmetry is broken off in favor of a longer downstroke as the generation of a lift is more efficient due to the free-stream velocity which penalizes consequently the upstroke motion. To maneuver gently, the insect modifies the symmetry between its wing motion with for example larger amplitude on the right wing for a left turn, like in kayaking.

Thanks to the high flapping frequency at stake, the various changes on the wing motion and stroke plane are almost instantaneous, explaining therefore a good part of the impressive capabilities of the insect flight, the other being its aerodynamic phenomena.

1.2.2 Aerodynamic phenomena

The aerodynamics of insect flight is now for almost 80 years a field of intense scientific researches towards its understanding. The associated flow is incompressible, laminar, unsteady, and occurring at low Re. For large insects, Re, based on the wing tip velocity and its chord, lies between 5000 and 10 000, but approaches 10 for the smallest ones. It means that the viscous effects are, here, becoming more important as size decreases leading to diverse unusual and unexpected aerodynamic phenomena.

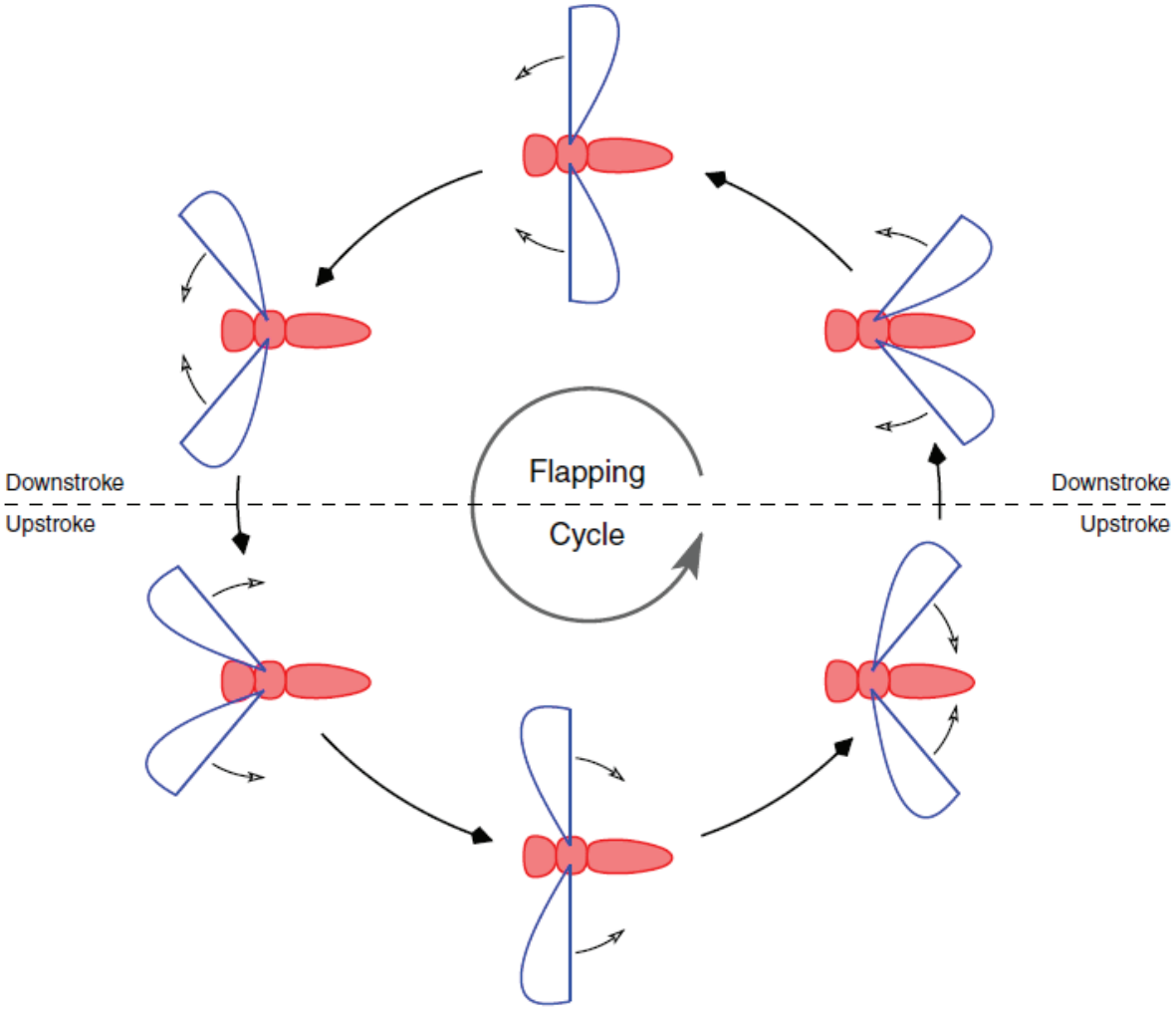

(a) Insect flapping cycle from top view

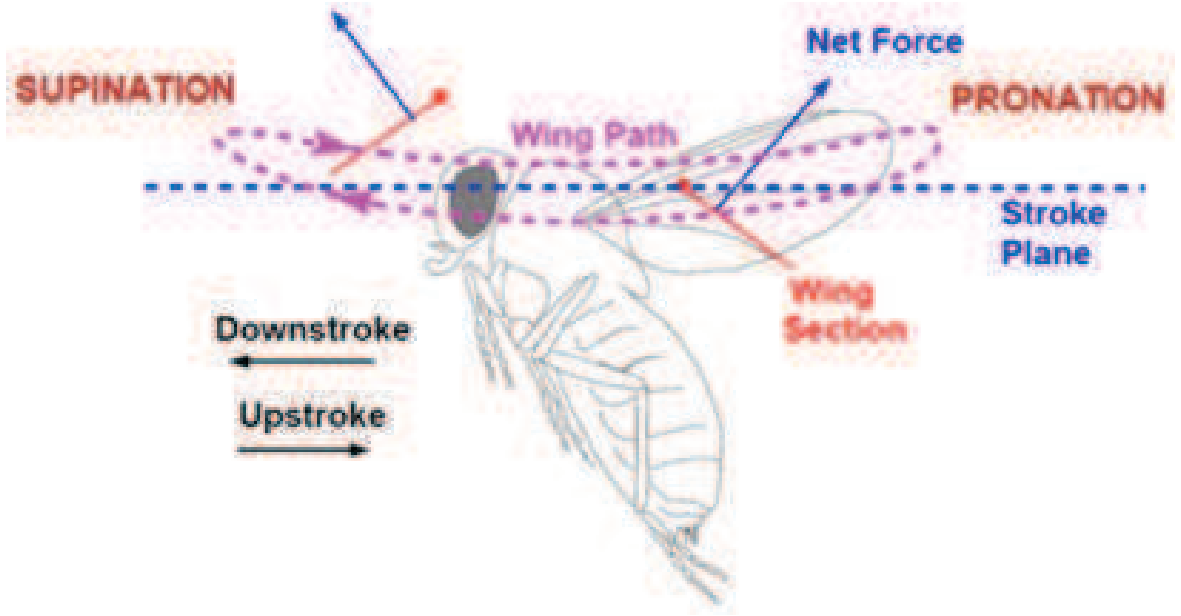

(b) Insect flapping cycle from side view

Figure 1.11: Typical insect wing kinematics taken from Ansari et al. [2006c] and Seshadri et al. [2012] with the leading-edge, the thick line in 1.11(a) and the thick dot in 1.11(b) always leading. The accurate timing of each wing movement is the key to the amazing flight capabilities of insects.

Indeed as seen in the figure 1.7, the wing span of insects tends to decrease over time, which might be interpreted, in terms of evolution, as an optimization of their flight. This is not coherent with the classical aerodynamics experienced on aircraft or helicopter where large wingspan are actively sought to minimize the overall power. In addition to that, insect wings operate at relatively large AOA which is again contrary to the traditional aerodynamics where the AOA of the wing is usually below 15 ° to avoid stall behavior. However from an energetic point of view, the insect wing performs better, at their scale, than a wing flapped at 10 ° even if the lift-to-drag ratio tends to decrease with the Re.

With progress in flow visualization and with the help of computational fluid dynamics, various flight mechanisms have been identified and brought up to understand the insect flight and justify its physicality. The leading-edge vortex (LEV) is one of them being responsible for the improved performance of the wing at large AOA. Only the most relevant flow characteristics are here further discussed so as to provide a clear picture of the phenomena involved. Comprehensive reviews of various aerodynamic phenomena, included those described below, are available in Mueller [2001],Sane [2003],Wang [2005] and Ansari et al. [2006c].

The aerodynamic phenomena described below are the main ones occurring during a 'typical' stroke and are presented according to their onset in the stroke.

1.2.2.1 Wagner effect

An emblematic feature of the insect flapping cycle is the continuous acceleration, deceleration and reversal of its wing. Each time a wing starts from rest, the circulation around it does not immediately reached its steady-state value, but rises slowly towards it. This effect, called the Wagner effect, takes shape through the shedding of starting vortices from the trailing-edge. These vortices are of opposite sense to the bound circulation of the wing and are thus delaying its steady-state, until they are shed sufficiently far. This effect comes into play whenever an inclined wing starts from rest or also when its AOA increases suddenly. A similar phenomena happens also when the wing is decelerating and stopping vortices are shed then from the trailing edge, delaying the lift drop before stroke reversal but emphasizing the next Wagner effect.

1.2.2.2 Wing-wake interaction

With the periodic motion used by insects and its relatively high frequency, the fluid surrounding the insect can no longer be considered quiescent, especially at hovering or at low-speed flight. As a consequence, the wing interacts with its own wake. Vortices shed from previous stroke, but still in the close vicinity of the wing, are sources of potential lift enhancement and energy recovery sources for the insect, particularly around the wing reversal. Ansari et al. [2006c] propose a scheme of wing-wake interaction at wing reversal, where stopping vortices and leading-edge vortices from the previous half-stroke as well as starting vortices of the new half-stroke are of wrong circulation sign for the new half-stroke and thus increasing the overall lift, as depicted in the figure 1.12.

This scheme was also corroborated with experiments on the OVMI prototype (Vanneste et al. [2011b]).

1.2.2.3 Added-mass effects

As explained before, a representative characteristic of insect flight is the continuous acceleration and deceleration of its wing. As it accelerates or decelerates, the neighboring fluid has also to be accelerated or decelerated like an additional mass generating an inertial aerodynamic force. Thus a reaction force opposed to the wing motion is induced. Typically when the wing is accelerating, the fluid in front is preventing the motion of the wing pushing it backward generating forces that are locally perpendicular to the airfoil surface. Similarly when the wing is decelerating, the fluid behind is pushing the wing forward creating also an additional perpendicular forces.

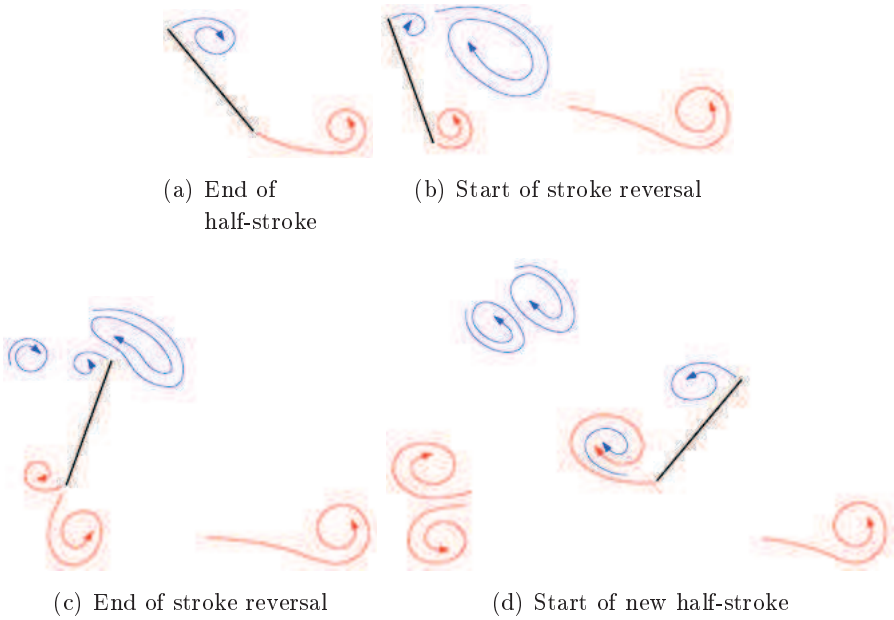

(a) End of half-stroke (b) Start of stroke reversal

(c) End of stroke reversal (d) Start of new half-stroke

Figure 1.12: Typical wake generated by an insect-like flapping wing in the hover taken from Ansari et al. [2006c]. Vortices from the leading-edge are shown in blue while those from the trailing-edge are in red.

In incompressible and irrotational fluid, the variations of the fluid energy due to the acceleration are instantaneous. Therefore the added-mass forces are said to be proportional to the instantaneous acceleration without any delay effect as the phenomena is free of any vortex shedding.

1.2.2.4 Leading-edge vortex

With the high AOA achieved by insects, the flow tends to separate from the leading-edge and reattach upstream of the trailing-edge. In the separation zone, a leading-edge vortex (LEV) is formed thus smoothing the high AOA and enabling the fluid to reattach smoothly. The LEV is thus preventing stall as well as increasing the lift through a suction effect. Topologically speaking, the LEV starts close to the root and spirals towards the tip, which is under-pressured due to the higher velocity. There it coalesces with the tip vortex and converts into the wake, as depicted in the figure 1.13.

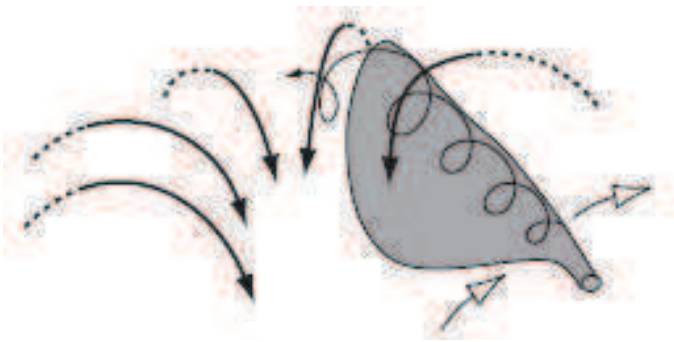

Figure 1.13: Structure of the LEV as proposed by Sane [2003].

The LEV remains attached for most of the half-stroke and is shed away only when the stroke reversal occured, as it was already outlined by the figure 1.12 of Ansari et al. [2006c]. The exact mechanism governing its stability is still under discussion but involves spanwise flows, downwash from the tip vortices as well as a dependency to the Re for its spiralling nature (Ellington et al. [1996]; Willmott et al. [1997]; van den

Berg and Ellington [1997a,b]; Birch and Dickinson [2001]; Birch et al. [2004]; Wilkins [2008]; Lentink and Dickinson [2009]). Nevertheless the presence of LEVs for a wide range of kinematics, wing configurations, and Re, has led to the hypothesis that the LEV is the main unsteady mechanism in flying insects.

1.2.2.5 Kramer effect

At the end of each half-stroke, the wing rotates rapidly upward around its spanwise axis, while at the same time translating farther. As a result, the flow deviates from the Kutta condition at the trailing-edge bringing the stagnation region upstream. Due to its viscosity, the fluid tends to resist and additional circulation is generated in order to re-establish the Kutta condition. As this re-establishment is not instantaneous and as long as the wing continues to rotate rapidly, additional circulation is generated until the Kutta condition is met again. In other words, the wing generates a rotational circulation in the fluid to counteract the effects of wing rotation which, in return, affects positively the lift generation. Similarly and unfortunately at the beginning of each half-stroke, the wing rotates downward which pushes the stagnation region downstream affecting negatively the lift generation.

In a nutshell, the insect flight are due to two key features: the wing kinematics and its induced aerodynamics phenomena. When considering the development of a design tool for FWNAVs, these features, among others, have to be closely modeled, apprehended and tied together which is not without challenges.

1.2.3 Challenges facing the modeling of insect flight

To model properly the insect flight and its flapping, the phenomena induced by the wing stroke have to be rendered both in terms of structural and aerodynamic forces but also their interactions as they are interdependent. This raises several issues for the modelers.

1.2.3.1 Structural challenges

Flapping wings generate various forces as they move through air. Some of these forces are aerodynamic forces, due to the fluid surrounding the wing motion, while others are purely determined by their mechanical properties such as the inertial-elastic forces. All these forces bend and twist the wing during which, through passive shape changes, influence the flight performance (Combes and Daniel [2003b,c]). Furthermore due to the lack of muscles controlling the wing shape, these passive shape changes are primarily determined by the architecture of the wing (venation pattern, etc.) and its mechanical properties (mass, flexibility, etc.).

For example, some species have limited wing bending and twisting while others endure large bending and twisting during flapping as illustrated in the figure 1.14. Depending on the flapping frequency, those phenomena may be strongly emphasized and even more in the case of a resonant actuation, as for the OVMI.

Thus from a structural point of view, the challenge facing the modeling of insect flight is the handling of flexible structures in large deflection and also possibly in large deformation.

1.2.3.2 Aerodynamic challenges

Due to their wing motion, insects are capable of achieving high aerodynamic forces. As seen in the section 1.2.2, various unsteady mechanisms are present in the insect flight that are specific to low Re aerodynamics. Therefore from an aerodynamic point of view, the challenge facing the modeling of insect flight is to handle this unsteady and low Re aerodynamics within an unified and coherent model accounting for the most critical phenomena.

(a) Wasp (b) Moth

(c) Ichneumon (d) Click beetle

Figure 1.14: Wing deformation in various insect species (Copyright, Linden Gledhill at `http://www.flickr.com/photos/13084997@N03/sets/72157610450102014/`)

Also as highlighted by the figure 1.14, the shape of the wing might change dramatically within a stroke, in both the spanwise and the chordwise directions, and such wing shape alteration has to be taken into account by any candidate model.

1.2.3.3 Aeroelastic challenges

Various forces are generated in a flapping-wing system due to the continuous acceleration, deceleration and rotation of the wing resulting in dynamic shape changes of the wing throughout the stroke. From an aerodynamic point of view, the instantaneous shape of the wing determines the direction and magnitude of the aerodynamic forces. However from a structural point of view, the instantaneous shape is determined by the forces acting on the wing such as the aerodynamic forces but also the inertial forces. Both disciplines are thus interdependent and rise the question of the fluid-structure interaction and in particular of the fidelity level of the aeroelasticity coupling required when modeling a flapping sequence.

If the aerodynamic forces are preponderant, a high-fidelity coupling, i.e. implicit, is needed so as to find an equilibrium wing shape between the aerodynamic load and its structural response. This can be time-consuming and tricky as sub-iterations between the structural and aerodynamic solver are necessary to reach a converged shape. However, if the inertial forces dominate, a low-fidelity coupling, i.e. explicit, is sufficient and the aerodynamic forces are calculated using the structural response of the wing due primarily to the inertial forces. The uncertainty about the relative importance of aerodynamic to inertial forces in determining the dynamic wing shape is a concern (Combes and Daniel [2003a]; Tang et al. [2007]; Thiria and Godoy-Diana [2010]) and neither approach can be privileged *a priori* in the design from scratch of FWNAVs.

Therefore from an aeroelastic point of view, the challenge facing the modeling of insect flight is the appropriate handling of the wing shape determination and its structural response to aerodynamic forces as well as inertial-elastic forces.

The challenges faced by modelers to properly account and model the insect flight specificity are numerous especially from an aerodynamic and aeroelastic point of view. To choose the best options available for the FWNAV design tool envisioned in this work and to set its scope, a literature review is here mandatory before rushing into any development.

1.3 Literature review

Numerous studies have been undertaken by the scientific community to analyze several aspects of the insect-like flapping flight. Among the ones of interest for this work are any model dealing first, with the aerodynamic phenomena of insect flight, and second, with its aeroelasticity, either applied to the understanding of the insect-flight or to the design of a flapping-wing system. But prior to this inventory, a review of experimental works is essential as most of the above models are developed using or benchmarked against these experiments and also as the design tool considered in this thesis will have, at some point, to be validated. Such database needs to be comprehensively documented in terms of mechanical properties of the wings, of wing shape and of actuation kinematics to be exploitable for validation purposes. Finally, a bunch of design tools for flapping-wing systems are already operating and have to be scrutinized so as to set the best launch pad for this thesis.

1.3.1 Experiments on flapping-wing

The review of experiments made on flapping-wing is classified into two categories: the experiments made in a liquid medium and the ones in air. The former enables to acquire and visualize the aerodynamic phenomena at approximately the same Re as insect but at a lower flapping frequency than the latter at the cost of the inertial-elastic phenomena. Indeed the ratio of the fluid forces to the inertial forces is much

larger in water than in air enabling a direct measurement of unsteady hydrodynamic forces for a rigid wing. Nonetheless both experiments are complementary.

Only the experiments helping the modeling of aerodynamic or aeroelastic phenomena of insect-like flapping-wing or its benchmarking are here discussed. In another words, values of interest for validation purposes are either qualitative flow visualization, such as smoke flow visualization, or quantitative flow and force measurements, such as particle image velocimetry (PIV) or balance data, with precise data of the wing geometry and of its root actuation. Some experiments (Walker et al. [2009]; Young et al. [2009]) have been made on real insects to measure the instantaneous wing deformation in flight. However their applicability for validation purpose might be too specific and too cumbersome for a preliminary design tools and are therefore, here, not more lengthily discussed.

1.3.1.1 Experiments in a liquid medium

Various studies have been done in a liquid medium to investigate the flight phenomena of insects. However only a few might be used to validate an aerodynamic or aeroelastic model. They are summarized in the table 1.1 and a sample of them, extensively used by other researchers, is discussed below more lengthily.

Dickinson et al. [1999] design a robotic apparatus mimicking the fruit fly wing equipped at its root with a two-components force transducer measuring the vertical and horizontal forces. The wings are driven by stepper-motors allowing three-dimensional rotational motions about their root and are immersed in a tank of mineral oil, as depicted in the figure 1.15. The viscosity of the oil, the length of wing ($\sim 25cm$), and the flapping frequency of the model ($\sim 0.145Hz$) are chosen so as to match the Re typical of fruit fly ($Re \sim 136$). The polar curves of the wing, giving the lift C_L and the drag C_D coefficients versus the AOA α, are estimated and fitted by moving the wing through a 180 ° arc at constant velocity and fixed AOA including thus the LEV effect. Furthermore, the force histories for various actuation kinematics patterns, here tuning only the stroke and pitch angles, are measured in order to understand the effect of the wing reversal timing on the aerodynamic forces.

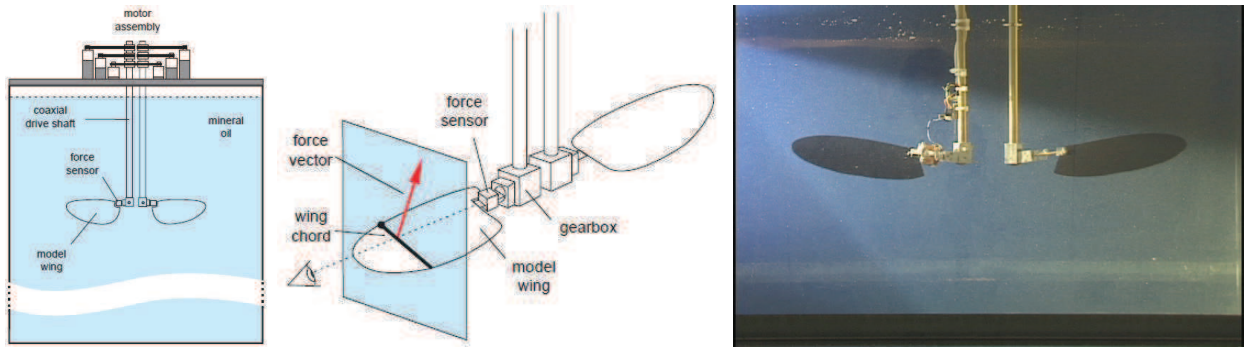

(a) Schematic overview of the apparatus (b) Schematic overview of the wings (c) Close-up view on the wings

Figure 1.15: Robofly apparatus used by Dickinson et al. [1999] to investigate the insect-flight mechanisms. (Source: Dickinson et al. [1999] and `http://www.berkeley.edu/news/media/releases/99legacy/robofly1.jpg`)

Sane and Dickinson [2001] pursue the investigations on more actuation kinematics patterns by using the additional third rotational motion of the apparatus. Parameters such as the stroke amplitude, the stroke deviation shape and magnitude, the wing reversal timing and duration are thus tuned. These investigations offer, in addition to the comprehensive experimental database, some evidences of the aerodynamic mechanisms used by insects to modulate their aerodynamic performance in lift generation or maneuvers.

Table 1.1: Summary table of available experimental data in liquid for validation purposes of an aerodynamic or aeroelastic model of insect flight.

Reference	Medium	Wing	Data type	Actuation frequency [Hz]
			- Flow visualization	
Dickinson and Gotz [1993] Dickinson [1994]	54% sucrose solution	Rectangular "plate'	- Flow visualization - 2D Force measurement	n/a
Dickinson et al. [1999] Sane and Dickinson [2001] Sane and Dickinson [2002]	Mineral oil	Fruit fly scaled-model	- 2D Force measurement	0.145 0.17 0.17
Birch and Dickinson [2001] Birch and Dickinson [2003] Birch et al. [2004]	Mineral oil	Fruit fly scaled-model	- Flow visualization - PIV - 2D Force measurement	0.168
Dickson and Dickinson [2004]	Mineral oil	Fruit fly scaled-model	- 2D Force measurement	n/a
Heathcote et al. [2004]	Water	Airfoil/plate combinations	- Wing deformation - PIV - 2D Force measurement	1-2.5
Heathcote et al. [2008]	Water	NACA0012 airfoils	- Wing deformation - PIV - 2D Force measurement	0-6
Paquet and Bourez [2006] Huon [2007]	Water	NACA0012 SD7003 airfoil	- Flow visualization - 5D Force measurement	0.1-1
Lehmann and Pick [2007]	Mineral oil	Fruit fly scaled-model	- 2D Force measurement	0.17-0.35
Toomey and Eldredge [2008]	Water	Driven/passive airfoil combination	- Flow visualization - Wing deformation	0.15
Ansari et al. [2009]	Water	Rectangular 'plate'	- PIV	0.126-3.77
Lentink and Dickinson [2009]	Mineral oil	Fruit fly scaled-model	- Flow visualization - 2D Force measurement	0.15
Han et al. [2010]	Water	Fruit fly model	- Flow visualization - 1D Force measurement	0.0868-0.278
Lua et al. [2010]	Water	Hawkmoth model	- Flow visualization - 4D Force measurement	0.1
Zhao et al. [2010]	Mineral oil	Fruit fly scaled-model	- 2D Force measurement	n/a
Czekalowski et al. [2011]	Water	Flat 'plate'	- Flow visualization - Pressure measurement - 5D Force measurement	0.025-0.679

Sane and Dickinson [2002] follow their work to, this time, evaluate the aerodynamic effects of wing rotation at wing reversal by varying the wing rotational velocity as well as the position of the axis of rotation along the wing. By comparing their experiments to an in-house quasi-steady aerodynamic model, presented in the section 1.3.2, the authors acquire and tabulate the effects of wing rotation to improve their numerical prediction. These experimental data provide a close and comprehensive look in the wing reversal, a complex and vital motion for the insect flight. They also offer, once again, a complete experimental database for the modeling of insect flight and its benchmarking.

Heathcote et al. [2004] study the thrust generation for a chordwise flexible airfoil heaving at zero freestream velocity and immersed in a water tank, in a setup similar to the one presented in the figure 1.16 but without the free flow velocity U_c. The airfoil is a steel plate of uniform thickness attached to a tear-drop thick aluminium leading-edge, whereby the chordwise flexibility of the plate is tuned by taking three different thicknesses. The tests are carried out for frequencies in the range of 1-2.5Hz for heaving amplitudes of 5 to 25mm. By measuring the deformation, the flow velocity field, the thrust and the ratio of thrust to input power, several conclusions on the influence of chordwise flexibility for the thrust generation are made. The authors suggest that an optimum airfoil stiffness exists for a given heaving frequency and amplitude and also that the ratio thrust/input power is greater for flexible airfoil than for a rigid airfoil. In addition, these investigations offer a clear database for testing the aeroelastic coupling of a wing at hovering against its chordwise deformation with a relative simpler flow as the complete insect one as well than a simple wing geometry.

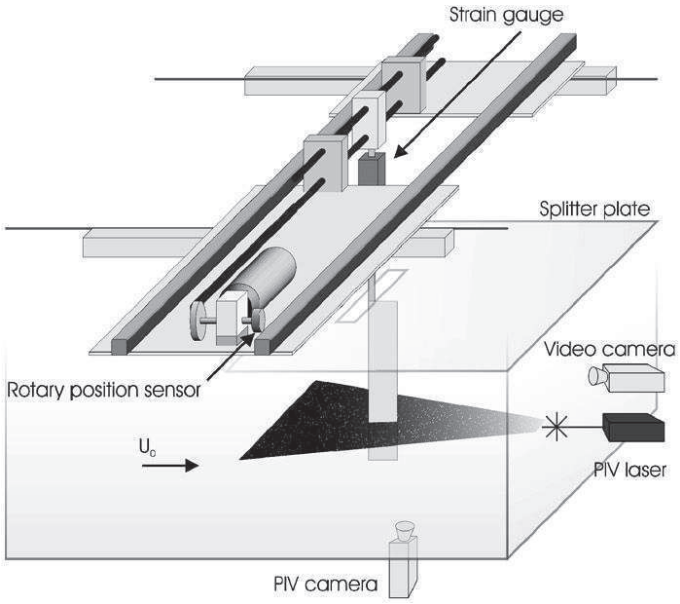

Figure 1.16: Schematic view of the experimental setup used in Heathcote et al. [2008]

Heathcote et al. [2008] pursue their investigation in the role of flexibility in the thrust generation by this time studying the effect of spanwise flexibility in a non-zero freestream velocity. The tests are carried out in the setup presented in the figure 1.16 for actuation frequencies in the range of 0-6Hz, a constant heaving amplitude of 17.5mm and a freestream velocity in the range of 0-0.45$m.s^{-1}$. The airfoil is now a NACA012 profile with different flexibilities in the spanwise direction, through different materials for the spars. Using the same measuring method, the authors conclude that introducing a degree of spanwise flexibility may be beneficial for the thrust and its efficiency, but a larger degree could be detrimental due to a weaker and more fragmented vorticity pattern. They found also that the range of Strouhal numbers Sr [5] for which spanwise flexibility is beneficial overlaps the one found in nature ($0.2 < Sr < 0.4$). As for their previous work, these

[5] The Strouhal number is a dimensionless number describing oscillating flow mechanisms, defined as $Sr = \frac{fc}{V}$ with f the frequency of vortex shedding, c the airfoil chord and V the velocity of the free-stream velocity.

investigations offer a clear database for testing an aeroelastic coupling of a wing in forward flight against its spanwise deformation.

Paquet and Bourez [2006] conduct experiments in a water towing tank to understand the aerodynamic of rigid flapping wings and also to get energy efficient actuation kinematics. Using an ad-hoc mechanism, two quasi-rigid profiles, a $100mm$ chord and $450mm$ span NACA0012 and a $120mm$ chord and $500mm$ span SD7003, are driven in a pitch and plunge motion for actuation frequencies in the range of 0.1-1Hz while a five-components force balance measured the hydrodynamic forces generated. Using the measured forces, an optimizer iterates on the actuation kinematics so as to generate an actuation law that is energy-efficient for a given lift coefficient. Quasi-sinusoidal kinematics are thus found to be optimal. Flow visualizations are also conducted to investigate both the wing wake but also its direct surrounding for phenomena such as stalled or reversed flow. Despite the flight dynamic model of bird-like flapping-wing, an extensive database is available for validating an aerodynamic model in forward flight on a geometry much simpler than the fruit fly scaled-model. The study is also extended with insect-like flapping-wing kinematics in Huon [2007], even if not academically available, by modifying the flapping mechanisms.

Zhao et al. [2010] use a custom-made version of the Robofly to measure the aerodynamic forces on flapping wings of variable flexural stiffness at $Re \sim 2000$ so as to understand the role of flexibility on the aerodynamic forces generation and control them. The authors highlight that for low to medium angles of attack, as flexibility of the wing increases, its ability to generate aerodynamic forces decreases monotonically while its lift-to-drag ratio remains approximately constant. However they demonstrate that a simple venation pattern is sufficient to restore the ability of flexible wings to generate forces closed to rigid values by influencing the camber and at a lower inertial power and weight costs than a rigid one. An extensive database of aerodynamic forces as a function of several variables including material properties, kinematics, aerodynamic forces and center of pressure is thus available to validate an aeroelastic model of insect flight.

1.3.1.2 Experiments in air

For a better understanding of the inertial-elastic phenomena in insect-flight, various studies have been done in air. However only a few might be used to validate an aerodynamic or aeroelastic model. They are summarized in the table 1.2 and a sample of them, extensively used by other researchers, are here discussed.

Singh [2006] uses a flapping mechanism, depicted in the figure C.5, emulating insect wing kinematics to measure the thrust generated by various wing designs at different wing pitch settings. To measure the force, a custom load cell using piezoresistive strain gages is designed and incorporated near the wing. In order to extract the aerodynamic from the measured forces, vacuum chamber tests are conducted at $914mbar$ to determine the inertial forces and subtract them from the air measurement. Experiments on various wing configurations are thus done for actuation frequency in the range of 6-16Hz depending on the wing material and geometry. However this frequency is limited first by the high inertial power requirement of the flapping mechanism, second, by the wing mass and third, by the pitch actuator bumps at each stroke reversal. By modifying the flapping mechanism with a passive torsion spring of variable stiffnesses, the actuation frequency is increased to $\sim$22.5Hz and the effect of passive pitching, due to the aerodynamic and inertial forces, is investigated. Thus, a soft torsion spring leads to a greater range of pitch variation during the stroke while producing more thrust at a slightly lower power than a stiff one. This work is interesting for two reasons. First, a comprehensive database for flapping wing in air is available for frequency up to 22.5Hz with force measurement and flow visualization. Second, a methodology to retrieve the aerodynamic forces from air measurement is given based on inertial forces measurement in vacuum.

Wu et al. [2008, 2009a] develop an experimental setup, depicted in the figure 1.18, capable of investigating the performance of flapping wings in a hover station by measuring simultaneously the wing deformation and the force production up to 30Hz and $\pm 35^\circ$. To differentiate the inertial forces from the aerodynamic one,

Table 1.2: Summary table of available experimental data in air for validation purposes of an aerodynamic or aeroelastic model of insect flight.

Reference	Wing type	Wing at resonance	Data type	Actuation frequency [Hz]
Saharon and Luttges [1987] Saharon and Luttges [1988]	Dragonfly scaled-model	No	- Flow visualization	n/a
Ellington et al. [1996] van den Berg and Ellington [1997b]	Hawkmoth scaled-model	No	- Flow visualization	0.3
Usherwood and Ellington [2002]	Hawkmoth scaled-model	No	- Flow visualization - 2D Force measurement	0.1
Okamoto and Azuma [2005]	Rectangular	No	- 2D Force measurement	4.7-12.6
Tarascio et al. [2005]	Flat 'plate'	No	- Flow visualization	7
Singh [2006]	Fruit fly inspired Rectangular	No	- Flow visualization - 2D Force measurement	10-22.3
Wu et al. [2008] Wu et al. [2009a] Sällström et al. [2009] Wu and Ifju [2010] Wu et al. [2011]	Flat Zimmerman wing	Yes but not exclusively	- Wing deformation - PIV - 6D Force measurement	5-40
Agrawal and Agrawal [2009]	Hawkmoth scaled-model	No	- 6D Force measurement	0.9
Watman and Furukawa [2009]	Half ellipse	No	- 6D Force measurement	5-50
Phillips and Knowles [2011]	Flat 'four-ellipse' wing	No	- Wing deformation - Force measurement	5-20
Tanaka et al. [2011]	Hoverfly alike	No	- Force measurement	150

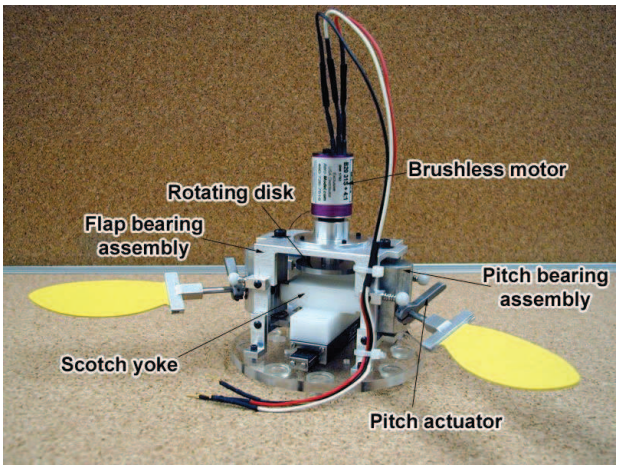

Figure 1.17: Flapping mechanism developed by Singh [2006] enabling the measurement of aerodynamics forces in combination with a force balance and a vacuum chamber.

vacuum chamber tests are conducted at about -1000$mbar$ relative to the surrounding air pressure. Digital image correlation is used all along to track the wing deformation while a commercial load cell is used for the forces. Zimmerman planform wings are investigated versus their thrust performance so as to draw various correlations between their instantaneous wing deformation and force generation. This work constitutes a comprehensive database for an aeroelastic validation both in terms of frequency but also of complementary of the data types.

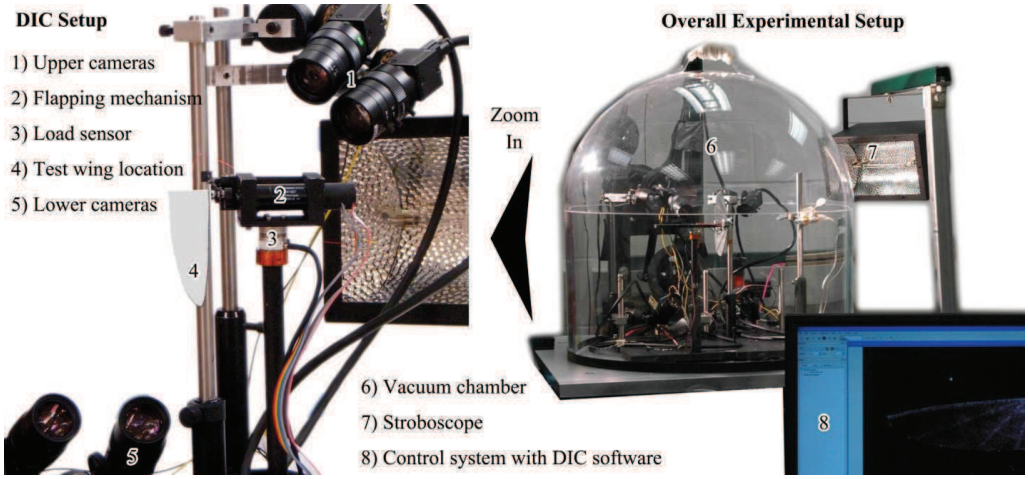

Figure 1.18: Experimental setup used by Wu et al. [2008, 2009a] and in their later works based around a vacuum chamber enclosing a 6D force balance and a digital image correlation system.

Using the same test bench but without the force measurement, Sällström et al. [2009] investigate the effects of spanwise flexibility on the three-dimensional averaged flow field for the same set of flapping wings using stereoscopic PIV. The wings are here actuated at 25Hz with flapping amplitude of about 35 $^\circ$. Using a superimposition of wing deformation data and PIV one, the study shows that a too compliant wing in the spanwise direction suffers from poor thrust performance due to the phase lag between the root and the tip, but that a too rigid wing does not generate the same velocity or cover such a large path and thus has suboptimal performance in thrust generation. Due to the flexibility of the wings and the large amounts of scattered light from the surfaces of the wing, the flow in its close vicinity can not be determined leaving the exact nature of vorticity formation unknown. However this work can be used to validate an aerodynamic model including the wing wake as it is clearly outlined by the PIV data.

Wu and Ifju [2010] introduce the power measurement capacity to the test bench while pushing further

the maximal actuation frequency to about $35Hz$. The correlations introduced in Wu et al. [2009a] are here extended and discussed further under the consideration of the power efficiency new meter. It is more clearly outlined that wings with more bending compliance produce more thrust at lower frequencies while stiffer wings produce more thrust at higher frequencies. Thus this work completes the database already developed in Wu et al. [2008, 2009a] for an aeroelastic validation with new data under air and vacuum.

Wu et al. [2011] summarize these works while showing data up to $40Hz$. The results show that for a specific spatial distribution of flexibility, there is an effective frequency range in thrust production due the wing resonance phenomena and its passive deformation. The authors conclude their work by two essential remarks. First, that the aeroelastic behavior in air is substantially different from that in vacuum, meaning that the structure-fluid interaction is significant and the deformation consists of both aerodynamic and inertial effects. Second, that the flexibility and mass distribution should be tailored to a particular flapping frequency to enable passive deformation that is beneficial in generating forces.

Phillips and Knowles [2011] develop a mechanical flapping-wing apparatus, depicted in the figure 1.19, capable of reproducing a wide range of insect-like wing motions in air on bio-inspired wing. The three degrees of freedom (DOF) required to produce the three separate motions necessary to mimic an insect-like trajectory are controlled up to $20Hz$. Various kinematics parameters and their effects on the mean lift are investigated: the flapping frequency, the AOA at mid-stroke, the rotation phase, the stroke amplitude and the plunge amplitude. Rules of thumb are defined to maximize the mean lift for a FWMAV application such as setting the AOA around 45° or advancing the wing reversal. High-speed visualization of the wing deformation is also done to check the aeroelastic behavior of the wing within a more global uncertainty analysis giving more credits to the overall test bench. This work provides precious data to validate an aeroelastic model against several actuation kinematics other than a traditional sine and along the 3 DOFs of the wing root.

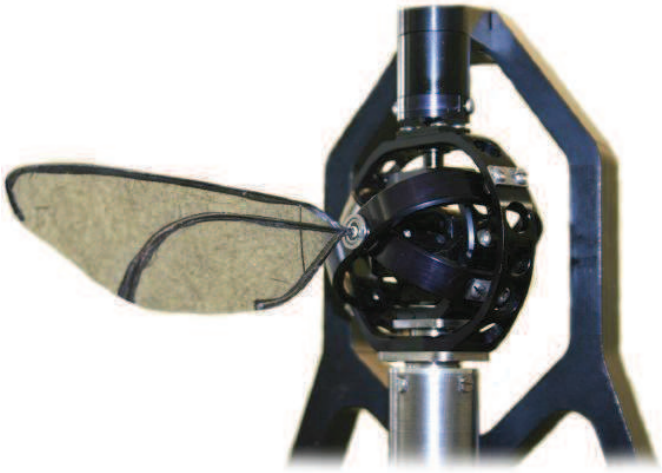

Figure 1.19: Flapping mechanism developed by Phillips and Knowles [2011] enabling a wide range of insect-like wing motion and lift measurement when mounted on top of a force balance.

Tanaka et al. [2011] investigate the effects of flexural and torsional wing flexibility on the lift using an at-scale mechanical model and the force sensor developed by Wood et al. [2009]. A polymer wing mimicking the venation and corrugation profiles as well as the flexural stiffness of hoverfly is compared to a similar shaped, rigid, flat, carbon-fiber wing using a flapping mechanism driven sinusoidally at $150Hz$. Torsional flexibility at the wing-body joint is emulated with a set of hinges encompassing the torsional stiffness of pronation and supination in hoverfly. Maximum lift is achieved with a hinge stiffness similar to the hoverfly one for both wings with, however, better performance for the rigid wing. The authors conclude by suggesting that intrinsic compliance can be exploited to generate the desired motions of the wing and that, for the same flapping motions, a rigid wing could be more suitable for producing large lift. They also acknowledged that more output criteria i.e. drag and efficiency have to be investigated to conclude further

given the conclusion of Shyy et al. [2010]. However this work is the first aeroelastic investigation available at high frequency under air even if its use as a reference for validating a numerical model might be quite difficult given the already very detailed wing and its actuation mechanism blurring the proper wing actuation.

The major experiments made to understand either aerodynamic or structural phenomena occurring in the insect flight have been here reviewed highlighting the strong commitment of the scientific community in the past decade. These works given the wide range of techniques and test cases are also a comprehensive support for the partial or full validation of an aerodynamic or aeroelastic model.

1.3.2 Aerodynamic modeling of insect-like flapping-wing

Given the substantial amount of literature on CFD studies of flapping-wing (Shyy et al. [2010]; Liu et al. [2010]), it can be noted that the computed aerodynamic forces have shown good quantitative agreement with experimental data for a variety of configurations, kinematics and flow conditions. However as CFD requires substantial computer load and time, such an option proves itself to be inadequate and too expensive for the preliminary design stage of a FWNAV where quick iterative studies are expected to rough out a design. Therefore various attempts have been made to model the aerodynamic force generated by an insect-like flapping-wing offering a compromise between the computational efficiency and accuracy needed for such design studies.

The usual theories in unsteady aerodynamics are generally based on the computation of induced velocities due to the vortices convected far from the wing. This fact does not hold with the phenomena observed in the insect flight as the wing interacts with its own wake. Additionally, the added-mass forces are usually assumed to be negligible on traditional aerodynamic configurations, which is not the case for insect flight given their size and weight. The well-established modeling methods developed for aircraft are, therefore, not appropriate and novel models addressing the specificity of insect flight are necessary.

Following the classification scheme given by Ansari et al. [2006c] in their review, aerodynamic models of insect-like flapping-wing can be classified into steady-state methods, quasi-steady methods, semi-empirical methods and finally unsteady methods. Others methods covering only some aspects of the insect-like flapping flight or less analytical such as the panel method are also included in the review made by Ansari et al. [2006c], but are here not discussed. Steady-states or quasi-steady methods assume that the forces on an insect wing at any time-step are the steady-state values that would be achieved by the wing at the same velocity and AOA. The difference between steady-state and quasi-steady methods is that the steady-state analysis applies only once a steady-state has been reached limiting their use to mean-quantities studies. To compensate the moderate accuracy of those simplified models, semi-empirical methods were introduced with an empirical 'correction' added to increase the accuracy of the model while still relying on fairly simple equations. Finally, unsteady methods are analytic methods relying purely on unsteady aerodynamics, such as the wake modeling. Ansari et al. [2006c] provide extensive review of the various, at-the-time, available models and only a selection of those models are here reviewed as well as relevant models published since then. These works are summarized in the table 1.3.

Sane and Dickinson [2002] present a quasi-steady semi-empirical method based on a blade-element approach to describe the forces measured in their earlier experiments made on the *Robofly* (Sane and Dickinson [2001]). In their model, the aerodynamic forces are decomposed on each blade into a sum of four components: translational, added-mass, rotational, and wake-capture forces. Both translational and rotational components are computed using a quasi-steady assumption with experimental coefficients and potential theory. Added-mass component is computed using a two-dimensional flat plate formulation developed by Sedov [1965]. Wake-capture is then assumed to be the remaining measured forces after

Table 1.3: Summary table of available aerodynamic model of insect flight.

Category	Remarks on the category	Reference	Advantages	Disadvantages
Steady-state	+ Simple formulation - 'Reverse-engineering' from output data - Wing geometry and kinematics not accounted - Ignore the aerodynamic mechanisms	Weis-Fogh and Jensen [1956]	+ Simple momentum theory	- Assumed a 180 ° stroke amplitude - Stroke frequency not accounted
		Rayner [1979]	+ Vortex-wake method	- Assumed a 180 ° stroke amplitude
		Ellington [1984e]	+ Simple momentum theory + Vortex-wake method + Accounting for the stroke amplitude	
		Sunada and Ellington [2001]	+ Accounting for wing kinematics + Accounting for all forward speed	
Quasi-steady	+ Simple formulation + Wing geometry and kinematics accounted - Limited accuracy - Unsteady effects not accounted	Osborne [1951]	+ Blade-Element approach coupled to a momentum theory	- Constant C_L and C_D along the stroke - 'Reverse-engineering' for C_L and C_D
		Weis-Fogh [1973]	+ Blade-Element approach coupled to a momentum theory	- Constant C_L and C_D along the stroke - 'Reverse-engineering' for C_L and C_D
		Ellington [1984a] Ellington [1984d]	+ Blade-Element approach coupled to thin airfoil theory	- 'Reverse-engineering' for C_D
		Azuma [1992]	+ Blade-Element approach coupled to a Theodorsen function	- Based on flat plate - Limited treatment of the drag
		Ansari [2004]	+ Blade-Element approach coupled to a Glauert-type analysis	- Limited treatment of the drag
Semi-empirical	+ Simple formulation + Wing geometry and kinematics accounted + Experimental correction factor - Flow physics not properly reflected - Lump together different types of flow - Wake interaction generally not modeled	Walker and Westneat [2000]	+ Blade-Element approach + Use of a Wagner's function + Added-mass and skin-friction effects	- Wing as a rectangular plate
		Sane and Dickinson [2002]	+ Blade-Element approach + Added-mass	- Based partially on a flat plate - Wake capture component loose
		Traub [2004]	+ Simple actuator disk theory + Polhamus' leading-edge analogy	- Devised for time-averaged data - Small-angles approximations
		Tarascio et al. [2005]	+ Free vortex blob method + Modeling of the wake	- Limited to 2D-plate and to the wake - Based on a flat plate
		Berman and Wang [2007]	+ Blade-Element approach + Added-mass	- Based partially on a flat plate
Unsteady	+ Unsteady phenomena accounted + Wing kinematics accounted + Wing geometry accounted (except for 2D-wing) + Accuracy without resorting to experiments + Flow physics - More complex formulation - Computational cost - Limited to 2D or quasi-3D	Minotti [2002]	+ Conformal mapping + 2D potential method with a stationary LEV	- 2D resolution of the wing - Based on a thin flat plate
		Pedersen [2003]	+ Blade-Element approach + Circulatory and non-circulatory forces + Wagner and Küssner functions	- 2D resolution on each blade - 2D resolution on each blade - Based on a thin flat plate
		Yongliang et al. [2003]	+ Conformal mapping + Potential methods	- 2D resolution of the wing - Based on a thin flat plate
		Pullin and Wang [2004]	+ Conformal mapping + Similarity approach (spiral vortex sheet)	- 2D resolution of the wing - Based on a thin flat plate
		Ansari et al. [2006a] Ansari et al. [2006b]	+ Radial Blade-Element approach + Conformal mapping on each blade + Potential method	- 2D resolution on each blade
		Singh [2006]	+ Blade-Element approach + Circulatory and non-circulatory forces + Wagner and Küssner functions	- - 2D resolution on each blade
		Gogulapati [2011]	+ Based on Ansari et al. [2006a,b] + Compatible with forward flight and flexibility	- 2D resolution on each blade
		Taha et al. [2013]	+ Duhamel superposition principle	- Developed for dynamic stability analysis

subtracting all the other components, when wake re-entry experiments are made. But physically only a portion of the remaining forces can be associated with wake-capture as the far wake also influences the wing, like in an airplane, discarding this last component. However, this model is quite straightforward in its formulation while being sufficiently accurate through its experimental resort that accounts for the LEV for example.

Berman and Wang [2007] use also a quasi-steady method based on blade-element approach to compute the aerodynamic forces by decomposing them in translational, rotational and added-mass forces. The first two are computed through the circulation and the viscous dissipation using experimental coefficients. The added-mass component is similarly developed from Sedov [1965] but with contribution both from the wing chord and thickness. This decomposition is fitted to various Re by using the experimental coefficients acquired on various insects or experiments. The model is used to compare different wing kinematics patterns in order to minimize the power consumption for three different species and gain insight in the insect kinematics. The formulation of the model is still straightforward with the equations being slightly more complex than Sane and Dickinson [2002] and available for several Re.

Minotti [2002] develops a two-dimensional unsteady aerodynamic model for flapping-wing using a potential analytic approach. As support for its development, a flat plate is taken with a concentrated stationary LEV above the wing, whose position is set arbitrarily in order to give the best agreement with experiments from Dickinson et al. [1999] and Sane and Dickinson [2001]. Rotational as well as added-mass effects are automatically taken into account by the potential approach. Effects of wake capture as well as vorticity shed are not explicitly modeled but partially introduced by changing the bound vorticity and the position of the LEV. While inexpensive computationally, the model provides good agreement with the experiments of Dickinson et al. [1999] and Sane and Dickinson [2001] where the wake capture is quite strong. But the model is applied to a two-dimensional wing which is not appropriate for studying the effect of wing geometry.

Ansari et al. [2006a,b] develop an inviscid and non-linear unsteady aerodynamic model of insect-like flapping-wing in hover based on a blade-element approach. Using potential-based methods and a two-dimensional approach on each blade, the aerodynamic forces are decomposed in a wake-free, the contribution of free-stream velocity and of the unsteady motion of the wing, and a wake-induced component, the contribution of the leading-edge vortex and of the trailing-edge wake, as illustrated in the figure 1.20(a). A continuous distribution of bound vortices is issued on each blade for both components with the wake-free vortices moving with the airfoil whereas the wake-induced ones are free and move within the fluid. To better account for the specificity of insect flight, radial chords are used instead of spanwise chords to solve the flow on each two-dimensional cylindrical cross-plane associated with a blade element, as illustrated in the figure 1.20(b). For this reason and also as the bound and tip vortices are modeled, the authors refer to the methods as being a 'quasi-three-dimensional' model. The model is benchmarked versus the flow visualization made by Dickinson and Gotz [1993] and with the Robofly force measurement of Sane and Dickinson [2002], showing very good agreement for a moderate computational load. Nevertheless, the computational load is reported to be strongly influenced by the vortices convection computation as well as the number of stroke reversal in the simulation. However, this model is quite novel in its approach and avoids the resort to experimental coefficient which is very interesting for design application.

Singh [2006] develops a blade-element approach splitting the aerodynamics forces into 6 components: the translational, added-mass and rotational forces based on thin airfoil theory, the leading-edge vortex through the Polhamus analogy (Polhamus [1966]), the effect of starting vortices using the Wagner function, and the effect of shed wake and tip vortex using the Kussner function, as illustrated in the figure 1.21. Comparison with the experiments on Robofly (Birch and Dickinson [2003]) are made showing the same general trend in the evolution of aerodynamic forces through a stroke cycle except the force peak observed at the beginning of each half-stroke which is missed due to the non-circulatory forces. Additionally to better match the experimental data, the lift and drag coefficients are taken from the Robofly apparatus. However, the aerodynamic model is interesting as it handles already the wing flexibility and a large panel of aerodynamic forces encountered

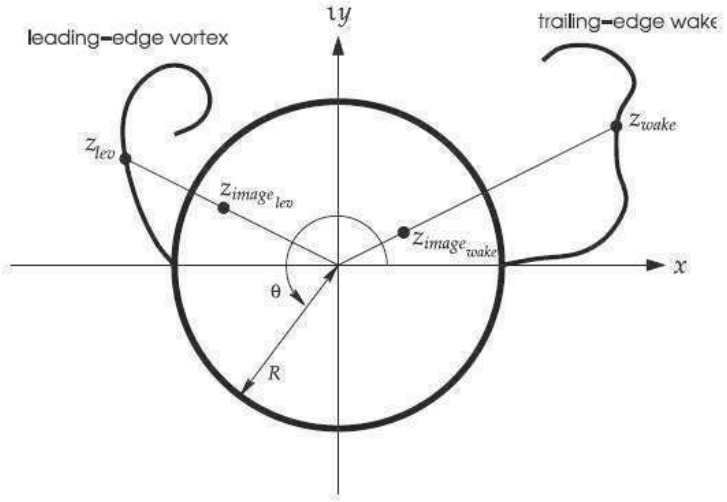

(a) Wake system

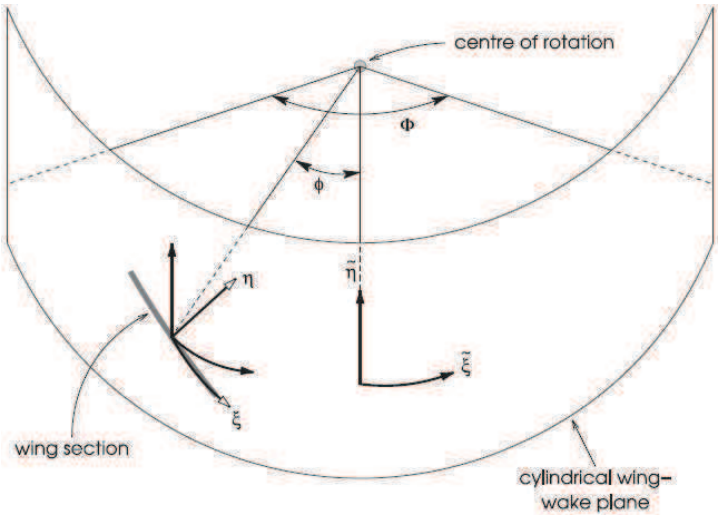

(b) 'Wrapped' cylindrical cross-plane

Figure 1.20: Details of the method of Ansari et al. [2006a,b] based on a cylindrical cross-plane on each blade to solve the unsteady flow using a conformal mapping accounting for the LEV and trailing-edge wake.

in insect flight for a moderate computational load.

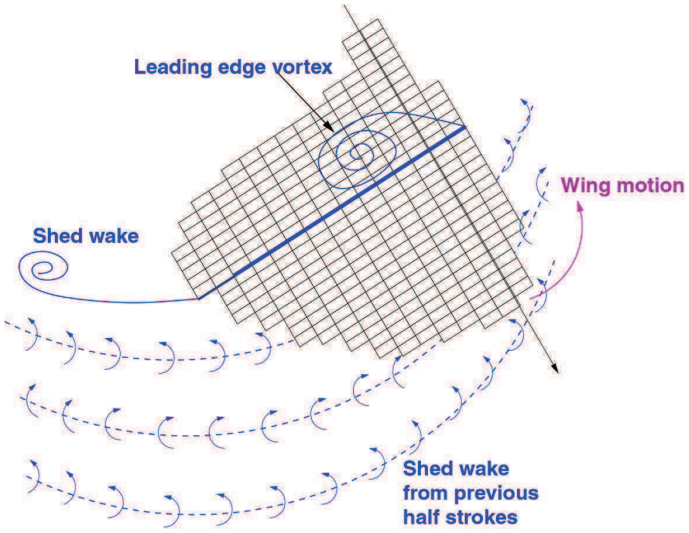

Figure 1.21: Wake structure at one station along the span modeled in Singh [2006]

Gogulapati [2011] modifies the aerodynamic model developed in Ansari et al. [2006a,b] to incorporate wing flexibility as well as forward flight respectively by averaging the radial deformation over two consecutive time-steps (Gogulapati and Friedmann [2008]) and by making an analogy with the prescribed skewed cylindrical wake for helicopters in forward flight (Gogulapati et al. [2010]). With these slight changes in the formulation, the model is tailor-made for intensive aeroelastic studies with a high-fidelity aerodynamic model.

1.3.3 Framework for the aeroelasticity of insect-like flapping-wing

Numerous studies of insect flight focus on explaining one specific aspect, either from a structural point of view like the role of flexibility or from an aerodynamic point of view such as the role of the wake. Generally, several assumptions are made to simplify the study for examples by assuming rectangular plate for the wing, rigid wing, simple actuation kinematics. These assumptions are valid within their context and are needed to speed up our understanding of the insect flight. The developed frameworks are also specialized and can not encompassed most of the specificity of the insect flight, such as various wing geometry and flexibility, actuation, aeroelastic effects and so on. Nonetheless, a few framework are developed aiming at taking a comprehensive picture of the insect flight and of its diversity. They are here summarized in the table 1.4 and a sample of them are here more extensively reviewed.

Smith [1996] develops a model of a tethered flapping moth using an unsteady aerodynamic panel method for aerodynamic computation and FEM for the wing flexibility. The wing is discretized by tubular beams for the veins and orthotropic stress membrane otherwise both with varying thicknesses. The finite surface spline method is used to transfer the load from the aerodynamic computation to the FE model. The framework is validated with literature data for the plunging of an inclined flat plate and pitch oscillation of a NACA0012 section wing (Katz and Plotkin [1991]). Once validated, the aeroelastic response of a tethered moth is computed showing good agreement with experimental data once the wake is accounted. However, the framework takes a small displacement assumption for the wing deformation and is displayed only for a forward flight case.

Ho et al. [2003] use a commercial software to compute the aeroelastic response of an arbitrary flapping-wing using CFD for the flow and FEM for the structural dynamics response. The framework is validated in a two-steps approach. First, a mesh convergence study is done by comparing the computed data, with and without coupling, to experimental ones for a fixed AOA (30°) and free-stream velocity ($1.7m.s^{-1}$). Thus

Table 1.4: Summary table of available aeroelastic framework of insect flight.

Reference	Aerodynamic method	Finite-Element used	Dynamic stiffening	Isotropic / Anisotropic	Aeroelastic coupling	Remark(s)
Smith [1996]	Unsteady aerodynamic panel method	- Tubular beam - Plane stress membrane	- No	Anisotropic (Orthotropic)	Implicit	- Applied to the forward flight of a moth
Ho et al. [2003]	CFD	n/a	n/a	n/a	Implicit	+ Used for optimization purposes - Applied to forward flight cases
Singh [2006]	Unsteady aerodynamic model	- Composite Plate	Yes	n/a	Implicit	+ Applied to hovering cases + Extensive validation
Blair et al. [2007]	Quasi-steady aerodynamic model	- Linear beam	No	Isotropic	Implicit	+ Used for a preliminary design tool
Hamamoto et al. [2007]	CFD	- Shell	n/a	n/a	Implicit	+ Applied to a hovering case
Tang et al. [2008]	CFD (RANS)	- Non-linear beam - Linear plate	Yes/No	Isotropic	Explicit / Implicit	- Applied to a forward flight case - Applied in a pure heave motion of the wing root
Gopalakrishnan [2008]	CFD (LES)	- Linear elastic membrane	No	n/a	Explicit	- Applied to forward flight cases
Chimakurthi [2009]	CFD (RANS)	- Non-linear plate/shell	Yes	Isotropic	Explicit / Implicit	+ Extensive validation + Applied to 'hovering' cases
Aono et al. [2010]	CFD (RANS)	- Non-linear plate/shell	Yes	Isotropic / Anisotropic	Explicit / Implicit	+ Applied to hovering and forward flight cases
Liu et al. [2010]	CFD	- Shell	Yes	Anisotropic	Explicit	+ Applied to hovering insects + Used for a dynamic flight simulator
Su and Cesnik [2010]	Unsteady aerodynamic models	- Non-linear beam	Yes	n/a	n/a	+ Used for a dynamic flight simulator - Applied to forward flight cases
Gogulapati [2011]	Unsteady aerodynamic model	- Beam - Plate/shell	Yes	Isotropic / Anisotropic	Implicit	+ Applied to hovering and forward flight cases
Kang et al. [2011]	CFD (RANS)	- Linear Beam - Non-linear shell	No/Yes	n/a	Implicit	+ Applied to hovering and forward flight cases
Combes et al. [2012]	Potential flow model	- Shell - Frame	Yes	n/a	Implicit	- Restricted to forward flight cases + Ready for optimization purposes
Stanford et al. [2012a]	Unsteady aerodynamic model	- Beam - Membrane	No	Isotropic	n/a	- Restricted to forward flight cases + Used for optimization purposes
Dawson et al. [2013]	CFD	- Shell - 3D Volumic	n/a	n/a	Explicit	+ Applied for hovering case

the authors outline that resolving large-scale flow separation requires many more cells than for smoothly attached flow i.e. more computation load. Second, a flapped wing with rigid and flexible membrane is computed and compared to flow visualization and force measurement made in a wind tunnel showing a very good agreement. However, very few details are given about the choices made for the FEM and the framework is demonstrated only for a forward flight case.

Singh [2006] combines the aerodynamic model presented in the previous section to a structural finite-element analysis based on plate element capable of handling large motion and dynamic stiffening. Once each component of the framework is validated, the framework is used to compare the aeroelastic response of several experiments made on several wings of an in-house FWMAV showing an overall good agreement. Furthermore prior to the aeroelastic model, a interpolation module is approximating the input wing geometry using plate element is implemented offering a greater adaptability to change in wing shape as well as increasing the reliability of the simulation by reducing the effects of mesh skewness.

Blair et al. [2007] propose an aeroelastic framework based on a quasi-steady aerodynamic model derived from Sane and Dickinson [2002] coupled to a linear beam model, handling the spanwise deformation, in a spectral method. The framework handles the complete process of evaluation from wing definition to computation of the aeroelastic response with three levels of abstraction depending on the end-user. The model is validated using the experiments of Dickinson et al. [1999] and shows a good agreement. The aeroelastic framework is part of an overall project aiming at developing a complete computational design framework for FWMAV adressing here the preliminary design stage. Further results are discussed in the section 1.3.4.

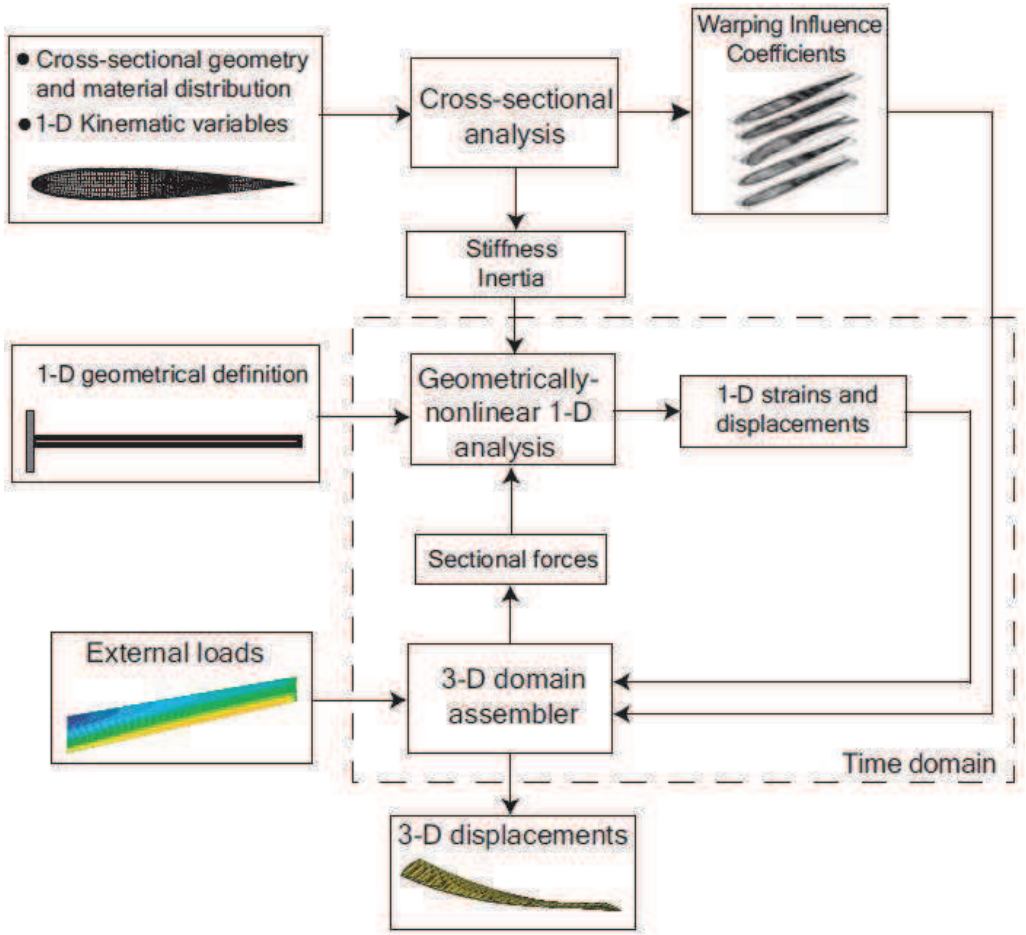

Figure 1.22: Flowchart of the structural method used in Tang et al. [2008] to compute the wing deformation under aerodynamic loads using a non-linear beam and the warping influence coefficients of a linear plate.

Tang et al. [2008] extend the capacity of their two-dimensional aeroelastic framework developed in Tang et al. [2007] by including three-dimensional effects through CFD and an in-house nonlinear beam/linear plate FEM solver. The flow is computed within a structured mesh while the structural deformation is decomposed in two independent problems, as illustrated in the figure 1.22. First, the spanwise larger deformation is handled with the non-linear beams. Second, the chordwise smaller deformations are computed on each beam element using the warping influence coefficients of a linear plate matching the airfoil cross-section. Given a set of control points on the CFD grid, the aerodynamic loads are transferred first to the plate and then to the beam giving the quasi-3D wing deformation. For the coupling between the structural and fluid solvers, both the explicit and implicit methods are available. To validate the framework, the experiments of Heathcote et al. [2008] are used and agree quantitatively. However the framework is applied for a forward flight case and with only a pure heave actuation missing the typical flapping motion of insects.

Chimakurthi [2009] pursues the development of this aeroelastic framework by adding two complementary environments for the computation of the wing deformation: one based on an in-house nonlinear plate/shell finite element solver and the other by interfacing a commercial structural solver *MSC.Marc*. Both solutions are handling non-linearities either due to material behavior, large deformation, or boundary conditions, by using non-linear plate/shell elements. An higher fidelity is achieved but limited to isotropic wing structures. The complete aeroelastic framework is validated first, using again a rectangular NACA0012 airfoil in pure heaving (Heathcote et al. [2008]), second, using an isotropic elliptic wing in pure flapping (Wu et al. [2009a]), and finally a pure rectangular in pure flapping (Wu et al. [2009b]). An overall good agreement is shown demonstrating the strong capabilities of the framework. However a slight free-stream velocity is needed for each computation at hovering.

Aono et al. [2010] advance further the computational capabilities of this framework by adding an unstructured Navier-Stokes solver as well as an anisotropic structural solver. Remeshing techniques are implemented to handle the airfoil deformation and motion within the CFD unstructured grid. Anisotropy is introduced by implementing a composite model based on laminate plate theories. The framework is validated again, among others, with the experiments of Heathcote et al. [2008], with the anisotropic wing of Wu et al. [2009a] showing an overall good agreement. The aeroelastic framework is thus reliable to investigate a broaden variety of wing geometry and actuation thanks to the unstructured mesh and to the anisotropy feature.

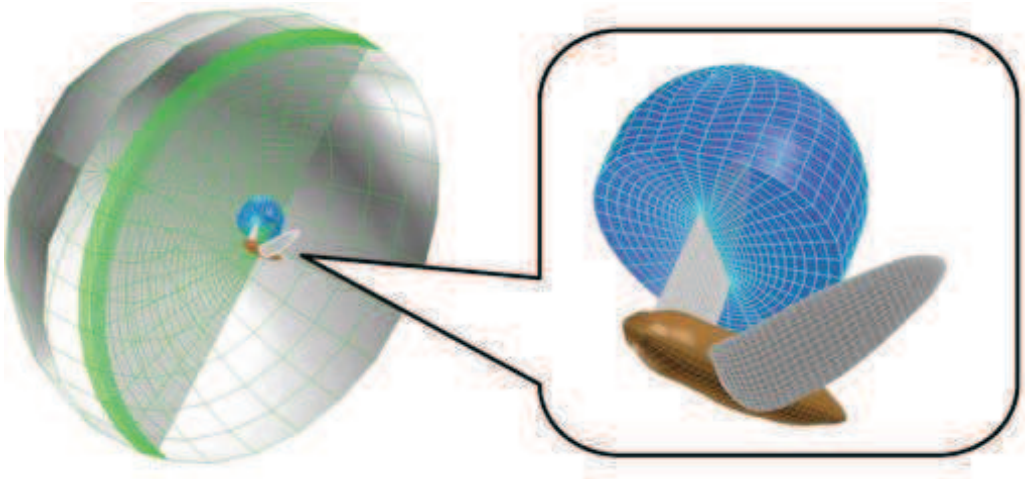

Figure 1.23: Global and local grid blocks about a hawkmoth model used in Liu et al. [2010] and highlighting the Chimera techniques.

Liu et al. [2010] propose a comprehensive computational framework, which integrates aerodynamics, flight dynamics, vehicle stability and maneuverability. The aeroelastic part of this framework consists of a Navier-Stokes solver, using Chimera techniques as illustrated in the figure 1.23, coupled to a non-linear FEM model, based on very thin and anisotropic shells. The aeroelastic coupling is here explicit to maintain the

computation load low given the objective of the framework as a dynamic flight simulator. Each component is thus properly validated and results are presented for hovering hawkmoth and fruitfly with rigid and flexible wings giving a strong insight in the flow structure.

Gogulapati [2011] develops an aeroelastic framework for wings undergoing prescribed rigid body motion and moderate-to-large flexible deformation. The framework is obtained by coupling a nonlinear structural dynamic model with a modified version of the unsteady aerodynamic model of Ansari et al. [2006a,b]. The structural solver handled beam, plate, shell and membrane elements with both isotropic and anisotropic material. The framework is validated using experiments for rigid and flexible Zimmerman wing in hover and in forward flight and shows reasonable agreement.

1.3.4 Wing design for insect-based flapping-wing system

Even with computational frameworks developed to study the flight insect, the design from scratch of a wing for a flapping-wing system is still mainly done by trials-and-errors, which can become hard and time-consuming depending on the fabrication and design choices made. However a few studies have addressed the problem of determining numerically the appropriate wing geometry for a flapping-wing system. They are summarized in the table 1.5 and reviewed below. The appendix F is describing the various optimization techniques used here and might be of assistance for unfamiliar readers.

Ho et al. [2003] use its aeroelastic framework presented in the previous section and combine it to a Gur Game algorithm to optimize the force coefficients by setting the appropriate stiffness for six arbitrary membrane areas, representing stiffness actuators. The optimization is done for a fixed stroke angle of the wing and a fixed free-stream velocity on a rectangular and a bio-inspired wing. The optimized wing tends to perform similarly in lift and in thrust but minimizes the drag. However the optimization does not addressed the definition from scratch of a wing geometry and is more like an advanced design optimization with local tuning.

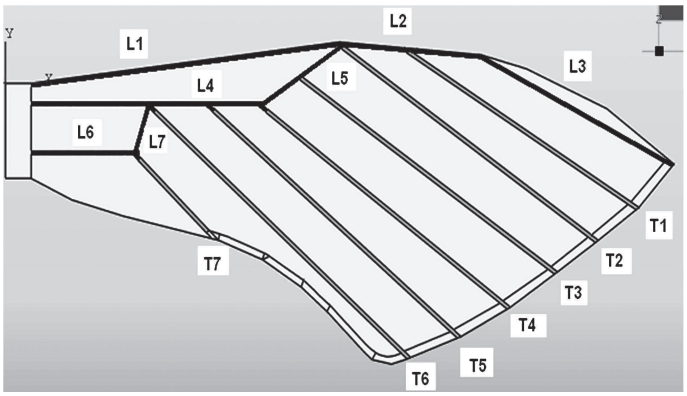

Figure 1.24: Structural model of the hawkmoth wing, as used in Agrawal and Agrawal [2009], showing longitudinal veins (LE) and transversal veins (TE) and whose Young moduli are optimized to match the load-deformation profile of a real wing.

Agrawal and Agrawal [2009] develop a structural model of a hawkmoth-inspired wing with its venation pattern using FEM, as illustrated in the figure 1.24. In order to mimic the load-deformation profile of the hawkmoth wing under static load deformation, the structural model is coupled to an gradient-based optimization module available in *MATLAB* in order to minimize the deformation error between the real hawkmoth and the synthetic wing by adjusting the Young modulus of the veins. A scaled-version, due to fabrication constraints, of the optimized wing is then fabricated and tested on a robotic flapper showing larger thrust performance for various kinematics patterns in comparison to a rigid version of the wing with almost the same lift performance. However the optimization does not included any aerodynamic aspects

Table 1.5: Summary table of wing design studies for flapping-wing system.

Reference	Aerodynamic method	Aeroelastic coupling	Design stage	Optimization approach	Optimization goal	Optimization variables	Remark(s)
Ho et al. [2003]	CFD	Yes	Advanced	Gur Game algorithm	Force Coefficients C_L and C_T	Stiffness of specific area	- Applied to forward flight cases - Not applied to the wing geometry
Agrawal and Agrawal [2009]	None	No	Early	Gradient-based method	Wing deformation	Young modulus of veins	- Not applied to the wing geometry
Beran et al. [2007]	Model	Yes	Intermediate to advanced	Gradient-based method	-	-	- No results shown
Isogai et al. [2010]	CFD	Yes	Early to advanced	Complex method	Mean lift and thrust	Wing geometry and kinematics	+ Applied to a hovering case + Applied to the wing geometry
Stanford et al. [2012a]	Model	Yes	Advanced	Genetic Algorithm	Mean lift, thrust and peak power	Wing venation pattern	- Restricted to forward flight cases + Not applied to the wing geometry
Stewart et al. [2012]	Model	No	Early	Gradient-based method	Mean lift, wing area and power	Wing geometry	+ Applied to forward flight and hovering cases

and does not addressed the definition from scratch of a wing geometry. But this is an successful attempt to mimic a natural flapper.

Isogai et al. [2010] propose an aeroelastic framework based on a two DOF resonance-type flapping-wing system, the equations of two torsional spring at the root giving the structural response, coupled to a CFD solver, giving the pressure load on the wing. This framework, intended for a dragonfly-like FWMAV, is plugged to a complex-method optimization algorithm so as to maximize the mean lift and thrust of the hovering FWMAV through various geometrical and kinematics parameters of the fore- and hind-wings. Thus the optimized wings demonstrate numerically that sufficient lift, to sustain the weight, and sufficient thrust, to overcome the body drag, are generated while minimizing the actuation power. The authors also show that the optimized parameters hold for forward flight. Even if applied on a dragonfly-like FWMAV and using a loose structural model, the study outlines that the optimization of a complete wing geometry and kinematics is possible.

Beran et al. [2007] pursue the development of the aeroelastic framework of Blair et al. [2007] by presenting two new components of their framework: an adjoint method for calculating sensitivities of the system with respect to changing structural design variables and an optimization component built upon existing gradient-based methods. No results are given outlining the performance and capabilities of their framework even if some hints are found in latter papers such as the one of Stanford et al. [2012a]

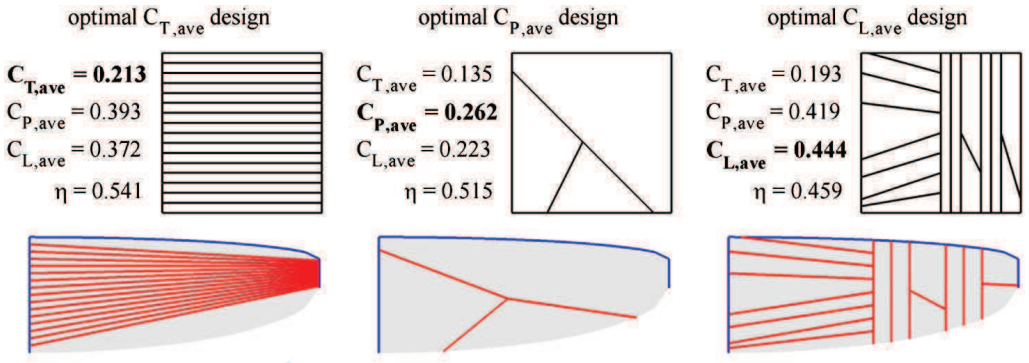

Figure 1.25: Single-objective optimal designs for a flexible wing skeleton found in Stanford et al. [2012a] with the mean thrust, the mean power and the mean lift optimized design respectively from left to right.

Stanford et al. [2012a] use their aeroelastic framework, coupling CFD and FEM in a spectral method, to optimize the venation pattern of Zimmerman planform wing in forward flight versus the mean lift, the mean thrust and the mean actuation power. The venation pattern is modeled by a cellular division approach where the membrane is split iteratively in cells. The design is then evaluated by a genetic algorithm which used the aeroelastic framework as its evaluation function enabling to locate the global Pareto optima in a gradient-free manner. The authors note that spanwise battens tends to favor thrust optimal design while diagonal battens favor power optimal one. But even if the approach is original and successful, the wing outer geometry is given as input while the inner wing is optimized making the framework useful for advanced design optimization.

Stewart et al. [2012] investigate the effects of wing planform on the aerodynamic performance of a rigid wing in forward flapping flight and hovering configurations. To do so, the design space is parameterized as a Zimmerman wing. No aeroelasticity is here accounted and the aerodynamic forces are computed using an unsteady aerodynamic model. A gradient-based optimizer is used to launch a multi-objective optimization approach for three objectives: the wing area, the peak actuation power, and an aerodynamic force based on the kinematic configuration, either lift for hovering or thrust for forward flight. The choice of primary and secondary objective functions is important in determining the optimal planform, the Pareto differing drastically from one to another.

1.4 Conclusion on the state of the art and on the literature review

Flapping-wing vehicles are becoming more and more popular in the scientific and engineer communities due to their appealing hover and size capabilities opening new operation theaters and applications. Fully functional and autonomous FWMAVs have been demonstrated such as the Hummingbird from *Aerovironment* or the DelFly from the University of Delft. However FWNAVs, closer to insects, are scarcer and at an earlier development stage as none has yet shown autonomous flight in the sense of self-powered flight (Wood [2007b]; Nagai et al. [2012]). Two categories are emerging: the first driving the wing to its desired motion through an appropriate transmission system and the second exploiting the wing mode shape i.e. resonance to generate the appropriate motion such as the OVMI. Given the success encountered by UAVs in general, flapping-wing vehicles are expected to have also their share of success.

However their design from scratch is an arduous tasks for engineers which is currently based mostly on trial and error due to the lack of well-established know-how. This work intends to provide a robust, efficient and modular aeroelastic framework of insect-flight so as to assist designers through the preliminary design stage of their flapping-wing vehicles whatever their requirements. To do so, the framework has to account for both the structural and aerodynamic specificity of insects. The challenges are here to account for flexible wing in large deflection actuated, most probably, in the range of $5Hz$ to $200Hz$ and under the non-linear loads of unsteady aerodynamic forces. Following the precepts outlined by Zbikowski [2002], Combes and Daniel [2003a] and Blair et al. [2007] and to comply with the preliminary design tool requirements in terms of accuracy and of rapidity, the kernel of the framework is a FEM solver coupled to an aerodynamic model.

Several aerodynamic models have been here reviewed and two categories are particularly interesting given their good agreement with experimental data and their capability to account for several unsteady phenomena: the semi-empirical methods like the one from Sane and Dickinson [2002] and the unsteady methods like the one from Ansari et al. [2006a,b]. The former benefits from a simple formulation but needs experimental correction factor to improve its accuracy while the latter requires a more complex formulation but does not need the experimental resorting.

Several aeroelastic frameworks of the insect flight have also been reviewed. The majority of these works were oriented towards the comprehension of the aeroelastic phenomena in the insect flight such as the role of the flexibility. All of them are using the FEM for the structural computation while relying mainly on CFD for the aerodynamic computation. Given the accuracy offered by CFD and to benefit fully from its computation cost, an implicit coupling is generally used along with the dynamic stiffening of the wing due to its flexibility. Aeroelastic frameworks using an aerodynamic model are scarcer but are generally devised for engineering applications such as optimization or flight dynamics studies given their lower computation cost and rapidity. This confirms the choice of the approach envisioned in this work to use an aerodynamic model and a FEM solver.

One of the task of the framework being to determine aerodynamic interesting wing geometry, several studies addressing the numerical design of a wing have been also reviewed even if their number is quite limited for insect-like flapping-wing. Most are more appropriate to an advanced design stage as they are tuning locally the wing geometry and are applied preferentially to forward flight cases. In the ones devised more for preliminary design stage, where determining the overall wing geometry is relevant, the aeroelastic phenomena might be accounted but not the large deflection of the wing. These points are essential for resonant wing FWNAVs, where the chordwise and the spanwise deformations are emphasized by the mode shape which is influenced itself by the aeroelasticity, especially at the FWNAV scale where actuation frequencies around or over $100Hz$ might be expected.

As any numerical model, the aeroelastic framework has to be, at some point, validated. Therefore numerous experimental studies, both in a liquid medium or in air, providing data for qualitative and

quantitative comparison have been reviewed. The majority of the studies are however made in liquid where the aerodynamic forces are considerably larger than the structural forces, perfect for the validation of a rigid wing (Sane and Dickinson [2002]) or moderately flexible wing (Heathcote et al. [2004, 2008]), and where the actuation frequency are limited to a few Hz. Experiments in air are more complicated as the actuation frequency increases, for example up to $40Hz$ in Wu et al. [2011] which is one of the highest frequencies reported. Most do not even considered the case of resonant wing, except Wu et al. [2011] where the resonant frequencies are around $20Hz$. Therefore to validate the framework for FWNAV applications such as the OVMI, a novel database that accounts for resonance, high-frequency ($\geq 100Hz$) and large deflection is needed to back the framework and its applications.

In a nutshell, an aeroelastic framework for the preliminary design stages of a FWNAV is not yet available especially for resonant design. An approach coupling a FEM solver to an aerodynamic model of insect flight is sound given its applications, evaluating quickly the performance of a wing and eventually iteratively. For validation purpose, a dedicated experimental database is also required for high-frequency resonant wings under large deflection.

Chapter 2

Definition of an aerodynamic model of flapping flight compatible with a bidirectional flexible approach

Contents

As reviewed in the chapter 1.2.2, the phenomena encountered and generated by the insect flight are numerous and still need some more researches to get a comprehensive understanding of how insects exploit so perfectly each mechanism. This objective is beyond the goal of this thesis, but still research and engineering can be started based on our current knowledge to size a FWNAV. At the early design stage, whereby only a rough estimation of the amount of aerodynamic forces is needed, aerodynamic models offer an attractive and interesting alternative to CFD mainly by simplifying their computation. Within these models, the wing deformation throughout the strokes is handled either by assuming a rigid wing or a flexible wing, in the spanwise and eventually in the chordwise direction, depending on the envisioned application. As the main goal of the aeroelastic framework is to assist in the design of a resonant FWNAV, it is expected that the deformation of the wing, dictated by the mode-shape, plays a critical role in the generation of aerodynamic forces and even more so in the case of flexible resonant wing as both bending and torsion have to be attained. Thus any aerodynamic model, that will be later on incorporated in the aeroelastic framework, has to take those local deformations into account both in the spanwise and in the chordwise direction, i.e. accounting for the full wing flexibility.

In order to appreciate the meaning of a "bidirectional flexible approach", a proper definition and description of its benefits when compared to the simplest rigid or unidirectional approaches is first discussed in this chapter. With these aspects in mind, the major aerodynamic models reviewed in the chapter 1.3.2 are once again scrutinized versus both the requirements of the bidirectional flexible approach and of a preliminary design tool in order to select a robust, simple and efficient aerodynamic model of the insect flight. Finally, the selected model is formulated in terms of local deformations in order to prepare its integration within the finite element solver that is used to model the wing structure and its response to various loads.

2.1 Definition and benefits of a bidirectional flexible approach

An usual method to model the aerodynamics forces generated by a wing with varying velocity and angles of attack along its span, like a propeller or a flapping wing, is the blade-element method. As illustrated in the figure 2.1(a), the wing is stripped in a finite amount of blades, whereby the aerodynamic forces are computed on each blade assuming a 2D flow and using the blade kinematics and geometry (velocity, acceleration, span, chord, etc.). A side effect of this method is that 3D-phenomena resulting from a spanwise flow cannot be properly modeled such as the leading edge vortex or the tip vortex. Nevertheless the method has proven itself to be highly satisfactory for a number of experimental and numerical cases as seen in the chapter 1.3.2. This method is therefore also considered in the aeroelastic framework for computing the aerodynamic forces.

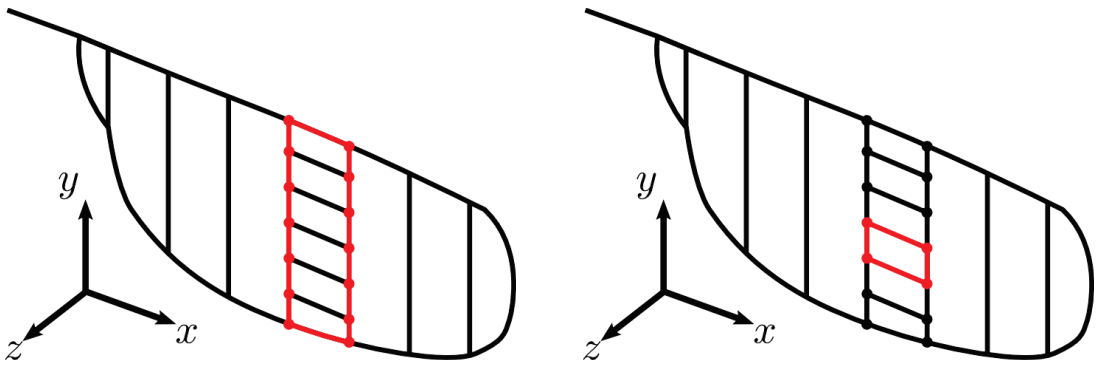

(a) Rigid or unidirectional flexible approach (b) Bidirectional approach

Figure 2.1: Principles of the unidirectional vs the bidirectional flexible approach within the blade-element method. In the rigid unidirectional approach, the wing deformation is either not taken into account (rigid) or only along the spanwise direction (unidirectional) and thus any chordwise deformation is either averaged or prescribed by the aerodynamic model. In the bidirectional flexible approach, both the spanwise and chordwise deformation are taken into account by the aerodynamic model.

Within the blade-element method based aerodynamic model, two categories are distinguished: the one assuming a rigid or unidirectional flexible approach, e.g. Sane and Dickinson [2002] or Ansari et al. [2006a], and the one using bidirectional flexible approach such as Singh [2006] or Gogulapati [2011]. In the former, as illustrated in the figure 2.1(a), the aerodynamic model uses the kinematics information, either prescribed or computed, of each blade but the effect of chordwise deformation is not taken into account as each blade is assumed to be rigid along its chord. On the contrary, a bidirectional flexible model considers also the effects of chordwise deformation as the aerodynamic forces are computed using a chordwise discretization, as seen in the figure 2.1(b), and their associated local information in terms of kinematics or structural shape. By taking the chordwise flexibility into account, these aerodynamic models capture several issues that may affect

strongly the aerodynamic forces such as: computation on real blade profile, change in the local AOA and in the effective AOA due to the local velocities, difference in terms of acceleration within the blade, position of the shedding vortices, relative position of the wake against the wing. So to sum up, the bidirectional approach offers a lot of advantages in terms of characterization of the flow but at the cost of a slightly more complicated model and implementation as chordwise averaged values cannot be used anymore.

Since in the aeroelastic framework, the wing is discretized in both directions in order to compute the structural response, local kinematics and shape data are available making the bidirectional flexible approach an obvious choice for the aerodynamic model. Furthermore with the prospect of flexible resonant wing, a strong chordwise deformation is sought and a bidirectional flexible approach is thus mandatory in order to maximize the capability of our aeroelastic framework and its fidelity. The local information are, now on, denoted with the subscript i. For example, c_i will refer to the chord of an chordwise element or α_i to its AOA.

2.2 Selection of an appropriate model

The selection of an appropriate model has to be a compromise between the fidelity of the flow model, its robustness, its easiness of implementation, and the requirements imposed by a preliminary design tool i.e. to evaluate quickly and fairly the potential of a wing versus various performance items. Due to the limited technical support available with the commercial finite element solver used, a strong attention is paid to the easiness of implementation as our objective is to offer a first working and sufficiently robust framework that might, in future works, be completed and improved.

As seen in the previous section, an aerodynamic model handling a bidirectional flexible approach is sought. Within the numerical model reviewed in the section 1.3.2, only the models of Singh [2006] and of Gogulapati [2011] fall into this category. Both offer a reasonably accurate picture of the flow by featuring major difficulties in terms of aerodynamic modeling in their formulation: the leading edge vortex and the shed wake. Their formulation requires a number of integrals and derivatives in time and space in addition to intensive matrix computation that, in the end, influences strongly the computation time and load. This is even more true in the case of the model of Gogulapati [2011] where the convection of the wake is taken into account through a computation-intensive convection routine. Furthermore the integration and derivation mathematical operators within the finite element solver, used as the kernel of the proposed aeroelastic framework, are not so practical and convenient to use. The implementation and debugging can thus be expected to be quite long and laborious. So as the main criteria for the selection of the aerodynamic model is its practicality, its simplicity, and its ease of implementation, both models are discarded, even if their flow description are very satisfactory.

Thus a new model accounting for the bidirectional flexible approach has to be formulated. When looking at the model developed for rigid or unidirectional flexible approach, the quasi-steady semi-empirical model of Sane and Dickinson [2002] seems to be quite promising with respect to its simplicity and accuracy with experimental data. The computation on each blade is limited to a set of very simple equations depending on a few kinematics and geometric parameters which also limit drastically its computational load. These advantages are a good starting point for a straightforward and efficient model of flapping wing adapted to a bidirectional flexible approach and complying with the requirements of a preliminary design tool in terms of speed and accuracy.

2.3 Adaptation of the Sane and Dickinson [2002] model to a bidirectional flexible approach

As reviewed in the section 1.3.2, the model of Sane and Dickinson [2002] is decomposed in four components: the translational forces, the added mass forces, the rotational forces, and the wake-capture forces. However the last component has proved itself to be discarded by later authors due to its non-physicality, as seen in the section 1.3.2. So only the three first components remain of interest in the aerodynamic model and in its adaptation to a bidirectional flexible approach.

2.3.1 Presentation of the Sane and Dickinson [2002] model and discussion on its adaptation

Using the Robofly experiments, Sane and Dickinson [2002] formulate a blade-element method based on the quasi-steady assumption enabling the calculation of the aerodynamic forces generated by a flapping wing using kinematics and geometric parameters, as illustrated in the figure 2.2.

In their case, the wing motion was prescribed which enables the determination of some coefficients in the model and a close match between modeling and experiments. Given their kinematics and decomposition, the main forces are the translational forces accounting for the majority followed by the added-mass and rotational forces of almost equal contribution but with the added-mass forces delayed. Each component of the model is briefly introduced in order to point out how the bidirectional flexible approach might be introduced.

It has to be noted that the kinematics parameters in their approach are U_t the translational wing tip velocity, ϕ the flapping angle, and α the morphological angle of attack.

2.3.1.1 Translational forces

First, the translational forces are given for each blade by the equation 2.1:

$$F_{trans} = \frac{\rho S U_t^2 \hat{r_2}^2(S)}{2} \left[C_L^2(\alpha) + C_D^2(\alpha)\right]^{1/2} \tag{2.1}$$

where ρ is the fluid density, S is the projected surface area of the wing, $\hat{r_2}^2(S)$[1] is the non-dimensional second moment of wing area as defined by Ellington [1984b], and where C_L and C_D are respectively the lift and drag coefficients found by the experiments of Dickinson et al. [1999], which include the enhancement effect of the leading edge vortex both on the lift and on the drag. They are reminded below in the equations 2.2 and 2.3.

$$C_L = 0.225 + 1.58 \sin(2.13\alpha - 7.2) \tag{2.2}$$

$$C_D = 1.92 + 1.55 \cos(2.04\alpha - 9.82) \tag{2.3}$$

To introduce the bidirectional flexible approach, the idea is here to introduce the local chordwise deformation by computing the force on each chordwise element using their local velocity and AOA and by assuming that each chordwise element is rigid and has its own free-stream velocity. Furthermore the local velocities induce a slight shift in the AOA, as each chordwise element is subjected to a vertical motion, that is considered through the effective AOA α'.

[1] $\hat{r_2}^2(S) = \int_0^1 \hat{c}\hat{r}^2 \, \mathrm{d}\hat{r}$ with $\hat{r}$ being the ratio of the radial position along the wing r to the wing length R and with $\hat{c}$ being the ratio of the wing chord c to the mean chord $\bar{c}$.

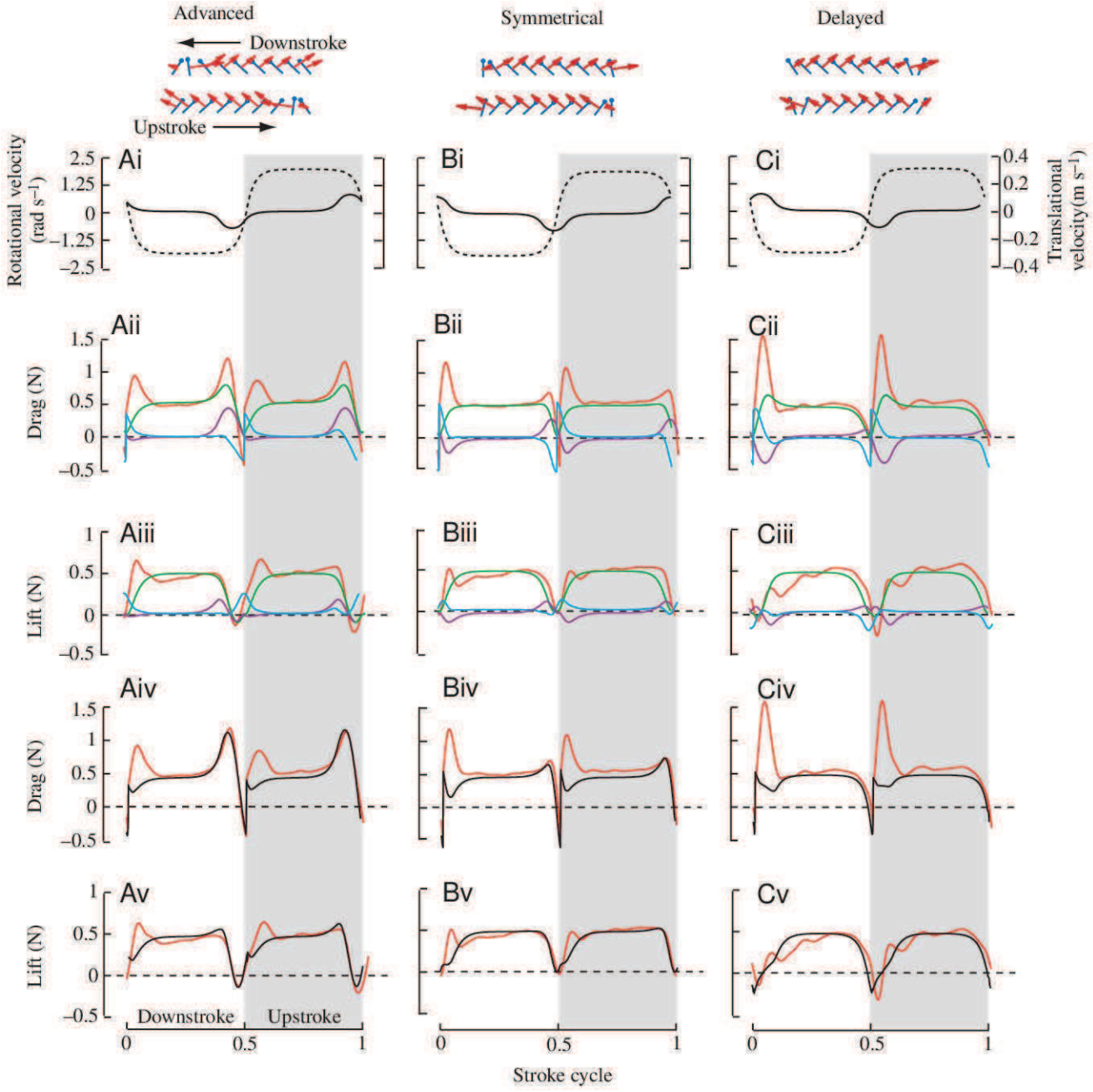

Figure 2.2: Aerodynamic forces measured, in red, and computed, in black, by Sane and Dickinson [2002] using the Robofly apparatus. The computed forces are split into translational forces, in green, rotational forces, in purple, and the added-mass forces in blue. Three different wing reversal timings are presented from left to right: advanced, symmetrical and delayed. Note that the drag is here conventionally taken as opposed to the wing motion, what makes sense for rigid wings.

2.3.1.2 Added mass forces

Second, the added mass forces are given for each blade by the equation 2.4:

$$F_{added} = \rho\frac{\pi}{4}R^2\bar{c}^2\left(\ddot{\phi}\sin\alpha + \dot{\phi}\dot{\alpha}\cos\alpha\right)\int_0^1 \hat{r}\hat{c}^2\left(\hat{r}\right)\,\mathrm{d}\hat{r} - \ddot{\alpha}\rho\frac{\pi}{16}\bar{c}^3R\int_0^1 \hat{c}^2\left(\hat{r}\right)\,\mathrm{d}\hat{r} \tag{2.4}$$

where ρ is the fluid density, R is the wing length, $\hat{r}$ is the non-dimensional radial position along the wing, $\hat{c}\left(\hat{r}\right)$ is the non-dimensional chord length as defined by Ellington [1984b].

It is essential to understand that the first integral depicts the aerodynamic forces opposing any normal acceleration of the wing whereas the second integral models the ones opposing any angular acceleration of the wing, as defined originally by Sedov [1965]. The former term can easily incorporate local chordwise information, whereas the latter is simply put on hold as any angular acceleration of the wing, whatever its rotation axis, should be reflected automatically in the local approach by a higher normal acceleration for elements distant from the rotation axis.

2.3.1.3 Rotational forces

Finally, the rotational forces are given for each blade by the equation 2.5:

$$F_{rot} = C_{rot,exp}\rho U_t\dot{\alpha}\bar{c}^2R\int_0^1 \hat{r}\hat{c}^2\left(\hat{r}\right)\,\mathrm{d}\hat{r} \tag{2.5}$$

where $C_{rot,exp}$ is the rotational force coefficient which is tabulated against various values of angular velocity $\dot{\alpha}$ and rotation axis. This term models the extra circulation generated by an airfoil rotating while translating that adds or subtracts to the one generated by the overall translational motion. But it is definitely depending on the blade overall shape, kinematics and location of the rotation axis.

For sake of simplification, the rotational forces are not yet considered within the proposed model. However the effects of rotational velocity should partly be modeled in the bidirectional flexible approach through the translational formulation. Indeed a rotational velocity of the blade will reflect into a local higher translational velocity and thus higher forces.

To sum up, inspired by the Sane and Dickinson [2002] model, a bidirectional flexible approach can reasonably be formulated by incorporating local chordwise information into their equations. Only two components of the original, the translational and the added mass forces, are reformulated as it is assumed that introducing the chordwise discretization tends to extend slightly their capabilities.

2.3.2 Formulation of the translational forces

From the formulation given by Sane and Dickinson [2002], the introduction of the bidirectional flexible approach is almost straightforward. As illustrated in the figure 2.3, accounting for the effective AOA α'_i, induced by the vertical velocity $\dot{y}_i$, can dramatically change the performance of the wing as the angle seen by the airfoil is either increased or decreased when compared to the purely geometrical one α_i. Similarly the free-stream velocity, further denoted as $V_{\mathrm{inf},i}$, is also increased as it is now the vector addition of the horizontal velocity $\dot{z}_i$ and of the vertical velocity $\dot{y}_i$ of the element.

Within the formulation of the translational forces, the stroke periodicity has to be accounted for the free-stream velocity $V_{\mathrm{inf},i}$. Indeed when the wing is flapped back and forth, the direction of the free-stream velocity is periodically changed and the squared expression of the velocity can not anymore be held with respect to a fixed coordinate system. This is easily solved by multiplying the expression of the free-stream velocity by its absolute value. Thus the translational forces are computed for a chordwise element along its

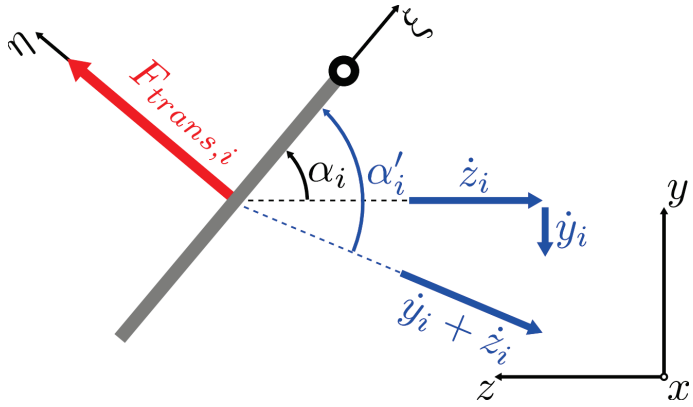

Figure 2.3: Translational forces on a sectional view of a chordwise element. Using the local velocities of the element $\dot{y}_i$ and $\dot{z}_i$, the translational force $F_{trans,i}$ is computed using the effective AOA α'_i along the element normal η. The empty black circle represents the leading edge side of the element.

normal η as:

$$F_{trans,i} = \frac{1}{2}\rho c_i s_i \left[C_L\left(\alpha'_i\right)^2 + C_D\left(\alpha'_i\right)^2\right]^{1/2} V_{\text{inf},i}\,|V_{\text{inf},i}| \tag{2.6}$$
$$\text{with} \quad \alpha'_i = \alpha_i - atan\left(\frac{\dot{y}_i}{\dot{z}_i}\right)$$
$$\text{and} \quad V_{\text{inf},i} = \vec{\dot{y}_i} + \vec{\dot{z}_i}$$

where ρ is the density of the surrounding fluid, c_i is the chord of the element, s_i is its span, α_i is its AOA, C_L and C_D the lift and drag coefficients of Dickinson et al. [1999].

2.3.3 Formulation of the added mass forces

The formulation of Sane and Dickinson [2002] originates from the one given by Sedov [1965] for the case of a flat plate rotating at one-quarter chord length from the leading edge under normal and angular acceleration. Its adaptation to a bidirectional approach is somehow a bit trickier than the translational forces. As the local information are used and for sake of simplicity, the formulation is written for the case of a two-dimensional flat plate rotating at mid-chord on each chordwise element. The formulation of Sedov [1965] gives the tangential F_ξ and the normal F_η forces generated by the motion of an airfoil in a fluid. Given that $\ddot{\eta}$ and $\dot{\alpha}$ are the normal and angular velocities respectively, the formulation of F_ξ and F_η for an airfoil of chord C and span s is then:

$$F_\xi = \lambda_\eta \dot{\eta}\dot{\alpha} \tag{2.7}$$
$$F_\eta = -\lambda_\eta \ddot{\eta} \tag{2.8}$$
$$\text{with} \quad \lambda_\eta = \rho\pi\frac{C^2}{4}s$$

In our case, only the terms proportional to accelerations are of interest and thus the tangential component F_ξ is discarded as it is a product of two velocities modeling a Magnus effect[2] which is not physical on a flat

[2]The Magnus effect is that commonly observed and striking effect in which a spinning ball (or cylinder) curves away from its principal flight path. The spinning ball spins a boundary layer of air that clings to its surface as it travels along. On one side of the ball, the boundary layer of air collides with the air passing by. The collision causes the air to decelerate, creating a high-pressure area. On the opposing side, the boundary layer is moving in the same direction as the air passing by, so there is no collision and the air collectively moves faster. This sets up a low-pressure area. The pressure differential, high on one side and low on the other, creates a lift force: the Magnus force. However its action is limited to object without a streamlined shape. (Source: `http://www.humankinetics.com/excerpts/excerpts/magnus-effect-`)

plate. Thus only the expression of F_η is going to be modified to take into account the bidirectional flexible approach and the chordwise element information, as illustrated in the figure 2.4.

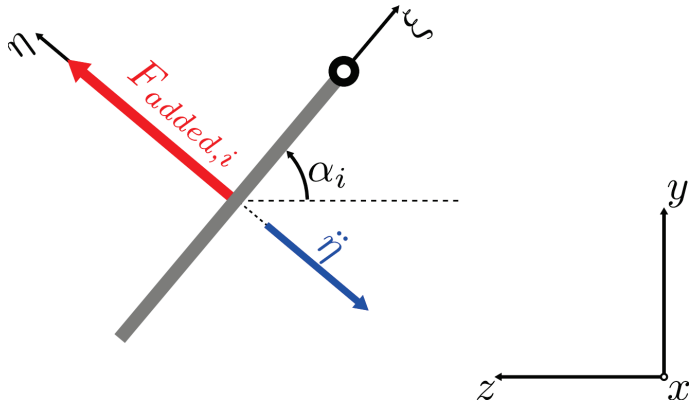

Figure 2.4: Added mass forces on a sectional view of a chordwise element. Using the local normal acceleration of the element $\ddot{\eta}_i$, the added mass force $F_{added,i}$ is directed along the element normal η and always opposed to the acceleration. The empty black circle represents the leading edge side of the element.

This modification is yet still not straightforward as some physical considerations regarding the discretization of the forces are mandatory. First, in the equation 2.8, C is the chord of the plate and λ_η models the volume of fluid influenced by the normal acceleration of the airfoil which is assimilated to a cylinder of diameter C and length s. Therefore, if C is substitute directly by c_i, the sum of all the tiny cylinder of diameter c_i will not be equal to the bigger cylinder of diameter C, as illustrated in the figure 2.5. Therefore the coefficient λ_η has to be pondered in order to find a trade-off between the volume of fluids influenced locally by the cylinder c_i, and the overall volume of the blade cylinder C_{blade}. Second, some chordwise elements have a greater acceleration, typically the ones closer to the trailing edge, and so should generate more added mass forces. This local acceleration has to be accounted in the formulation by finding a trade-off between the local acceleration and the overall acceleration of the blade, used in the equation 2.8.

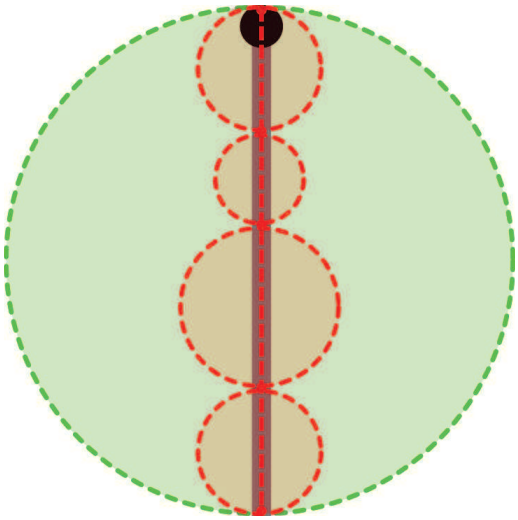

Figure 2.5: Problematic of trade-off between local formulation and global effect. The green area is the volume of fluid accelerated by the unidirectional flexible approach, while the red one is the one using a straightforward local formulation.

Therefore the bidirectional formulation for the added mass forces results in the following equation:

$$F_{added,i} = -\lambda_{\eta,i}\frac{\ddot{\eta}_i}{N_{FE}} \quad \text{with} \quad \lambda_{\eta,i} = \rho\pi\frac{c_i C_{blade}}{4}s_i \tag{2.9}$$

where N_{FE} is the number of chordwise elements in the blade, C_{blade} is the mean chord of the blade. The other notations are the same as for the translational formulation. To check our trade-off between local and global effects, one can take the case of a single chord element ($n = 1$ and $c_i = C_{blade}$) whereby the equation 2.8 is found again. This formulation is not physical from an aerodynamic point of view but it is just a local reformulation and adaptation of the physically correct equations defined by Sane and Dickinson [2002] providing simple equations for aerodynamic forces.

2.4 Adaptation of the Sane and Dickinson [2002] model to a unidirectional flexible approach

To check if this formulation is coherent and gives results in line with the original one of Sane and Dickinson [2002], a unidirectional approach is also derived. The formulation takes up the one given by Sane and Dickinson [2002] but stays at the blade level by using chordwise averaged data, denoted by the $\overline{\ }$ symbol.

2.4.1 Formulation of the translational forces

To compute the translational forces on a blade element, the equation 2.6 is taken back and adapted to the unidirectional flexible approach by just introducing chordwise averaged data. The resulting equation is:

$$F_{trans} = \frac{1}{2}\rho C_{blade}s_{blade}\left[C_L\left(\overline{\alpha'}\right)^2 + C_D\left(\overline{\alpha'}\right)^2\right]^{1/2}\overline{V_{\text{inf}}}\left|\overline{V_{\text{inf}}}\right| \tag{2.10}$$

$$\text{with} \quad \overline{\alpha'} = \bar{\alpha} - atan\left(\frac{\bar{\dot{y}}}{\bar{\dot{z}}}\right)$$

$$\text{and} \quad \overline{V_{\text{inf}}} = \sqrt{\bar{\dot{y}} + \bar{\dot{z}}}\cdot sgn\left(\bar{\dot{z}}\right)$$

2.4.2 Formulation of the added mass forces

To compute the added mass forces on a blade element, the original equation from Sedov [1965] and the derived equation 2.4 from Sane and Dickinson [2002] are taken back and adapted to chordwise averaged data by dropping the integration as follow and by assuming a rotation axis at ΔC from the blade mid-chord. The resulting equation is:

$$F_{added} = \lambda\bar{\ddot{z}} + \lambda\Delta C\bar{\ddot{\alpha}} \quad \text{with} \quad \lambda = \rho\frac{\pi}{4}C_{blade}^2 s_{blade} \tag{2.11}$$

2.4.3 Formulation of the rotational forces

To compute the rotational forces on a blade element, the original equation from Sane and Dickinson [2002] is taken up. Instead of using the tabulation of the coefficient $C_{rot,exp}$ versus experimental data, the theoretical coefficient C_{rot} is introduced using the non-dimensional location of the rotation axis $\Delta\widehat{C}$. The resulting equation is:

$$F_{rot} = C_{rot}\rho\bar{\dot{z}}\bar{\dot{\alpha}}C_{blade}^2 s_{blade} \quad \text{with} \quad C_{rot} = \pi\left(0.75 - \Delta\widehat{C}\right) \tag{2.12}$$

2.5 Conclusion on the definition of the aerodynamic model

Two new aerodynamic models have been defined, one relying on a bidirectional flexible approach and the other on a unidirectional approach. Both are derived the aerodynamic model from Sane and Dickinson [2002] with the later being the closest, by leaving out the blade integration. The resulting equations for the former, although more complicated in principle, are still fairly simple with dependency to the local chord c_i, local span s_i, local kinematics and geometric data, and should account for some major components of the aerodynamic phenomena identified on insects making it appropriate for this study. The latter offers even simpler equations with dependency only to chordwise averaged kinematics and geometric data but is developed primarily to verify that the implementation of the bidirectional model is coherent. As required, the computation of the aerodynamic forces might be rather fast as the finite element solver is providing all the necessary data on each chordwise element while also easing its implementation.

Combining both aerodynamic models to a finite element solver constitutes the kernel of the proposed aeroelastic framework, with the bidirectional flexible one preferred for detailed analysis and the unidirectional one for basic analysis.

Chapter 3

Development of an aeroelastic framework of flapping flight using the finite-element method

Contents

To solve an aeroelastic problem, a wing can be seen as a structure in motion with external forces acting on it and thus the classical motion equation of an N degree-of-freedom (DOF) system can be written under the form:

$$\mathbf{M}\ddot{q} + \mathbf{C}\dot{q} + \mathbf{K}q = F(t) \tag{3.1}$$

where $\mathbf{M}$, $\mathbf{C}$, $\mathbf{K}$ are the mass, the viscous damping, and the stiffness matrix of the structure respectively, $F(t)$ is the external force vector, and q is the displacement vector of the structure. In the case of steady-state aeroelasticity, such as the one made on aircraft in cruise flight, the time dependency can be dropped and so are the matrices $\mathbf{M}$ and $\mathbf{C}$. In dynamic analysis such as the one made for flutter (resonance of an aircraft wing) or for flapping wing, the time-dependency is primordial, as the structural response is a trade-off between the inertial, elastic, and aerodynamic forces.

To solve this equation, the usual approach in structural mechanics is to use the finite element method (FEM), whereby a continuous domain, in our case the structure, is discretized into a set of discrete sub-domains, the finite elements (FE). The global matrices $\mathbf{M}$, $\mathbf{C}$, and $\mathbf{K}$ are then defined by assembling the local matrix of the FEs together, whereby each one is defined by geometric and material properties. Note that in the case of geometric nonlinearity, such as in large displacement, the stiffness matrix $\mathbf{K}$ has a dependency

to the structural displacement q. The resolution of the equation 3.1 is usually solved automatically, using standard numerical schemes, once the external force vector $F(t)$ is known. This vector is, in our case, the sum of the gravity component, which is obviously known, and of the aerodynamic components, which have to be calculated depending on the wing shape or/and the flow history. To compute them, CFD or an aerodynamic model can be introduced. As seen in the previous chapter, the latter is used in this thesis and the external force vector $F(t)$ can be rewritten to highlight its dependency to the kinematics variable q within the aerodynamic model as:

$$\mathbf{M}\ddot{q} + \mathbf{C}\dot{q} + \mathbf{K}(q)q = F(t, q, \dot{q}, \ddot{q}) \tag{3.2}$$

However only the bidirectional aerodynamic model enables aeroelastic studies, i.e. with coupling, as the unidirectional aerodynamic loads can not be transferred individually to the FEs. Although various FEM-solvers exist, the aeroelastic framework is developed within the commercial software *Ansys* (Ansys Inc [2007]), available at the IEMN, as some previous analysis within the OVMI project (Dargent et al. [2009]; Dargent [2010]) were already done, as each command is quite well documented, and as it supports scripting and bash mode. Furthermore *Ansys* is very well suited for large displacement computation as demonstrated by Fotouhi [2007]. Thus the approach will have some *Ansys* specific contents but can be extended quite easily to other solvers.

This chapter is organized along the resolution of the equation 3.2. First, the discretization of the structure in FEs is described in order to determine the **M**, **C**, **K** matrices. Second, the determination of the aerodynamic component of $F(t, q, \dot{q}, \ddot{q})$ i.e. the integration of the aerodynamic models of the chapter 2 within *Ansys* are discussed prior to the coupling procedure. Finally, an overview of the complete aeroelastic framework is presented.

3.1 Modeling of the wing structure

To model properly the wing, the FEM offers an attractive solution to determine the **M**, **C**, **K** matrices. These matrices have to be carefully defined as the structural response of the wing to aerodynamic loads will depend on them as well as its resonant behavior. The determination of **M** and **K** is quite easy as they depend only on material and geometric properties and comes downto selecting the appropriate FE within the software library. Unfortunately the determination of **C** is not so straightforward and the Rayleigh method is used in *Ansys* to formulate this structural damping matrix.

3.1.1 Selecting the finite elements

In the wing structure of insects, two major and distinctive components are noted: the vein and the membrane patterns. As illustrated by the figure 3.1, insect wings exhibit various vein and membrane patterns whose role and properties were quite intensively investigated ([Wootton, 1992; Kesel et al., 1998; Wootton et al., 2000; Smith et al., 2000; Herbert et al., 2000; Wootton et al., 2003; Combes and Daniel, 2003a,b; Ganguli et al., 2009; Sims et al., 2010]). The main conclusion of these studies is that the vein and membrane patterns enable a fine tuning of the torsional and bending moment of inertia of the wing as well as of its rigidity allowing its efficient flight, but also its morphological role like in the spreading of wing.

In the design of FWNAVs, the morphological role might be dropped out as it is of secondary importance when compared to its flight capability. Therefore the aeroelastic framework is focused strictly on the distribution of moments of inertia and rigidity from an aerodynamics point of view. As the design of FWNAVs is mainly drawn by bio-inspiration, the vein and membrane patterns are of interest and have to be modeled, with beam elements for vein and with shell elements for the membrane. From a mechanical point of view, membranes are more restrictive in terms of deformations as shells, but shell elements are

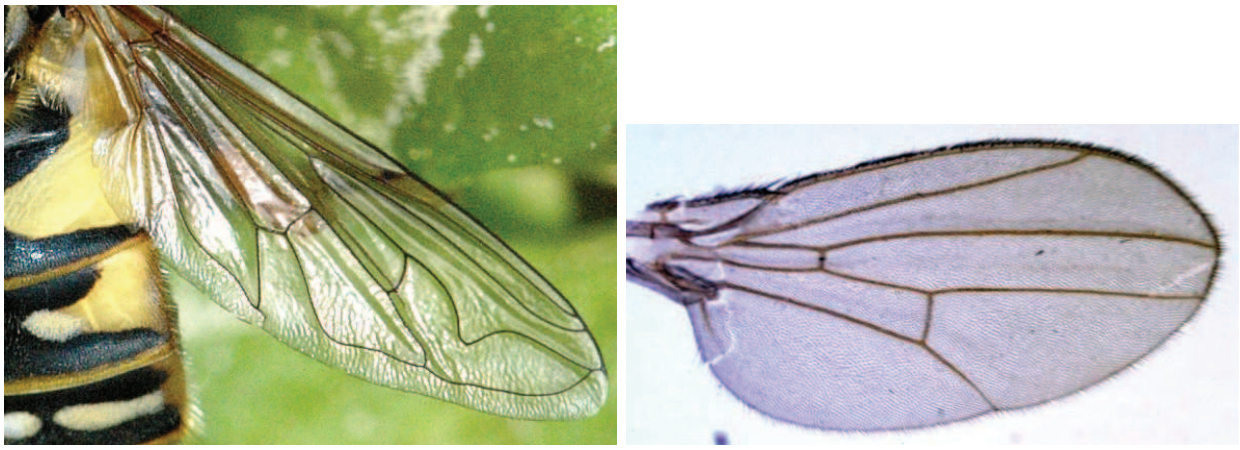

(a) Helophilus Pendulus (Lindsey [2004]) (b) Drosophila Melanogaster (Daily [2008])

Figure 3.1: Examples of vein and membrane patterns on insect wing.

more convenient in practice.

The requirements for those FEs are first, the number of DOFs available at each node as the aerodynamic model requires 6 DOFs per node element (3 translations and 3 rotations), and second, their compatibility with large deflection computation.

3.1.1.1 Beam element

To model the vein pattern of the wing, the *BEAM4* element is chosen in *Ansys* which is a 3D elastic beam element defined by two nodes at each extremity. As required, it offers large deflection capability and has 6 DOFs per node. To fully define the element, three material properties are needed, the Young's modulus E, the Poisson's ratio ν and the density ρ, as well as various section characteristics such as its surface and diverse moments of inertia. These last characteristics are dictated by the shape of the beam, either cylindrical, rectangular or even more complex. For sake of simplification, a self-centered rectangular section is here by default handled. All the necessary properties for a *BEAM4* element are summed up in the table 3.1.

Table 3.1: Material and section properties necessary for the definition of a *BEAM4* element in *Ansys* for a rectangular section of thickness t and width w.

Name	Description	Unit	Definition
E	Young's modulus	$[Pa]$	-
ρ	Density	$[kg.m^{-3}]$	-
ν	Poisson's ratio	$[-]$	-
A	Cross-sectional area	$[m^2]$	tw
I_t	Area moment of inertia along the thickness of the section	$[m^4]$	$\frac{tw^3}{12}$
I_w	Area moment of inertia along the width of the section	$[m^4]$	$\frac{wt^3}{12}$
t	Thickness of the beam section	$[m]$	-
w	Width of the beam section	$[m]$	-
J	Torsional moment of inertia	$[m^4]$	$0.333t^3w$ as $\frac{t}{w} < 10$

3.1.1.2 Shell element

To model the membrane pattern of the wing, the *SHELL93* element is chosen in *Ansys* which is a 3D structural shell element defined by eight nodes, four corners plus four mid-nodes. As required, it offers large deflection capability as well as 6 DOFs per node and is particularly well suited to model curvature, an useful feature in the case of flexible flapping wing. To define the element, along the same material properties as for the *BEAM4* element, only the shell thickness is mandatory. All the necessary properties for the *SHELL93* element are summed up in the table 3.2.

Table 3.2: Material and section properties necessary for the definition of a *SHELL93* element in *Ansys* of thickness t.

Name	Description	Unit
E	Young's modulus	$[Pa]$
ρ	Density	$[kg.m^{-3}]$
ν	Poisson's ratio	$[-]$
t	Thickness of the membrane	$[m]$

Both elements offer also stress stiffening and added mass capabilities which are by default turn off, as the data necessary to set these capabilities are not known either from know-how or from charts. Also they are mainly optional parameters to model even more closely experimental behaviors in combination with to more dominant parameters such as the Young modulus E and the structural damping.

3.1.2 Integrating the structural damping

In equation 3.2, only the $\mathbf{C}$ matrix is left unknown in the structural term and has to be determined. This matrix represents the structural damping of the wing and its expression is problematic for the equation resolution as if solved directly the complexity of the numerical scheme might increased. Nonetheless several solutions have been addressed to alleviate this bottleneck and the Rayleigh method is the one used within *Ansys*.

The Rayleigh method assumes that the damping matrix $\mathbf{C}$ is proportional to the mass matrix $\mathbf{M}$ and to the stiffness matrix $\mathbf{K}$ through two coefficients α and β as written in equation 3.3.

$$\mathbf{C} = \alpha\mathbf{M} + \beta\mathbf{K} \tag{3.3}$$

These coefficients α and β can be determined using the viscous damping ratio ζ_i defined for several modes as explained by Chowdhury and Dasgupta [2003]. Thus with at least two modes, the value of α and β is determined using first the equation 3.4 and then the equation 3.5 when the values of viscous damping ratio ζ_i are known for two eigenpulsation ω_i.

$$\beta = \frac{2\zeta_1\omega_1 - 2\zeta_2\omega_2}{\omega_1^2 - \omega_2^2} \tag{3.4}$$

$$\alpha = 2\zeta_1\omega_1 - \beta\omega_1^2 \tag{3.5}$$

The values of ζ_i and ω_i might be determined experimentally if an accurate model is needed or assessed from know-how otherwise.

Taking a look at the equation 3.2, only the right hand side of the equation is now left unknown with the external forces vector $F(t, q, \dot{q}, \ddot{q})$, which encompasses the contribution from gravity as well as from aerodynamic loads. The gravity is handled automatically by the FE solver which leaves only the aerodynamic contribution to be determined at each time step using the aerodynamic model defined in the chapter 2.4.

3.2 Integration of the bidirectional aerodynamic model

As described in the chapter 2.3, an aerodynamic model of flapping flight compatible with a bidirectional flexible approach has been developed. The resulting model consists of a set of two components, the translational and added mass forces, acting on the wing with the equation 2.6 and 2.9 respectively. Each equation uses local information from the chordwise element to compute along its normal, which is noted η in the figures 2.3 and 2.4, the associated aerodynamic forces.

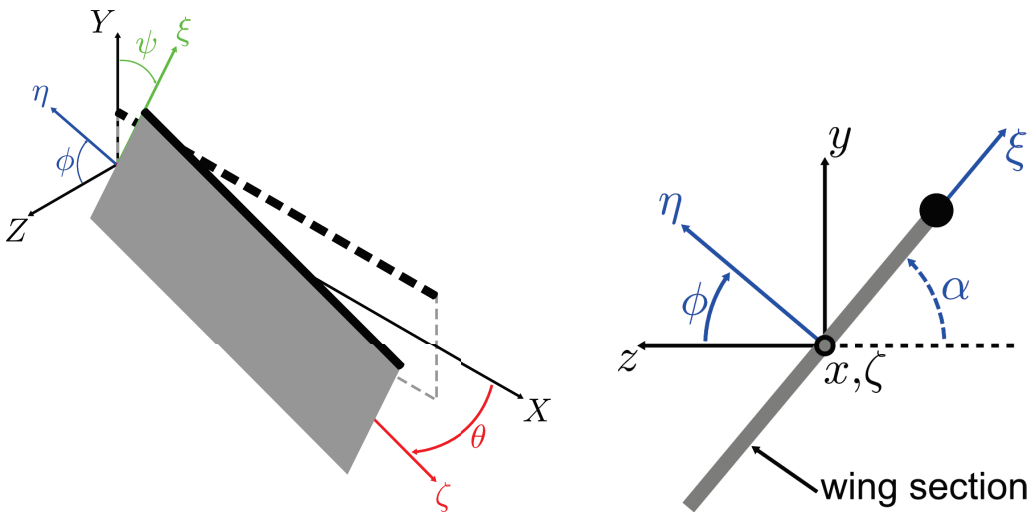

(a) Positioning of the local coordinate system vs the global one

(b) Local coordinates system on a wing section

Figure 3.2: The (X, Y, Z) system defines the global coordinates system used by the Finite-Element solver whereas the (ζ, ξ, η) is the local to each FE and used for the computation of its aerodynamic forces.

Unfortunately the kinematics data necessary for the computation are not defined in the local coordinate system (ζ,ξ,η) as illustrated in the figure 3.2. Instead the kinematics data are known in the global coordinate system (X,Y,Z) and thus have to be projected for each element in its local frame. To do so, Euler-angles are used. First, the kinematics data are subjected to a rotation around the Z-axis of angle ψ, being set to the mean Z-angle made by the chordwise element with its initial position, using the $\mathbf{Rot_{Z,i}}$ matrix defined in the equation 3.6. Second, a rotation around the resulting y-axis of angle θ, being set to the mean Y-angle made by the chordwise element with its initial position, is made using the $\mathbf{Rot_{Y,i}}$ matrix defined in equation 3.7.

$$\mathbf{Rot_{Z,i}} = \begin{bmatrix} \cos\psi & -\sin\psi & 0 \\ \sin\psi & \cos\psi & 0 \\ 0 & 0 & 1 \end{bmatrix} \tag{3.6}$$

$$\mathbf{Rot_{Y,i}} = \begin{bmatrix} \cos\theta & 0 & \sin\theta \\ 0 & 1 & 0 \\ -\sin\theta & 0 & \cos\theta \end{bmatrix} \tag{3.7}$$

At the end of both rotations, the kinematics are known in the (x,y,z) coordinate system but the aerodynamic forces are still computed in the (ζ,ξ,η) system while the mandatory kinematics information are expressed in either the same system or another depending on the component. In the case of added mass forces, as illustrated by the figure 2.4, the kinematics information needed is the normal acceleration $\ddot{\eta}$ which is easily retrieved by a rotation around the ζ-axis of angle ϕ, which is equal to the complementary geometrical AOA α_i i.e. the mean X-angle made by the chordwise element with its initial position, using the matrix $\mathbf{Rot_{X,i}}$ defined in equation 3.8.

$$\mathbf{Rot_{X,i}} = \begin{bmatrix} 1 & 0 & 0 \\ 0 & \cos\phi & -\sin\phi \\ 0 & \sin\phi & \cos\phi \end{bmatrix} \tag{3.8}$$

Unfortunately for the translational case, the forces are expressed in the (ζ,ξ,η) system but required the effective free-stream velocity, noted $\dot{y}+\dot{z}$ in the figure 2.3. Therefore an extra X-Rotation matrix $\mathbf{Rot_{X_{trans},i}}$, similar to the original $\mathbf{Rot_{X,i}}$ but with a different ϕ' angle which is equal to the effective AOA α_i' minus the geometrical AOA α_i, is necessary to retrieve the amplitude and direction of the free-stream-velocity.

When all aerodynamic components are computed and added in the (ζ,ξ,η) system, the resulting force vector is projected back to the (X,Y,Z) global coordinate system to ensure the correct computation of the wing structural response by the FE solver. To do so, the forces vector in (ζ,ξ,η) system is projected in the (X,Y,Z) system, by counter-rotating first around the ζ-axis, then the y-axis and finally the Z-axis using the inverse matrices of $\mathbf{Rot_{X,i}}$, $\mathbf{Rot_{Y,i}}$ and $\mathbf{Rot_{Z,i}}$. The complete inverse matrix for a finite element is given in the equation 3.9.

$$\mathbf{Rot_{Z,i}^{-1}Rot_{Y,i}^{-1}Rot_{X,i}^{-1}} = \begin{bmatrix} \cos\psi\cos\theta & \cos\psi\sin\theta\sin\phi+\sin\psi\cos\phi & -\cos\psi\sin\theta\cos\phi+\sin\psi\sin\phi \\ -\sin\psi\cos\theta & -\sin\psi\sin\theta\sin\phi+\cos\psi\cos\phi & \sin\psi\sin\theta\cos\phi+\cos\psi\sin\phi \\ \sin\theta & -\cos\theta\sin\phi & \cos\theta\cos\phi \end{bmatrix} \tag{3.9}$$

The whole procedure of projection forth and back is sum up in the figure 3.3, for the definition of each coordinate system, and in the figure 3.4 with a flowchart of the projections.

3.3 Coupling the aerodynamic forces with the structural response

Once the aerodynamic forces for each chordwise element are known, they are divided equally among the active nodes of each element without resorting to the interpolations functions of each element. The external force vector $F(t, q, \dot{q}, \ddot{q})$ is thus now completely defined and consequently the equation 3.2 is solved by the FE solver and thus gives rise to the aeroelastic framework.

At each time step, no sub-iteration is made between the structural response of the wing and the aerodynamic forces computation. Thus the coupling can be qualified as an explicit approach. Nonetheless the coupling is enhanced by the periodicity of the transient analysis as several strokes are computed in order to reach a steady-state response of the wing.

3.4 Integration of the unidirectional aerodynamic model

As mentioned in the chapter 2.4, an aerodynamic model compatible with an unidirectional flexible approach has been also defined. This model is not used to compute any aeroelastic response of wing, as it is, for now on, too complicated to distribute judiciously the forces between each node. However this model will serve primarily as a baseline to verify the implementation of the bidirectional aerodynamic model, as detailed in the chapter 4.2. Another application is to evaluate even more quickly the performance of a wing, as detailed in the chapter 6.2. Its computation will run either in parallel to the bidirectional or independently but without coupling.

For this model, no rotation matrices are used to compute the kinematics variables as quick calculations are seek in order to lighten further the computation load. Indeed, the kinematics variable are taken at each time-step directly in the (X,Y,Z) system on each element of the blade and are averaged.

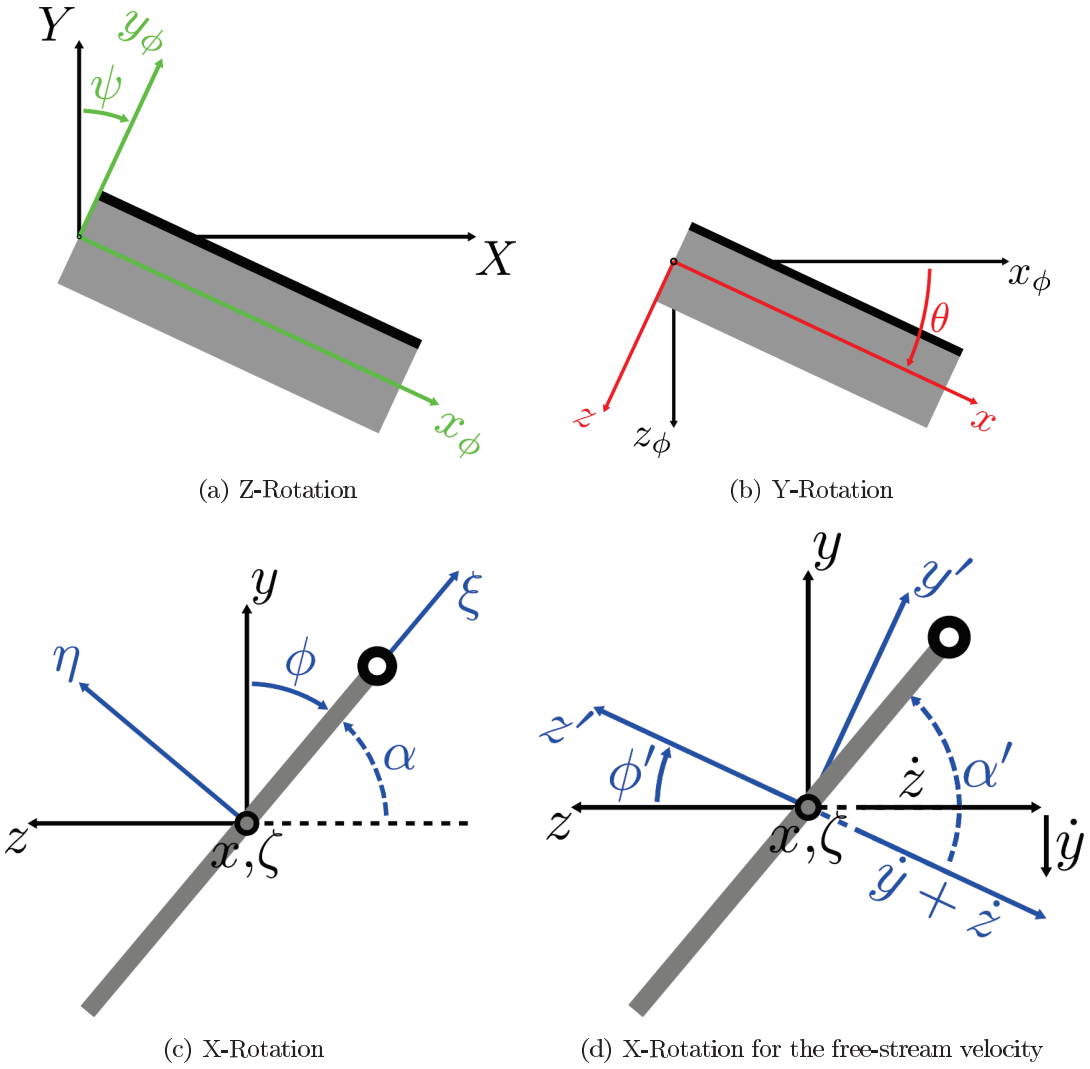

(a) Z-Rotation (b) Y-Rotation

(c) X-Rotation (d) X-Rotation for the free-stream velocity

Figure 3.3: Definition of the various coordinates systems and theirs rotation angles to switch from one to another.

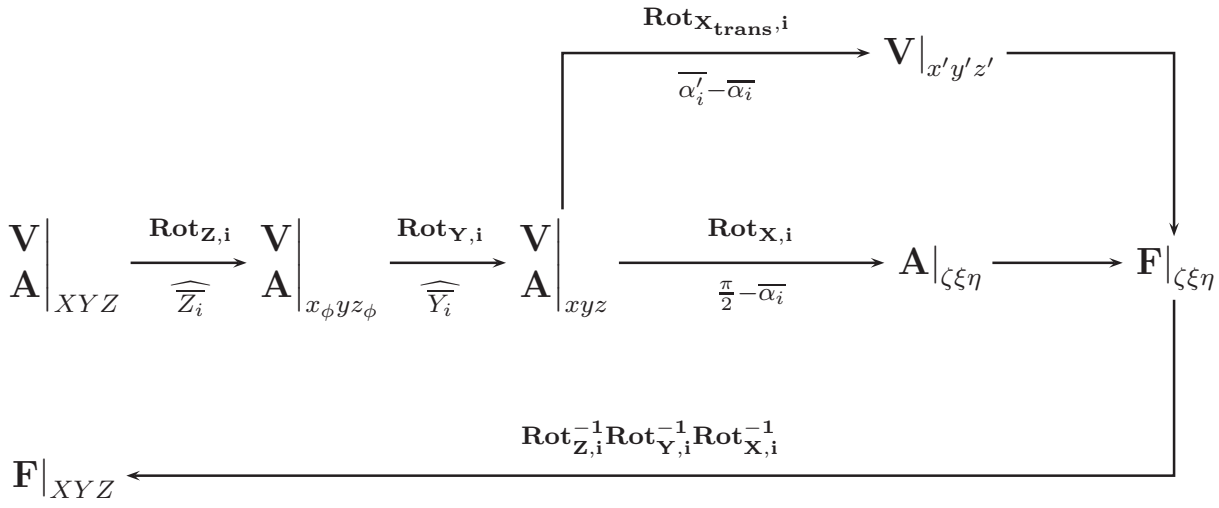

Figure 3.4: Flowchart of the kinematics projections made for the computation of the aerodynamic forces vector according to the bidirectional model and of its projection back to the main coordinate system of *Ansys*. This procedure is repeated on each chordwise element at each time step.

Similarly the geometric data are retrieved at the beginning of the calculation process. The data are saved to be post-processed later by using the equations of the chapter 2.4 and by summing along the blades at each time step.

3.5 Overview of the aeroelastic framework

As explained in the previous sections, the aeroelastic framework solves the equation 3.2 for various wing geometry and/or actuation motion in order to quickly but fairly evaluate diverse performance items such as the mean lift or the peak-to-peak actuation power. before stepping more deeply into the framework, it is important to define properly the drag and the lift that will be outputted as performance items.

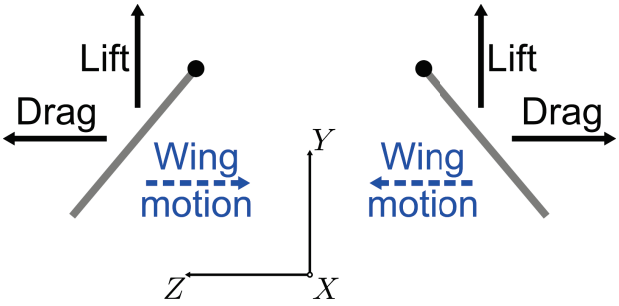

Figure 3.5: Definition of the drag and the lift versus the wing motion. The drag is taken positively in the Z direction.

The drag is defined as the aerodynamic forces acting on the wing in the direction of the relative flow velocity. However as the evaluated wings are most probably flexible, each portion of the wing is not submitted simultaneously to the same motion which makes it quite problematic to define a proper sign for the drag. Therefore the drag is, in this work, defined as positive in the Z direction. Thus a negative drag is here not a thrust force, but the drag resulting from a portion of wing moving towards the positive Z (downstroke). More simply, the lift is defined as the aerodynamic forces acting on the wing in the vertical direction opposed to the gravity. The figure 3.5 summarizes these definitions.

The complete aeroelastic computation is divided in three steps in the framework: the generation of the wing geometry and mesh, the computation of the resonant frequencies, and finally the simulation of the aeroelastic response. The overall flowchart of the framework is given in the figure 3.6. Note that the framework is originally intended to assist the design of a resonant FWNAV which requires the computation of the resonant frequencies. Non-resonant design can also be considered which makes then the modal analysis optional.

Before getting into the details of each step, a quick explanation of the workflow is provided. With a wing geometry inputted, the aeroelastic framework starts by modeling the wing and by generating the mesh. Once defined, analysis to determine the wing mass, for the non-dimensionalization of variables in the post-processing, the wing blades, for the unidirectional aerodynamic model, and the modal analysis, which computes the resonant frequencies of the wing necessary for the actuation signal, are achieved. Finally the most intensive part of the framework is launched with the computation over several strokes of the aeroelastic response of the wing, after a static analysis initializing the transient one. The whole transient analysis is divided in a number of time steps where, in the case of the bidirectional aerodynamic model, the aerodynamic forces are computed and applied on each elements using their local information or, in the case of the unidirectional one, just the kinematics variables are retrieved. At the end of this process, the aeroelastic response of the wing, the aerodynamic forces and the actuation power are available for post-processing among other output data. All these steps are implemented in *Ansys* using macro files. In addition to the

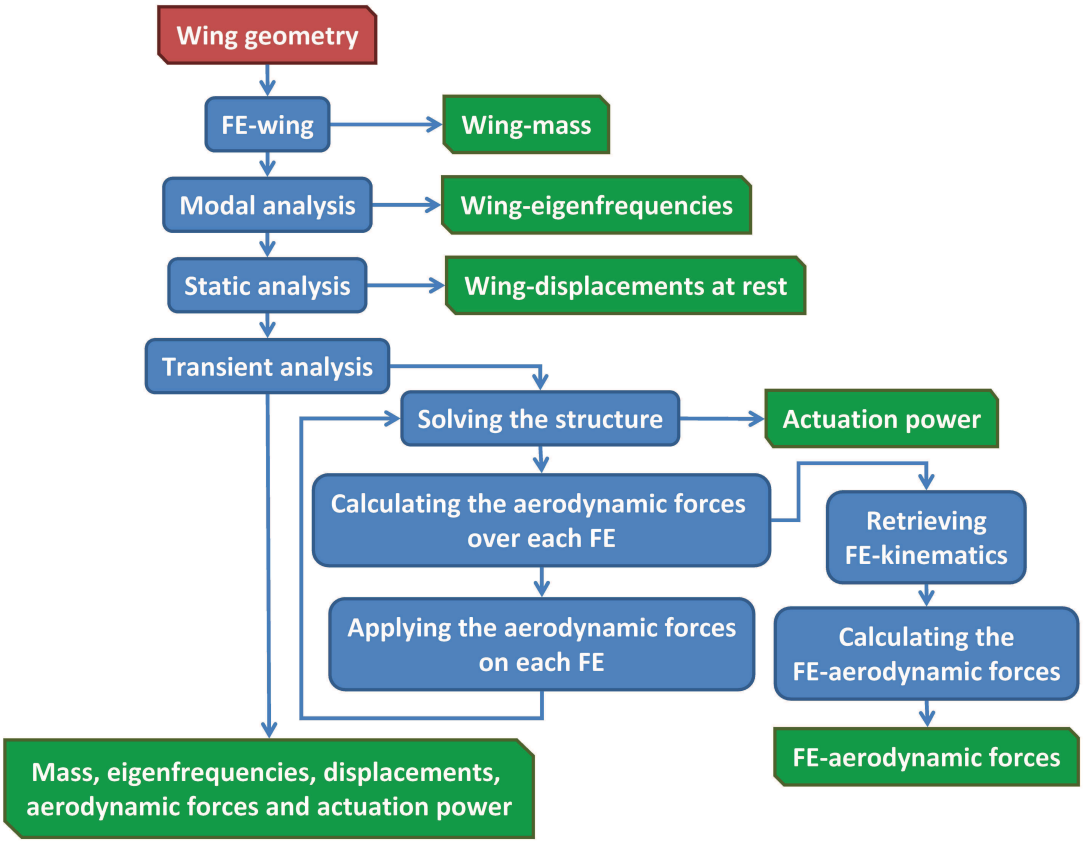

Figure 3.6: Flowchart of the aeroelastic framework. The mandatory input data are indicated in red whereas the outputs are in green. Although each analysis is mandatory to compute the aeroelastic response of a wing at resonance, the framework can be adapted to non-resonant design with the modal analysis being thus optional. Similarly a sinusoidal heaving motion will by default simulated for the actuation but other motions might be investigated.

computation itself, a *Python* script is integrated into the framework to manage and oversee each analysis properly, autonomously and efficiently.

3.5.1 Generating the wing

The first step of the aeroelastic framework is to generate the wing geometry and to mesh it using the elements presented in the section 3.1.1, using *BEAM4* element for venation pattern and *SHELL93* element for membrane features. In order to automatize the whole framework, a parametric wing geometry is adopted as seen in the figure 3.7 and described more lengthily in the chapter 5.1.2.

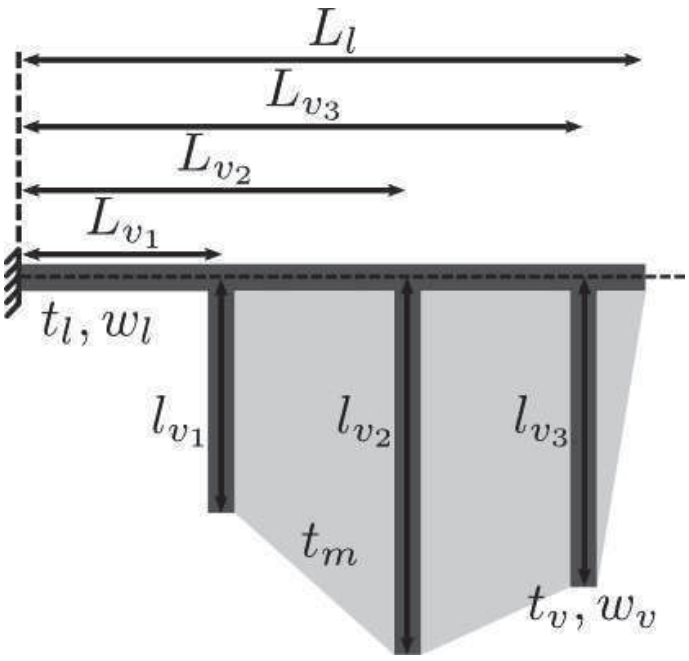

Figure 3.7: Parametric design of the validation wings

Thus with only 7 to 11 parameters, a large range of insect-like wing skeletons, wing constituted only of beam elements, can be generated and with an additional parameter also wings with membranes. Thanks to this parametric definition, keypoints, lines, and eventually areas are created. In order to lower the computation load and due to the symmetry of FWNAVs, only an individual wing is modeled and simulated.

For the mesh generation, up to three element types are defined, the one for the leading-edge, the one for the perpendicular vein(s) and eventually the one for the membrane(s).The material and geometric parameters required for the definition of these types are summed up in the table 3.3 along with their default values. The material properties are the ones used by default in the prototype, the SU-8, and taken from the literature (Lorenz et al. [1997]; Chang et al. [2000]; Hopcroft et al. [2005]) but other materials can be used. Once defined, the wing is automatically meshed with the mesh size adjusted through the number of finite-elements per beam segments, which is given along the parametric geometry as input.

The structural damping is also here defined using the coefficient α and β of the Rayleigh method computed as in the section 3.1.2. The necessary values of ζ_i and f_i are taken by default from previous experiments under vacuum with SU-8 micro-beams and are defined in the table 3.4. Nonetheless they can be refined from experimental data as shown in the chapter 5.1.3.1.

Once the geometry and the mesh is generated, a first analysis is completed in order to retrieve the numerical wing mass as well as the wing blade geometry and saved them into text-files for later use in the post-processing. Currently as the aerodynamic model is limited to a cartesian mesh, two constraints are generated on the geometry handled by the framework: first, only perpendicular veins are available, and

Table 3.3: Material and section properties necessary for the definition of the three element types within the aeroelastic framework. The material values are the ones used in the prototype with SU-8.

(a) Leading-edge: *BEAM4*

Property	Unit	Value
E	$[Pa]$	4.6e9
ρ	$[kg.m^{-3}]$	1190
ν	$[-]$	0.22
t	$[m]$	t_l
w	$[m]$	w_l

(b) Vein: *BEAM4*

Property	Unit	Value
E	$[Pa]$	4.6e9
ρ	$[kg.m^{-3}]$	1190
ν	$[-]$	0.22
t	$[m]$	t_v
w	$[m]$	w_v

(c) Membrane: *SHELL93*

Property	Unit	Value
E	$[Pa]$	4.6e9
ρ	$[kg.m^{-3}]$	1190
ν	$[-]$	0.22
t	$[m]$	t_m

Table 3.4: Default damping properties used to compute the coefficients α and β of the Rayleigh damping. These data are taken from experiments under vacuum with SU-8 micro-beams of $5mm$ in length, $750\mu m$ in width and $48\mu m$ in thickness.

Name	Unit	Value
f_1	$[Hz]$	699.1
ζ_1	$[-]$	0.0069
f_2	$[Hz]$	4362.8
ζ_2	$[-]$	0.0069

second, only convex quadrilateral membrane are supported. Those constraints constitute slight drawbacks of the aeroelastic framework which have to be taken care of in later works.

3.5.2 Solving the modal analysis

Following the generation of wing geometry and mesh, the modal analysis is completed in two steps. First, the boundary conditions are applied by clamping the 6DOFs of the wing root so as to avoid any rigid mode. Second, the modal analysis is done by solving the equation:

$$\mathbf{M}\ddot{q} + \mathbf{K}q = 0 \tag{3.10}$$

The first fourth modes of the structure are extracted using a Block Lanczos method and saved within a text-file. Only the first one is used to compute the actuation period, in case of a resonant actuation design, and consequently the time step for the transient analysis.

3.5.3 Solving the transient analysis

The final step of the aeroelastic framework and its kernel is the transient analysis, where the aeroelastic response of the wing is computed over several strokes using a full implicit[1] transient dynamic analysis. There, the equation 3.2 is solved directly without any further assumption using a Newton-Raphson method[2] coupled

[1] Implicit in the sense of implicit method for the resolution of time-dependent ordinary and partial differential equations and therefore opposed to explicit methods.

[2] The Newton-Raphson method is an iterative process of solving nonlinear equations as, for example, $\mathbf{K^T_{n,i}}(q_{n+1,i+1} - q_{n,i}) = F^{ext}_{n+1} - F^{nr}_{n,i}$ where $\mathbf{K^T_{n,i}}$ is the tangent stiffness matrix and F^{nr}_i the restoring force vector calculated from the element stresses, instead of $\mathbf{K}q_{n+1} = F^{ext}_{n+1}$.

to a HHT[3] time integration method or a Newmark[4] one with when the large deflection capability of the FEs is turned on (Ansys Inc [2007]). The analysis is divided in three consecutive steps: the application of the initial and boundary conditions, the computation of the aeroelastic response and finally the saving of data for post-processing.

3.5.3.1 Initializing

Before computing the aeroelastic response, it is essential to known the position of the wing at rest under gravity so as to initialize the transient analysis and thus reduce the transient state occurring at the beginning of the aeroelastic computation when the actuation kicks in. To do so, a static analysis is conducted under the influence of gravity whereby the displacements of all nodes are stored and applied as initial conditions to the transient analysis.

Similarly the boundary condition i.e. the actuation motion is applied to the wing root as a prescribed displacement. In order to match the experiments done on the validation wing, a sinusoidal heaving motion along the Z-axis (see figure 3.2(a) for the orientation) is applied by default while all the other DOFs of the root are clamped. The amplitude of the actuation sine is given as input to the aeroelastic framework (by default $100\mu m$) while its frequency is set to the first resonant frequency of the wing, retrieved from the modal analysis. Other actuation motions can be applied, if necessary, depending on the actuation strategy selected for the FWNAV.

Once the initial and boundary conditions set, a few options of the transient analysis are tuned. Among the options, the most important one is either to switch on the large deflection option of the elements or not, referred later on as LD or SD respectively. By default, this option is turned off in order to increase the computation speed and stability. Another important option is the number of substeps per time step (by default set to 4), which influences the computation of the kinematics derivatives (velocity and acceleration) to whom both aerodynamic models are highly sensitive. Those options are given as input to the aeroelastic framework along with the number of strokes to simulate and the number of time steps per stroke.

3.5.3.2 Computing

Finally, the computation of the aeroelastic response itself begins and is divided roughly in 3 phases: a transient state without aerodynamic coupling, i.e. in vacuum, in order to reach smooth and steady kinematics variables, a transient state with aerodynamic coupling, i.e. in air, that fades out ultimately in a steady state response of the wing. Only the first phase is prescribed in the framework, while the two other phases are independent and depend on the number of simulated strokes to occur. The coupling between the structure and the aerodynamic forces is an option, given as an input to the framework, but in any case the aerodynamic forces computation starts right after the first phase.

[3] The Hilber-Hughes-Taylor algorithm is an implicit method of numerical integration used to solve differential equations derived from the Newmark method. Based on two additional integration parameters α_f and α_m to interpolate the acceleration and the displacement, velocity and loads, it solves the displacement q at the time t_{n+1} as:

$$\left(\tfrac{1-\alpha_m}{\alpha\Delta t^2}\mathbf{M}+\tfrac{(1-\alpha_f)\delta}{\alpha\Delta t}\mathbf{C}+(1-\alpha_f)\mathbf{K}\right)q_{t_{n+1}}=(1-\alpha_f)F^{ext}_{t_{n+1}}+\alpha_f F^{ext}_{t_n}-\alpha_f F^{int}_{t_n}+\left(\tfrac{1-\alpha_m}{\alpha\Delta t^2}q_{t_n}+\tfrac{1-\alpha_m}{\alpha\Delta t}\dot{q}_{t_n}+\left(\tfrac{1-\alpha_m}{2\alpha}-1\right)\ddot{q}_{t_n}\right)\mathbf{M}$$
$$+\left(\tfrac{(1-\alpha_f)\delta}{\alpha\Delta t}q_{t_n}+\left(\tfrac{(1-\alpha_f)\delta}{\alpha}-1\right)\dot{q}_{t_n}+(1-\alpha_f)\left(\tfrac{\delta}{2\alpha}-1\right)\Delta t\ddot{q}_{t_n}\right)\mathbf{C}$$

where F^{int} are the internal forces. It offers unconditional stability and the second order accuracy while α_f and α_m increase the amount of numerical damping present without degrading the order of accuracy.

[4] The Newmark method is an implicit method of numerical integration used to solve differential equations that uses finite difference expansions in the time interval Δt to solve the displacement q at the time t_{n+1} as:

$$\left(\tfrac{1}{\alpha\Delta t^2}\mathbf{M}+\tfrac{\delta}{\alpha\Delta t}\mathbf{C}+\mathbf{K}\right)q_{t_{n+1}}=F^{ext}_{t_{n+1}}+\left(\tfrac{1}{\alpha\Delta t^2}q_{t_n}+\tfrac{1}{\alpha\Delta t}\dot{q}_{t_n}+\left(\tfrac{1}{2\alpha}-1\right)\ddot{q}_{t_n}\right)\mathbf{M}+\left(\tfrac{\delta}{\alpha\Delta t}q_{t_n}+\left(\tfrac{\delta}{\alpha}-1\right)\dot{q}_{t_n}+\tfrac{\Delta t}{2}\left(\tfrac{\delta}{\alpha}-2\right)\ddot{q}_{t_n}\right)\mathbf{C}$$

where α and δ are the Newmark integration parameters and F_{ext} the external forces applied. It offers unconditional stability for nonlinear systems and second-order accuracy

In the case of the bidirectional aerodynamic model, the computation of the forces is made at each time step iteratively over the elements, blade-by-blade. Within each blade, the mean chord and number of chordwise elements are retrieved and the aerodynamic forces computed on each chordwise elements by averaging the kinematics variables of its nodes, by rotating the averaged kinematics according to the order defined in the section 3.2, by computing the formula 2.6 and 2.9, by counter-rotating the force vector to the main coordinate system (X,Y,Z) and finally by distributing the resulting forces equally among its active nodes.

In the case of the unidirectional aerodynamic model, the kinematics data are retrieved at each time iteratively over the blade, and averaged over each blade and stored into a text-file. No coupling is made in anyway with this model as the aerodynamic forces are computed later on within *Python*.

3.5.3.3 Saving

Once all the intended strokes are computed and the aeroelastic response of the wing known, various data are stored in text-files. Among these data are the displacement of the wing extremities, the actuation power computed as the reaction load, the force or torque needed to counteract the instantaneous sum of the inertial/elastic and aerodynamic forces, at the wing root times its actuation velocity, either linear or angular, the aerodynamic forces and its components at each node for the bidirectional aerodynamic model or the geometric and kinematics data of each blade for the unidirectional one.

3.5.4 Post-processing and case management

Once the aeroelastic computation is complete, the data are available in various text-files and need to be post-processed so as to summarize clearly, concisely and graphically various performance items of the wing.

As stated before, a *Python* script oversees the overall analysis, managing the *Ansys* macros as well as the various files generated by the computation, and also post-processing them. Among the processing tasks, the main one is to concatenate the aerodynamic forces, stored at each node and at each time step, so as to extract the global aerodynamic forces generated by the wing. Another essential task is to post-process the unidirectional aerodynamic model by retrieving the appropriate data in the text-files, by computing the aerodynamic forces using the equations 2.10 to 2.12 and by summing the blades at each time step. To evaluate graphically and quickly the performance of the wing, various curves in dimensional and in non-dimensional form are plotted along with a brief summary of the analysis containing statistics about important performance items such as the peak-to-peak actuation power, the mean lift and drag.

In parallel to this post-processing tasks, the *Python* script handles also all the pre-processing operation prior to the *Ansys* computation. Originally the *Ansys* macros are written as template files encoded by a bunch of parameters and options. The *Python* script first copies all those macros to a distant computational directory and then modifies them interactively according to the wing geometry and to the calculation parameters before launching the *Ansys* computation.

This combination of a *Python* script handling *Ansys* computations offers great advantages in terms of practicality, rapidity, and also autonomy. First, the user interaction time and load are greatly reduced as file management and input errors are nonexistent. Second, once the input data are given the whole computation is made without any interaction from the user, which enables intensive computation as highlighted in the chapter 6. Third, once the computation data are available in text-files special post-processing requests can be addressed easily and quickly. Fourth, due to the high modularity of the *Ansys* template files and of the *Python* script, the aeroelastic framework can be adapted quickly and easily to alternative applications.

Chapter 4

Numerical investigations

Contents

With the aeroelastic framework formulated and its implementation done, a mandatory step, before an experimentally validation, is to assess its numerical behavior versus the calculation parameters but also to verify that the computation of aerodynamic forces is, in somehow, coherent with the ones predicted by the literature model of Sane and Dickinson [2002] represented here by the unidirectional flexible aerodynamic model. This chapter intends to be a numerical stress-test for the framework so as to bring out best practice in its use and back them.

The chapter is organized around four points. First, the framework is based on a FEM solver relying strongly, to solve the transient analysis and to evaluate the wing performance, on the mesh size and on the time step size to succeed a computation. Therefore a convergence study for both parameters is mandatory. Second, the aerodynamic forces predicted by the bidirectional flexible aerodynamic model are compared to the unidirectional one so as to check the coherence of each component. Third and as a direct consequence of this comparison, the effect of the chordwise discretization on the added-mass component of the bidirectional model is investigated in order to correct its underestimation. Fourth and ultimately, the sensitivity of the aeroelastic framework towards the material input data is assessed providing guidance about the accuracy

required for the experimental characterization of the chapter 5.2.1.

Except for the convergence study, the actuation and material data are taken from the experiments considered in the chapter 5.2 and all computations, except otherwise stated are at iso-mesh. The wing used here are the one defined in the chapter 5.1.2 for validation purpose.

4.1 Convergence study

Even if the aeroelastic framework is defined and implemented, its sensitivity and its stability towards the mesh size and the time step size is yet unknown but essential for this study. Indeed a satisfactory balance between the accuracy and the computing load is primordial to fulfill one of the framework requirement: a fast and sufficiently accurate evaluation of the wing performance. Furthermore such study provides guidelines for adapting properly the two parameters to the requirements needed by a application, less accuracy and more rapidity for example.

To define a trusted computation zone for designers, 6 output data are scrutinized after 10 wing strokes: the mean lift and drag, the amplitude for the lift and the drag, the displacement amplitudes of the leading-edge tip and of the trailing-edge tip. To control the mesh size, two input parameters are available: the number of elements per segment in the spanwise $N_{FE_{Span}}$ and in the chordwise direction $N_{FE_{Chord}}$. Similarly to control the time step size, two input parameters are used: the number of iterations/steps per period N_{Steps} and the number of sub-iterations $N_{Substeps}$.

In each case, the large deflection capabilities of the FE is alternatively turned off (SD) and on (LD). The bidirectional aerodynamic model is used and coupled. The wing is actuated at its root in a pure heaving motion with a large actuation amplitude (LA) of $100\mu m$. An arbitrary 2.5% error zone is defined, based on the most discretized and available result taken as reference, to evaluate the performance and define the "trusted" computation zone within the 2.5% area. The convergence study occurs consecutively, for both the mesh size and the time step size, for a wing without and with membrane.

4.1.1 Convergence study for wing skeleton

The convergence study for wing skeleton, i.e. wing without membrane, is made on the L1 wing, shown in figure 4.1. This wing is the simplest geometry available making the computation necessary for the overall study quick.

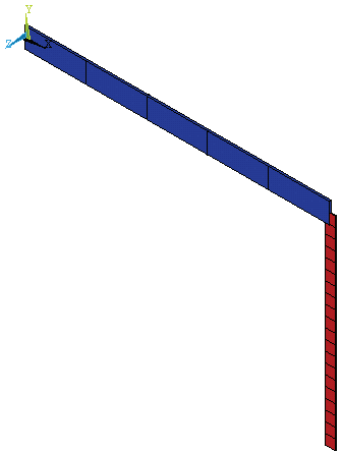

Figure 4.1: View of the L1 wing within Ansys. 10 spanwise (blue) and 20 chordwise (red) beam elements are meshing the wing.

4.1.1.1 Mesh study

Calculations are made for several sets of these parameters: 5, 10, 20, 30 for $N_{FE_{Span}}$ and 5, 10, 20, 50, 100, 200 for $N_{FE_{Chord}}$. Two time-steps known to work conveniently are used either $N_{Steps} = 50$ or $N_{Steps} = 100$ with each time $N_{Substeps} = 4$. The results are presented in the figure 4.2 for the SD case and in the figure 4.3 for the LD one.

In figure 4.2 for the SD case, a convergence is quickly reached for the displacement variables. However the aerodynamic variables are more problematic especially given the small computed values at stake. In average, the drag reaches the convergence more quickly than the lift for its mean value and its amplitude. But where the mean drag is quickly within its error zone, the mean lift converges slowly giving a thin error zone and requiring a fine mesh. For the amplitude values, conversely, the convergence is quicker for the lift whereas the drag is doing the splits. The definition of the error zone is here rough and slightly meaningless given the very small references. A first fact about the aerodynamic forces computation in SD is here then highlighted: the mean lift is sensitive to the mesh size and the drag amplitude even more. On the contrary the mean drag and the lift amplitude are quite robust versus the mesh size. A second fact is that the computation is relatively insensitive to the spanwise discretization as all the curves overlap almost each other. From this SD study, a convenient point of computation for wing skeleton might be defined at $N_{FE_{Span}} = 5$ and $N_{FE_{Chord}} = 50$. However as a 2.5% error zone is already quite restrictive for a preliminary design tool, where only the trends are of interest, $N_{FE_{Chord}} = 20$ is also an interesting option.

With the LD option on, the same conclusions are almost found in the figure 4.3 except that, this time, the drag amplitude converges and quite quickly. The LD option tends therefore to stabilize the computation of the aerodynamics forces by concealing any spanwise discretization effect and by making them less sensitive to mesh size effect. However the computation load is heavier for the LD computation but a combination of $N_{FE_{Span}} = 5$ and $N_{FE_{Chord}} = 20$ is here again a good starting point and $N_{FE_{Chord}} = 50$ an even better but more costly.

An important remark is that each metrics tends to converge towards the same value whatever the computation options are. For the SD computation, the discrepancy due to the time-steps between each metrics are quite pronounced highlighting its time-dependency for accuracy. On the contrary for the LD computation, a finer time-steps is not affecting the computation outlining the benefit of the large deflection option.

4.1.1.2 Time step study

Calculations are made for several sets of these parameters: 2, 4, 10, 20 for $N_{Substeps}$ and 50, 100, 200, 500, 1000 for N_{Steps}. Given the conclusion of the mesh size study, two combinations are here considered: a $N_{FE_{Span}} = 5$ with either $N_{FE_{Chord}} = 20$ or $N_{FE_{Chord}} = 50$. Results are presented in the figure 4.4 for the SD case and in the figure 4.5 for the LD one.

For the SD case, each variable is quite sensitive to N_{Steps} with the continuously decreasing curve but less to $N_{Substeps}$ as the curves overlap almost each other. No convergence is clearly outlined except possibly for the mean drag. Furthermore as highlighted by the stars in the figure 4.4(b), the number of substeps might even be the source of instabilities followed by crashes. Given the close values reported and that the priority for the framework is its stability, a convenient choice might defined as $N_{Steps} = 100$ and $N_{Substeps} = 4$ as each computation is working for these combinations and even $N_{Steps} = 50$ to minimize the computational load.

For the LD case in figure 4.3, convergence is reached quickly for all variables. Some crashes are however occurring but the computation is less sensitive to the time step. The combination of $N_{Steps} = 100$ and

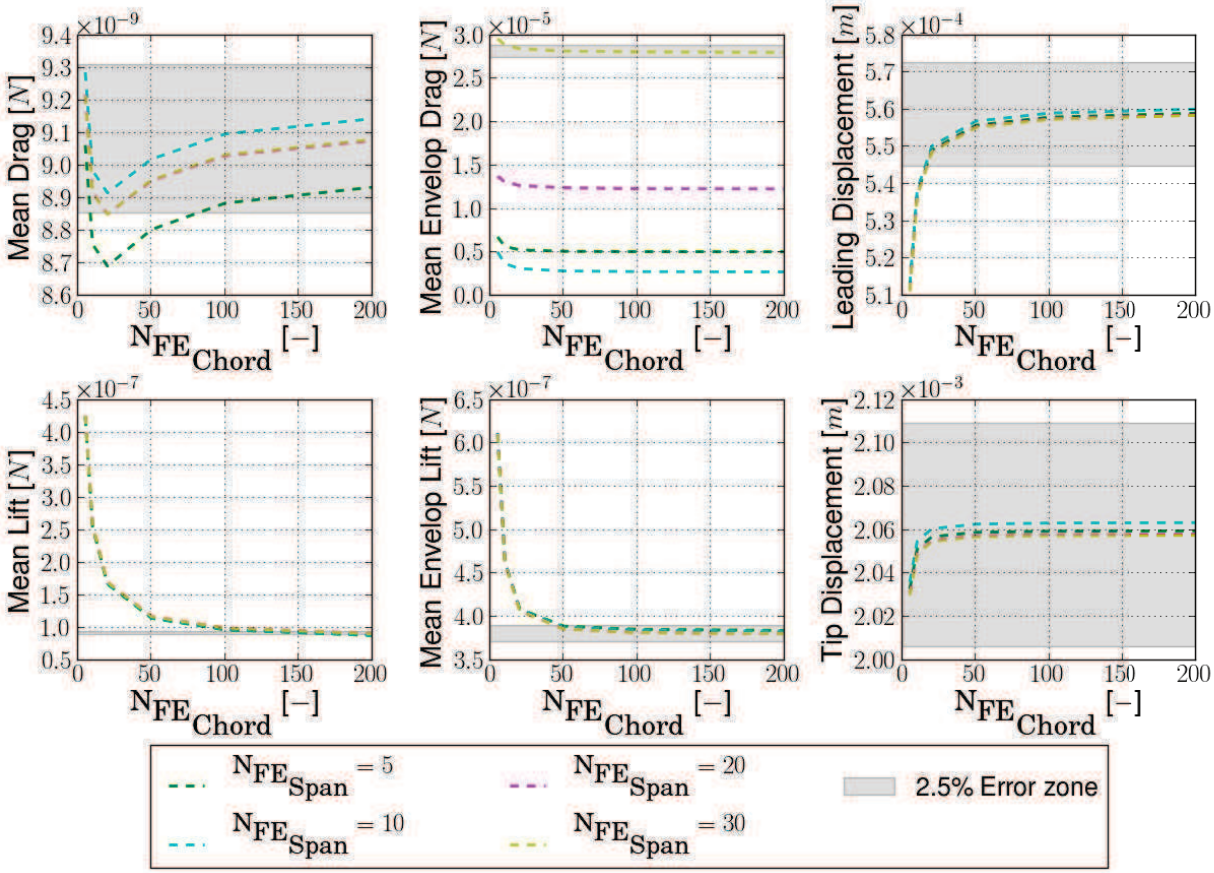

(a) 50 iterations per periods

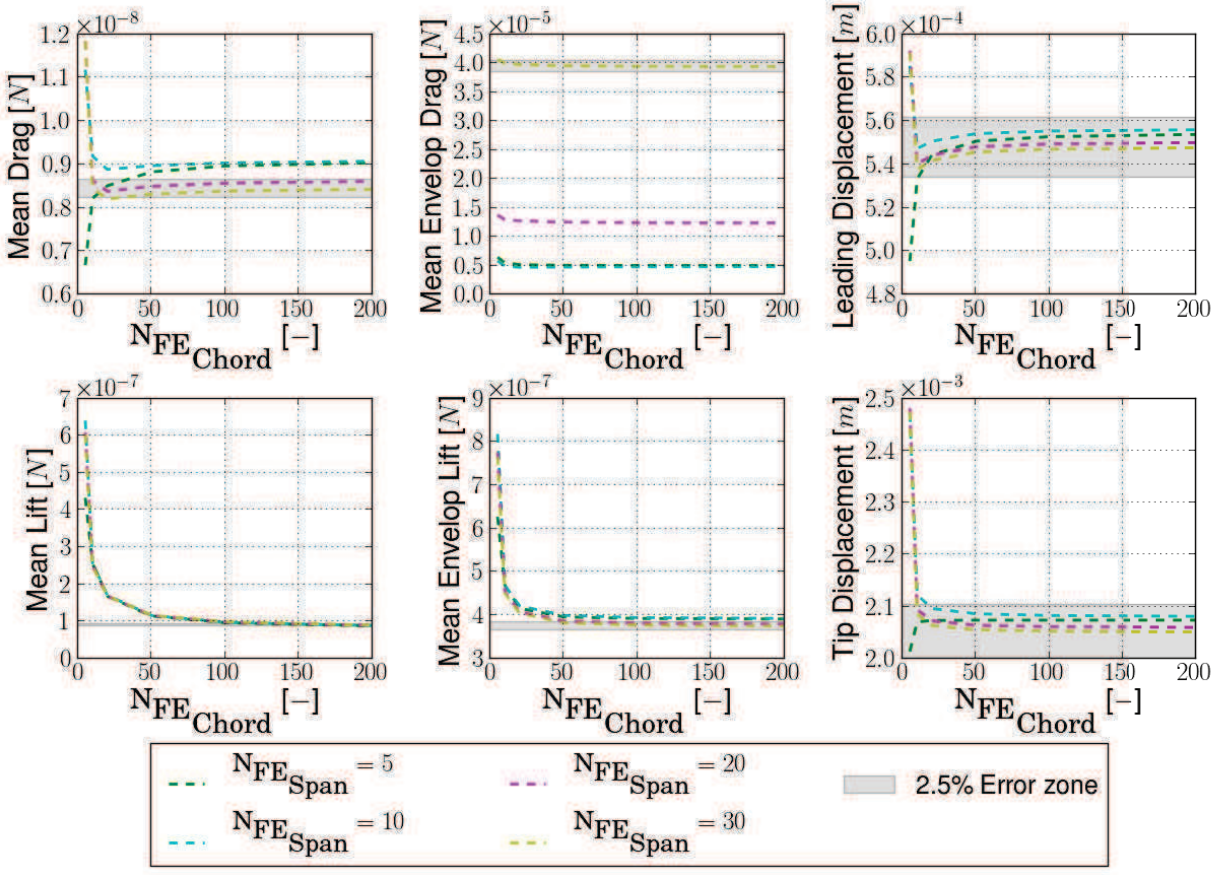

(b) 100 iterations per periods

Figure 4.2: Mesh convergence study on a wing skeleton (L1) in SD.

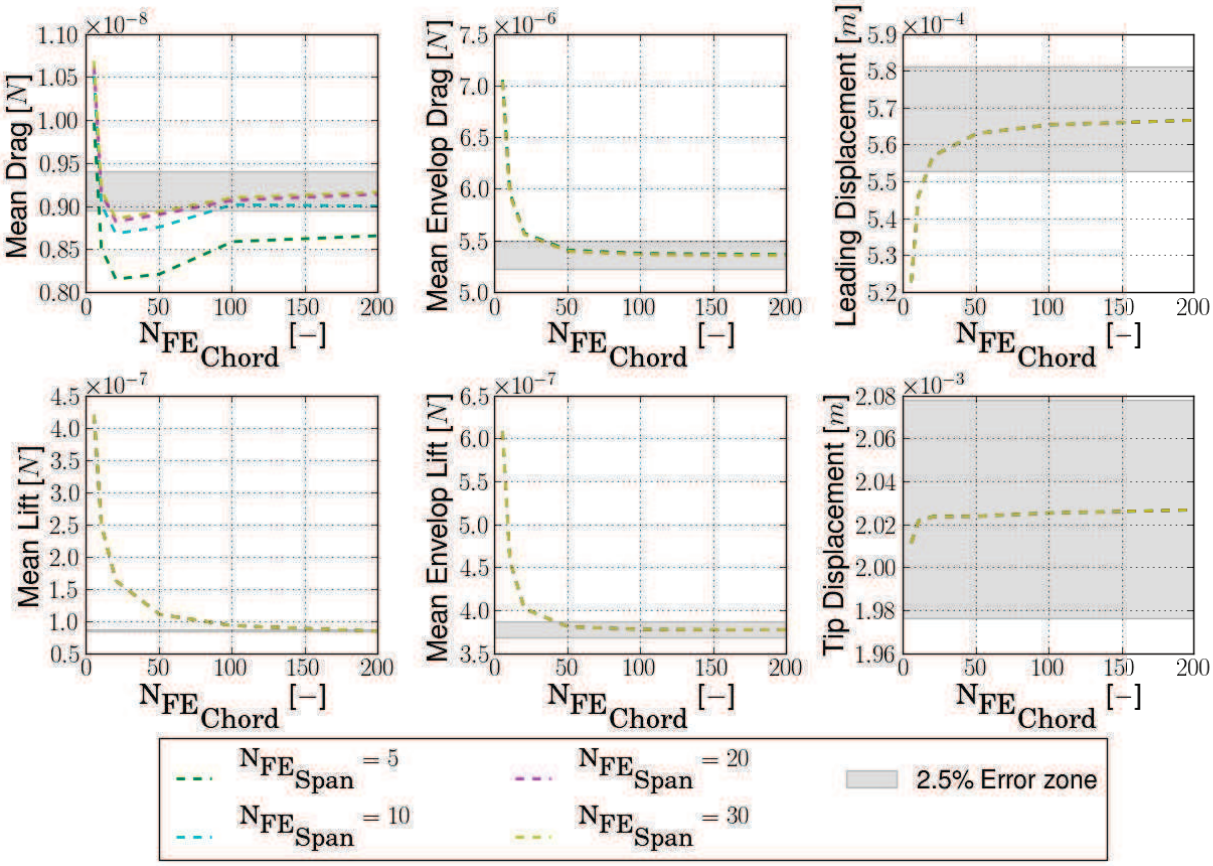

(a) 50 iterations per periods

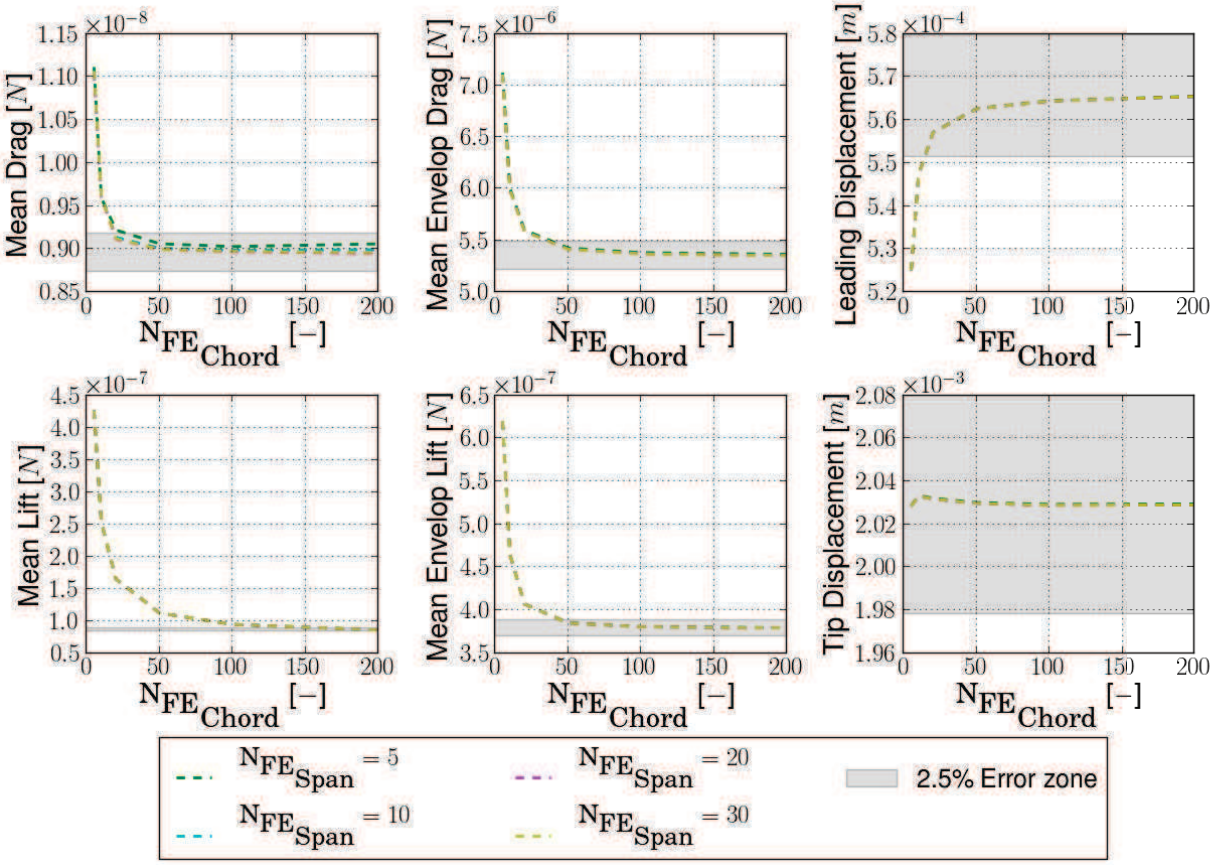

(b) 100 iterations per periods

Figure 4.3: Mesh convergence study on a wing skeleton (L1) in LD.

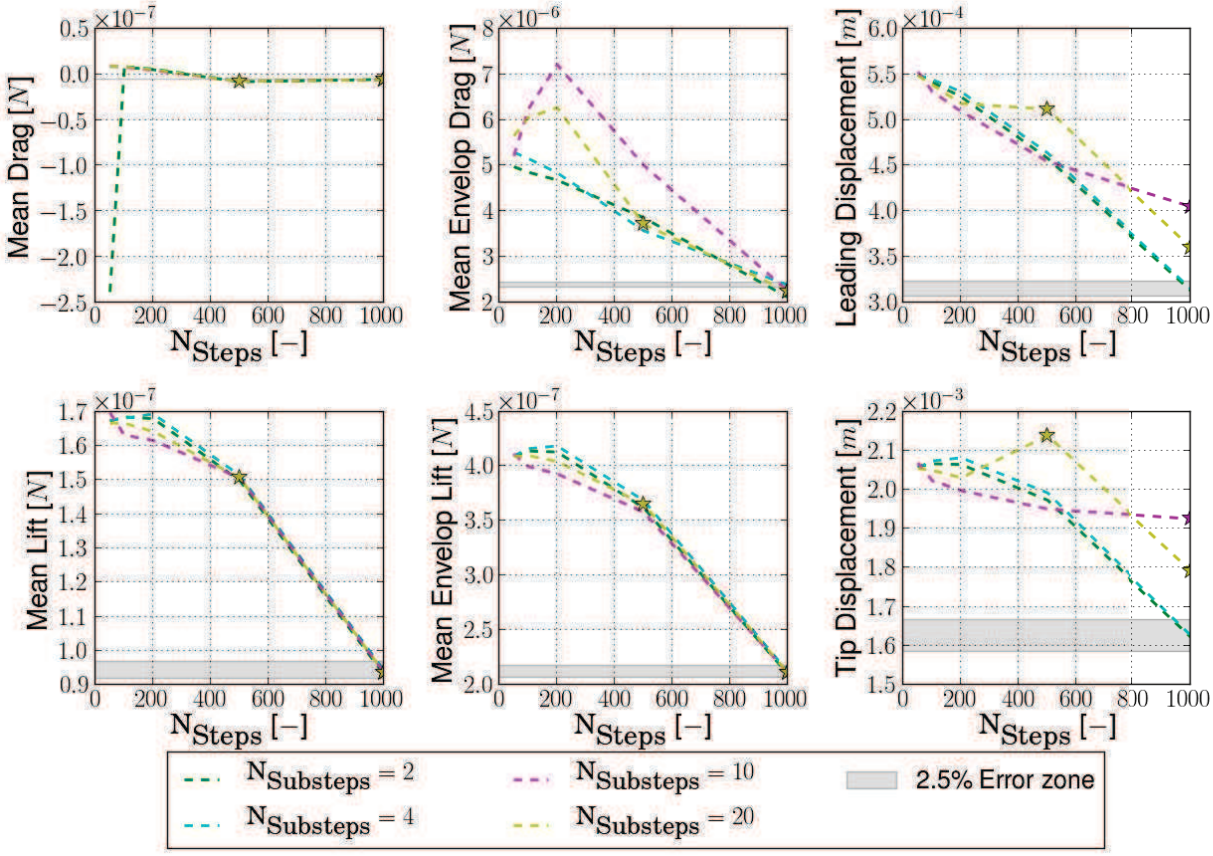

(a) 20 chordwise-elements

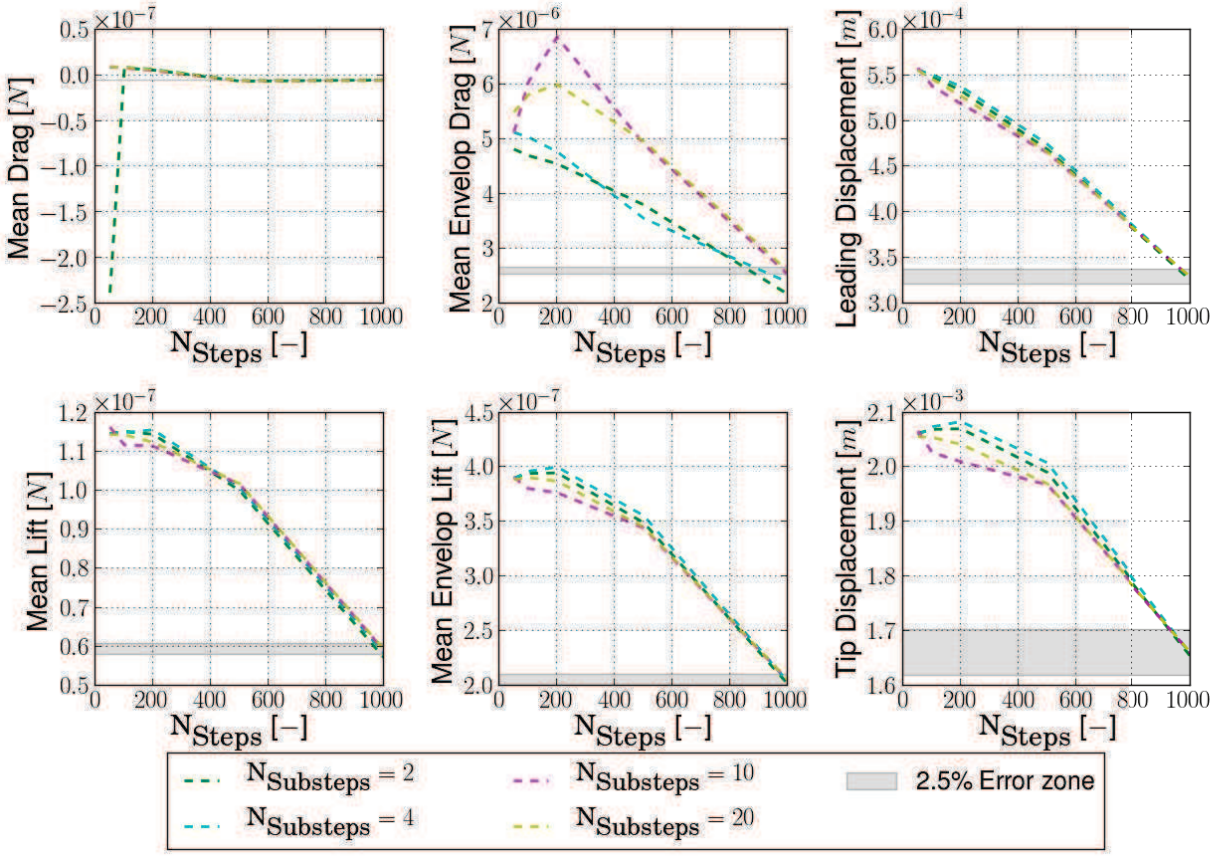

(b) 50 chordwise-elements

Figure 4.4: Time convergence study on a wing skeleton (L1) discretized with 5 spanwise-elements and 20 or 50 chordwise- elements in SD. Star marker indicates an abnormal value or a computation failure. The star value is then the mean value of the other working values.

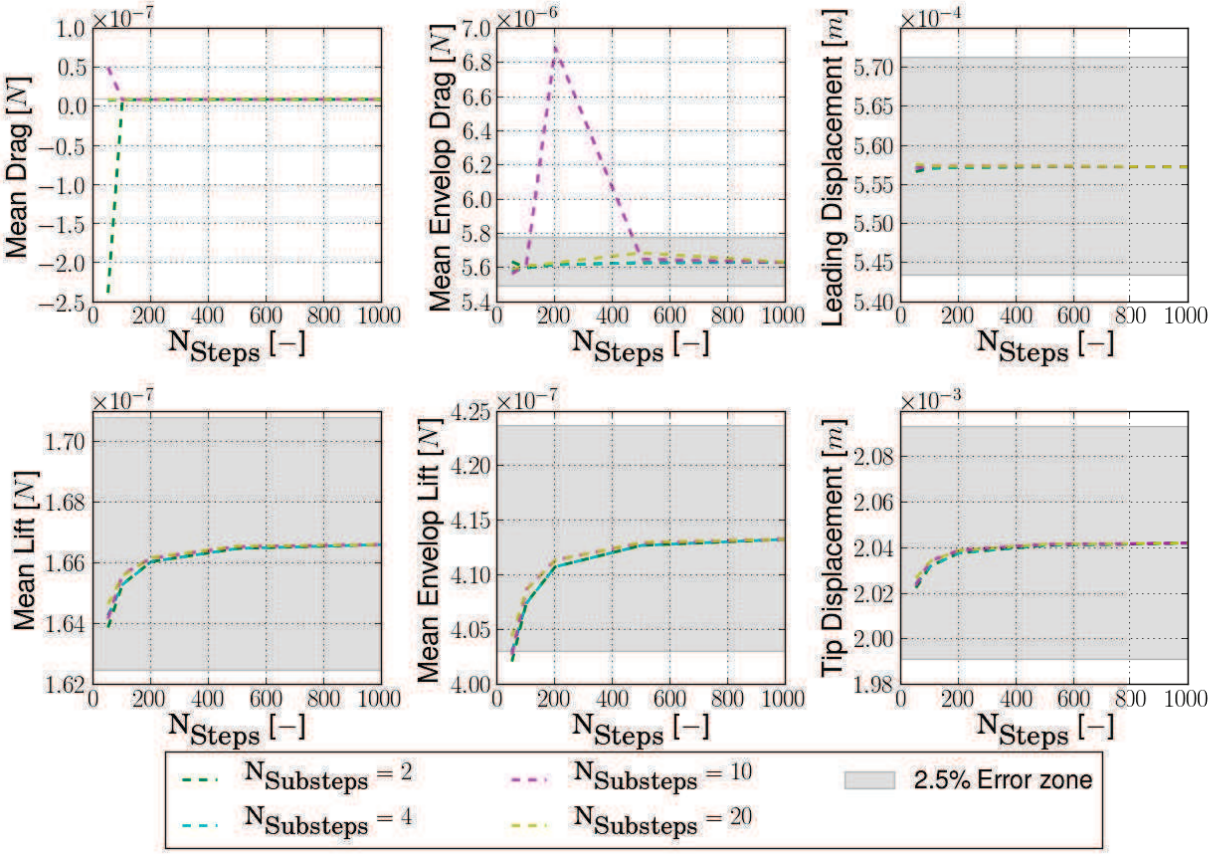

(a) 20 chordwise-elements

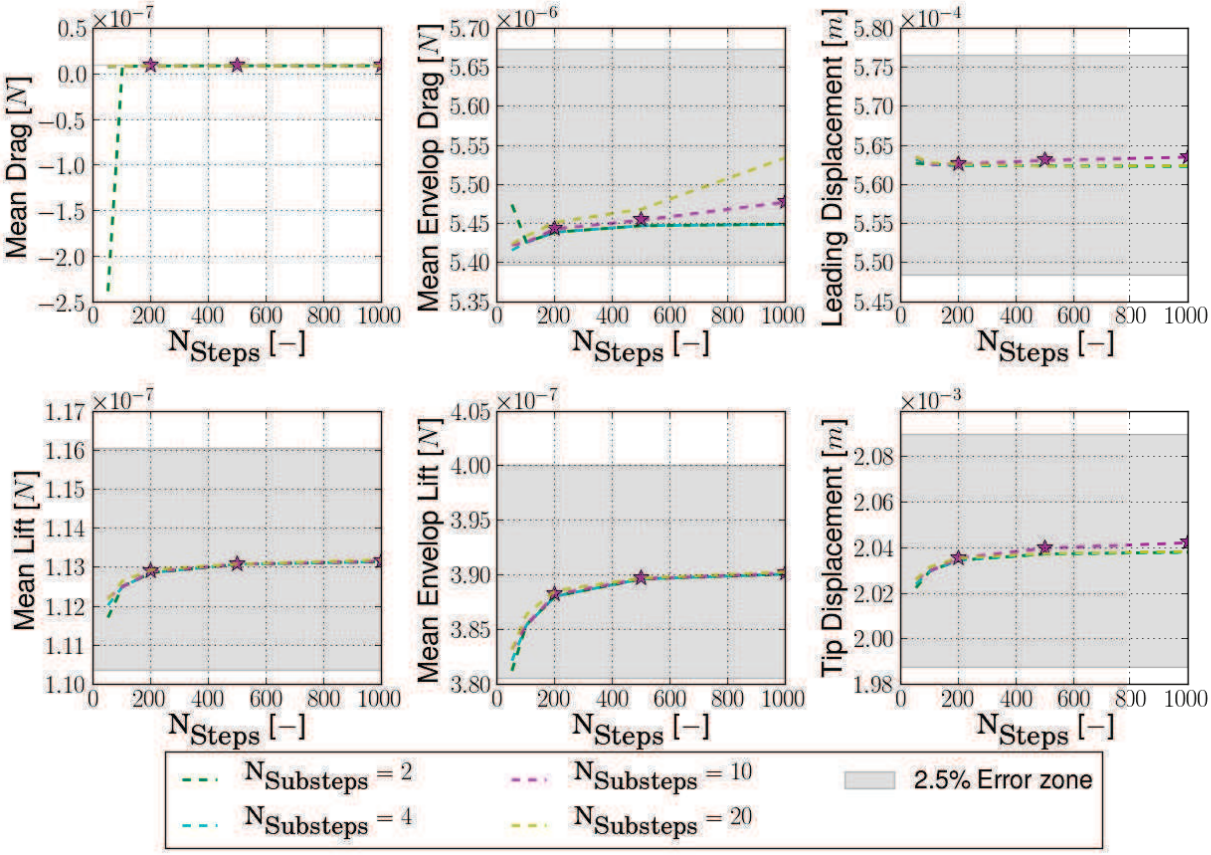

(b) 50 chordwise-elements

Figure 4.5: Time convergence study on a wing skeleton (L1) discretized with 5 spanwise-elements and 20 or 50 chordwise elements in LD. Star marker indicates an abnormal value or a computation failure. The star value is then the mean value of the other working values.

$N_{Substeps} = 4$ is here again a good starting point and $N_{Steps} = 50$ an even better choice so as to minimize the computational load which is increasing considerably in LD.

When comparing now both SD and LD cases, the values obtained for the SD case are about the same order of magnitudes from the one obtained in the LD case, which is essential for trend studies. However the LD compputations are more stable versus the time discretization and the accuracy highlighting its advantages over the SD ones to complete refined design study.

4.1.2 Convergence study for wing with membrane

For the convergence study for wing with membrane, the validation wing shape FM2 is chosen, shown in figure 4.6. This wing is the simplest geometry available as the membrane is rectangular making the computation necessary for the study quicker with the shell elements now introduced for the membrane. The mesh size is also controlled by the parameters $N_{FE_{Span}}$ and $N_{FE_{Chord}}$ as a membrane is always encompassed between a leading-edge segment and two vein segments and meshed in a cartesian way.

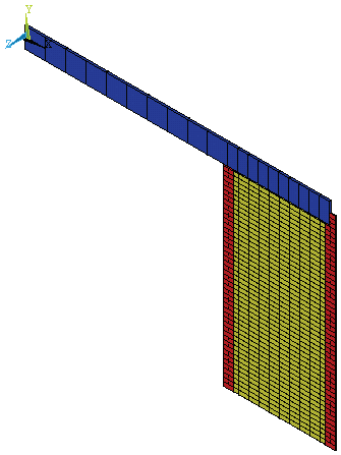

Figure 4.6: View of the FM2 wing within Ansys. 10 spanwise (blue) and 50 chordwise(red) beam elements and 500 (yellow) shell elements are meshing the wing.

4.1.2.1 Mesh study

Calculations are made for several sets of these parameters: 5, 10, 20, 30 for $N_{FE_{Span}}$ and 10, 20, 50, 100, 200 for $N_{FE_{Chord}}$. The time steps are set either to $N_{Steps} = 50$ or $N_{Steps} = 100$ to with each time $N_{Substeps} = 4$. The results are presented in the figure 4.7 for the SD case and in the figure 4.8 for the LD one.

For the SD case in figure 4.7, convergence occurs for every variables but at lower rate than the wing skeleton highlighting the need for a finer mesh for the membrane. The observations made for the wing skeleton are also here observed: the drag amplitude is doing the splits and the variables are almost insensitive to the spanwise discretization. In any case, the error zone is much narrower outlining the need for a finer mesh than the wing skeleton. Therefore a convenient point of computation for wing skeleton might be defined at $N_{FE_{Span}} = 5$ and $N_{FE_{Chord}} = 50$. However, as a 2.5% error zone is already quite restrictive for a preliminary design tool, where only the trends are of interest, and given the small values reported and that the computation load is strongly affected by the mesh size, $N_{FE_{Chord}} = 20$ might also be used for later wing evaluation in combination with $N_{FE_{Span}} = 10$ to increase the stability of the computation.

For the LD case in figure 4.8, the convergence is even more clear as the error zone is broader and the drag amplitude convergences to a single value. The same stabilizing effect of the LD option is observed as

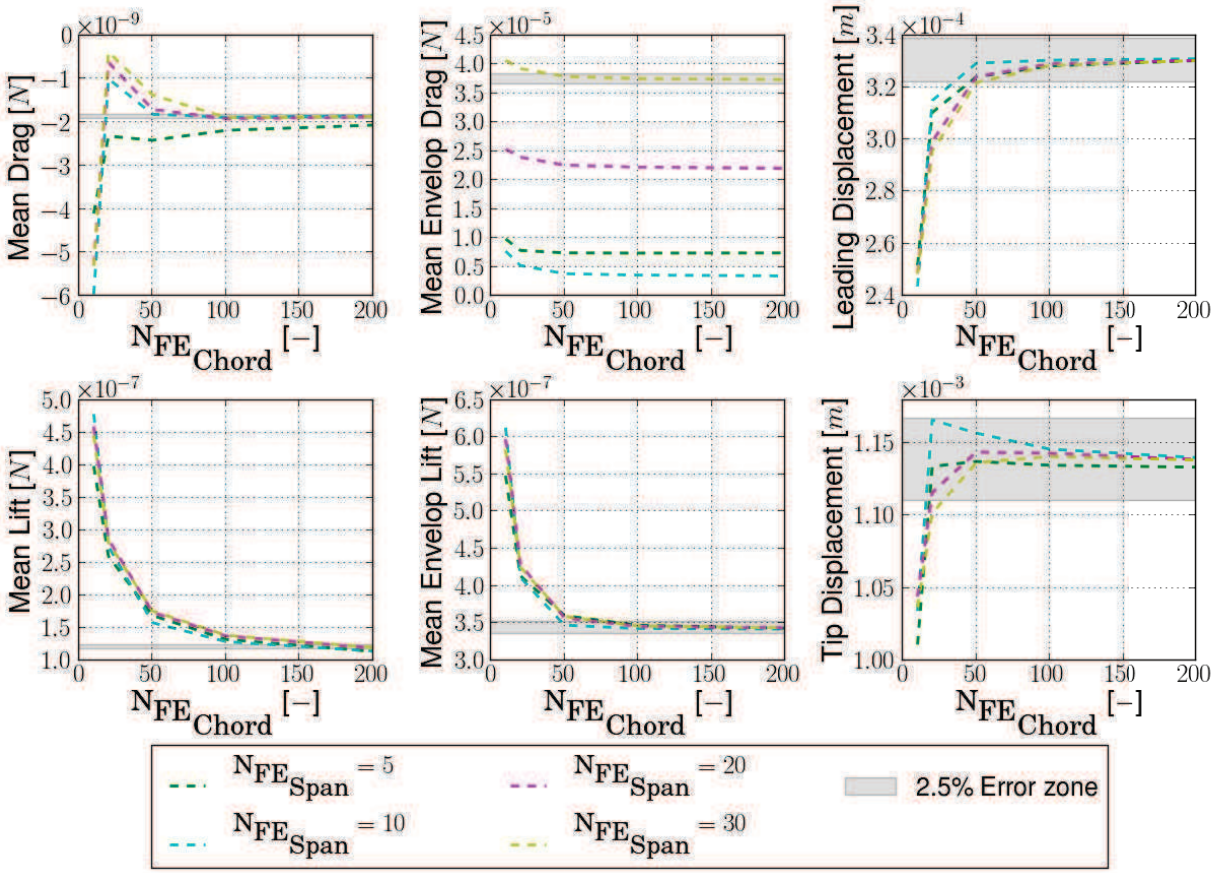

(a) 50 iterations per periods

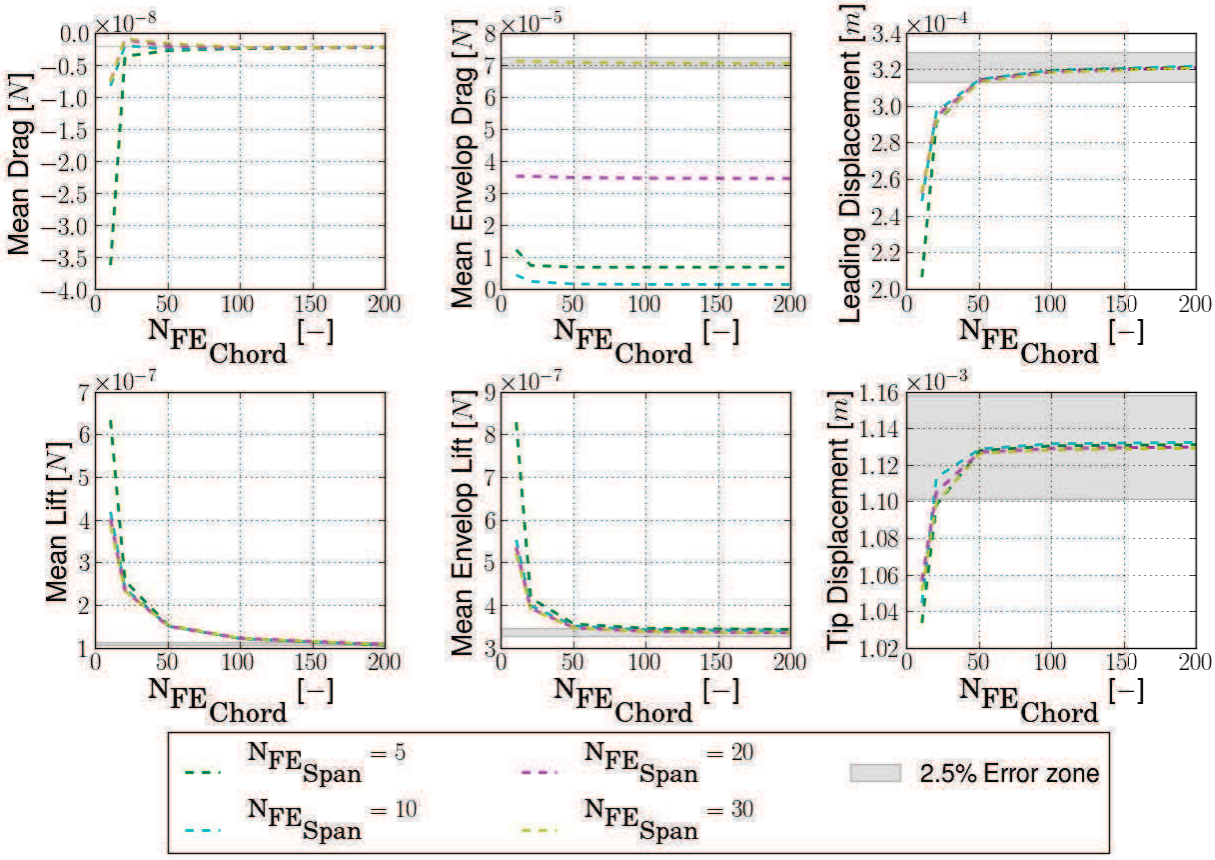

(b) 100 iterations per periods

Figure 4.7: Mesh convergence study on a wing with membrane (FM1) in SD.

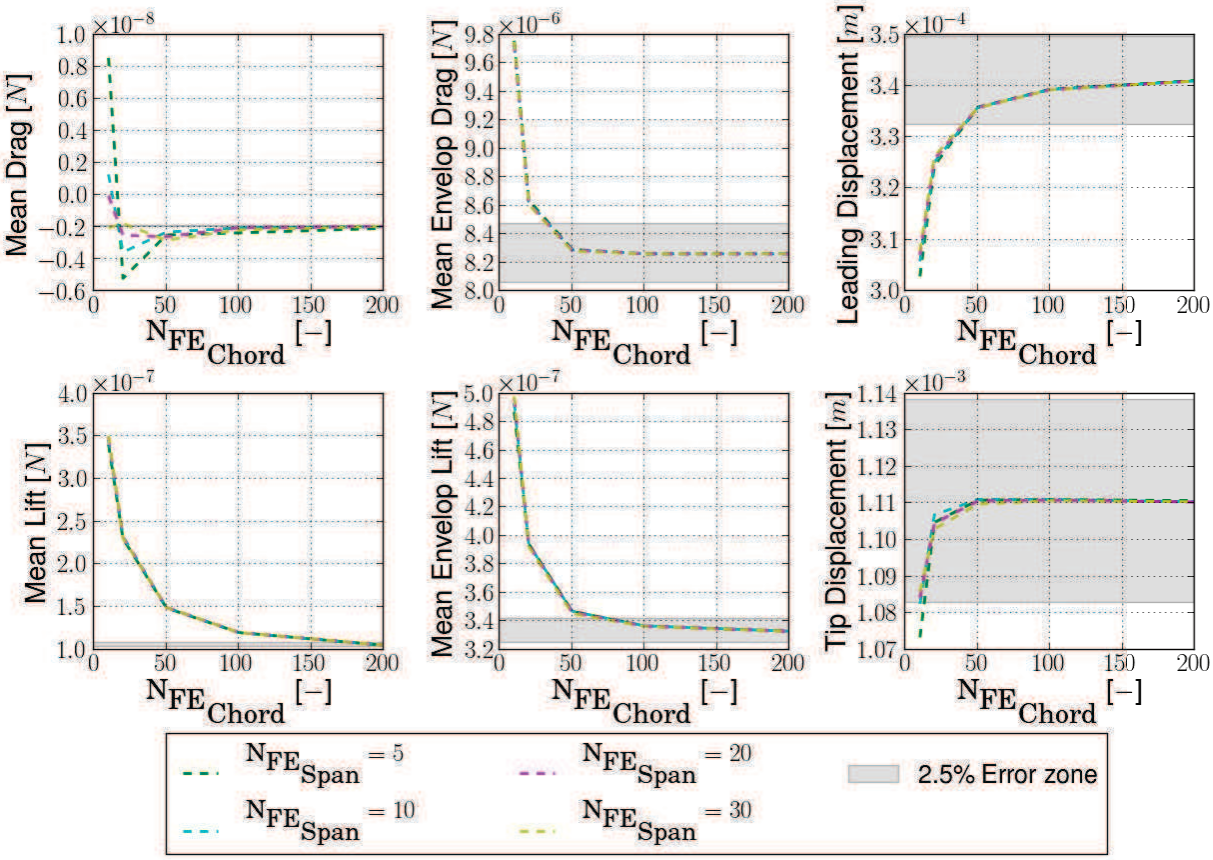

(a) 50 iterations per periods

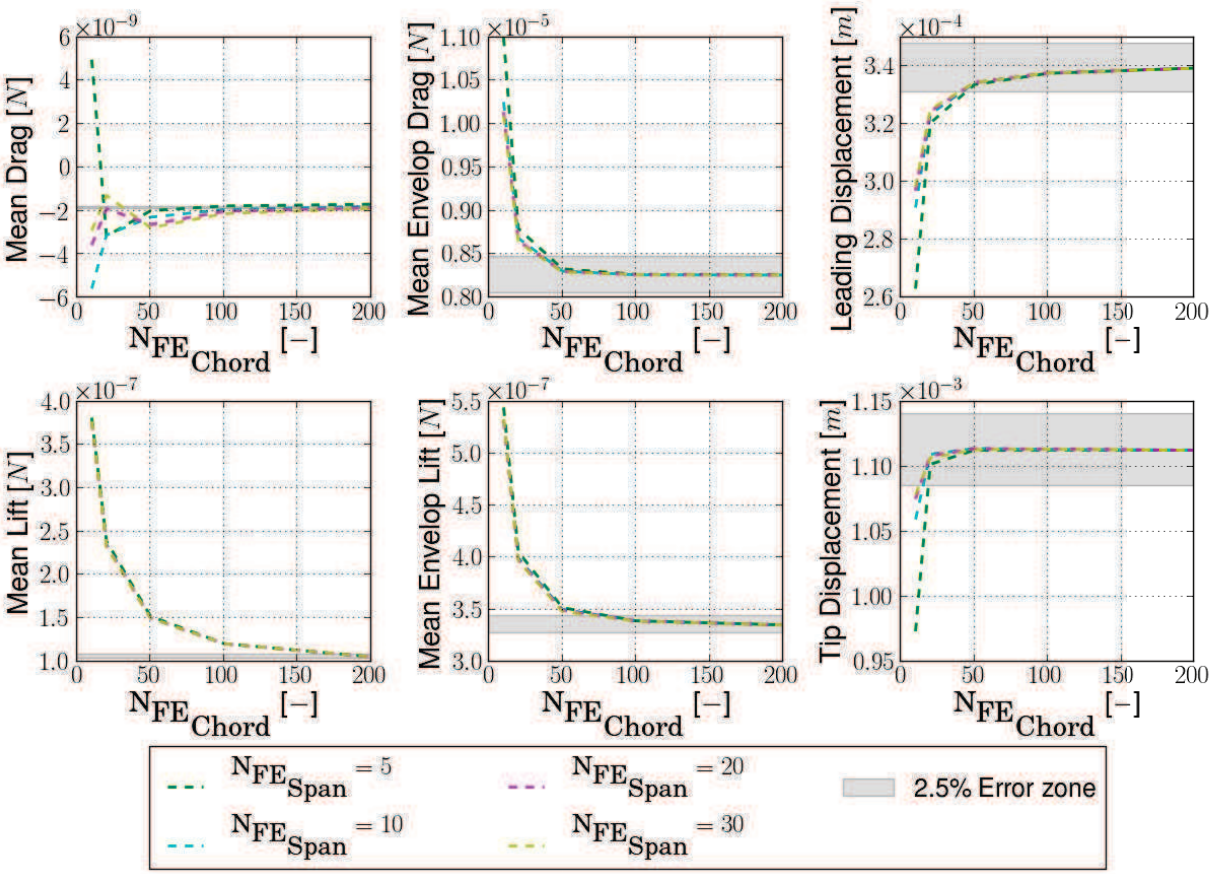

(b) 100 iterations per periods

Figure 4.8: Mesh convergence study on a wing with membrane (FM1) in LD.

in the wing skeleton. However the computation for wing with membrane is a lot more trickier as the shell elements are highly sensitive to large deflection and might therefore requires a very fine mesh to avoid any computational crash. Nonetheless the combination of $N_{FE_{Span}} = 5$ and $N_{FE_{Chord}} = 20$ is here again a good starting point and $N_{FE_{Chord}} = 50$ an even better but more costly.

An important remark is that, once again, each metrics tends to converge towards the same value whatever the computation options are. For the SD computation, the discrepancy due to the time-steps between each metrics are less pronounced than for the wing skeleton, most probably due to a smaller wing deformation as the membrane tends to stiffen the wing and 'damps' its deformation. Similarly as for wing skeleton, the LD computation is not affected by a finer time-steps outlining the benefit of a large deflection option.

4.1.2.2 Time step study

For the time convergence study, calculations are made at: 2, 4, 10, 20 for $N_{Substeps}$ and 50, 100, 200, 500 for N_{Steps}. Given the conclusion of the mesh size study, a combination of $N_{FE_{Span}} = 5$ and $N_{FE_{Chord}} = 50$ is chosen. The combination with $N_{FE_{Chord}} = 20$ has also be investigated but proves itself to be too unstable for every cases when the substep is larger than 10. The results are presented in the figure 4.9 for both the SD and LD cases.

Almost the same conclusions as for the wing skeleton can be drawn, with an insensitivity to the number of substeps, except that the slope are here gentle over the time discretization highlighting the benefit of the membrane which 'damps' the wing deformation. Furthermore, the reported values are almost all about the same order or magnitude which is highlighted by a broader error zone when compared to the wing skeleton study. It highlights also the adequacy of the SD assumption for trends studies for wing with membrane. For SD study, a wise combination is here again $N_{Steps} = 100$ and even $N_{Steps} = 50$ with each time $N_{Substeps} = 4$ so as to minimize the computational load and maximize the stability.

Following the same course as the wing skeleton, the LD case on wing with membrane converges at high rate even if some crashes occur at larger number of substeps. Overall in LD, the computation of each variables is less sensitive to N_{Steps} and almost insensitive to $N_{Substeps}$. Given the close values reported, a convenient choice is here again $N_{Steps} = 100$ and even $N_{Steps} = 50$ with each time $N_{Substeps} = 4$ so as to minimize the computational load and maximize the stability.

When comparing now both SD and LD cases, the values obtained for the SD case are about the same order of magnitudes from the one obtained in the LD case, which is essential for trend studies. However the LD computations are more stable versus the time discretization and the accuracy highlighting, once again, its advantages over the SD ones to complete refined design study.

4.1.3 Remarks on the convergence study

For the wing without membrane, a convenient combination is $N_{FE_{Span}} = 5$ and $N_{FE_{Chord}} = 20$ or $N_{FE_{Chord}} = 50$. For the wing with membrane, a convenient combination is $N_{FE_{Span}} = 10$ and $N_{FE_{Chord}} = 20$ or $N_{FE_{Span}} = 5$ and $N_{FE_{Chord}} = 50$. Finer combinations are also possible depending on the accuracy requirements. For the time-step size, either $N_{Steps} = 50$ or $N_{Steps} = 100$ and $N_{Substeps} = 4$ is recommended as they work fairly well. These parameters have been earlier arbitrarily chosen to conduct each convergence study and are here strengthened.

Even if a convergence study should normally be done on each computation case, the aim of this study is to provide some guidelines for functional, accurate and fast computations. Therefore the conclusions of this study are not definitive and have to be adapted to any difficult computational case, especially in the

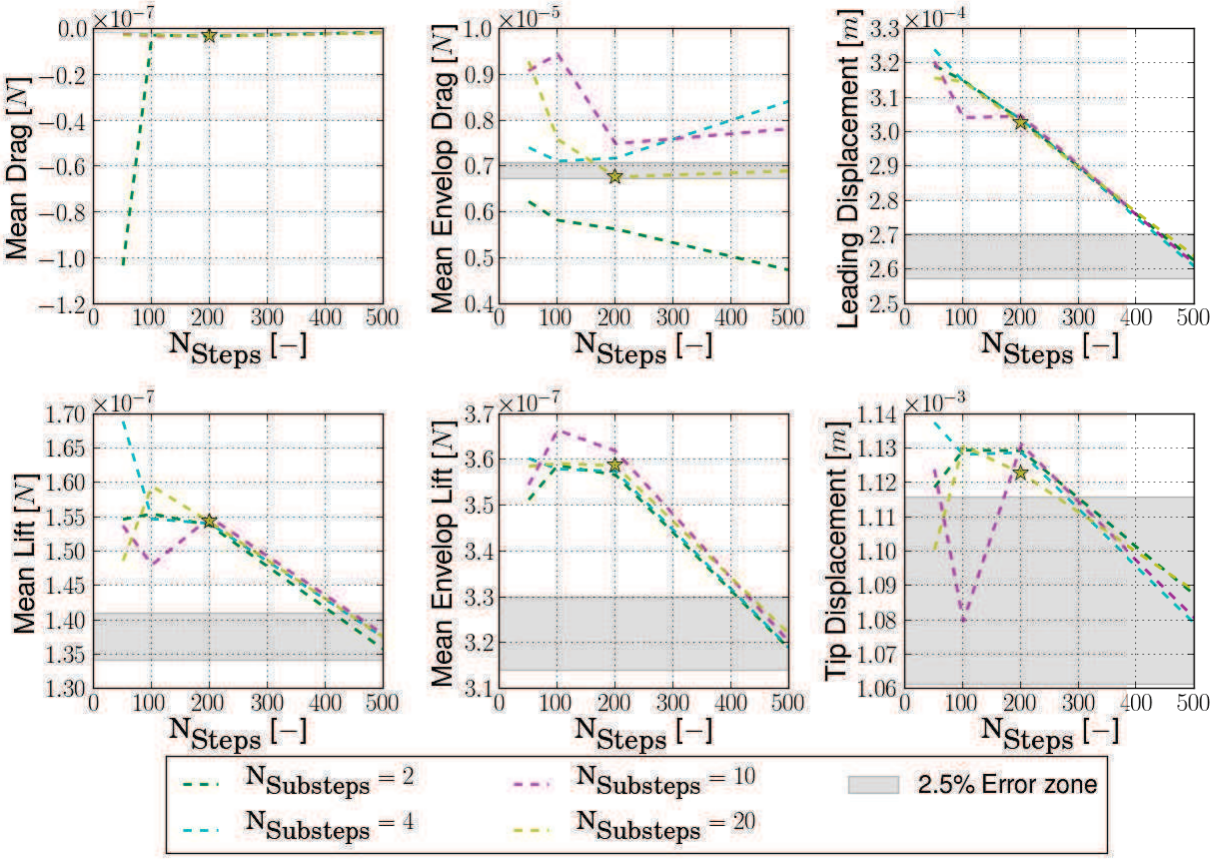

(a) Large deflection capability turned off

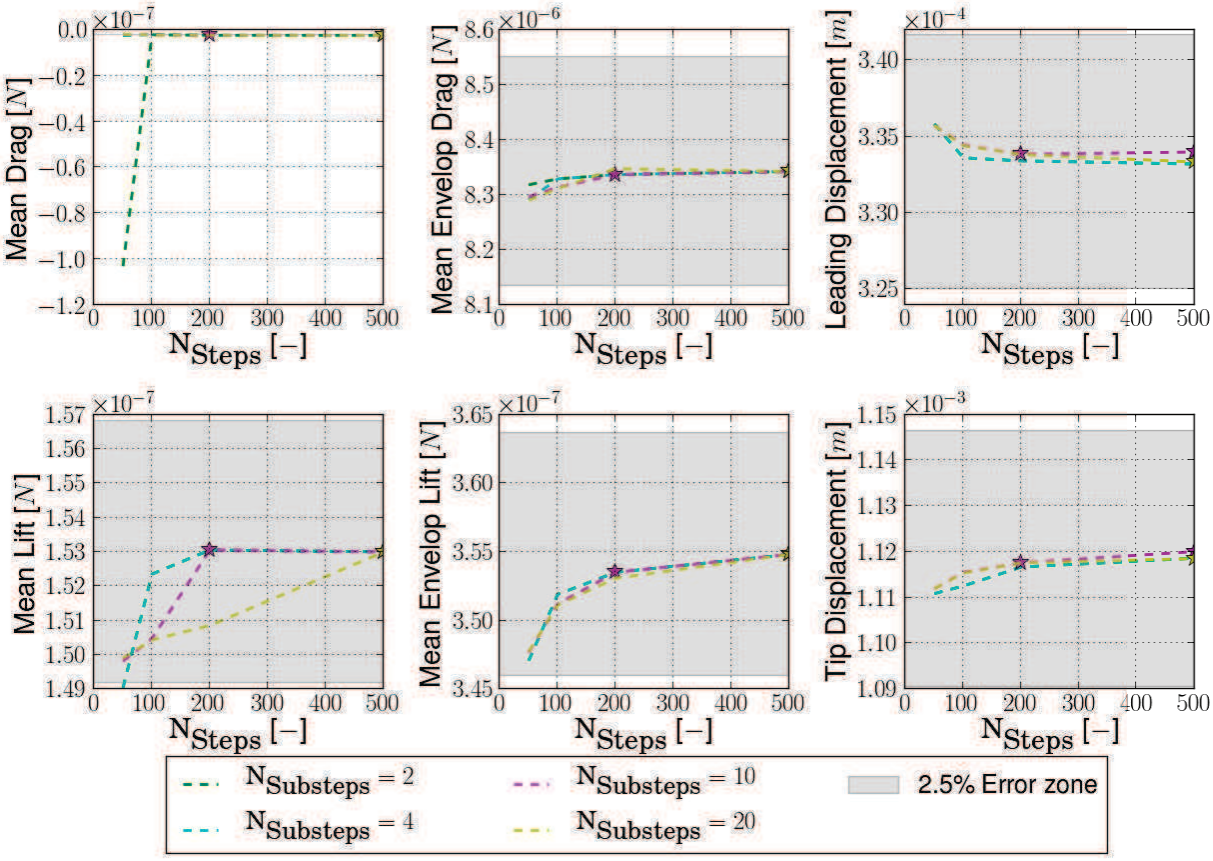

(b) Large deflection capability turned on

Figure 4.9: Time convergence study on a wing with membrane (FM1) discretized with 5 spanwise-elements and 50 chordwise elements.

case of a coarse mesh with very large deflection over an element. In these configurations and when a crash occurred, the first action should be to increase the mesh size and then to refine the time step so as to smooth the deflection between two consecutive time steps and thus to carry on the computation successfully.

However, a general rule is that the computation are quicker when the time-step and elements discretization are kept low, but at the cost of accuracy and eventually of a crash. Also computations in LD requires more computation load and are more subjects to crashes than the ones in SD, but here again at the cost of a bit of accuracy, which is more extensively discussed in the chapter 5.6. But first, it is important to assess the consistency of the bidirectional flexible aerodynamic model before drawing more conclusions.

4.2 Comparison of the bidirectional aerodynamic model with the unidirectional one

To validate or at least quantify the differences induced by the bidirectional flexible approach in the aerodynamic formulation, the unidirectional flexible approach is used as a baseline for validation. Even if both models are derived from Sane and Dickinson [2002], the unidirectional one is the closest in terms of formulation as it replaces the spanwise integration by a finite sum of blades and thus account for spanwise flexibility by averaging the chordwise deformation. It can therefore be used as a reference. Discrepancies are expected given the different treatments of the flexibility but results from both models should not fall far. Here both models are run in parallel: while the wing is simulated under aerodynamic load computed with the bidirectional approach, the unidirectional forces are also computed. Thus any discrepancy introduced by the bidirectional approach might be identified and quantified while the assumptions made can be discussed.

4.2.1 Beam wing

As the wetted surface of the wing in the case of beam wing is relatively small, it is a good starting point to analyze the effects introduced by the bidirectional approach. The table 4.1 and the figure 4.11 summarize the comparison for the wing L2, shown in the figure 4.10, between the unidirectional and the bidirectional flexible approach. For the wing F3 and E4, the comparison are summarized in the tables 4.2 and 4.3 respectively but the graphical comparisons are presented in the appendix B for sake of brevity.

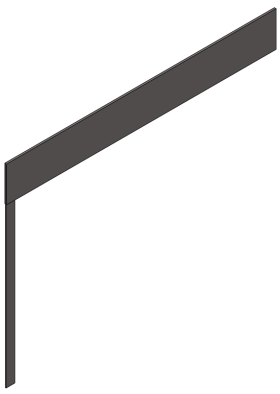

Figure 4.10: CAD view of the L2 wing.

Regarding the lift performance, the total force is underestimated with the overall difference going between -42% to -68% for L2, between -43% to -66% for F3 and between -43% to -69% for E4, almost monotonically. By looking at the force decomposition, the added-mass forces in the bidirectional approach are quite low when compared to the unidirectional one. This is due to the formulation of the added-mass forces where the local information, c_i and $\ddot{\eta}_i$, tends to minimize the forces when compared to the blade averaged value.

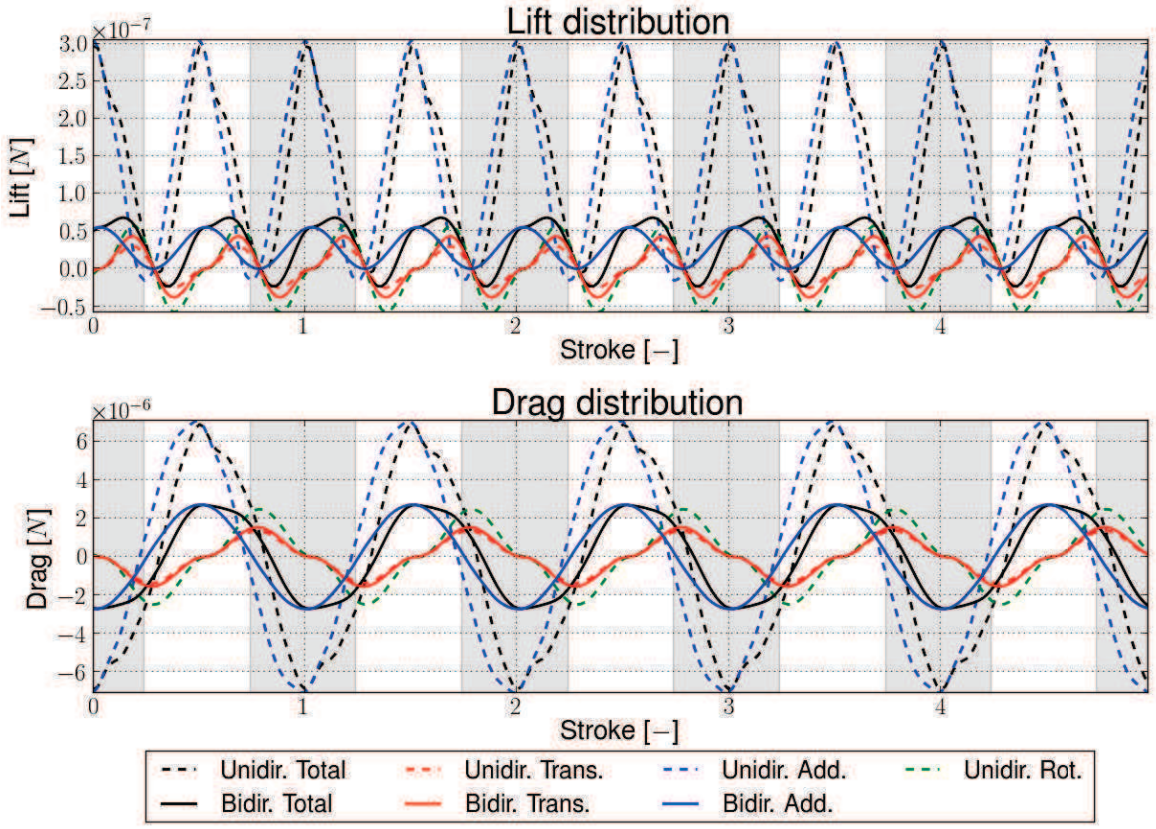

(a) Small actuation displacement (SA)

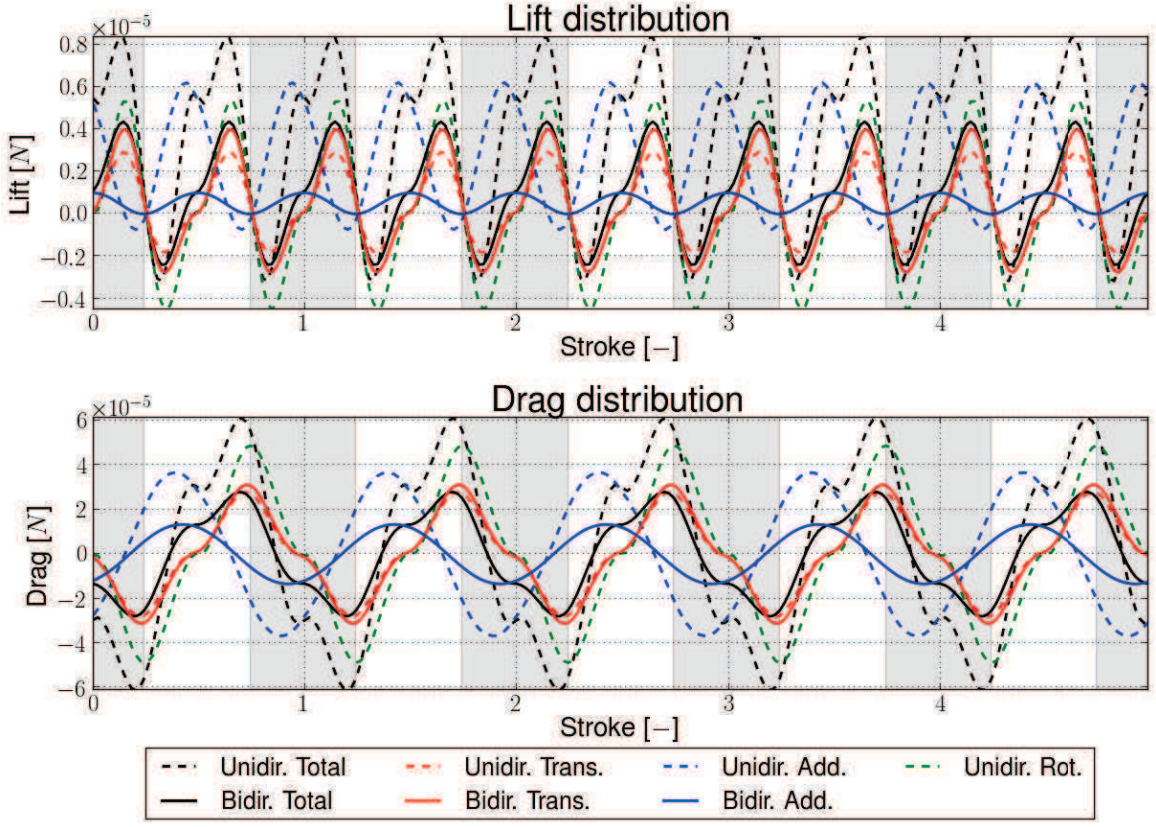

(b) Large actuation displacement (LA)

Figure 4.11: Graphical comparison between the aerodynamic forces calculated using the unidirectional and bidirectional flexible approach for the wing L2 when actuated at the vacuum resonant frequency in air. Calculations were done in the same conditions as in 5.2.2. More metrics about the comparison are given in the table 4.1.

Table 4.1: Summary of the bidirectional/unidirectional comparison for L2. The difference between the bidirectional and the unidirectional values is defined as $(F_{bi} - F_{uni})/F_{uni}$ with F_{bi} and F_{uni} the unidirectional and bidirectional computed forces respectively.

Component		**Lift**		**Drag**	
Actuation type		SA	LA	SA	LA
Translational forces	Difference Bidir./Unidir. on means [%]	12	10	-104	-102
	Difference Bidir./Unidir. on amplitudes [%]	46	42	13	11
Added-mass forces	Difference Bidir./Unidir. on means [%]	-80	-81	-106	-94
	Difference Bidir./Unidir. on amplitudes [%]	-82	-86	-61	-63
Total forces	Unidir. mean [μN]	0.14	3.42	0.00	0.00
	Bidir. mean [μN]	0.03	0.97	0.00	-0.00
	Difference Bidir./Unidir. on means [%]	**-79**	**-72**	**-99**	**-111**
	Unidir. amplitude [μN]	0.14	5.20	6.54	54.83
	Bidir. amplitude [μN]	0.05	3.04	2.86	25.49
	Difference on Bidir./Unidir. amplitudes [%]	**-68**	**-42**	**-56**	**-54**

Table 4.2: Summary of the bidirectional/unidirectional comparison for F3. The difference between the bidirectional and the unidirectional values is defined as $(F_{bi} - F_{uni})/F_{uni}$ with F_{bi} and F_{uni} the unidirectional and bidirectional computed forces respectively.

Component		**Lift**		**Drag**	
textbfActuation type		SA	LA	SA	LA
Translational forces	Difference Bidir./Unidir. on means [%]	12	9	-108	-96
	Difference Bidir./Unidir. on amplitudes [%]	45	40	11	9
Added-mass forces	Difference Bidir./Unidir. on means [%]	-81	-82	-90	-94
	Difference Bidir./Unidir. on amplitudes [%]	-83	-86	-67	-68
Total forces	Unidir. mean [μN]	0.20	3.97	0.00	0.00
	Bidir. mean [μN]	0.04	1.08	0.00	-0.00
	Difference Bidir./Unidir. on means [%]	**-80**	**-73**	**-99**	**-108**
	Unidir. amplitude [μN]	0.21	6.24	8.93	63.69
	Bidir. amplitude [μN]	0.07	3.55	3.47	29.09
	Difference on Bidir./Unidir. amplitudes [%]	**-66**	**-43**	**-61**	**-54**

Nonetheless, the trend in terms of lift is caught by the bidirectional approach as well as the periodicity of the added-mass. A slight phase-shift is also observed, when comparing with the unidirectional approach, resulting from the natural phase-shift existing between the leading-edge and the trailing-edge of the wing which is better depicted by the bidirectional approach. In terms of translational forces, the bidirectional component is slightly larger than the unidirectional one while the two approaches are synchronous. As expressed in the chapter 2.3, the translational formulation captures some of the rotational forces as highlighted graphically by the difference between the approaches occurring when rotational forces are generated. This is also another plus for the bidirectional approach, even if not all the rotational forces are captured.

Regarding now the drag performance, the results are slightly better with the overall difference going between -54% to -56% for L2, between -54% to -61% for F3 and between -55% to -66% for E4, again almost monotonically. Similarly, the main source of discrepancies is the added-mass component while the bidirectional translational component captures some effects of the unidirectional rotational component.

Interestingly, the rotational capture by the bidirectional approach seems to decreased with the wetted

Table 4.3: Summary of the bidirectional/unidirectional comparison for E4. The difference between the bidirectional and the unidirectional values is defined as $(F_{bi} - F_{uni})/F_{uni}$ with F_{bi} and F_{uni} the unidirectional and bidirectional computed forces respectively.

Component		Lift		Drag	
Actuation type		SA	LA	SA	LA
Translational forces	Difference Bidir./Unidir. on means [%]	11	9	-107	-97
	Difference Bidir./Unidir. on amplitudes [%]	44	38	10	7
Added-mass forces	Difference Bidir./Unidir. on means [%]	-82	-83	-92	-95
	Difference Bidir./Unidir. on amplitudes [%]	-83	-87	-71	-73
Total forces	Unidir. mean [μN]	0.18	3.92	0.00	0.00
	Bidir. mean [μN]	0.03	1.04	0.00	-0.00
	Difference Bidir./Unidir. on means [%]	**-81**	**-74**	**-99**	**-113**
	Unidir. amplitude [μN]	0.18	5.87	9.26	63.16
	Bidir. amplitude [μN]	0.06	3.33	3.10	28.65
	Difference on Bidir./Unidir. amplitudes [%]	**-69**	**-43**	**-66**	**-55**

area as highlighted by the slightly decreasing overestimation of the translational components for both the lift and the drag.

4.2.1.1 Conclusions on the numerical validation on beam wing

The bidirectional approach by means of its translational and added-mass components enables to model the same aerodynamic effects as the unidirectional one based on three components. Both models can be compared qualitatively as the curves shapes look strongly similar with the peaks and slope changes of the overall aerodynamic forces occurring simultaneously and as the mean values are about the same order of magnitudes capturing scrupulously the aerodynamic trend. However quantitatively, the bidirectional approach tends to minimize the aerodynamic force, in average by 56%, mainly due to the added-mass component and to the lack of a formulation for the rotational forces, even if the translational component captures some of them.

Thus the aerodynamic model is fit for trend-study like at the preliminary design stage and evaluate the performance of a flapped beam wing.

4.2.2 Membrane wing

Even if the aeroelastic framework is validated for beam wing, insect and FWNAV wings contain membranes which are mandatory for flying. Thus the aerodynamic model has to be validated above all on membrane wing. The comparison between the unidirectional and the bidirectional approach is for the membrane wing not straightforward. Indeed the kinematics data needed for the unidirectional approach prove to be quite noisy especially for the added-mass component as shown in the figure 4.12. Therefore to compare more easily the approaches, the kinematics data of the unidirectional approach are here filtered using an additional low-pass Butterworth filter. The table 4.4 and the figure 4.14 summarize the comparison for the wing FM3, shown in the figure 4.13, between the unidirectional and the bidirectional flexible approach. For the wing EM4, the comparison are summarized in the table 4.5 but the graphical comparisons are presented in the appendix B for sake of brevity.

Regarding the lift performance, the total force is underestimated with the overall difference going between -57% to -81% for FM3 and between -62% to -84% for EM4. By looking at the force decomposition,

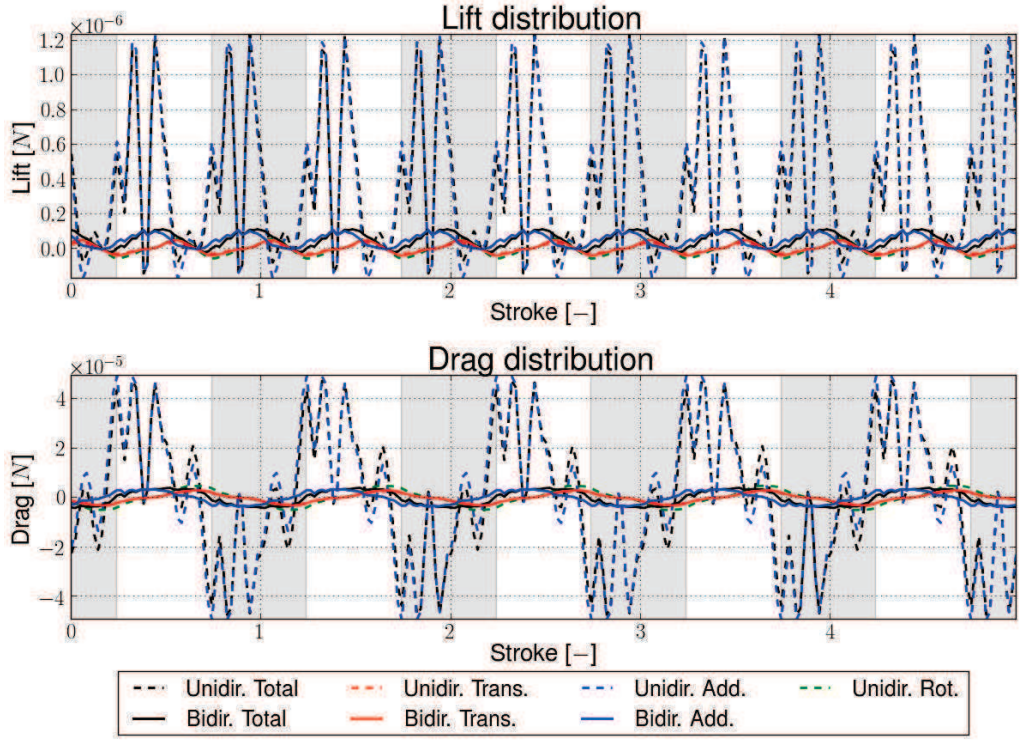

Figure 4.12: Example of comparison on a wing with membrane, here EM4, with noisy kinematics data interfering the unidirectional computation

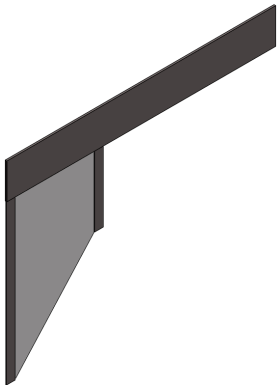

Figure 4.13: CAD view of the FM3 wing.

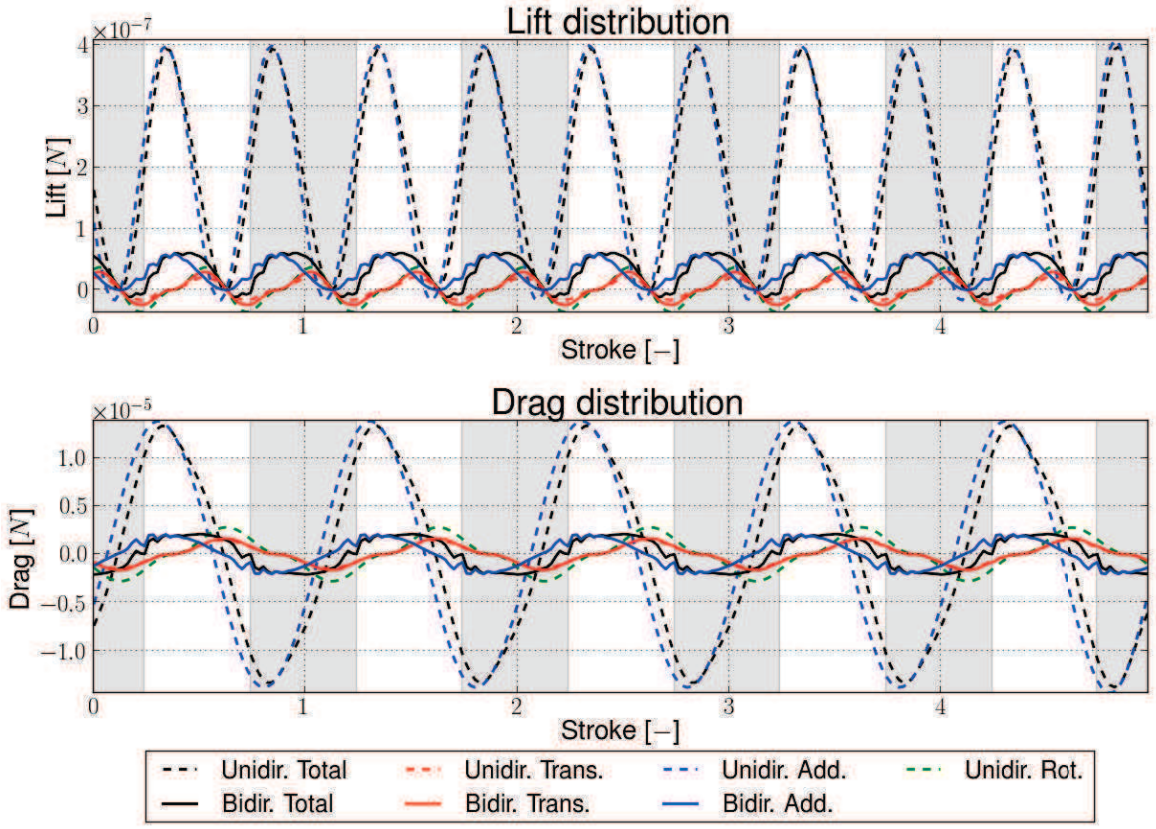

(a) Small actuation displacement (SA)

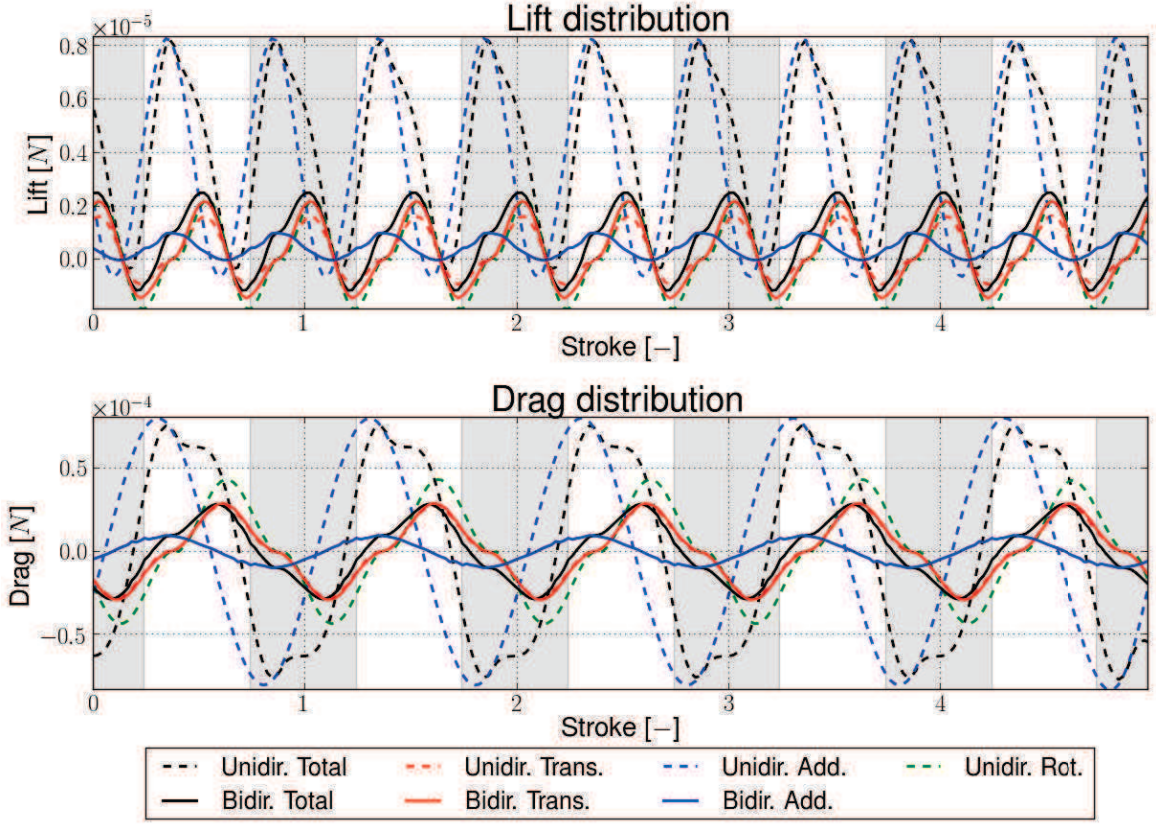

(b) Large actuation displacement (LA)

Figure 4.14: Graphical comparison between the aerodynamic forces calculated using the unidirectional and bidirectional flexible approach for the wing FM3 when actuated at the vacuum resonant frequency in air. Calculations were done in the same conditions as in 5.2.3. More metrics about the comparison are given in the table 4.4.

Table 4.4: Summary of the bidirectional/unidirectional comparison for FM3. The difference between the bidirectional and the unidirectional values is defined as $(F_{bi} - F_{uni})/F_{uni}$ with F_{bi} and F_{uni} the unidirectional and bidirectional computed forces respectively.

Component		**Lift**		**Drag**	
Actuation type		SA	LA	SA	LA
Translational forces	Difference Bidir./Unidir. on means [%]	8	4	-126	-99
	Difference Bidir./Unidir. on amplitudes [%]	44	43	10	5
Added-mass forces	Difference Bidir./Unidir. on means [%]	-85	-88	-100	-100
	Difference Bidir./Unidir. on amplitudes [%]	-86	-89	-86	-88
Total forces	Unidir. mean [μN]	0.19	4.20	0.03	0.09
	Bidir. mean [μN]	0.03	0.75	0.00	-0.00
	Difference Bidir./Unidir. on means [%]	**-84**	**-82**	**-100**	**-100**
	Unidir. amplitude [μN]	0.19	4.03	12.89	77.89
	Bidir. amplitude [μN]	0.04	1.72	2.30	25.36
	Difference on Bidir./Unidir. amplitudes [%]	**-81**	**-57**	**-82**	**-67**

Table 4.5: Summary of the bidirectional/unidirectional comparison for EM4. The difference between the bidirectional and the unidirectional values is defined as $(F_{bi} - F_{uni})/F_{uni}$ with F_{bi} and F_{uni} the unidirectional and bidirectional computed forces respectively.

Component		**Lift**		**Drag**	
Actuation type		SA	LA	SA	LA
Translational forces	Difference Bidir./Unidir. on means [%]	20	9	-100	-100
	Difference Bidir./Unidir. on amplitudes [%]	37	37	9	6
Added-mass forces	Difference Bidir./Unidir. on means [%]	-87	-88	-100	-100
	Difference Bidir./Unidir. on amplitudes [%]	-87	-90	-89	-91
Total forces	Unidir. mean [μN]	0.38	8.00	0.06	0.13
	Bidir. mean [μN]	0.05	1.39	0.00	-0.00
	Difference Bidir./Unidir. on means [%]	**-86**	**-83**	**-100**	**-100**
	Unidir. amplitude [μN]	0.38	7.39	29.85	160.63
	Bidir. amplitude [μN]	0.06	2.79	4.19	48.33
	Difference on Bidir./Unidir. amplitudes [%]	**-84**	**-62**	**-86**	**-70**

the main sources of discrepancies are the added-mass and also the rotational components, as the bidirectional translational component captures them marginally due to the increased wetted surfaces. The curve shapes can not be straightforwardly compared given that the added-mass peak tends to distort the total forces. However the curves are all similar to a sine like function with slight slope changes around each added-mass maximum. A larger phase-shift between the bidirectional and the unidirectional curves is also observed, most probably due the phase-shift between the leading-edge motion and the trailing-edge one and also between the inboard and outboard parts of the wing.

Regarding now the drag performance, the results are comparable with the overall difference going between -67% to -82% for FM3 and between -70% to -86% for EM4. The main sources of discrepancies are again the added-mass and the rotational components. While the former stays in line with the other results for beam and membrane wing, a change is observed for the latter. Indeed some of its effects were previously accounted by the bidirectional translational component, even if it was very moderate for the drag, but a negative gap occurs now on between the two approaches. This might be explained by the flexibility of the wing, accounted more properly by the bidirectional approach, which tends to reduce the drag as the wetted area decreased.

The curve shapes are also not straightforwardly comparable as the added-mass component tends to distort the total forces, but the same conclusion than for the lift might be drawn: a sine like function but with this time, two noticeable plateaus around a peak even if the plateau slope is inverted between the unidirectional and the bidirectional approach due to the added-mass peaks.

4.2.2.1 Conclusions on the numerical comparison on membrane wing

Even if the results are less convincing and more subject to discussion than for beam wing, the bidirectional approach captures qualitatively the main aerodynamic features occurring on a membrane wing. Additionnally, the bidirectional means and amplitudes for the drag and lift are of the same order of magnitude than the unidirectional ones. However the bidirectional added-mass component seems to be slightly under-estimated as it is missed its peak but still caught the average order of magnitude. The curve shapes are also roughly similar in terms of periodicity and in location of the slope changes. A larger phase-shift between the unidirectional and the bidirectional aerodynamic model is also observed most probably due to the wing flexibility better accounted by the bidirectional approach.

To sum up, given that the order of magnitude on the mean lift, relevant for the take-off of a FWNAV, and on the peak-to-peak forces in LA, relevant for the wing aeroelastic response, are correctly caught, the aeroelastic framework is cleared for trend studies and might be used for the preliminary design stage of a FWNAV.

4.3 Effect of the chordwise discretization on the added-mass forces

As just mentioned, the added-mass forces as formulated by the bidirectional flexible approach tend to miss the peak depicted by the unidirectional one even if the phase and the order of magnitude of the computed forces are overall satisfactory. The added-mass formulation is based on the works of Sedov [1965] for a flat plate and to trade-off between local and global effects, a formulation has been adopted in the chapter 2 depending on the local acceleration $\ddot{\eta}_i$ and chord c_i as reminded in the equation 4.1.

$$F_{added,i} = -\lambda_{\eta,i}\frac{\ddot{\eta}_i}{N_{FE}} \quad \text{with} \quad \lambda_{\eta,i} = \rho\pi\frac{c_i C_{blade}}{4}s_i \tag{4.1}$$

The aims were to take into account local acceleration, creating more added-mass forces locally, and also the shape of the FEs, a larger FE moving more fluid than a small one, so as to stay in line with the formulation defined by Sedov [1965] while accounting for the flexibility in the chordwise direction.

The observed discrepancies between the unidirectional and the bidirectional aerodynamic model might be linked to the chordwise discretization and its use in the added-mass formulation both in the added mass coefficient $\lambda_{\eta,i}$ and in the local acceleration $\ddot{\eta}_i$.

4.3.1 Exemple on a I-Wing

To highlight the influence of the chordwise discretization, the aeroelastic framework is used on a cantilever sized as the leading-edge of L2. The decomposition of the aerodynamic forces is given in the figure 4.15.

Given that the wing motion is merely the one of a flat plate perpendicular to the flow, the main force acting on the wing is the drag. When taking a closer look at the components of both the unidirectional and bidirectional aerodynamic models, each component matches with its counterpart while the rotational component is null given that the wing axis of rotation lays at mid-chord and inherently produces no forces. The same occurs for the lift, even if some discrepancies are noted resulting from the small values at stake

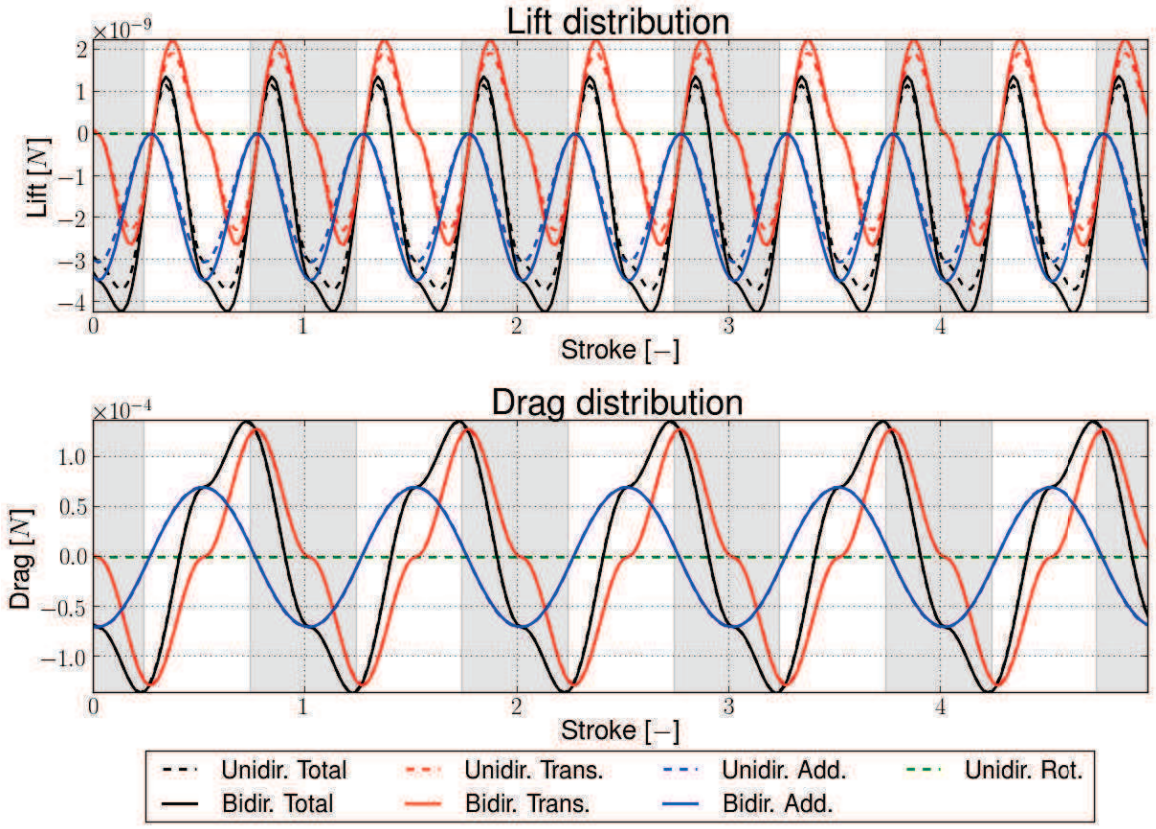

Figure 4.15: Comparison of the bidirectional/unidirectional approach on a cantilever sized as the leading-edge of L2.

and from the unidirectional approach which uses none projected data. Thus on a non chordwise discretized wing, the two approaches converge logically towards the same results.

However with a chordwise discretization, both approaches are doing the splits due to the rotational forces and the added-mass forces as depicted previously in the figure 4.11(b) for the wing L2 in LA. Of course, the rotational forces are not assumed to be taken into account by our model, except slightly by the translational forces, and is one reason of the observed discrepancy. However some refinements on the added-mass formulation might improve the quantitative discrepancy occurring between the unidirectional and the bidirectional aerodynamic model.

Two approaches are here discussed in order to fill the gap between the added-mass forces of the unidirectional and the bidirectional aerodynamic model. The first one is focused on the added mass coefficient $\lambda_{\eta,i}$ while the second on the local acceleration $\ddot{\eta}_i$.

4.3.2 Influence of the added-mass coefficient $\lambda_{\eta,i}$ formulation

The added-mass coefficient $\lambda_{\eta,i}$ models the volume of fluid set into motion by the wing when accelerating or decelerating. The theory from Sedov [1965] depicts this volume as a cylinder of diameter the blade chord C_{blade} and of length the blade span s_i, as illustrated by the figure 4.16(a) with the green disk. The original idea, developed in this work, should model the fluid as a sum of tiny cylinders, the red ones. Some kind kind of trade-off is achieved by using the local chord c_i and the blade chord C_{blade} simultaneously, but the volume of fluid is in any case underestimated. This approach has been chosen for sake of simplicity and ease of implementation as well as an inherent robustness.

To reduce the discrepancy between the approaches, a novel approach might be used where the volume of moved fluid is interpolated from the position of the FE in the blade as seen in the figure 4.16(b) by the red

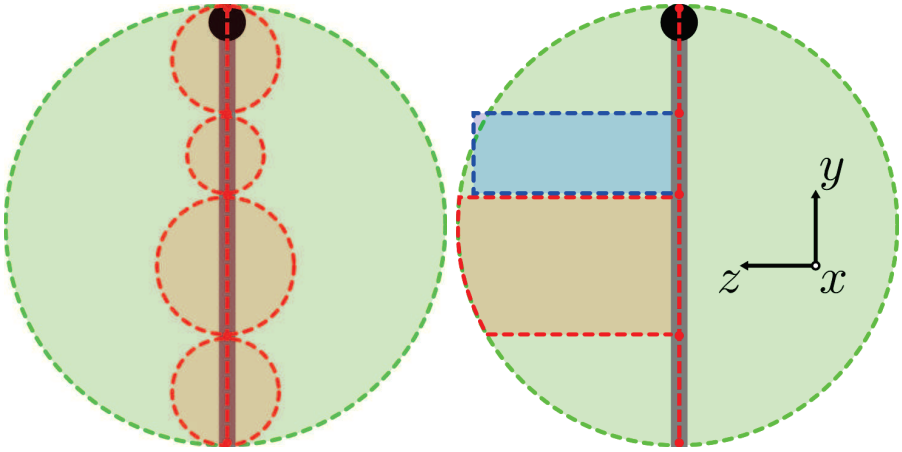

(a) Formulation with local information (b) Formulation with local information and volume interpolation

Figure 4.16: Scheme of possible added-mass formulations and theirs volume of fluid at stake.

area. Given the equation of a cylinder of diameter C_{blade} centered at mid-chord and of length s_i, the volume of fluid $V_{fluid,i}$ between the position y_i and y_{i+1} is defined as:

$$V_{fluid,i} = s_i \int_{y_i}^{y_{i+1}} \sqrt{C_{blade} y - y^2}\, \mathrm{d}y \tag{4.2}$$

However the primitive of such function is fairly complicated and a simplest approach is chosen, derived from a Riemann sum, with $V_{fluid,i}$ approximated by the rectangle beneath the curve, the blue area in the figure 4.16(b), times the local span:

$$V_{fluid,i} = 2 s_i c_i \frac{\left(\sqrt{C_{blade} y_{i+1} - y_{i+1}^2}\right) + \left(\sqrt{C_{blade} y_i - y_i^2}\right)}{2} \tag{4.3}$$

The added-mass forces are then reformulated as:

$$F_{added,i} = -\lambda_{\eta,i} \frac{\ddot{\eta}_i}{N_{FE}} \quad \text{with} \quad \lambda_{\eta,i} = \rho V_{fluid,i} \tag{4.4}$$

To test this assumption, the wing L2 in LA is recomputed and its results are given in the figure 4.17 and summarized in the table 4.6.

The gap between the unidirectional and the bidirectional approach is then slightly better with the novel approach especially for the mean performance but still not filled. In addition, it further credits to the original formulation indicating that the use $c_i C_{blade}$ is a good correction factor of the FE-shape effects given that the volume of fluid used here is almost identical to the one formulated by Sedov [1965].

Thus the reason for the discrepancies between the unidirectional and the bidirectional added-mass force stems from the other part of the equations 4.1 or 4.4: the local acceleration and its averaging factor.

4.3.3 Influence of the local acceleration factor

In the bidirectional added mass formulations adopted until now, the local acceleration $\ddot{\eta}_i$ is divided by N_{FE}, the number of FEs in the blade, so as to match the mean acceleration of the blade, when all elements are summed up. This assumption might be too restrictive and other arbitrary weighting factor might improve the

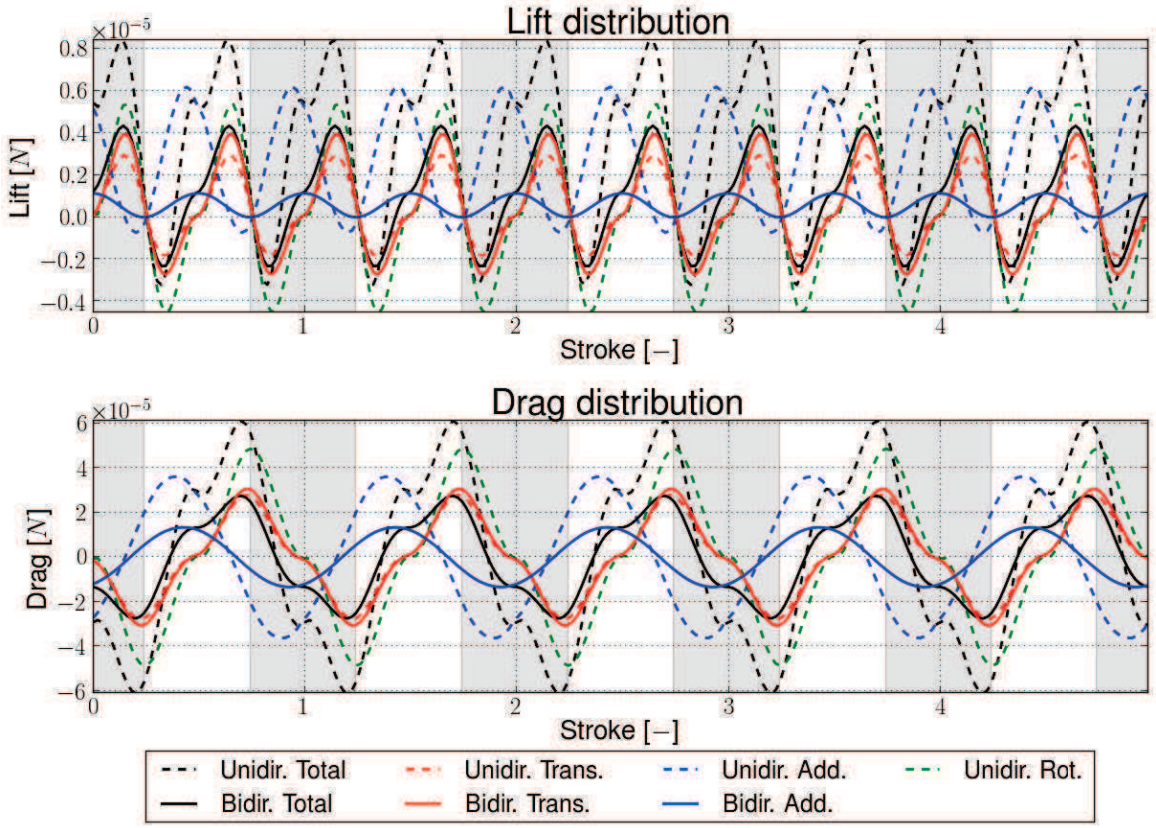

Figure 4.17: Graphical comparison between the bidirectional/unidirectional approach using $\lambda_{\eta,i} = \rho V_{fluid,i}$ and averaged $\ddot{\eta}_i$.

Table 4.6: Summary of the bidirectional/unidirectional comparison for L2 using $\lambda_{\eta,i} = \rho V_{fluid,i}$ and averaged $\ddot{\eta}_i$. The difference between the bidirectional and the unidirectional values is defined as $(F_{bi} - F_{uni})/F_{uni}$ with F_{bi} and F_{uni} the unidirectional and bidirectional computed forces respectively.

		Lift	Drag
Translational forces	Difference Bidir./Unidir. on means [%]	8.5	-110
	Difference Bidir./Unidir. on amplitudes [%]	40	10
Added-mass forces	Difference Bidir./Unidir. on means [%]	-79	-88
	Difference Bidir./Unidir. on amplitudes [%]	-84	-62
Total forces	Unidir. mean [μN]	3.41	0.00
	Bidir. mean [μN]	1.02	-0.00
	Difference Bidir./Unidir. on means [%]	**-70**	**-105**
	Unidir. amplitude [μN]	5.21	54.58
	Bidir. amplitude [μN]	3.00	25.23
	Difference on Bidir./Unidir. amplitudes [%]	**-42**	**-54**

accuracy of the added-mass computation and reduce the gap between the unidirectional and the bidirectional computation.

4.3.3.1 Using non-averaged local acceleration $\ddot{\eta}_i$

A first natural guess is to rely only on the local acceleration $\ddot{\eta}_i$, by dropping the weighting factor N_{FE}, so that the added-mass forces can be reformulated as:

$$F_{added,i} = -\lambda_{\eta,i}\ddot{\eta}_i \tag{4.5}$$
$$\text{with} \quad \lambda_{\eta,i} = \rho\pi\frac{c_i C_{blade}}{4}s_i$$

To test this assumption, the wing L2 in LA is recomputed and the results are given in the figure 4.18 and summarized in the table 4.7.

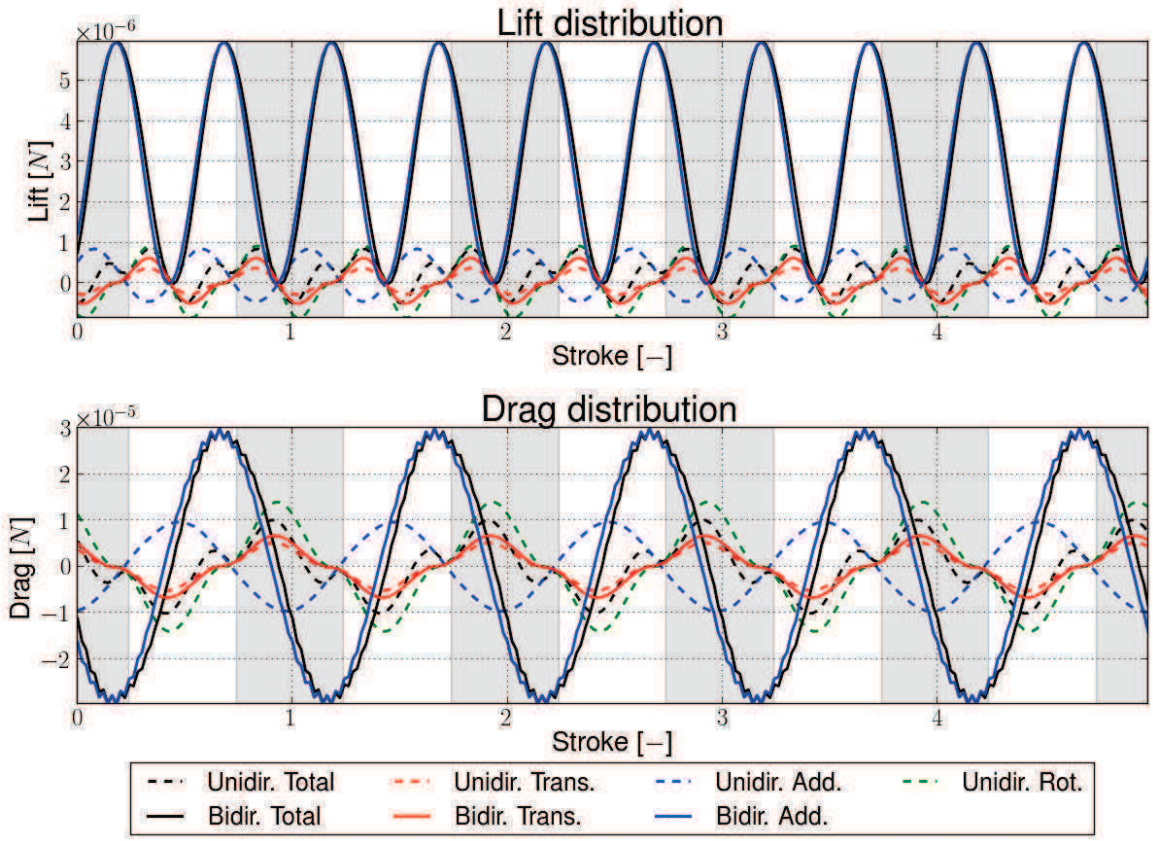

Figure 4.18: Graphical comparison between the bidirectional/unidirectional approach using non-averaged $\ddot{\eta}_i$.

Table 4.7: Summary of the bidirectional/unidirectional comparison for L2 using non-averaged $\ddot{\eta}_i$. The difference between the bidirectional and the unidirectional values is defined as $(F_{bi} - F_{uni})/F_{uni}$ with F_{bi} and F_{uni} the unidirectional and bidirectional computed forces respectively.

		Lift	**Drag**
Translational forces	Difference Bidir./Unidir. on means [%]	18	-98
	Difference Bidir./Unidir. on amplitudes [%]	73	30
Added-mass forces	Difference Bidir./Unidir. on means [%]	1523	-119
	Difference Bidir./Unidir. on amplitudes [%]	358	-206
Total forces	Unidir. mean [μN]	0.25	0.00
	Bidir. mean [μN]	3.03	-0.00
	Difference Bidir./Unidir. on means [%]	**1120**	**83**
	Unidir. amplitude [μN]	0.54	7.79
	Bidir. amplitude [μN]	3.00	29.26
	Difference on Bidir./Unidir. amplitudes [%]	**458**	**275.39**

The performance are dreadful with a huge overestimation of the aerodynamic forces by the bidirectional model, as highlighted by the differences on the total forces. The main reason lays with the strong local acceleration occurring on some elements that are highly boosted by the added-mass coefficient $\lambda_{\eta,i}$. Therefore the local acceleration can not be used on its own and really has to be pondered by a more appropriate factor than N_{FE}.

4.3.3.2 Iterative search of an appropriate weighting factor for the local acceleration

Given that the discrepancies between the unidirectional and the bidirectional computation occurred only on wing part with a chordwise discretization and that the bidirectional formulation stands otherwise, typically on the leading-edge elements, the added-mass formulation is split into two: the usual formulation for non-chordwise discretized wing blades and an acceleration pondered one otherwise as indicated in the equation 4.6.

$$F_{added,i} = \begin{cases} -\lambda_{\eta,i}\ddot{\eta}_i & \text{if } N_{FE} = 1 \\ -\lambda_{\eta,i}\frac{\ddot{\eta}_i}{WF} & \text{if } N_{FE} > 1 \end{cases} \tag{4.6}$$
$$\text{with} \quad \lambda_{\eta,i} = \rho\pi\frac{c_i C_{blade}}{4}s_i$$

To find the correct weighting factor WF, an iterative search is undertaken so as to retrieve almost the unidirectional performance with the bidirectional formulation. Two different cases are sought: the first where the bidirectional mean lift due to the added-mass forces is roughly equal to the unidirectional and the second where the bidirectional peak-to-peak drag of the added-mass forces is close to the unidirectional one. The former is of interest for the designer as it is one of the first variables of interest in the design of a FWNAV. The latter is of interest as the drag, in this configuration, is the major forces acting on the wing.

a) Iterative search on the mean lift

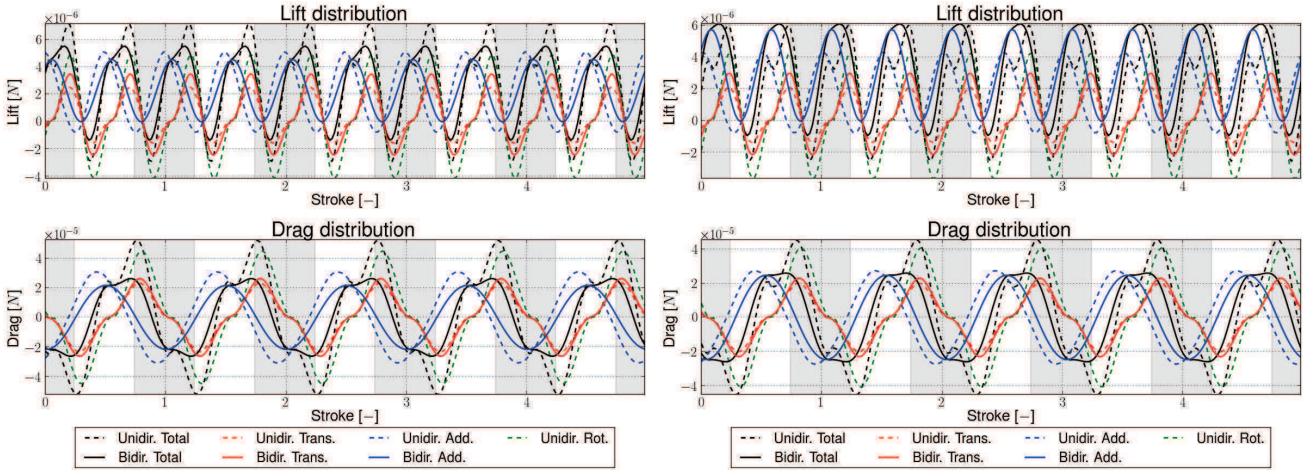

(a) $WF = N_{FE}/5$ to match the mean lift

(b) $WF = N_{FE}/7$ to match the peak-to-peak drag

Figure 4.19: Aeroelastic result for L2 with the weighting factor set to $WF = N_{FE}/5$ and $WF = N_{FE}/7$ so that respectively the unidirectional and the bidirectional added-mass mean lift and peak-to-peak drag are alike.

A weighting factor of $WF = N_{FE}/5$ is found to match fairly the mean lift as shown by the figure 4.19(a) and in the table 4.8 with only a 7% error on the mean added-mass lift. As expected, the overall forces are also better approximated with a mean error down to -31.5% for the peak-to-peak forces, which are sizing the system, and of -3% on the mean lift, which is essential for the designer.

b) Iterative search on the peak-to-peak drag

When now focusing on the peak-to-peak drag of the added-mass forces, the weighting factor becomes $WF = N_{FE}/7$ as depicted by the figure 4.19(b) and in the table 4.8 with only a error on the peak-to-peak drag of -7%. Similarly, the overall forces are better approximated in terms of peak-to-peak values with a mean error of only of -15% but the mean lift is overestimated with a 42% difference and compensates the rotational forces that are not modeled.

Table 4.8: Summary of the bidirectional/unidirectional comparison for L2 using pondered $\ddot{\eta}_i$ to match either the added mass mean lift with $WF = N_{FE}/5$ or the peak-to-peak drag with $WF = N_{FE}/7$. The difference between the bidirectional and the unidirectional values is defined as $(F_{bi} - F_{uni})/F_{uni}$ with F_{bi} and F_{uni} the unidirectional and bidirectional computed forces respectively.

		$WF = \frac{N_{FE}}{5}$		$WF = \frac{N_{FE}}{7}$	
		Lift	**Drag**	**Lift**	**Drag**
Translational forces	Difference Bidir./Unidir. on means [%]	10	-123	11	-140
	Difference Bidir./Unidir. on amplitudes [%]	45	13	48	15
Added-mass forces	Difference Bidir./Unidir. on means [%]	**7**	3	64	6
	Difference Bidir./Unidir. on amplitudes [%]	-22	-28	15	**-7**
Total forces	Unidir. mean [μN]	2.73	0.00	2.24	0.00
	Difference Bidir./Unidir. on means [%]	**-3**	**-95**	**42**	**-86**
	Unidir. amplitude [μN]	4.44	45.82	3.74	39.42
	Difference on Bidir./Unidir. amplitudes [%]	**-24**	**-39**	**-4**	**-26**

Given the number of FEs used to discretize the vein (20), a weighting factor of about $WF = \frac{20}{6} = 3.33$ seems to be a good approximation of both cases studied above. This factor is independent of the chordwise discretization as highlighted by the figure 4.20(a), where the wing L2 was recomputed with 5 FEs for the vein, and might even be extended reasonably to other wings, such as the wing FM3 in figure 4.20(b).

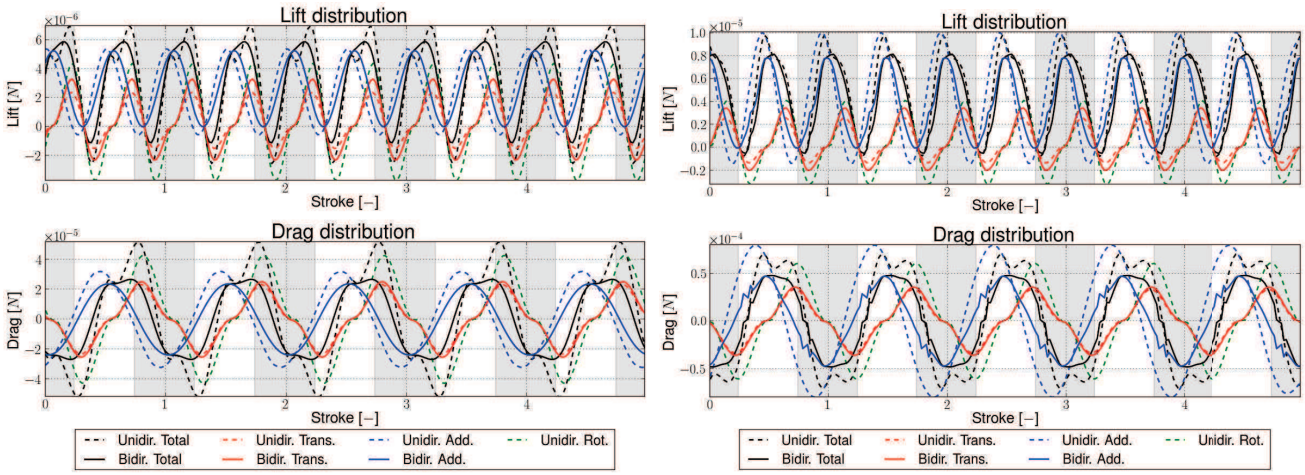

(a) Wing L2 with a coarser mesh (5x5)

(b) Wing FM3

Figure 4.20: Extension of the weighting factor to other meshes and wings with $WF = 3.33$ such as the wing L2, recomputed with a coarser mesh, and the wing FM3.

4.3.4 Remarks on the added-mass formulation

The added-mass formulation adopted in this work using the local information of the FE is fairly appropriate to depict these forces and a good basis opens to basic refinements. As seen with the added-mass coefficient $\lambda_{\eta,i}$, the original formulation using the local chord c_i and the blade chord C_{blade} is already a good approximation of the volume of moved fluid and might be enhanced by interpolating a more realistic volume from the cylinder predicted by Sedov [1965]. However the most significant improvement is done by adjusting the local acceleration factor enabling a more accurate prediction of the aerodynamic forces experienced by the wing both in terms of mean lift, essential for designers, and in terms of peak-to-peak values which sized the aeroelastic response. It also influences the wing deformation and the phase-shift positively as reported in the chapter 5.3.

However given its arbitrary value, the weighting factor is not used systematically in the rest of this work. Instead the original bidirectional formulation is used as being the common denominator to these refinements and enabling sounder comparison without any artificial bias.

Before rushing into any design or validation process, the influence of the material parameters on both the wing deformation and the aerodynamic forces has to be determined so as to define proper safety margins.

4.4 Sensitivity of the aeroelastic model to material parameters

In the design process of the OVMI, typical values from SU-8 are used that might be slightly different from the experimental one especially given its fabrication and time dependency. Similarly, the validation process defined in the chapter 5.1 aims at determining the material properties of a wing which depends on the measurement uncertainties. Therefore, it is necessary to assess the sensitivity of the aeroelastic framework towards the material parameters and gives thus insight and credit into the aeroelastic performance computed.

4.4.1 Sensitivity towards the Young modulus

To outline the influence of the Young modulus, the wing L2 is computed with values varying from $\pm 10\%$ and compared to the baseline value of $7.3GPa$ for the displacement and the aerodynamic forces. The results are shown in the figure 4.21 and summarized in the table 4.9

Table 4.9: Summary of the Young modulus sensitivity analysis on L2. The difference between the modified Young and the baseline, determined in the chapter 5.2, is defined as (Mod − Bsl) /Bsl with Mod and Bsl the modified and the baseline value respectively. The drag mean error is overestimated as the reference value is very small.

		90% E_{exp}	**110%** E_{exp}
Displacement	Difference on leading-edge amplitudes [%]	-0.12	0.09
	Difference on tip amplitudes [%]	-0.13	0.10
Aerodynamics forces	Baseline mean lift [μN]	0.97	
	Baseline lift amplitude [μN]	3.04	
	Difference on lift means [%]	-10.25	10.23
	Difference on lift amplitudes [%]	-10.32	10.32
	Baseline mean drag [μN]	0.00	
	Baseline drag amplitude [μN]	25.49	
	Difference on drag means [%]	-9.84	9.89
	Difference on drag amplitudes [%]	-10.22	10.21

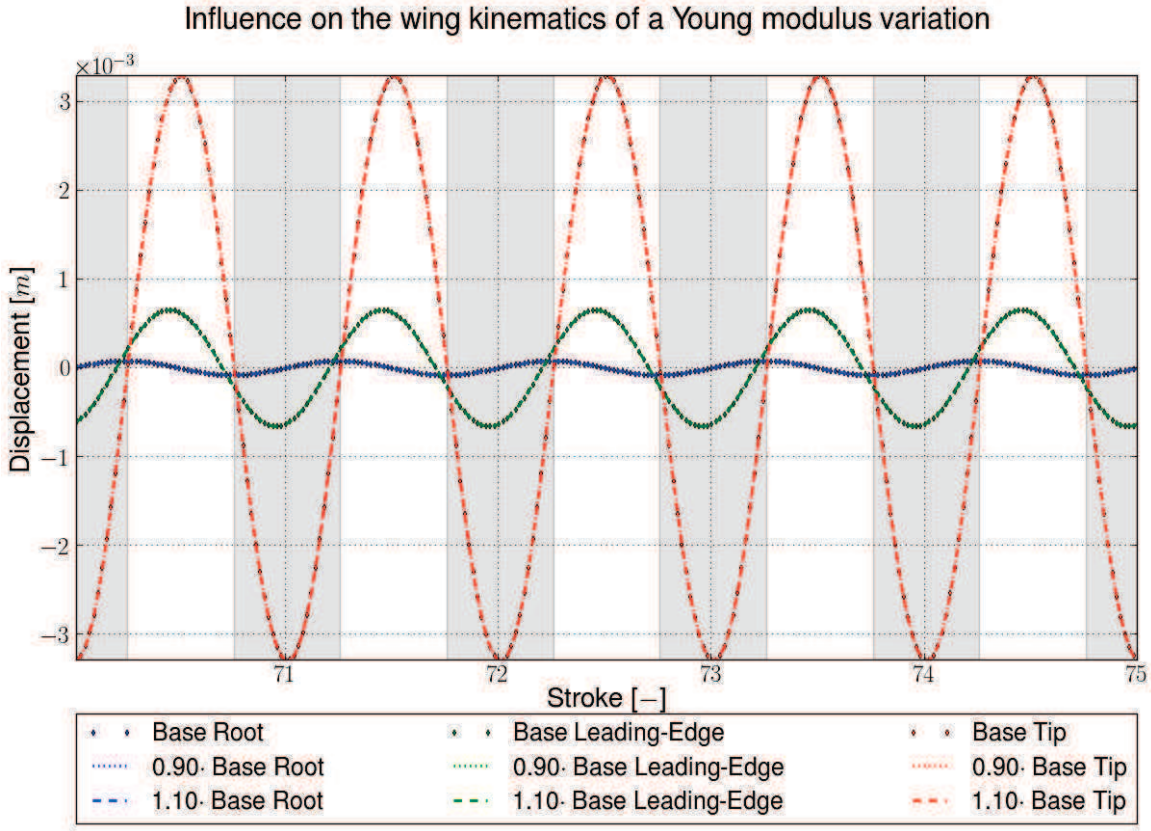

(a) Displacement

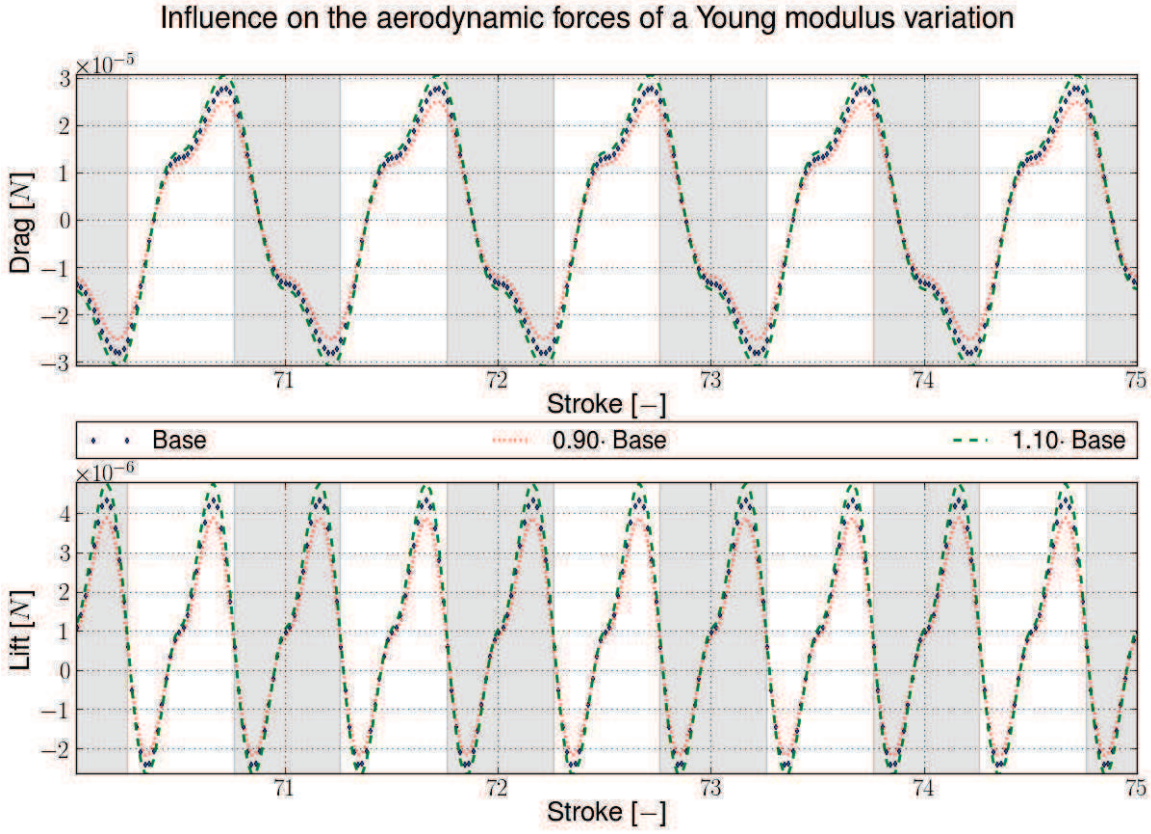

(b) Aerodynamic forces

Figure 4.21: Graphical comparison of a 10% variation of the L2 Young modulus on the displacement and on the aerodynamic forces. Otherwise calculations are done with the same settings as in the chapter 5.2.2. More details about the comparison are given in table 4.9.

In terms of displacement, the influence of the Young modulus is very limited as the difference is below the percent for both the means and the amplitudes of about a hundredth of the Young modulus variation. However the aerodynamic forces are quite sensitive but follow the variation of ±10%. To explain the gap, one as to keep in mind that the velocity and the acceleration vary as $A \cdot f_{wing}$ and $A \cdot f_{wing}^2$ respectively. Thus for the 90% case, the decreased resonant frequency of the wing, $127.2Hz$, implies lower velocities and accelerations resulting in lower aerodynamic forces. For the 110% case, the explanation is similar: an higher resonant frequency, $140.7Hz$, induces higher kinematics and thus higher aerodynamic forces.

From an validation point-of-view, the influence of the Young modulus is minim given that only wing deformation is needed. From a design point-of-view, the influence of the Young modulus is more critical. Indeed if the Young modulus is strongly fabrication dependent, as reported and experienced with the SU-8, the numerical prediction, using literature values, might be far-off from what is endured by the prototype. Thus special cares are necessary during the fabrication so as to minimize this drift or at least contains it. However a rule of thumb might be defined: the aerodynamic forces vary like the Young modulus perturbation and the displacement like its hundredth.

4.4.2 Sensitivity towards the density

To outline the influence of the density, the wing L2 is computed with the values varying from ±10% and compared to the baseline value of $1190kg.m^{-3}$ for the displacement and the aerodynamic forces. The results are shown in the figure 4.22 and summarized in the table 4.10

Table 4.10: Summary of the density sensitivity analysis on L2. The difference between the modified density and the baseline, defined in the chapter 3.5, is defined as $(\text{Mod} - \text{Bsl})/\text{Bsl}$ with Mod and Bsl the modified and the baseline value respectively.

		90% ρ	**110% ρ**
Displacement	Difference on leading-edge amplitudes [%]	-4.46	4.13
	Difference on tip amplitudes [%]	-4.38	4.07
Aerodynamics forces	Baseline mean lift [μN]	0.97	
	Baseline lift amplitude [μN]	3.04	
	Difference on lift means [%]	2.30	-2.23
	Difference on lift amplitudes [%]	-2.32	1.96
	Baseline mean drag [μN]	0.00	
	Baseline drag amplitude [μN]	25.49	
	Difference on drag means [%]	-7.82	8.80
	Difference on drag amplitudes [%]	1.28	-1.32

In terms of displacement, the influence of the density is noticeable with a difference slightly below the half of the density perturbation. However, the aerodynamic forces are more insensitive with a lower difference of about 2%. This is understandable for both cases considering the resonant frequencies and the lower amplitudes observed. For the 90% case, while the wing amplitudes decrease, the resonant frequency of the wing increase to $141.3Hz$ and counterbalance the lack of amplitude by higher kinematics. As a result, the aerodynamic are almost unchanged. The reasoning is similar for the 110% case. The wing amplitude is higher but the resonant frequency crashes to $127.9Hz$ thus canceling the increase of amplitude and giving almost identical aerodynamic forces.

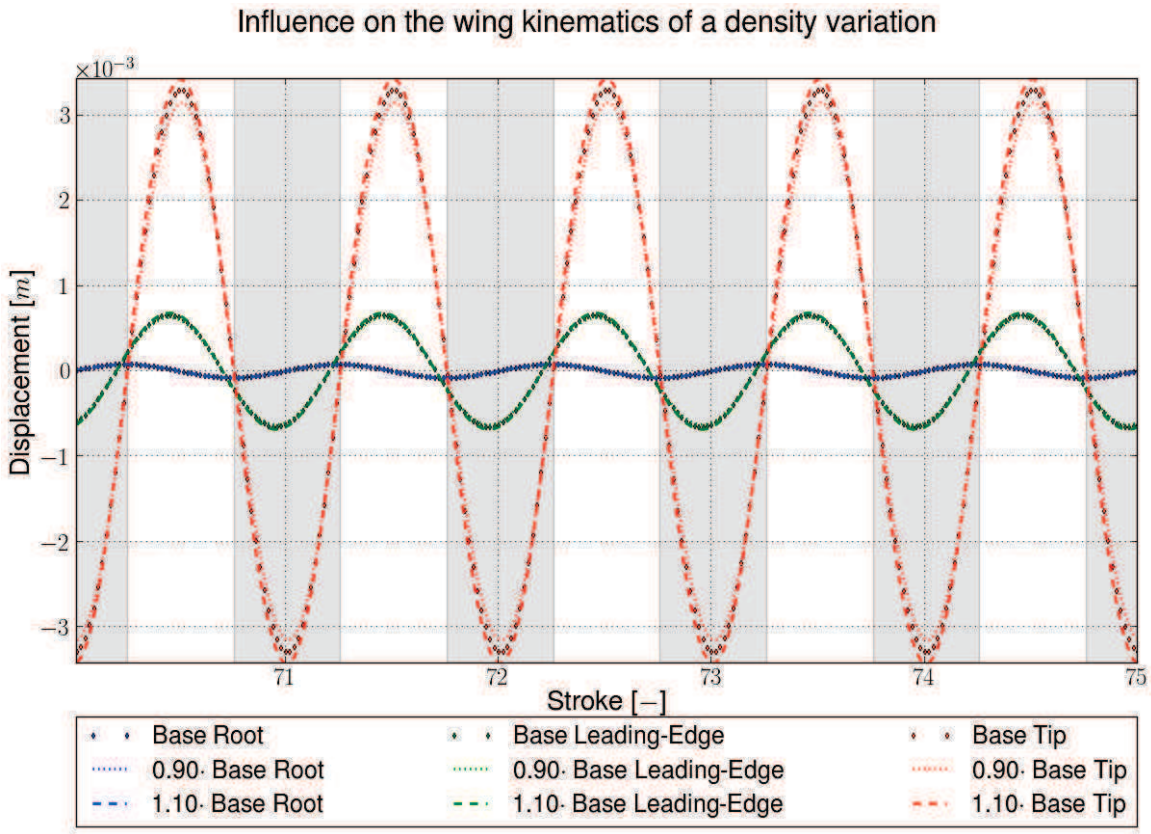

(a) Displacement

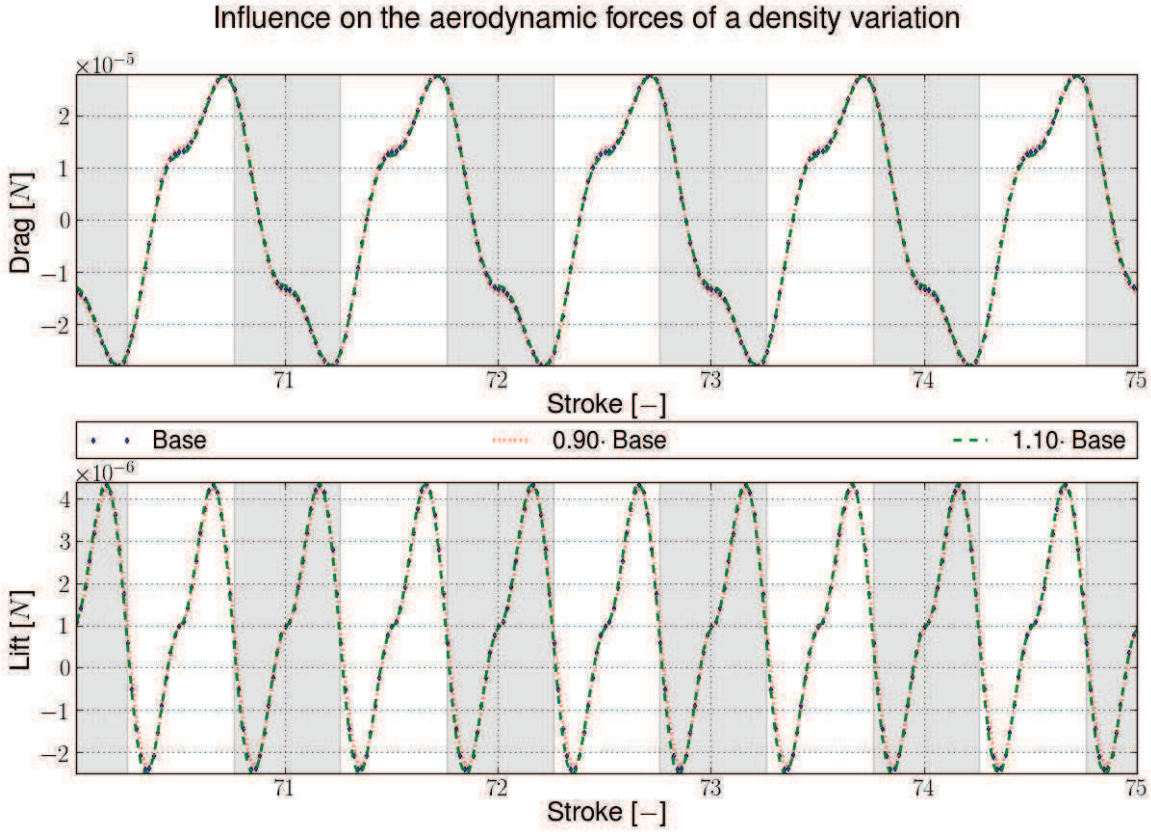

(b) Aerodynamic forces

Figure 4.22: Graphical comparison of a 10% variation of the L2 density on the displacement and on the aerodynamic forces. Otherwise calculations are done with the same settings as in the chapter 5.2.2. More details about the comparison are given in table 4.10.

The effect of a slight density change is thus moderate. The change of resonant frequency tends to be countered by a loss or gain of amplitude resulting in almost identical aerodynamic forces. For the aeroelastic framework and its validation, it means that the hypothesis of constant density is valid. Furthermore from a designer point of view, this implies that literature value might be used without problems and no special care is required for the fabrication. However a rule of thumb might be defined: the aerodynamic forces vary like the fifth of the density perturbation and the displacement like its half.

4.4.3 Sensitivity towards the damping ratio ζ_i

To outline the influence of the damping, the influence of the damping ratio ζ_i is investigated instead of the influence of the Rayleigh coefficients. Indeed even if the FE-model is using the latter, their values are still computed using the former which are given as inputs by the designers or determined experimentally. Thus the influences of predominant damping ratio might be investigated.

4.4.3.1 Damping ratio of the first mode

For ζ_1, the wing L2 is computed with the values varying from $\pm 10\%$ and compared to the baseline value of 0.0087 for the displacement and the aerodynamic forces. The results are shown in the figure 4.23 and summarized in the table 4.11.

Table 4.11: Summary of the ζ_1 Rayleigh coefficient sensitivity analysis on L2. The difference between the modified ζ_1 Rayleigh coefficient and the baseline, determined in the chapter 5.2, is defined as (Mod − Bsl) /Bsl with Mod and Bsl the modified and the baseline value respectively.

		90% ζ_1	**110% ζ_1**
Displacement	Difference on leading-edge amplitudes [%]	1.29	-1.30
	Difference on tip amplitudes [%]	1.14	-1.11
Aerodynamics forces	Baseline mean lift [μN]	0.97	
	Baseline lift amplitude [μN]	3.04	
	Difference on lift means [%]	2.43	-2.34
	Difference on lift amplitudes [%]	3.26	-3.12
	Baseline mean drag [μN]	0.00	
	Baseline drag amplitude [μN]	25.49	
	Difference on drag means [%]	-0.14	1.35
	Difference on drag amplitudes [%]	2.39	-2.33

In terms of displacement, the influence of ζ_1 is limited with the difference varying like the tenth of the perturbation which is in line with the physics, the structure being less or more damped respectively. This reflects in terms of aerodynamics on a slightly larger variation of about a fifth of the perturbation. This is understandable as the amplitude of the wing motion is decreased but no frequency shift occurs to counterbalance this change of amplitude. Thus the damping ratio of the first mode is having a slight effect on both the displacement and the aerodynamic forces but which is not as critical as the Young modulus or the density.

4.4.3.2 Damping ratio of the second mode

For ζ_2, the wing L2 is computed with the values varying from $\pm$ 10% and compared to the baseline value of 0.0085 for the displacement and the aerodynamic forces. The results are shown in the figure 4.24 and summarized in the table 4.12.

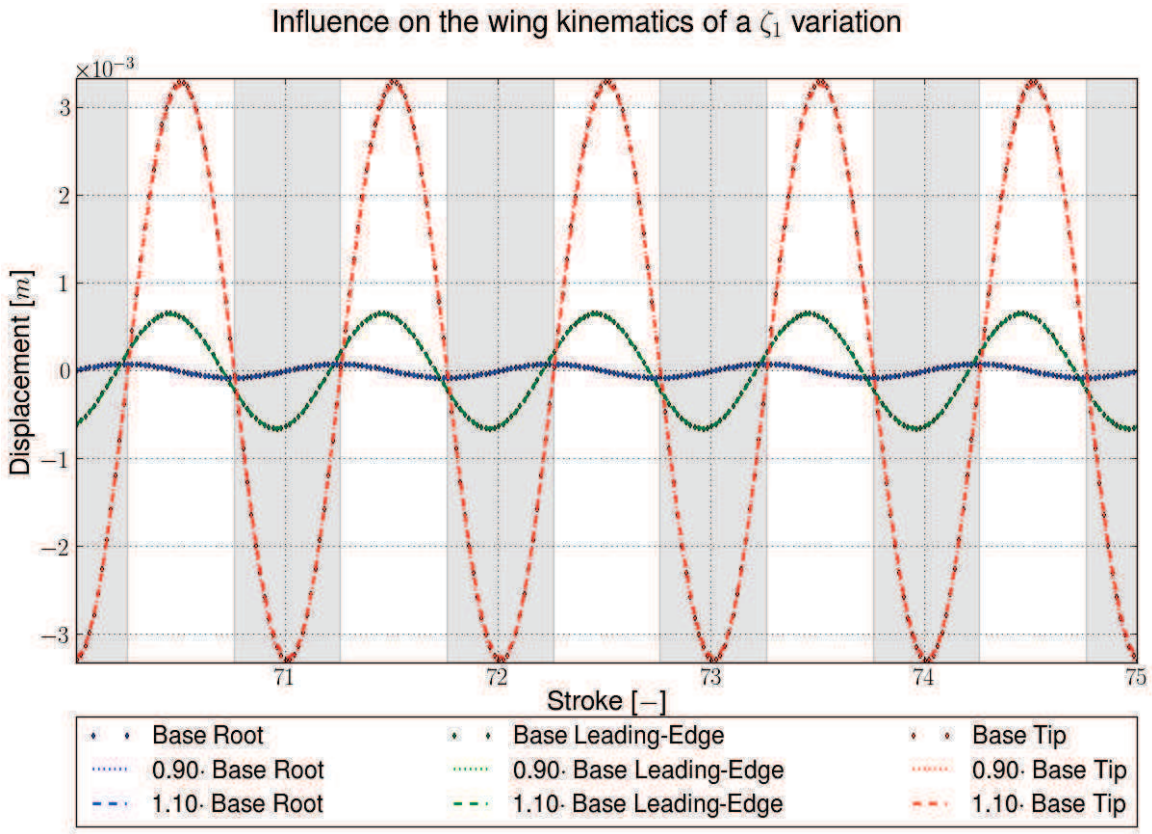

(a) Displacement

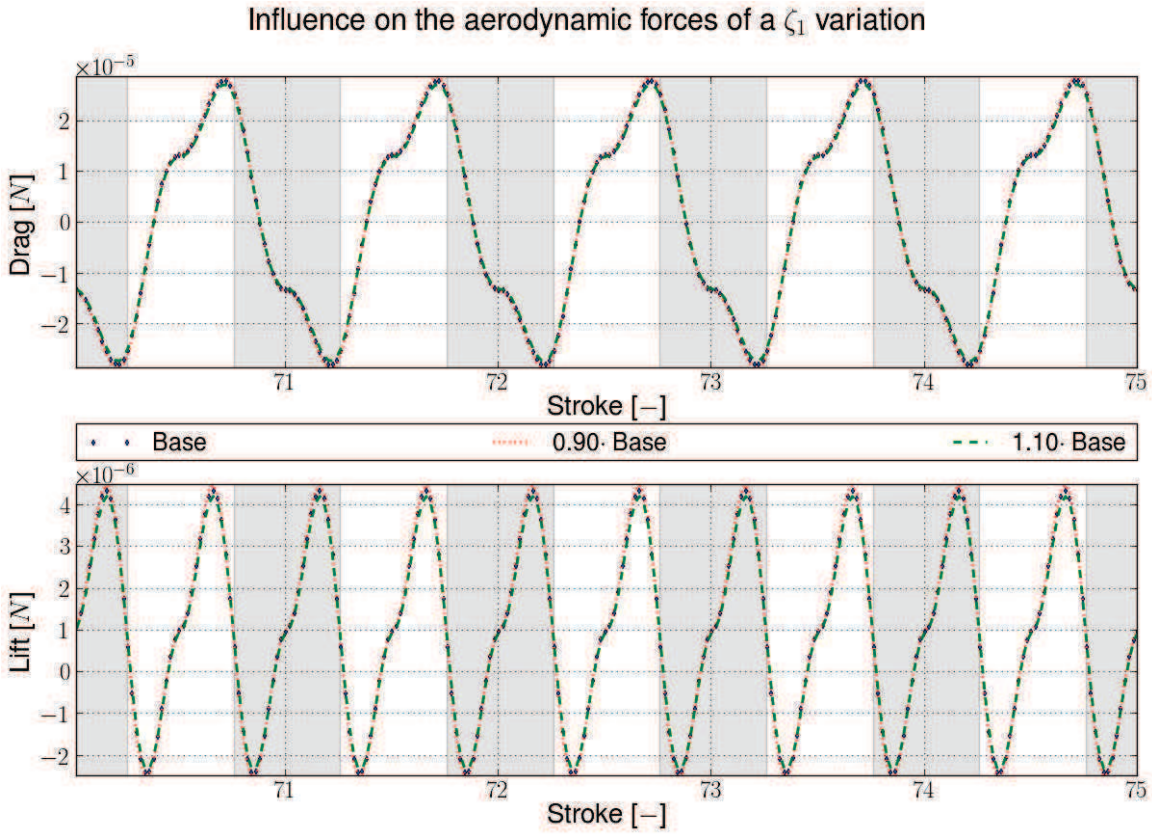

(b) Aerodynamic forces

Figure 4.23: Graphical comparison of a 10% variation of the ζ_1 Rayleigh coefficient on the displacement and on the aerodynamic forces for L2. Otherwise calculations are done with the same settings as in the chapter 5.2.2. More details about the comparison are given in table 4.11.

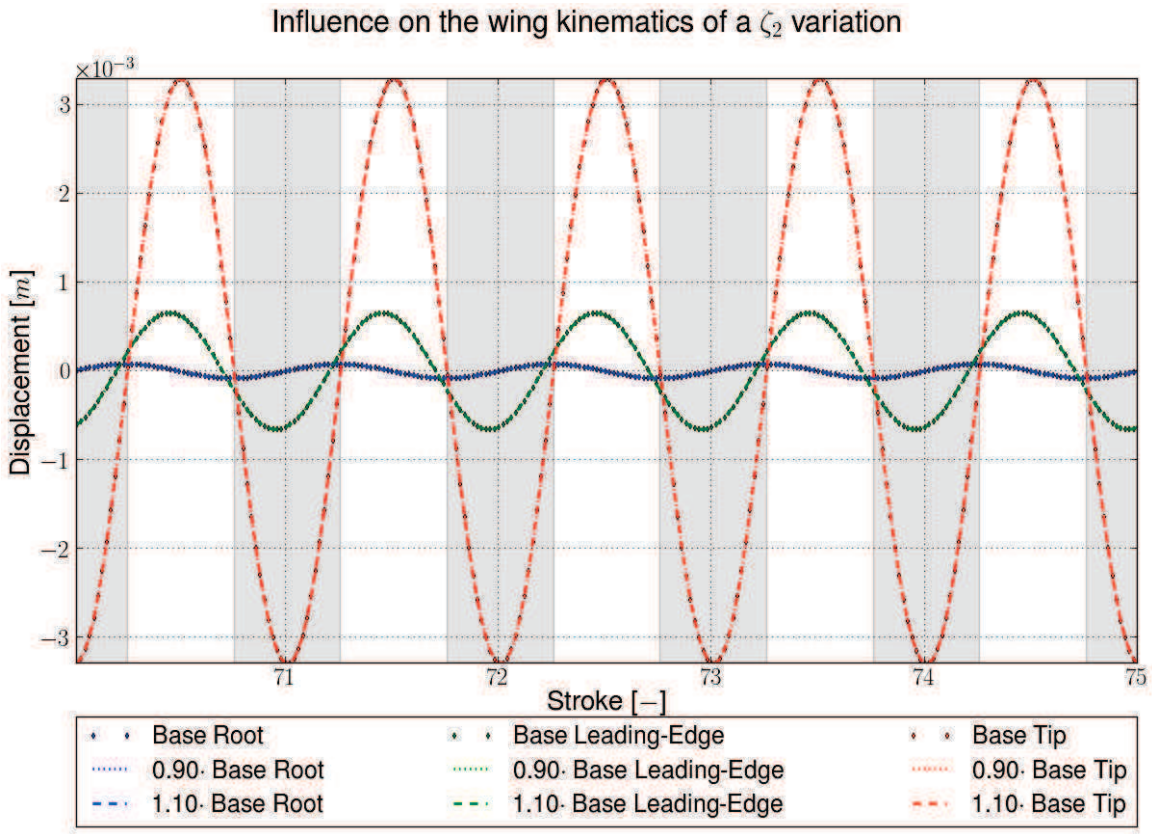

(a) Displacement

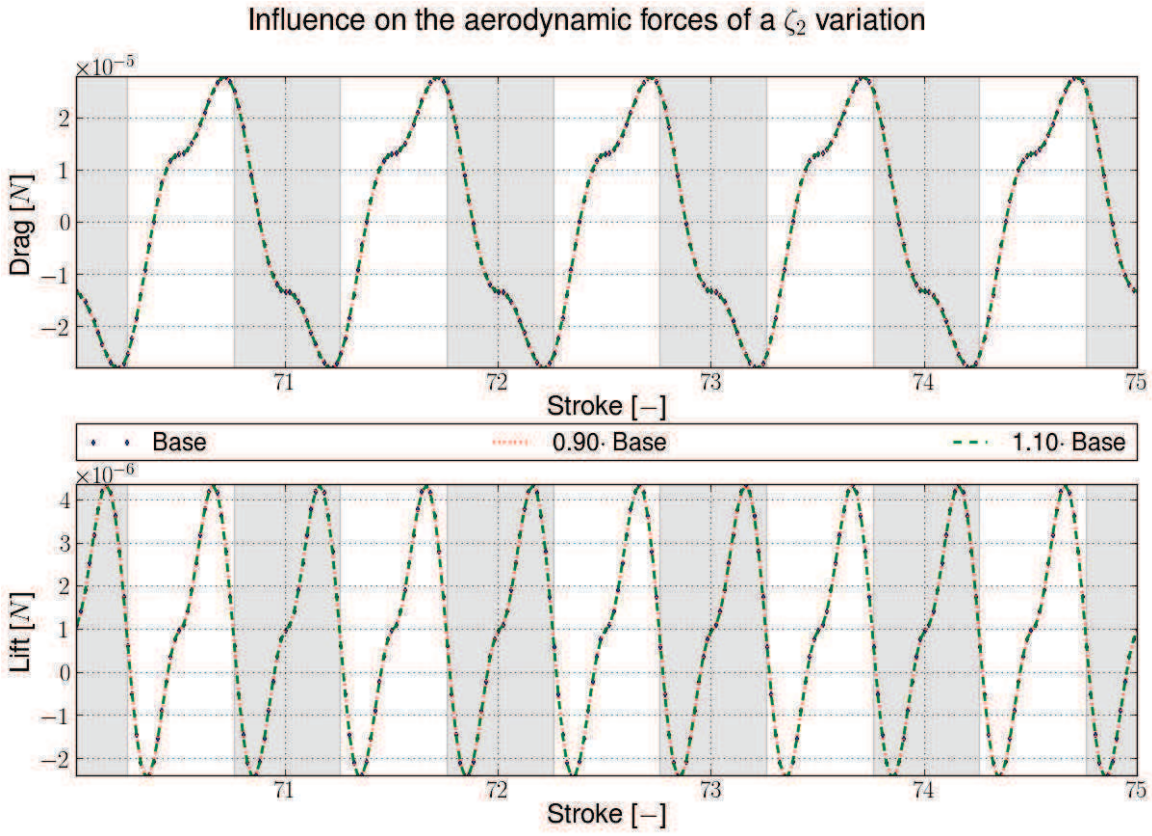

(b) Aerodynamic forces

Figure 4.24: Graphical comparison of a 10% variation of the ζ_2 Rayleigh coefficient on the displacement and on the aerodynamic forces for L2. Otherwise calculations are done with the same settings as in the chapter 5.2.2. More details about the comparison are given in table 4.12.

Table 4.12: Summary of the ζ_2 Rayleigh coefficient sensitivity analysis on L2. The difference between the modified ζ_2 Rayleigh coefficient and the baseline, determined in the chapter 5.2, is defined as (Mod – Bsl) /Bsl with Mod and Bsl the modified and the baseline value respectively.

		90% ζ_2	**110% ζ_2**
Displacement	Difference on leading-edge amplitudes [%]	-0.06	0.07
	Difference on tip amplitudes [%]	0.06	-0.07
Aerodynamics forces	Baseline mean lift [μN]	0.97	
	Baseline lift amplitude [μN]	3.04	
	Difference on lift means [%]	0.13	-0.13
	Difference on lift amplitudes [%]	0.17	-0.21
	Baseline mean drag [μN]	0.00	
	Baseline drag amplitude [μN]	25.49	
	Difference on drag means [%]	3.69	1.69
	Difference on drag amplitudes [%]	-0.01	0.01

In terms of displacement, the influence of ζ_2 is even more limited with the differences below the hundredth of the perturbation which is in line with the physics, the structure being actuated at its first resonant frequency. This reflects almost not on the aerodynamic forces with an error of about a hundredth. Thus a variation of the damping ratio of the second mode is not critical at all for both the displacement and the aerodynamic forces.

4.4.3.3 Remarks on the damping ratio sensitivity study

To sum up, the performance of the aeroelastic framework in terms of displacement and aerodynamic forces are not affected by a slight perturbation of the damping ratio. From the two damping ratios needed to translate the damping into Rayleigh coefficients, only the first one has a moderate effect on the performance of about a tenth and a fifth on the displacement and the aerodynamic force respectively which is comprehensible given that the wing is actuated at the first resonant frequency. Thus the designer can used literature data as only slight discrepancies occur but the experimenter has to take great care in the frequency scanning of the first peak.

The aeroelastic framework has been here intensively stress-tested to assess its numerical behavior versus its calculations parameters and also to credit the bidirectional flexible aerodynamic model. Good practices are thus provided to complete successfully aeroelastic computation, to improve the prediction of the aerodynamic model and to anticipate the effect of material uncertainties. The next step is to proceed with the experimental validation of the aeroelastic framework and further validate its potential for the preliminary design applications of flapping-wing systems.

Chapter 5

Experimental investigations

Contents

With the aeroelastic framework formulated, implemented and stress-tested, the next mandatory step before operating it is its validation. Each component of the framework, the structural and the bidirectional aerodynamic models as well as the aeroelastic coupling, has in somehow to be compared to real world data to check if the framework predictions are coherent and depict real performance. As stated in the literature review of chapter 1.3.1, few experimental data are available for a very flexible, high-frequency resonant wing. Therefore new data have to be generated to carefully and gradually validate the aeroelastic framework. To do so, a complete methodology, based on the time-history of the wing deformation, has been devised to conduct experiments on a dedicated test bench with some validation wings providing the deflection of several wing extremities versus time in both vacuum and air. These data allow to verify the structural model of the framework and also its aeroelastic coupling respectively.

Experiments were also originally considered to validate the aerodynamic model along with the aeroelastic coupling by measuring the aerodynamic forces, but the appropriate sensor is not yet available, see appendix C for details. However the aerodynamic model has been already partially 'validated' in the chapter 4.2 and the results on the aeroelastic response of the wing will complete further this validation.

This chapter is organized around the experimental validation. First, the experimental setup and methodology used to acquire the validation data are described. Second, the experimental results are presented along their numerical counterparts. Third, several factors are investigated to improve the agreement between the experimental and numerical data in terms of phase-shift or amplitudes for example. Fourth, as experimental results are available as references, the relevance of the large deflection capability of the FEs is discussed.

5.1 Experimental environment and methodology for the validation of the aeroelastic framework

The whole experimental process, i.e. the environment and the methodology, aims to acquire proper data so as to enable a step-by-step validation of the aeroelastic framework. To this end, a dedicated test bench and methodology have been devised. This section describes them extensively and introduces also a set of academic wing geometries used for the validation process as guinea pigs. These wings have already been used partially for the numerical benchmarking of the chapter 4.

5.1.1 Presentation of the test bench

In order to size the test bench, it is important to understand what are the damping sources which influence the aeroelasticity phenomena encountered by a vibrating wing. The wings are fabricated using MEMS technologies, see appendix A for more details, which are commonly used to fabricate micro (length below the mm), high-frequency (over the $1kHz$) resonant structure as sensors. There, common damping sources for resonant structures are essentially caused by material and thermoelastic damping, clamping and support loss, and airflow force (Ono and Esashi [2002]; Hosaka and Itao [1999]). However the wings are envisioned to be over $10mm$ in span and vibrating around $100Hz$. At this scale, Hao et al. [2003] demonstrate that clamping loss is too small to play a dominant role in the damping behavior of the wing. Moreover, since the system stays more or less in a thermal equilibrium (isothermal state) for the frequencies (Schmid and Hierold [2008]), it is obvious that thermoelastic damping can be neglected too. Therefore only the material damping, referred now on as structural damping, and the air damping are assumed to be relevant in the aeroelastic modeling of the wing. Obviously their role and determination are quite important for a structure at resonance as they determine the amplitude of the mode shape.

As seen in figure 5.1 for the case of SU-8 micro-cantilevers at resonance, the quality factor, inversely proportional to the damping, increases with the vacuum level until it reaches a plateau. In terms of deflection, it means that the cantilever deflection increases gradually until the plateau and that the deflection amplitude is imposed by the damping sources. Three different regions are thus characterized for the overall damping mechanisms: the viscous, the molecular and the intrinsic region. The first two are related to the collision of air molecules with the structure damping its motion while the latter is strictly due to the structure and its material. Before explaining each regions, the mean free path λ has to be introduced as the average distance traveled by a moving particle between successive impacts with other moving particles. It is commonly used to quantify the quality of a vacuum level.

Close to atmospheric pressure ($10^3 - 10^5 Pa$), the viscous flow of the air caused by the movement of the structure is a major damping source i.e. a low mean free path. In low vacuum ($10^1 - 10^3 Pa$), the mean free path of the gas molecules becomes larger than the typical dimensions of the structure and the damping is caused by the collision of non-interacting air molecules with the structure. Finally in the intrinsic region ($< 10^1 Pa$), the vacuum is low enough so that air damping is negligible, i.e. very large mean free path, and only the structural damping remains. Even if those results stand for high-frequency micro-cantilevers,

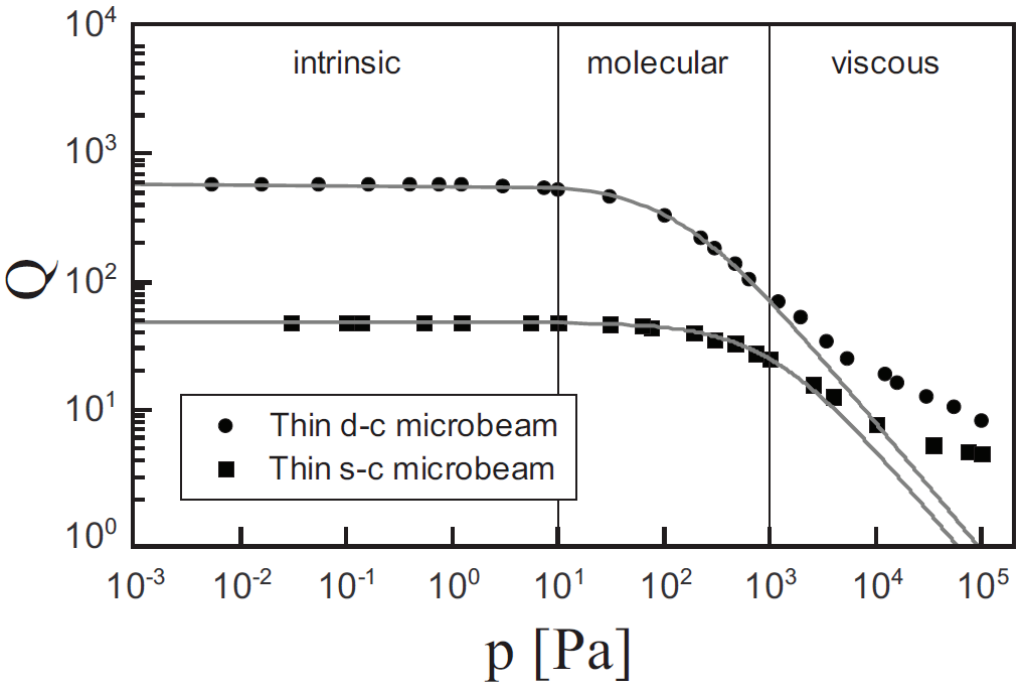

Figure 5.1: Quality factor of two SU-8 micro-cantilevers plotted against air pressure taken from Schmid and Hierold [2008]. A plateau is reached for vacuum level below $10Pa$ in the intrinsic damping region, where air damping is neglected. The thin s-c microbeam is a single clamped $55\mu m$ long, $1.45\mu m$ high, $14\mu m$ wide beam resonating at $138.3kHz$. The thin d-c microbeam is a double clamped $250\mu m$ long, $1.45\mu m$ high, $14\mu m$ wide beam resonating at $222.7kHz$.

the propensity to reach a plateau in the intrinsic region stays with larger and lower-frequency resonant cantilever (Blom et al. [1992]; Hosaka and Itao [1999]).

Therefore to validate the aeroelastic framework, it is compulsory to isolate each damping source and to characterize them at best. As the air damping is modeled by the computation of aerodynamic forces, only the structural damping has to be carefully identified within the intrinsic region where air damping is negligible. Hence a test bench is developed around a vacuum chamber and a piezoelectric actuator to characterize the aeroelastic response of flexible structure at resonance in vacuum and in atmosphere. Various instruments compatible with vacuum are deployed within and around the vacuum chamber to track and acquire the deformation of resonant flapping wings.

5.1.1.1 Vacuum chamber

The requirements for the vacuum chamber are apart from the vacuum level to be reached, discussed below, pretty straightforward with a $30cm$-side cube for the inner volume, allowing a convenient manipulation of the experimental material, with several windows and feedthroughs, allowing the instrumentation within and around the vacuum chamber to monitor the aeroelastic response of the wing. An overall view of the test bench is given in figure 5.2.

Apart from these practical consideration, the main requirement for the vacuum chamber is to achieve a vacuum level sufficiently high so as to reach the intrinsic damping region and thus characterize the structural damping of the structure. As shown in figure 5.1, the targeted vacuum level is below 10^1Pa for the SU-8 micro-cantilevers. To account for the scale difference between these cantilevers and the wing, the Knudsen number Kn is used to determine the target vacuum level. This dimensionless number, defined as the ratio of

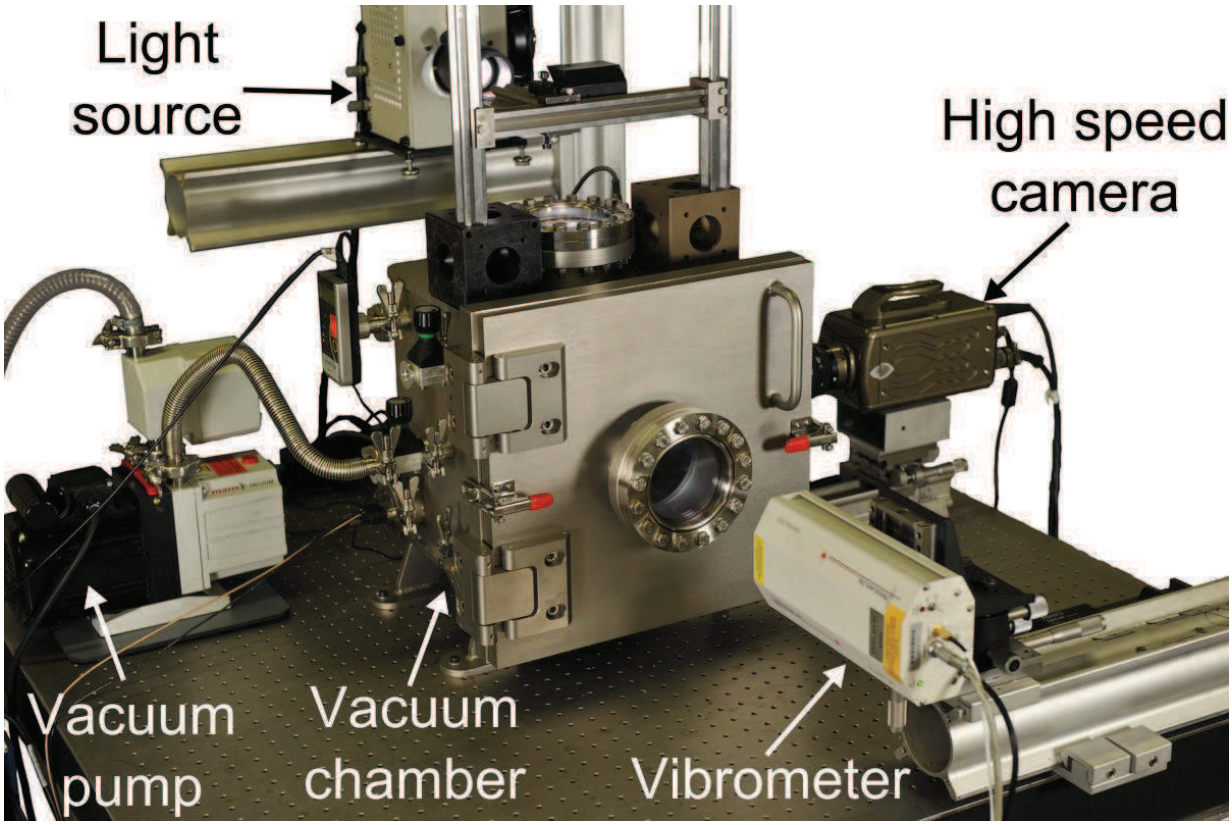

Figure 5.2: Overview of the test bench centered around the vacuum chamber. The vacuum pump is on the left, the high speed camera on the right with its light source above the chamber and the vibrometer in the front.

the mean free path length λ to a representative physical length scale L, compares the scale of a problem to the one of the surrounding fluid and will normally determine whether statistical mechanics or the continuum mechanics formulation of fluid dynamics should be used. Here the same Kn is sought for a different beam length, the physical length scale chosen here, and thus the corresponding mean free path i.e. pressure. Indeed for an ideal gas, the mean free path is inversely proportional to the pressure p as highlighted in equation 5.1 with k_{B} is the Boltzmann constant in J/K, T is the temperature in K, p is pressure in Pa, and d is the diameter of the gas particles in m.

$$\lambda = \frac{k_{\mathrm{B}} T}{\sqrt{2}\pi d^2 p} \tag{5.1}$$

Thus by taking the case of the d-c micro-beam of the figure 5.1 and by cross-multiplying it with the wing span ($\sim 15mm$), the targeted vacuum level for the chamber is slightly over $0.1Pa$ or $10^{-3}mbar$. Thus the vacuum pump should normally have to be sized for a pressure level at least an order magnitude lower than $0.1Pa$ making a high vacuum multi-stage pump mandatory. However such a pump is out of the budget allowed for this work and in light of the work of Dargent [2010], a vacuum level around this target might be sufficient. Therefore a *Pfeiffer Vacuum* DUO 2.5 Dual Stage Rotary Vane Vacuum Pump mounted to an ONF16 oil mister filter is chosen. The maximum vacuum level achieved with this pump and the vacuum chamber design is then about $2.5e^{-3}mbar$.

In order to validate the sizing of the vacuum pump, two tests are done with a 'L-Beam' without membrane and a 'E-Beam' with membrane (see the section 5.1.2 for description of the wings) actuated at various vacuum levels and at the associated resonance frequency. Both wings are extrema in terms of available wing shape, the 'L-Beam' without membrane being the one with the less wetted surface while the 'E-Beam' with membrane is the one with the maximum wetted surface. They are therefore reliable references for checking the sizing of the vacuum pump. To do so, two actuation scenarios are investigated, one with a small amplitude actuation (SA), about $20\mu m$, and one with a large one (LA), about $175\mu m$, where the wing deformation is tracked at its resonance versus the pressure. For sake of practicality, the leading-edge tip is tracked in SA through the vibrometer, enabling a direct post-processing, while the trailing-edge tip is tracked in LA through the high-speed camera, as its deflection is over the vibrometer measuring range and as the post-processing is more straightforward at this location. By plotting the amplification ratio versus the pressure, the characteristic plateau of the intrinsic region might be spotted. Results are given in the figure 5.3 for the 'L-Beam' and in figure 5.4 for the 'E-Beam' respectively.

For both wings, a plateau is reached highlighting thus the intrinsic damping region. This plateau is best outlined by the exponential curve fitting, given the sensitive nature of resonance and also the measurement and post-processing uncertainties. Thus the vacuum level achieves by both the pump and the chamber is sufficient to reach the intrinsic region of the wing and therefore to determine the structural damping of the wing. Even if the amplification factor are not comparable between SA and LA, the amplification factor under air pressure tends to be always more than the half of the one under vacuum indicating a first rule of thumb for designers interested in modeling roughly the aerodynamic damping. Also the amplification factor in air tends to decrease drastically with an increased wetted area of the wing which is understandable given the increases aerodynamic forces at stake.

5.1.1.2 Piezoelectric actuator

To actuate the wing at its resonance within the vacuum chamber, a *Cedrat Technologies* APA200M piezoelectric actuator, see figure 5.5 is used as a shaker compatible with vacuum. It enables the generation of a pure sine heaving motion of the wing root in the amplitude range of 0-200μm within at least the frequency range 0-200Hz.

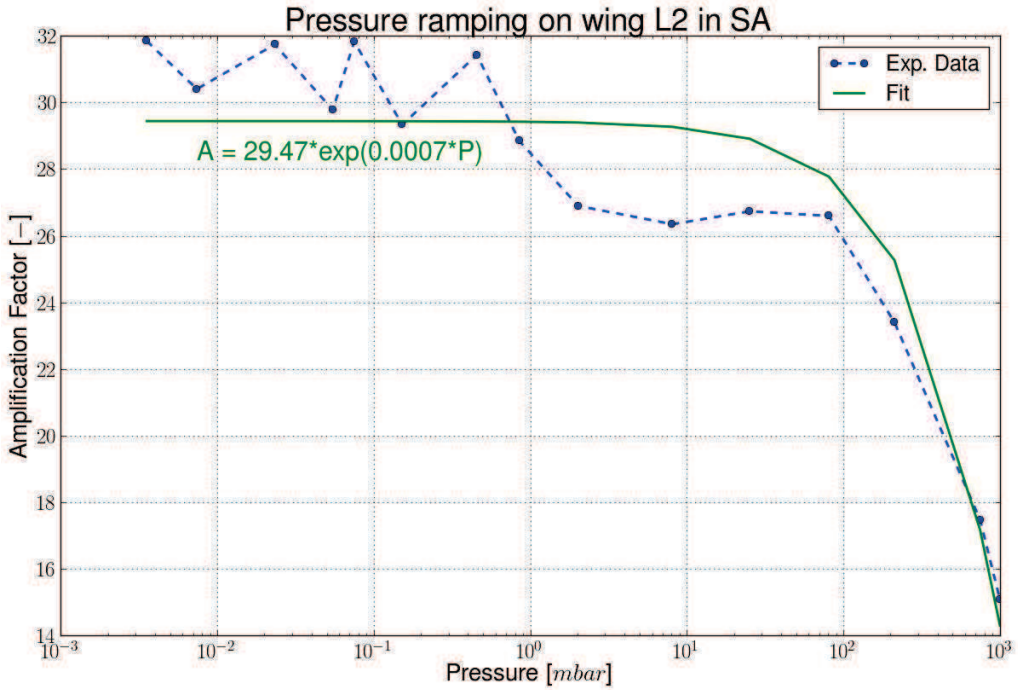

(a) Small amplitude actuation (SA)

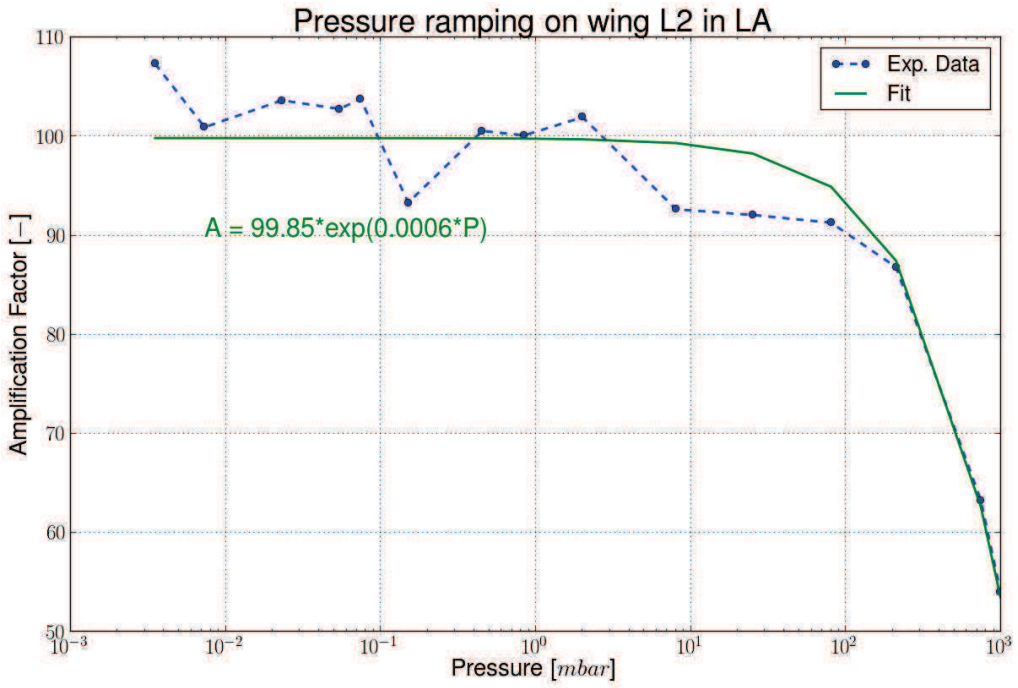

(b) Large amplitude actuation (LA)

Figure 5.3: Pressure ramping for the wing L2. The amplification factor of the wing, defined as the ratio of the leading-edge tip motion amplitude to its root one with the small amplitude actuation (SA), about $20\mu m$, and as the ratio of the trailing-edge tip motion amplitude to its root one with the large amplitude actuation (LA), about $175\mu m$, is plotted against the surrounding pressure and an exponential curve is fitted to highlight the plateau of the intrinsic region. Each measurement is done with the wing actuated closed to its local resonance frequency in pure heaving motion. Three measurements are made consecutively for small amplitude actuation and only one measurement for large amplitude actuation.

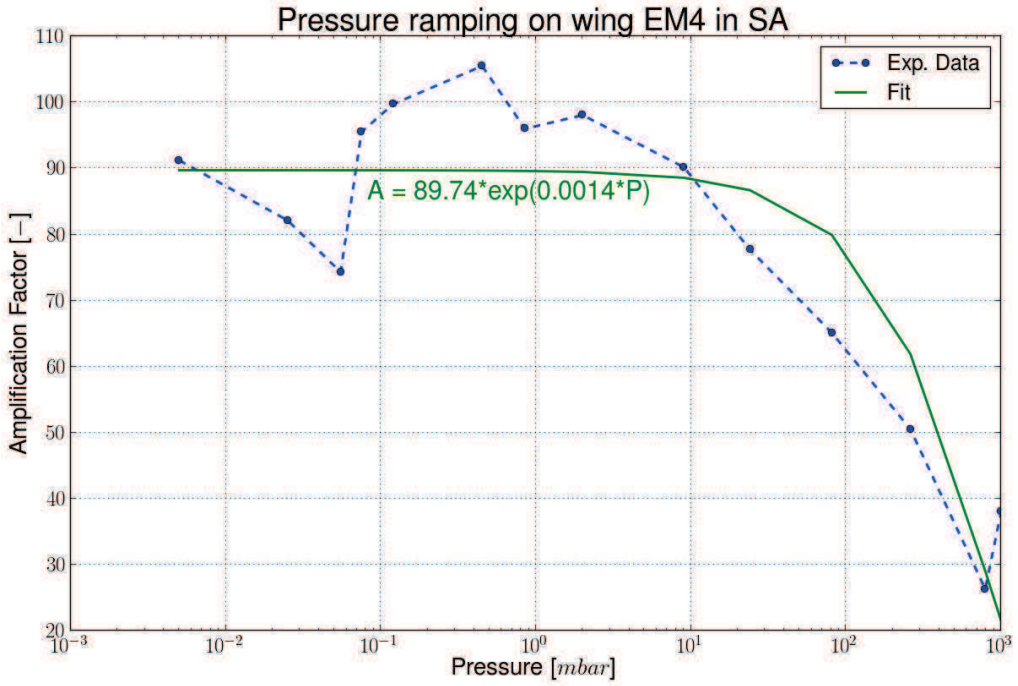

(a) Small amplitude actuation (SA)

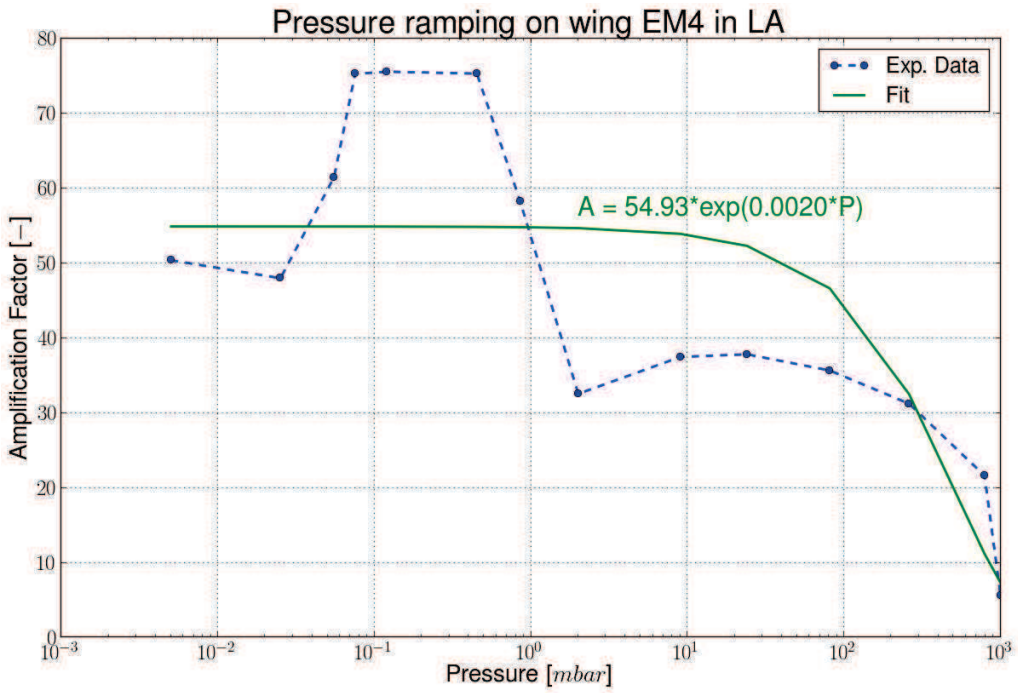

(b) Large amplitude actuation (LA)

Figure 5.4: Pressure ramping for the wing EM4. The amplification factor of the wing, defined as the ratio of the leading-edge tip motion amplitude to its root one in SA and as the ratio of the trailing-edge tip motion amplitude to its root one in LA, is plotted against the surrounding pressure and an exponential curve is fitted to highlight the plateau of the intrinsic region. Each measurement is done with the wing actuated closed to its local resonance frequency in pure heaving motion. Three measurements are made consecutively for small amplitude actuation and only one measurement for large amplitude actuation.

Figure 5.5: Piezoelectric actuator APA200M

The figure 5.6 shows the inside of the vacuum chamber with the piezoelectric actuator ready to actuate a wing. As seen in this figure, strain gages are positioned on each side of the piezoelectric sandwiches which enables a precise monitoring and setting of the actuation motion, in terms of frequency and amplitude, thanks to a proportional-integral-derivative (PID) controller and a *Labview*-based software provided with the hardware. Other actuation signals can also be accommodated if necessary such a triangle or square signal but with decreasing frequency range and amplitude.

5.1.1.3 Vibrometer

To capture the deflection on one point of the wing, a *MetroLaser* VibroMet 500V laser doppler vibrometer is used, as shown in figure 5.2. Even if the vibrometer measures a velocity, the displacement might be computed, by direct integration, from 0.1nm to 10mm. The vibrometer is positioned perpendicularly to the wing as seen in the figure 5.6.

5.1.1.4 High-speed camera

To capture the wing deformation, a *Vision Research* Phantom v7.2 high-speed camera is positioned on the side of the wing, as shown in figures 5.2 and 5.6. This camera is equipped with a 800x600 pixel SR-CMOS monochrome imaging sensor array and can acquire up to 6600 pictures per second (pps) in full resolution. With 4Gb on board, the camera captures the wing deformation for around 0.45s.

Due to the high speed acquisition rate and the associated low exposure time, a XBO 150 W Xenon light source is placed above the vacuum chamber in order to get a sufficient depth of field. The videos are later analyzed with the motion tracking software TEMA Trackeye from *Image Systems* to extract the deflection of several points of interest, here the wing extremities.

5.1.1.5 Acquisition hardware and software

To synchronize each hardware with one another, to generate the wing actuation signal i.e. piezoelectric input and to acquire the vibrometer signal and the piezoelectric output, a *National Instrument* USB-6259 module and various *Labview* programs are used.

5.1.2 Wing shape for the experimental validation

In order to validate the aeroelastic framework, a set of simple wings has been defined inspired by the one used in Dargent et al. [2009] with the 'L-Beam' that demonstrated kinematics similar to the insect one. The principles is extended to wings with one, two and three perpendicular veins without membrane forming L-, F-, and E-wing skeletons respectively. These designs are then extended to wings with a membrane positioned

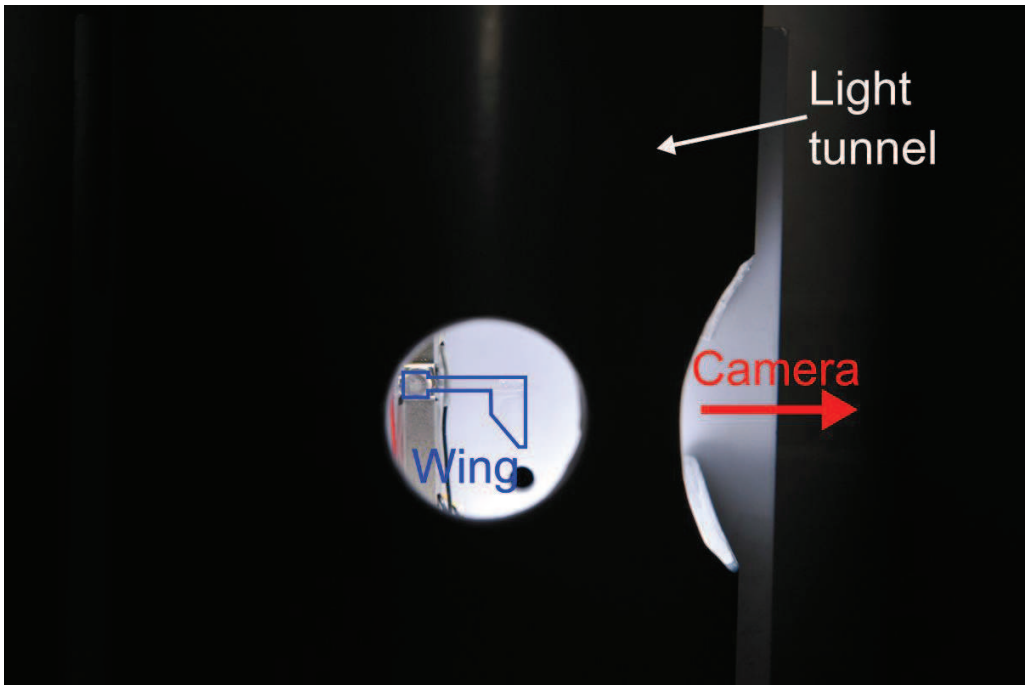

(a) Vibrometer view

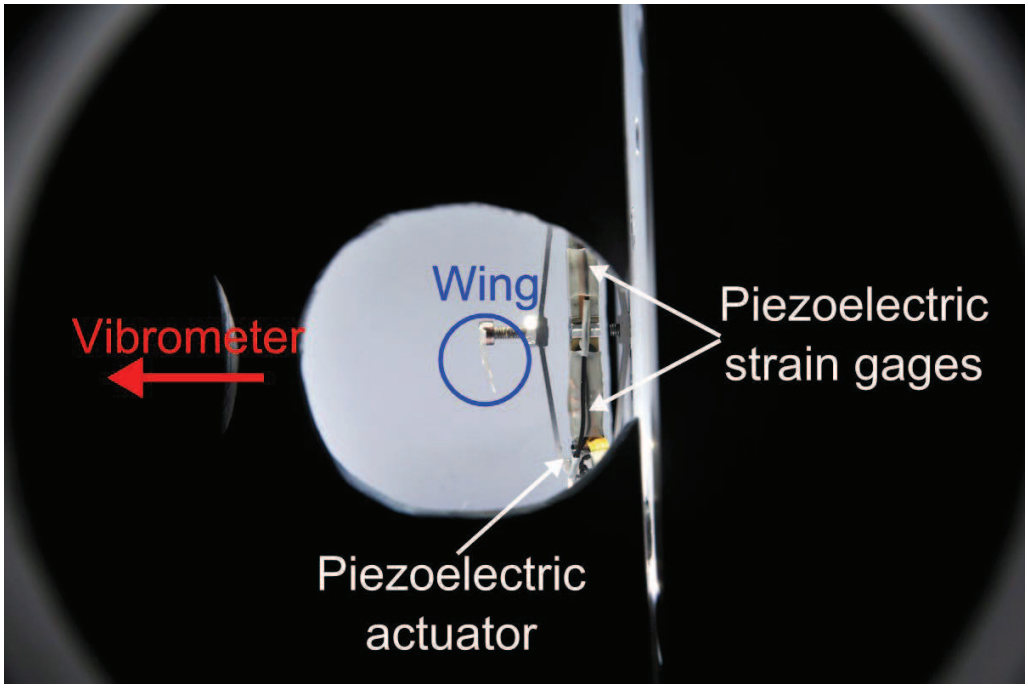

(b) Camera view

Figure 5.6: Piezoelectric actuator mounted within the vacuum chamber and positioned inside the light tunnel. The actuator is mounted vertically so as to have a horizontal heaving motion of the wing root with strain gages on each side. A wing (blue) is mounted on top of the actuator and is ready to be characterized by the camera and the vibrometer.

between two consecutive veins forming F- and E-wings and named hereafter FM or EM to differentiate them from their counterparts without membrane. The perpendicular veins are due to the technical limitation of the aeroelastic framework, yet restricted to a cartesian mesh, but are still sufficiently challenging from a phenomenology point of view while being easily modeled. In order to describe those wings, the parametric design introduced in the chapter 3.5.1 and reminded in the figure 5.7 is used again.

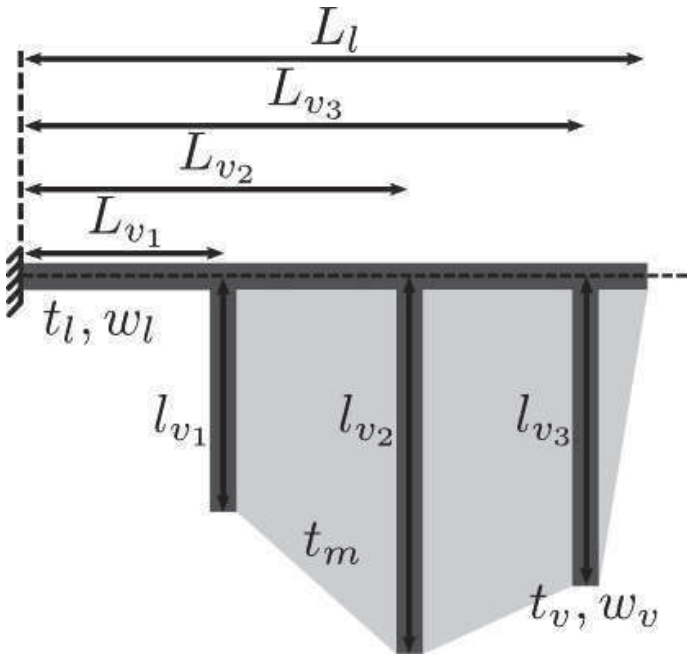

Figure 5.7: Parametric design of the validation wings

Overall 12 wing designs without membrane and 10 with membrane have been defined to benchmark the aeroelastic framework versus experiments. Their dimensions are given in the table 5.1 and details about their fabrication are given in the appendix A.

A tiny alteration is made experimentally on each wing in order to ease the post-processing, in the way of a slight layer of correction fluid on each wing extremities (vein(s) and leading edge). Thus the contrast of wing extremities on the camera is strengthened as well as the signal of the vibrometer. This tiny layer is not modeled in any way numerically but is assumed to be negligible.

5.1.3 Characterizing the wing aeroelastic response

Three features of the proposed aeroelastic framework have to be independently validated: the structural model, the aerodynamic model and the aeroelastic coupling. To do so a complete methodology has been established to generate the compulsory data.

Before presenting this methodology, it has to be mentioned that the proposed aeroelastic framework computes the resonant frequency of the wing in vacuum and thus does not account for the effect of the surrounding air in its modal analysis as illustrated in figure 5.8. A non-negligible resonant frequency shift and amplitude decrease in the amplification factor, defined as the ratio of wing tip motion amplitude to the wing root one, between air and vacuum. These discrepancies are legitimate and are solely due to the air playing a damping and an added-mass role on the wing. Therefore the current inability of the framework to compute the wing resonant frequency in air has to be handled by the proposed methodology.

Three complementary steps are required: the frequency characterization, the time-history of the wing deformation, and the one of the forces generated by the wing. First, the frequency characterization

Table 5.1: Characteristics of the validation wings using the parametric design of the figure 3.7

Wing	L1	L2	F1	F2	F3	F4	E1	E2	E3	E4	E5	E6
Leading edge												
Length L_l $[mm]$							15					
Width w_l $[mm]$	1	2	1	1	2	2	1	1	1	2	2	2
Thickness t_l $[\mu m]$							100					
Vein												
Width w_v $[mm]$							0.5					
Thickness t_v $[\mu m]$							40					
Vein 1												
Position along the LE L_{v_1} $[mm]$	15	15	10	10	10	10	5	5	7.5	5	5	7.5
Length l_{v_1} $[mm]$	10	10	5	10	5	10	5	10	5	5	10	5
Vein 2												
Position along the LE L_{v_2} $[mm]$	-	-	15	15	15	15	10	10	11.25	10	10	11.25
Length l_{v_2} $[mm]$	-	-	10	10	10	10	7.5	10	7.5	7.5	10	7.5
Vein 3												
Position along the LE L_{v_3} $[mm]$	-	-	-	-	-	-			15			
Length l_{v_3} $[mm]$	-	-	-	-	-	-			10			
Membrane												
Thickness t_m $[\mu m]$	-	-						5				

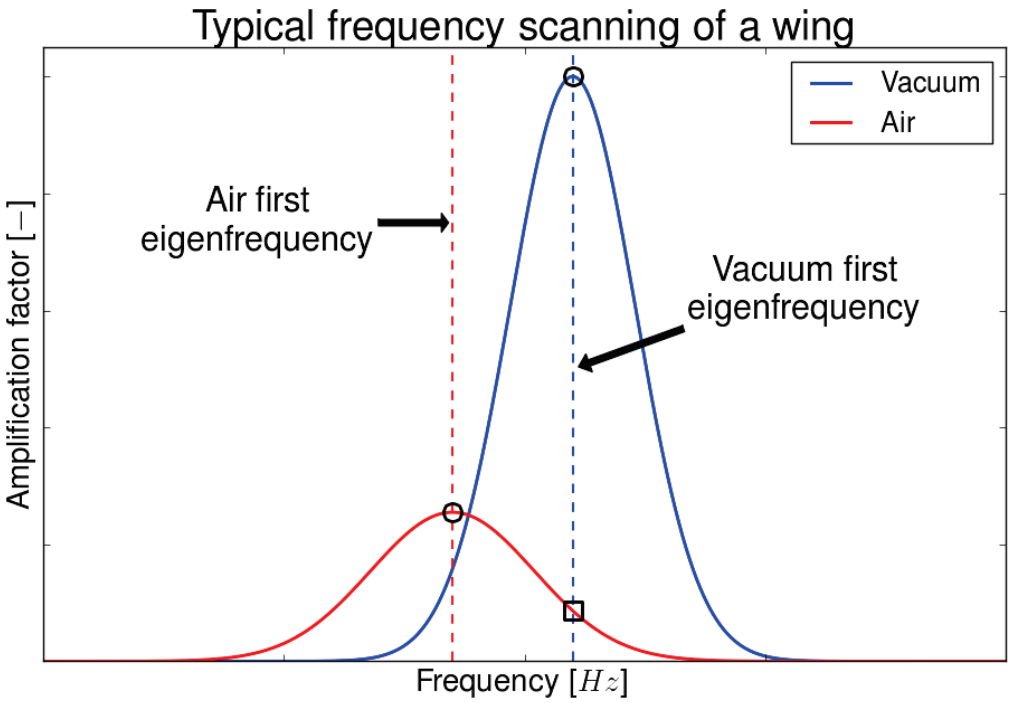

Figure 5.8: Typical frequency response of a wing in vacuum and in air under a small actuation amplitude generating no non-linearities within the structure. The circle markers indicate the resonant frequency and the amplification achieved in vacuum or air whereas the square marker indicates the amplification level where the computation is done by the aeroelastic framework, as the resonant frequency computation is limited to vacuum.

determines key material parameters of a wing closing the gap between experimental and numerical wing data. Second, by tracking the wing deformation throughout several strokes in vacuum and in air, both the structural model and the aeroelastic coupling can be validated. Third, the acquisition of the forces generated by the wing will validate the aerodynamic model while checking further the aeroelastic coupling. As mentioned earlier, this last step is here not reported as the proper sensor is not yet sufficiently reliable. More details about it are available in appendix C.

5.1.3.1 Frequency characterization of a wing

Due to the lack of well-established mechanical data and to their strong-dependency to the fabrication process (see Chang et al. [2000]; Feng and Farris [2002, 2003] for more details), the polymer wings are characterized by two mechanical properties: the Young's modulus E and the structural damping ratio ζ. The first one dictates strongly the resonance frequency while the second stabilizes passively the resonant motion along with its amplitude.

To determine these properties, a simple method exists and consists in tracking the amplification factor, i.e. the ratio of wing tip motion amplitude to the wing root one, versus the actuation frequency over several resonant frequencies. The resulting curves are typically the ones shown in the figure 5.8 whereby the material data are extracted from them.

For the sake of clarity, this process is first introduced theoretically on a cantilever and then extended numerically to the wing. Ultimately the experimental process to acquire the amplification ratio of a wing versus its actuation frequency is described.

a) Explanation on a cantilever

In the case of a cantilever, it is established (Lalanne et al. [1984]) that the first resonant frequency f_c and the damping ratio ζ_c are determined by the equation 5.2 and 5.3, where Δf is the half-power frequency bandwidth.

$$f_c = \frac{3.516}{2\pi\sqrt{12}} \frac{t_c}{l_c^2} \sqrt{\frac{E}{\rho}} \tag{5.2}$$

$$\zeta_c = \frac{\Delta f}{2 f_c} \tag{5.3}$$

Reading the amplification factor curve, the position of the resonance frequency f_c is clearly indicated by a large and high peak. Assuming that the density ρ as well as the cantilever dimension are known, here t_c and l_c are respectively the thickness and the length, the value of the Young's modulus E can then be deduced using equation 5.2. Similarly, once the resonant amplitude is known, the half-power bandwidth Δf is computed as the frequency width around the peak where the amplification factor is equal to the resonant amplitude divided by $\sqrt{2}$. The damping ratio ζ_c is then easily deduced using equation 5.3.

b) Extension to a wing

When now handling a wing, its resonant frequency f is not analytically available clouding the determination of the Young modulus. However the Young modulus E might be retrieved numerically once at least a resonant frequency is know. Indeed the aeroelastic framework might be reassigned to perform only modal analysis and called iteratively with modified Young modulus until the resonant frequency found in the experiments is at best approached.

To avoid time-consuming hand-made iterations, the genetic algorithm environment of the chapter 6 is modified to minimize the distance between the numerical and the experimental resonant frequency. Thus the experimental Young modulus E_{exp} is determined usually within a couple of hours.

Unfortunately the damping ratio ζ is not tackled so easily. Indeed the finite element solver of the framework accepts the damping only in the manner of a Rayleigh damping, as explained later in section 3.1.2, using two coefficients α and β. To determine these coefficients and as explained in Chowdhury and Dasgupta [2003], at least two resonant peaks f_i along with the associated damping ratio ζ_i are necessary as shown in the equations 5.4 and 5.5.

$$\beta = \frac{2\zeta_1\omega_1 - 2\zeta_2\omega_2}{\omega_1^2 - \omega_2^2} \tag{5.4}$$

$$\alpha = 2\zeta_1\omega_1 - \beta\omega_1^2 \tag{5.5}$$

Thus the amplification factor curve has to be extended beyond the first resonant frequency towards at least the second.

Additionally, the amplification curve has to be determined in vacuum so as to characterize only the structural damping the associated Young modulus and damping ratios. The associated frequencies are noted $f_{v,1}$ and $f_{v,2}$ for the first and second resonant frequencies in vacuum. Experiments in air will also occur to estimate the bias between the resonant state at the air resonant frequency and at the vacuum one and also to generate the data for later validation studies once the aeroelastic framework is capable of computing the resonant frequency in air. The associated air resonant frequency is then noted $f_{a,1}$ and only an amplification factor curve with one peak is needed.

A drawback to this method is that its validity is limited to the case of symmetrical peaks characteristics of a small displacement assumption. Non-linearities raised by large displacement and/or within the material tends to bend the resonance peak in a smurf hat fashion, as observed by Guedama [2010], making the notion of resonant frequency and half-power bandwidth more complicated. Therefore each amplification curve is determined when the wing is under the small displacement hypothesis usually with a heaving actuation of about $20\mu m$.

5.1.3.2 Acquiring the amplification curve

To establish the amplification curve of a wing up to its second peak, it is necessary to track successfully the displacement of the wing root and of an other point on the wing surface. With a wing mounted at its root to the piezoelectric actuator within the vacuum chamber, the displacement of the wing root is easily tracked by the strain gages mounted on the actuator. To track the second point, the vibrometer is preferentially used. The camera might also be used but its low resolution for small displacement and its time-consuming post-processing makes it here undesired. The position of this point of interest is a trade-off between the vibrometer capacities (size of the laser spot, maximal velocity, etc.) and the relevance of the position towards the two expected mode shapes i.e. the displacement being noticeable on both modes. A convenient place for this point is the tip of the leading edge as it offers a large enough area for the laser beam and is significantly influenced by the first two mode shapes for all the wings. It is essential to not touch the vibrometer for the complete duration of the characterization process as any slight change will shift strongly the measured point and thus discard the whole process.

For the acquisition of each signal, a *Labview* program and the *NI* USB-6259 module are used to generate the heaving sine, to acquire simultaneously the input signal of the piezoelectric actuator, the signal provided by the strain gages mounted on the actuator and the output signal of the vibrometer. Finally the data are stored in a text-file for post-processing.

After a quick evaluation of the two resonant peaks and with a constant actuation amplitude, the frequency is gradually increased so as to sweep through the two resonant peaks. At each frequency step, three

acquisitions are made for $5s$ at 2500 Hz. The scanning starts at least $15Hz$ before the first resonant peak and ends $15Hz$ after the second resonant peak. The frequency step decreases gradually as the resonant peak come closer from $1Hz$ up $\pm 7.5Hz$ of the peak, to $0.5Hz$ up to $\pm 2.5Hz$, and finally to $0.25Hz$ within its neighborhood. By doing so and by adjusting continuously the velocity range of the vibrometer, maximizing thus the signal-to-noise ratio, each frequency peak is well captured without damaging too much the post-processing by lacking data on the width of the peak or on its height. The acquisition starts with the air amplification curve, in order to set the vibrometer quickly and easily, and is followed by the vacuum curve which requires more time mainly due to the pumping time.

For the post-processing, a *Python* script is launched which handles all the files, plots the amplification curve using smooth averaged data and determines the resonant frequencies as well as the associated damping factors. Data are filtered using a 5- or 7-order Butterworth bandpass filter centered on the actuation frequency. The amplification factor is computed using the mean envelope value of each signal while a cubic spline is used to determine precisely the bandwidth of each peak. Examples of measurement and data extraction are given in the section 5.2.1.1.

5.1.3.3 Time-history of the wing deformation

With the wing characterized in terms of frequency and of mechanical properties, the next step of the methodology is to validate the structural model and the aeroelastic coupling by tracking the wing deformation throughout several strokes in vacuum and in air respectively. Only the resonant frequency in vacuum, $f_{v,1}$, is relevant for the validation purpose of this study both in air and in vacuum. However the resonant frequency in air is also investigated in order to establish the validation database for air resonant frequency.

The wing deformation is monitored easily using the high speed camera coupled to the motion tracking software which enables to track the deflection of several wing extremities, such as veins and the leading edge. To scale the image, a steel rule is positioned perpendicular to the wing in the focused area and an image is taken.

The same *Labview* program as in section 5.1.3.2 is used and synchronized with the high-speed camera by the way of a digital trigger. The high-speed camera acquires the wing deformation at $6600pps$ until its memory is full ($\sim 0.45s$ of acquisition) while the *NI* acquisition module generates and acquires the actuation motion at a frequency rate of $10kHz$ during $1s$. Two actuation amplitudes are investigated: a small displacement actuation (SA) with a heaving amplitude around $20\mu m$ and a large displacement actuation (LA) around $175\mu m$. For each configuration, three consecutive runs are made in order to average the instantaneous wing deformation. After each run, the *Labview* and the camera data are saved for post-processing.

For the post-processing of the wing deformation, two consecutive processes occur. First, the motion tracking software *Image Systems* TEMA Motion is used to extract the image scale and save it, then to track the deflection of the wing extremities throughout several strokes and saved them in a text-file. Second, a *Python* script is launched synchronizing each run (*Labview*+*Tema*) with one another using the input signal of the piezoelectric actuator as a reference. The wing data are then averaged, plotted and stored for their later juxtaposition to the computation made on the aeroelastic framework under the same actuation and load conditions as well as numerically tuned material properties.

In order to check the capability of the framework to compute the aeroelastic response of flexible flapping wings at resonance, a complete methodology and test bench have been defined enabling to validate step-by-step each component: the structural model, the aerodynamic model, and the aeroelastic coupling. By comparing the numerical prediction to the experimental data for each wing, the capability and accuracy of the aeroelastic framework might be determined, paving the way for more complex computation using the

framework as a reliable kernel for preliminary design tasks.

5.2 Experimental validation through the deformation method

As stated above, the validation process is twofold. First, the material properties of the wing need to be characterized as no well-established mechanical data are available and as they are strongly dependent of the fabrication process. Second, the wing deformation is tracked for several strokes under different actuation and atmosphere conditions. By doing so, both the structural model and the aeroelastic coupling might be validated along with partially the aerodynamic model through the coupling. Eventual discrepancies can thus be identified.

From the validation wing shape, only the wings L2, F3, E4 for the wing without membrane and FM3, EM4 for the wing with membrane are here reported due to the relatively large measuring spot of the vibrometer compared to the leading edge limiting the frequency characterization process. Thus each wing type is tested and numerically benchmarked. In line with the convergence studies of the chapter 4.1, the default mesh is set to $N_{FE_{Span}} = 5$ and $N_{FE_{Chord}} = 20$ for the wings without membrane and to $N_{FE_{Span}} = 10$ and $N_{FE_{Chord}} = 20$ for the ones with.

5.2.1 Characterization of the wing

The wing characterization aims at extracting, from an experimental wing, the mechanical properties essential for the FE-computation: the damping ratio $\zeta_{exp,i}$ of two resonant modes and the Young modulus E_{exp}. To do so and as explained in the section 5.1.3.1, the amplification factor versus actuation frequency curve is acquired in vacuum and its peak indicates then a resonant frequency $f_{v,exp,i}$ and the associated damping ratio $\zeta_{exp,i}$. Using these inputs as reference, the aeroelastic framework computes iteratively the resonant frequencies $f_{num,i}$ for different Young modulus E_{num} until the experimental ones are found. As seen in the chapter 4.4, the Young modulus is the most sensible material parameter in the framework and the genetic algorithm method is suitable to handle its determination properly.

5.2.1.1 Retrieving the resonant frequencies $f_{v,exp,i}$ and damping ratios $\zeta_{exp,i}$

Using the method defined in the section 5.1.3.2, the wing is actuated in vacuum at various frequencies but at a constant amplitude while the vibrometer is tracking the leading-edge displacement. The amplification factor, the ratio of the leading-edge displacement to the root one, is acquired for the first two resonant frequencies under a small actuation amplitude. The amplification curve is also done in air to determine the air resonant frequency $f_{a,exp}$.

Results are shown in the figures 5.9 to 5.11 and summarized in the table 5.2 for the wing without membrane and for the one with membrane in the figures 5.12 and 5.13 and in the table 5.3.

As highlighted by the curves, the amplification factor is strongly decreased in air while the resonant frequency is shifted. This is in complete agreement with the effects of the added-mass forces, which shift the resonant frequency due the increased apparent mass of the wing, and of the aerodynamic forces, which damp the wing motion.

With the experimental resonant frequencies $f_{exp,i}$ and the associated damping ratio $\zeta_{exp,i}$ determined, only the Young modulus is left unknown in the mechanical characterization of the validation wing.

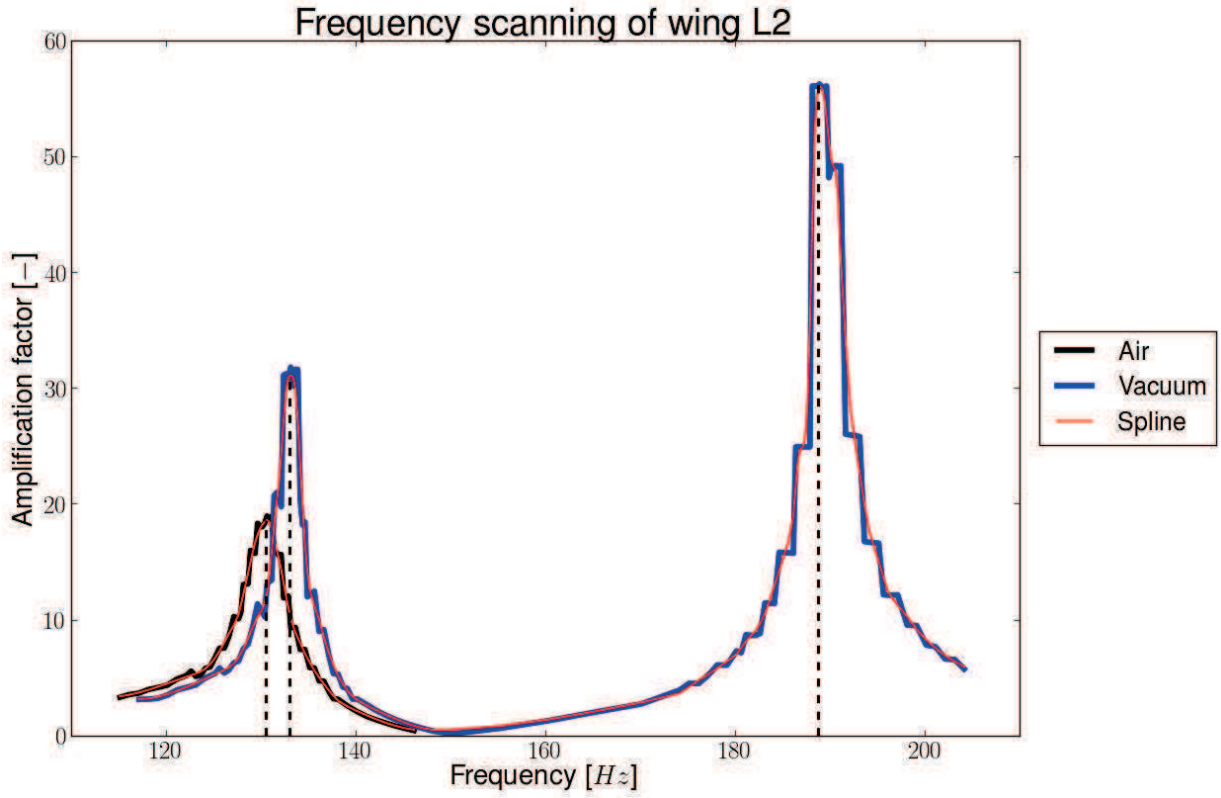

Figure 5.9: Frequency analysis of the wing L2 in air and in vacuum. The red line indicates for each curve, the spline used for the calculation of the damping ratio. Results are summarized in table 5.2.

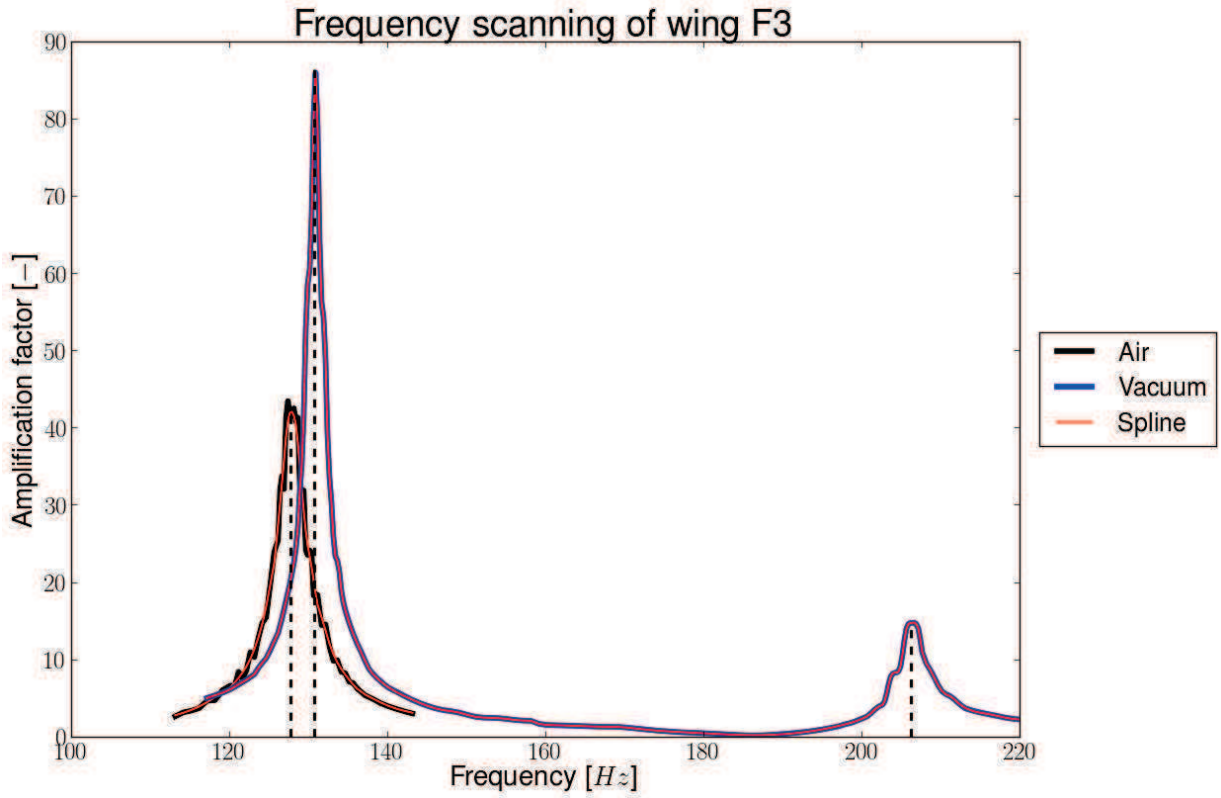

Figure 5.10: Frequency analysis of the wing F3 in air and in vacuum. The red line indicates for each curve, the spline used for the calculation of the damping ratio. Results are summarized in table 5.2.

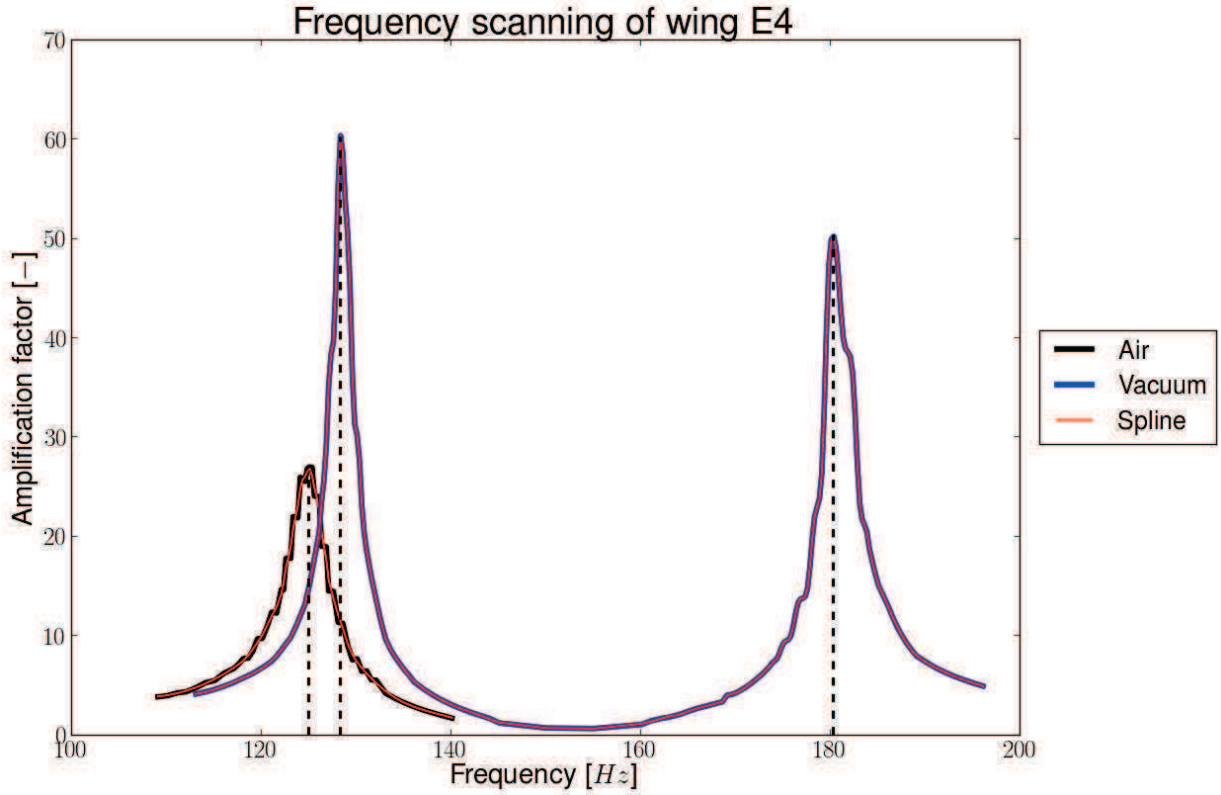

Figure 5.11: Frequency analysis of the wing E4 in air and in vacuum. The red line indicates for each curve, the spline used for the calculation of the damping ratio. Results are summarized in table 5.2.

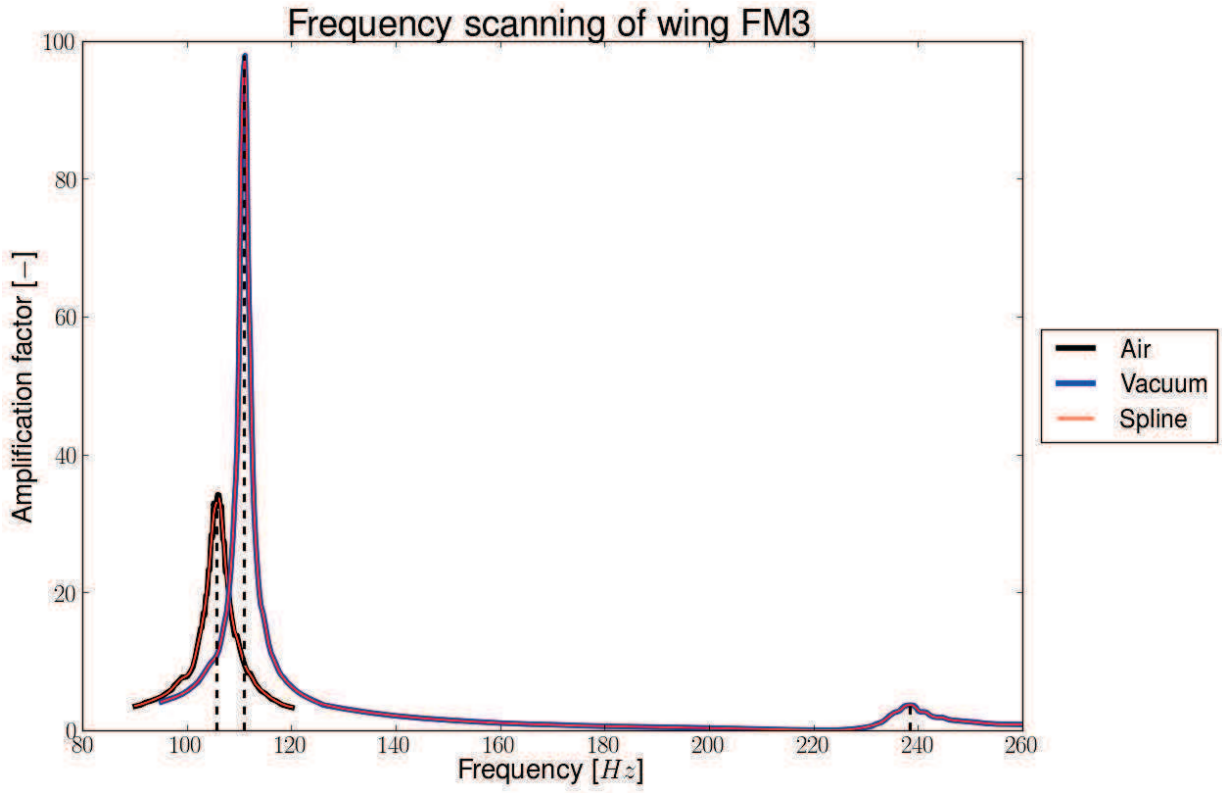

Figure 5.12: Frequency analysis of the wing FM3 in air and in vacuum. The red line indicates for each curve, the spline used for the calculation of the damping ratio. Results are summarized in table 5.3.

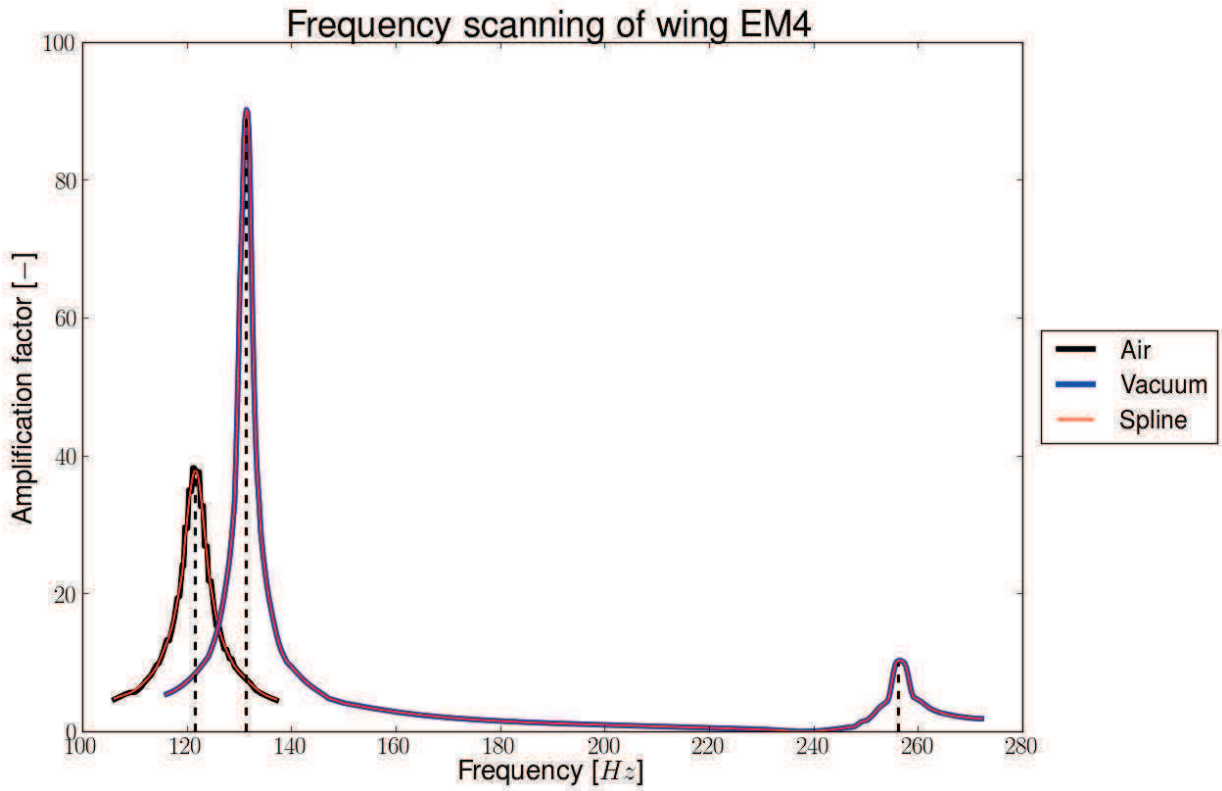

Figure 5.13: Frequency analysis of the wing EM4 in air and in vacuum. The red line indicates for each curve, the spline used for the calculation of the damping ratio. Results are summarized in table 5.3.

5.2.1.2 Determining the experimental Young modulus E_{exp}

To determine the experimental Young modulus E_{exp} and described in the section 5.1.3.1, the genetic algorithm is used with the following objective function:

$$J_{E_{exp}} = 0.75\frac{\|f_{v,exp,1} - f_{num,1}\|}{f_{v,exp,1}} + 0.25\frac{\|f_{v,exp,2} - f_{num,2}\|}{f_{v,exp,2}} \tag{5.6}$$

This translates the distance between each resonant frequencies weighted by some factors aimed at driving the optimizer towards the first resonant frequency. Results are summarized in the table 5.2 for the wing without membrane and in the table 5.3 for the one with membrane.

Table 5.2: Experimental characterization of the beam wing. The resonant frequencies $f_{v,exp,i}$ and $f_{a,exp}$ as well as the damping ratio $\zeta_{exp,i}$ are determined from experimental data as defined in section 5.1.3.1 while the Young modulus is approximated numerically so as to match at best the experimental resonant frequencies. The numerical resonant frequencies $f_{v,num,i}$ computed with E_{exp} are also given.

Wing	$f_{v,exp,1}$ $[Hz]$	$\zeta_{exp,1}$ $[-]$	$f_{v,exp,2}$ $[Hz]$	$\zeta_{exp,2}$ $[-]$	E_{exp} $[GPa]$	$f_{a,exp}$ $[Hz]$	$f_{v,num,1}$ $[Hz]$	$f_{v,num,2}$ $[Hz]$
L2	133	0.0087	188.75	0.0085	7.3	130.5	134.10	196.03
F3	130.75	0.0050	206.25	0.0064	7.1	127.75	131.41	191.08
E4	128.25	0.0065	180.25	0.0083	6.8	125	127.81	184.82

With the experimental validation wing characterized in terms of mechanical properties, their numerical counterparts can now be simulated in vacuum and in air by coupling the aerodynamic model to the structural model and thus validate the structural model and the aeroelastic coupling.

Table 5.3: Experimental characterization of the beam-shell wing. The resonant frequencies $f_{v,exp,i}$ and $f_{a,exp}$ as well as the damping ratio $\zeta_{exp,i}$ are determined from experimental data as defined in section 5.1.3.1 while the Young modulus is approximated numerically so as to match at best the experimental resonant frequencies. The numerical resonant frequencies $f_{v,num,i}$ computed with E_{exp} are also given.

Wing	$f_{v,exp,1}$ $[Hz]$	$\zeta_{exp,1}$ $[-]$	$f_{exp,2}$ $[Hz]$	$\zeta_{exp,2}$ $[-]$	E_{exp} $[GPa]$	$f_{a,exp}$ $[Hz]$	$f_{v,num,1}$ $[Hz]$	$f_{v,num,2}$ $[Hz]$
FM3	111	0.0068	238.5	0.013	6.5	105.75	111.67	174.92
EM4	131.25	0.0090	256.25	0.0065	9.5	121.5	131.35	211.12

5.2.2 Validation on beam wing

In order to validate the structural model and the aeroelastic model on wings with relatively low aerodynamic forces, the validation is done first on wing without membrane. Using the method described in the section 5.1.3.3, the deflection of the wing extremities throughout several strokes are available for comparison with their numerical counterpart under several actuation, in small (SA) and in large (LA) amplitude.

As a reminder, experiments are made at the resonant frequency of the wing in vacuum. Results for the one in air are given in appendix E.1.

5.2.2.1 Presentation of the results

The tables 5.4 to 5.6 summarize the experimental/numerical comparison for the wing L2, F3 and E4 in vacuum and in air while the figure 5.15, for vacuum, and the figure 5.16, for air, depict graphically the comparison between the wing extremities of L2 outlined in the figure 5.14. For the wing F3 and E4, the figures are available in the appendix D.1. Due to a numerical instability on the lift component, the last rotation $\mathbf{Rot_{Z,i}}$ has been disabled in the computation which has no drastic influence on the computation in light of the complete inverse matrix (see equation 3.9) and of the very small angles ψ at stake.

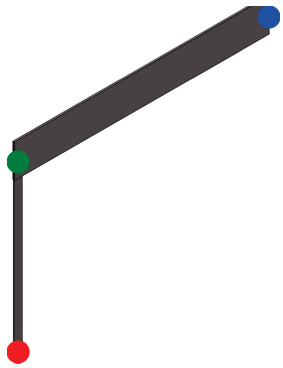

Figure 5.14: CAD view of the L2 wing with its extremity colored as in the figures 5.15 and 5.16.

5.2.2.2 Validation in vacuum

For the experiments in vacuum, the numerical simulations match very closely the experimental data for each extremity both in SA and in LA for both the wing L2 and E4, the experiments being not done for wing F3. For the wing L2, the SA error is of 15-19% and the LA error of 0-2%. Similarly for the wing E4, the SA error is of 7-18% and the LA error of 7-29%. Given the mean experimental errors reported, the numerical results can be considered as matching pretty well the experimental ones.

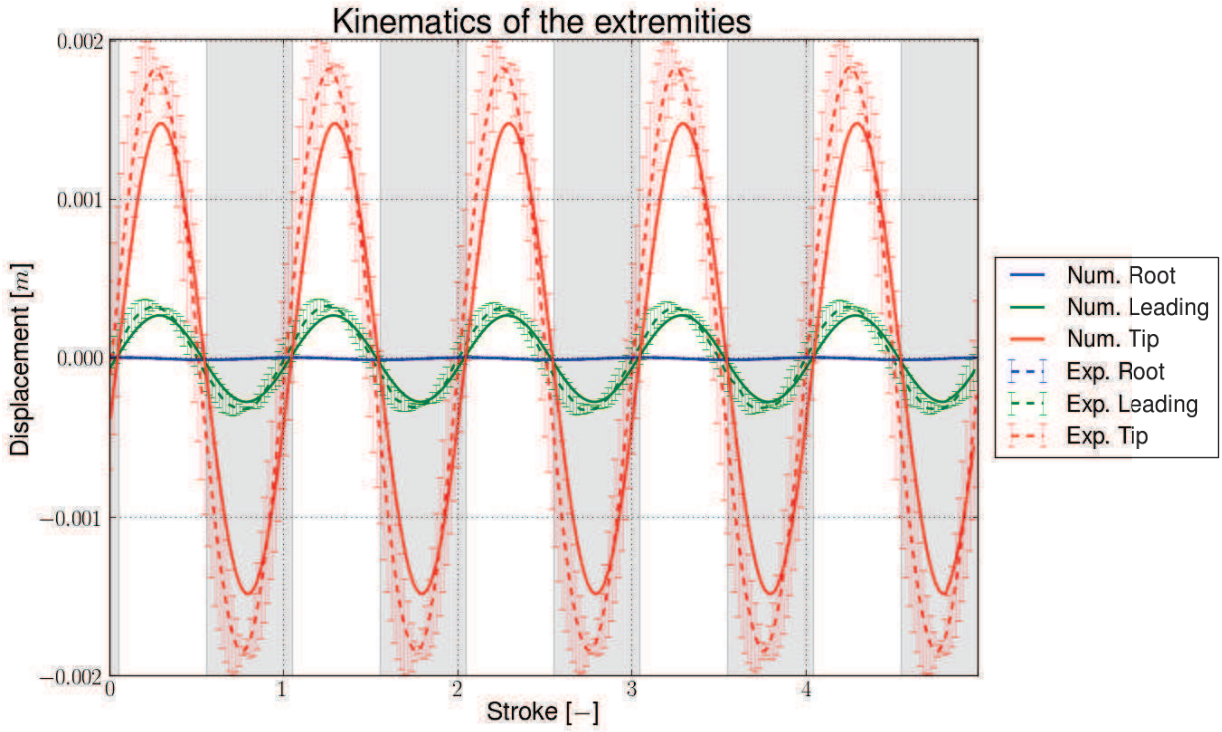

(a) Small actuation displacement (SA)

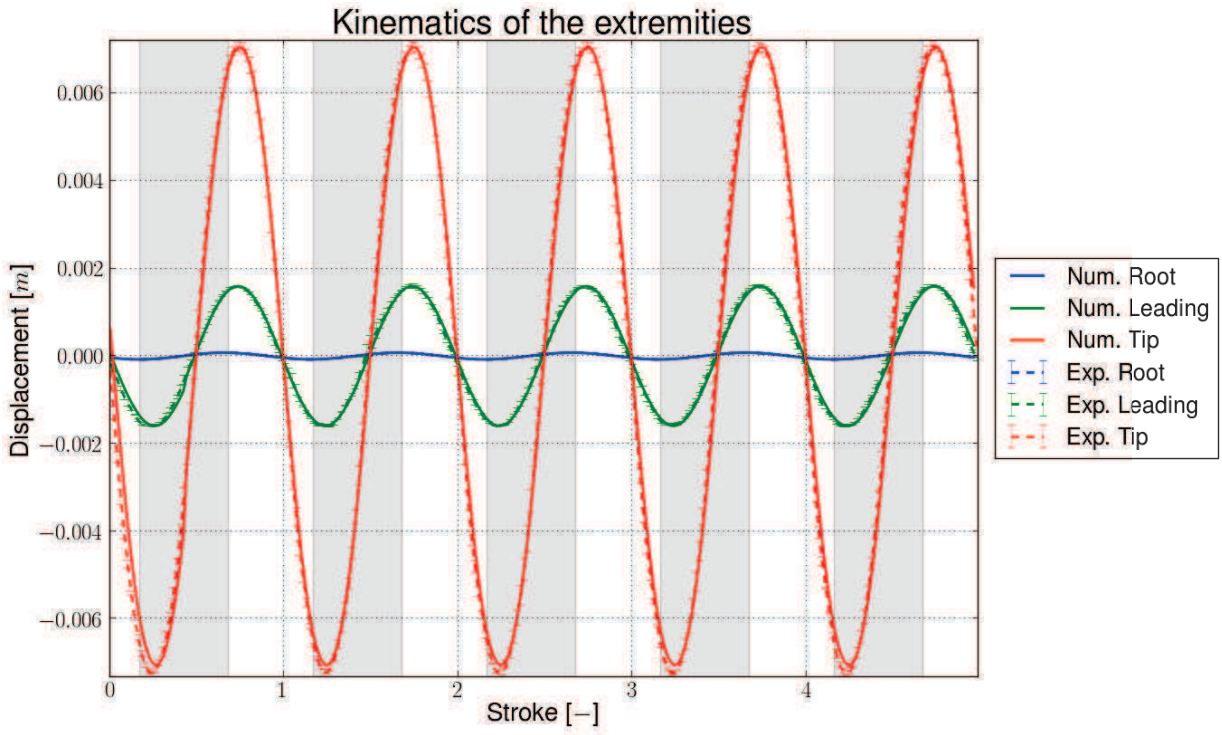

(b) Large actuation displacement (LA)

Figure 5.15: Graphical comparison between experimental and numerical data for the wing L2 when actuated in vacuum i.e. without aerodynamic coupling. Calculations are done with the large deflection of the FEs turned on and with the relevant experimental actuation amplitude. 125 periods are simulated to overturn the transient state. More details about the comparison are given in table 5.4.

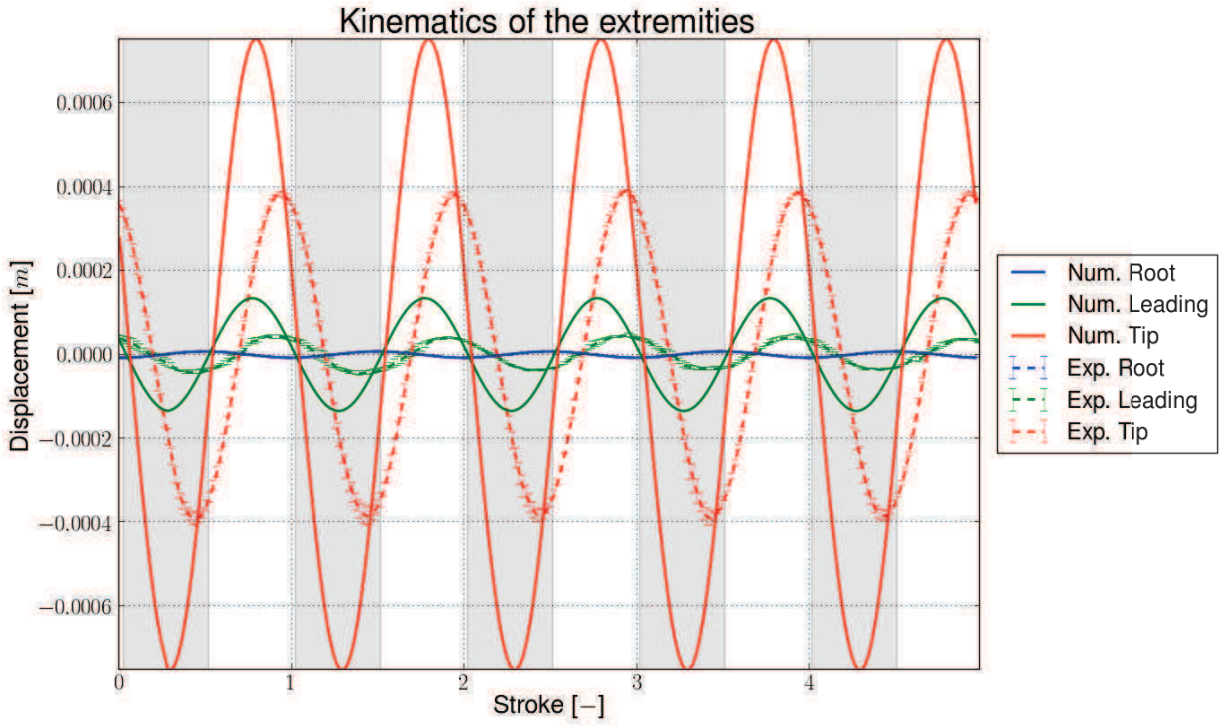

(a) Small actuation displacement (SA)

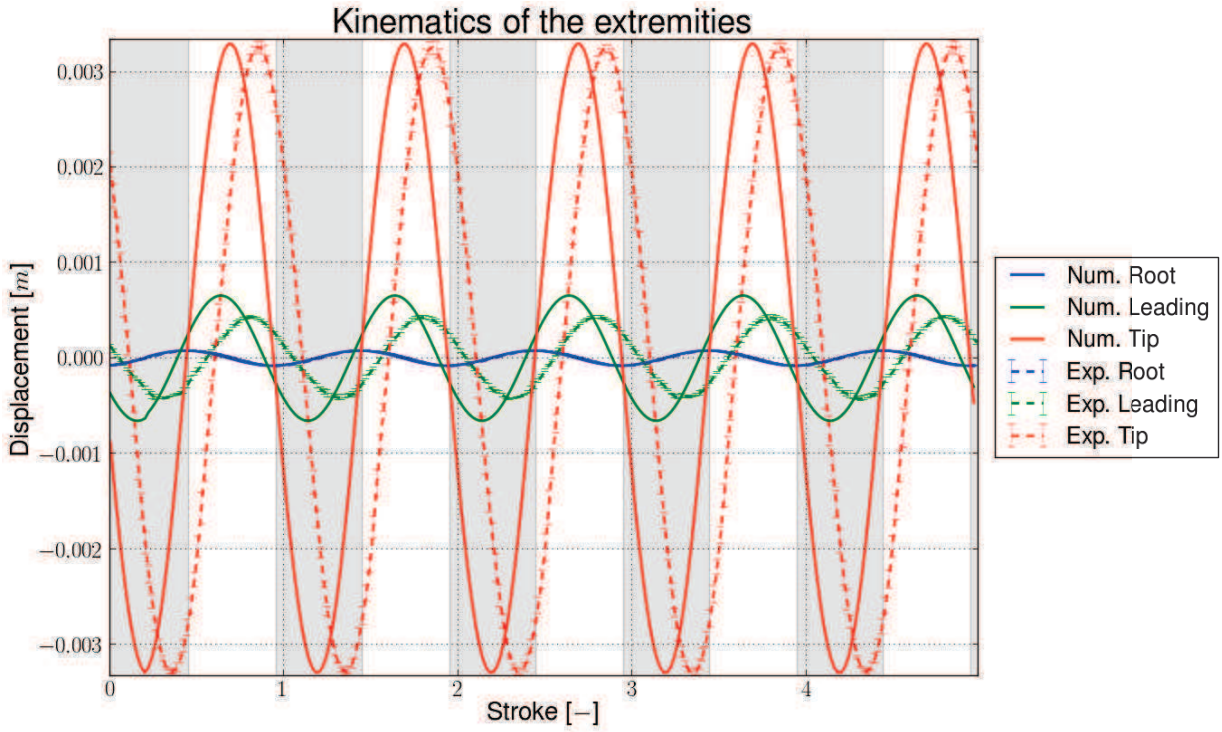

(b) Large actuation displacement (LA)

Figure 5.16: Graphical comparison between experimental and numerical data for the wing L2 when actuated in air i.e. with aerodynamic coupling. Calculations are done with the large deflection of the FEs turned on and with the relevant experimental actuation amplitude. The first rotation $\mathbf{Rot_{Z,i}}$, see chapter 3.2, is disabled for LA as it causes instabilities in the computation of the lift forces. 75 periods are simulated to overturn the transient state. More details about the comparison are given in table 5.4.

Table 5.4: Summary of the experimental/numerical comparison for L2. In order to quantify the experimental error of each extremity, its mean and standard-deviation values are given. Other items are based on the displacement amplitude of the extremity. The error between the numerical and the experimental values is defined as $\left(\overline{A_{num}} - \overline{A_{exp}}\right) / \overline{A_{exp}}$ with $\overline{A_{num}}$ and $\overline{A_{exp}}$ the numerical and experimental displacement amplitudes respectively.

Medium		**Vacuum**		**Air**	
Exp. Pressure [*mbar*]		3.3e-3 to 4.1e-3		992	
Actuation type		SA	LA	SA	LA
Root	Mean Exp. Error [μm]	0.1	1.6	0.1	1.9
	STD on Exp. Error [μm]	0.1	0.8	0.0	0.9
	Exp. Amp. [μm]	7.6	76.9	7.5	79.1
	Num. Amp. [μm]	7.6	77.1	7.5	79.3
	Error Num./Exp. Amp. [%]	0	0	0	0
	Phase-shift between Num. and Exp. [*rad*]	0.00	0.00	0.00	0.00
Leading-edge	Mean Exp. Error [μm]	66.0	42.8	4.4	17.8
	STD on Exp. Error [μm]	33.0	32.6	2.7	8.2
	Exp. Amp. [μm]	321.8	1596.9	41.0	420.5
	Num. Amp. [μm]	272.0	1594.0	134.3	655.5
	Error Num./Exp. Amp. [%]	**-15**	**0**	**227**	**56**
	Phase-shift between Num. and Exp. [*rad*]	**-0.25**	**-0.13**	**0.88**	**1.01**
Tip	Mean Exp. Error [μm]	380.2	140.0	12.3	88.4
	STD on Exp. Error [μm]	182.9	68.7	7.5	46.2
	Exp. Amp. [μm]	1834.9	7314.2	386.5	3291.9
	Num. Amp. [μm]	1482.7	7192.7	752.3	3304.1
	Error Num./Exp. Amp. [%]	**-19**	**-2**	**95**	**0**
	Phase-shift between Num. and Exp. [*rad*]	**-0.25**	**-0.13**	**0.88**	**0.88**

Table 5.5: Summary of the experimental/numerical comparison for F3. In order to quantify the experimental error of each extremity, its mean and standard-deviation values are given. Other items are based on the displacement amplitude of the extremity. The error between the numerical and the experimental values is defined as $\left(\overline{A_{num}} - \overline{A_{exp}}\right) / \overline{A_{exp}}$ with $\overline{A_{num}}$ and $\overline{A_{exp}}$ the numerical and experimental displacement amplitudes respectively.

Medium		**Air**	
Exp. Pressure [*mbar*]		1001	
Actuation type		SA	LA
Root	Mean Exp. Error [μm]	0.1	0.9
	STD on Exp. Error [μm]	0.0	0.3
	Exp. Amp. [μm]	7.6	78.5
	Num. Amp. [μm]	7.7	78.6
	Error Num./Exp. Amp. [%]	0	0
	Phase-shift between Num. and Exp. [*rad*]	0.00	0.00
Leading-edge	Mean Exp. Error [μm]	13.1	79.1
	STD on Exp. Error [μm]	7.4	30.7
	Exp. Amp. [μm]	206.8	1469.9
	Num. Amp. [μm]	167.0	727.6
	Error Num./Exp. Amp. [%]	**-19**	**-50**
	Phase-shift between Num. and Exp. [*rad*]	**0.88**	**1.00**
Vein	Mean Exp. Error [μm]	5.7	43.3
	STD on Exp. Error [μm]	3.0	16.3
	Exp. Amp. [μm]	107.1	792.8
	Num. Amp. [μm]	108.4	480.3
	Error Num./Exp. Amp. [%]	**1**	**-39**
	Phase-shift between Num. and Exp. [*rad*]	**0.88**	**1.00**
Tip	Mean Exp. Error [μm]	24.3	184.2
	STD on Exp. Error [μm]	12.5	73.6
	Exp. Amp. [μm]	496.2	3606.1
	Num. Amp. [μm]	902.2	3538.4
	Error Num./Exp. Amp. [%]	**82**	**-2**
	Phase-shift between Num. and Exp. [*rad*]	**0.75**	**0.75**

Table 5.6: Summary of the experimental/numerical comparison for E4. In order to quantify the experimental error of each extremity, its mean and standard-deviation values are given. Other items are based on the displacement amplitude of the extremity. The error between the numerical and the experimental values is defined as $\left(\overline{A_{num}} - \overline{A_{exp}}\right) / \overline{A_{exp}}$ with $\overline{A_{num}}$ and $\overline{A_{exp}}$ the numerical and experimental displacement amplitudes respectively.

Medium		**Vacuum**		**Air**	
Exp. Pressure [*mbar*]		4.8e-3 to 5.4e-3		1007	
Actuation type		SA	LA	SA	LA
Root	Mean Exp. Error [μm]	0.2	1.6	0.1	0.6
	STD on Exp. Error [μm]	0.1	0.8	0.1	0.3
	Exp. Amp. [μm]	7.6	79.6	7.3	77.9
	Num. Amp. [μm]	7.6	79.7	7.3	78.0
	Error Num./Exp. Amp. [%]	0	0	0	0
	Phase-shift between Num. and Exp. [*rad*]	0.00	0.00	0.00	0.00
Leading-edge	Mean Exp. Error [μm]	131.9	91.4	14.1	67.9
	STD on Exp. Error [μm]	64.7	51.5	6.8	36.4
	Exp. Amp. [μm]	484.9	2608.3	95.1	917.2
	Num. Amp. [μm]	395.9	1839.9	160.2	744.2
	Error Num./Exp. Amp. [%]	**-18**	**-29**	**68**	**-19**
	Phase-shift between Num. and Exp. [*rad*]	**0.00**	**-0.06**	**0.63**	**0.50**
Vein 1	Mean Exp. Error [μm]	27.7	117.8	2.6	13.6
	STD on Exp. Error [μm]	14.8	58.9	0.9	7.0
	Exp. Amp. [μm]	78.3	494.4	0.7	137.8
	Num. Amp. [μm]	85.5	450.0	33.2	184.6
	Error Num./Exp. Amp. [%]	**9**	**-9**	**4251**	**34**
	Phase-shift between Num. and Exp. [*rad*]	**0.00**	**0.06**	**0.63**	**0.38**
Vein 2	Mean Exp. Error [μm]	106.8	71.3	4.3	34.1
	STD on Exp. Error [μm]	49.1	34.0	2.0	15.8
	Exp. Amp. [μm]	398.7	2035.4	85.8	772.9
	Num. Amp. [μm]	366.0	1708.2	147.4	689.8
	Error Num./Exp. Amp. [%]	**-8**	**-16**	**72**	**-11**
	Phase-shift between Num. and Exp. [*rad*]	**0**	**-0.06**	**0.63**	**0.50**
Tip	Mean Exp. Error [μm]	591.5	288.4	11.4	195.2
	STD on Exp. Error [μm]	272.4	157.5	6.8	101.9
	Exp. Amp. [μm]	2216.2	8858.2	539.8	4589.2
	Num. Amp. [μm]	2015.8	7693.9	841.7	3523.8
	Error Num./Exp. Amp. [%]	**-8**	**-13**	**56**	**-23**
	Phase-shift between Num. and Exp. [*rad*]	**0**	**-0.06**	**0.50**	**0.38**

Additionally each numerical extremity is almost or in phase with its experimental counterpart for both wings in SA and in LA.

Thus the structural deformation of beam wing is thus well modeled and simulated in vacuum.

5.2.2.3 Validation in air

For the experiments in air, the performance in terms of amplitude are satisfactory for SA with an error of 95-227% for L2, of 1-82% for F3 and of 56-71% for E4 (the displacement of the vein 1 in SA being discarded due to post-processing hiccup). It gets better for LA with an error of 0-56% for L2, of 2-51% for F3 and of 11-35% for E4. These values might seem high but the percentage tends to skyrocket as they are related to small values, especially in SA. Additionally the error goes generally quickly down for extremity with large amplitude and for the LA actuation as the post-processing is eased on the motion tracking software.

In terms of phase-shift, the numerical displacements are in advance on the experimental ones, probably induced by the explicit coupling or by some aerodynamic effects not accounted yet, such as a Wagner effect or a wing-wake interaction, given the small distance traveled by the high-frequency resonant wing when compared to its chord.

Even so, the damping role of air is captured quite well with high-kinematics extremities being damped further than low-kinematics ones, which is in adequacy with the aerodynamic model where the aerodynamic forces are proportional to the motion amplitude. Thus the correct trend in terms of aeroelastic response is caught which validates the aeroelastic coupling.

5.2.2.4 Remarks on the experimental validation on beam wing

Given the experimental and numerical results found for the beam wing, the aeroelastic framework is validated for these wings. The performance both in vacuum and in air are quite good and encouraging. The damping effect of air is caught pretty well whatever the wing configuration. Furthermore the methodology, determining first the structural damping and second the Young modulus, is efficient enabling very good comparison between numerical and experimental data for a relatively low workload.

5.2.3 Validation on membrane wing

With the aeroelastic framework validated on beam wing, the next step is to extend this validation to the wings with membrane. Here again, the same methodology is used to characterize the wing deformation throughout several strokes and to compare it with its numerical prediction. However the focus is here more from a qualitative point of view so as to highlight better the performances of the framework for trend studies, i.e. preliminary design tasks.

As a reminder, experiments are made at the resonant frequency of the wing in vacuum. Results for the one in air are given in appendix E.2.

5.2.3.1 Presentation of the results

The table 5.8 summarizes the experimental/numerical comparison for the wing FM3 while the figure 5.18, for vacuum, and the figure 5.19, for air, depict graphically the comparison between the wing extremities of FM3 outlined in the figure 5.17. The wing EM4 has been also investigated but is not here discussed because the vacuum level reaches during the experiments was not sufficient to characterize properly the material damping as depicted in the appendix D.2, where the numerical wing displacements are over-damped both in SA and in LA.

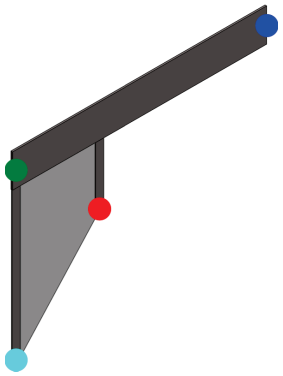

Figure 5.17: CAD view of the FM3 wing with its extremity colored as in the figures 5.18 and 5.19.

Table 5.7: Summary of the experimental/numerical comparison for FM3. In order to quantify the experimental error of each extremity, its mean and standard-deviation values are given. Other items are based on the displacement amplitude of the extremity. The error between the numerical and the experimental values is defined as $\left(\overline{A_{num}} - \overline{A_{exp}}\right) / \overline{A_{exp}}$ with $\overline{A_{num}}$ and $\overline{A_{exp}}$ the numerical and experimental displacement amplitudes respectively.

Medium		**Vacuum**		**Air**	
Exp. Pressure [$mbar$]		2.5e-3		1015	
Actuation type		SA	LA	SA	LA
Root	Mean Exp. Error [μm]	0.0	0.7	0.1	0.8
	STD on Exp. Error [μm]	0.0	0.3	0.0	0.4
	Exp. Amp. [μm]	7.7	78.7	7.7	80.5
	Num. Amp. [μm]	7.7	78.8	7.7	80.6
	Error Num./Exp. Amp. [%]	0	0	0	0
	Phase-shift between Num. and Exp. [rad]	0.00	0.00	0.00	0.00
Leading-edge	Mean Exp. Error [μm]	26.7	57.4	9.8	17.6
	STD on Exp. Error [μm]	12.9	18.8	4.4	11.5
	Exp. Amp. [μm]	142.3	1151.7	55.1	657.2
	Num. Amp. [μm]	101.6	626.9	100.1	508.0
	Error Num./Exp. Amp. [%]	**-29**	**-46**	**82**	**-23**
	Phase-shift between Num. and Exp. [rad]	**2.64**	**2.64**	**2.01**	**1.88**
Vein	Mean Exp. Error [μm]	15.6	46.4	7.5	29.3
	STD on Exp. Error [μm]	8.1	28.6	2.8	24.1
	Exp. Amp. [μm]	126.4	667.3	42.9	323.4
	Num. Amp. [μm]	96.1	638.9	96.0	510.1
	Error Num./Exp. Amp. [%]	**-24**	**-4**	**124**	**58**
	Phase-shift between Num. and Exp. [rad]	**2.51**	**2.64**	**2.01**	**1.88**
Tip	Mean Exp. Error [μm]	23.8	79.4	18.0	22.1
	STD on Exp. Error [μm]	10.6	26.4	8.6	8.7
	Exp. Amp. [μm]	213.9	1651.9	99.5	1045.4
	Num. Amp. [μm]	465.7	2243.8	478.0	1864.7
	Error Num./Exp. Amp. [%]	**118**	**36**	**380**	**78**
	Phase-shift between Num. and Exp. [rad]	**2.51**	**2.64**	**2.01**	**1.76**

5.2.3.2 Validation in vacuum

The numerical simulations are not as striking as for the beam wing but still satisfactory in terms of amplitudes both in SA and LA. The errors go from 24% to 118% in SA and decrease drastically between 4%

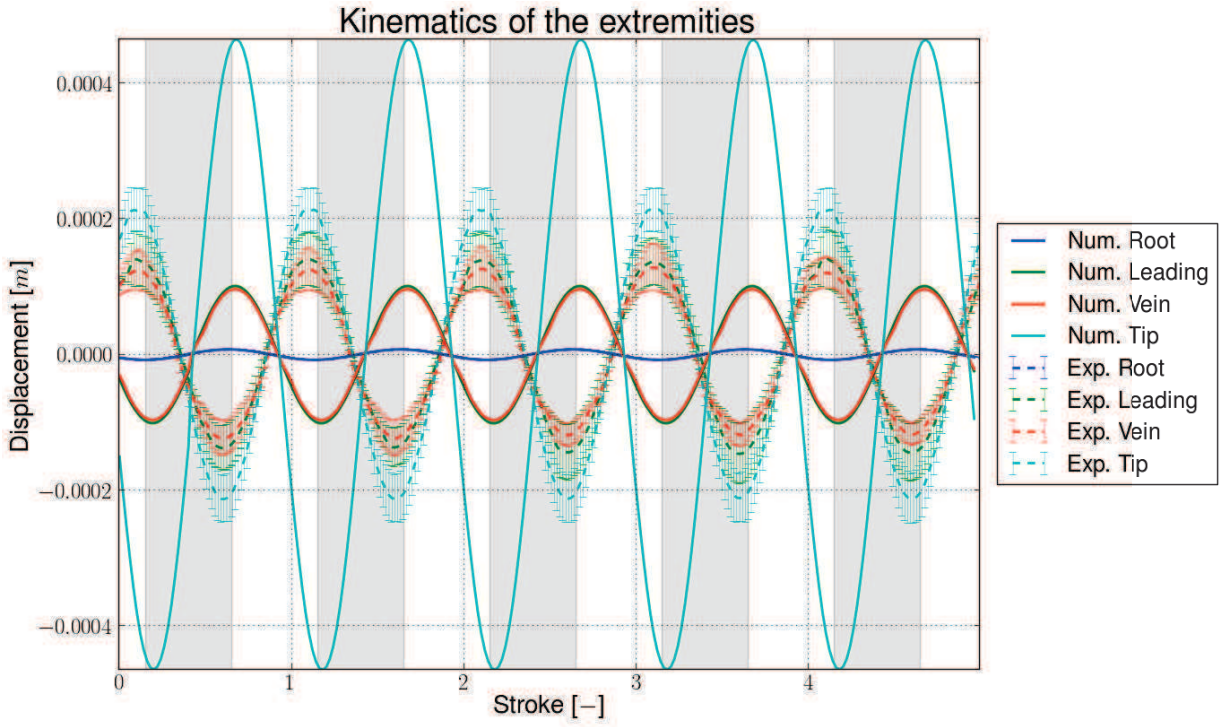

(a) Small actuation displacement (SA)

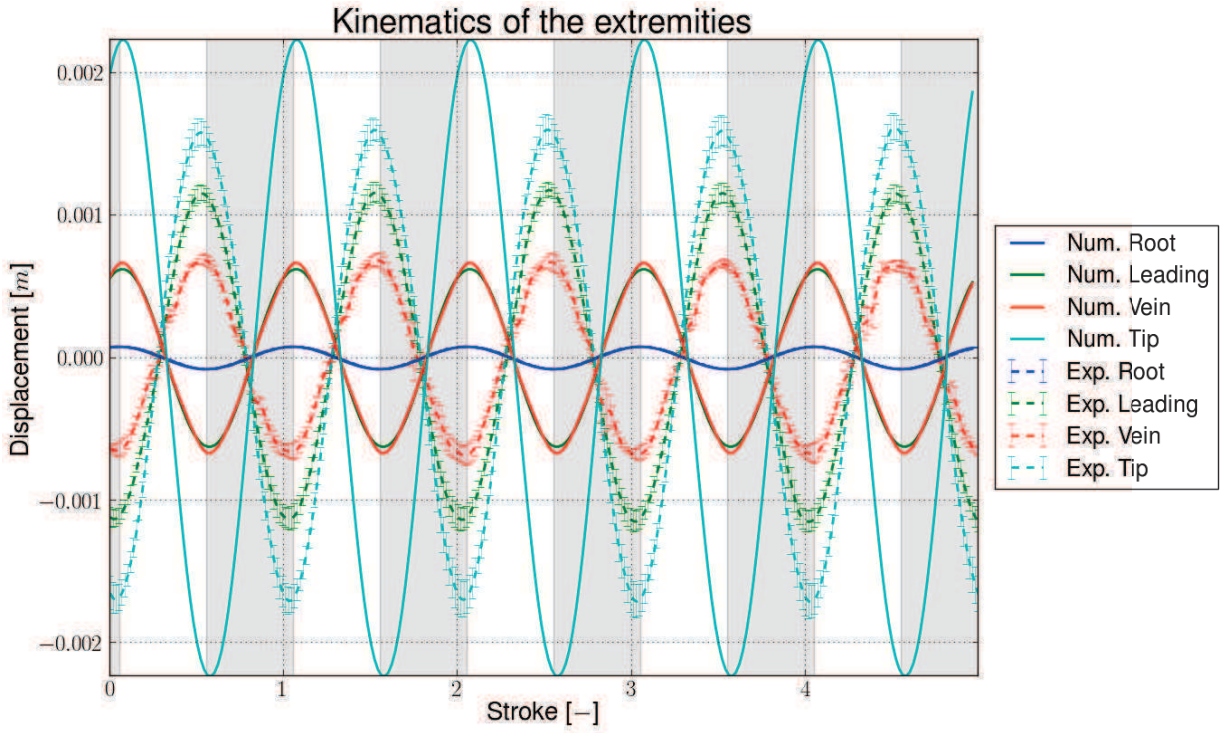

(b) Large actuation displacement (LA)

Figure 5.18: Graphical comparison between experimental and numerical data for the wing FM3 when actuated in vacuum i.e. without aerodynamic coupling. Calculations are done with the large deflection of the FEs turned on and with the relevant experimental actuation amplitude. 125 periods are simulated to overturn the transient state. More details about the comparison are given in table 5.7.

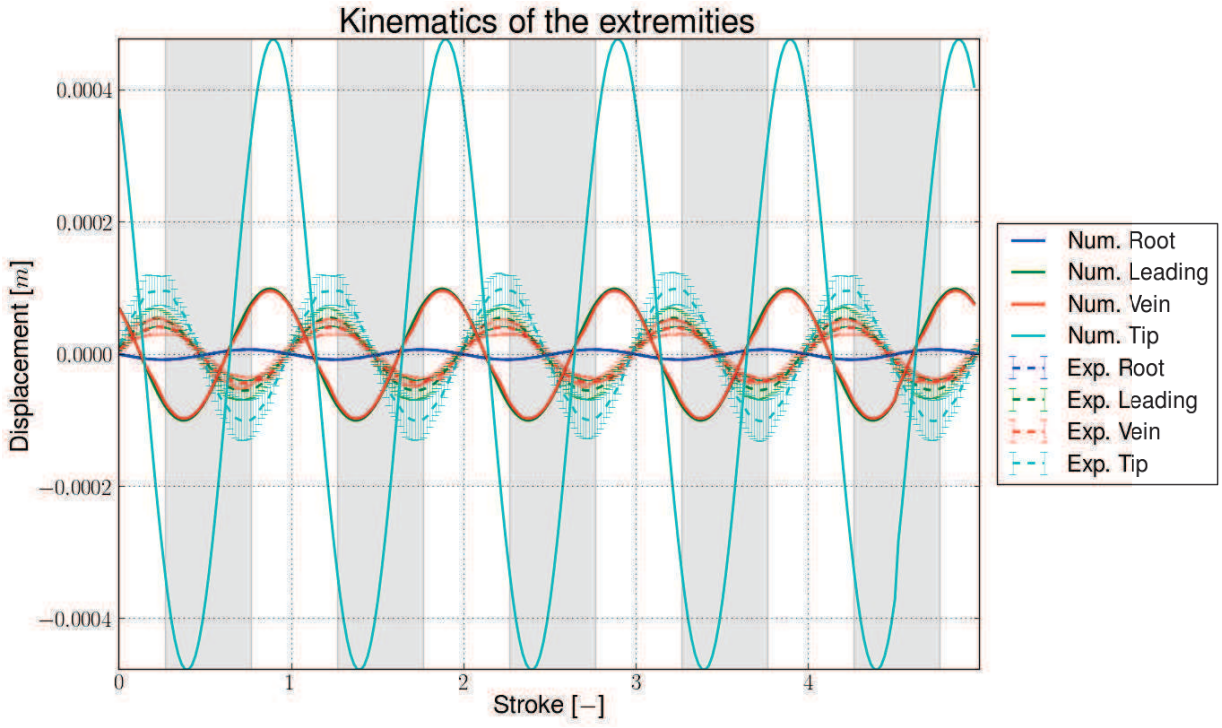

(a) Small actuation displacement (SA)

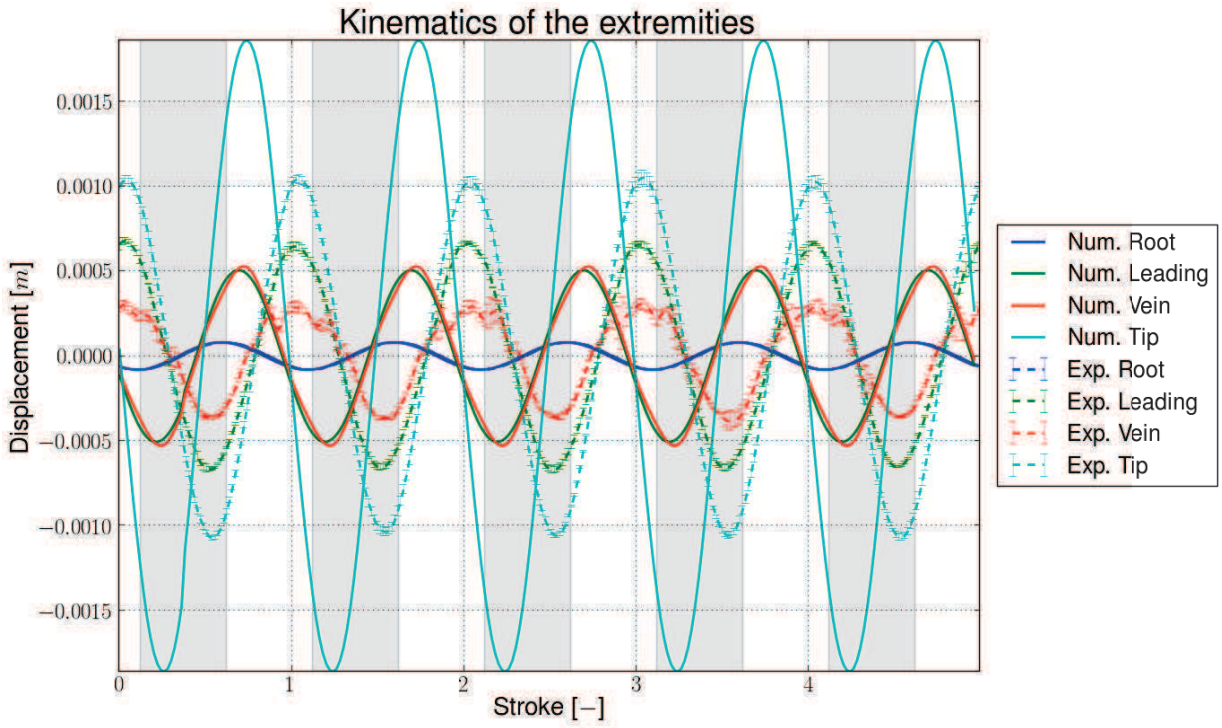

(b) Large actuation displacement (LA)

Figure 5.19: Graphical comparison between experimental and numerical data for the wing FM3 when actuated in air i.e. with aerodynamic coupling. Calculations are done with the large deflection of the FEs turned on and with the relevant experimental actuation amplitude. 50 periods are simulated to overturn the transient state. More details about the comparison are given in table 5.7.

Table 5.8: Summary of the experimental/numerical comparison for FM3. Amplification factor of each extremity are here reported being defined as the ratio betweeen the amplitude of the extremity to the one of the root. The damping factor is defined as the ratio of the amplification factor in vacuum to the one in air. The error between the numerical and the experimental values is defined as $\left(\overline{D_{num}} - \overline{D_{exp}}\right)/\overline{D_{exp}}$ with $\overline{D_{num}}$ and $\overline{D_{exp}}$ the numerical and experimental damping factors respectively. All computations are made using the values reported in the table 5.7.

Actuation type		**SA**	**LA**
Leading-edge	Exp. amplification factor in vacuum [–]	18.5	14.6
	Exp. amplification factor in air [–]	7.2	8.2
	Num. amplification factor in vacuum [–]	13.3	8.0
	Num. amplification factor in air [–]	13	6.3
	Exp. damping factor [–]	2.57	1.78
	Num. damping factor [–]	1.02	1.27
	Error Num./Exp. damping factor [%]	**-60**	**-29**
Vein	Exp. amplification factor in vacuum [–]	16.4	8.5
	Exp. amplification factor in air [–]	5.6	4.0
	Num. amplification factor in vacuum [–]	12.6	8.1
	Num. amplification factor in air [–]	12.5	6.3
	Exp. damping factor [–]	2.93	2.13
	Num. damping factor [–]	1.01	1.28
	Error Num./Exp. damping factor [%]	**-66**	**-40**
Tip	Exp. amplification factor in vacuum [–]	27.8	21.0
	Exp. amplification factor in air [–]	12.9	13.0
	Num. amplification factor in vacuum [–]	60.9	28.5
	Num. amplification factor in air [–]	62.1	23.1
	Exp. damping factor [–]	2.16	1.62
	Num. damping factor [–]	0.98	1.23
	Error Num./Exp. damping factor [%]	**-55**	**-24**

to 46% in LA. Given the small displacement observed both in SA and in LA, the error goes again quickly up, these performances are acceptable especially for design applications where only the LA actuation is sought. Furthermore, by glancing at the vacuum results of EM4 in the appendix D.2, the structural performance are confirmed, even if over-damped, with a reasonable error of 47% in average for LA.

In terms of phase-shift, each signal, except the root, is in advance, not far from being in anti-phase with its counterpart. This bias might be explained by remembering the typical phase response of a resonant system near resonance as reminded in the figure 5.20. For very low damped system, like here with *zeta* typically below 0.01, the phase response tends to shift quickly to *pi* instead of $\frac{pi}{2}$. Given the frequency step used for the frequency scanning of the section 5.2.1.1, the actual resonant frequency might well lay between two consecutive steps and thus the experimental actuation might be slightly off the resonant frequency and thus induced this phase-shift response. With this point in mind, the bias is acceptable as the phases are secondary to the amplitudes.

Thus the structural deformation of membrane wing is cleared especially given that the framework is aimed at preliminary design studies where only LA and the overall trends are actively sought.

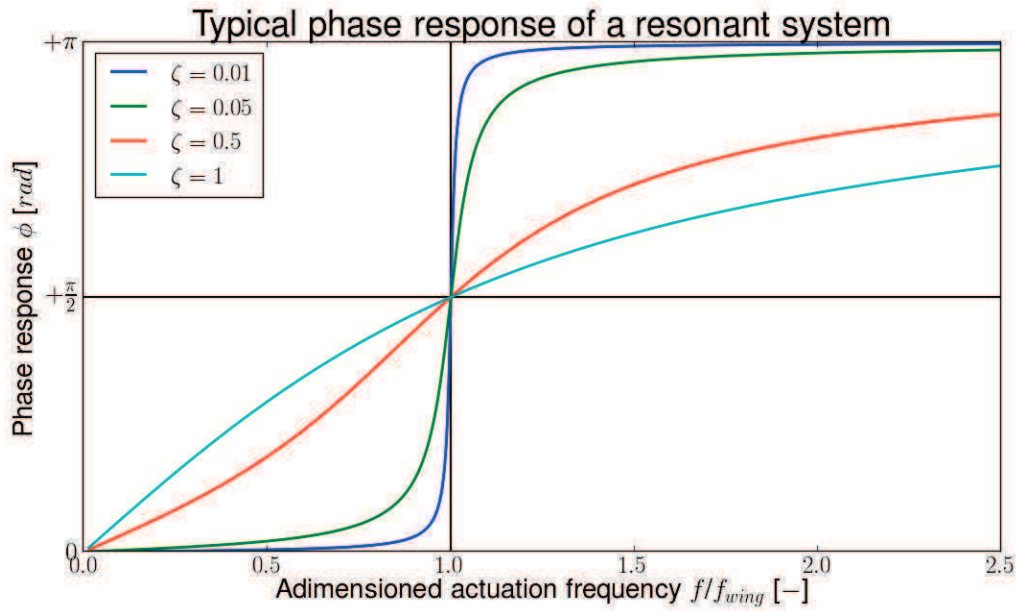

Figure 5.20: Typical phase response of a system near resonance as a function of the damping ratio ζ.

5.2.3.3 Validation in air

Similar results are observed for the experiments in air. The SA performance are slightly puzzling with an error of 82-380%. It gets way better for the LA performance with an error of 23-78%. The errors might seem high but the percentage goes again quickly up given the small values at stake. In any case, the aerodynamic damping is captured as highlighted by the table 5.8, where the numerical and experimental amplification factor of each extremity are compared along with their damping between vacuum and air. Differences of 60% in SA and only of 31% in LA are observed which is appropriate for trend studies.

In terms of phase-shift, the results are more satisfactory than in vacuum. Indeed when discarding the original anti-phase bias shown in vacuum and instead assuming in phase results in vacuum, a parallel might be established with the phase-shift observed in air for beam wing due most probably to the explicit coupling or some aerodynamic forces not yet accounted. This hypothesis is credited as the phase-shift response for FM3 in air is better than in vacuum, which is not physical. This backs the results in air even more and also ultimately the framework. Additionally, it points further towards an experimental error in the vacuum results where the wing might have been actuated short after the resonant frequency.

Thus the framework is appropriate for aeroelastic trend studies in LA especially as the aerodynamic damping is captured satisfactorily.

5.2.3.4 Remarks on the experimental validation on membrane wing

To validate more extensively the framework, wing with membrane should be investigated more intensively both numerically and experimentally on a larger database. First, due to the high computation load required for these wings, the study of the membrane behavior is very time-consuming as the fine tuning of each parameter needed for better comparison. Second, some improvements on the test bench are needed to minimize the uncertainties and handling errors. For example, the vacuum level might not be sufficient to characterize efficiently the structural damping of all wings with membrane and a more efficient pump might be needed. Also as the post-processing for wings with membrane is trickier due to the inboard extremities being almost always hidden to the camera, the overall experimental uncertainties is non-negligible and novel tracking techniques are needed to reduce them.

Even if the results are not as striking as for beam wing, the aeroelastic framework captures the effects of aerodynamic damping on the structure, especially for trend studies in LA, and can be cleared to assist the design of flapping-wing system.

Additionally it is, to our knowledge, the first time at this high-frequency, here about $100Hz$ whereas the one from Wu et al. [2011] is at $40Hz$ maximum, that such complete database is available for resonant flapping-wings in large deflection.

5.3 Effect of the added-mass formulation on the wing deformation

As seen in the chapter 4.3, the added-mass forces as computed by the bidirectional flexible approach are underestimated when compared to the unidirectional approach which is attributed to the chordwise discretization and its use in the added-mass formulation. Using an arbitrary weighting factor WF, the two approaches converge towards one another in terms of aerodynamic forces generated but its effect on the displacement has not been discussed and might be a source of discrepancy for the experimental validation. It might also improve further the experimental comparison both in terms of amplitude and phase-shift and is therefore here discussed.

The wing L2 is thus recomputed with the weighting factor of $WF = 3.33$. The results are presented in the figure 5.21 and in the table 5.9.

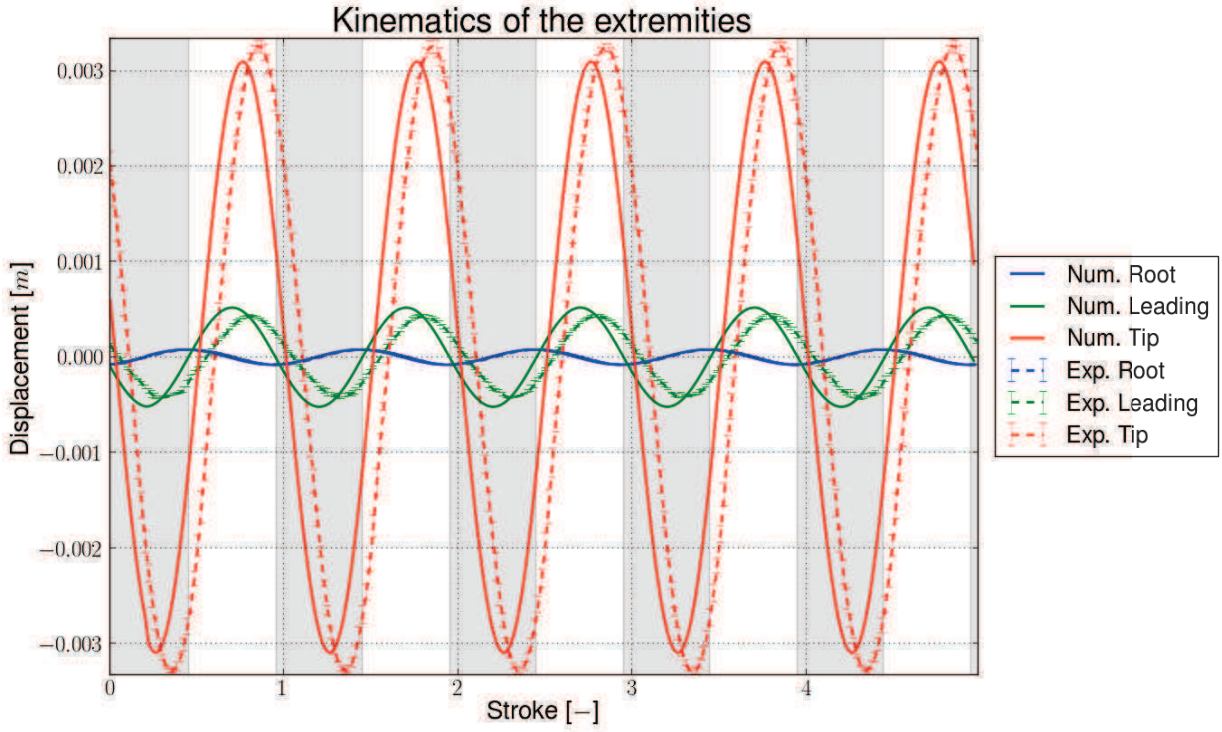

Figure 5.21: Experimental comparison with $WF = 3.33$ for the wing L2 in LA.

The numerical prediction is slightly better with a mean error of about 14.5% compared the original of 28%. Due the higher aerodynamic forces, the numerical displacements are slightly more damped, which is appropriate for the leading-edge but less for the wing tip. But in average the agreement is better crediting the weighting factor WF for its enhancement of the added-mass forces.

However the most noticeable improvement is still the phase-shift which is much closer to the experimental one highlighting the key role of the added-mass forces in the phase-shift between root and tip. This phase-shift is favorable to the generation of aerodynamic forces and an appropriate model of them is mandatory what the formulation adopted here, with some slight enhancements, does.

Table 5.9: Summary of the experimental/numerical comparison for L2 with $WF = 3.33$. The error between the numerical and the experimental values is defined as $\left(\overline{A_{num}} - \overline{A_{exp}}\right)/\overline{A_{exp}}$ with $\overline{A_{num}}$ and $\overline{A_{exp}}$ the numerical and experimental displacement amplitudes respectively.

		No WF	$WF = 3.33$
Root	Exp. Amp. [μm]	79.1	
	Error Num./Exp. Amp. [%]	0	0
	Phase-shift between Num. and Exp. [rad]	0.00	0.00
Leading-edge	Exp. Amp. [μm]	420.5	
	Error Num./Exp. Amp. [%]	56	23
	Phase-shift between Num. and Exp. [rad]	**1.01**	**0.63**
Tip	Exp. Amp. [μm]	3291.9	
	Error Num./Exp. Amp. [%]	0	-6
	Phase-shift between Num. and Exp. [rad]	**0.88**	**0.50**

5.4 Influence of the FE chosen to model membrane and of its thickness

As seen earlier, the experimental validation for the wings with membrane is not completely satisfactory. The damping effect of aerodynamic forces is caught, but the deformation for both the wings FM3 and EM4 is not sufficiently accounted. Experimental errors can explain some of the discrepancies, but the structural model itself might be also liable. Therefore to alleviate this doubt, the FE chosen to model the membrane and the influence of the membrane thickness have to be investigated.

5.4.1 Choice of FE

The original choice of FE has been driven by the robustness of the *SHELL93* with its mid-nodes reducing the number of elements necessary to discretize a membrane especially in LA. However a simpler FE is also available without mid-nodes improving thus potentially the accuracy and the rapidity of the framework: the *SHELL63*.

To evaluate this element, the wing FM3 is recomputed in LA both in vacuum and in air and is compared both the *SHELL93* computation and to the experimental data. To get a successful computation of the wing in LD, the mesh is densified to $N_{FE_{Span}} = 20$ and $N_{FE_{Chord}} = 40$. Results are summarized in the table 5.10.

The results speaks for themselves as no clear difference is observed between the two elements. Therefore the discrepancy between the numerical and the experimental data is independent of the FE choice. Furthermore by comparing the computation duration, the choice of the *SHELL93* FE to discretize the membrane is strengthened due mainly to the coarser mesh complying nicely with the LD intensive computation while enabling faster and more stable computation.

To improve the behavior and prediction of membrane wing, other parameters such as the stress-stiffening or the membrane thickness have to be investigated. However only the latter is here studied as the former required additional input data, the elastic foundation stiffness, which is yet unknown.

5.4.2 Influence of the membrane thickness

Given the very thin thickness of the membrane, its fabrication is quite sensitive to any micromachining disturbances and thus might introduce an important bias between the predicted and experienced behavior on the wing. The aim here is to study the influence of the membrane thickness on the numerical prediction.

To do so, the complete validation process is relaunched with a thinner and a thicker FM3, nominally $t_m = 4\mu m$ and $t_m = 6\mu m$ which falls typically within the fabrication tolerances. The experimental Young

Table 5.10: Comparison of the performance using *SHELL63* as FE for FM3 in LA both in vacuum and in air. The error between the numerical and the experimental values is defined as $\left(\overline{A_{num}} - \overline{A_{exp}}\right)/\overline{A_{exp}}$ with $\overline{A_{num}}$ and $\overline{A_{exp}}$ the numerical and experimental displacement amplitudes respectively.

Medium		**Vacuum**		**Air**	
Actuation type		*SHELL63*	*SHELL93*	*SHELL63*	*SHELL93*
Root	Exp. Amp. [μm]	78.7		80.5	
	Error Num./Exp. Amp. [%]	0	-1	0	0
	Phase-shift between Num. and Exp. [rad]	0.00	0.00	0.00	0.00
Leading-edge	Exp. Amp. [μm]	1151.7		656.1	
	Error Num./Exp. Amp. [%]	-45	-46	-24	-23
	Phase-shift between Num. and Exp. [rad]	**2.64**	**2.64**	**2.01**	**1.88**
Vein	Exp. Amp. [μm]	667.3		325.3	
	Error Num./Exp. Amp. [%]	-3	-5	54	57
	Phase-shift between Num. and Exp. [rad]	**2.64**	**2.64**	**1.88**	**1.88**
Tip	Exp. Amp. [μm]	1651.8		1043.9	
	Error Num./Exp. Amp. [%]	37	35	73	79
	Phase-shift between Num. and Exp. [rad]	**2.64**	**2.64**	**1.76**	**1.76**
Duration [h]		65.4	45.1	10.5	8

modulus E_{exp} is then defined using the same procedure as in the section 5.2.1.2 and its results are given in the table 5.11.

Table 5.11: Influence of the membrane thickness on the Young modulus of FM3.

Membrane thickness	$f_{v,exp,1}$ [Hz]	$\zeta_{exp,1}$ [$-$]	$f_{v,exp,2}$ [Hz]	$\zeta_{exp,2}$ [$-$]	E_{exp} [GPa]	$f_{v,num,1}$ [Hz]
$t_m = 4\mu m$	111	0.0068	238.5	0.013	6.3	111.50
$t_m = 6\mu m$	111	0.0068	238.5	0.013	6.6	111.23

The aeroelastic computation is then done in LA both in vacuum and in air and compared to the original thickness of $t_m = 5\mu m$. Results are summarized in the table 5.12 for the wing displacement and aerodynamic forces.

The influence of the membrane is thus significant both for the displacement and for the aerodynamic forces. Their variations follow the one of the thickness with in average 7% discrepancy induced on the displacement per μm, 8% for the mean lift and 5% for the peak-to-peak drag. Similarly, the computation load increases with thinner membrane as the mesh and time step have to be increased to accommodate the more fragile nature of the membrane.

Given the fabrication tolerances, it might explain some of the discrepancies observed experimentally and a better characterization of the wing is mandatory for example using a profilometer for example. Also special attention is needed during the fabrication process to control the tolerances and also during the design process to anticipate their effects on the aeroelastic response using the rule of thumb defined above.

5.5 Effect of the explicit approach in the transient analysis

As better outlined by the experimental comparison for beam wings, the structural response in vacuum is correctly predicted while in air the amplitude is very satisfactory but a phase-shift appears each time with the numerical wing being in advance. Some of the delay might be attributed to the underestimated

Table 5.12: Summary of the influence of the membrane thickness on the aerodynamic forces for FM3. The difference between the bidirectional and the unidirectional value is defined as $(F_{bi} - F_{uni})/F_{uni}$ with F_{bi} and F_{uni} the unidirectional and bidirectional computed forces respectively.

Medium		**Vacuum**		**Air**	
		$t_m = 4\mu m$	$t_m = 6\mu m$	$t_m = 4\mu m$	$t_m = 6\mu m$
Displacement	Difference on leading-edge amplitudes [%]	-5	7	-1	2
	Difference on vein amplitudes [%]	-8	11	-4	7
	Difference on tip amplitudes [%]	-6	8	-2	4
Aerodynamics forces	Baseline mean lift [μN]	-		0.75	
	Baseline lift amplitude [μN]	-		1.72	
	Difference on lift means [%]	-		-6	9
	Difference on lift amplitudes [%]	-		-6	11
	Baseline mean drag [μN]	-		0.00	
	Baseline drag amplitude [μN]	-		25.36	
	Difference on drag means [%]	-		52	-25
	Difference on drag amplitudes [%]	-		-4	6

added-mass forces, as seen in the section 5.3, but the main sources might be induced by the coupling and/or by some aerodynamic effects not accounted yet, such as a Wagner effect or a wing-wake interaction.

However as the strokes are periodic and once a steady state is reached, the phase-shift might be canceled by retrieving kinematics of the previous stroke and induced thus an artificial delay or advance on the applied forces. Thus, as highlighted by the figure 5.22 and the table 5.13 for the wing L2, any wings might be synchronized with its experimental counterpart easily. Here a forward-shift of 5 time-steps is used meaning that the aerodynamic model uses kinematics variables from the wing future of 5 time-steps. The explanation of this arbitrary shift is not known but the explicit coupling has its share of responsibility, given that the aerodynamic forces are always computed *at posteriori*.

Table 5.13: Summary of the experimental/numerical comparison for L2 with a 5 forward-shift in LA and the enhanced local acceleration weighting factor of $WF = 3.33$. The error between the numerical and the experimental values is defined as $\left(\overline{A_{num}} - \overline{A_{exp}}\right)/\overline{A_{exp}}$ with $\overline{A_{num}}$ and $\overline{A_{exp}}$ the numerical and experimental displacement amplitudes respectively.

Root	Exp. Amp. [μm]	79.1
	Error Num./Exp. Amp. [%]	0
	Phase-shift between Num. and Exp. [rad]	0.00
Leading-edge	Exp. Amp. [μm]	420.5
	Error Num./Exp. Amp. [%]	10
	Phase-shift between Num. and Exp. [rad]	**0.00**
Tip	Exp. Amp. [μm]	3291.9
	Error Num./Exp. Amp. [%]	4
	Phase-shift between Num. and Exp. [rad]	**0.00**

Apart from the fact that numerical results can be arbitrarily synchronized, the availability of previous and 'future' kinematics variable is appealing for future works as more advanced aerodynamic schemes implying wake modeling, such as the one of Ansari et al. [2006a,b], or advanced aerodynamic effects, such as Theodorsen function (Theodorsen [1935]) to model the wake, might be implemented.

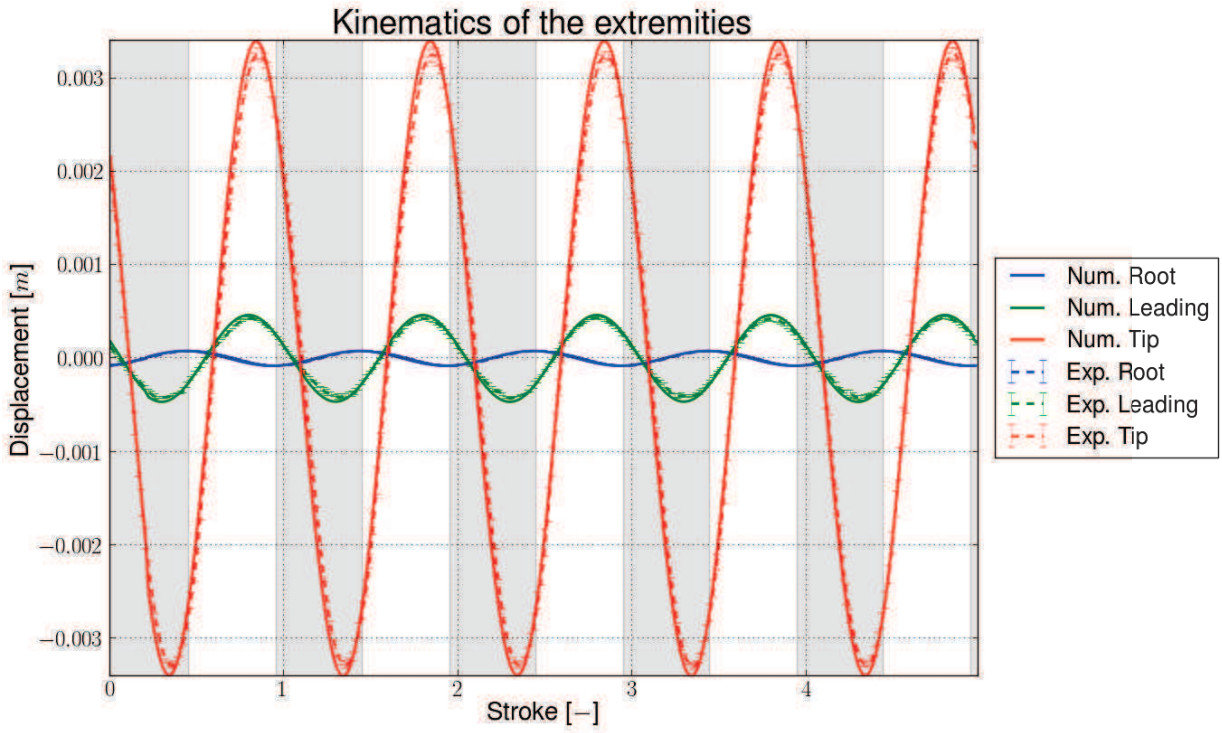

Figure 5.22: Graphical comparison of experimental/numerical data for the wing L2 with a 5 forward-shift in LA and the enhanced local acceleration weighting factor of $WF = 3.33$

5.6 Influence of the large deflection capability of the FEs

In this work, the large deflection capability of the FEs might be either turned off (SD) or on (LD) depending on the envisioned applications as a balance between accuracy and computation rapidity might be required. For example, in the experimental validation above, the accuracy is primordial and no time constraint is imposed. Thus the LD capability has been activated. On the contrary for typical preliminary design applications, the time constraint is more decisive and trends are more important. There the LD capability might be superficial given the strong impact of this option on the computation load. Therefore, it is essential to evaluate its impacts on the aeroelastic performance of both beam and membrane wings so as so to identify possible sources of discrepancy and enable faster but less accurate applications with the LD option turned off.

5.6.1 Beam-Wing

To benchmark the influence of the large deflection option on beam wing, the wing L2 is used first in vacuum and second in air. The wing are using the experimental data of the section 5.2.2 for the large amplitude actuation (LA), here of about $150\mu m$ peak-to-peak.

5.6.1.1 Vacuum comparison

The results for the computation both in SD and LD within vacuum are summarized in the table 5.14 and compared to the experimental results found previously.

As expected, due to the large deflection occurring in vacuum, the large deflection capability of the FE is mandatory to catch the experienced displacement as highlighted by the high percentage and also by the large phase-shift observed for the computation in SD. However in terms of computation duration, the SD is unbeatable mainly due to the reduced computation time between two consecutive time steps.

Table 5.14: Influence of the large deflection capability of the FEs for L2 under vacuum. The error between the numerical and the experimental values is defined as $\left(\overline{A_{num}} - \overline{A_{exp}}\right)/\overline{A_{exp}}$ with $\overline{A_{num}}$ and $\overline{A_{exp}}$ the numerical and experimental displacement amplitudes respectively. More details about the experimental data are given in the chapter 5.2.2.

		SD	**LD**
Root	Exp. Amp. $[\mu m]$	76.9	
	Error Num./Exp. Amp. [%]	0	0
	Phase-shift between Num. and Exp. $[rad]$	0.00	0.00
Leading-edge	Exp. Amp. $[\mu m]$	1596.9	
	Error Num./Exp. Amp. [%]	**72**	**0**
	Phase-shift between Num. and Exp. $[rad]$	**-1.26**	**-0.13**
Tip	Exp. Amp. $[\mu m]$	7314.2	
	Error Num./Exp. Amp. [%]	**110**	**-2**
	Phase-shift between Num. and Exp. $[rad]$	**-1.26**	**-0.13**
Duration $[min]$		71	117

5.6.1.2 Air comparison

The results for the computation both in SD and LD within air, i.e. with the aerodynamic coupling enabled and using the bidirectional flexible aerodynamic model, are summarized in the table 5.15 and are compared to the experimental data. Additionally and more importantly, the effect on the aerodynamic forces is presented in the table 5.16 where the ones computed by the bidirectional flexible aerodynamic model are compared to the unidirectional one.

Table 5.15: Influence of the large deflection capability of the FEs for L2 under air. The error between the numerical and the experimental values is defined as $\left(\overline{A_{num}} - \overline{A_{exp}}\right)/\overline{A_{exp}}$ with $\overline{A_{num}}$ and $\overline{A_{exp}}$ the numerical and experimental displacement amplitudes respectively. More details about the experimental data are given in the chapter 5.2.2.

		SD	**LD**
Root	Exp. Amp. $[\mu m]$	79.1	
	Error Num./Exp. Amp. [%]	0	0
	Phase-shift between Num. and Exp. $[rad]$	0.00	0.00
Leading-edge	Exp. Amp. $[\mu m]$	420.5	
	Error Num./Exp. Amp. [%]	**50**	**56**
	Phase-shift between Num. and Exp. $[rad]$	**0.88**	**1.01**
Tip	Exp. Amp. $[\mu m]$	3291.9	
	Error Num./Exp. Amp. [%]	**2**	**0**
	Phase-shift between Num. and Exp. $[rad]$	**0.75**	**0.88**
Duration $[min]$		38	43

The performances are better for the SD option in air than in vacuum in terms of displacement. Indeed due to the higher kinematics computed in SD prior to the coupling, i.e. in vacuum, the aerodynamic forces tends to be larger at the beginning which increases the aeroelastic response of the wing by damping further its displacement. It defines thus an auto-compensation mechanism that prove to be quite useful as both the computation in SD and in LD tends to converge towards almost the same equilibrium, both in terms of displacement and aerodynamic forces. However, the LD computation tends to provide a better prediction both in terms of displacement and of aerodynamic forces by modeling more closely the behavior of the wing.

Table 5.16: Comparison between the bidirectional/unidirectional aerodynamic forces for L2 in LA computed either in SD or in LD. The difference between the bidirectional and the unidirectional values is defined as $(F_{bi} - F_{uni})/F_{uni}$ with F_{bi} and F_{uni} the unidirectional and bidirectional computed forces respectively.

		Lift		Drag	
		SD	**LD**	**SD**	**LD**
Translational forces	Difference Bidir./Unidir. on means [%]	11	10	-100	-102
	Difference Bidir./Unidir. on amplitudes [%]	42	42	11	11
Added-mass forces	Difference Bidir./Unidir. on means [%]	-81	-81	-100	-94
	Difference Bidir./Unidir. on amplitudes [%]	-85	-86	-62	-63
Total forces	Unidir. mean [μN]	3.45	3.41	0.00	0.00
	Difference Bidir./Unidir. on means [%]	**-71**	**-72**	**-100**	**-111**
	Unidir. amplitude [μN]	5.70	5.20	55.55	54.83
	Difference on Bidir./Unidir. amplitudes [%]	**-44**	**-42**	**-56**	**-54**

In terms of computation duration, the SD computation keeps its advantage over the LD computation.

5.6.1.3 Remarks on the role of large deflection for beam wing

The SD option for beam wing is not appropriate for study in vacuum where accuracy is essential. Indeed with the large deflection experienced by the wing, the small deflection assumption used by the FE does not stand any longer. Thus the FE solver is overestimating the displacement at each step while no damping sources are here to correct this behavior. On the contrary, the SD assumption stands in air, as the aerodynamic forces are damping the displacement proportional to its overestimation.

Overall the SD performances are comparable to the LD ones for computation in air, but still better performance are achieved in LD in terms of accuracy both in air and in vacuum, but not in terms of speed.

5.6.2 Membrane-Wing

To benchmark the influence of the large deflection option on membrane wing, the wing FM3 is used alternatively in vacuum and in air.

5.6.2.1 Vacuum comparison

The results for the computation both in SD and LD within vacuum are summarized in the table 5.17 and compared to the experimental results found previously.

As expected, due to the large deflection occurring in vacuum and to the trickiest behavior of the membrane FE, the large deflection capability of the FE is mandatory to better estimated the experienced displacement as highlighted by the high percentages observed. However in terms of phase-shift and of computation duration, the SD option offers better performance especially for the latter.

5.6.2.2 Air comparison

The results for the computation both in SD and LD within air, i.e. with the aerodynamic coupling enabled, are summarized in the table 5.18. The effect on the aerodynamic forces are presented in the

Table 5.17: Influence of the large deflection capability of the FEs for FM3 under vacuum. The error between the numerical and the experimental values is defined as $\left(\overline{A_{num}} - \overline{A_{exp}}\right)/\overline{A_{exp}}$ with $\overline{A_{num}}$ and $\overline{A_{exp}}$ the numerical and experimental displacement amplitudes respectively. More details about the experimental data are given in the chapter 5.2.3.

		SD	LD
Root	Exp. Amp. [μm]	78.7	
	Error Num./Exp. Amp. [%]	0	-1
	Phase-shift between Num. and Exp. [rad]	0.00	0.00
Leading-edge	Exp. Amp. [μm]	1151.7	
	Error Num./Exp. Amp. [%]	**165**	**-46**
	Phase-shift between Num. and Exp. [rad]	**1.13**	**2.64**
Vein	Exp. Amp. [μm]	667.3	
	Error Num./Exp. Amp. [%]	**294**	**-4**
	Phase-shift between Num. and Exp. [rad]	**1.01**	**2.64**
Tip	Exp. Amp. [μm]	1651.9	
	Error Num./Exp. Amp. [%]	**993**	**36**
	Phase-shift between Num. and Exp. [rad]	**1.01**	**2.64**
Duration [h]		32	45

table 5.19 where the ones computed by the bidirectional flexible aerodynamic model are compared to the unidirectional one.

Table 5.18: Influence of the large deflection capability of the FEs for FM3 under air. The error between the numerical and the experimental values is defined as $\left(\overline{A_{num}} - \overline{A_{exp}}\right)/\overline{A_{exp}}$ with $\overline{A_{num}}$ and $\overline{A_{exp}}$ the numerical and experimental displacement amplitudes respectively. More details about the experimental data are given in the chapter 5.2.3.

		SD	LD
Root	Exp. Amp. [μm]	80.5	
	Error Num./Exp. Amp. [%]	0	0
	Phase-shift between Num. and Exp. [rad]	0.00	0.00
Leading-edge	Exp. Amp. [μm]	657.2	
	Error Num./Exp. Amp. [%]	**-41**	**-23**
	Phase-shift between Num. and Exp. [rad]	**1.26**	**1.88**
Vein	Exp. Amp. [μm]	323.4	
	Error Num./Exp. Amp. [%]	**0**	**58**
	Phase-shift between Num. and Exp. [rad]	**1.26**	**1.88**
Tip	Exp. Amp. [μm]	1045.4	
	Error Num./Exp. Amp. [%]	**105**	**78**
	Phase-shift between Num. and Exp. [rad]	**0.88**	**1.76**
Duration [h]		5	8

As for the beam wing, the SD computation in air offers a better estimate of the experienced displacement than in vacuum. The damping by the aerodynamic forces of the overestimated displacement stands again even if the damping does not equal the one observed with the beam element in terms of efficiency, the differences between the SD and LD computation being larger for membrane wings. However considering the original gap between the vacuum and the air computation observed, the auto-compensation is an efficient mechanism outlining the importance of the aeroelastic coupling in the study of resonant flapping wings. In

any case, the LD option has to be used when accuracy on the experienced displacement is sought.

This auto-compensation mechanism is also confirmed when looking specifically at the aerodynamic forces in table 5.19 where the higher kinematics tends to reduce the gap between the unidirectional and the bidirectional approach, by compensating further the rotational forces by the translational one and by slightly increasing the added-mass forces when compared to the LD computation. Therefore the results are quite similar and comparable as highlighted by the difference between the peak-to-peak drag, being the main forces acting on the system and sizing its aeroelastic response, and by the order of magnitude found.

Table 5.19: Comparison between the bidirectional/unidirectional aerodynamic forces for FM3 in LA computed either in SD or in LD. The difference between the bidirectional and the unidirectional values is defined as $(F_{bi} - F_{uni})/F_{uni}$ with F_{bi} and F_{uni} the unidirectional and bidirectional computed forces respectively.

		Lift		**Drag**	
		SD	**LD**	**SD**	**LD**
Translational forces	Difference Bidir./Unidir. on means [%]	9	4	-100	-99
	Difference Bidir./Unidir. on amplitudes [%]	47	43	11	5
Added-mass forces	Difference Bidir./Unidir. on means [%]	-80	-88	-100	-100
	Difference Bidir./Unidir. on amplitudes [%]	-87	-89	-65	-88
Total forces	Unidir. mean [μN]	3.74	4.20	0.00	0.00
	Difference Bidir./Unidir. on means [%]	**-71**	**-82**	**-65**	**-100**
	Unidir. amplitude [μN]	3.61	4.03	56.54	77.89
	Difference on Bidir./Unidir. amplitudes [%]	**-34**	**-57**	**-67**	**-67**

5.6.2.3 Remarks on the role of large deflection for membrane wing

The SD option for membrane wing is not appropriate for study in vacuum but is satisfactory in air.

In vacuum, the absence of external damping sources is detrimental as the wing experiences severe deflection emphasized by the trickiest behavior of the membrane FE. There only trend studies can be undertaken, such as the optimization application done in the chapter 6.2, as the displacements are completely overestimated but still complying with the overall mode shape of the wing, indicating its plausible aerodynamic potential in the case of the optimization applications.

In air, the SD performance are, like for beam wing, much more comparable to the LD one with slightly overestimated displacement and slightly better aerodynamic forces prediction. The compensation mechanism already found for beam wing is here fully efficient and essential.

Overall the main advantage of the SD computation is its reduction of the computation load while being sufficiently accurate to capture the trend. The LD is however more accurate and depicts more properly the aeroelastic response.

In a nutshell, the aeroelastic framework has been here experimentally stress-tested to assess its capability to conduct trend studies both for wing without and with membrane. Even if more experimental data are required to complete this study, the aeroelastic prediction are satisfactory for both wing types capturing successfully the damping effect of aerodynamic forces. Several factors have also been investigated to improve the agreement. To complete this experimental validation, the effect of large deflection capability of the FEs has been investigated to expand the capabilities of the framework towards more intensive preliminary design applications where less accuracy but more rapid evaluation are necessary.

As a consequence of this complete numerical and experimental stress-testing, the framework is cleared and ready to demonstrate its capabilities as a preliminary design tool for flapping-wing systems.

Chapter 6

Optimisation of the performance of a resonant FWNAV

Contents

With the aeroelastic framework validated for trend studies on both beam and membrane wings, its applications are now of interest. A major goal of this work is to develop a tool assisting the engineers and scientists in the sizing of a FWNAV and driving them quickly through the preliminary design stages. The aim is here to speed up the development time by limiting the experimental trial and error loops. Depending on the FWNAV specifications and on the technologies available, multiple design choices have to be made. Each choice induces additional requirements that may impact later on the overall FWNAV performance. Therefore it is critical to evaluate in advance the pro and con of a design choice and avoid thus costly engineering deadlock. The framework developed in this work is here a promising platform for such tasks due to its practicality, rapidity and also autonomy.

Among the wide variety of possible applications, the focus is here made on two of them being major concerns for the designers: the selection of an actuation strategy, how should I actuate my wings to maximize their performances, and the design of wing suitable to sustain a FWNAV, what is the best wing geometry considering my FWNAV specifications. The overall goal of such applications is to optimize gradually the performance of a FWNAV. Here the applications are considered for the OVMI, where among its specifications are the use of a resonant design, i.e. the wing mode-shape generating the necessary aerodynamic forces for flight by itself without any active mechanical link as explained in the chapter 1.1.3.

6.1 Choosing an actuation strategy

A major difficulty in sizing a FWNAV is to define how to actuate the wing so that the wing maximizes its aerodynamic potential for example. Indeed given the FWNAV specifications, the wing root can be actuated

on various DOFs and a strategy for actuation has to be devised. An actuation strategy is here defined as the combination of an actuation mode, which DOF is actuated, and of its kinematics, how it is actuated. This task is important as it defines the core of any FWNAV and each system has to be designed towards this goal such as the actuator, any mechanical link and all the electronics equipment necessary for flight control.

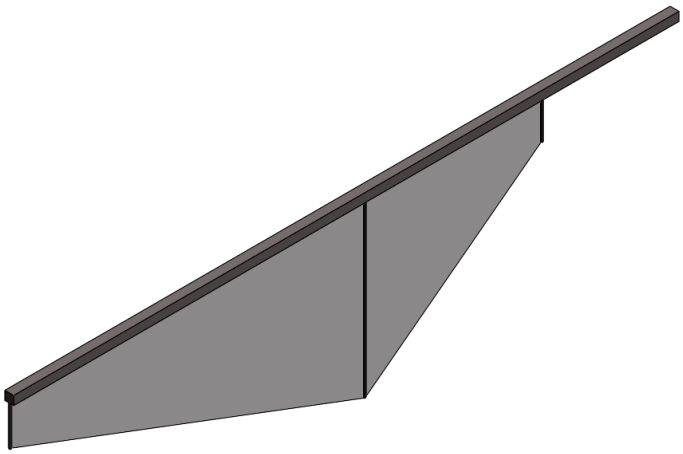

Figure 6.1: CAD view of the wing where the actuation strategy study is made.

Both items are discussed below using the aeroelastic framework to evaluate various actuation scenarios with the aerodynamic forces and the actuation power as meters. The idea is here to follow the same pace as a designer for the preliminary design where results are expected quickly. Therefore calculations are made with the large displacement capability of the FE turned off, i.e. in SD. To benchmark the different actuation strategies, the wing of the figure 6.1 is used. Also by default, the wing is actuated in heaving with a $300\mu m$ sine which constitutes the baseline of these studies.

6.1.1 Choosing an actuation mode

One specification of the OVMI is to avoid any complex mechanical link between the actuator and the wings so as to minimize the energy-losses and increase its reliability. Therefore a single DOF actuation is here considered. In terms of DOF, two actuation modes are here investigated: a heaving and flapping actuation mode as defined in the figure 6.2. The former is investigated first, as it is a common actuation mode for cantilever at resonance and second, as the test bench provides such actuation enabling experimental cross-examinations once a force sensor available. The latter is bio-inspired by the insects and is therefore of interest.

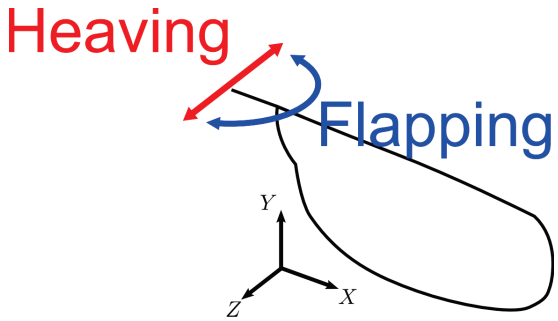

Figure 6.2: Definition of the heaving/flapping actuation.

As the electromagnetic actuator chosen in the OVMI provides only a translational motion, the flapping amplitude is determined using the dimension of the prototype, i.e. the actuator positioned in the middle of a thorax of 1 cm in diameter, and is here of $0.06rad$ ($\sim 3.4^\circ$). The heaving and the flapping actuations

are set to a pure sine at the first resonant frequency of the wing in vacuum. The resulting aerodynamic forces and actuation power are given in the figure 6.3 and depicted slightly after mid-stroke in the figure 6.4.

Regarding the aerodynamic forces, the flapping actuation proves itself to be more efficient than the heaving one by generating about 2.5 times more drag and 3.3 more lift in terms of peak-to-peak values and 3.6 times more mean lift. This behavior is expected since that, with a flapping actuation, the wing tip is experiencing a higher translational velocity, i.e. a larger drag force, combined to a larger torsion angle inducing by higher inertial forces in the veins.

Concerning the actuation power, the flapping actuation is also more efficient by reducing the peak-to-peak and mean values to about a fifth of the heaving one. As the actuator is sized according to the peak-to-peak values, this result implies that, in the case of a heaving actuation, the actuator will be probably much larger, penalizing the FWNAV with some additional weight and thus reducing its payload. Furthermore for the same wing motion, the actuator motion will be much smaller for a flapping motion requiring thus less power.

To sum up, a flapping actuation proves itself to be more efficient than a heaving actuation and is therefore, since this work, implemented on the OVMI using a compliant link as a rotational axis as shown earlier in the figure 1.9(b) and described extensively in Bontemps et al. [2013].

6.1.2 Choosing an actuation kinematics

Similarly, results in the literature (Berman and Wang [2007]; Bos et al. [2008]; Khan and Agrawal [2011]; Nagai and Isogai [2011]; Phillips and Knowles [2011]; Ghommem et al. [2012]; Stanford et al. [2012b]) indicate that the actuation kinematics influences the aerodynamic forces generation. Therefore various simple actuation kinematics are here evaluated: a sine, a triangle and a square waveforms. The triangle and square waveforms are given by the equations 6.1 and 6.2 respectively where f is the first resonant frequency of the wing $f_{num,1}$.

$$z(t) = \frac{\arcsin\left(0.99 \sin\left(2\pi f t\right)\right)}{\arcsin\left(0.99\right)} \tag{6.1}$$

$$z(t) = \frac{\tanh\left(3 \cdot \sin\left(2\pi f t\right)\right)}{\tanh\left(3\right)} \tag{6.2}$$

More complicated actuation kinematics can also be investigated if necessary by the framework playing for example on the duty cycle or the edge time of the signal. However, these settings belong already to the detailed design stage of a FWNAV and the aim of this study is to evaluate common signals available on any waveform generator. The results are presented in the figure 6.5 for a heaving actuation mode. The heaving actuation is kept as reference due to the potential experimental cross-examination once a proper force sensor is available.

The discussion about the results is here not as straightforward as for the actuation mode. Indeed depending on the FWNAV specifications, on its flight phase or mission requirements, either the power or the aerodynamic forces have to be favored.

When only pure aerodynamic performance is sought, such as for take-off or hovering, the square waveform performs better in lift than the other waveforms with about 1.4 more peak-to-peak lift and above all show 1.5 more mean lift, while the performances in drag are comparable.

When now the actuation power comes into play, like for long range or long endurance mission, a strong peak-to-peak amplitude is characterizing the square waveform indicating an oversized actuator which might limit consequently the payload and overall the endurance. Therefore the sine is a better compromise for the actuation of a resonant wing in heaving when both the energy-efficiency and lift are sought, as it offers the lower peak-to-peak value and an intermediate level of lift.

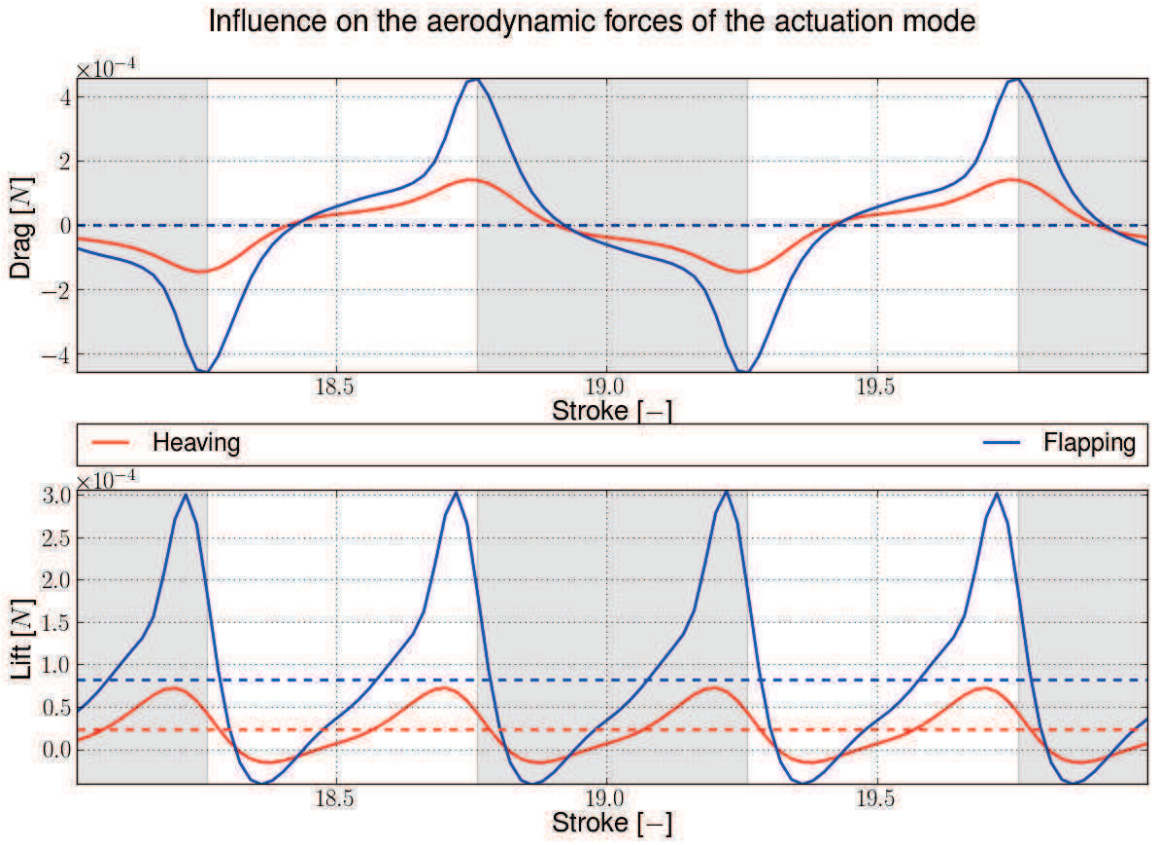

(a) Aerodynamic forces

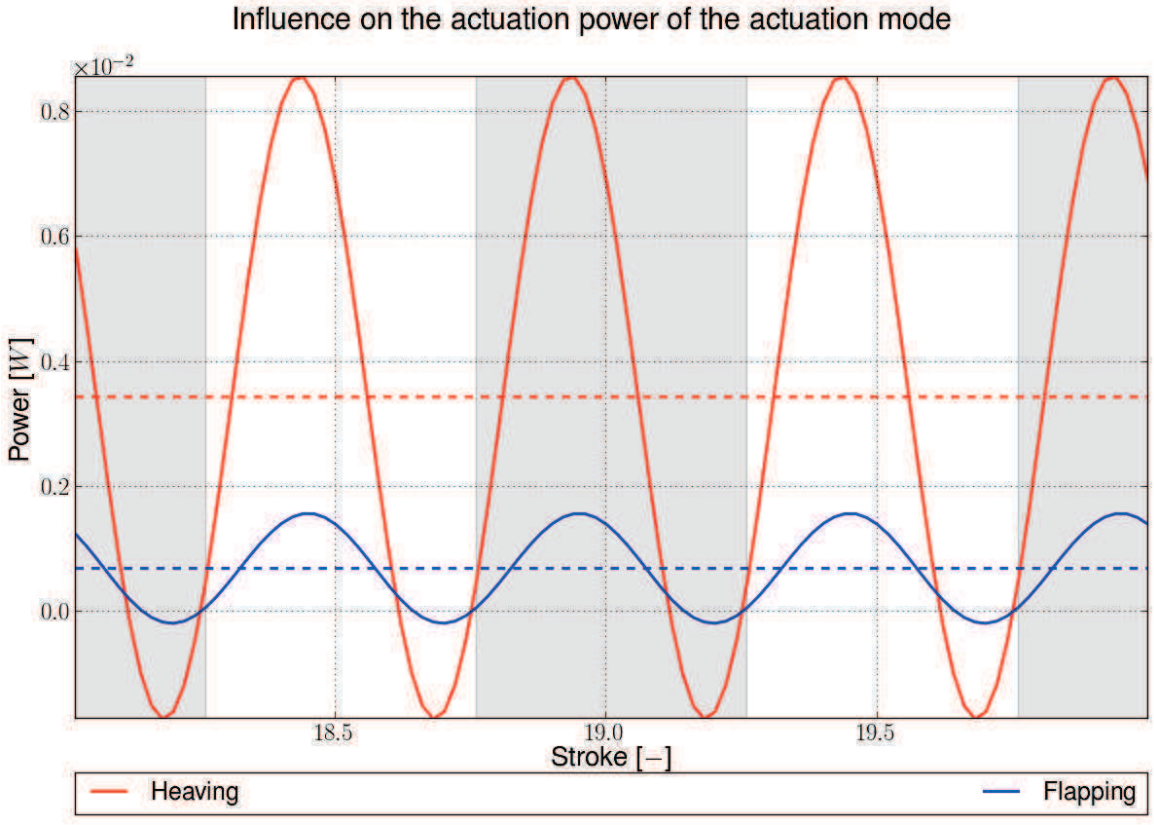

(b) Actuation power

Figure 6.3: Comparison between a heaving (red) and a flapping (blue) sine excitation of the wing root. Shaded areas indicate the downstroke motion and dashed lines the mean values.

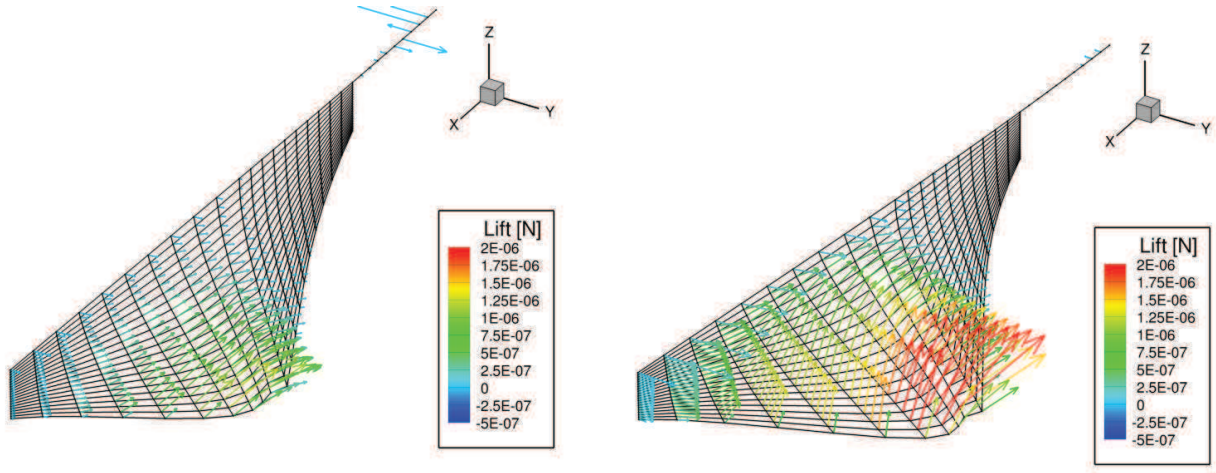

(a) Heaving actuation

(b) Flapping actuation

Figure 6.4: Aerodynamic forces slightly after mid-stroke at $t = 0.0981s$ for a heaving and a flapping sine excitation of the wing root

To sum up, a square waveform will generate more aerodynamic forces when compared to a sine one making it suitable for lift-demanding flight phase for example. However given the higher number of harmonics presents in the square waveform, other resonant modes might also slightly be excited that leads to some counter-performances. Thus, a sine waveform is a better compromise in terms of aerodynamic forces and actuation power and is the default waveform on our prototype.

6.2 Definition of an optimized wing geometry

Another challenge faced by designers is to define the proper wing geometry to get an airborne FWNAV. As illustrated in the figure 6.6 for the *Aerovironment* NAV, the task can be tremendous when using a trial and error method. This task is even more time-consuming in the absence of previous know-how or with novel actuation concept, as encountered on the OVMI. Bio-inspiration might be a solution as outlined by the variety and the number of insects flying in nature. However, it does not necessarily match the FWNAV specifications and is, foremost, not necessarily engineerable.

Therefore to assist and speed up the design of an 'optimized' wing capable of sustaining the prototype, the aeroelastic framework can perform as a kernel to evaluate iteratively various wing geometries until one might be used as a baseline for refinement using a trial and error or a higher fidelity aeroelastic model. This defines an optimization problem.

Several algorithms, briefly described in the appendix F, are able to solve such problem. However, given the number of flying insects, local extrema are expected and the optimization strategy has to be sufficiently robust and efficient to find the global extremum. Furthermore given that the design space might be rather broad depending on the variables and constraints set for the optimization and that no fair starting point is *a priori* known, the algorithm should be able to scan the design space autonomously. Despite an increasing computation load when compared to more classical iterative methods, heuristic algorithms have better chance in completing this task. Given that the aeroelastic framework is aimed at limiting the computation load, the optimization strategy is thus based on a genetic algorithm (GA) using the framework as a kernel for the wing evaluation.

The optimization environment is here below introduced and some applications on membrane wing are presented so as to benchmark the environment and identify bottlenecks. The idea is here really to

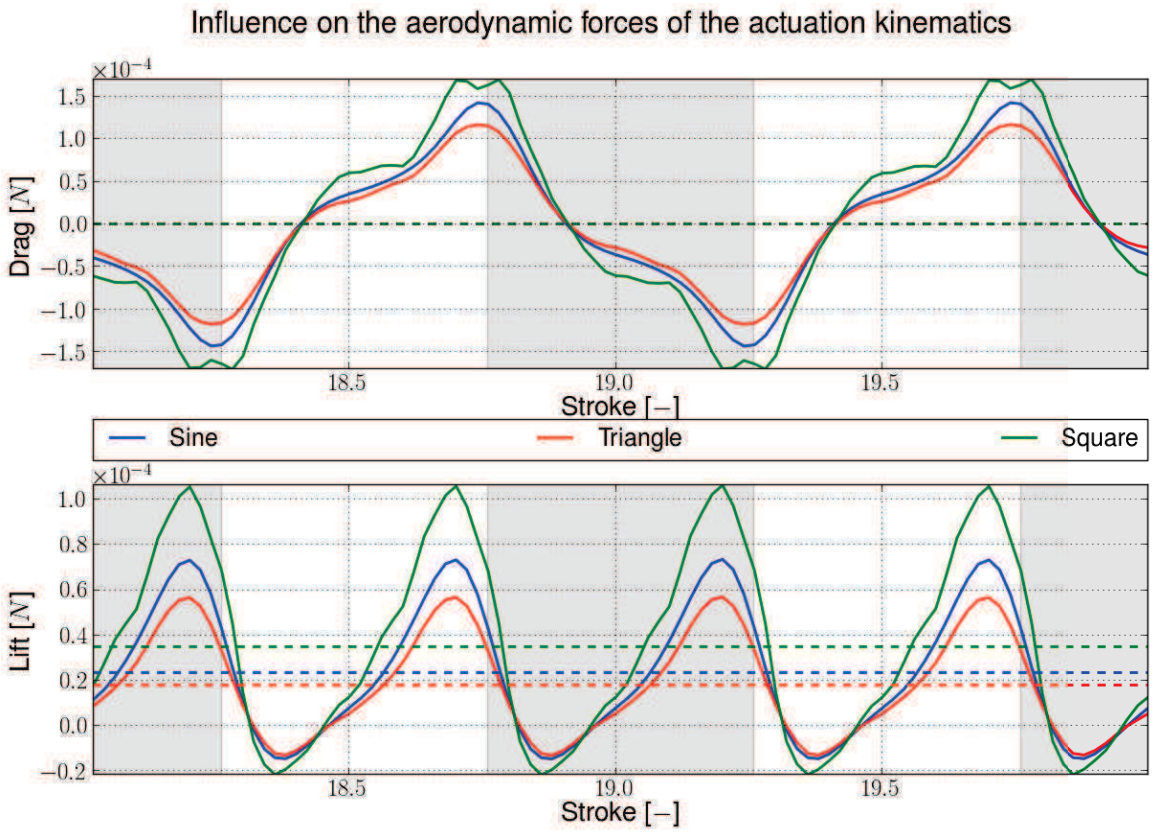

(a) Aerodynamic forces

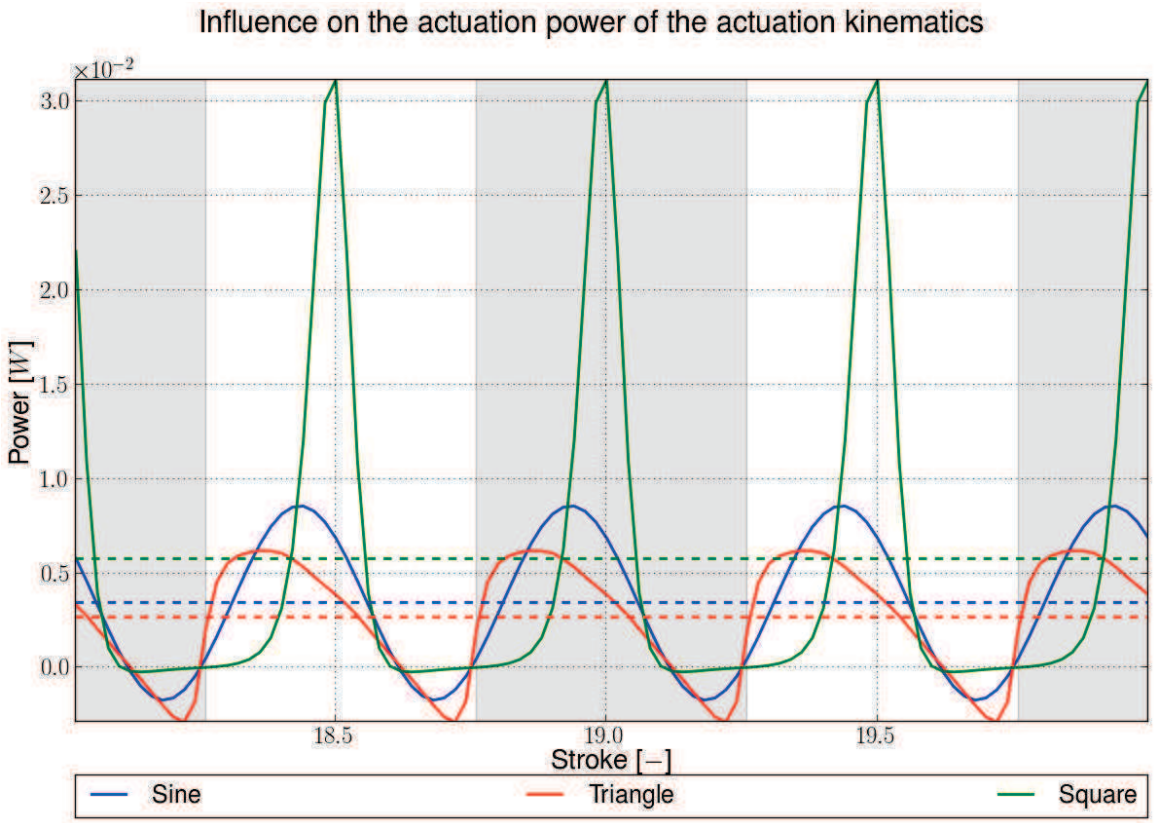

(b) Actuation power

Figure 6.5: Comparison between a sine, a triangle and a square signal for a heaving excitation of the wing root of 300μm at the first resonant frequency of the wing. Shaded areas indicate the downstroke motion and dashed lines the mean values.

Figure 6.6: Set of wings used by *Aerovironment* to design successfully their NAV (Source: Keennon [2012]).

provide a good starting point in terms of wing geometry so that the designers might refine it using more advanced models or trial and error.

6.2.1 Genetic algorithm environment

As mentioned earlier in the chapter 3.5, the aeroelastic framework is build as a combination of *Ansys* templates and of a *Python* script. Various performance items can thus be autonomously evaluated once a wing geometry is supplied. This integration provides a perfect kernel for an iterative optimizer.

In order to ease its implementation, an additional Python layer based on the *Pyevolve* module is added to support the GA (Perone [2010]). By using an open source *Python* module, the implementation of the optimizer is quasi-straightforward and a higher modularity is achieved when compared to a stand-alone optimizer as the overall optimization process is handled within *Python*. This is especially relevant for the score function, where the diversity of outputs (mass, aerodynamic forces, actuation power, etc.) enables its quick and easy tuning so as to address a large variety of optimization problems. The overall optimization process is summarized in the figure 6.7.

To optimize a given score function J, the module generates a population of individuals from a given design space. Each individual is defined by the simplified parametric geometry of the figure 6.8, evaluated in the aeroelastic framework, and scored using its output data. Once an entire population is evaluated, the module generates a new population by selecting the best individuals and combining them as well as breeding randomly new individuals to the population. The module iterates until it hits convergence or the maximum number of generations allowed. The only input parameters are here the geometrical parameters to optimize, the design space, the size of population and the maximum number of generations and foremost the score function.

However a downside of the GA is its increased computation load inherent to its random approach. Therefore to keep the computation time satisfactory, the computational parameters of the aeroelastic framework are set to their minima so that the computation can run smoothly for the majority of wing geometries. These

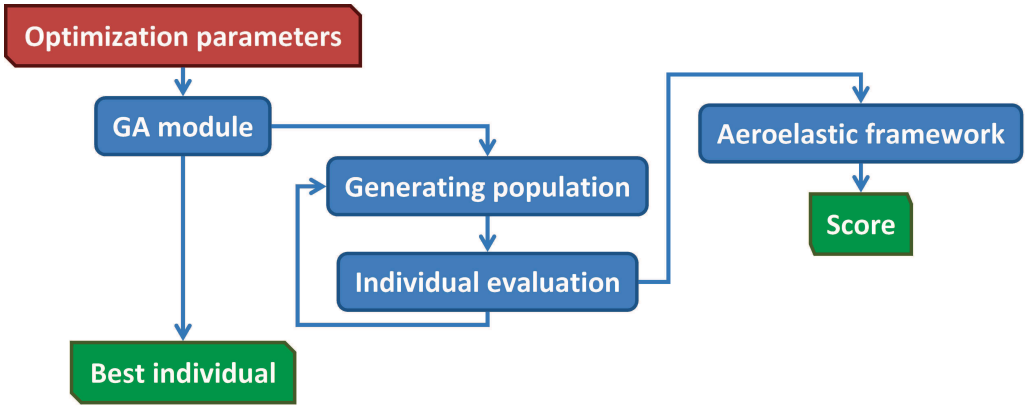

Figure 6.7: Optimization flowchart using the *Pyevolve*-module as a genetic algorithm optimizer and our aeroelastic framework as evaluation function.

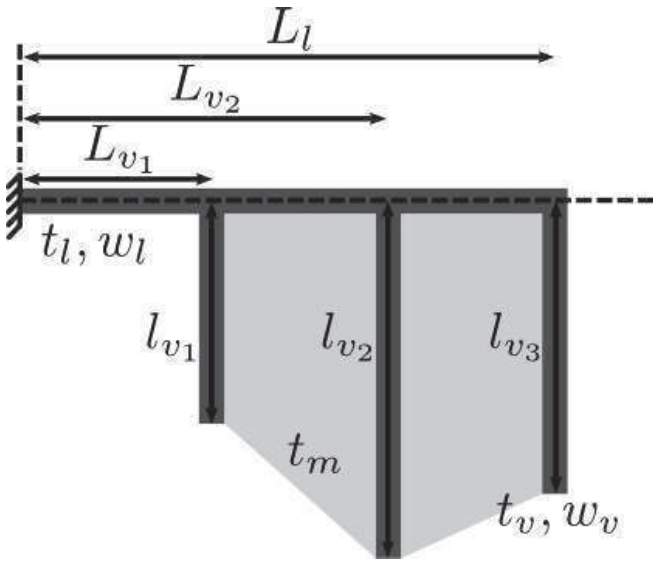

Figure 6.8: Parametric geometry for optimization.

parameters are essentially the grid and time step size and the number of periods computed.

Due to these limitations, the output data might become noisy and have to be filtered to avoid any optimization deadlock. To do so, a FFT-filter is implemented and checks the frequency spectrum of the aerodynamic forces for inconsistencies due to a disrupted computation. A FFT on the drag signal is achieved and normalized by its maximal amplitude. The computation is then eventually discarded if more than three frequencies contribute to more than 10% to the signal. The framework accommodates also computation crashes by penalizing them drastically so as to push the optimizer far away from these individuals.

Using this environment, three complementary stages of the preliminary design of a flapping-wing system can be covered with increasing fidelity and cost.

The first one is using the unidirectional approach in SD to compute the aerodynamic forces with no aeroelastic coupling. It is therefore assumed that once the coupling is made, only the amplitude of the motion will decrease and thus the aerodynamic forces, but the mode-shape will be sized correctly. The advantage is here fully taken from the rapidity and robustness of the unidirectional approach to sweep through a very broad design space for promising design.

The second one is using the bidirectional approach, still in SD, to compute the aerodynamic forces with yet the aeroelastic coupling activated. Even if the numerical forces might be less than the real forces, as seen in the chapter 4.2, the sizing of the mode-shape will be more precise narrowing the wing geometry gradually towards a more suitable design.

The third one is using the bidirectional approach to compute the aerodynamic forces with simultaneously the aeroelastic coupling and the LD option activated. Thus the mode-shape might be refined nailing the wing geometry towards an optimal design ready for refinements using more high-fidelity models or trial and error.

To test the validity and robustness of this optimization environment, several benchmarks are here accomplished on an increasingly more complex wing geometry before clearing the optimization environment for release.

6.2.2 Optimization benchmarks

To assess the capacities of the optimization environment and to provide guideline for designers, only the two first design stages, described above, are here investigated as the third one is too computational intensive on our server.

In terms of calculation parameters for the benchmarks, the population size is limited to 10 while the maximal number of generations is fixed to 50. The evaluation of each wing individual is done in SD for 8 periods, with $N_{FE_{Span}} = 5$ and $N_{FE_{Chord}} = 10$ for the mesh along with $N_{Steps} = 50$ and $N_{Substeps} = 4$ for the time-step discretization. By default, the optimizations are performed using a pure sine heaving actuation of $100\mu m$ so that the best individuals might be prototyped and tested. The computation duration are indicative but all the optimizations are done on the same server.

6.2.2.1 Optimization in SD using the uncoupled unidirectional approach

Benchmarks are here made for a F-wing and a E-wing of increasing complexity. As no aeroelastic coupling occurred, the mean lift reported is not representative of the real performance but indicates just a promising geometry.

a) Applications on a F-wing

Several optimizations are made for the F-wing, which are summarized and sorted by complexity in the table 6.1. The table indicates for each run the geometric variables to optimize, their design spaces,

the objective function to maximize along with the optimized value of the geometric variables, the score obtained, the wing first resonant frequency, the mean lift obtained, the wing mass and the optimization duration. This is thus a complete overview of one optimization.

Runs 3 and 4 aim at optimizing the mean non-dimensional lift, the ratio of the mean lift and of the wing weight, on a F-wing with two veins of same length, referred here as a flat F-wing. The best individuals share the same features, a massive leading-edge (400x400μm) with a very short membrane ($1mm$) attached at $8mm$ from the wing root, and differ only on the vein characteristics: run 3 favors a slender but thicker vein (100x80μm) while run 4 chooses a larger but thinner vein (700x10μm). However both cross-sections are almost identical. Therefore the final scores are very close to one another as are the resonant frequencies. Unfortunately these resonant frequencies are too high to sustain reasonably the OVMI given its specifications. Indeed as highlighted by Ellington [1999] in its chart reported in the figure 6.9, a frequency around 50 to $80Hz$ is more likely for a $15mm$ wingspan FWNAV of about $100mg$.

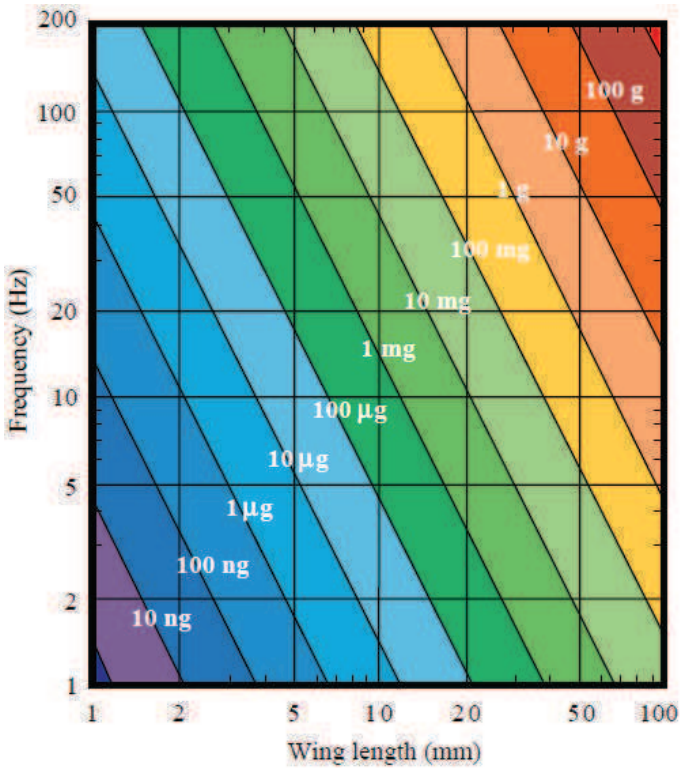

Figure 6.9: Mass supported as functions of wingbeat frequency and wing length for a hovering insect-based flying machine (Source: Ellington [1999]).

To enforce this condition and for sake of simplicity, the objective function is penalized based on the distance between the computed resonant frequency and the objective one instead of an optimization under constraint. The penalty factor is essential and has to be carefully set as highlighted on one hand by the run 10, 11, 12 and in the other hand by the run 13, 14, 15. For the first set, the resonant frequency crashes dramatically to about $2Hz$ except for the run 12. However the membrane becomes more important, its length increasing to $14mm$, highlighting its necessity for the generation of aerodynamic forces. Similarly the leading-edge is also thinner (40x40 or 200x200μm) favoring its torsion. By adjusting the penalty factor to a lower value, in the second set, the resonant frequency stabilizes about $70Hz$ which is in the appropriate range described by Ellington [1999]. However by applying this frequency criterion, the discrepancy between each individual increases sharing fewer characteristics except a large membrane area. The most probable explanation is that with the calculation parameters set to their minima, the kinematics data supplied by the membrane FEs are highly sensitive, as seen earlier in the figure 4.12, and 8 periods are not sufficient to

Table 6.1: Summary of the optimization of a F-wing with the unidirectional aerodynamic model uncoupled to the structural model. Apart from the geometrical parameters to be optimized, the leading-edge length L_l and the membrane thickness t_m are keep constant to $15mm$ and $5\mu m$.

	Range	**Parameter**	**Objective function** J_F	**Best individual**	**Score** $[-]$	f_{wing} $[Hz]$	$\overline{Lift}$ $[\mu N]$	M_{wing} $[mg]$	**Duration** $[h]$
Run 3	$w_l = t_l$	40 - 560μm per 40	$J_F = \frac{\overline{Lift}}{M_{wing} \cdot g} \cdot 1000$	400/400	5193.8	550.81	-	-	~ 12
	w_v	100 - 1400μm per 100		100/700					
	t_v	10 - 140μm per 10		80/10					
Run 4	L_{v_1}	1 - 14mm per 1		8/8	5963.0	550.76	-	-	~ 8.5
	$l_{v_1} = l_{v_2}$	1 - 14mm per 1		1/1					
Run 10	$w_l = t_l$	40 - 560μm per 40	$J_F = \frac{\overline{Lift}}{M_{wing} \cdot g} \cdot 1000 - \mid f_{wing} - 80 \mid \cdot 50$	40/40/200	3917.0	1.66	0.0	7	~ 18
	w_v	100 - 1400μm per 100		1400/1400/100					
Run 11	t_v	10 - 140μm per 10		140/140/110	3881.5	2.37	0.0	7.5	~ 17.6
	L_{v_1}	1 - 14mm per 1		10/4/2					
Run 12	$l_{v_1} = l_{v_2}$	1 - 14mm per 1		14/14/14	7227.0	49.46	121	2.2	~ 15.6
Run 13	$w_l = t_l$	40 - 560μm per 40	$J_F = \frac{\overline{Lift}}{M_{wing} \cdot g} \cdot 1000 - \mid f_{wing} - 80 \mid \cdot 40$	120/240/400	2456.1	86.58	17	0.6	~ 10
	w_v	100 - 1400μm per 100		100/400/1000					
Run 14	t_v	10 - 140μm per 10		50/100/40	3224.2	56.23	134	3.3	~ 4.7
	L_{v_1}	1 - 14mm per 1		1/2/2					
Run 15	$l_{v_1} = l_{v_2}$	1 - 14mm per 1		4/13/7	1114.4	73.67	67.2	4.1	~ 24.4
Run 17	$w_l = t_l$	40 - 560μm per 40	$J_F = \frac{\overline{Lift}}{M_{wing} \cdot g} \cdot 1000 - \mid f_{wing} - 80 \mid \cdot 40$	560/200	-102.7	80.60	-5.2	6.7	~ 11.5
	w_v	100 - 1400μm per 100		900/900					
	t_v	10 - 140μm per 10		40/70					
	L_{v_1}	1 - 14mm per 1		9/2					
Run 18	l_{v_1}	1 - 14mm per 1		6/14	1386.3	54.89	83.4	3.6	~ 5.4
	l_{v_2}	1 - 14mm per 1		12/11					
Run 19	$w_l = t_l$	40 - 560μm per 40	$J_F = \frac{\overline{Lift}}{M_{wing} \cdot g} \cdot 1000 - \mid f_{wing} - 80 \mid \cdot 40$	520	33981.6	598.22	2921	5.4	~ 6.8
	w_v	100 - 1400μm per 100		500					
	t_v	10 - 140μm per 10		100					
	L_{v_1}	1 - 14mm per 1		12					
	l_{v1}	1 - 14mm per 1		4					
	l_{v_2}	1 - 14mm per 1		5					

reach a complete steady state response of membrane FEs in terms of velocity and acceleration. Even if the filtering is enforced, it is not sufficient to drive repetitively the optimizer towards the same best individual.

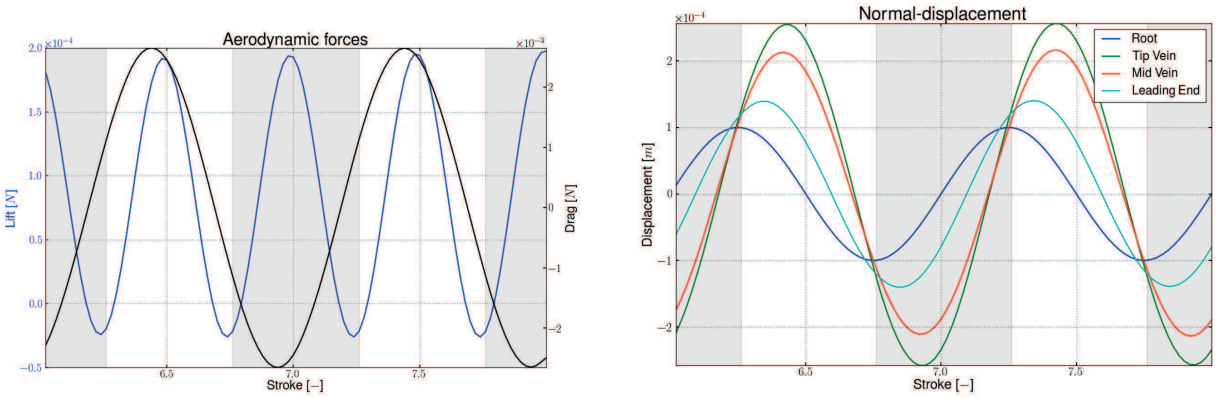

(a) Aerodynamic forces

(b) Displacement of the wing extremity

Figure 6.10: Best individual of Run 18 for a F-wing in heaving at $54.89Hz$ with its aerodynamic forces generated by the wing displacement. Shaded areas indicate the downstroke motion.

When now releasing the constraint on the vein length, in run 17 and 18, the results are slightly more puzzling as the score are even lower than for the flat wing and even negative. However the large membrane is once again found which is reassuring. This highlights again the extreme sensitivity of the framework to the membrane FEs given the large surface they mesh and the limited mesh size. By examining now the aerodynamic force generated by the best individual of run 18 and the displacement of its extremities, given in the figure 6.10, a promising phase-shift is observed between the leading-edge, the blue curves, and the trailing-edge, the red and green curves, but also between the wing root and the wing tip, the dark and light blue curves respectively. This phase-shift generates large lift ($83.4\mu N$) with the membrane expanding along almost the entire leading-edge, starting at $2mm$ from the wing root with a $14mm$ vein on its root side and a $11mm$ vein of its tip side.

Given the conclusion on the section 6.1, an optimization is made with a flapping actuation in the run 19. As expected the aerodynamic forces generated are much larger ($2921\ \mu N$) but the frequency penalty factor has to be increased to bring back the frequency within the design range. The best individual is almost a flat F-wing but with only a relatively small membrane to the most outboard part of the wing. This positioning of the membrane might be explained as the kinematics are maximal around this area and are known to be especially favorable for aerodynamic forces (Shyy et al. [2010]).

b) Applications on a E-wing

Optimizations are also made for the E-wing to test the optimizer on more complex geometry. Results are summarized and sorted by complexity in the table 6.2 using the same column organization.

The benchmarks start with the run 6 on a E-wing with three veins of the same length, referred here as a flat E-wing, by optimizing the mean non-dimensional lift penalized by the distance between the computed resonant frequency and the objective one, as earlier. The optimization load is higher than for the F-wing as the mesh size increased due to the intermediate vein in the membrane. However the performances are satisfactory, the resonant frequency falls well within the $50\text{-}80Hz$ range. The design takes some characteristics of the flat F-wing optimized in the same conditions, especially of the run 14, with a membrane going almost over the complete leading-edge. The mean lift achieved is about $126\mu N$ for a mass of $3.6mg$ similar to the ones of the flat F-wing of run 14.

With run 5, the flat E-wing is allowing its two inner veins to have a different length than the tip vein, to

Table 6.2: Summary of the optimization of a E-wing with the unidirectional aerodynamic model uncoupled to the structural model. Apart from the geometrical parameters to be optimized, the leading-edge length L_l and the membrane thickness t_m are keep constant to $15mm$ and $5\mu m$.

	Range	**Parameter**	**Objective function** J_F	**Best individual**	**Score** $[-]$	f_{wing} $[Hz]$	$\overline{Lift}$ $[\mu N]$	M_{wing} $[mg]$	**Duration** $[h]$
Run 6	$w_l = t_l$	40 - 560μm per 40	$J_F = \frac{\overline{Lift}}{M_{wing} \cdot g} \cdot 1000 - \mid f_{wing} - 80 \mid \cdot 40$	320	2845.1	62.42	125.7	3.6	~ 46.5
	w_v	100 - 1400μm per 100		100					
	t_v	10 - 140μm per 10		140					
	L_{v_1}	1 - 14mm per 1		2					
	L_{v_2}	1 - 14mm per 1		14					
	$l_{v_1} = l_{v_2} = l_{v_3}$	1 - 14mm per 1		14					
Run 5	$w_l = t_l$	40 - 560μm per 40	$J_F = \frac{\overline{Lift}}{M_{wing} \cdot g} \cdot 1000 - \mid f_{wing} - 80 \mid \cdot 40$	120	-121.6	72.35	1.2	0.7	~ 36
	w_v	100 - 1400μm per 100		700					
	t_v	10 - 140μm per 10		30					
	L_{v_1}	1 - 14mm per 1		1					
	L_{v_2}	1 - 14mm per 1		7					
	$l_{v_1} = l_{v_2}$	1 - 14mm per 1		1					
	l_{v_3}	1 - 14mm per 1		6					
Run 2	$w_l = t_l$	40 - 560μm per 40	$J_F = \frac{\overline{Lift}}{M_{wing} \cdot g} \cdot 1000 - \mid f_{wing} - 80 \mid \cdot 40$	320/400	90.3	78.33	1.8	1.1	~ 42
	w_v	100 - 1400μm per 100		800/700					
	t_v	10 - 140μm per 10		30/110					
	L_{v_1}	1 - 14mm per 1		9/1					
	L_{v_2}	1 - 14mm per 1		14/5					
Run 3	l_{v_1}	1 - 14mm per 1		2/1	3268.5	90.71	236.7	6.5	~ 27.8
	$l_{v_2} = l_{v_3}$	1 - 14mm per 1		8/14					
Run 7	$w_l = t_l$	40 - 560μm per 40	$J_F = \frac{\overline{Lift}}{M_{wing} \cdot g} \cdot 1000 - \mid f_{wing} - 80 \mid \cdot 40$	280	28376.1	183.36	1336.7	4.2	~ 44.7
	w_v	100 - 1400μm per 100		800					
	t_v	10 - 140μm per 10		140					
	L_{v_1}	1 - 14mm per 1		4					
	L_{v_2}	1 - 14mm per 1		9					
	$l_{v_1} = l_{v_2} = l_{v_3}$	1 - 14mm per 1		6					

see if an inboard membrane might be suitable. The results indicate, as the run 19 for the F-Wing, that the aerodynamic forces are generated mostly at the outboard of the leading-edge, as the membrane is enlarging gradually between the second and the tip vein from $1mm$ to $6mm$. This attitude mimics the one observed in insects. However the performances are not satisfactory as outlined by the low mean lift ($1.2\mu N$) most probably due to a too small membrane area.

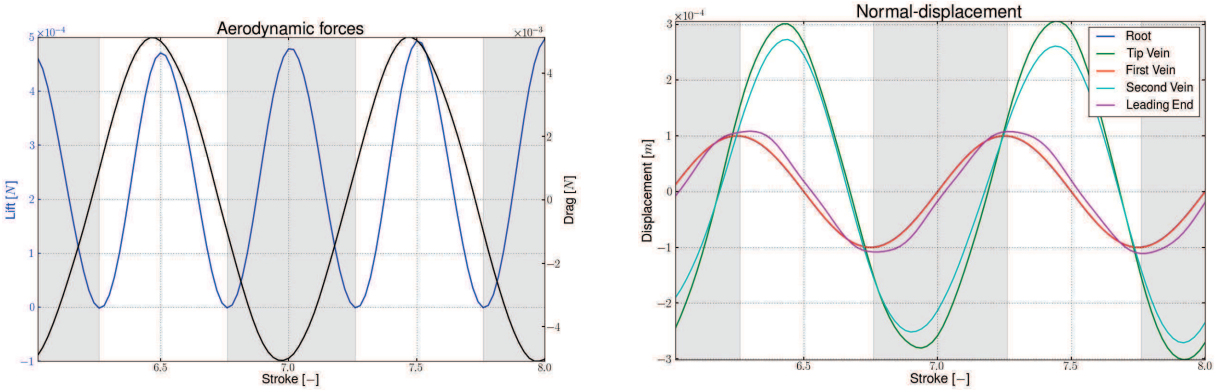

(a) Aerodynamic forces

(b) Displacement of the wing extremity

Figure 6.11: Best individual of Run 3 for a E-wing in flapping at $90.71Hz$ with its aerodynamic forces generated by the wing displacement. Shaded areas indicates the downstroke motion. The wing root curve is hidden by the overlapping curve of the first vein.

Therefore the optimization is modified, in the run 2 and 3, to this time favors the outboard part of the wing by allowing the second and the tip vein to share the same length and the first one being released from any constraint. Here the results become appealing, as the wing also tends to highlight a small inboard membrane and a larger outboard membrane as previously but at a larger scale. The frequencies are falling for each run within the design range, but only the mean lift of the run 3 is appealing ($236.7\mu N$) being well above the wing weight ($6.5mg$). By looking at the aerodynamic forces and the displacement of the extremities, depicted in the figure 6.11, an important phase-shift between the leading-edge and the trailing-edge is coupled to a stiff leading-edge producing large aerodynamic forces on a similar fashion as in Nagai et al. [2012].

A flapping optimization is also made on a flat E-wing to demonstrate further the environment capacity with the run 7. Here again the optimizer tends to favor a small membrane located mostly on the outboard part of the wing as in the run 19 for the F-wing. However here the resonant frequency is much lower ($183.36Hz$) but still outside the design range and the mean lift is more than halved ($1336.7\mu N$).

The optimizer is working more smoothly on E-wing as on F-wing as the intermediate vein stiffens the membrane and smooths its kinematics, but also as the mesh is more dense on the E-wing which increases the computation load. Special care is required to set properly the computation parameters and the objective function and balance the computation load, the stability and the repetitivity with the computing power available. Furthermore some mechanical and aerodynamic intuitions and know-how are required to drive properly the optimizer towards a promising design. However the optimization environment, using the uncoupled unidirectional approach in SD, is working smoothly and quite robust, once tuned, making it perfect for the first stage of preliminary design optimization.

6.2.2.2 Optimization in SD using the coupled bidirectional approach

Due to the increased computational load required by the bidirectional approach and the aeroelastic coupling, only the F-wing is here investigated. The optimizations are summarized and sorted by complexity in the table 6.3 in the same manner as previously.

Table 6.3: Summary of the optimization of a F-wing with the bidirectional aerodynamic model coupled to the structural model. Apart from the geometrical parameters to be optimized, the leading-edge length L_l and the membrane thickness t_m are keep constant to $15mm$ and $5\mu m$.

	Range	**Parameter**	**Objective function** J_F	**Best individual**	**Score** $[-]$	f_{wing} $[Hz]$	$\overline{Lift}$ $[\mu N]$	M_{wing} $[mg]$	**Duration** $[h]$
Run 1	$w_l = t_l$	40 - 560μm per 40	$J_F = \frac{\overline{Lift}}{M_{wing} \cdot g} \cdot 1000$	520/360	2953.9	632.06	-	-	~ 25.7
	w_v	100 - 1400μm per 100		1200/100					
	t_v	10 - 140μm per 10		90/130					
Run 2	L_{v_1}	1 - 14mm per 1		11/11	1563.3	418.25	-	-	~ 19.2
	$l_{v_1} = l_{v_2}$	1 - 14mm per 1		2/5					
Run 3	$w_l = t_l$	40 - 560μm per 40	$J_F = \frac{\overline{Lift}}{M_{wing} \cdot g} \cdot 1000 - \mid f_{wing} - 80 \mid \cdot 40$	320/160/120	822.5	87.03	32.6	3	~ 34.2
	w_v	100 - 1400μm per 100		200/100/700					
Run 4	t_v	10 - 140μm per 10	$J_F = \frac{\overline{Lift}}{M_{wing} \cdot g} \cdot 1000 - \mid f_{wing} - 100 \mid \cdot 40$	140/90/90	4.5	100.77	0.4	1	~ 30.8
Run 5	L_{v_1}	1 - 14mm per 1	$J_F = \frac{\overline{Lift}}{M_{wing} \cdot g} \cdot 1000 - \mid f_{wing} - 50 \mid \cdot 40$	4/7/1	1114.4	28.46	68.3	3.5	~ 31.6
	$l_{v_1} = l_{v_2}$	1 - 14mm per 1		9/8/14					
Run 6	$w_l = t_l$	40 - 560μm per 40	$J_F = \frac{\overline{Lift}}{M_{wing} \cdot g} \cdot 1000 - \mid f_{wing} - 80 \mid \cdot 40$	280	2877.6	50.11	83.2	2.1	~ 57.2
	w_v	100 - 1400μm per 100		100					
	t_v	10 - 140μm per 10		60					
	L_{v_1}	1 - 14mm per 1		1					
	l_{v_1}	1 - 14mm per 1		1					
	l_{v_2}	1 - 14mm per 1		13					

To check if in this computation configuration, the optimizer tends to drive towards high frequency when no penalization is made on the objective function, run 1 and 2 are made on a flat F-wing. The results speak for themselves as high resonant frequencies are obtained, with $632.06Hz$ and $418.25Hz$ respectively. The computation load is also higher increasing dramatically the optimization duration. The membrane tends to reduce to an outboard small rectangle with its area decreasing with increasing frequency.

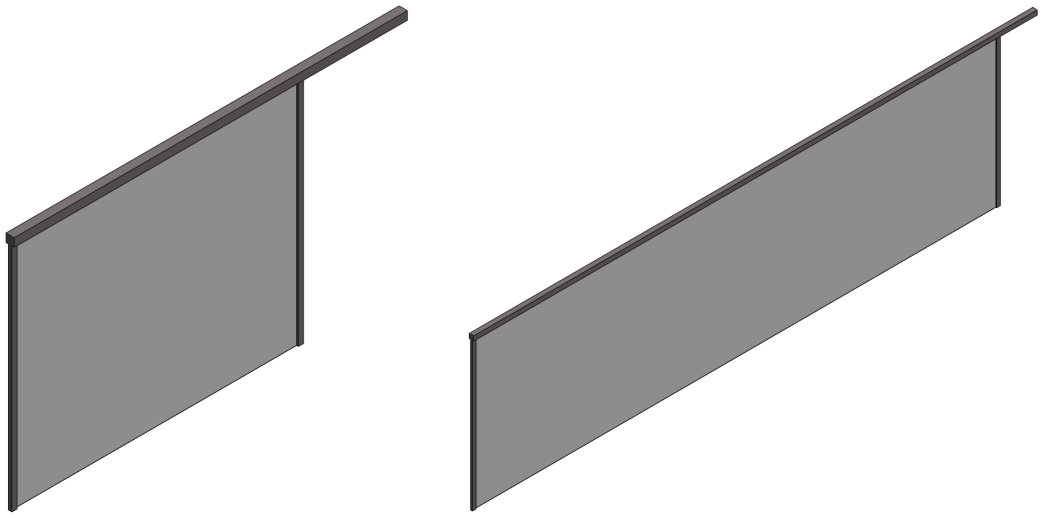

(a) Run 3 (b) Run 13

Figure 6.12: CAD view of the best individual of Run 3 of the coupled bidirectional approach compared to the one of Run 13 of the uncoupled unidirectional approach.

The objective function is thus modified to take into account the frequency penalization and several tests (run 2, 3 and 4) are made to check the correct response of the optimizer to find an individual around a specified actuation frequency: 80, 100 and 50 Hz respectively here. The response of the optimizer to such constraint is quite satisfactory even for the last run where the penalizing factor was probably slightly to high with 87.03, 100.77 and $28.4Hz$. The size of the membrane tends to decrease with increasing frequency, confirmed by the previous results of the run 1 and 2, and also its position tends to be shifted slowly to the outboard part of the wing. When comparing the run 3 with the run 13 of the uncoupled unidirectional optimization, depicted in the figure 6.12, due to their similar resonant frequency, the activation of the aeroelastic coupling tends to reduce its inboard area while simultaneously increasing the outboard one, by lengthening the veins, and also to add some weight on the veins, by thickening and enlarging them, so as to increase the torsion of the leading-edge. Furthermore the mean lift is in the same order of magnitude as for the run 13 with about $33\mu N$ instead of $17\mu N$.

Finally, an optimization is made on unconstrained wing with the run 6. The resonant frequency falls shortly within the design range of 50-80Hz with $50.11Hz$. The best individual performance are comparable with the run 18 of the uncoupled unidirectional optimization, with similar resonant frequency ($50.11Hz$), mean lift ($83.2\mu N$) and mass ($2.1mg$). CAD views of them are given in the figure 6.13. The differences in terms of geometry are that, in the coupled optimization, the wing mimics behavior seen on an insect wing, with a short membrane near the root and a large membrane near the wing tip, and that, in the uncoupled analysis, the wing looks more like a plate with an almost constant membrane along the leading-edge. Such behavior is understandable given that the wing tip is a place more favorable for aerodynamic forces given its natural higher velocity and acceleration which are accounted by the coupled analysis and the bidirectional model.

When looking at the performance of the coupled best individual in the figure 6.14, the aerodynamic forces are still perturbed as no steady-state is established. However they have already found their periodicity

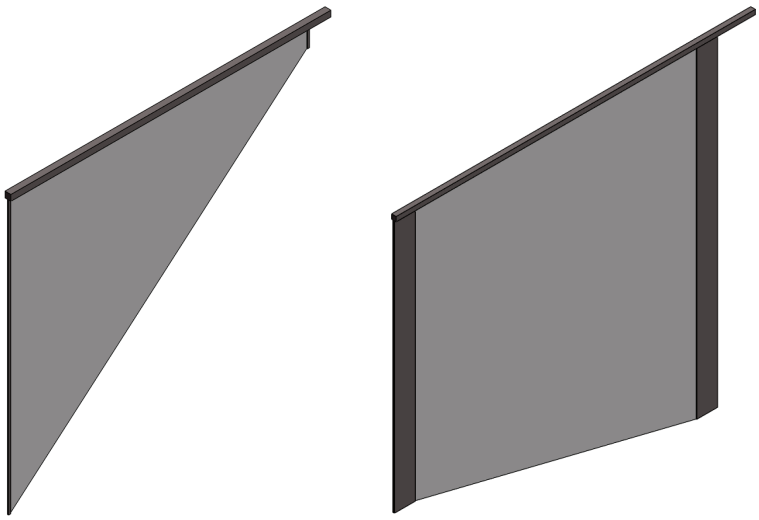

(a) Run 6 (b) Run 18

Figure 6.13: CAD view of the best individual of Run 6 of the coupled bidirectional approach compared to the one of Run 18 of the uncoupled unidirectional approach.

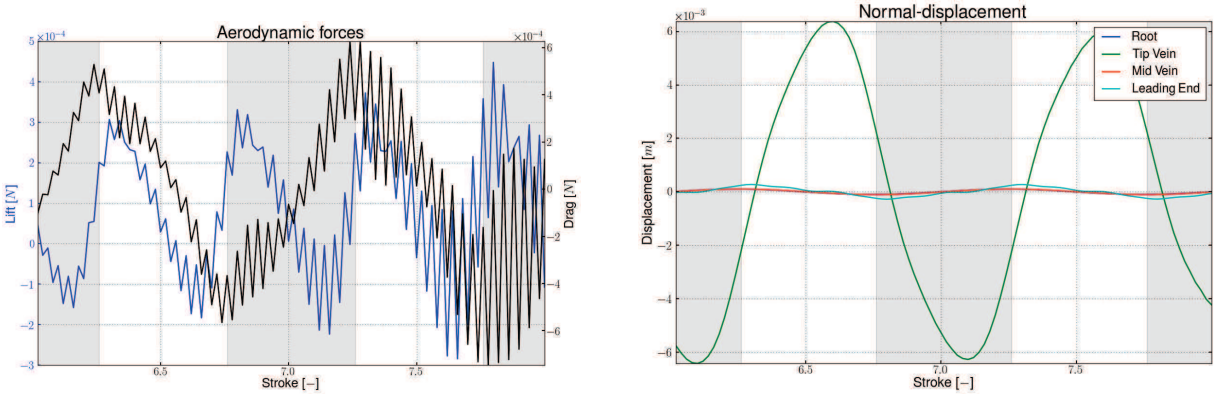

(a) Aerodynamic forces (b) Displacement of the wing extremity

Figure 6.14: Best individual of Run 6 for a F-wing in heaving at $90.71Hz$ with its aerodynamic forces generated by the wing displacement. Shaded areas indicate the downstroke motion. The wing root is hidden by the overlapping curve of the mid vein.

and amplitudes. The displacement curves are also encouraging, even if the SD assumption overestimates the displacement of the extremities especially here for the tip vein, as the phase lag between the trailing-edge and the leading-edge is observed and increased along the span.

The optimizer is working smoothly for F-wing using the coupled bidirectional approach in SD and is therefore quite promising for later investigations on more complex wing. The same recommendations regarding the computation parameters and the use of designer intuitions are also here formulated. Additionally, the computation load for the coupled bidirectional optimization is increasing quite strongly when compared to the uncoupled unidirectional approach and the question of the computing power is becoming primordial. However the optimization environment, using the coupled bidirectional approach in SD, is working smoothly and quite robust, once tuned, making it suitable and ready for the second stage of preliminary design optimization.

6.2.3 Conclusion on the optimization environment

The optimization environment first two design stages have been here benchmarked to highlight their complementarity. This is highlighted by the optimization on the flat F-wing and on the normal F-wing where the best individuals using the second approach are refined versions of the first approach, sharing the same characteristics in terms of frequency, mass and mean lift. Even if the optimization are occurring in SD so as to contain the computation time and that the displacement might be overestimated, the best individuals are already correctly sized in terms of mode-shape and their trends in terms of performance is sound. Additionally, the convergence and repeatability of the optimization environment can be improved by using a larger population which increases the diversity and the scanned design space.

Thus the optimization environment with its two stages is cleared and might be released to designers so that the potential FWNAVs might be unleashed.

For future works, the optimization environment third design stage has to be benchmarked to benefit from the coupled bidirectional approach in LD so as to narrow again the design. Also, to complete the optimization environment, testing the 'optimized' design on the test bench might be a definitive plus for later studies.

Conclusion and perspectives

In this thesis, a preliminary design tool for FWNAVs has been devised to assist designers in their choices and unleash the potential of FWNAVs. An aeroelastic framework of insect flight is the backbone of such design tool and it has been developed and applied throughout this work.

The first part of this thesis has been dedicated to the development of the framework itself. Its first end use being the OVMI case and the sizing of its wing mode shape, strong considerations have been given to handle correctly the flexibility of the wing, both in the spanwise and in the chordwise direction, and its effects on the aerodynamics. Thus an analytic aerodynamic model of insect flight, derived from the one defined by Sane and Dickinson [2002], has been defined and coupled to a FEM based structural solver. Thus using local information, such as the FE shape and kinematics for example, wing flexibility is accounted and various performance figures can be computed and brought to light. To comply with the requisites of a preliminary design tool, the framework has been designed for robustness, efficiency and modularity so as to evaluate quickly and accurately enough a broad design space of wing geometries, material and actuation strategies.

The second part of this thesis has been committed to the validation of the aeroelastic framework by comparing the numerical prediction with experimental and numerical data. An experimental database has been generated covering the validation of each module of the framework: the structural model, the aerodynamic one and the coupling. To do so a complete test bench has been devised along with the appropriate methodologies. Using a vacuum chamber, the material properties of a set of experimental wings have been first determined and fed to their numerical counterparts to validate both the structural model and the aeroelastic coupling using high-speed acquisition of the wing deformation. As reported in the appendix C, the development of a force sensor has been attempted to validate further the aerodynamic model and the aeroelastic coupling, but has lacked maturity at the end of this work. An alternative has been devised by comparing the bidirectional aerodynamic results to a chordwise averaged aerodynamic model of Sane and Dickinson [2002]. In terms of wing deformation, the results are quite astonishing for beam wing and satisfactory for membrane wing. In terms of aerodynamic forces, the bidirectional model tends to underestimate the total aerodynamic forces especially with the added-mass component. However at the preliminary design stage, only the trends in terms of displacements and aerodynamic forces are of interest and these are correctly predicted, which is satisfactory and validate the aeroelastic framework. Furthermore as highlighted in the discussion, some tuning within the aerodynamic model reduce further those discrepancies and provides more accurate prediction. Additionally, this database is also a first in terms of data available for high-frequency resonant and very flexible wing.

The third and last part of this thesis have been devoted to demonstrate the capabilities of the framework as a preliminary design tool on the OVMI case to optimize its performance. Among the first challenges faced by designers are the definition of an appropriate actuation strategy and foremost of an aerodynamic potentially interesting wing. For the former, it has been demonstrated that a flapping actuation with a square actuation signal is interesting for lift intensive flight phase such as take-off or hovering but that a sine signal is better for cruise flight as it improves the power consumption. For the latter, an optimization

strategy based on genetic algorithm has been devised offering at least three complementary levels of design: two neglecting the large deflection capabilities of the FE, a rough one using the uncoupled unidirectional aerodynamic model and an intermediate one using the coupled bidirectional model, and a more realistic one accounting for these. Thus a designer might choose and refine gradually its wing design according to his specifications. Only the first two have been carried out on the OVMI case in this thesis. The best individuals found are in somehow making sense by positioning each time the membrane to the outboard of the leading-edge where the generation of aerodynamic forces is the most efficient copying thus the nature and paving the way for more complex optimizations.

Recommendation for future works

Several modifications and enhancements might improve the predictive capabilities of the aerodynamic framework as well as the experimental process and its post-processing. Some recommendations are provided next, ordered by priorities:

1. The force measurement capabilities of the test bench has to be consolidated either by pursuing the development of the in-house balance or finding an appropriate sensor either available academically or commercially. It will first enable a faster improvement of prototypes by providing clear figures on the aerodynamic performances while increasing the trial and error turnover. Second, it will also complete the experimental data necessary for the complete validation of the aeroelastic framework as it was originally devised.

2. The experimental validation has to be pursued to complete the database and better understand the discrepancies observed between the numerical and experimental data. Thus numerical investigations can be initiated so as reduce this gap. Stress-stiffening and pure membrane FEs instead of shell FEs are among the possible lines of approach for improving the numerical prediction.

3. The efficiency and capabilities of the optimization environment have also to be refined but required more computational power and support. This can be temporized by limiting the computational noise induces by the membrane, either by acknowledging the conclusions of the previous point or by better processing the data with, for example, a better filter on the kinematics data such as a Butterworth filter.

4. The comparison between experimental and numerical data using the wing deformation is quite time-consuming especially for the motion tracking. Thus easing its post-processing should become a priority when more complex wing are going to be studied either by adding better markers (roughcast or colored points) on the wing or by changing the test bench configuration. However the best option might be to automate completely the tracking of the wing deformation by, for example, adopting a digital image correlation system retrieving the 3D displacement of the wing. This might provide highly valuable information both for the validation of the aeroelastic framework but also for the current trial and error method adopted in the OVMI project.

5. The aerodynamic model defined is quite simple, consisting of a set of two equations, and has thus some drawbacks, which can be limited reasonably if needed. Improving its accuracy and robustness is essential as it will extend and strengthen the range of its application as well as increase its credibility towards designers. For example, releasing the cartesian mesh constraint might be considered broadening easily the design space and imitating more closely the nature. More complicated and accurate aerodynamic model, such as the one of Gogulapati [2011], might also be implemented extending thus the capabilities of the framework towards more detailed design stage of FWNAVs.

Finally, this work has been quite intensively promoted in various conferences, as listed in the appendix G. While some improvements and more know how might be necessary, the preliminary design tool devised in this work is already fully functional and might be released cautiously to designers. Its capabilities are tremendous for preliminary design tasks and are ready to be unleashed for FWNAV applications.

Appendix A

Material choice and fabrication of SU-8 wing

The driving idea of the OVMI project is to create a MEMS bio-inspired FWNAV. Material and fabrication process are therefore inspired by the ones commonly available in MEMS environment. This appendix sum up just these two points. Please refers to existing works for more details about the design and fabrication method (Dargent et al. [2008, 2009]; Dargent [2010]; Vanneste et al. [2010]; Bao et al. [2011a]; Vanneste et al. [2011a]).

A.1 Choice of material

The material choice for the wing is straightforward when considering the mechanical properties of insect vein/membrane and comparing them with the common available MEMS materials as showed in figure A.1. Drawn lines and their weighted counterpart are representative of reported mechanical properties of insect nervure/membrane and define our criterion lines.

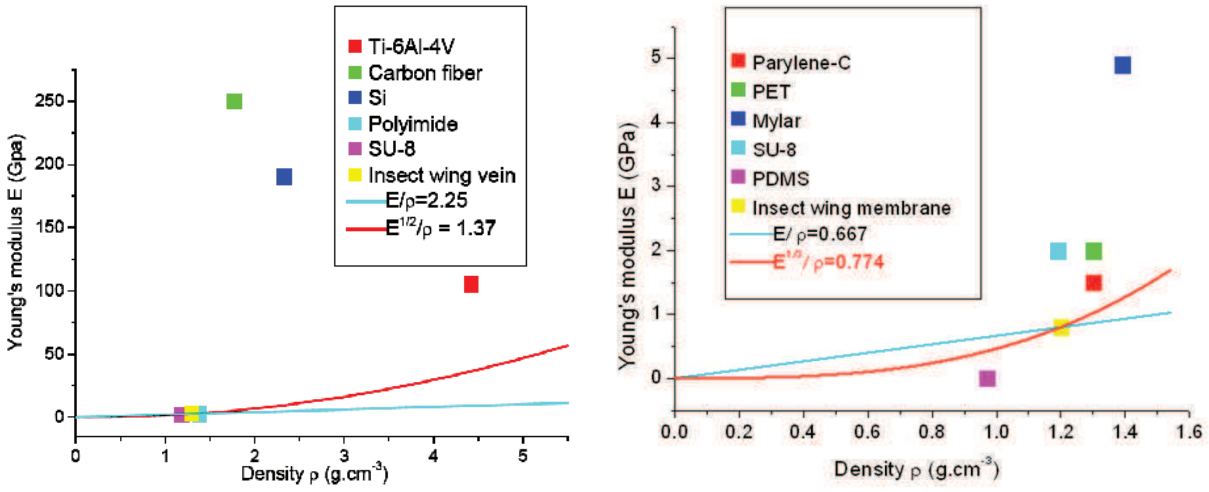

(a) Nervure (b) Membrane

Figure A.1: Comparison of different material, commonly available in micromachining, with the insect ones for nervure (left) and membrane (right) based on the Young Modulus E and density ρ. The superscript number for E refers to the efficiency of a material into a given application (Wegst and Ashby [2004]), here 1/2 for beam (nervure) in flexure and 1/3 for plate (membrane) in flexure

A common material for MEMS micromachining is the epoxy-based negative photoresist resin SU-8 which matches fairly the insect vein and membrane properties. Furthermore its mechanical properties are process-

dependent and might be adjusted. Another pro is also its compatibility with classical micromachining technologies.

A.2 Fabrication process

The fabrication process of SU-8 wing relays heavily on spin-coating and lithography techniques. An example of the process is given in figure A.2 for a part (upper ring of the thorax) from an old configuration of the OVMI prototype, but the principle stays.

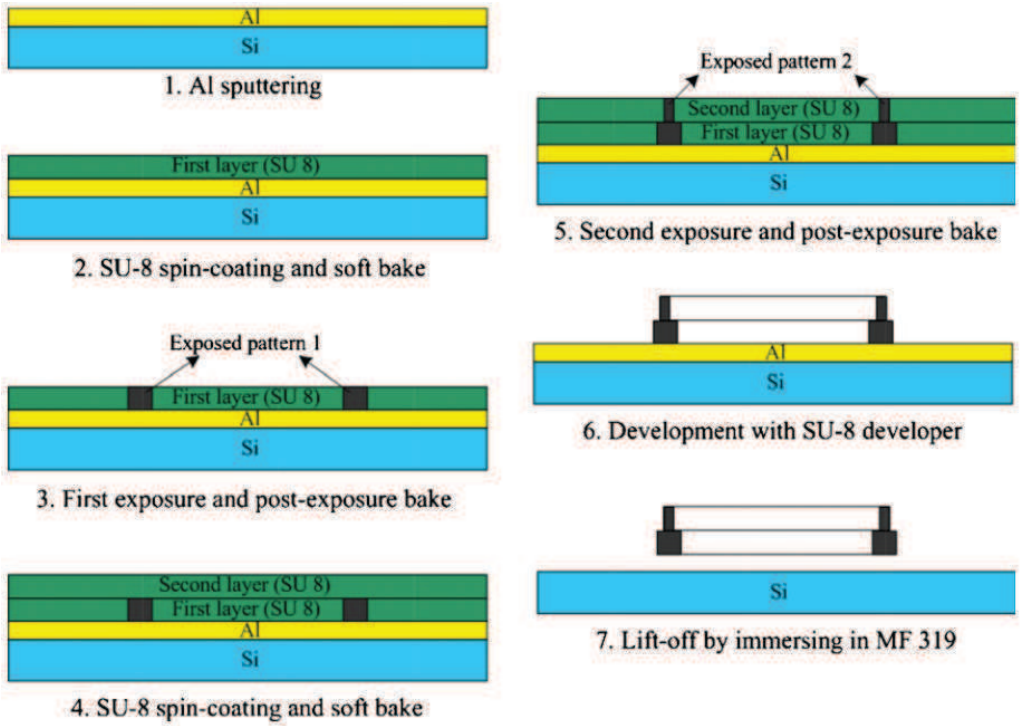

Figure A.2: Fabrication process of a SU-8 structure, here the upper ring of the thorax taken from Dargent et al. [2009]. The process can be summarized as consecutive steps of spin-coating, baking, exposing and development.

Taking a wafer and sputtering a sacrificial layer (here aluminium) on it, SU-8 is deposited and spin-coated to a desired thickness. It is then insulated with ultraviolet-light through an adequate mask representing our structure. The SU-8 will cross-link where exposed and uncrosslinked part will be dissolved when immersed into solvent. By repeating these steps several times for different thicknesses and masks shapes, SU-8 structure (wing, thorax, etc.) could be fabricated easily. Thickness can goes from $1\mu m$ to $400\mu m$ and mask shape up to $7.5cm$.

Appendix B

Comparison of the bidirectional and the unidirectional aerodynamic model: supplementary material

B.1 Wing F3

Table B.1: Reminder summary of the bidirectional/unidirectional comparison for F3.

Component / Actuation type		Lift		Drag	
		SA	LA	SA	LA
Translational forces	Difference Bidir./Unidir. on means [%]	12	9	-108	-96
	Difference Bidir./Unidir. on amplitudes [%]	45	40	11	9
Added-mass forces	Difference Bidir./Unidir. on means [%]	-81	-82	-90	-94
	Difference Bidir./Unidir. on amplitudes [%]	-83	-86	-67	-68
Total forces	Unidir. mean [μN]	0.20	3.97	0.00	0.00
	Bidir. mean [μN]	0.04	1.08	0.00	-0.00
	Difference Bidir./Unidir. on means [%]	**-80**	**-73**	**-99**	**-108**
	Unidir. amplitude [μN]	0.21	6.24	8.93	63.69
	Bidir. amplitude [μN]	0.07	3.55	3.47	29.09
	Difference on Bidir./Unidir. amplitudes [%]	**-66**	**-43**	**-61**	**-54**

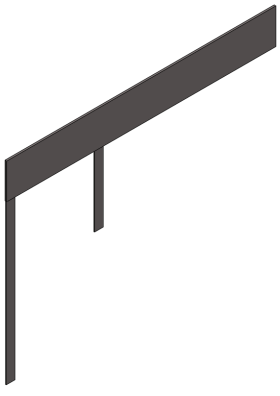

Figure B.1: CAD view of the F3 wing.

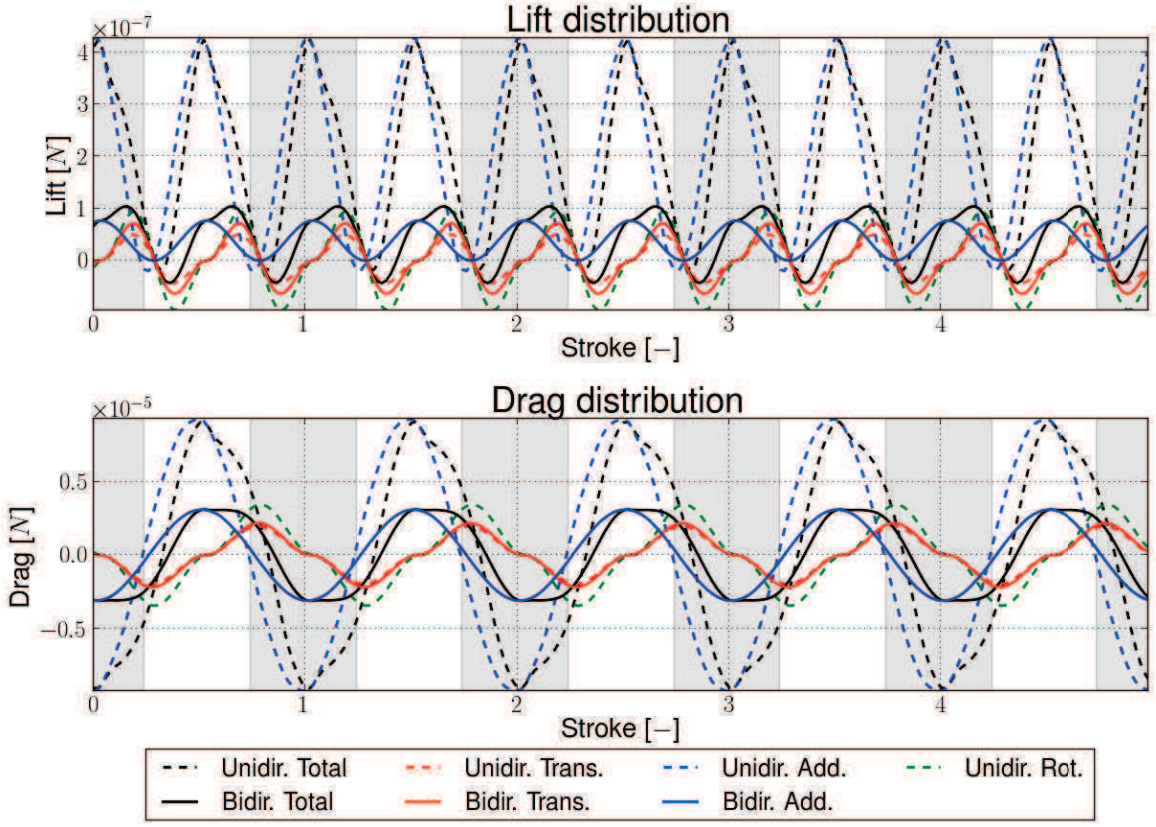

(a) Small actuation displacement (SA)

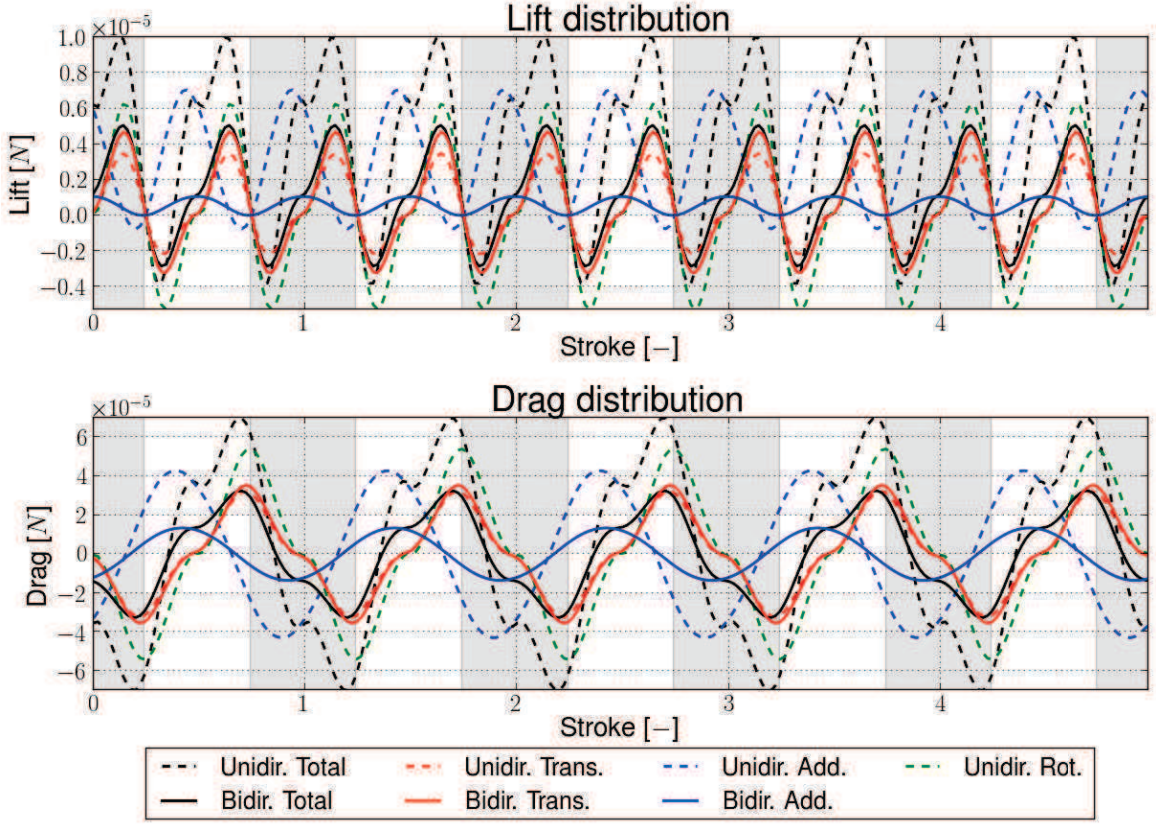

(b) Large actuation displacement (LA)

Figure B.2: Graphical comparison between the aerodynamic forces calculated using the unidirectional and bidirectional flexible approach for the wing F3 when actuated at the vacuum resonant frequency in air. Calculations are done in the same conditions as in 5.2.2. More metrics about the comparison are given in the table B.1.

B.2 Wing E4

Table B.2: Reminder summary of the bidirectional/unidirectional comparison for E4.

Component / Actuation type		Lift SA	Lift LA	Drag SA	Drag LA
Translational forces	Difference Bidir./Unidir. on means [%]	11	9	-107	-97
	Difference Bidir./Unidir. on amplitudes [%]	44	38	10	7
Added-mass forces	Difference Bidir./Unidir. on means [%]	-82	-83	-92	-95
	Difference Bidir./Unidir. on amplitudes [%]	-83	-87	-71	-73
Total forces	Unidir. mean [μN]	0.18	3.92	0.00	0.00
	Bidir. mean [μN]	0.03	1.04	0.00	-0.00
	Difference Bidir./Unidir. on means [%]	**-81**	**-74**	**-99**	**-113**
	Unidir. amplitude [μN]	0.18	5.87	9.26	63.16
	Bidir. amplitude [μN]	0.06	3.33	3.10	28.65
	Difference on Bidir./Unidir. amplitudes [%]	**-69**	**-43**	**-66**	**-55**

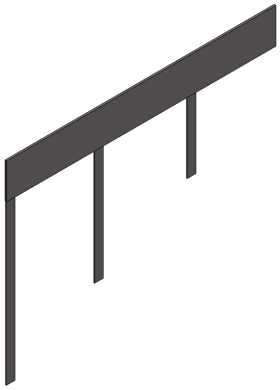

Figure B.3: CAD view of the E4 wing.

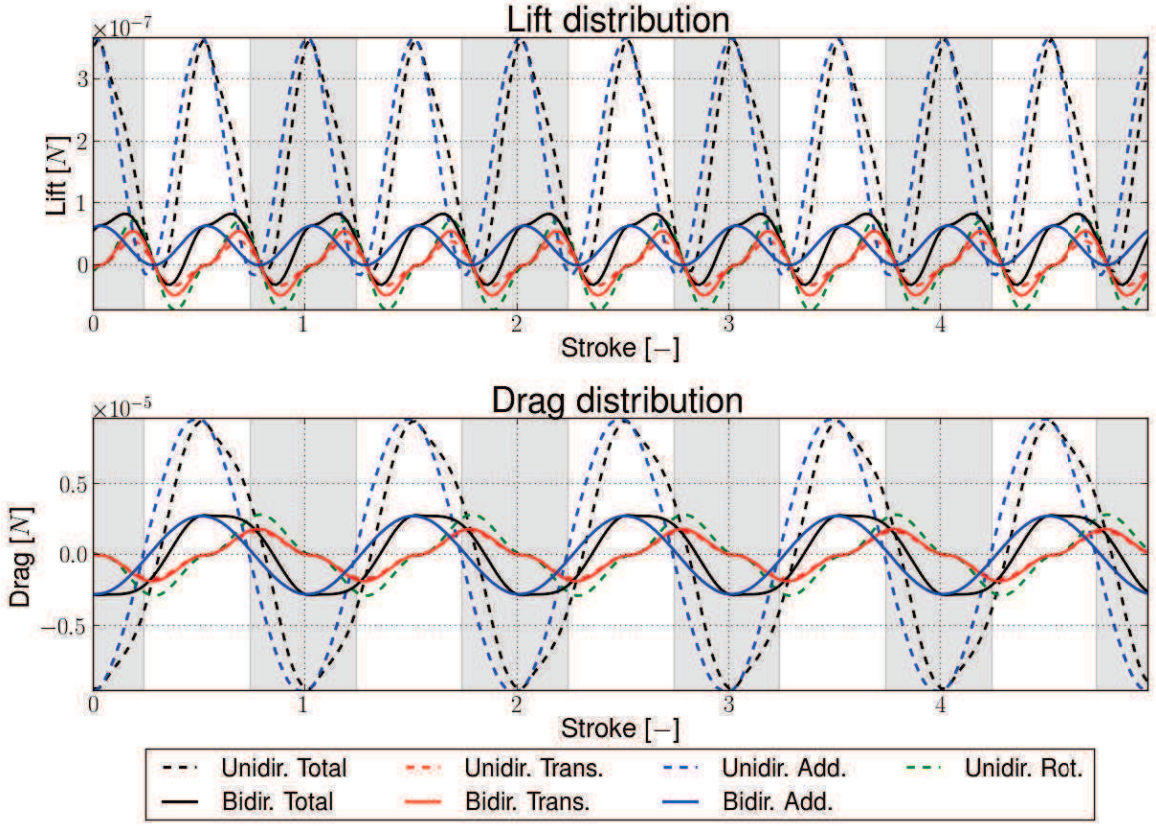

(a) Small actuation displacement (SA)

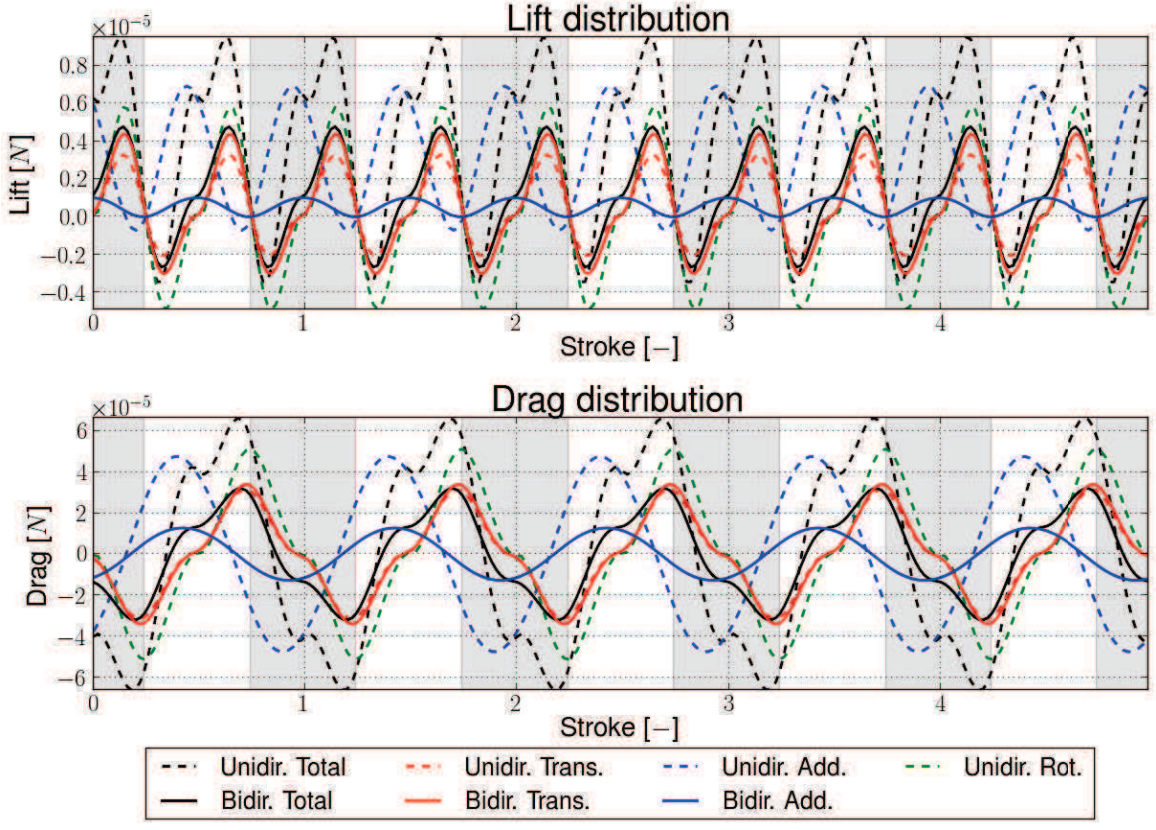

(b) Large actuation displacement (LA)

Figure B.4: Graphical comparison between the aerodynamic forces calculated using the unidirectional and bidirectional flexible approach for the wing E4 when actuated at the vacuum resonant frequency in air. Calculations are done in the same conditions as in 5.2.2. More metrics about the comparison are given in the table B.2.

B.3 Wing EM4

Table B.3: Reminder summary of the bidirectional/unidirectional comparison for EM4.

Component		**Lift**		**Drag**	
Actuation type		SA	LA	SA	LA
Translational forces	Difference Bidir./Unidir. on means [%]	20	9	-100	-100
	Difference Bidir./Unidir. on amplitudes [%]	37	37	9	6
Added-mass forces	Difference Bidir./Unidir. on means [%]	-87	-88	-100	-100
	Difference Bidir./Unidir. on amplitudes [%]	-87	-90	-89	-91
Total forces	Unidir. mean [μN]	0.38	8.00	0.06	0.13
	Bidir. mean [μN]	0.05	1.39	0.00	-0.00
	Difference Bidir./Unidir. on means [%]	**-86**	**-83**	**-100**	**-100**
	Unidir. amplitude [μN]	0.38	7.39	29.85	160.63
	Bidir. amplitude [μN]	0.06	2.79	4.19	48.33
	Difference on Bidir./Unidir. amplitudes [%]	**-84**	**-62**	**-86**	**-70**

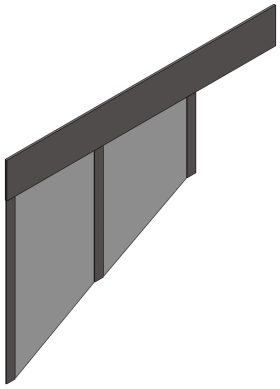

Figure B.5: CAD view of the EM4 wing.

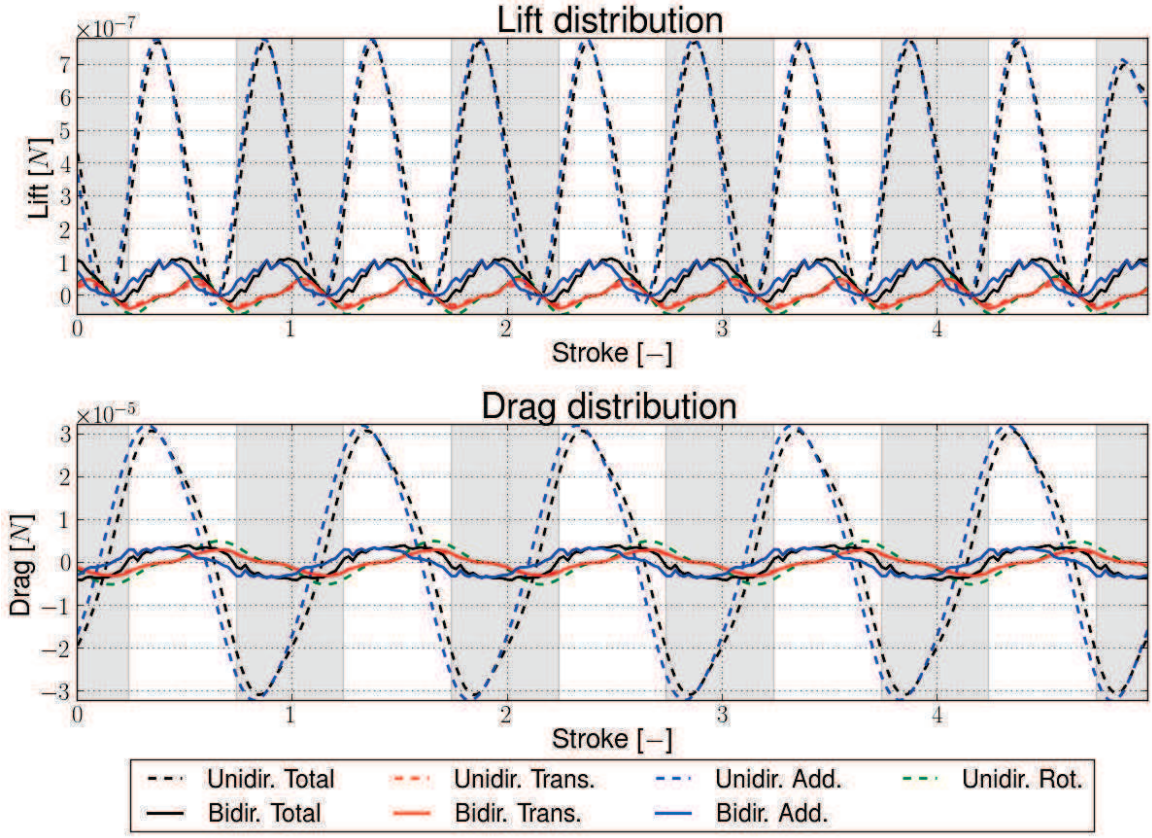

(a) Small actuation displacement (SA)

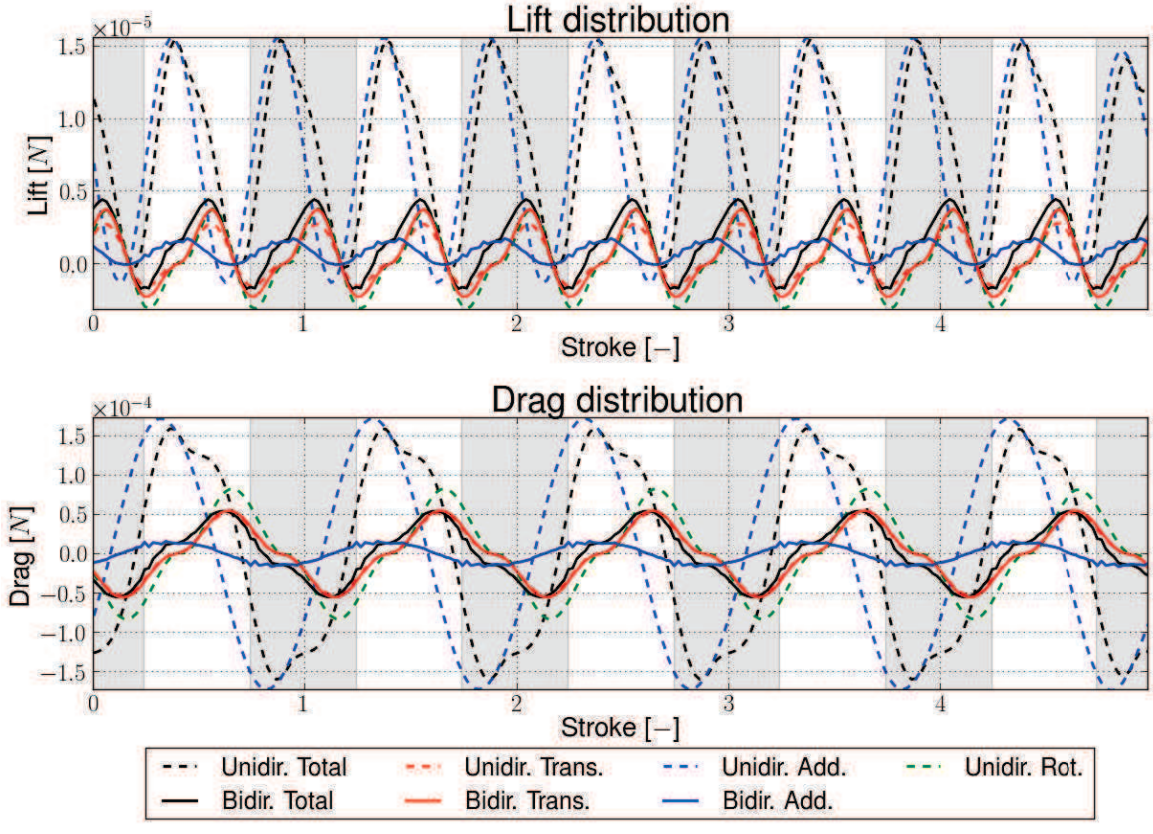

(b) Large actuation displacement (LA)

Figure B.6: Graphical comparison between the aerodynamic forces calculated using the unidirectional and bidirectional flexible approach for the wing EM4 when actuated at the vacuum resonant frequency in air. Calculations are done in the same conditions as in 5.2.3. More matrics about the comparison are given in the table B.3.

Appendix C

Development of a force sensor for flapping-wing nano-air vehicle

Contents

One of the initial objective of the thesis was to develop a balance capable of measuring the force generated by the wing and thus validating further the aeroelastic framework. The requirements are nevertheless a bit drastic, when compared to the usual balances in wind tunnel, as the typical forces are around the μN at $100Hz$ requiring a balance with high bandwidth and high sensitivity. Unfortunately, this development is quite challenging and, at the end of this work, is not sufficiently mature to fulfill its validation tasks. Therefore it has to be set aside from the main outline of this work for clarity sake.

This appendix reports the work done on this subject and is organized in four sections: a literature review of aerodynamic balance designed for flapping wings, a presentation of the balance concept developed in this work, the methodology used for aerodynamic forces measurement and finally some experimental results outlining the capability of the balance. The experimental parts of this work have been partly accomplished by Hodara [2011] and mostly by Labarrere [2012] as part of their internship.

C.1 Literature review

The literature review is synthesized in the table C.1 where each reference is weighted against seven criteria: the number of components, its vacuum compatibility, its use as a static balance (measuring the overall system

response) or a dynamic balance (measuring directly near the wing), its sensor type, a reported measured value along with its other advantages and disadvantages. Among all the references synthesized in the table C.1, only reference, which might be of interest for this work, are later on discussed. The focus is here on devices capable of measuring the force generated by an insect or by a flapping device.

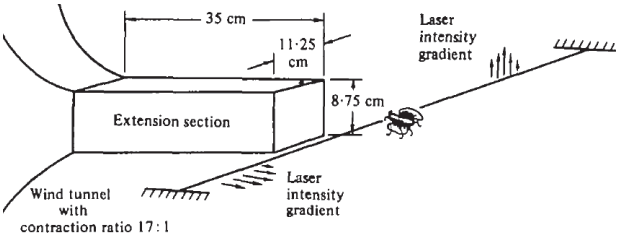

Figure C.1: Balance design by Buckholz [1981].

Buckholz [1980] and Buckholz [1981] proposes a two-component dynamic wind tunnel balance for the measurement of the instantaneous lift and drag of a mounted blowfly. The force balance is a simple string with fixed ends and an insect mounted near the middle point, as seen in figure C.1. Using two laser beams crossing the wire at two different positions, the horizontal and vertical motions of the wire are transformed into signals by collecting the intensity gradient of each laser beam through a photo-diode proportional to the displacement. The author succeeds in measuring about $15\mu N$ but no details are given about the repetitivity and the accuracy. However, the balance requires an extensive optical setup i.e. two laser beam, lenses and photo-diodes and an intensive calibration. The measurement is done behind an open wind tunnel to browse a wide variety of wind speed and might not be appropriate for hovering.

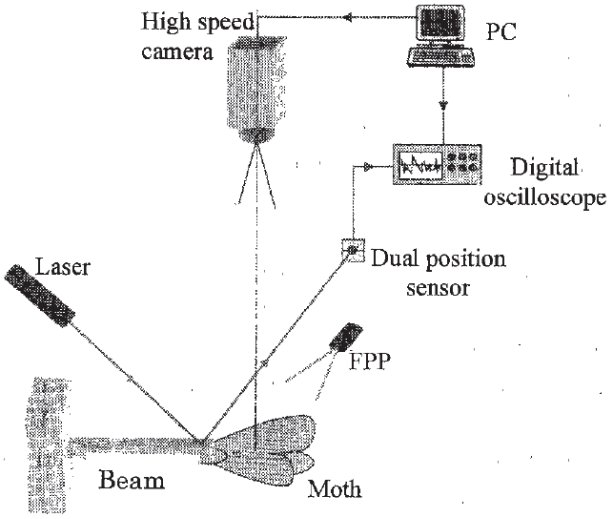

Figure C.2: Balance design by Sunada et al. [2002].

Sunada et al. [2002] use a clamped-free beam to measure the vertical aerodynamic force of a tethered Moth as illustrated in figure C.2. Coupled to an high-speed camera and fringe pattern projector, both the wing motion and the vertical force generated are measured. The aerodynamic vertical force is estimated by subtracting from the total vertical forces, measured by the beam deflection, the inertial and centrifugal forces acting on the wings, estimated from the flapping motion, from the measured vertical forces. The average aerodynamic vertical force, reported here, is around $7mN$. This work is very promising as it gives both the wing deformation and force generation. Both are relying on optical sensors for acquisition: the laser focused on the beam and the high-speed camera coupled to the fringe pattern projector. The former is quite simple in its principle and the optical sensor enables a high sensitivity while the second is more complicated requiring extensive calibration, implementation and post-processing efforts.

Table C.1: Summary table of the literature review for balance design. Different criteria are used for comparison relevant to flapping wing system.

Reference	Number of components	Vacuum compatibility	Static/Dynamic setup	Sensor type	Typical value	Advantage(s)	Disadvantage(s)
Cloupeau et al. [1979]	1	-	Static	Piezoelectric probe	$200\mu N$	+ Wind tunnel setup	- Measurement of mean values
Buckholz [1980] Buckholz [1981]	2	Yes	Static	Optical	$15\mu N$ (Min)	+ Simplicity of the montage + Wind tunnel setup	- Laser equipment and setup required - Difficult calibration
Wilkin [1990]	2	-	Static	Semiconductor strain gages	$25mN$ (Mean)	+ Wind tunnel setup	- Bulky
Sunada et al. [2002]	1	Yes	Static	Optical	$7mN$ (Mean)	+ Measurement of both wing force and deformation	- Laser equipment and setup required - Extensive post-processing
Nasir et al. [2005]	3	Yes	Static	Piezoelectric strain gage	$100\mu N$ (Min)	+ Compactness	- Temperature derivation
Sun et al. [2005] Graetzel et al. [2008] Graetzel et al. [2010]	1	Yes	Static	MEMS	$0.68\mu N$ (Min)	+ Simplicity of the montage + Compactness and availability + Bandwidth	- Robustness to forces applied perpendicular to the sensing axis - Limited displacement of the comb driver
Singh [2006]	1	Yes	Dynamic	Piezoelectric strain gage	$\sim 4mN$ (Mean)	+ Simplicity of the montage	- Decomposition of the normal force to the appropriate axis
Steltz et al. [2007]	1	No	Static	Precision balance	$1400\mu N$ (Mean)	+ Off-the-shelf	- Bulky
Wood and Fearing [2001]	1	Yes	Dynamic	Semiconductor strain gages	$10\mu N$ (Min)	+ Within the prototype	- Placement of gages and stiffening due to the wires
	2	Yes	Static	Strain sensors	$40\mu N$ (Min)	+ Compactness + Bandwidth	- Fabrication
Yan [2003]	1	No	Static	Precision balance	$1\mu N$(Min)	+ Off-the-shelf	- Measurement of mean values - Bulky
Wood et al. [2009] Tanaka et al. [2011]	2	No	Static	Capacitive sensors	$5.12\mu N$ (Min)	+ Compactness + Bandwidth	- Fabrication
Watman and Furukawa [2009]	1	-	Static	Load cell	$250\mu N$ (Min)	+ Off-the-shelf	- Measurement of mean values - Bulky setup
Wu et al. [2009a] Wu and Ifju [2010] Wu et al. [2011]	6	Yes	Static	Silicon strain gages	$3.1mN$ (Min)	+ Off-the-shelf + Bandwidth	- Measurement of mean values
Groen [2010]	2	-	Static	Load Cell	$1.92mN$ (Min)	+ Wind tunnel setup	- Setup resonance falling within the measurement range
Mueller et al. [2010]	1	-	Static	Load cell	$250\mu N$ (Min)	+ Off-the-shelf + Setup measuring lift and drag alternatively	- Low reported frequency bandwidth
Nguyen et al. [2010]	6	Yes	Static	Silicon strain gages	$781\mu N$ (Min)	+ Off-the-shelf + Bandwidth	- Bulky setup
	1	Yes	Static	Optical	-	+ Simple measurement principle	- Difficult calibration - Measurement of mean values
	1	Yes	Static	Optical	-	+ Simple measurement principle	- Measurement of mean values
Takahashi et al. [2010]	1	Yes	Dynamic	Pressure	$0.1Pa$ (Min)	+ Pressure gradient on the wing	- No direct measurement of the forces
Thiria and Godoy-Diana [2010]	1	No	Static	Precision balance	$\sim 2mN$ (Min)	+ Off-the-shelf	- Measurement of mean values and bulky
Azuma et al. [2012]	3	Yes	Static	MEMS	$\sim 1\mu N$ (Min)	+ Compactness + Bandwidth	- Fabrication

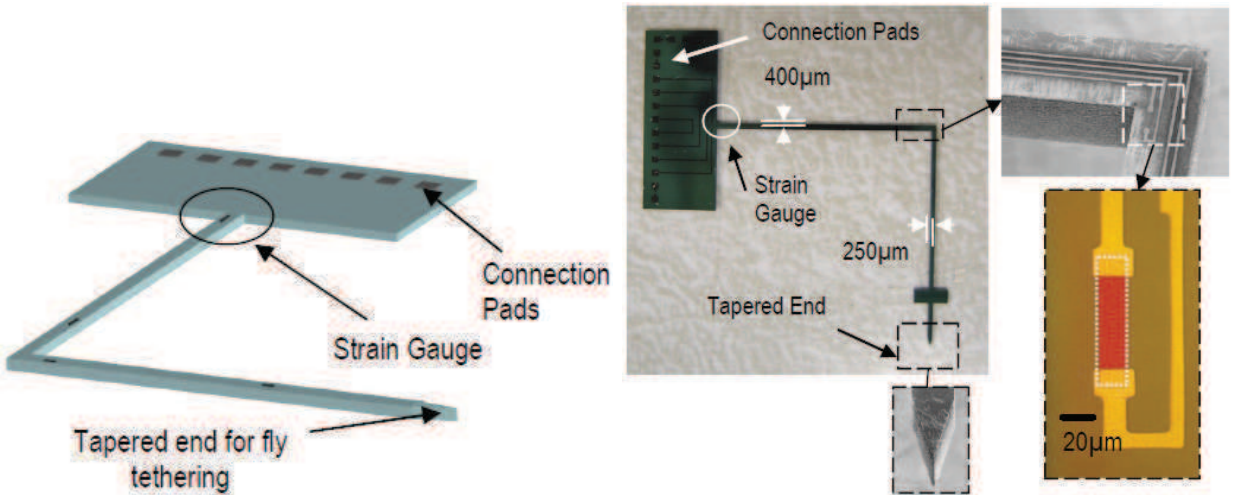

(a) Schematic design (b) Fabricated balance

Figure C.3: Balance by Nasir et al. [2005].

Nasir et al. [2005] develop a three components MEMS sensor that used piezoresistive strain gages in a quarter bridge configuration to measure the lift, thrust and yaw force, as illustrated in figure C.3. The paper verify the proof of concept and forces as small as $100\mu N$ are measured during calibration and the bandwidth seems promising. The measurement of the force generated by a fruit fly at $200Hz$ is also tempted but failed due to a lack of resolution. Large temperature drift of the gages is also reported even when compensated, making vacuum tests arduous. However possible updates to the design are given so as to increase the resolution and reduce the temperature drift. Such device, once fully developed, might be an asset for experimental work for high-frequency low-force application due to its sensitivity and bandwidth and especially its three components characterization.

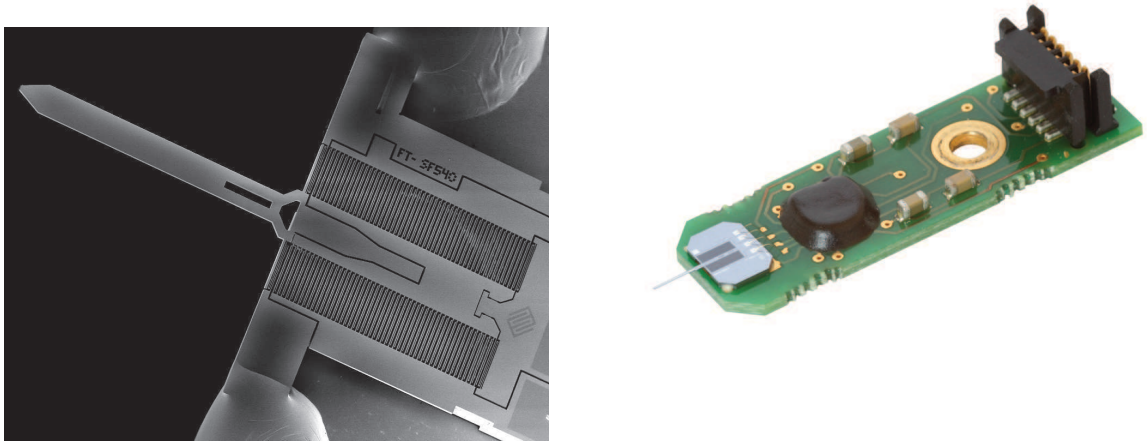

(a) SEM view (b) Overview

Figure C.4: Balance design by Sun et al. [2005] and available through *FemtoTools GmbH*.

Sun et al. [2005] develop an one component MEMS microforce sensor in the way of a capacitive sensor arranged in a differential triplate comb drive configuration with the sensor probe attached to the movable comb set, as illustrated in figure C.4. The sensor has high sensitivity ($1.35mV/\mu N$), high resolution ($0.68\mu N$), good linearity ($<4\%$), and a large bandwidth ($7.8kHz$). To fabricate the sensor, MEMS technologies (dry-

etching, lithography, etc.) are heavily used benefiting thus from all their advantage in term of fabrication and reliability, making the sensor available commercially via the *FemtoTools*. The authors conclude by measuring the instantaneous lift of a tethered fruit fly with an average of $9.3\mu N$ ($\pm$ 2.3 μN). This system is promising due to its compactness, its sensitivity, its high bandwidth making it available for high-frequency low-force application and now its commercial availability. However due the comb driver configuration, the system is quite fragile to forces applied off the sensing axis and also to the mass attached to its probe.

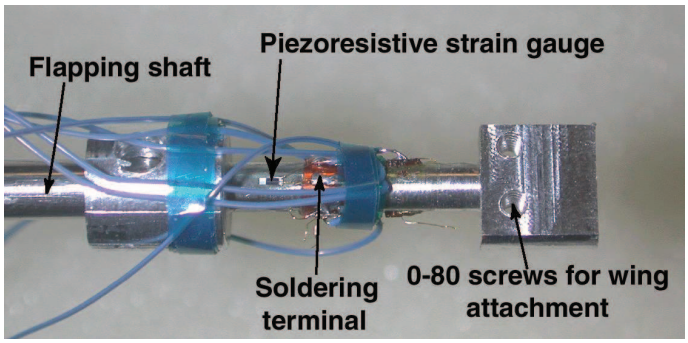

Figure C.5: Balance by Singh [2006].

Singh [2006] uses a biomimetic flapping mechanism to measure the thrust generated by various wing geometries at different wing pitch setting. To measure the force, a custom load cell using piezoresistive strain gages is designed and incorporated near the wing root. Due to high inertial power requirement, the maximum frequency of the flapping mechanism is influenced by the wing mass and is in the range of 10-22.3Hz depending on the wing material and geometry. In order to quantify the inertial forces acting on the wing, vacuum chamber tests are conducted and subtracted to the experiments made in air, thus determining only the aerodynamic forces contribution with for example a minimal average force around $4mN$. This work is relevant as it gives a methodology to subtract the inertial forces from the total forces in the case of resonant wing using a vacuum chamber. However as the strain gages are mounted directly at the wing root, the decomposition of the normal forces into drag and lift requires additional sensors.

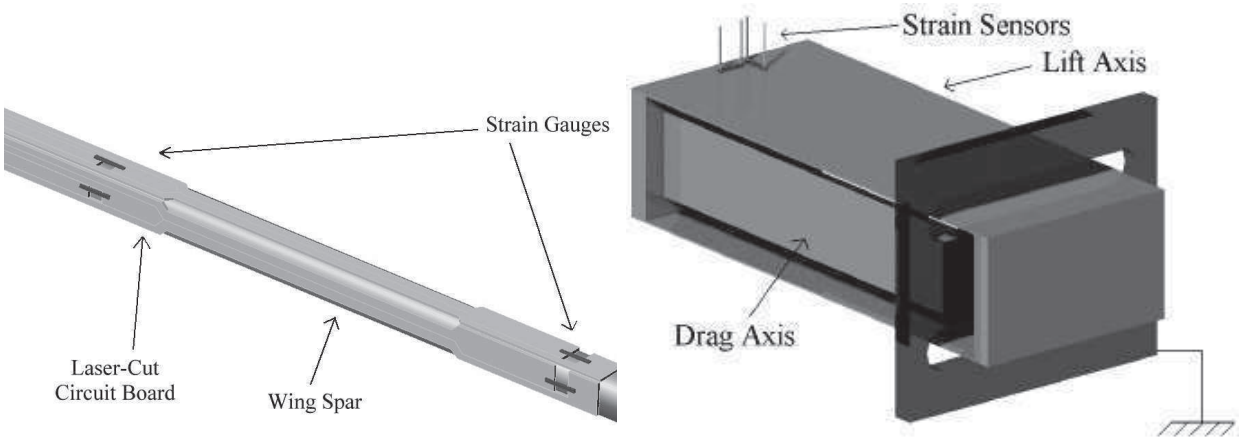

(a) Design 1 (b) Design 2

Figure C.6: Balance designs by Wood and Fearing [2001].

Wood and Fearing [2001] propose also three approaches to measure the instantaneous aerodynamic forces generated by the UC Berkeley Micromechanical Flying Insect (MFI). The first approach measures the forces directly on the wing spars using a two-axis semiconductor strain gage configuration. Although capable of measuring quite correctly the forces on the MFI at $85Hz$, a noticeable issue is the lack of sensitivity as well as practical issues such as the bounding of gages and the stiffening due to the wires. Therefore, a second

approach measuring the forces directly on the thorax is developed using two parallel cantilever body force sensors to constitute a two-component force sensor, as illustrated in figure C.6. This approach provides a good trade-off between sensor bandwidth, resonant frequency at $325Hz$, and sensitivity, $45\mu N$ and is applied to measure both the lift and drag generated by a blowfly at a wingbeat of $160Hz$ measuring maximal forces. However, its fabrication and especially the strain sensor are here unreported.

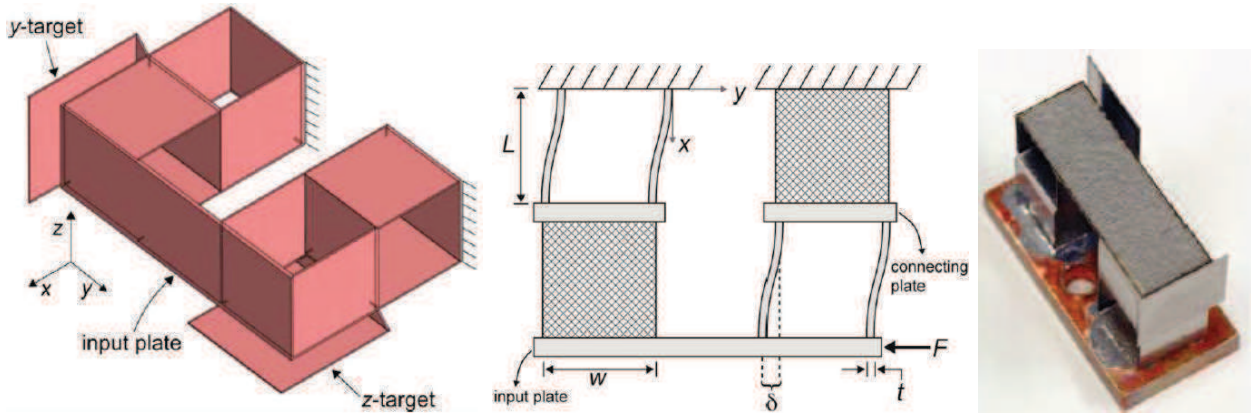

(a) CAD view (b) Functional principle (c) Fabricated balance

Figure C.7: Balance design by Wood et al. [2009].

Wood et al. [2009] develop further its last concept of a two parallel cantilever body force sensor and realized a two-component force sensor consisting of four parallel dual cantilever arranged in a series-parallel configuration, as seen in figure C.7. Through capacitive displacement sensors, the deformation of the two-component sensor is tracked. The series-parallel configuration enables high bandwidth ($630Hz$ for a $200mg$ load mass), high sensitivity, high resolution ($5.12\mu N$), and a good linearity. To fabricate the sensor, the folding process used in the Robobees is also used which allows quick production of sensors and fine tuning to measure various force ranges. The authors conclude this study by measuring the lift and drag of a Robobees-like prototype with maximum drag and lift forces around 80 μN. This work is promising as it detailed the concept of a two-axis component balance including the fabrication, calibration and practical application. Its sensitivity and bandwidth is compatible with high-frequency low-force device. Nonetheless, to measure the head displacement, capacitive sensors are used making it not compatible with vacuum.

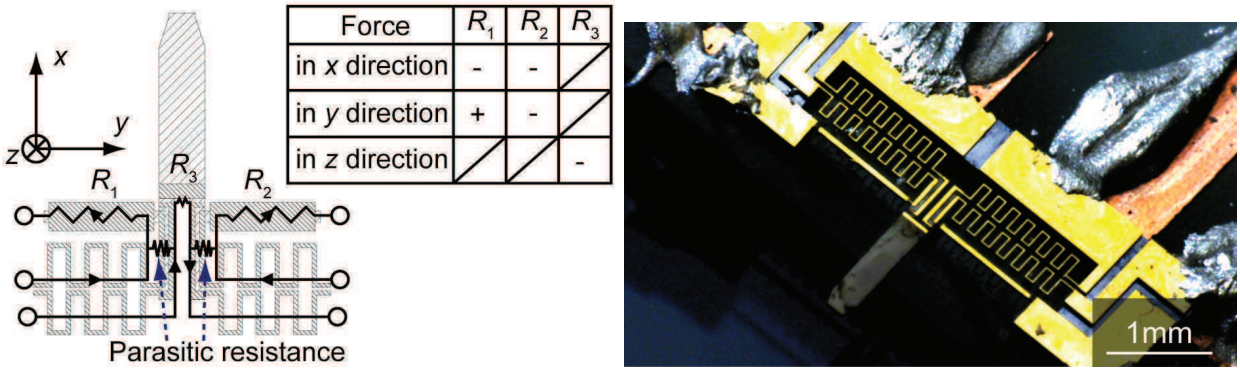

(a) Schematic design (b) Fabricated balance

Figure C.8: Balance design by Azuma et al. [2012].

Azuma et al. [2012] develop a three-component force sensor consisting of a cantilever probe, two sensing beams and four wiring beams. The sensor is fabricated using MEMS technologies with piezoresistors on the top surface of the cantilever and on each side of the sensing beam, as illustrated in figure C.8. The sensitivities

of the sensor vary among the axis considered but remained high so as to measure the instantaneous forces generated by a tethered fruit fly at $240Hz$. They report a maximum value of $40\mu N$ for the lift and the drag components. Its sensitivity and bandwidth are compatible with high-frequency low-force device and its piezoresistors make it compatible with vacuum. However, the electronics used is here not reported and its fabrication requires MEMS micro-machining tools.

C.2 Presentation and characterization of the in-house balance

Experimental investigations involving force measurements have been initially considered. To achieve this an in-house balance has been developed as no commercial device meeting the requirements of the OVMI was available especially in terms of sensitivity, bandwidth and vacuum compatibility. Another application of the balance is to evaluate the prototype performance in order to improve it by trial and error.

C.2.1 Requirements and design choices

In order to measure the aerodynamic forces generated by flapping wing, the balance should have a sufficient large bandwidth to acquire vibrating frequencies up to $100Hz$, while being sensitive enough to acquire force around or below the μN. These requirements are generally opposing themselves in balance and a compromise is here necessary. Few commercial balances are available within those range, to our knowledge only the *FemtoTools* sensor of Sun et al. [2005] which proves to be quite fragile in our application as reported by Labarrere [2012]. Furthermore, an extra requirement to the device is its role as a transmitter of the excitation from the piezoelectric actuator to the wing such that the wing can vibrate and generate its aerodynamic forces. Therefore an in-house balance has been developed aiming at measuring at least the mean aerodynamic forces with a satisfactory compromise between its accuracy, its bandwidth and its excitation transmitter duty.

Inspired by a weighting spoon capable of measuring $0.1g$ and by the design of Sunada et al. [2002], the balance is designed as a mono-component balance using strain gages in a full bridge configuration mounted on a foil. One side of the foil is glued to a screw, enabling its mounting, while the wing is positioned on the other side. When lift is generated by the wing, the foil will bend and thus induces strain within the foil, which is expected to be maximal near the foil root. To increase the sensitivity, the strain gages are positioned sufficiently apart so as to increase theirs integration region as seen in figure C.9. Typical foil strain gages are used in the design for reasons of cost and practicality.

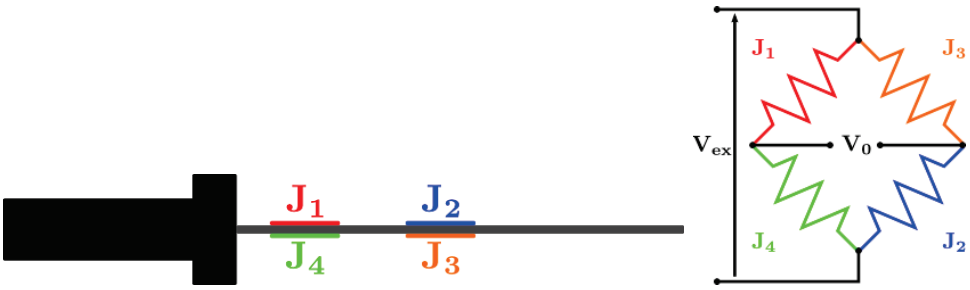

(a) Positioning of the strain gages on the foil

(b) Wiring of the strain gages within the bridge

Figure C.9: Strain gages on the foil using a full bridge configuration and an extended integration region set by the distance between the gages.

SU-8 and steel have been tested as material for the foil. The SU-8 one has been rapidly put aside due to

premature wear and fragility introduced when mounting of the strain gages (chemical reaction of the glue, heating due to the welding) and due to its laborious handling when removing wing that results generally in the destruction of the foil. Therefore steel is chosen due to its practicability and wide availability enabling fast improvement and repair of our design. To size the foil, its first resonant frequency f_f is set using the equation C.1 to be around $250Hz$ by adjusting its length l_f. The thickness t_f and the width w_f are imposed by the available foils in stock and by the width of the strain gages. The deflection of the foil, influencing the sensibility of the balance, is given by the equation C.2 for an arbitrary load F at the free foil tip as an additional decision-making parameter. A strong influence of the foil thickness t_f is noted.

$$f_f = \frac{3.516}{2\pi\sqrt{12}} \frac{t_f}{l_f^2} \sqrt{\frac{E}{\rho}} \tag{C.1}$$

$$\frac{\Delta l_f}{l_f} = \frac{6Fl_f}{Ew_f t_f^2} \tag{C.2}$$

Two sets of balance are built so as to increase the chances of finding the appropriate trade-off between the bandwidth i.e. the resonant frequency and the sensitivity i.e. the deflection. Theirs dimensions are summarized in the table C.2 along with their first resonant frequency and the deflection for a $10\mu N$ weight ($\sim 1mg$).

Table C.2: Dimensions of the two steel foils used in the two versions of the in-house balance with E=$210GPa$ and ρ=$7800kg \cdot m^{-3}$

	l_f $[mm]$	w_f $[mm]$	t_f $[\mu m]$	f_f $[Hz]$	$\frac{\Delta l_f}{l_f}$ [-]
Balance A	18	4	100	254.9	1.2857e-7
Balance B	17	4	80	228.6	1.8973e-7

To increase the robustness and the reliability of the design, a washer is added as a dispatcher on the screw side in order to avoid short-circuits between the strain gages wires by increasing the mean free path between each wire. The washer also increases the handling of the balance by preventing malicious fingers from bumping unexpectedly into the wires. Furthermore to reduce the strain induced by the connection wires on the foil and avoid guy-wires effects, several turns are made on each wire prior to their mounting. The balance is then connected to a *National Instruments* SCXI-1520 acquisition module which handles all the strain gages powering, nulling and measuring. A snapshot of the balance final design is given in figure C.10.

In order to measure the aerodynamic forces using the balance, it is compulsory to characterize the in-house balance first from a static point of view, by determining its calibration curve, and second from a dynamic point of view, by establishing its bandwidth and behavior when mounted and actuated by the piezoelectric actuator.

C.2.2 Static calibration

To establish the calibration curves i.e. the relation between the load acting on the foil W and the voltage acquired by the strain gages U, various loads are applied to the free extremity of the foil while the strain is acquired and then averaged. For the calibration, the considered masses M are in mg: 0, 1, 2, 5, 10, 50, 100, 200, and 1000. To reduce the thermal drift, a constant excitation voltage of $2.5V$ is applied which enables a fair output voltage within the range of loads considered with minimal thermal effects.

Using a *Labview* program, each acquisition starts by nulling the strain gages with the balance unloaded. When completed, the balance is loaded carefully with a mass and the acquisition starts for $10s$ at $2.5kHz$. Each mass point is repeated at least five times so as to estimate the standard-deviation.

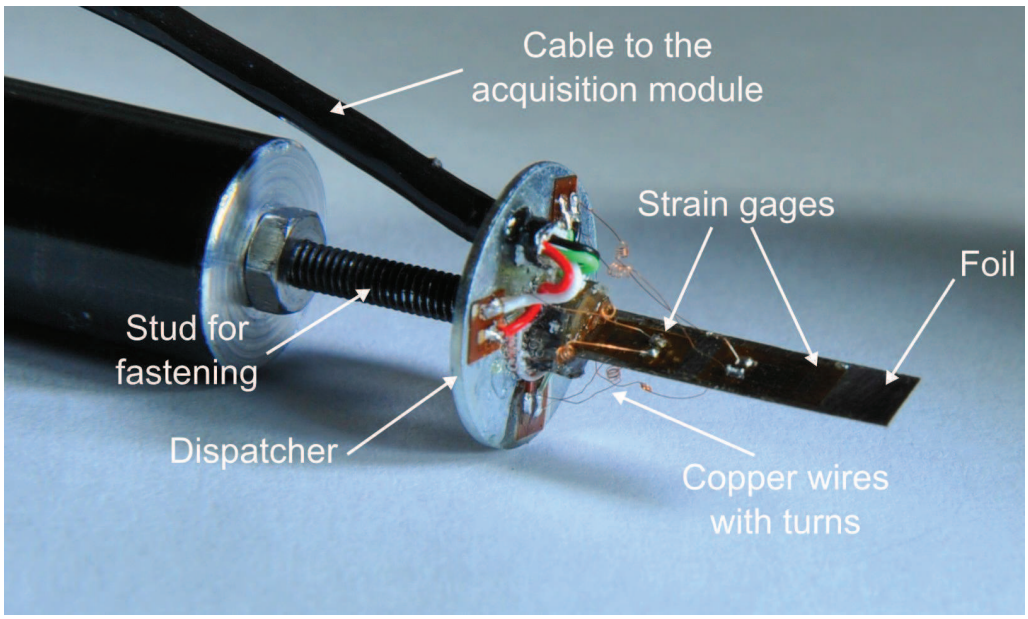

Figure C.10: Overview of an in-house balance, here the balance B. Four strain gages are mounted on a steel foil in a moment montage and wired to a washer using copper wires. The washer is used to dispatch the main cable wires to each strain gages. The stud enables a quick fastening of the balance to various support.

When all the acquisitions are completed, the post-processing started using a *Python*-script. First of all, the data are averaged for a given mass over each acquisition and then the mean output voltage of the unloaded balance is subtracted from those. At last, the standard-deviation and the mean value of each load are computed and plotted establishing the calibration curve. A linear interpolation is also computed so as to get a fast conversion between the measured voltage U and the applied load F i.e. the applied mass M. The calibration curves of the in-house balance are presented in the figure C.11 along with the linear interpolation and its equation.

The figure C.11 highlights the balance B which offers the best sensitivity i.e. the bigger linear coefficient.

C.2.3 Dynamic characterization of the balance

Even if the balance is capable of measuring load around the μN, the force measurement has to be free of any interference from the balance when the wing or a prototype vibrates or when the balance is used to transmit the piezo-excitation to the wing. In another words, its dynamic behaviour has to be characterized so as to check the bandwidth and sensitivity of the balance under excitation either at its free end or at its clamped end.

Thus four analysis are performed on each balance. First, the resonant frequency is quantified using a free vibration test. Second, the bandwidth is estimated by actuating the balance unloaded at various frequencies and by checking its data versus these frequencies. Third, the sensitivity is assessed by actuating the balance with a given mass at various frequency and by checking the deviation between the loaded and the measured mass. Fourth, the repetitivity is investigated by actuating the balance with various masses at a given frequency multiples times and by checking again the deviation between the loaded and the measured mass.

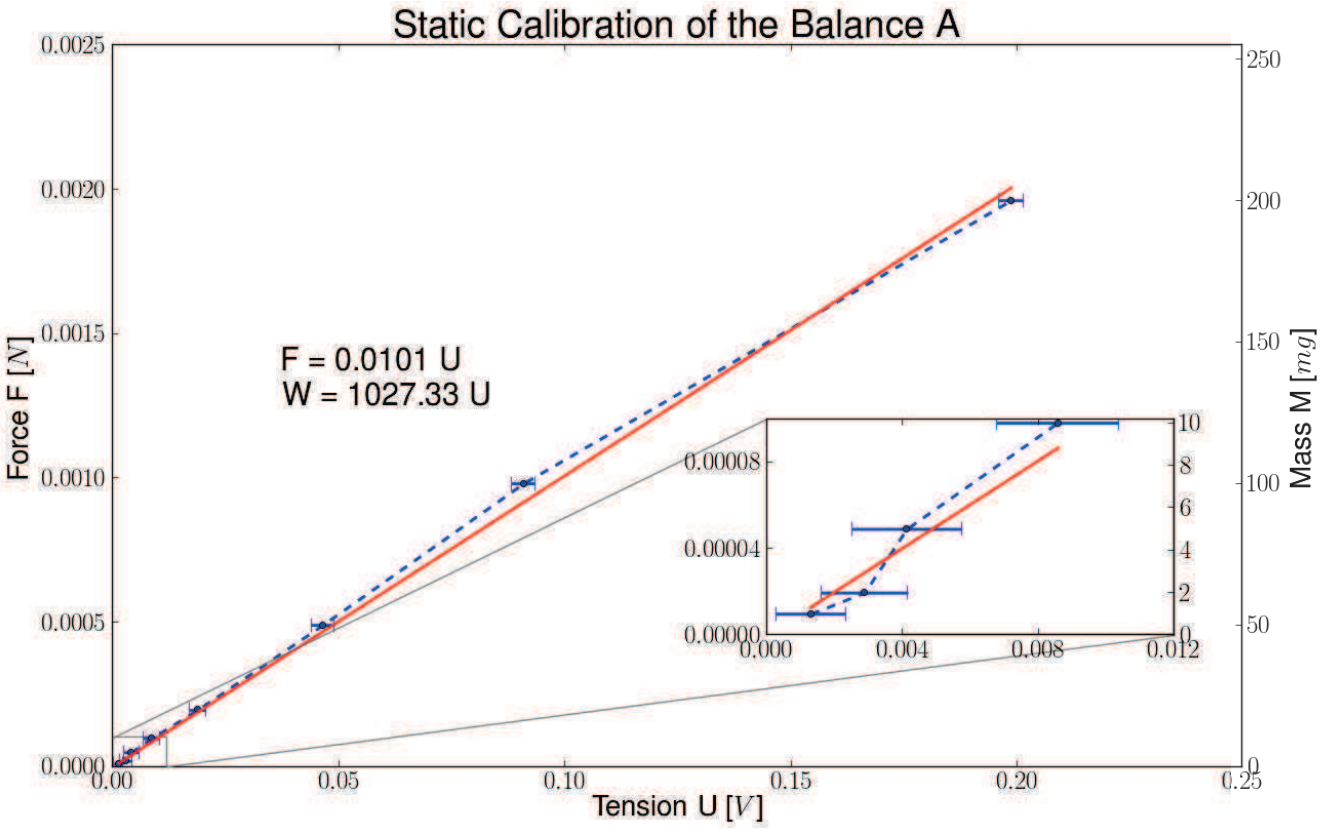

(a) Balance A

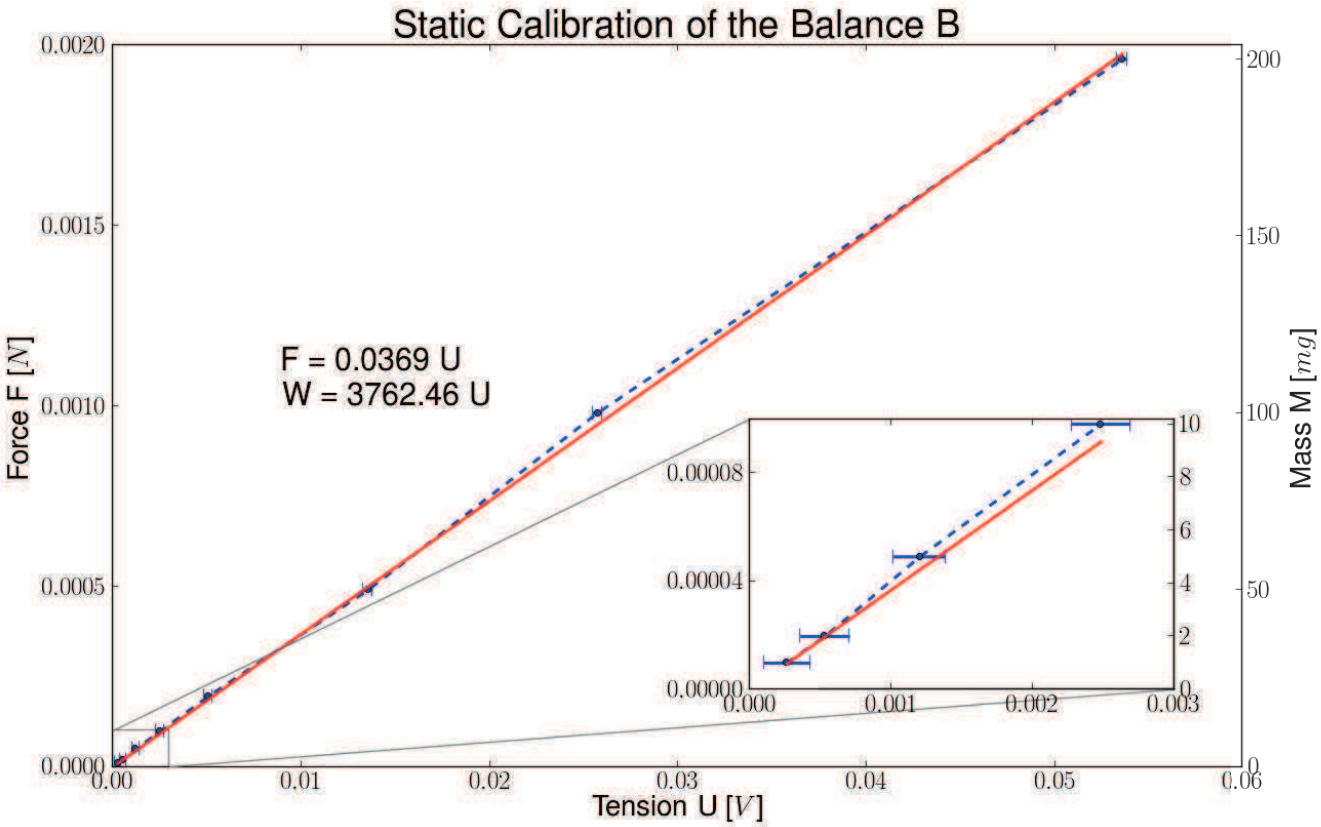

(b) Balance B

Figure C.11: Calibration curves of the two balances and the equation relating the output voltage to the load applied at the foil tip for an excitation voltage of $2.5V$. The calibration equation of the balance A is F=0.0101U. The one for the balance B is F=0.0369U. An equivalence is also given to related the output voltage to the weight (in mg).

C.2.3.1 Free vibration test

An important aspect of a balance is to determine its bandwidth which is mainly dictated by its resonant frequency. To determine it, a free vibration test is usual. To do so, the balance is set off with an initial flick of finger and its free vibration is acquired. By performing a FFT analysis of the output signal, the frequency spectrum provides the resonant frequency of the balance with a distinctive peak among others. For those tests, the acquisition is set to last $1s$ at $2500Hz$. Results are given in the figure C.12.

The resonant frequency of the balance A and B are characterized by the broader peak around $242.7Hz$ and $248.9Hz$ respectively. Those values are in the order of magnitude calculated in the table C.2, even if inverted. These differences might be explained by considering the role of the strain gages and the wires to the overall system. For the balance A, the weight tends to increase slightly while the stiffness is still dominated by the foil's one resulting in a slightly lower frequency. For the balance B, the weight increases still slightly, but this time, the strain gages and the wires plays a more important role in the stiffness of the balance and tends to increase its overall stiffness, which results in a significantly higher frequency. Another explanation might be simply the fabrication error inherited from the bonding between the foil and the screw head, such as for example a foil not completely or to deeply inserted in the notch.

As outlined by the numerous peaks at $50Hz$ and at its odd-multiples, a lot of noises due to electromagnetic interferences (EMI) are captured by the balances. This is unfortunate but comprehensible as the balance can be roughly described as a pair of raw copper wires much like an antenna. The Faraday cage provided by the vacuum chamber is not sufficient as its door is open for handling purposes. Connecting every components of the test bench to the same ground reduce slightly their amplitudes and has been here used.

C.2.3.2 Bandwidth test

Another important aspect of the bandwidth, more relevant maybe when the balance is used as a vibration transmitter, is to check up to which frequency is the balance capable of measuring something meaningful i.e. without the own vibration of the balance coming into play. To do so, the unloaded balance is actuated at various frequencies (15, 20, 50, 100, 150 and $200Hz$) by the piezoelectric and a FFT is performed to explore its frequency spectrum for a peak due to the balance. For those tests, the acquisition is set to last $1s$ at $2500Hz$. Results are given in figure C.13 and C.14 for respectively the balance A and B.

The FFT for each actuation frequency highlights the capability of the in-house balance of measuring phenomena up to $200Hz$ without inducing a noticeable dynamic response of the balance i.e. exciting the resonant frequency of the balance except around $100Hz$ where a sub-multiple of the resonant frequency seems to be excited ($\sim 80Hz$ for balance A and $\sim 83Hz$ for balance B). Furthermore, for low actuation frequency ($<50Hz$), the frequency is correctly captured by the balance but for higher frequency the EMI noise is a concern. For example, the $200Hz$ actuation frequency generates strong response at $150Hz$ and $250Hz$ for both balances and also the $100Hz$ actuation frequency with EMI peaks at $50Hz$ and $150Hz$.

However these results are mitigated by the fact that the balances are here unloaded and the EMI noise tends to vanish quickly when a load is applied as the output signal of the balance is stronger. The bad response around $100Hz$ is here unfortunate but will do the trick for these first draft design of balance. Higher resonant frequencies have to be considered for later design.

C.2.3.3 Sensitivity test

Now that the bandwidth of the balance is estimated, it is important to verify that the calibration curves hold when the balance is actuated with a load at its end, in another words to verify that $10mg$ shaked at $100Hz$ are still $10mg$. Therefore the calibration mass, from $1mg$ to $200mg$, is loaded, after the balance nulling, and actuated at various frequency, from $10Hz$ to $200Hz$. The mean load is then computed and

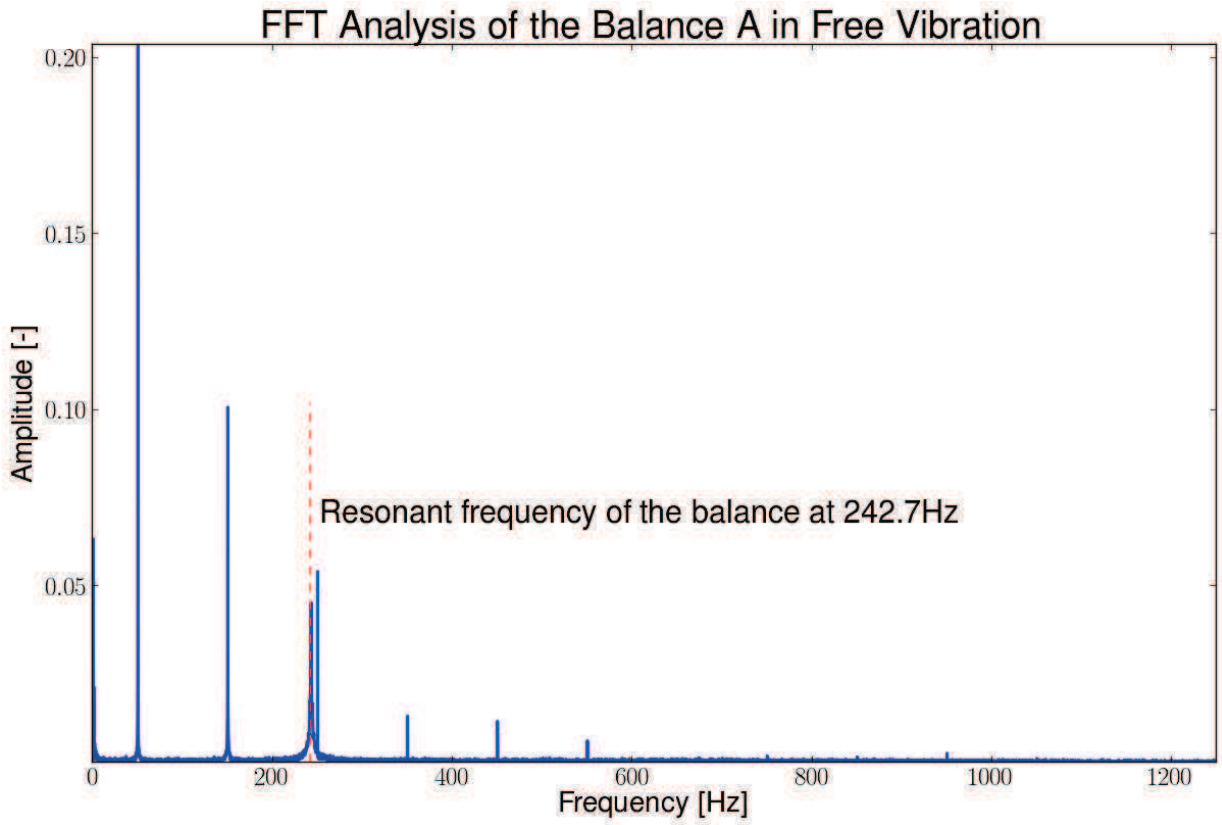

(a) Balance A

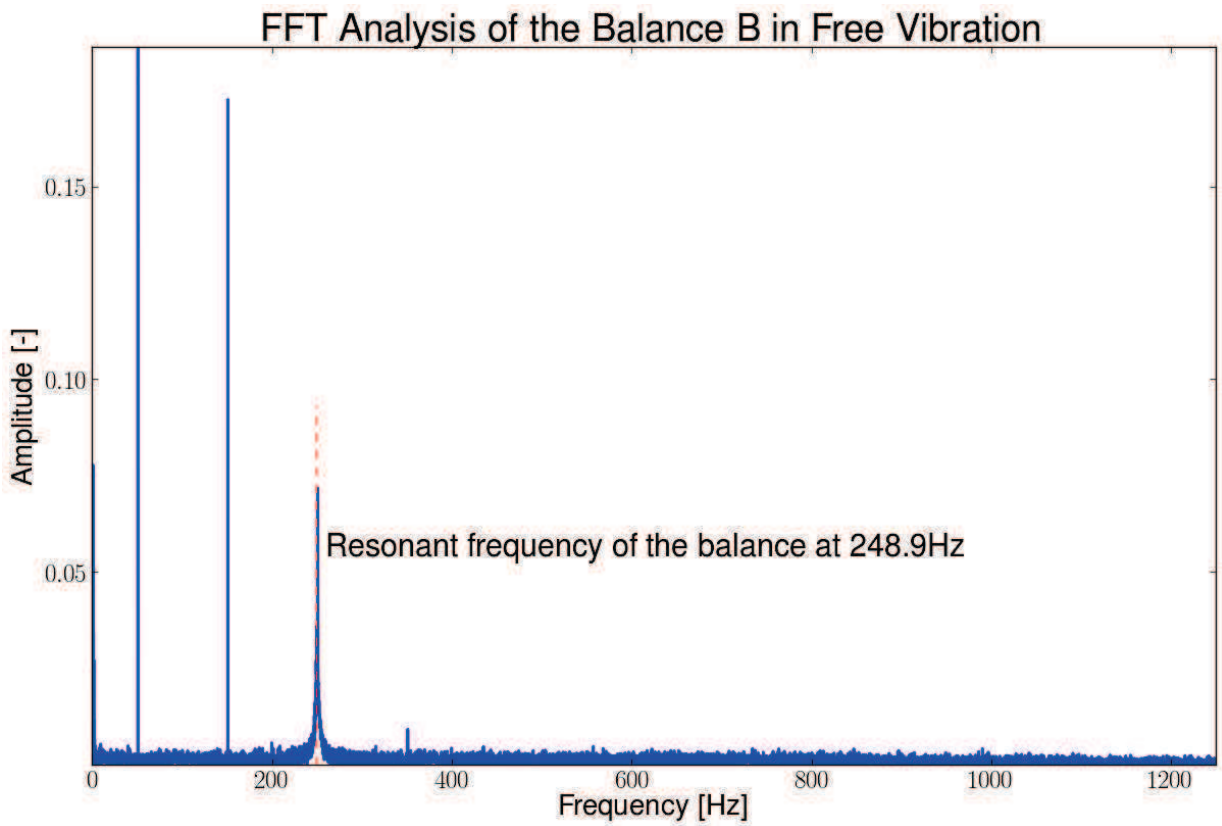

(b) Balance B

Figure C.12: Free vibration test of the in-house balances. The balance is set off and a FFT is performed to outline the frequency spectrum. Thus the resonant frequency of the balance A is 242.7Hz. The one of the balance B is 248.9Hz. As outlined by the peaks at 50Hz and at its odd-multiples, a lot of noises due to EMI are captured by the balances.

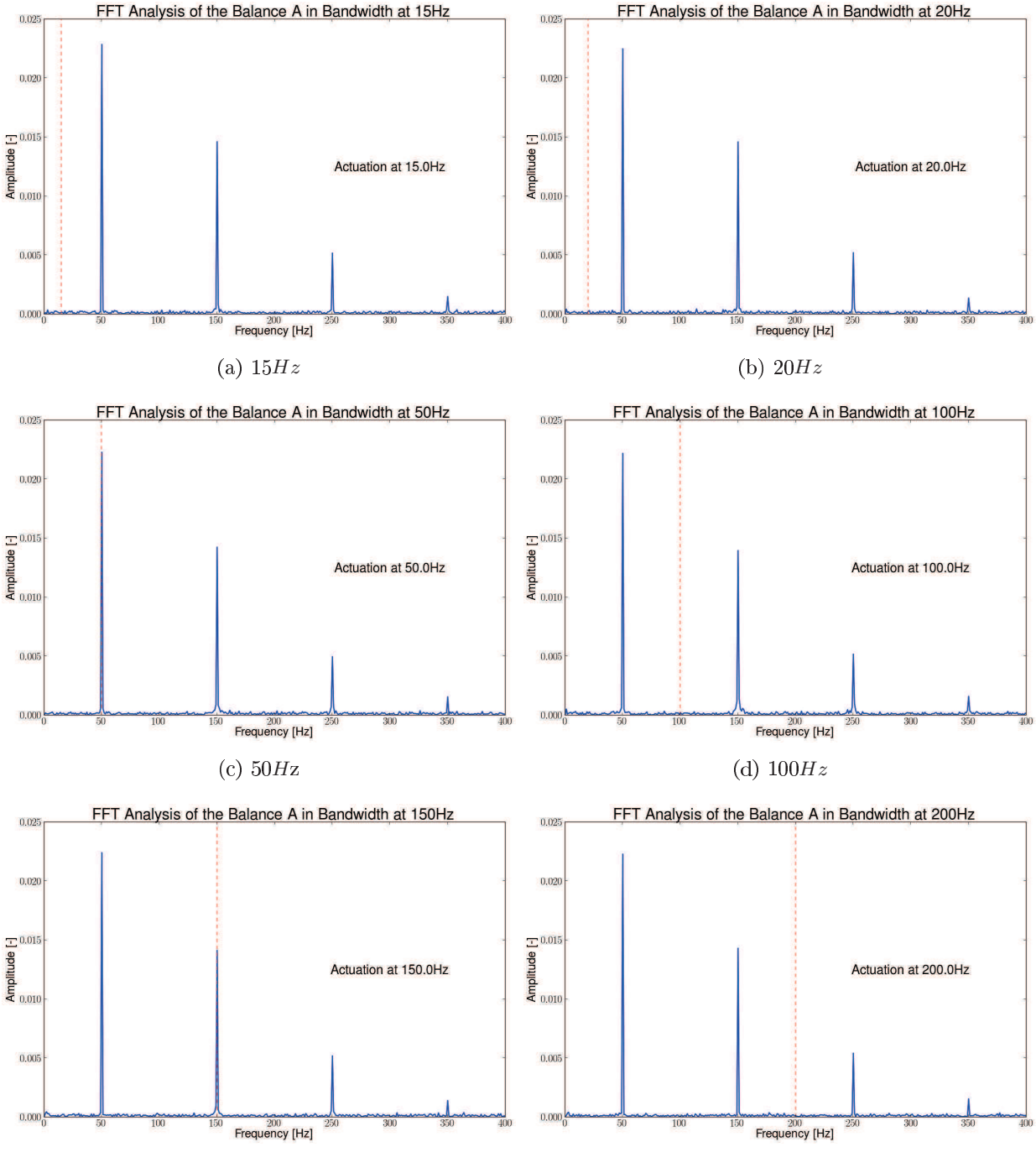

(a) $15Hz$ (b) $20Hz$

(c) $50Hz$ (d) $100Hz$

(e) $150Hz$ (f) $200Hz$

Figure C.13: Bandwidth test of the balance A. The balance is actuated at various frequencies and a FFT is performed to outline its frequency spectrum. The EMI noise is a concern.

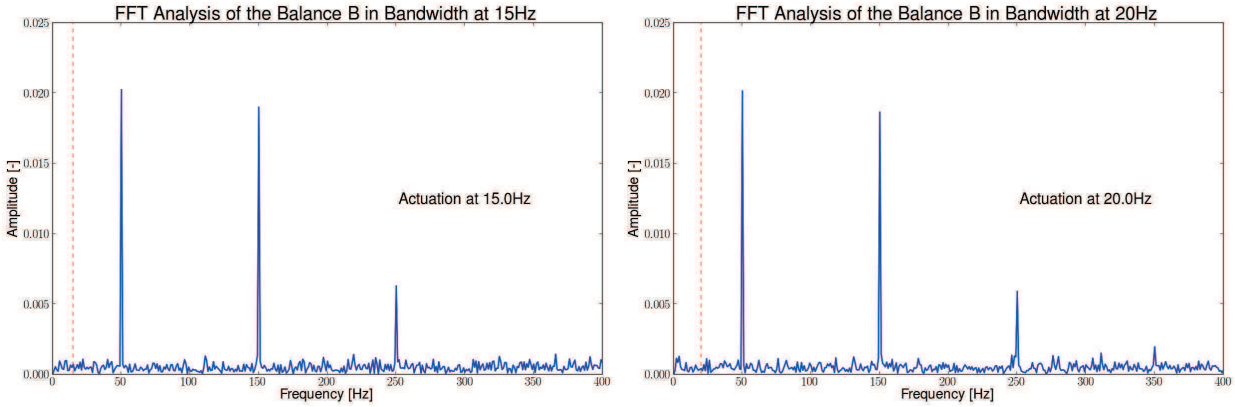

(a) $15Hz$

(b) $20Hz$

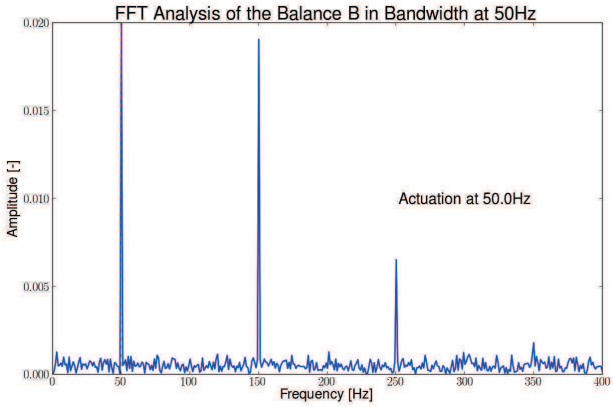

(c) $50Hz$

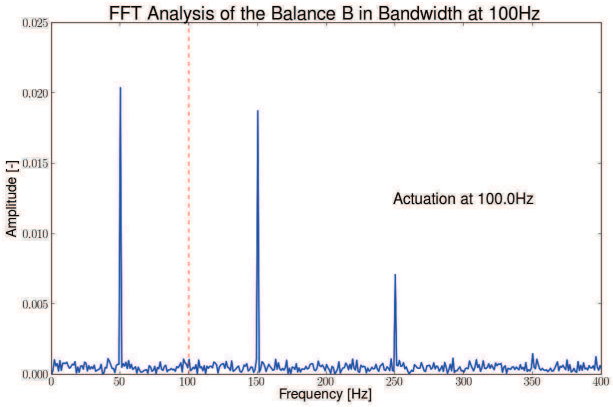

(d) $100Hz$

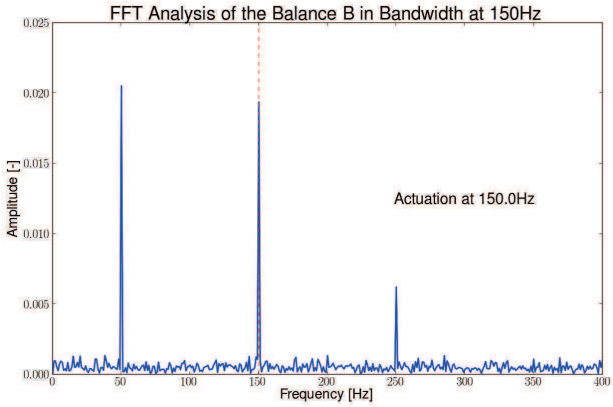

(e) $150Hz$

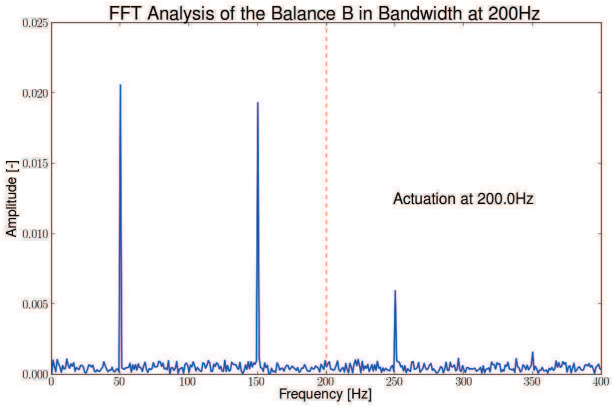

(f) $200Hz$

Figure C.14: Bandwidth test of the balance B. The balance is actuated at various frequencies and a FFT is performed to outline its frequency spectrum. The EMI noise is a concern.

compared to the reference mass to outline any drift in the balance when actuated by the piezoelectric. For these tests, the acquisition is set to last $1s$ at $2500Hz$ and a patch of double-sided tape is used to prevent the mass from being ejected during the test. Results are given in the figure C.15 and C.16 for respectively the balance A and B.

For the balance A, the results are slightly disappointing. The mean measured mass is for almost all cases less than the half of the calibration mass with a mean error around 70% except for the $1mg$ and $2mg$ masses where the error fall to 100%. These performances might be explained by experimental errors or simply by a bad calibration explaining the almost constant factor. However, the resonant frequency of the balance A is the lowest one from the two which makes it more sensitive to any disturbance even more with a mass at its end which decreases further its resonant frequency. The low sensitivity of the balance, as highlighted by the calibration curve in figure C.11(a), makes also the balance much more sensitive to noise. These bad performances will have to be understand further for later design.

For the balance B, the results are very encouraging. The mean measured mass is for almost all cases close to the calibration mass with a mean error around 10% except for the $1mg$ where the error falls to 100%. These performances might be explained by a larger resonant frequency of the balance B, a bigger sensitivity, as highlighted by the calibration curve in figure C.11(b), making the balance less sensitive to noise.

Therefore, the balance B is the best compromise between sensitivity and bandwidth for the balance as highlighted until now by the calibration curve, the free vibration test and now this sensitivity test. The mean measured masses at $100Hz$ are coherent with the ones at others frequencies for both balances, relieving thus some doubts about the ability to measure forces around $100Hz$, partially outlined by the forced vibration test.

C.2.3.4 Repetitivity test

One last item to check before concluding the dynamic characterization of the balances is the repetitivity of a measurement. It is important to verify that two measurements taken consecutively are alike. The task is accomplished for the static calibration with several acquisitions for a single reference mass, but not when the balance is actuated. The idea is to make several measurements for each calibration mass at various actuation frequencies and then compared the mean measured mass with each other. However, this task is quite time-consuming and has been partially accomplished with the sensitivity test, where each calibration mass was swept. Therefore it has been chosen to focus on the measurement at $100Hz$, which proves to be problematic with the resonant frequency of the balance being excited, as highlighted by the forced vibration test. For these tests, the acquisition is set to last $1s$ at $2500Hz$ for calibration masses ranging from $1mg$ to $200mg$. Results are given in figure C.17 and C.18 for respectively the balance A and B.

Once again, the results for the balance A are quite puzzling. The mean measured mass is for almost all cases less than the half of the calibration mass. However the standard-deviation values are quite low making the measurement consistent with one another. This result points out once again either a bad calibration or a bad compromise between sensitivity and bandwidth, giving awkward results.

For the balance B, the results are on the contrary very encouraging again. The mean measured mass is for almost all cases close to the calibration mass as highlighted by the reasonable standard-deviation values. The measurements are here again consistent with one another. The results also alleviated the doubt about the capability to measure forces around $100Hz$ as the mean measured masses are quite close to the calibration mass for each run.

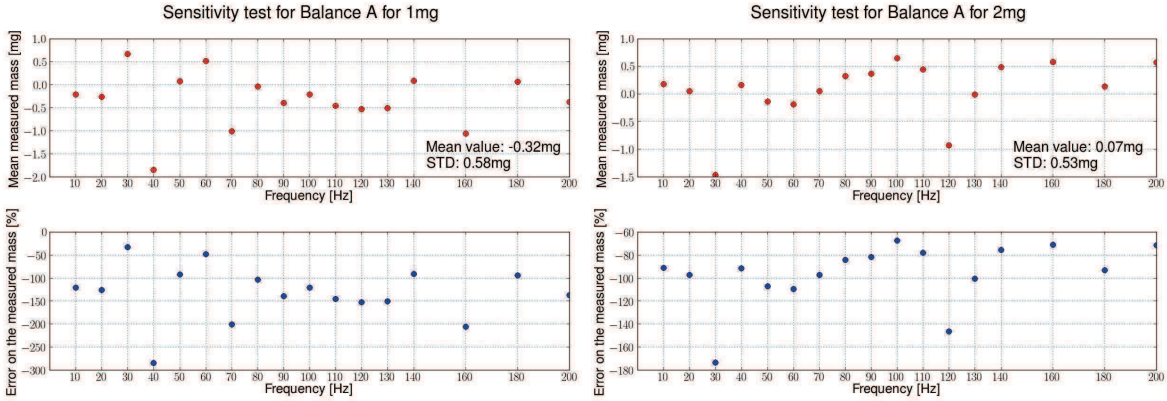

(a) $1mg$

(b) $2mg$

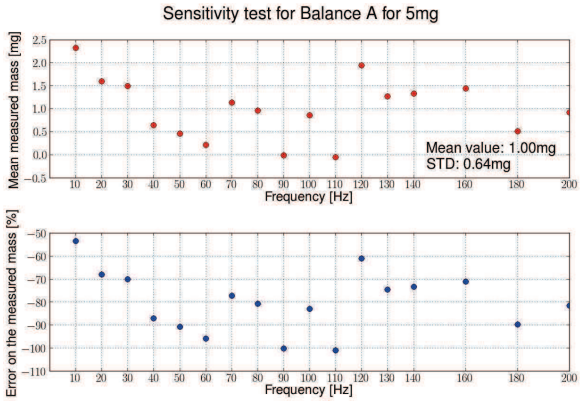

(c) $5mg$

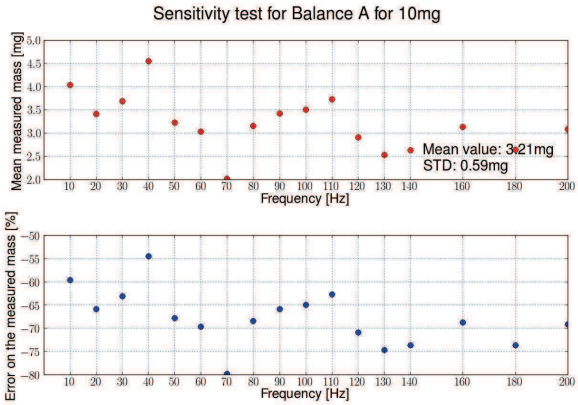

(d) $10mg$

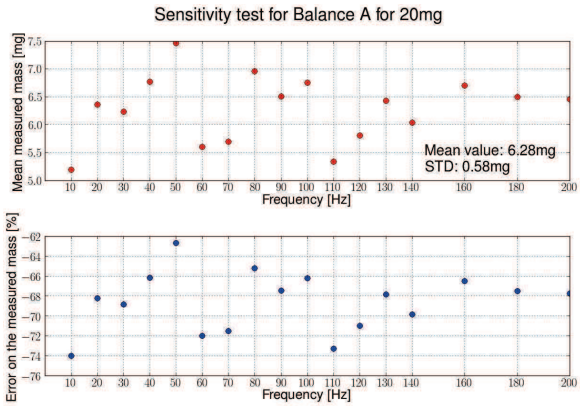

(e) $20mg$

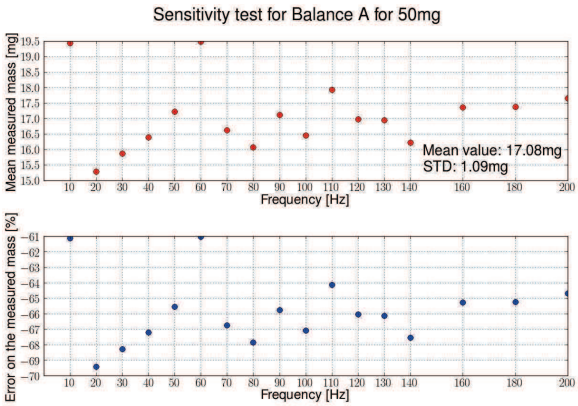

(f) $50mg$

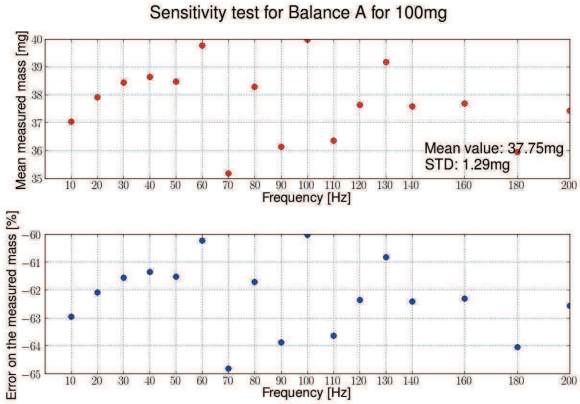

(g) $100mg$

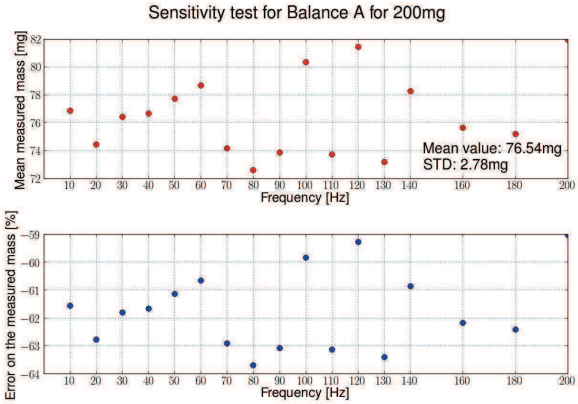

(h) $200mg$

Figure C.15: Sensitivity test of the balance A

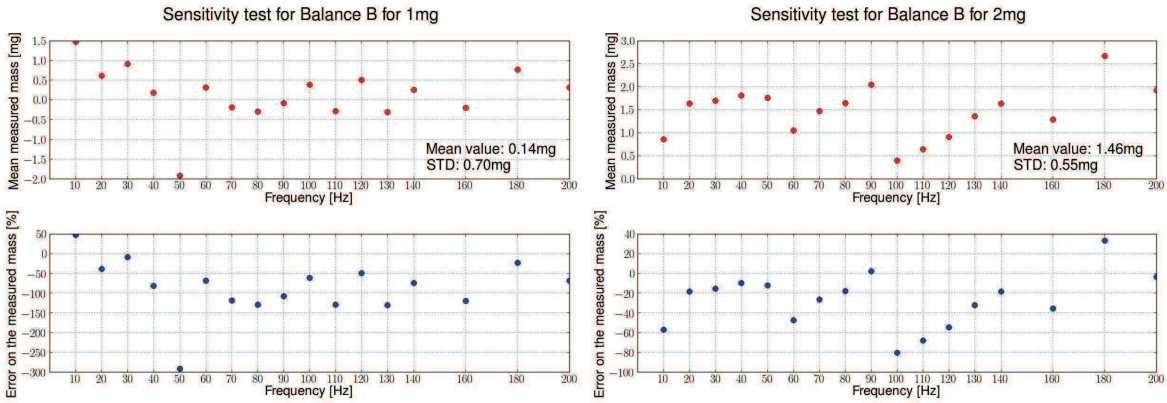

(a) $1mg$

(b) $2mg$

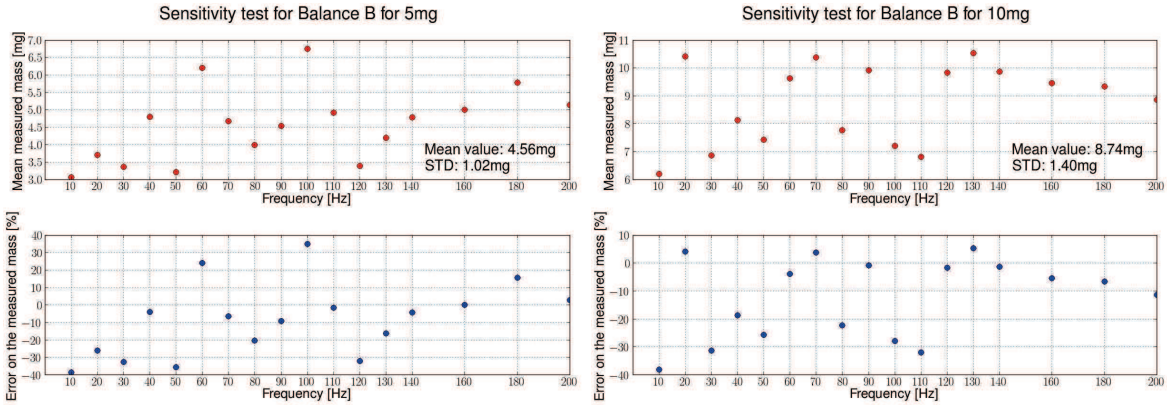

(c) $5mg$

(d) $10mg$

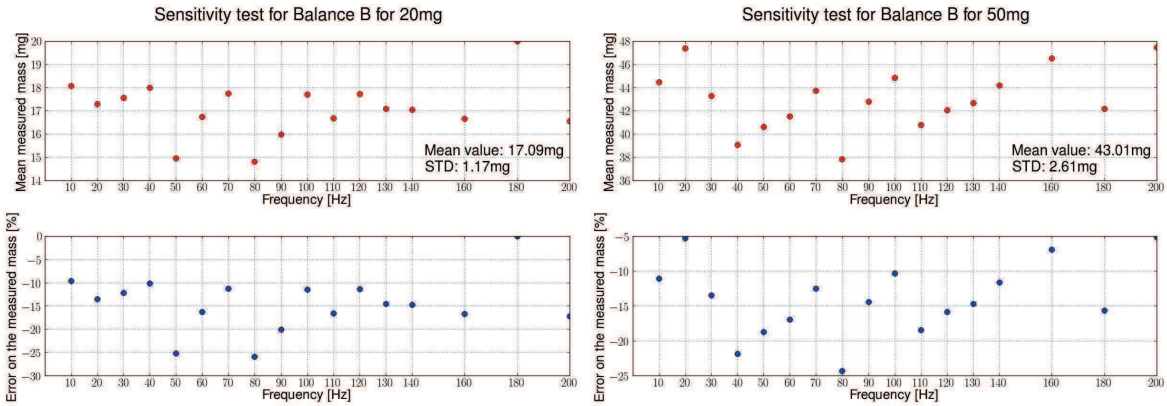

(e) $20mg$

(f) $50mg$

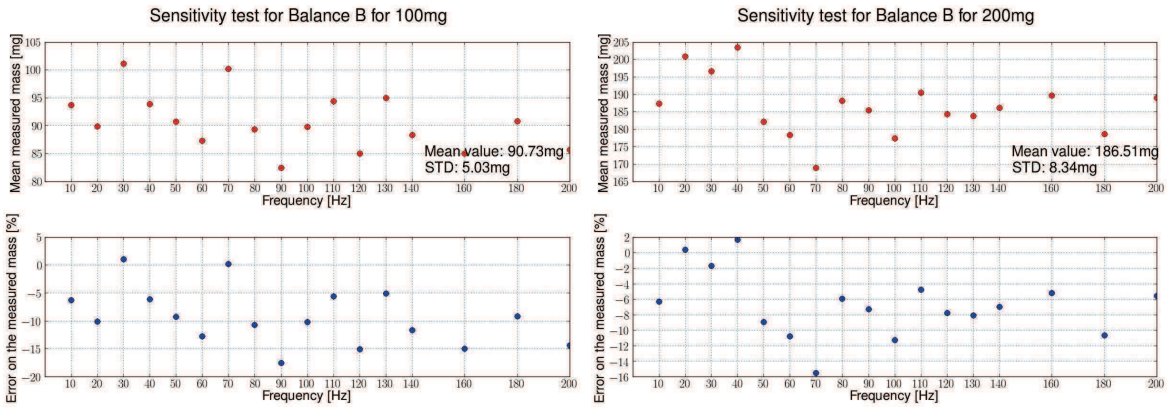

(g) $100mg$

(h) $200mg$

Figure C.16: Sensitivity test of the balance B

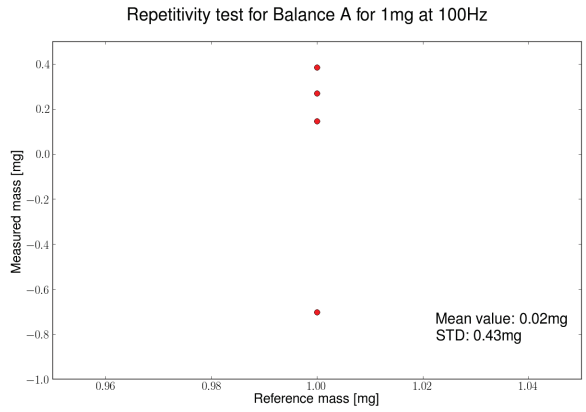

(a) $1mg$

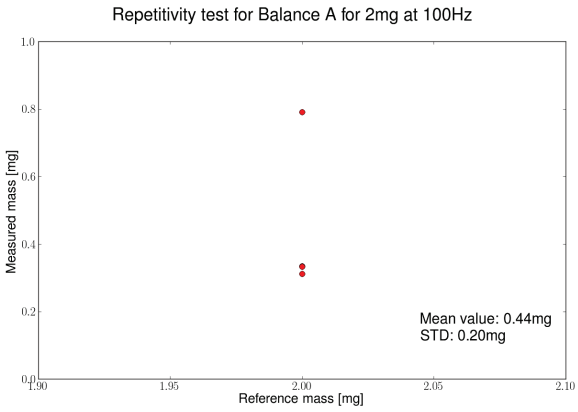

(b) $2mg$

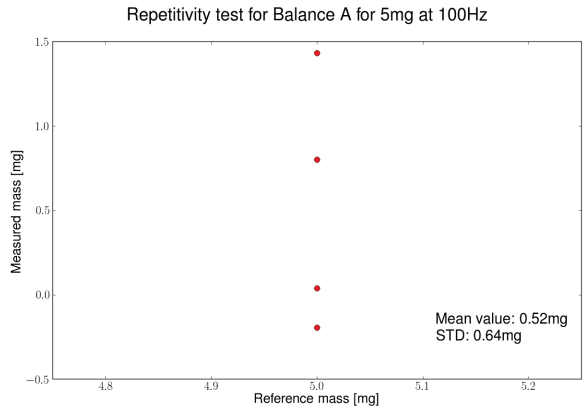

(c) $5mg$

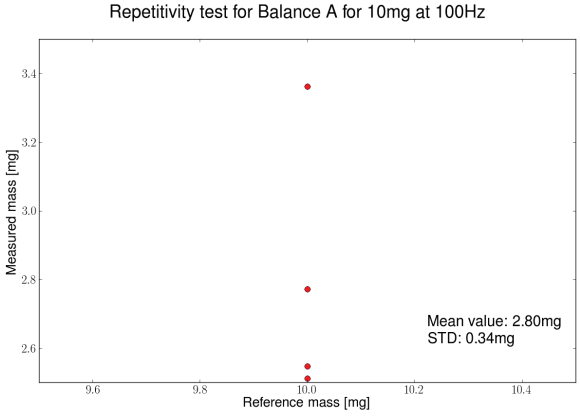

(d) $10mg$

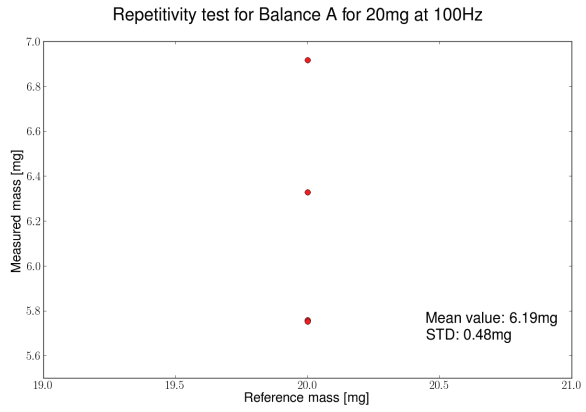

(e) $20mg$

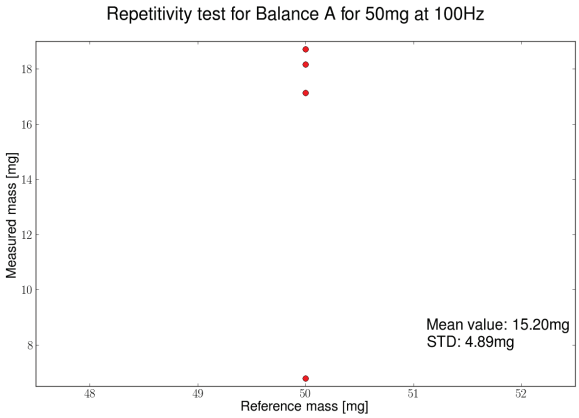

(f) $50mg$

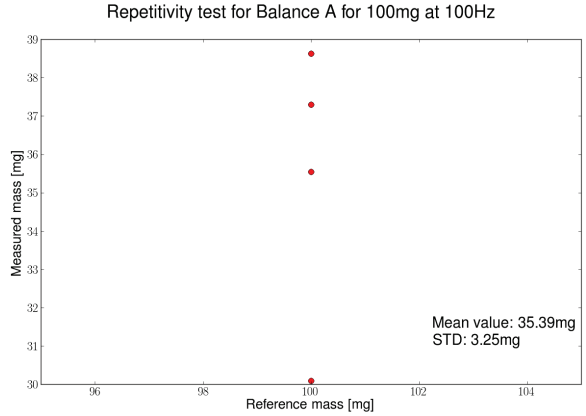

(g) $100mg$

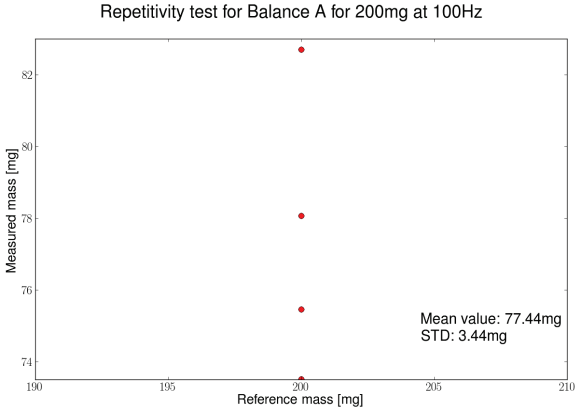

(h) $200mg$

Figure C.17: Sensitivity test of the balance A.

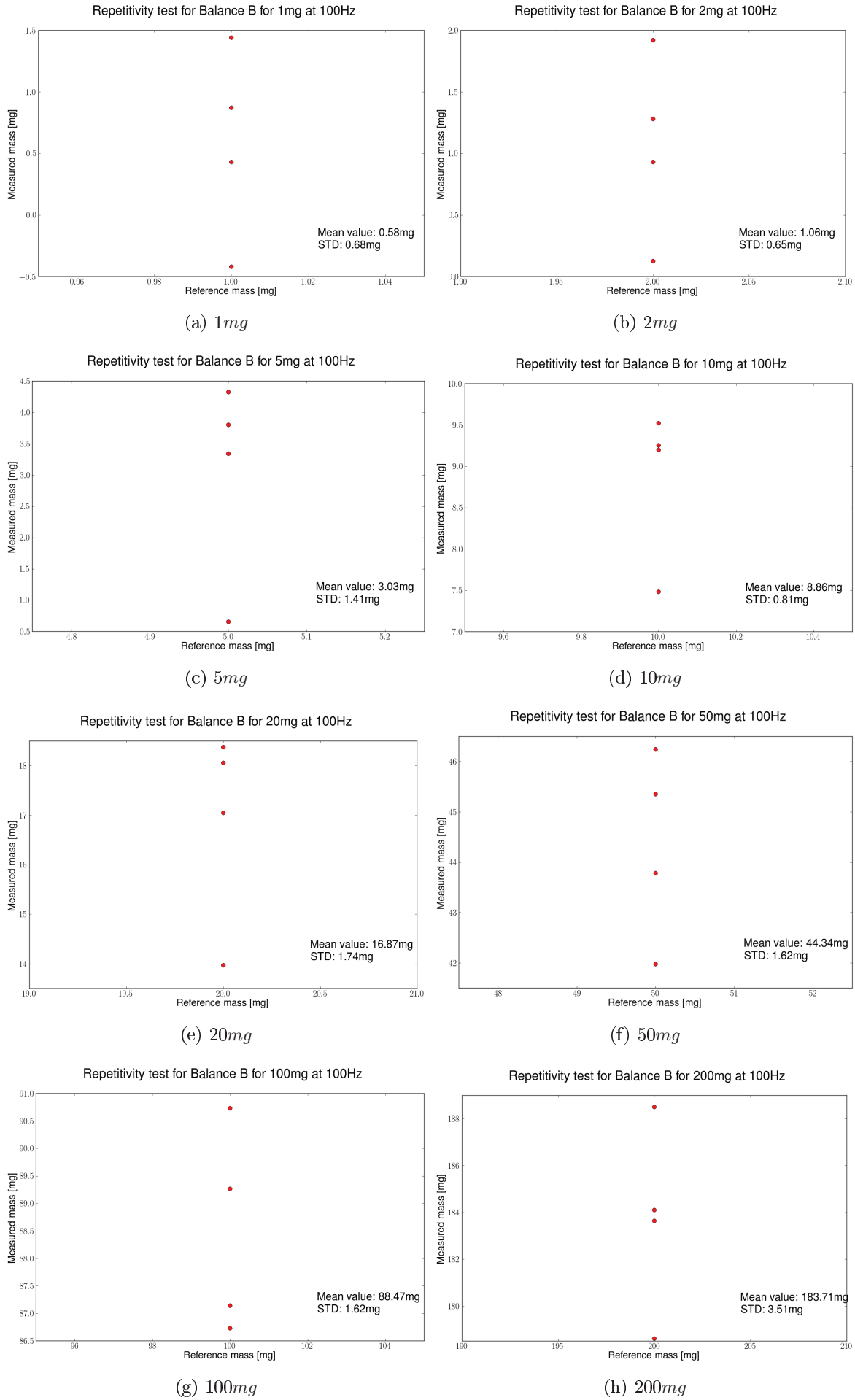

(a) $1mg$ (b) $2mg$

(c) $5mg$ (d) $10mg$

(e) $20mg$ (f) $50mg$

(g) $100mg$ (h) $200mg$

Figure C.18: Sensitivity test of the balance B.

C.2.4 Remarks on the characterization of the balance

The results given in the section C.2.2 and C.2.3 highlight that the balance B is the best compromise within the in-house balances to measure the aerodynamic forces on a flapping wing. However the balances are very sensitive to EMI and also to their calibrations influenced by the room temperature, the storage condition and so on. To counter the former or at least try, all electronic equipment is now on plugged to a power-inverter leaving the test bench free from any noise from the electrical network. To counter the latter, a calibration of the balance is recommended before each use or at least each time the balance is stored and/or unplugged. These remarks are illustrated in the section C.4 with the figure C.20 with novel calibration curves for the balance B.

C.3 Methodology for the acquisition of the aerodynamics forces generated by a wing

A methodology is here proposed to measure the aerodynamic forces and thereafter to further validate the aeroelastic framework by comparing experimental data to numerical one. It hereby could provide validations for the both the aerodynamic model and the aeroelastic coupling. Only the lift component is investigated as it represents the main bottleneck in the design of the OVMI.

To measure the forces, the in-house balances presented in C.2 are used in order to retrieve at least the mean or at best the instantaneous lift generated by several strokes. The key of the aerodynamic forces measurement lays first within the sensitivity and bandwidth of the balance and secondly by the appropriate subtraction of the inertial forces. The former is a constraint imposed by the hardware and almost no workaround are possible, whereas the latter can be handled appropriately with meticulous and methodical experiments. Measurements of the aerodynamic forces is here only reported for the resonant frequency of the wing in vacuum, but the methodology applies also to the one in air.

While the wing is mounted at its root to the free end of the balance, the other end is actuated by the piezoelectric actuator as illustrated in the figure C.19. The balance is here simultaneously used as an excitation transmitter and a force sensor. This is a minor bottleneck of this method as it reduces the sensitivity of the balance as underlined in the section C.2.3. However, the actuation has the merit to be highly repetitive and to have well-established boundary conditions when compared to direct measurement on prototype.

Assuming the resonant frequency of the wing under vacuum is known, the vibrometer is aimed at the wing so as to track the velocity magnitude of one point, as for example the leading edge tip on figure C.19. Starting in air and with the wing vibrating, the piezoelectric and the vibrometer data are acquired as well as the forces measured by the balance, i.e. the sum of the aerodynamic forces and of the inertial forces. Without altering the setup, the vacuum is made within the chamber and the wing is actuated. Due to the lack of air damping, the amplitude of the wing motion is larger than in air and is not anymore representative of the inertial forces encountered during the air motion. Thanks to the vibrometer and by assuming on one hand that the mode shape is unaffected by the vacuum and on another hand that the air damping on the balance probe is negligible (small deflection of foil is expected), the amplitude of one point of the wing is known in air and is measured again in vacuum. By adjusting the actuation amplitude, the same velocity magnitude is reached again and a new acquisition is launched to measure only the inertial forces. By synchronizing both acquisitions and subtracting them afterwards, the aerodynamic forces are then extracted.

For the acquisition, a *Labview* program is used as well as the associated *NI* modules. Both modules will generate and acquire data at $5kHz$ for $10s$. Three consecutive runs are made for each configuration in order to average the data and reduce the discrepancy.

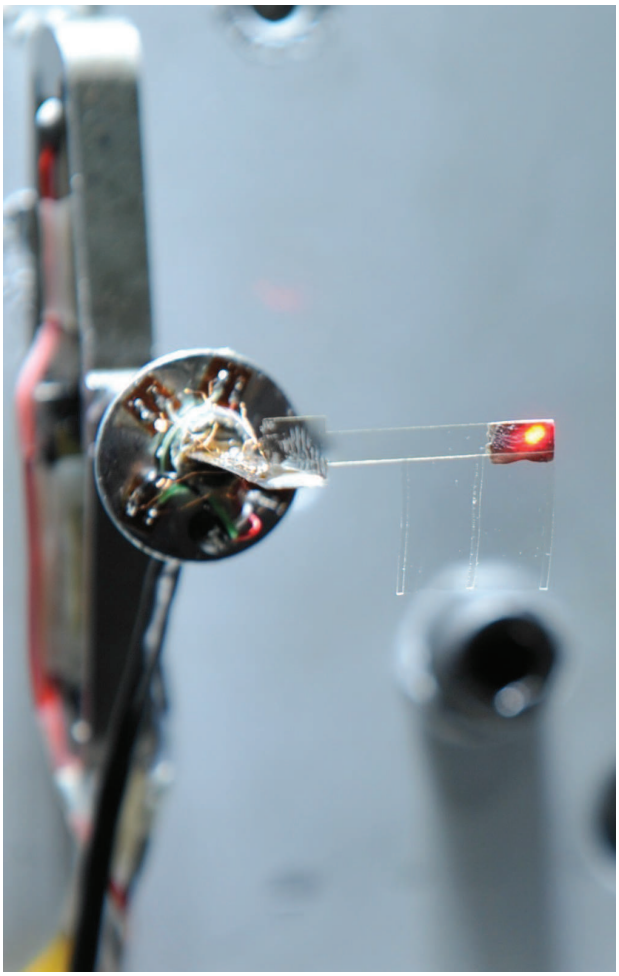

Figure C.19: Wing EM5 mounted on the balance B with the vibrometer (red spot) retrieving the leading edge amplitude in order to match the air and vacuum displacement of the structure and thus subtract the inertial forces from the forces measured in air leaving out only the aerodynamics forces.

For the post-processing, a *Python* script is used to synchronize data of each run on the piezoelectric input signal, to average them, to subtract the vacuum data from the air one, and finally to plot and store the final data for later review.

C.4 Proofs of concept

With both balances characterized, the balances have to be tested in real conditions for the two main applications: the measurement of the forces on real prototype, with the balance being static, and on validation wing, with yet the balance actuated at its root by the piezoelectric shaker. For both cases, only the balance B is further tested as it shown the best performance in both static and dynamic conditions. A calibration of the balance is done before each case as reported in the figure C.20.

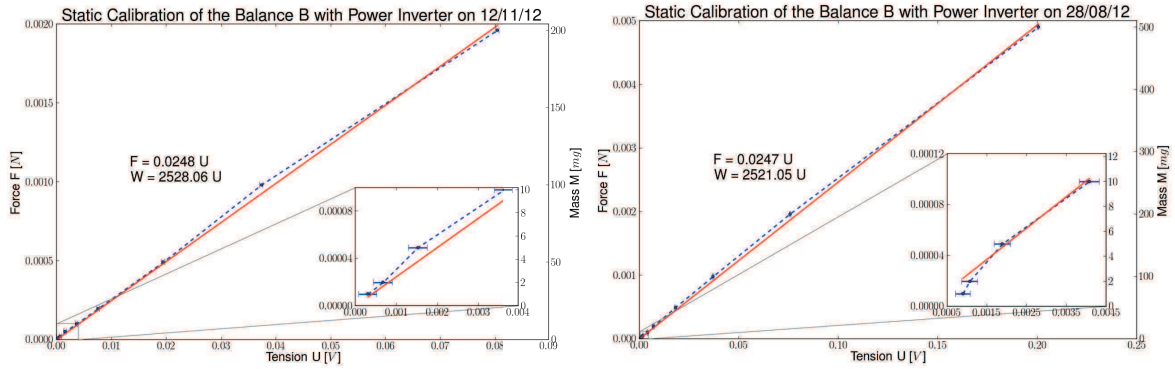

(a) Static demonstration (b) Dynamic demonstration

Figure C.20: Calibration curves of the balance for the proofs of concepts, the static and the dynamic force measurement. All electronic equipment is connected to a power-inverter to minimize the EMI noise. A large difference is observed with the previous calibration presented in the figure C.11(b).

C.4.1 Static force measurement

The aim of this demonstration is to assess the performance of the balance with a real OVMI prototype in order to get an estimate of its aerodynamic performances and thus to improve step-by-step the prototype and develop an airborne version of it more quickly.

To do so, the prototype is glued perpendicularly to the foil as shown in the figure C.21 so that the balance can 'see' the vertical force generated by the wing strokes. Two copper wires are stepping out of the prototype, one upwards and the other downwards, to power the electromagnet of the prototype. They are positioned such that the balance is not stiffened in anyway. The actuation frequency is set so that both wings flapped in phase, which is quite tricky, and the current is increased gradually to protect the prototype from breaking and the coil from melting. To measure the force generated, the balance is first nulled with the unpowered prototype weighting at its end. Then the prototype is powered and the acquisition is triggered shortly afterwards and the results are available for post-processing. Eventually, the high speed camera is adjusted to capture the wing deformation as well. Typical results are shown in the figures C.22 and C.23, which are almost identical prototypes, differing only by the placement of the flyweights.

For both prototypes, a periodic motion is seen with an average positive vertical force. As highlighted by the trace of the wing tip in figures C.22(b) and C.23(b), the first prototype has a larger stroke

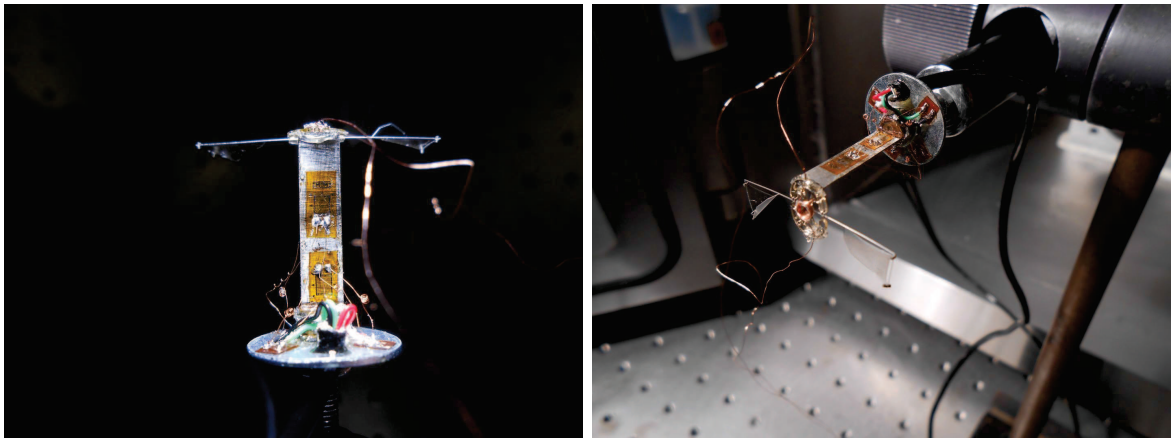

(a) Top view (b) Side view

Figure C.21: Overview of the setup for force measurement on a prototype, i.e. static configuration

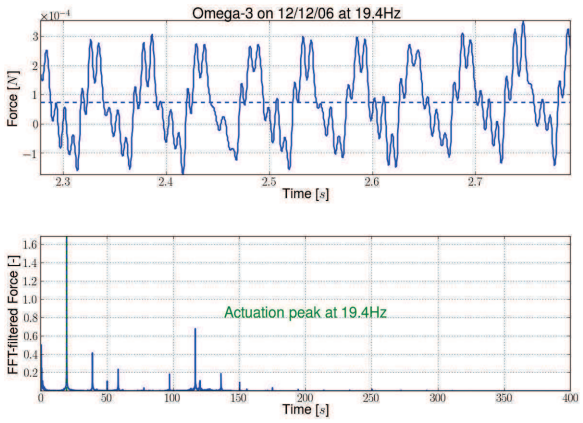

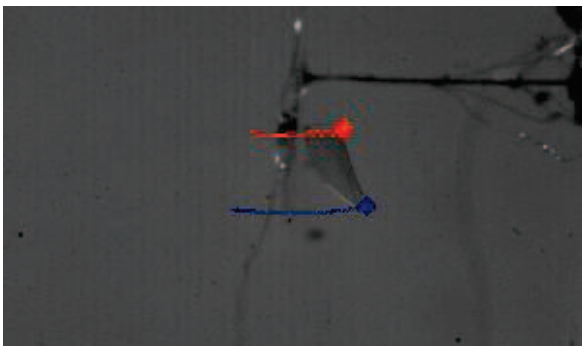

(a) Measured Force and its FFT (b) Trace of the wing tip

Figure C.22: Force measurement on a prototype at $19.4Hz$ where both wings flapped in phase. The forces measured, the sum of the aerodynamic and the inertial forces, during 10 strokes along with its frequency spectrum are presented in C.22(a), where the blue dotted line is the averaged force over the entire run $\bar{F} \sim 85\mu N$. In C.22(b), the trace of the wing type during those ten strokes is shown, where the red and blue dots represent the leading and the trailing edge respectively.

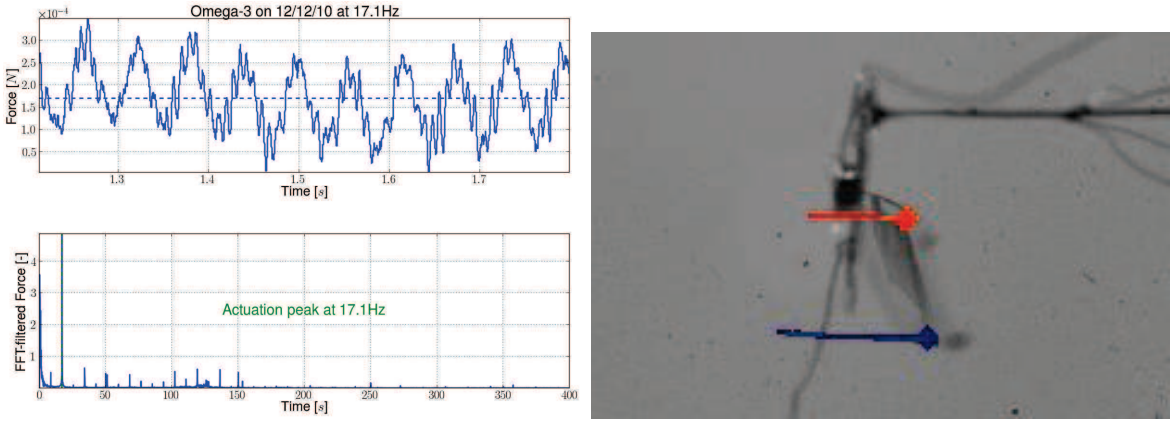

(a) Measured Force and its FFT

(b) Trace of the wing tip

Figure C.23: Force measurement on a prototype at $17.1Hz$ where both wings flapped in phase. The forces measured, the sum of the aerodynamic and the inertial forces, during 10 strokes along with its frequency spectrum are presented in C.23(a), where the blue dotted line is the averaged force over the entire run $\bar{F} \sim 202\mu N$. In C.23(b), the trace of the wing type during those ten strokes is shown, where the red and blue dots represent the leading and the trailing edge respectively.

amplitude which results in a larger force amplitude as captured by the balance. However, its wing stroke is almost symmetrical and both wing shapes slightly out of phase, resulting in a slightly positive mean force. In comparison the second prototype has a smaller wing stroke amplitude but both wings are more in phase resulting in a larger positive mean force. These observations are well correlated by the curves. Furthermore the resolution and time of response of the balance is also satisfactory as shown by the tiny oscillation captured and the repetitivity of such features.

Therefore the data given by the balance acknowledges that the force generated by the OVMI prototype are captured quite well, that the balance is correctly sized for this application and finally that the balance can be used to improve the design of the prototype towards an airborne design.

C.4.2 Dynamic force measurement

The aim of this demonstration is to assess the performance of the balance with a validation wing actuated through the balance. To do so, a wing is glued perpendicularly to the foil as shown in the figure C.19 so that the balance can 'see' the vertical force generated by the wing strokes. Using the methodology described in section C.3, the lift forces can be extracted from measurement made consecutively in air and in vacuum. The tricky part in this methodology is to match the vacuum wing motion with the air one in order to subtract the correct amount of inertial forces.

Results are given for both a E-Beam without membrane, in figures C.24 and C.25, and with membrane, EM4, in figures C.27 and C.28, at their air and vacuum resonant frequency. Each figure represents in the upper figure, the vertical force measured in air and in vacuum and their instantaneous difference i.e. the lift as well as a FFT analysis of those signals. Due to the high level of EMI noise on the signal, a noise-free version of them is plotted in the lower figure resulting generally in a much lower lift force. Each signal is filtered by zeroing the FFT coefficients at $50Hz$ and at each of its odd-multiples and converting the signal back to the time domain.

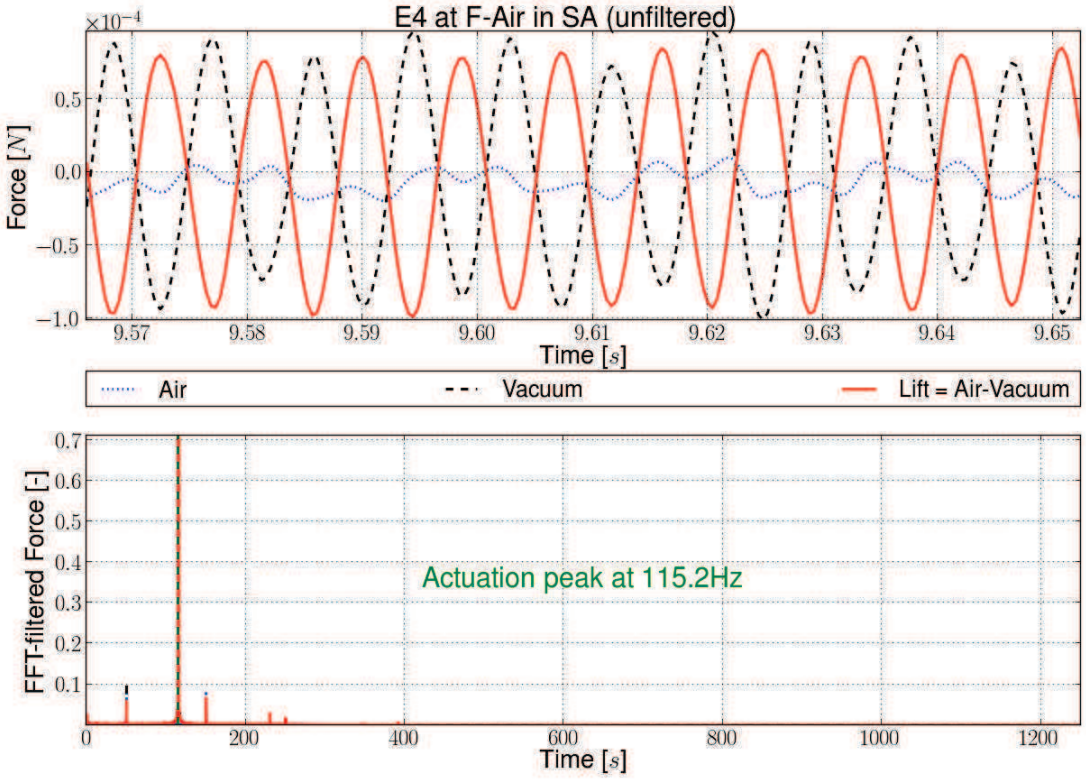

(a) Unfiltered

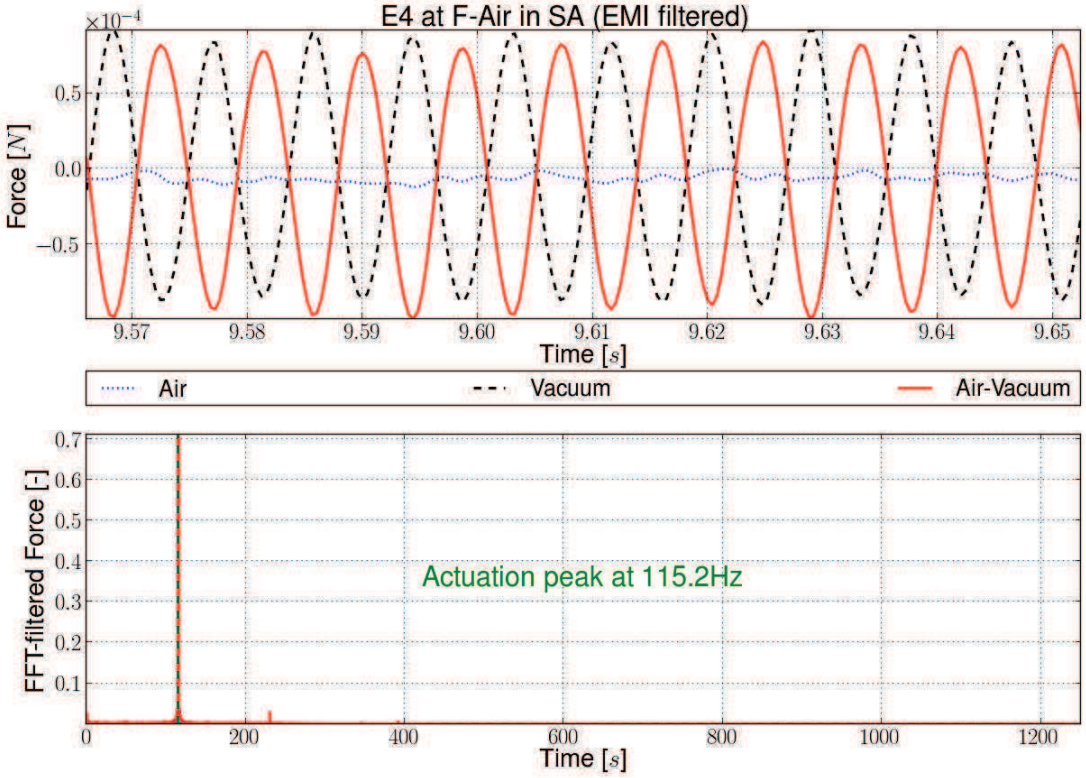

(b) Filtered

Figure C.24: Lift force generated by a E4 wing in small actuation at its air resonant frequency. C.24(a) illustrates the raw measured data for ten strokes along with an FFT analysis of the forces, highlighting EMI noise in the data. This noise is artificially suppressed by nulling the corresponding coefficient in the FFT analysis and recomposed. The amplitude of the forces is drastically reduced as shown in C.24(b). An average lift of -0.2μN is measured for a 18.95μm heaving actuation. However the results are here ambiguous due to the vacuum forces larger than the air forces.

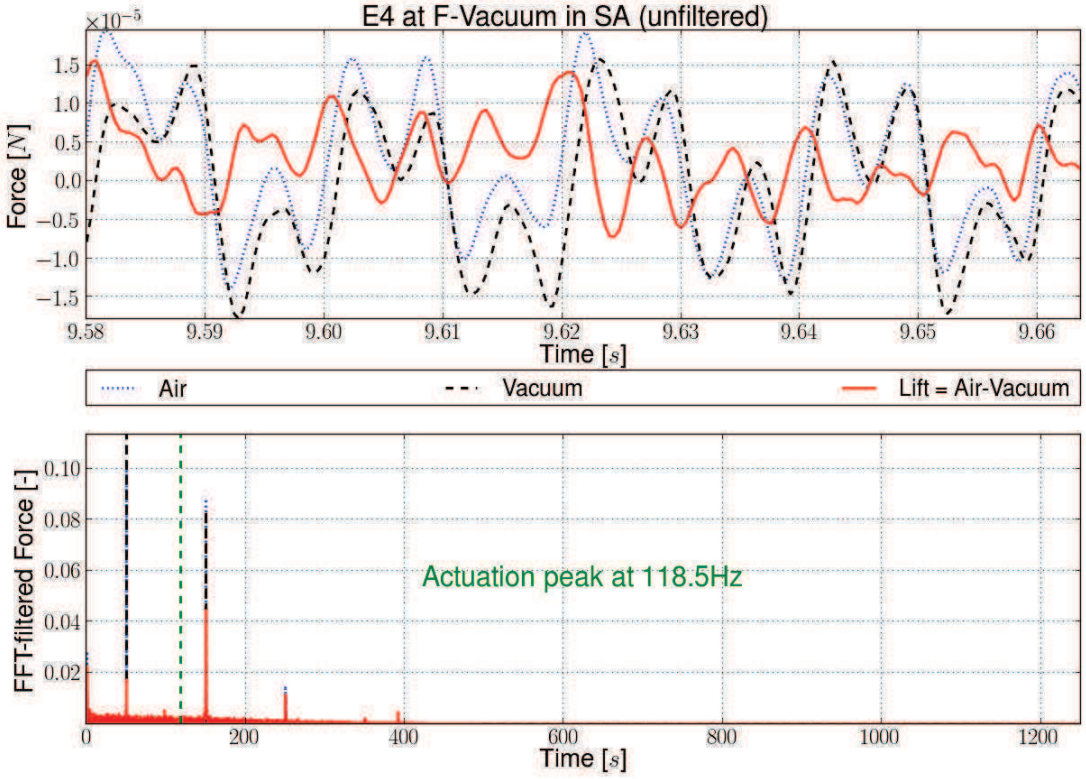

(a) Unfiltered

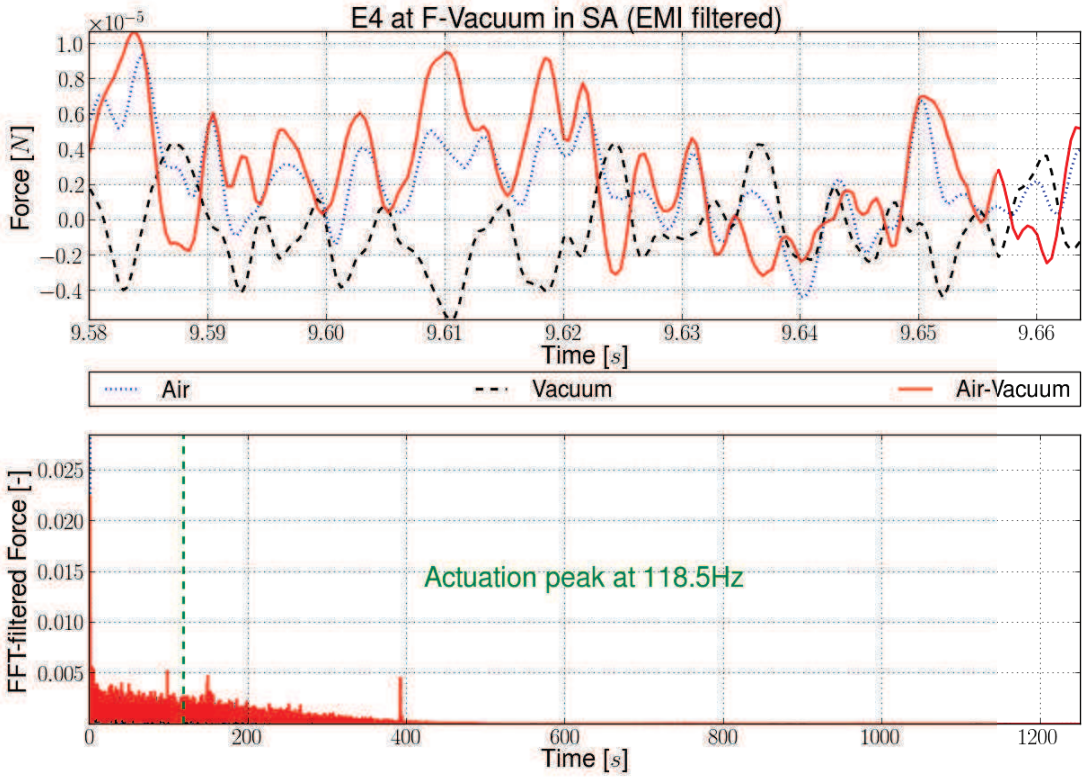

(b) Filtered

Figure C.25: Lift force generated by a E4 wing in large actuation at its vacuum resonant frequency. C.25(a) illustrates the raw measured data for ten strokes along with an FFT analysis of the forces, highlighting EMI noise in the data. This noise is artificially suppressed by nulling the corresponding coefficient in the FFT analysis and recomposed. The amplitude of the forces is drastically reduced as shown in C.25(b). An average lift of -1.9μN is measured for a 19.86μm heaving actuation.

C.4.2.1 Dynamic test on wing without membrane

For the wing without membrane at the resonant frequency in air, the results are quite puzzling as the forces measured in vacuum are larger than those in air as seen in the figure C.24. The most plausible explanation is an experimental handling error in the wing amplitude matching procedure resulting in larger inertial forces in vacuum than those measured in air. This error is partially confirmed by the fact that both signals are periodic and over the balance sensitivity, and above all by the measurement at the vacuum air frequency shown in the figure C.25.

At the resonant frequency in vacuum, the forces measured in vacuum are globally lower than the ones measured in air indicating the generation of aerodynamic forces by the wing. A periodic motion can clearly be seen in the unfiltered signals but much more hardly in the filtered signals. This lake of periodicity in the filtered signal might be due to the limited bandwidth of the in-house balance, as the wing actuation frequency, here $118.5Hz$, is around the half of the balance resonant frequency. Furthermore with the signal maxima reaching hardly $10\mu N$, the instantaneous value are well below the calibration range and can not therefore be trusted. However, a mean lift of -0.2μN is reported as a rough approximation of the lift. This value is in the same order of magnitude as the one given by the aeroelastic framework with a mean value of $0.2\mu N$ as seen in figure C.26(a) or even $0.6\mu N$ given by the unidirectional approach in figure C.26(b). Nonetheless, other comparisons are not possible and are purely speculative.

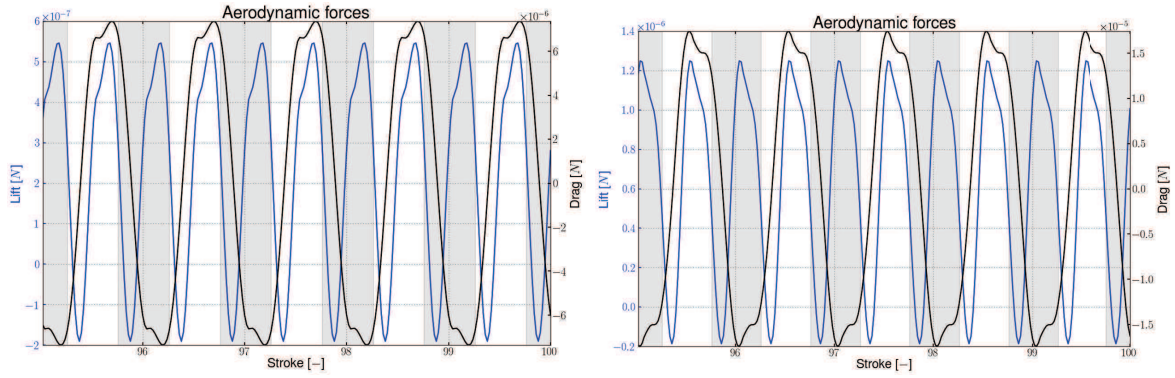

(a) Bidirectional flexible approach

(b) Unidirectional flexible approach

Figure C.26: Aerodynamic forces computed using the aeroelastic framework for the wing E4 with the same actuation at the vacuum resonant frequency. The mean lift force is $0.2\mu N$ using the bidirectional flexible approach and $0.6\mu N$ using the unidirectional flexible approach.

C.4.2.2 Dynamic test on wing with membrane

For the wing with membrane, very encouraging results are found as shown in the figure C.27 and C.28. A periodic motion is more clearly seen in both the unfiltered and filtered signals for both the resonant frequencies in air and in vacuum . This might be due to the lower actuation frequency at $85Hz$ and at $92.1Hz$ respectively as well as the higher aerodynamic generated by the membrane. Even if the actuation displacement are not comparable, the forces measured by the balance for wing with membrane are much higher, with at least an order of magnitude difference, catching this positive effect of the wing membrane on the generation of aerodynamic forces. However, the maximal values are again flirting below the calibration range of the balance and can not be therefore trusted. Indicative values for the mean aerodynamics are around $2.6\mu N$ for a $9.2\mu m$ heaving actuation at the resonant frequency in air and around $9\mu N$ for a $61.1\mu m$ heaving actuation at the one in vacuum. Those results are slightly larger but almost of the same order of magnitude than the one given by the aeroelastic framework with a mean value of $1.7\mu N$ as seen in figure

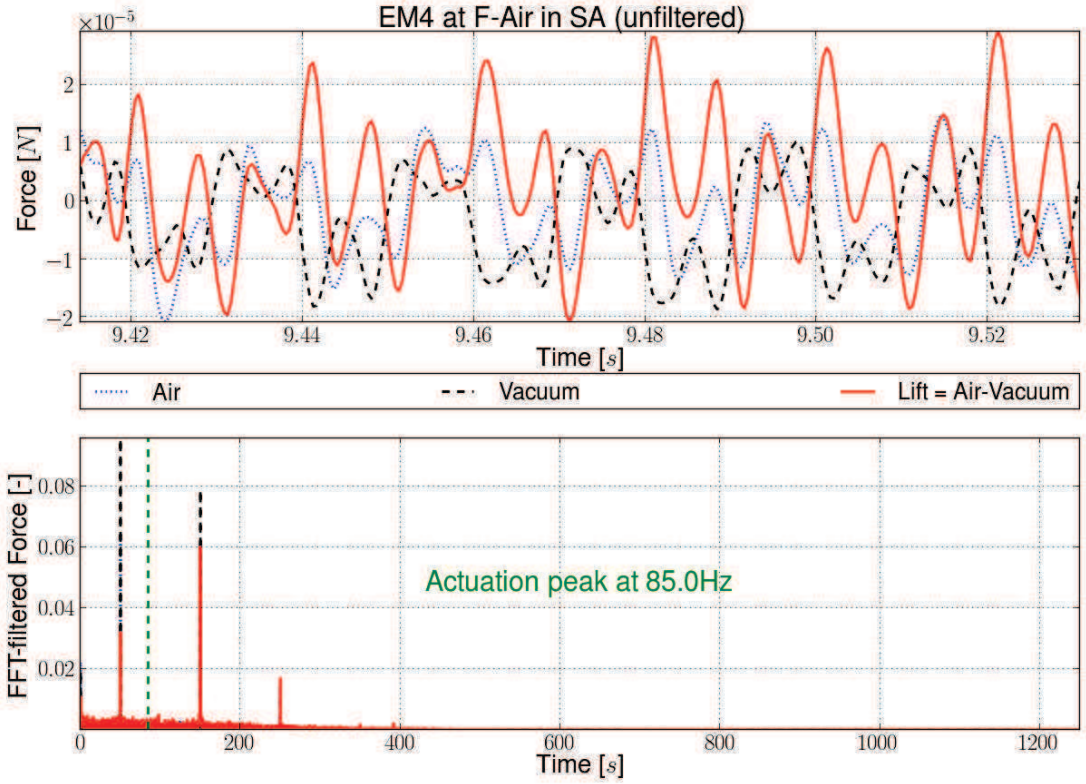

(a) Unfiltered

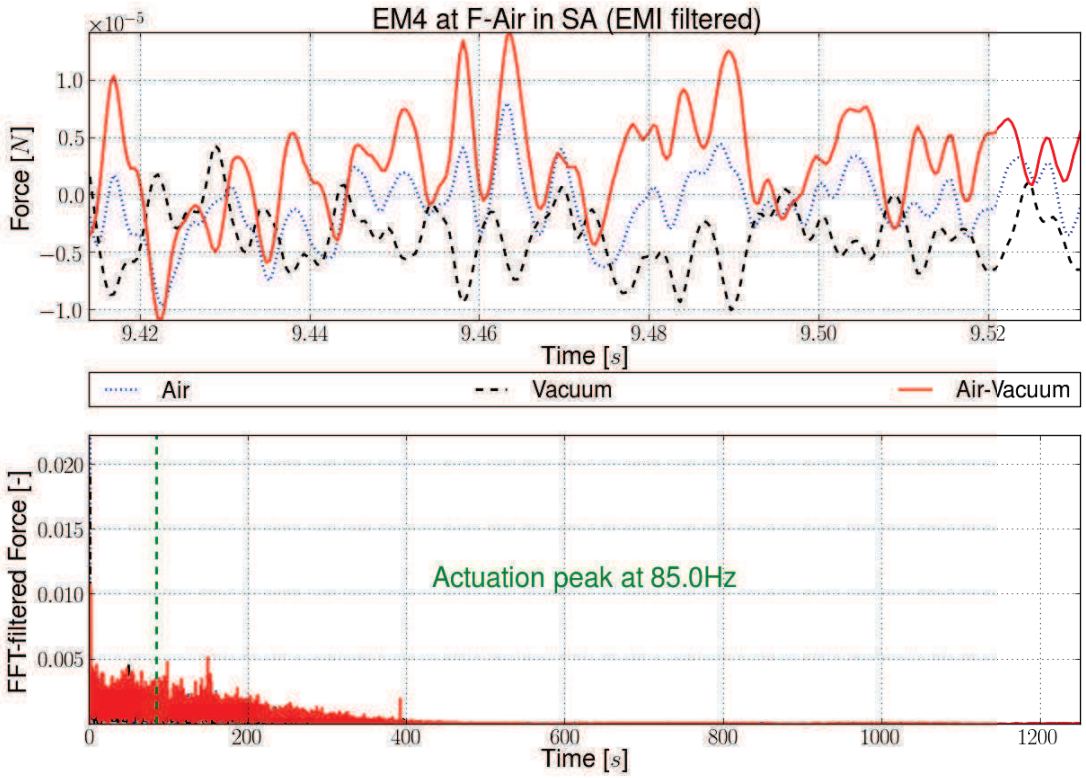

(b) Filtered

Figure C.27: Lift force generated by a EM4 wing in small actuation at its air resonant frequency. C.27(a) illustrates the raw measured data for ten strokes along with an FFT analysis of the forces, highlighting EMI noise in the data. This noise is artificially suppressed by nulling the corresponding coefficient in the FFT analysis and recomposed. The amplitude of the forces is drastically reduced as shown in C.27(b). An average lift of $2.6\mu N$ is measured for a $9.2\mu m$ heaving displacement at the wing root.

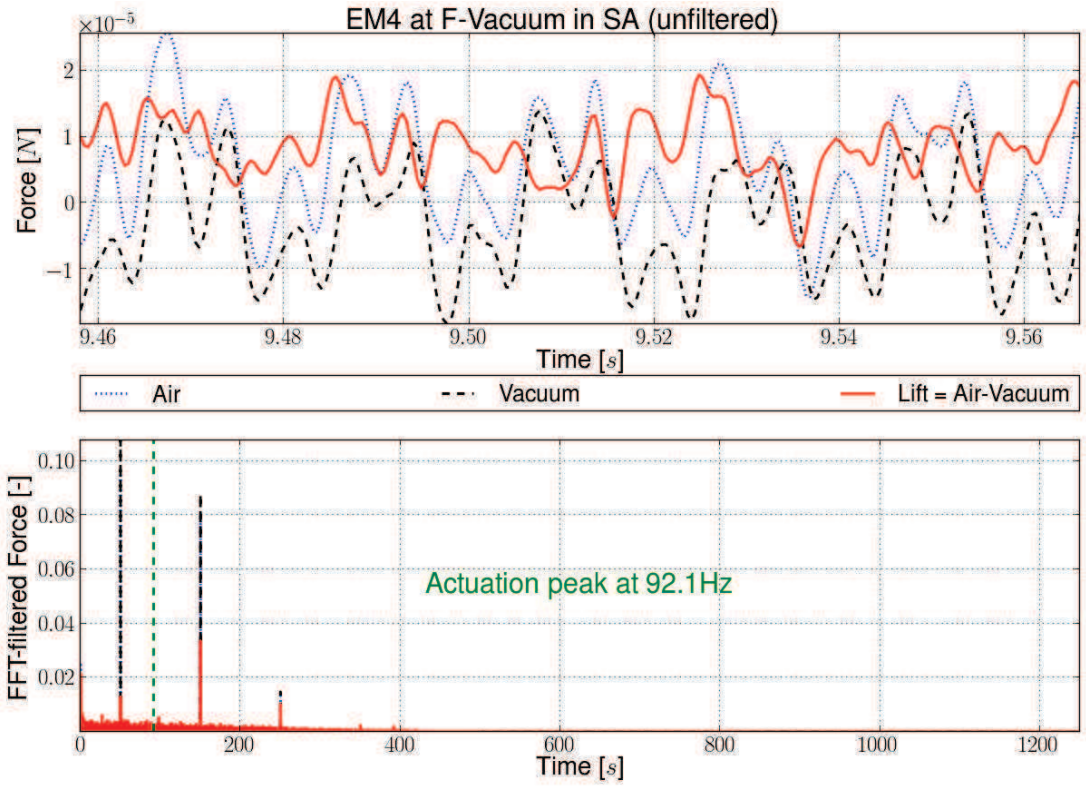

(a) Unfiltered

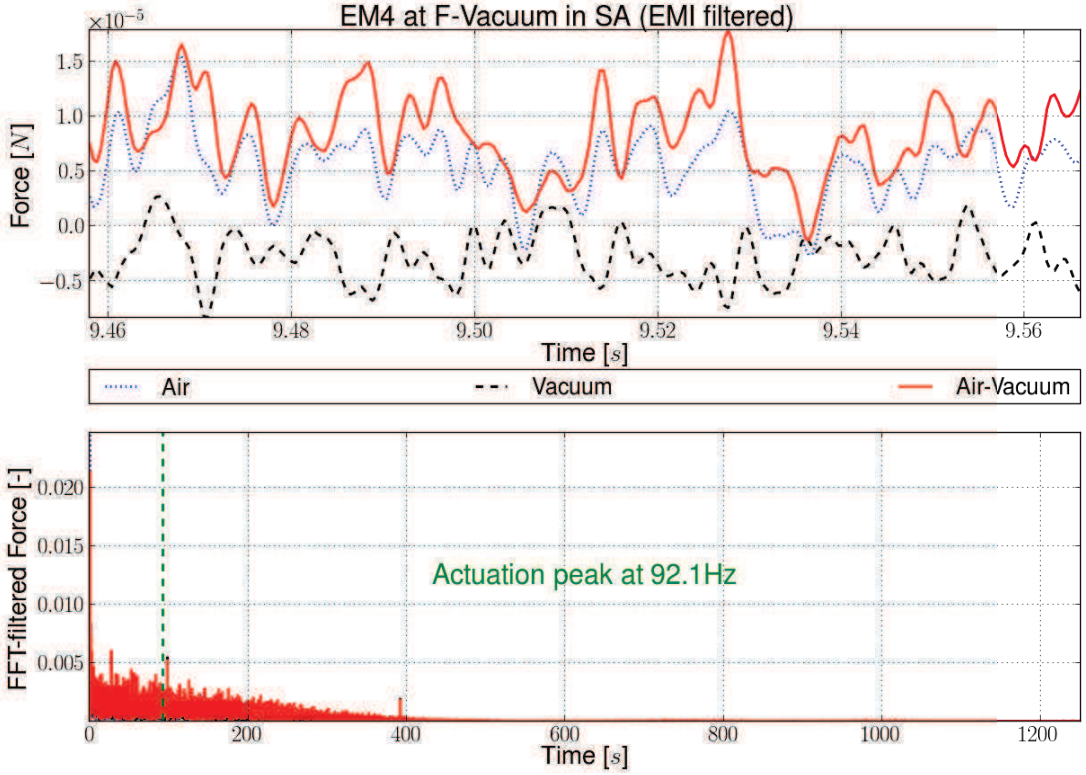

(b) Filtered

Figure C.28: Lift force generated by a EM4 wing in large actuation. C.28(a) illustrates the raw measured data for ten strokes along with an FFT analysis of the forces, highlighting EMI noise in the data. This noise is artificially suppressed by nulling the corresponding coefficient in the FFT analysis and recomposed. The amplitude of the forces is drastically reduced as shown in C.28(b). An average lift of $9\mu N$ is measured for a $61.1\mu m$ heaving displacement at the wing root.

C.29(a) or even $4.3\mu N$ given by the unidirectional approach in figure C.29(b). Nonetheless, other comparisons are not possible and are purely speculative.

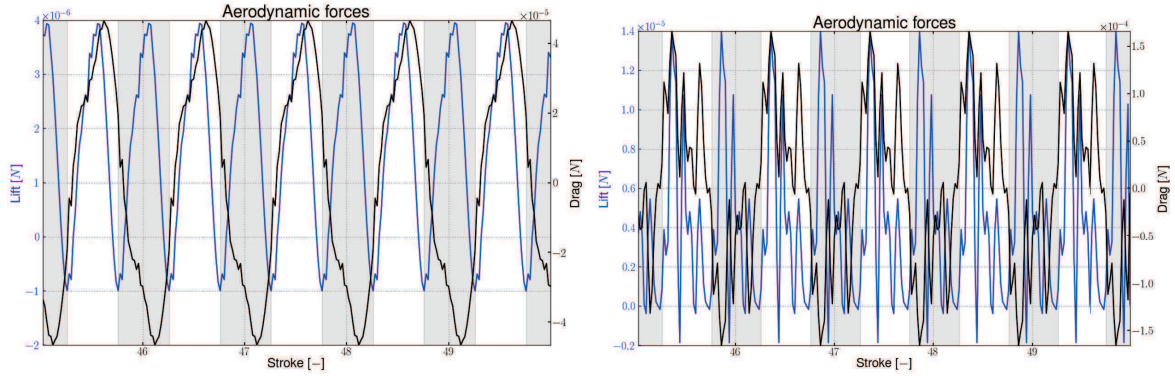

(a) Bidirectional flexible approach

(b) Unidirectional flexible approach

Figure C.29: Aerodynamic forces computed using the aeroelastic framework for the wing EM4 with the same actuation at the vacuum resonant frequency. The mean lift force is $1.7\mu N$ using the bidirectional flexible approach and $4.3\mu N$ using the unidirectional flexible approach.

C.5 Conclusion and development perspective on the in-house balance

One task of this work has been to develop a force sensor enabling the measurement of aerodynamic forces both for prototypes and for the validation wing shapes. The former with the actuation onboard does not need a outside actuation unlike the latter which requires the balance to transmit the actuation from the piezoelectric shaker to the wing. This dual role has proved itself to be tricky and challenging since a compromise has to be found between the sensitivity and the bandwidth, generally two opposing functions. Unfortunately this task is not completely fulfilled at the end of this work but, instead a simple design, relying on the bending of a foil, has been tested paving the way, hopefully, to more reliable and accurate solutions.

Concerning the measurement of forces generated by prototype, the balance is able to capture such forces and gives, qualitatively, consistent results, at least for wing at low frequency ($<20Hz$) as prototypes with higher frequency are not available at the time of this works. The mean values of lift are in agreement with the one computed by the aeroelastic framework using both approaches. The ability to cross-check the data with the wing motion, captured by the camera, gives an unique opportunity to improve the prototype towards an airborne design. Therefore the results for this application are very encouraging even if they have to be taken very cautiously and validated. To do so, a synchronized acquisition of the deformation of the two wings, enabling the computation of the aerodynamic and of the inertial forces using a quasi-steady approach, can be compared to the balance data. Another drawback of the method is that the pure aerodynamic forces are not extracted, which might drives designers in a dead end, but tracking the wing deformation might enable to numerically subtract the inertial forces.

Concerning the measurement of the forces generated by pure wings, it is hard to draw, for now on, some conclusions about the balance capability. The balance sees definitively some forces but several doubts are left concerning their validity. First, since the measured forces are below the calibration range of the balance and since the accuracy and repetitivity increased with the load, more static and dynamic characterization tests have to be undertaken below the $1mg$, defined initially as the lower boundary for the measurement capability, before trusting further the data. Second, the force subtraction process have to be improved. Indeed the displacement were matched near the leading-edge tip for convenience, but this spot is not where

the maximal inertial forces are acting. Thus even if the displacements near the leading-edge tip are alike, the displacement at the trailing-edge tip is most probably still over the one encountered in air and thus the subtraction process overestimates the inertial forces. Similarly, the assumption made on the mode shape that hold between air and vacuum is misleading as the phase-lag between the wing root and tip are different due to the aerodynamic load. A solution might be to use the camera to track the wing deformation, even if then the whole process becomes then quite time-consuming considering the number of iterations needed to adjust the amplitude, and to subtract the inertial using the FE model of the wing. Third, due to the high actuation frequencies of the wings, the quality of the measure is greatly affected by the limited bandwidth of the balance. Fourth, the balance calibration was completed under air and it was assumed that the calibration curve stays in vacuum, which is doubtful considering the lower heat dissipation in vacuum. Fifth, large amount of EMI noise are captured by the balance in this application which is the consequences of the design itself as the raw copper wires and also every unshielded parts act like an antenna. Furthermore no signal amplification is made directly after the sensor but only on the acquisition module and thus tends to propagate further and capture additional EMI noise.

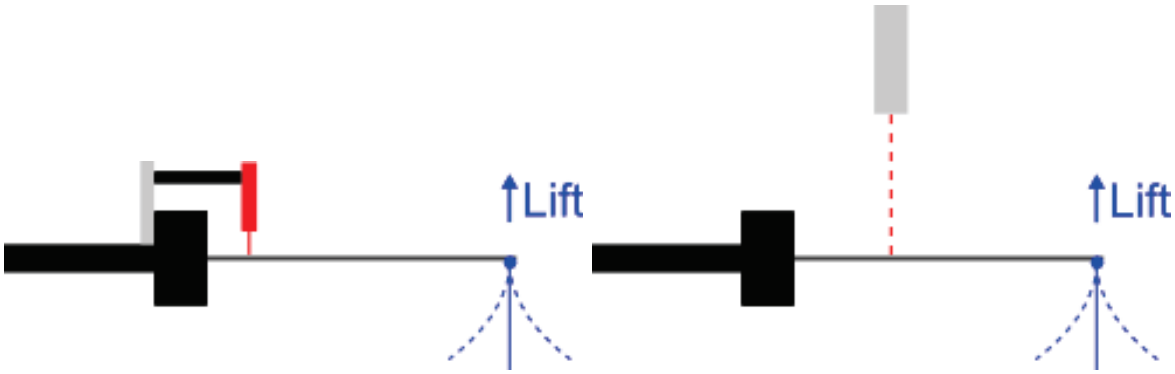

(a) Using a femtoTools sensor (b) Using an optical sensor

Figure C.30: Improvement concepts for the in-house balance. Both concepts are tracking the deflection of the foil at one point due to the forces generated by the wing, either using a FemtoTools sensor or an optical sensor. A two components balance (lift and yaw) can also be considered used more advance optical techniques such as stereo-correlation or digital holographic interferometry.

To improve the design of the in-house balance towards greater sensitivity and bandwidth, two approaches are suggested in figure C.30 that are trying to minimize the EMI noise by removing any EMI-sensitive part and also using more sensitive sensors than traditional foil strain gages. Additionally, the foil can be adjusted for a larger resonant frequency with both concepts.

The first one is replacing the strain gages by a FemtoTools sensor fixed above the balance with its probe linked by capillary action to the foil upper surface. The bending generated by the aerodynamic and the inertial forces of wing is then captured by the displacement of the probe. This sensor is vacuum compatible and has a very high sensitivity and bandwidth, two important aspects for the in-house balance. However, the probe has a limited displacement range and its comb is very fragile. This concept requires a very cautious operator or the balance might become quite costly both in time and in money.

The second one is replacing the strain gages by a optical sensor fixed above the balance. Two options are here available, either a laser displacement sensor, with an high resolution on one point at a long measuring distance allowing the sensor to be placed outside the vacuum chamber, giving a one component balance or using digital image correlation (Orteu [2002]) or a digital holographic interferometry techniques (Albe et al. [2000]; Desse et al. [2012]) to get a two component balance, using the bending for the lift and the torsion for the yaw, with high resolution.

The first concept is easily and quickly achievable offering a non-negligible gain in repetitivity, in accuracy and in sensitivity as the second one with the laser displacement sensor. These options are recommended for later works especially the latter. In contrast, the second option offering a two-dimensional balance is for more long term perspective but enables to account for more DOFs which might be suitable for flight mechanics purposes.

Another improvement is to move from traditional balance design based on metal to design based on MEMS. With the micromachining techniques available at the IEMN, this should not be a problem to design and fabricate such systems. A first step might be to adapt the design defined by Sun et al. [2005] or Azuma et al. [2012] to the specificity of our measures. Of course, it requires much more efforts but is of great interest to quantify also other MEMS systems in terms of forces.

In a nutshell, the balance designed in this work is capable of measuring the force generated by a prototype and see some forces generated by a pure wing actuated by the piezoelectric. Even if more works is needed to characterize the balance especially in a dynamic configuration but also in terms of measurement uncertainty, this in-house balance is a good starter to investigate more reliable and accurate devices. However, the development of this balance requires a lot of works and it should be, in the future, considered as a sole project and not as a by product.

Appendix D

Experimental validation: supplementary material

D.1 Graphical validation for wing without membrane

D.1.1 Wing F3

Table D.1: Reminder summary of the experimental/numerical comparison for F3.

Medium		**Air**	
Exp. Pressure [*mbar*]		1001	
Actuation type		SA	LA
Root	Mean Exp. Error [μm]	0.1	0.9
	STD on Exp. Error [μm]	0.0	0.3
	Exp. Amp. [μm]	7.6	78.5
	Num. Amp. [μm]	7.7	78.6
	Error Num./Exp. Amp. [%]	0	0
	Phase-shift between Num. and Exp. [*rad*]	0.00	0.00
Leading-edge	Mean Exp. Error [μm]	13.1	79.1
	STD on Exp. Error [μm]	7.4	30.7
	Exp. Amp. [μm]	206.8	1469.9
	Num. Amp. [μm]	167.0	727.6
	Error Num./Exp. Amp. [%]	**-19**	**-50**
	Phase-shift between Num. and Exp. [*rad*]	**0.88**	**1.00**
Vein	Mean Exp. Error [μm]	5.7	43.3
	STD on Exp. Error [μm]	3.0	16.3
	Exp. Amp. [μm]	107.1	792.8
	Num. Amp. [μm]	108.4	480.3
	Error Num./Exp. Amp. [%]	**1**	**-39**
	Phase-shift between Num. and Exp. [*rad*]	**0.88**	**1.00**
Tip	Mean Exp. Error [μm]	24.3	184.2
	STD on Exp. Error [μm]	12.5	73.6
	Exp. Amp. [μm]	496.2	3606.1
	Num. Amp. [μm]	902.2	3538.4
	Error Num./Exp. Amp. [%]	**82**	**-2**
	Phase-shift between Num. and Exp. [*rad*]	**0.75**	**0.75**

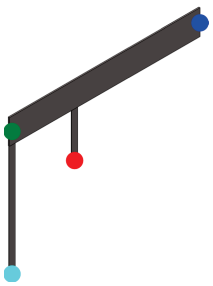

Figure D.1: CAD view of the F3 wing with its extremity colored as in the figure D.2.

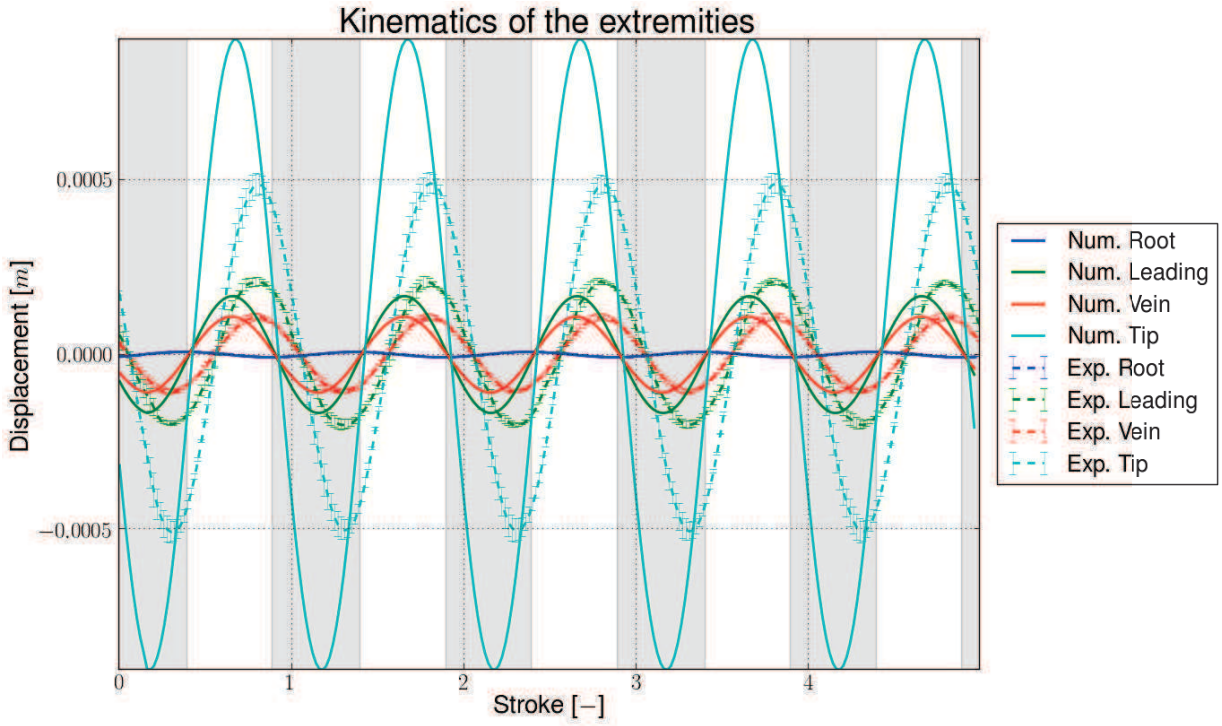

(a) Small actuation displacement (SA)

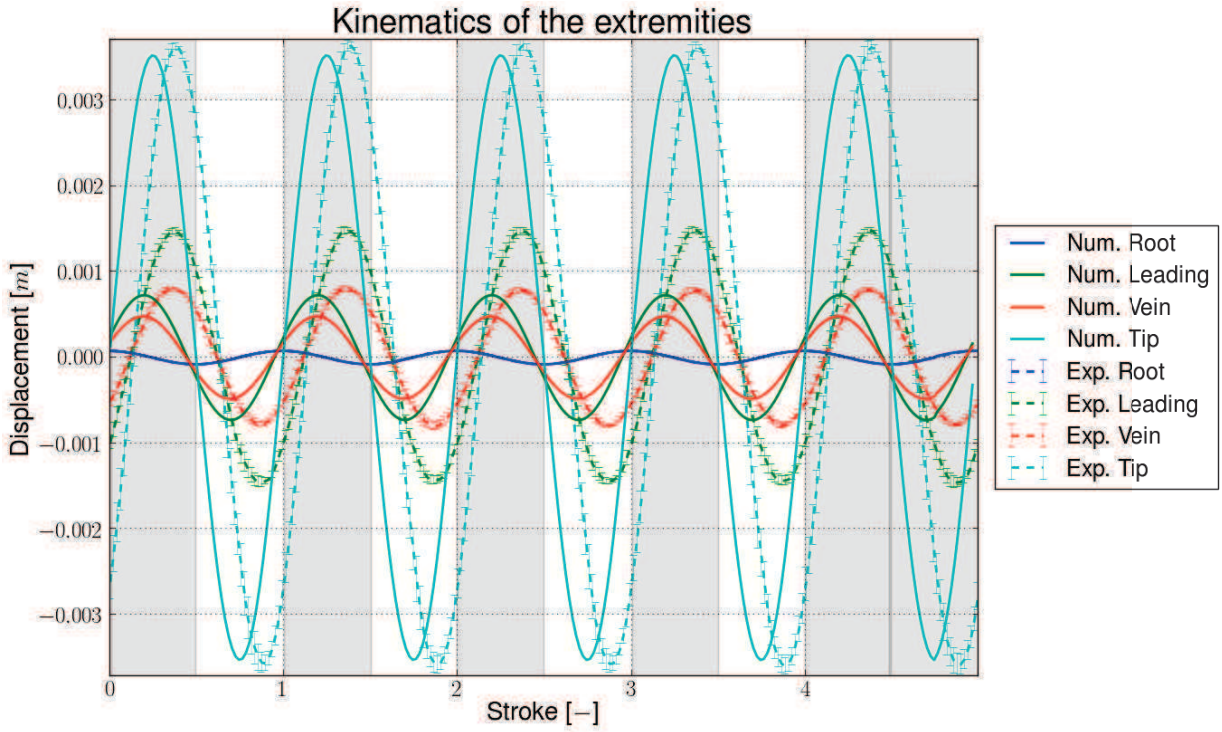

(b) Large actuation displacement (LA)

Figure D.2: Graphical comparison between experimental and numerical data for the wing F3 when actuated in air i.e. with aerodynamic coupling. Calculations are done with the large deflection of the FEs turned on and with the relevant experimental actuation amplitude. The first rotation $\mathbf{Rot_{Z,i}}$, see chapter 3.2, is disabled for LA as it causes instabilities in the computation of the lift forces. 75 periods are simulated to overturn the transient state. More details about the comparison are given in table D.1.

D.1.2 Wing E4

Table D.2: Reminder summary of the experimental/numerical comparison for E4.

Medium		**Vacuum**		**Air**	
Exp. Pressure [*mbar*]		4.8e-3 to 5.4e-3		1007	
Actuation type		SA	LA	SA	LA
Root	Mean Exp. Error [μm]	0.2	1.6	0.1	0.6
	STD on Exp. Error [μm]	0.1	0.8	0.1	0.3
	Exp. Amp. [μm]	7.6	79.6	7.3	77.9
	Num. Amp. [μm]	7.6	79.7	7.3	78.0
	Error Num./Exp. Amp. [%]	0	0	0	0
	Phase-shift between Num. and Exp. [*rad*]	0.00	0.00	0.00	0.00
Leading-edge	Mean Exp. Error [μm]	131.9	91.4	14.1	67.9
	STD on Exp. Error [μm]	64.7	51.5	6.8	36.4
	Exp. Amp. [μm]	484.9	2608.3	95.1	917.2
	Num. Amp. [μm]	395.9	1839.9	160.2	744.2
	Error Num./Exp. Amp. [%]	**-18**	**-29**	**68**	**-19**
	Phase-shift between Num. and Exp. [*rad*]	**0.00**	**-0.06**	**0.63**	**0.50**
Vein 1	Mean Exp. Error [μm]	27.7	117.8	2.6	13.6
	STD on Exp. Error [μm]	14.8	58.9	0.9	7.0
	Exp. Amp. [μm]	78.3	494.4	0.7	137.8
	Num. Amp. [μm]	85.5	450.0	33.2	184.6
	Error Num./Exp. Amp. [%]	**9**	**-9**	**4251**	**34**
	Phase-shift between Num. and Exp. [*rad*]	**0.00**	**0.06**	**0.63**	**0.38**
Vein 2	Mean Exp. Error [μm]	106.8	71.3	4.3	34.1
	STD on Exp. Error [μm]	49.1	34.0	2.0	15.8
	Exp. Amp. [μm]	398.7	2035.4	85.8	772.9
	Num. Amp. [μm]	366.0	1708.2	147.4	689.8
	Error Num./Exp. Amp. [%]	**-8**	**-16**	**72**	**-11**
	Phase-shift between Num. and Exp. [*rad*]	**0**	**-0.06**	**0.63**	**0.50**
Tip	Mean Exp. Error [μm]	591.5	288.4	11.4	195.2
	STD on Exp. Error [μm]	272.4	157.5	6.8	101.9
	Exp. Amp. [μm]	2216.2	8858.2	539.8	4589.2
	Num. Amp. [μm]	2015.8	7693.9	841.7	3523.8
	Error Num./Exp. Amp. [%]	**-8**	**-13**	**56**	**-23**
	Phase-shift between Num. and Exp. [*rad*]	**0**	**-0.06**	**0.50**	**0.38**

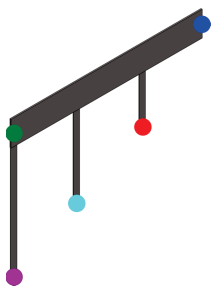

Figure D.3: CAD view of the E4 wing with its extremity colored as in the figures D.4 and D.5.

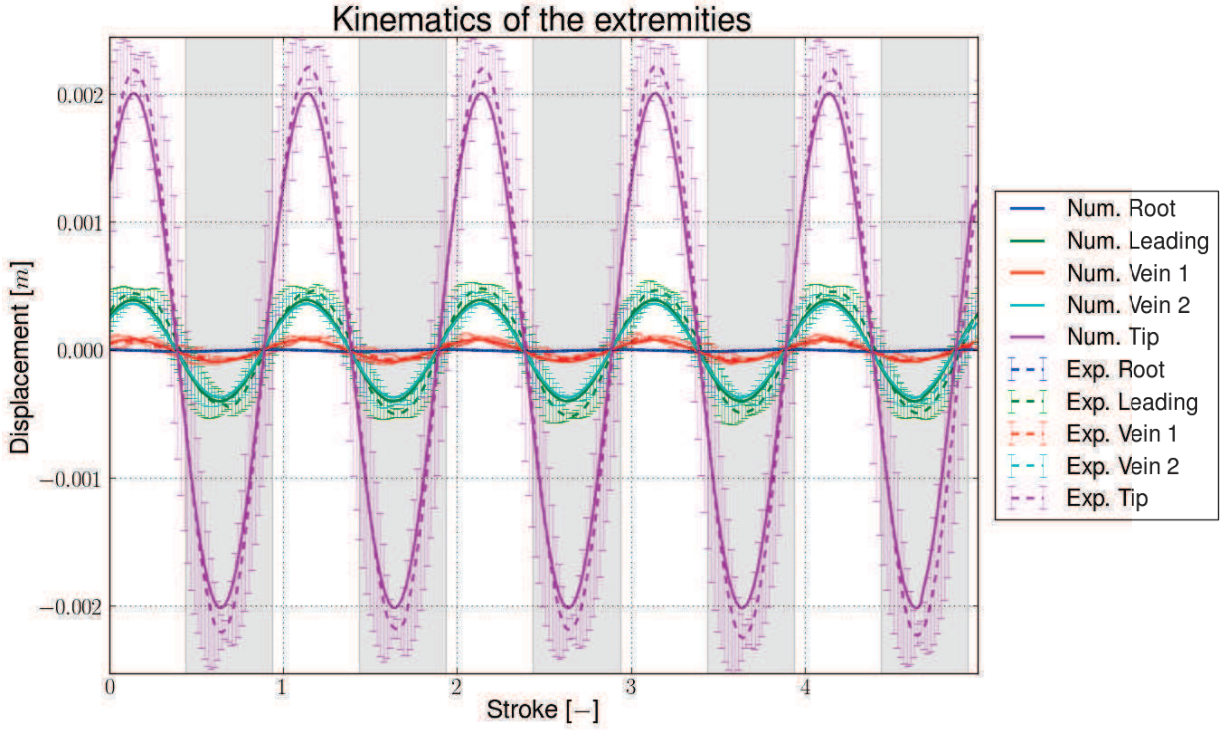

(a) Small actuation displacement (SA)

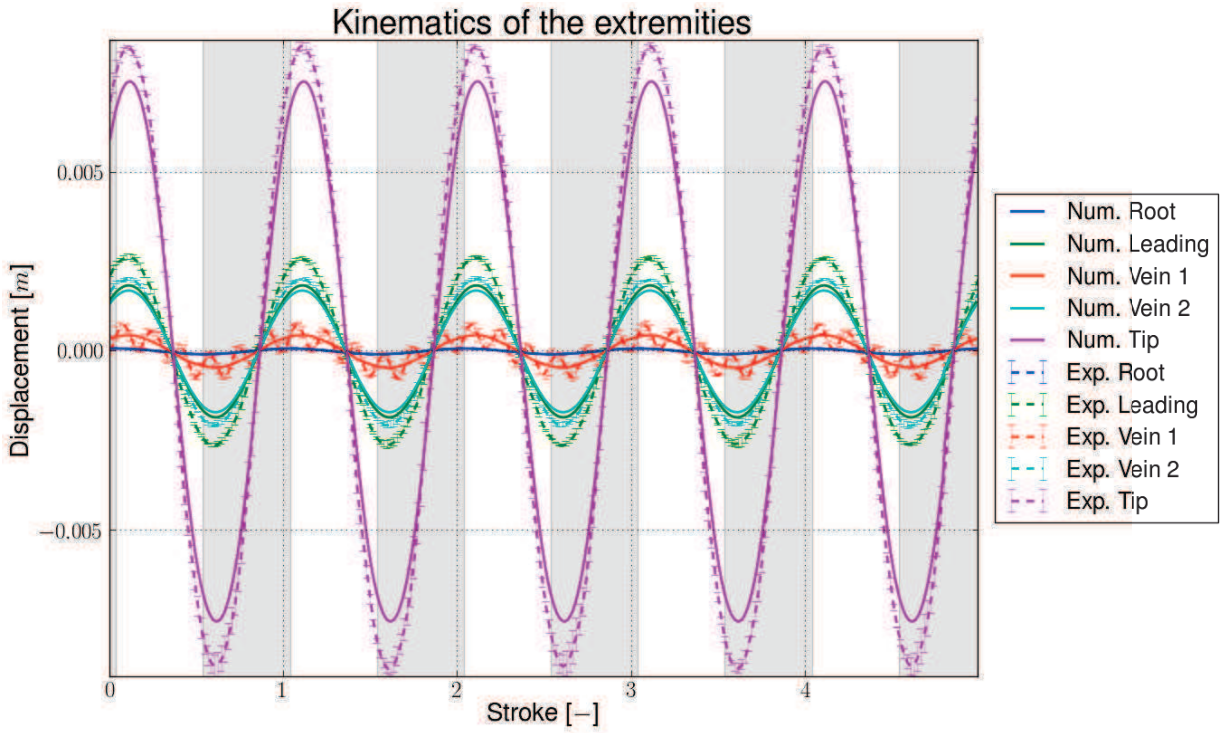

(b) Large actuation displacement (LA)

Figure D.4: Graphical comparison between experimental and numerical data for the wing E4 when actuated in vacuum i.e. without aerodynamic coupling. Calculations are done with the large deflection of the FEs turned on and with the relevant experimental actuation amplitude. 125 periods are simulated to overturn the transient state. More details about the comparison are given in table D.2.

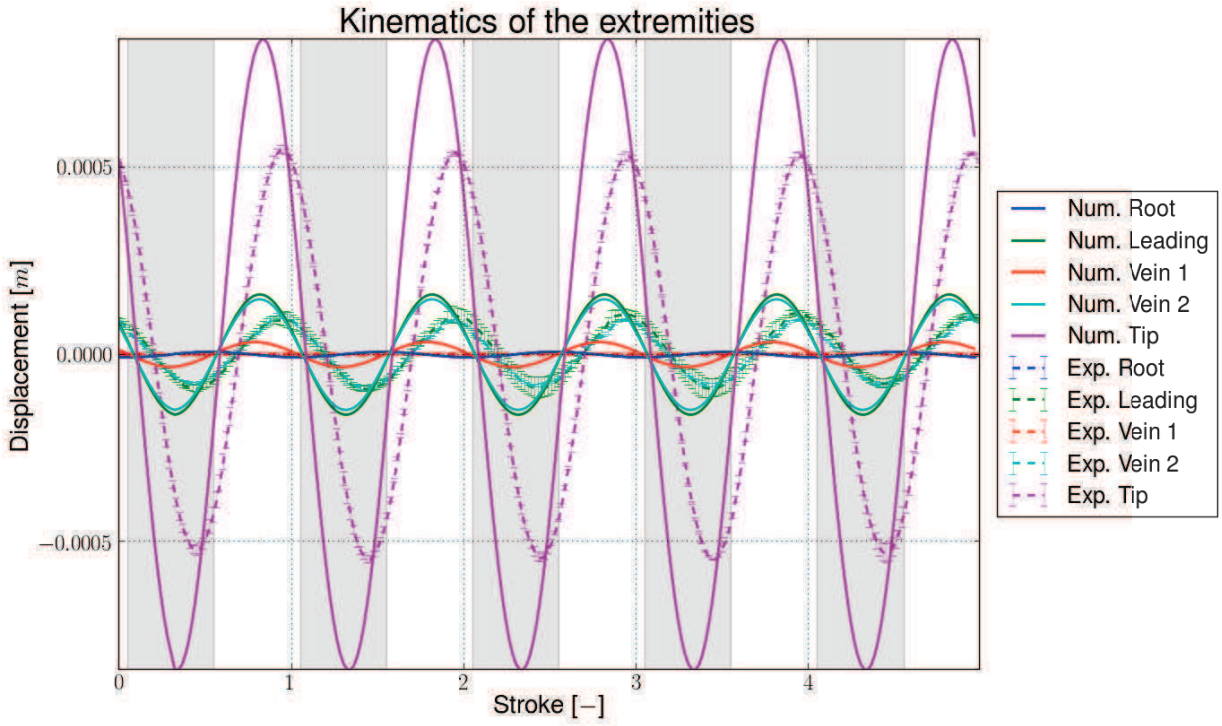

(a) Small actuation displacement (SA)

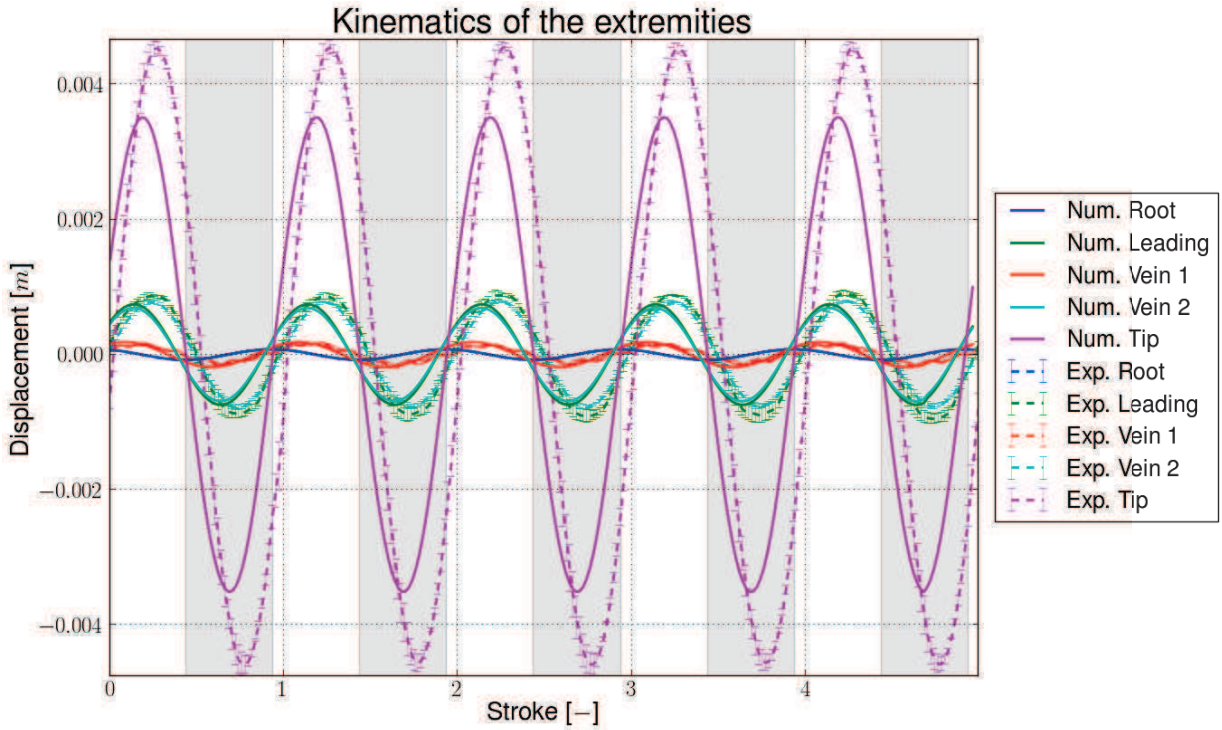

(b) Large actuation displacement (LA)

Figure D.5: Graphical comparison between experimental and numerical data for the wing E4 when actuated in air i.e. with aerodynamic coupling. Calculations are done with the large deflection of the FEs turned on and with the relevant experimental actuation amplitude. 75 periods are simulated to overturn the transient state. The first rotation $\mathbf{Rot_{Z,i}}$, see chapter 3.2, is disabled for LA as it causes instabilities in the computation of the lift forces. More details about the comparison are given in table D.2.

D.2 Experimental/numerical comparison for the wing EM4

Table D.3: Summary of the experimental/numerical comparison for EM4. In order to quantify the experimental error of each extremity, its mean and standard-deviation values are given. Other items are based on the displacement amplitude of the extremity. The error between the numerical and the experimental values is defined as $\left(\overline{A_{num}} - \overline{A_{exp}}\right) / \overline{A_{exp}}$ with $\overline{A_{num}}$ and $\overline{A_{exp}}$ the numerical and experimental displacement amplitudes respectively.

Medium		**Vacuum**		**Air**	
Exp. Pressure [$mbar$]		4.7e-3 to 6e-3		1001	
Actuation type		SA	LA	SA	LA
Root	Mean Exp. Error [μm]	0.1	1.2	0.2	1.0
	STD on Exp. Error [μm]	0.1	0.6	0.1	0.4
	Exp. Amp. [μm]	7.7	77.6	7.7	78.3
	Num. Amp. [μm]	7.7	77.6	7.7	78.5
	Error Num./Exp. Amp. [%]	0	0	0	0
	Phase-shift between Num. and Exp. [rad]	0.00	0.00	0.00	0.00
Leading-edge	Mean Exp. Error [μm]	43.9	79.7	0.8	22.1
	STD on Exp. Error [μm]	22.8	44.7	0.4	11.3
	Exp. Amp. [μm]	505.9	2508.8	12.9	209.3
	Num. Amp. [μm]	110.4	707.6	103.5	505.1
	Error Num./Exp. Amp. [%]	**-78**	**-72**	**699**	**141**
	Phase-shift between Num. and Exp. [rad]	**2.26**	**2.51**	**1.88**	**1.76**
Vein 1	Mean Exp. Error [μm]	9.5	24.4	1.5	11.6
	STD on Exp. Error [μm]	4.6	14.2	0.8	5.6
	Exp. Amp. [μm]	136.5	564.2	1.4	38.4
	Num. Amp. [μm]	44.9	359.9	41.5	251.4
	Error Num./Exp. Amp. [%]	**-67**	**-36**	**2960**	**555**
	Phase-shift between Num. and Exp. [rad]	**2.26**	**2.51**	**1.51**	**1.01**
Vein 2	Mean Exp. Error [μm]	31.4	74.0	1.8	23.9
	STD on Exp. Error [μm]	26.9	55.3	0.9	15.2
	Exp. Amp. [μm]	407.2	1895.5	20.0	173.9
	Num. Amp. [μm]	194.2	1170.4	188.8	843.1
	Error Num./Exp. Amp. [%]	**-52**	**-38**	**843**	**385**
	Phase-shift between Num. and Exp. [rad]	**2.26**	**2.51**	**1.76**	**1.51**
Tip	Mean Exp. Error [μm]	60.9	125.6	2.7	50.8
	STD on Exp. Error [μm]	33.5	84.2	1.2	29.5
	Exp. Amp. [μm]	845.2	4041.8	89.1	861.4
	Num. Amp. [μm]	458.6	2362.5	449.8	1767.4
	Error Num./Exp. Amp. [%]	**-46**	**-42**	**405**	**105**
	Phase-shift between Num. and Exp. [rad]	**2.13**	**2.51**	**1.88**	**1.76**

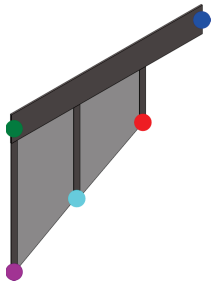

Figure D.6: CAD view of the EM4 wing with its extremity colored as in the figures D.7 and D.8.

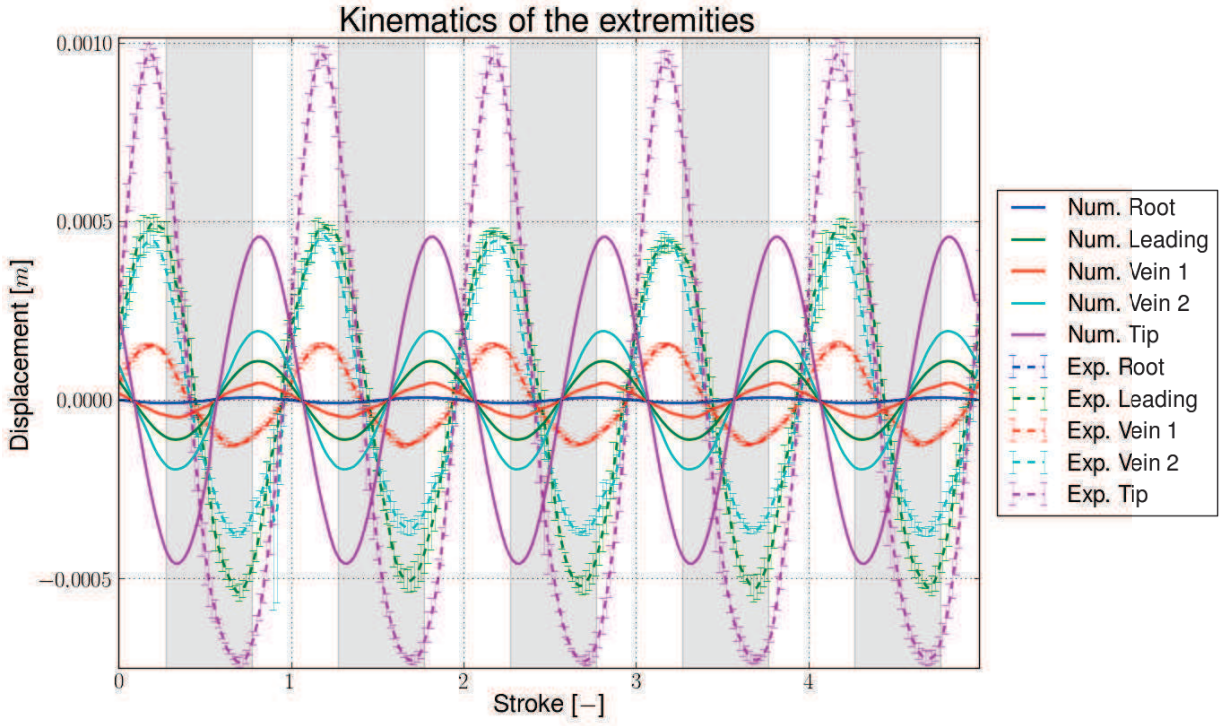

(a) Small actuation displacement (SA)

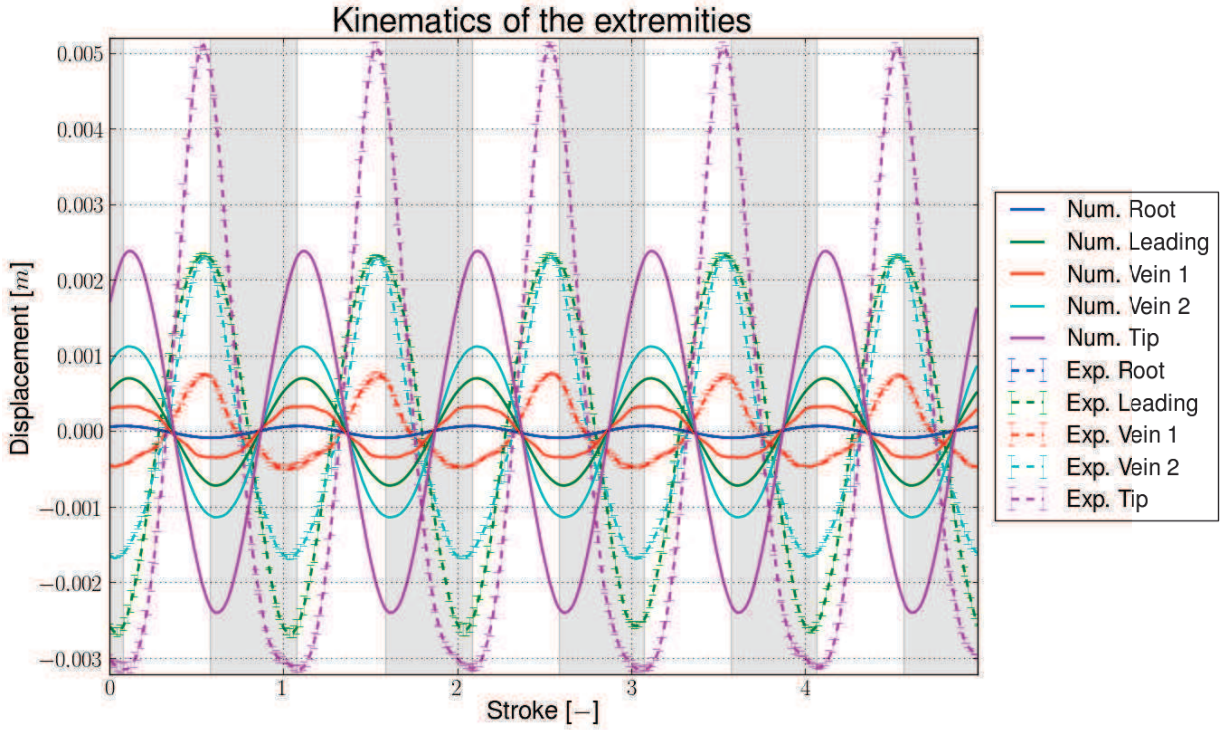

(b) Large actuation displacement (LA)

Figure D.7: Graphical comparison between experimental and numerical data for the wing EM4 when actuated in vacuum i.e. without aerodynamic coupling. Calculations are done with the large deflection of the FEs turned on and with the relevant experimental actuation amplitude. 125 periods are simulated to overturn the transient state. More details about the comparison are given in table D.3.

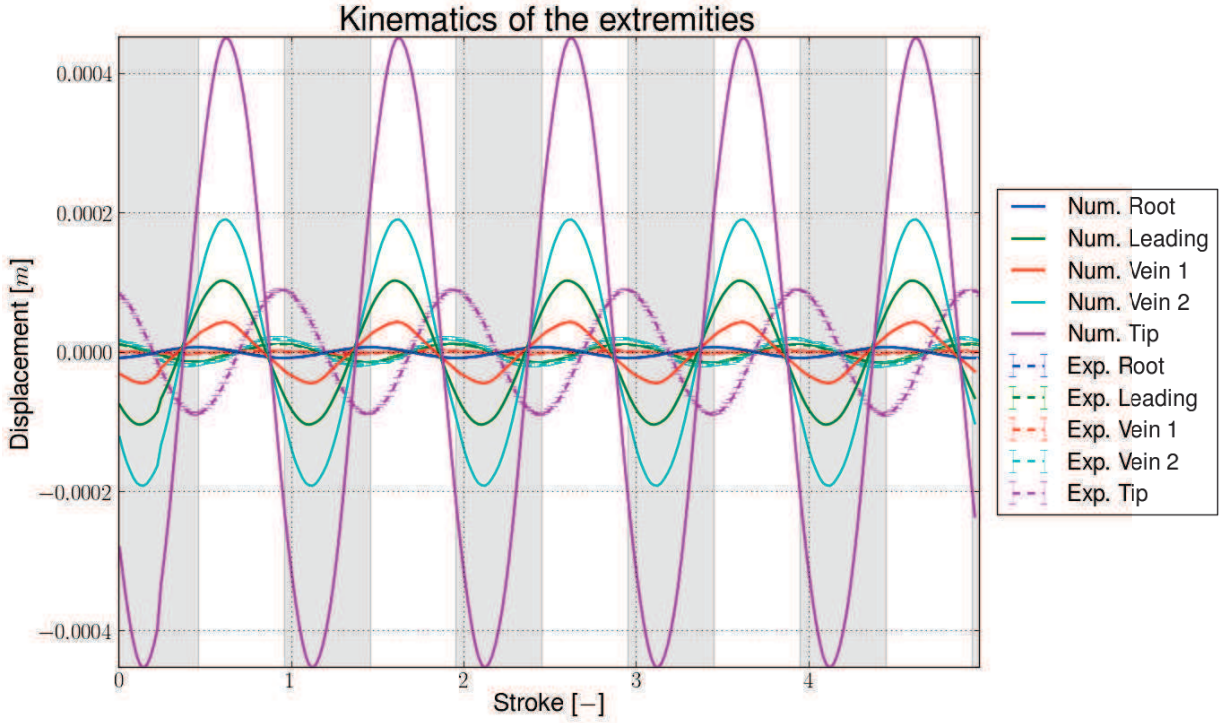

(a) Small actuation displacement (SA)

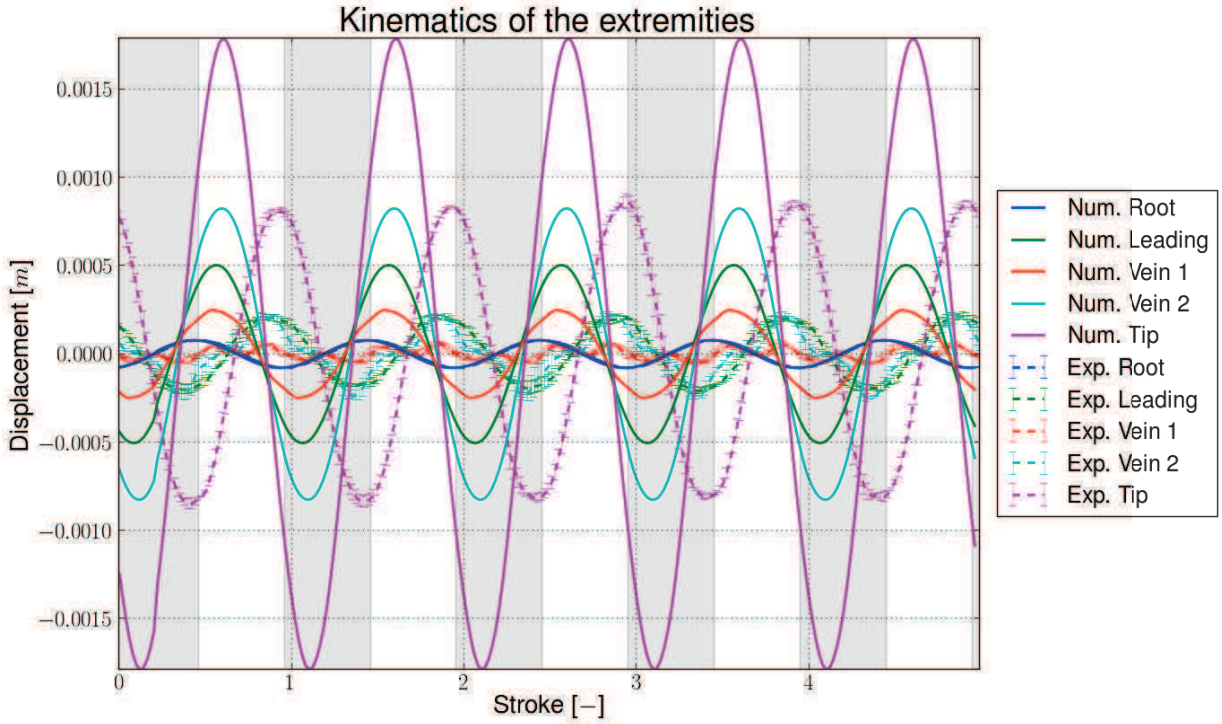

(b) Large actuation displacement (LA)

Figure D.8: Graphical comparison between experimental and numerical data for the wing EM4 when actuated in air i.e. with aerodynamic coupling. Calculations are done with the large deflection of the FEs turned on and with the relevant experimental actuation amplitude. 50 periods are simulated to overturn the transient state. The first rotation $\mathbf{Rot_{Z,i}}$, see chapter 3.2, is disabled for LA as it causes instabilities in the computation of the lift forces. More details about the comparison are given in table D.3.

Appendix E

Measurement of the wing deformation at air frequency

E.1 Beam Wing

E.1.1 L2

Table E.1: Summary of the experimental results for L2 actuated at its air resonant frequency.

Medium		**Vacuum**		**Air**	
Exp. Pressure [*mbar*]		3.3e-3 to 4.1e-3		992	
Actuation type		SA	LA	SA	LA
Root	Mean Exp. Error μm]	0.2	0.6	0.0	1.5
	STD on Exp. Error [μm]	0.1	0.3	0.0	0.8
	Exp. Amp. [μm]	7.6	76.7	7.4	77.8
Leading-edge	Mean Exp. Error [μm]	5.5	54.5	9.8	31.3
	STD on Exp. Error [μm]	2.6	24.1	6.2	15.2
	Exp. Amp. [μm]	93.7	1090.9	138.0	835.2
Tip	Mean Exp. Error [μm]	29.7	259.8	21.9	158.5
	STD on Exp. Error [μm]	13.5	118.9	11.5	81.0
	Exp. Amp. [μm]	521.6	5139.8	801.7	4356.3

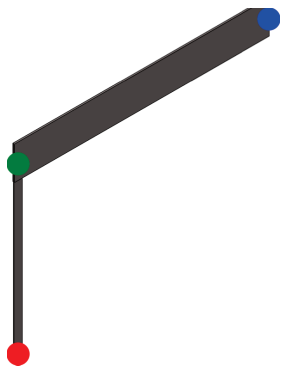

Figure E.1: CAD view of the L2 wing with its extremity colored as in the figures E.2 and E.3.

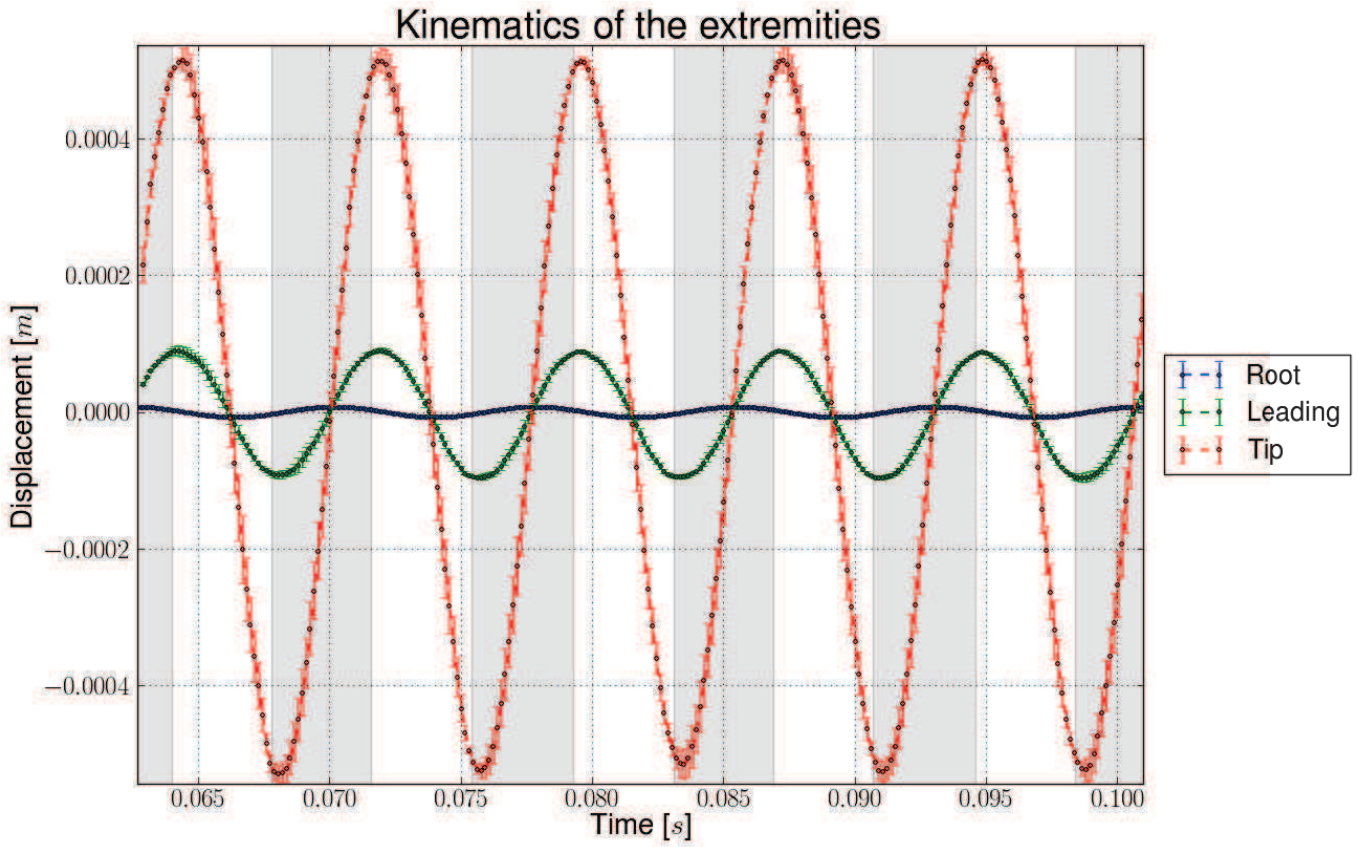

(a) Small actuation displacement

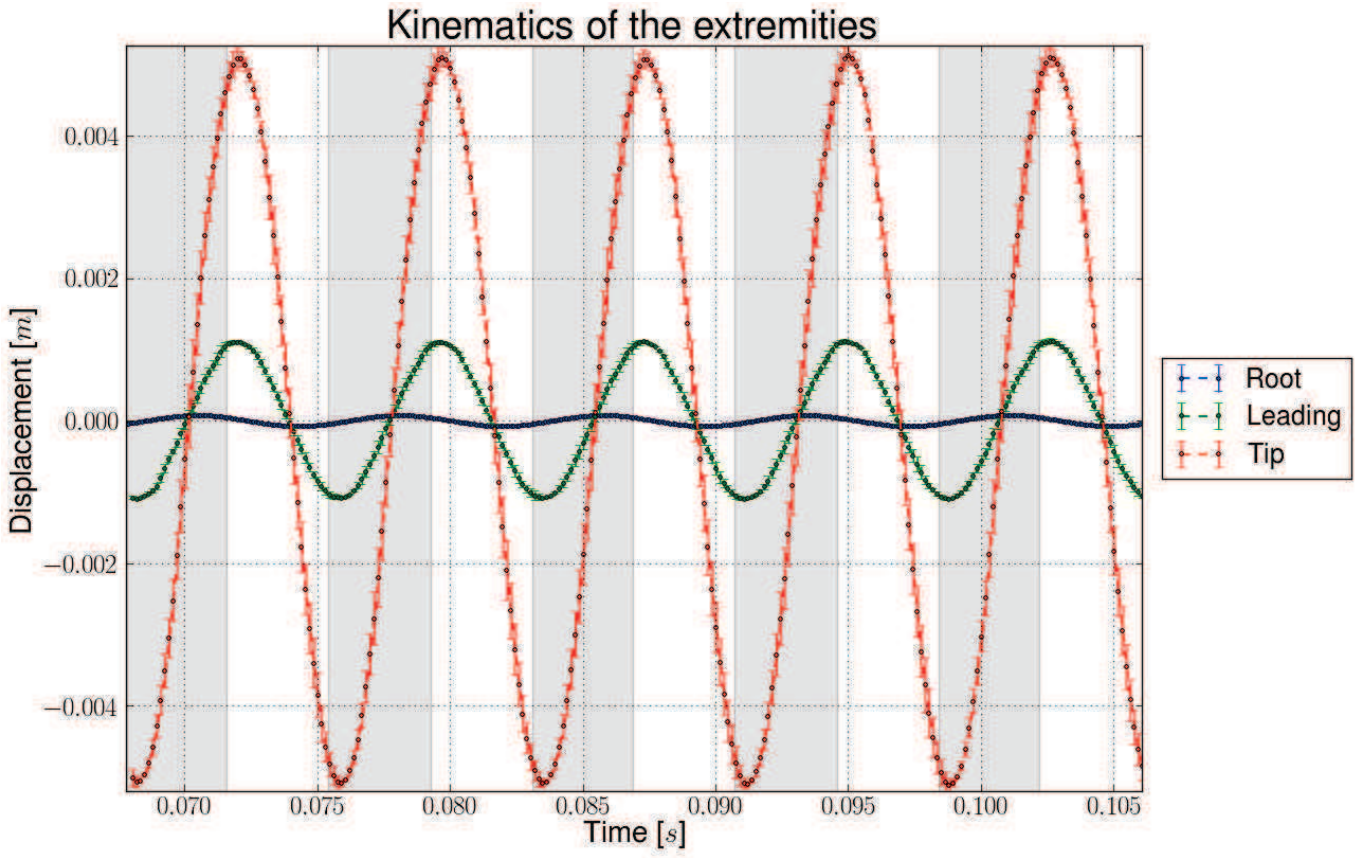

(b) Large actuation displacement

Figure E.2: Experimental data for the wing L2 when actuated in vacuum i.e. without aerodynamic coupling. More details about the experimental data are given in table E.1.

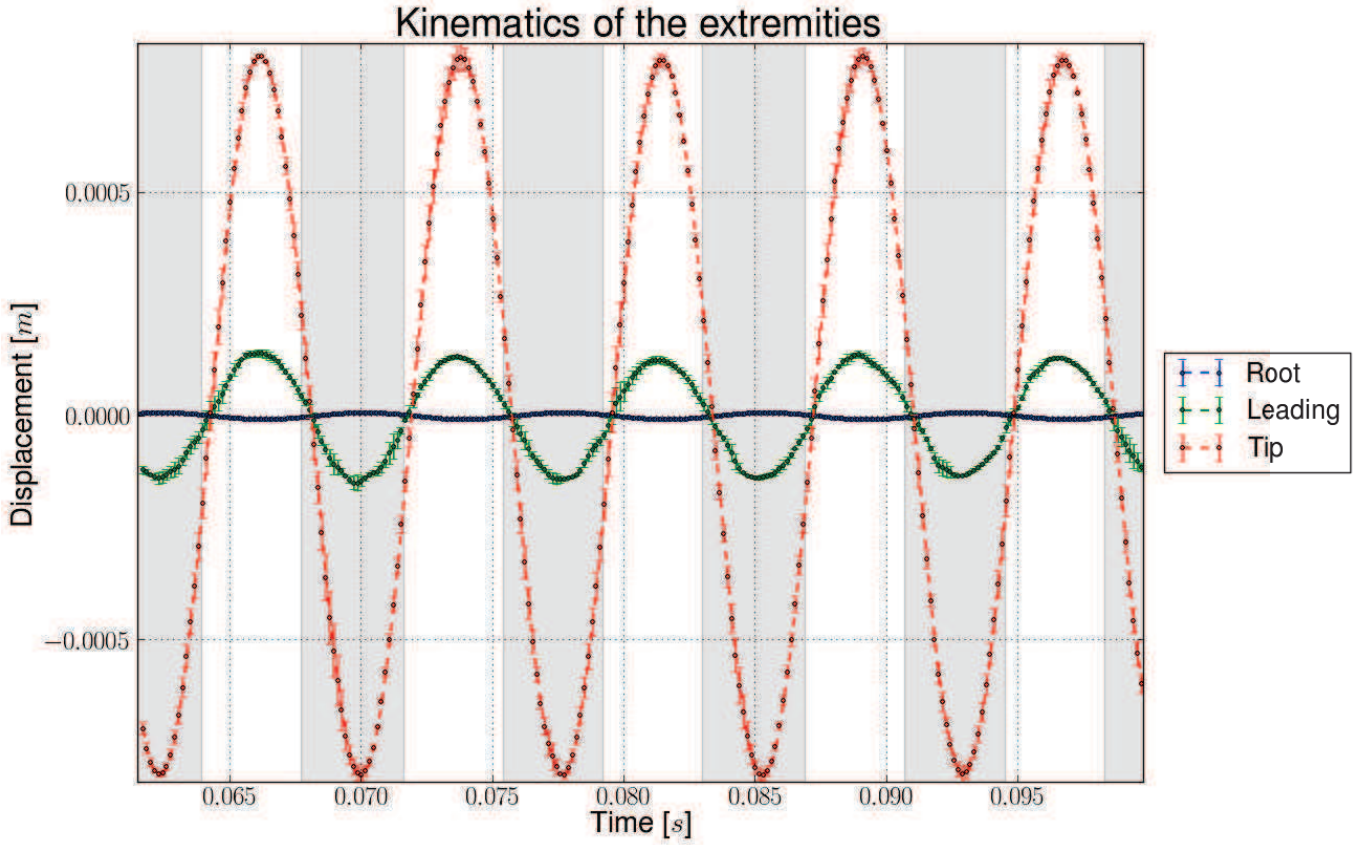

(a) Small actuation displacement

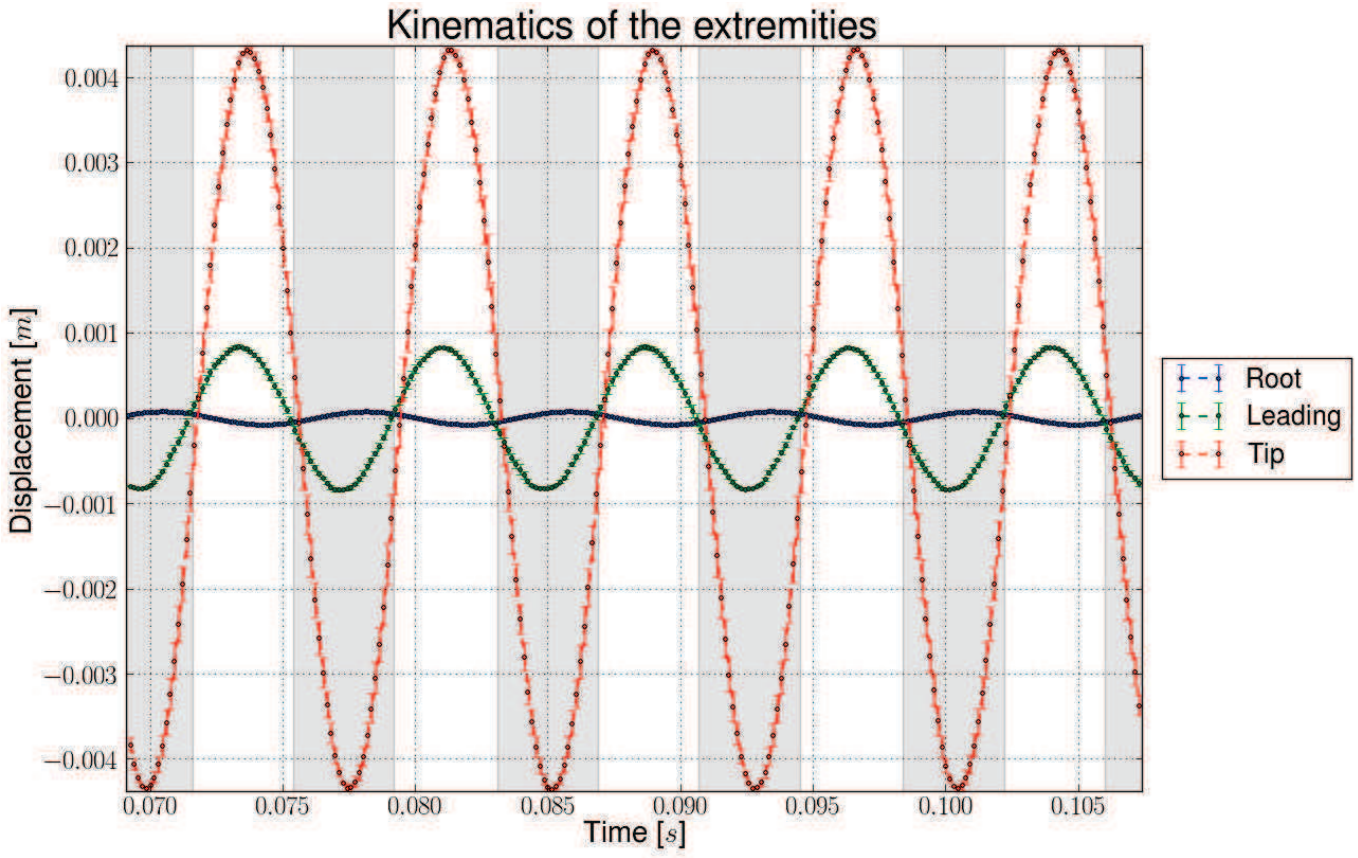

(b) Large actuation displacement

Figure E.3: Experimental data for the wing L2 when actuated in air i.e. with aerodynamic coupling. More details about the experimental data are given in table E.1.

E.1.2 F3

Table E.2: Summary of the experimental results for F3 actuated at its air resonant frequency.

Medium		**Vacuum**		**Air**	
Exp. Pressure [*mbar*]		3.3e-3 to 4.1e-3		992	
Actuation type		SA	LA	SA	LA
Root	Mean Exp. Error μm]	0.1	1.5	0.2	1.5
	STD on Exp. Error [μm]	0.0	0.6	0.1	0.7
	Exp. Amp. [μm]	7.5	77.6	7.7	78.3
Leading-edge	Mean Exp. Error [μm]	11.7	216.2	13.4	95.8
	STD on Exp. Error [μm]	4.3	79.0	6.5	83.1
	Exp. Amp. [μm]	173.5	2052.4	279.2	1742.5
Vein	Mean Exp. Error [μm]	3.5	117.9	10.0	60.0
	STD on Exp. Error [μm]	1.9	44.8	4.5	129.5
	Exp. Amp. [μm]	98.0	1112.6	152.0	974.0
Tip	Mean Exp. Error [μm]	14.0	471.0	21.9	299.6
	STD on Exp. Error [μm]	7.0	175.8	11.1	846.2
	Exp. Amp. [μm]	456.0	4893.1	673.9	4148.7

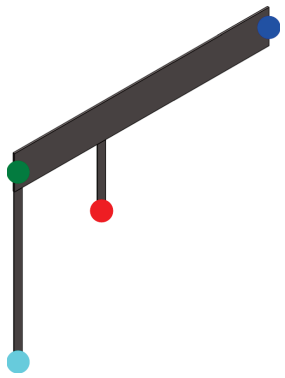

Figure E.4: CAD view of the F3 wing with its extremity colored as in the figures E.5 and E.6.

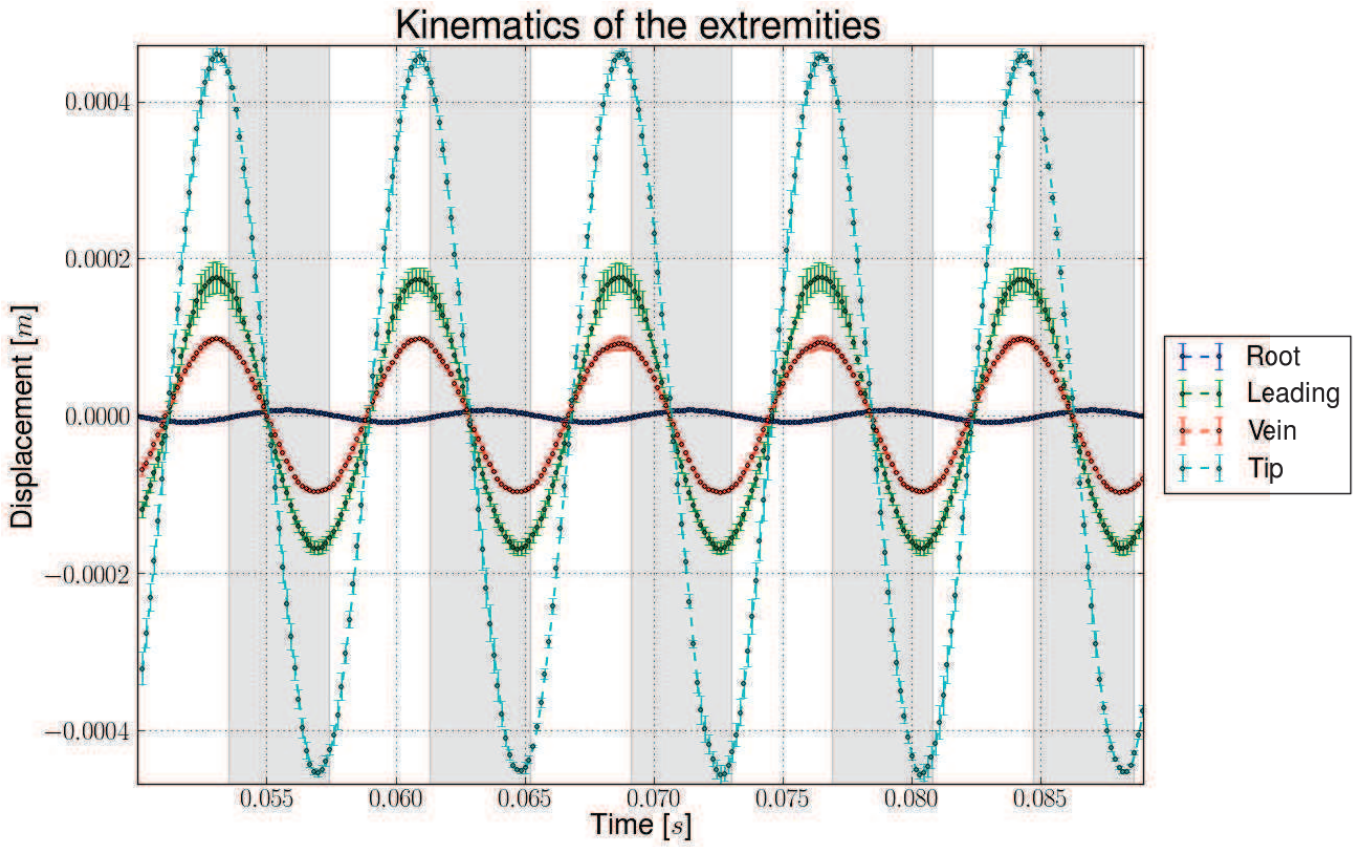

(a) Small actuation displacement

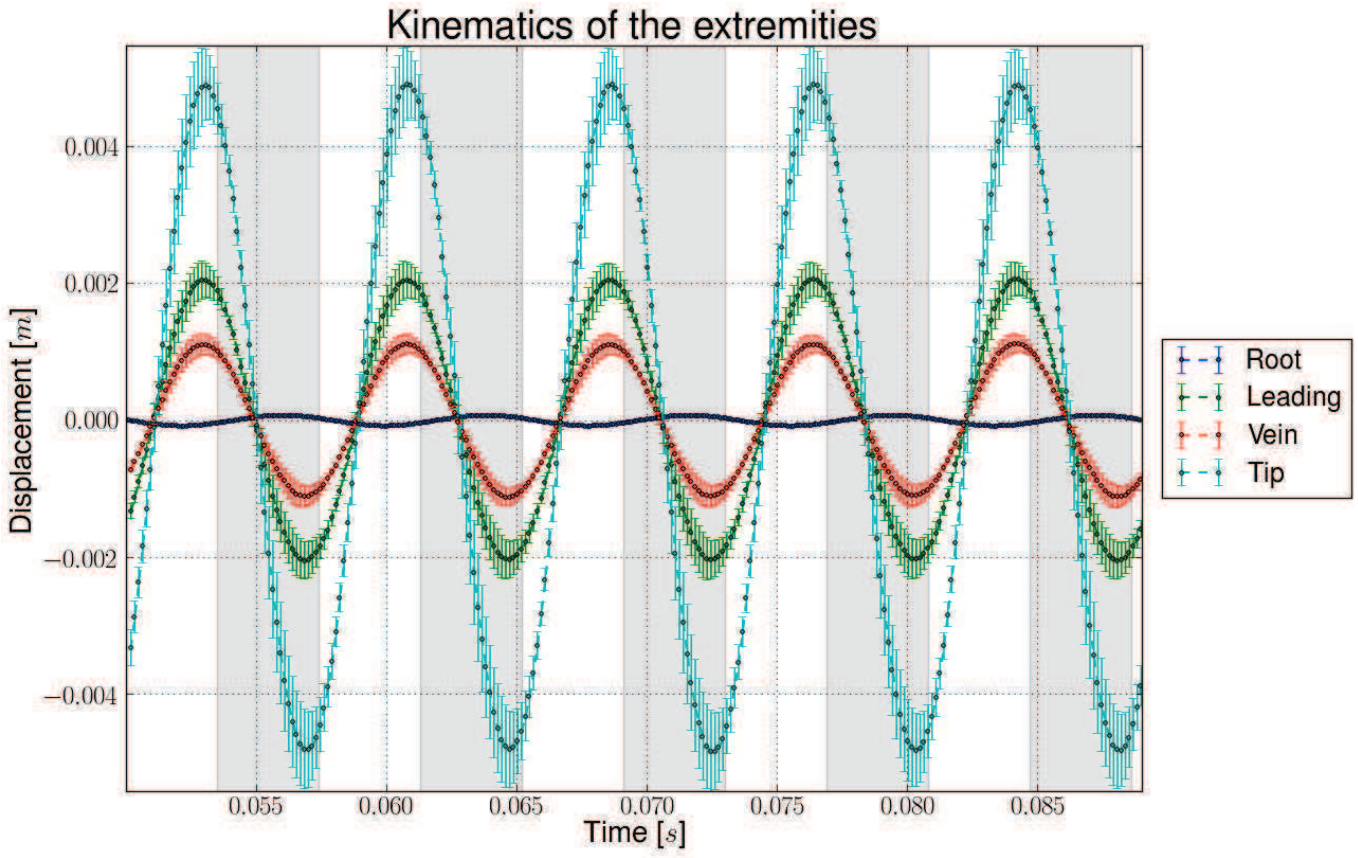

(b) Large actuation displacement

Figure E.5: Experimental data for the wing F3 when actuated in vacuum i.e. without aerodynamic coupling. More details about the experimental data are given in table E.2.

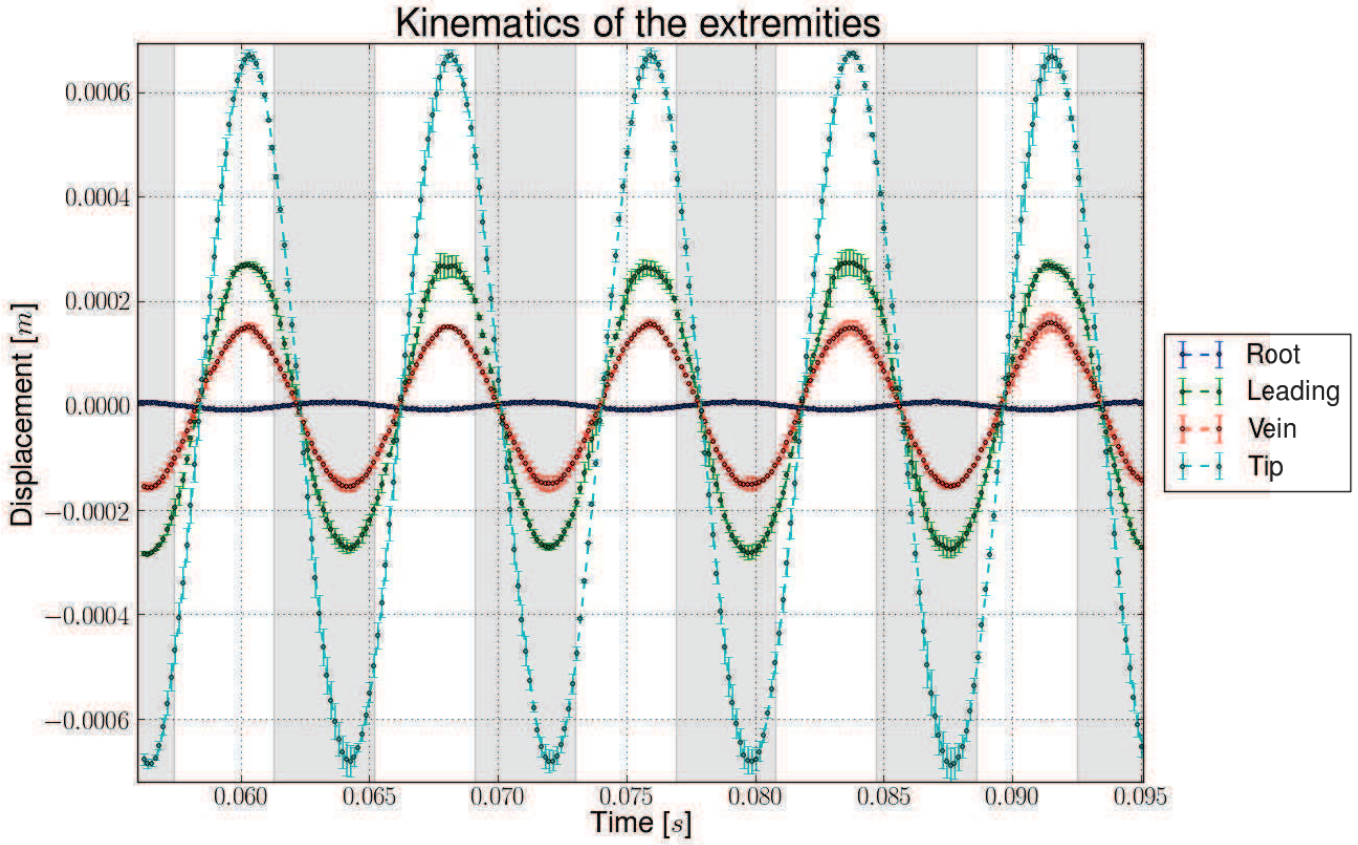

(a) Small actuation displacement

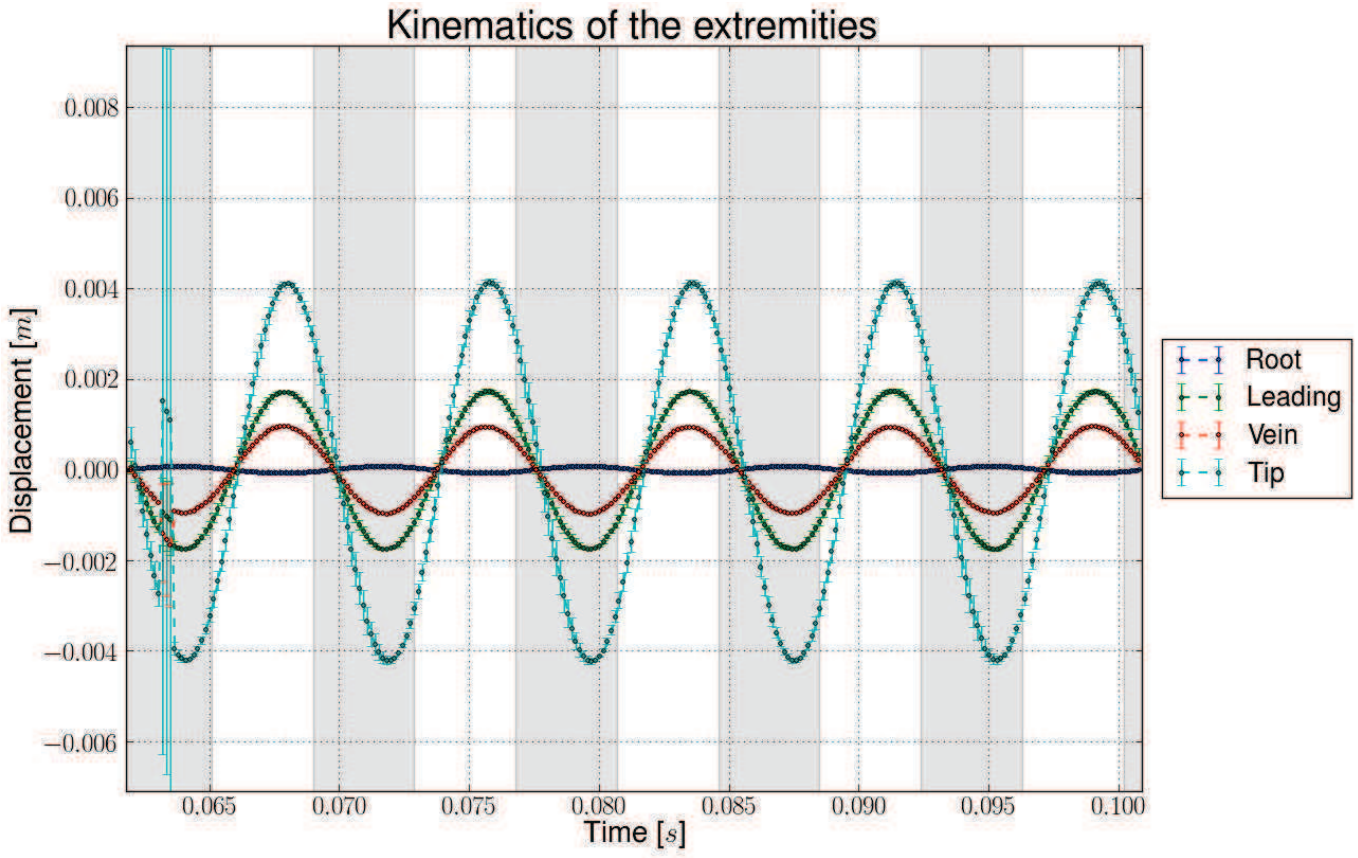

(b) Large actuation displacement

Figure E.6: Experimental data for the wing F3 when actuated in air i.e. with aerodynamic coupling. More details about the experimental data are given in table E.2.

E.1.3 E4

Table E.3: Summary of the experimental results for E4 actuated at its air resonant frequency.

Medium		**Vacuum**		**Air**	
Exp. Pressure [*mbar*]		3.3e-3 to 4.1e-3		992	
Actuation type		SA	LA	SA	LA
Root	Mean Exp. Error μm]	0.1	0.4	0.2	1.4
	STD on Exp. Error [μm]	0.0	0.2	0.1	0.7
	Exp. Amp. [μm]	7.5	79.2	7.2	78.2
Leading-edge	Mean Exp. Error [μm]	7.9	60.1	19.9	49.9
	STD on Exp. Error [μm]	3.4	38.6	11.2	28.1
	Exp. Amp. [μm]	121.3	1579.1	183.9	1167.4
Vein 1	Mean Exp. Error [μm]	9.9	20.3	10.0	11.4
	STD on Exp. Error [μm]	3.6	11.0	5.1	9.5
	Exp. Amp. [μm]	14.4	303.7	28.4	206.3
Vein 2	Mean Exp. Error [μm]	9.4	52.9	10.3	23.1
	STD on Exp. Error [μm]	3.9	25.3	5.4	11.8
	Exp. Amp. [μm]	107.7	1285.6	157.5	930.3
Tip	Mean Exp. Error [μm]	24.9	270.1	39.5	106.5
	STD on Exp. Error [μm]	12.8	111.1	19.7	60.4
	Exp. Amp. [μm]	538.2	6065.2	869.0	4815.6

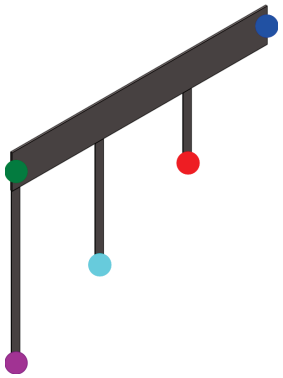

Figure E.7: CAD view of the E4 wing with its extremity colored as in the figures E.8 and E.9.

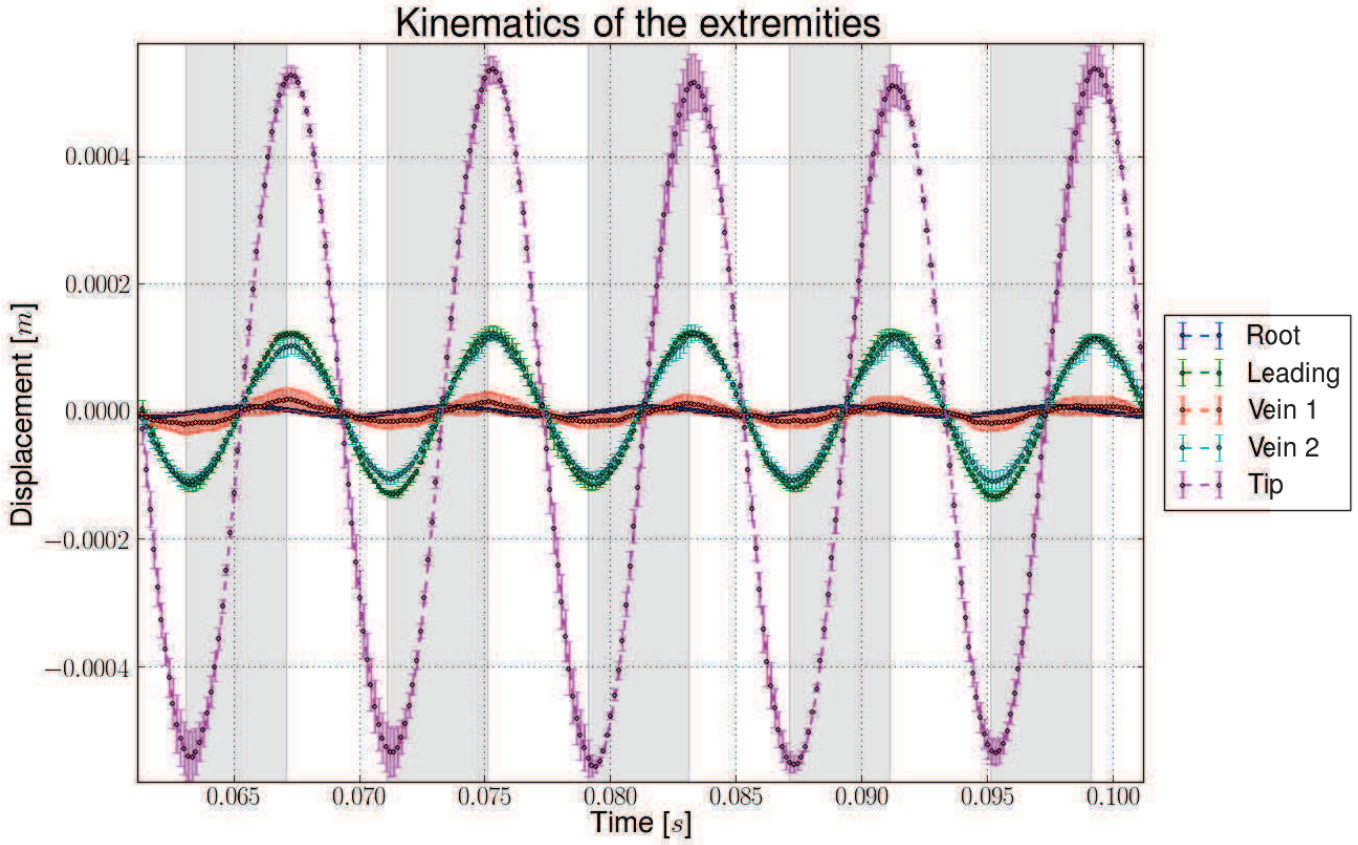

(a) Small actuation displacement

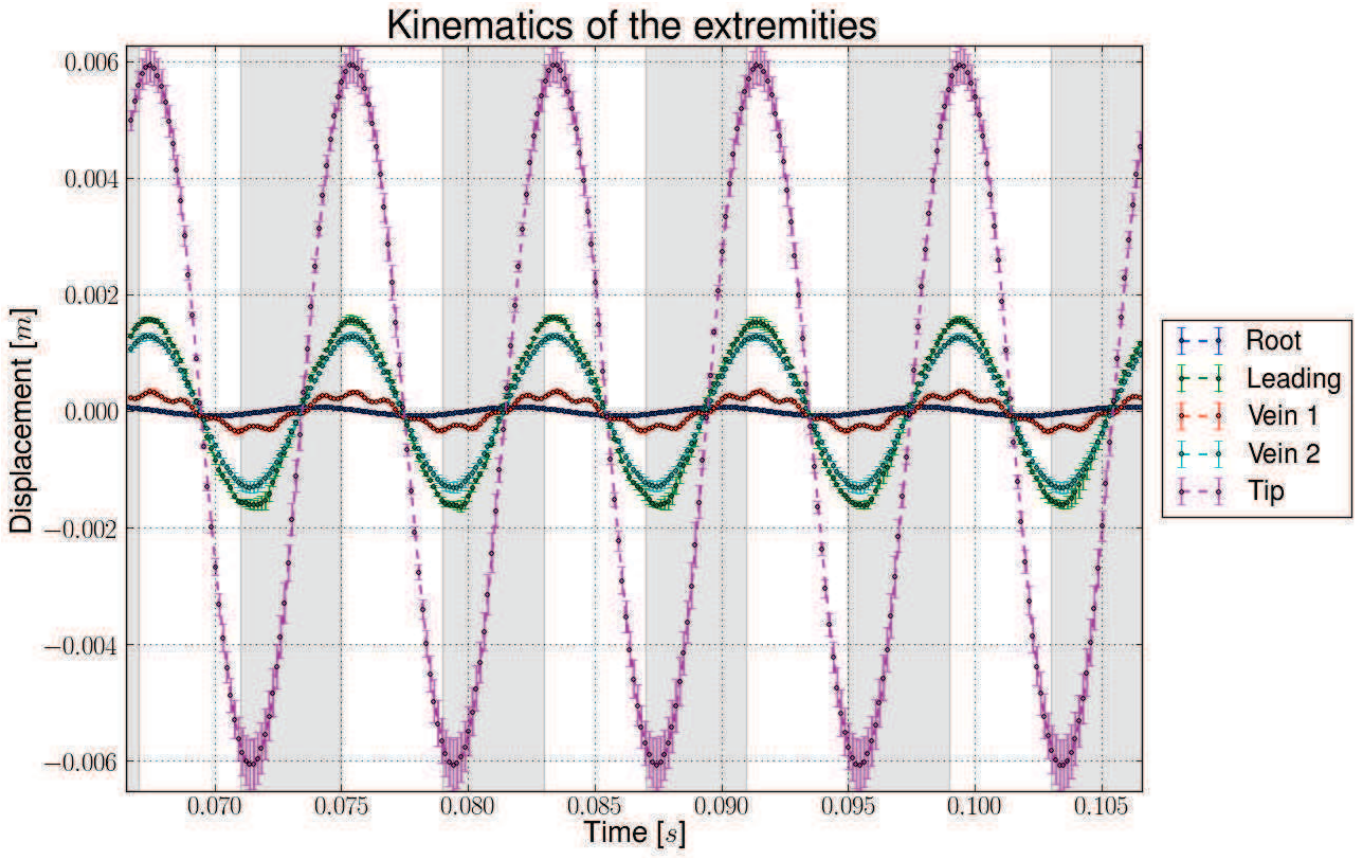

(b) Large actuation displacement

Figure E.8: Experimental data for the wing E4 when actuated in vacuum i.e. without aerodynamic coupling. More details about the experimental data are given in table E.3.

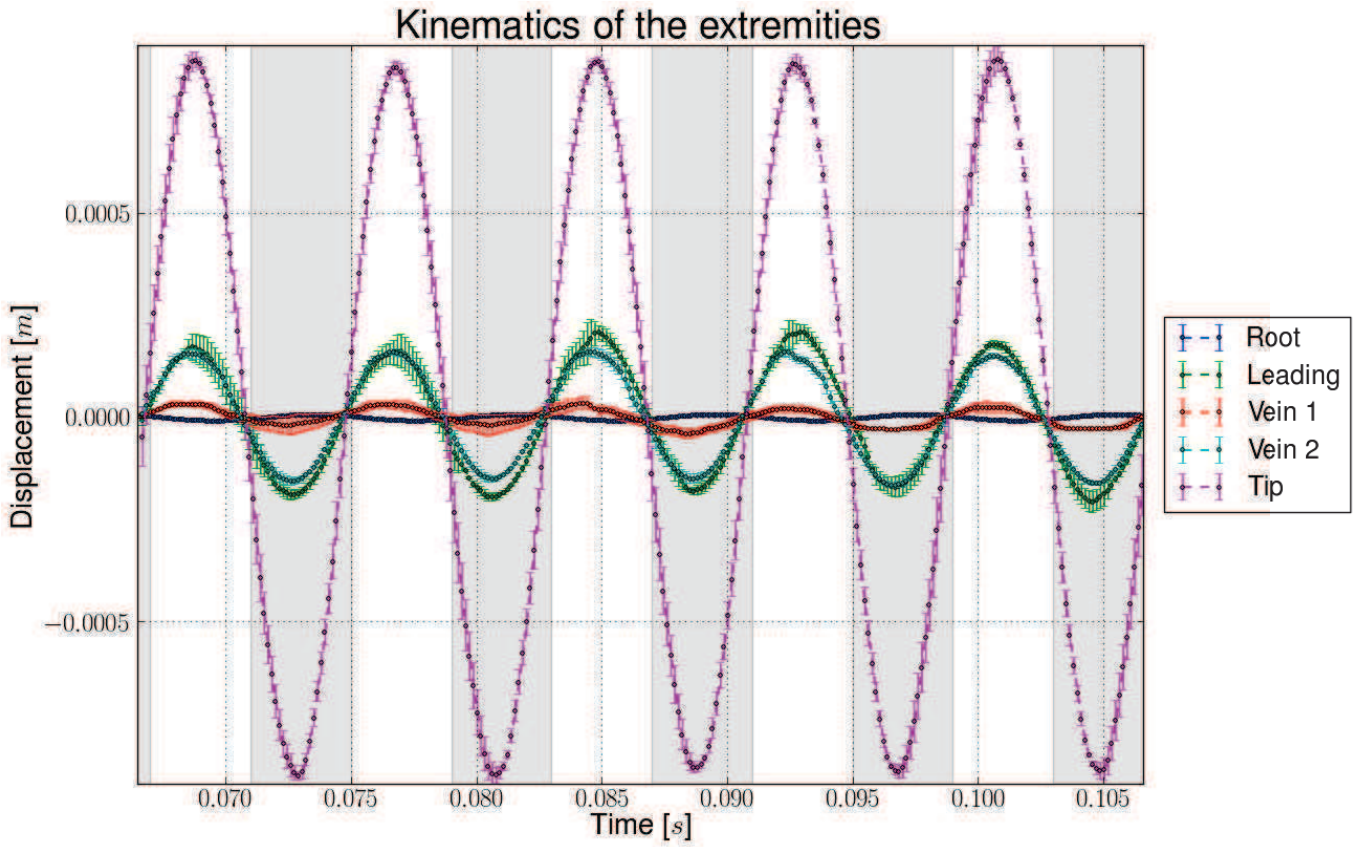

(a) Small actuation displacement

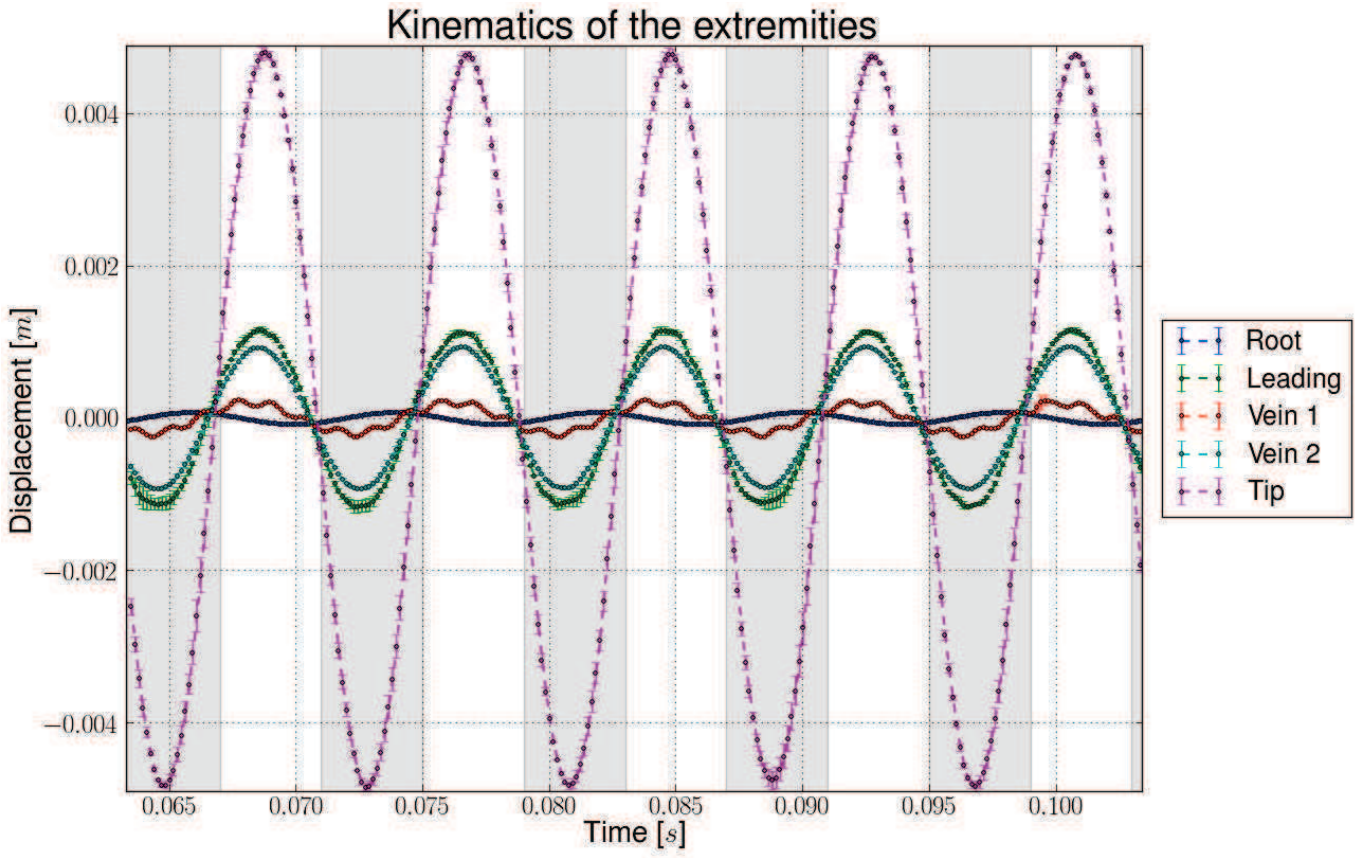

(b) Large actuation displacement

Figure E.9: Experimental data for the wing E4 when actuated in air i.e. with aerodynamic coupling. More details about the experimental data are given in table E.3.

E.2 Membrane Wing

E.2.1 FM3

Table E.4: Summary of the experimental results for FM3 actuated at its air resonant frequency.

Medium		**Vacuum**		**Air**	
Exp. Pressure [*mbar*]		3.3e-3 to 4.1e-3		992	
Actuation type		SA	LA	SA	LA
Root	Mean Exp. Error μm]	0.1	1.5	0.1	0.3
	STD on Exp. Error [μm]	0.0	0.7	0.1	0.1
	Exp. Amp. [μm]	7.5	78.7	7.6	80.9
Leading-edge	Mean Exp. Error [μm]	2316.3	497.1	13.9	61.4
	STD on Exp. Error [μm]	1068.8	231.1	7.0	26.7
	Exp. Amp. [μm]	2304.9	3688.3	223.1	1139.5
Vein	Mean Exp. Error [μm]	1394.7	313.3	14.6	50.4
	STD on Exp. Error [μm]	658.5	146.0	5.9	30.9
	Exp. Amp. [μm]	1386.9	2221.5	186.4	690.0
Tip	Mean Exp. Error [μm]	3882.3	815.3	23.2	93.6
	STD on Exp. Error [μm]	1852.5	369.2	9.8	41.9
	Exp. Amp. [μm]	3927.0	6238.5	372.2	1750.7

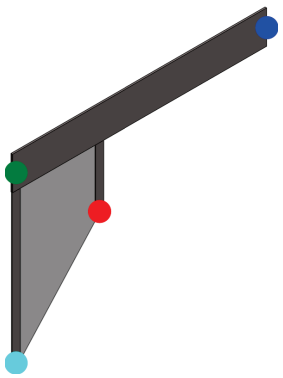

Figure E.10: CAD view of the FM3 wing with its extremity colored as in the figures E.11 and E.12.

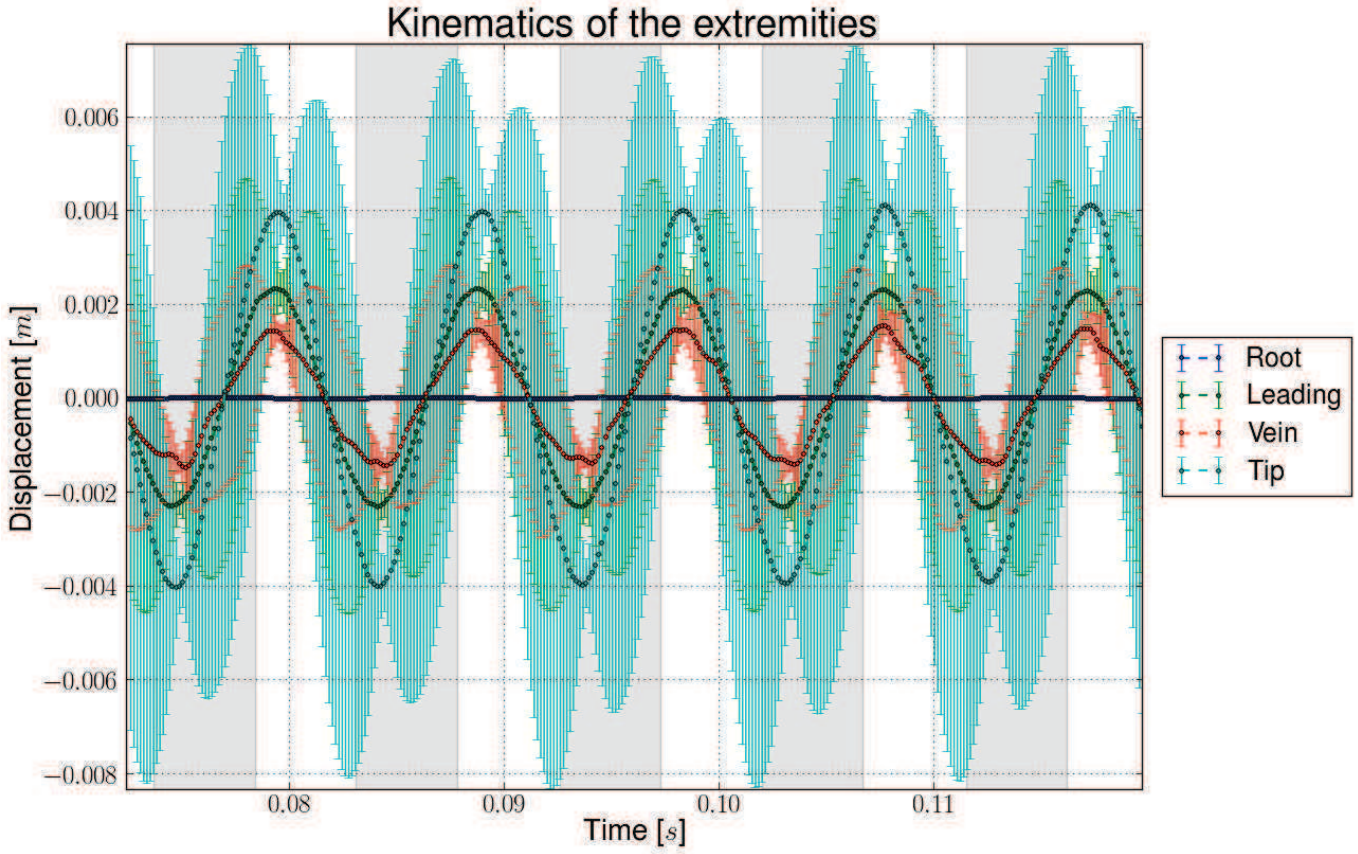

(a) Small actuation displacement

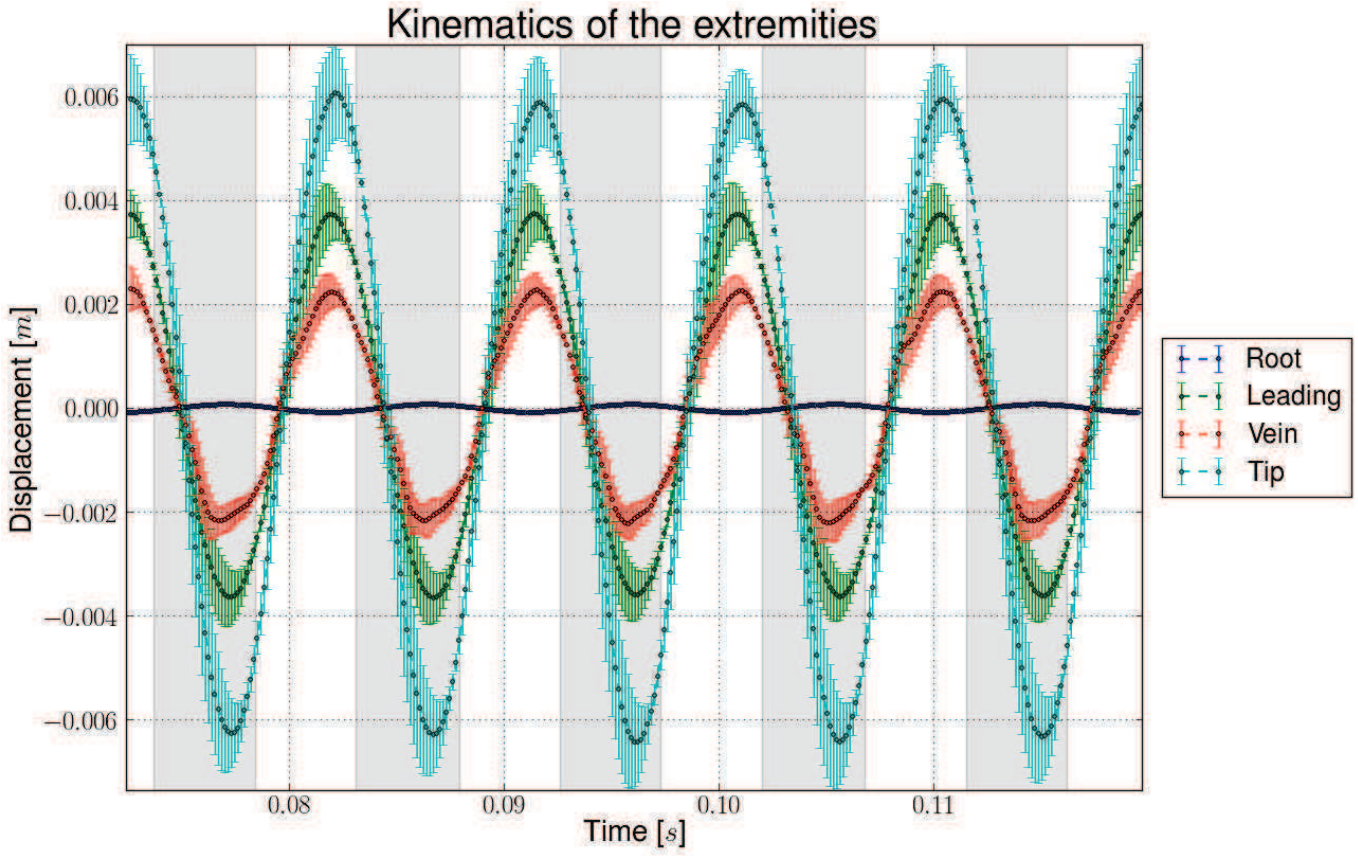

(b) Large actuation displacement

Figure E.11: Experimental data for the wing FM3 when actuated in vacuum i.e. without aerodynamic coupling. More details about the experimental data are given in table E.4.

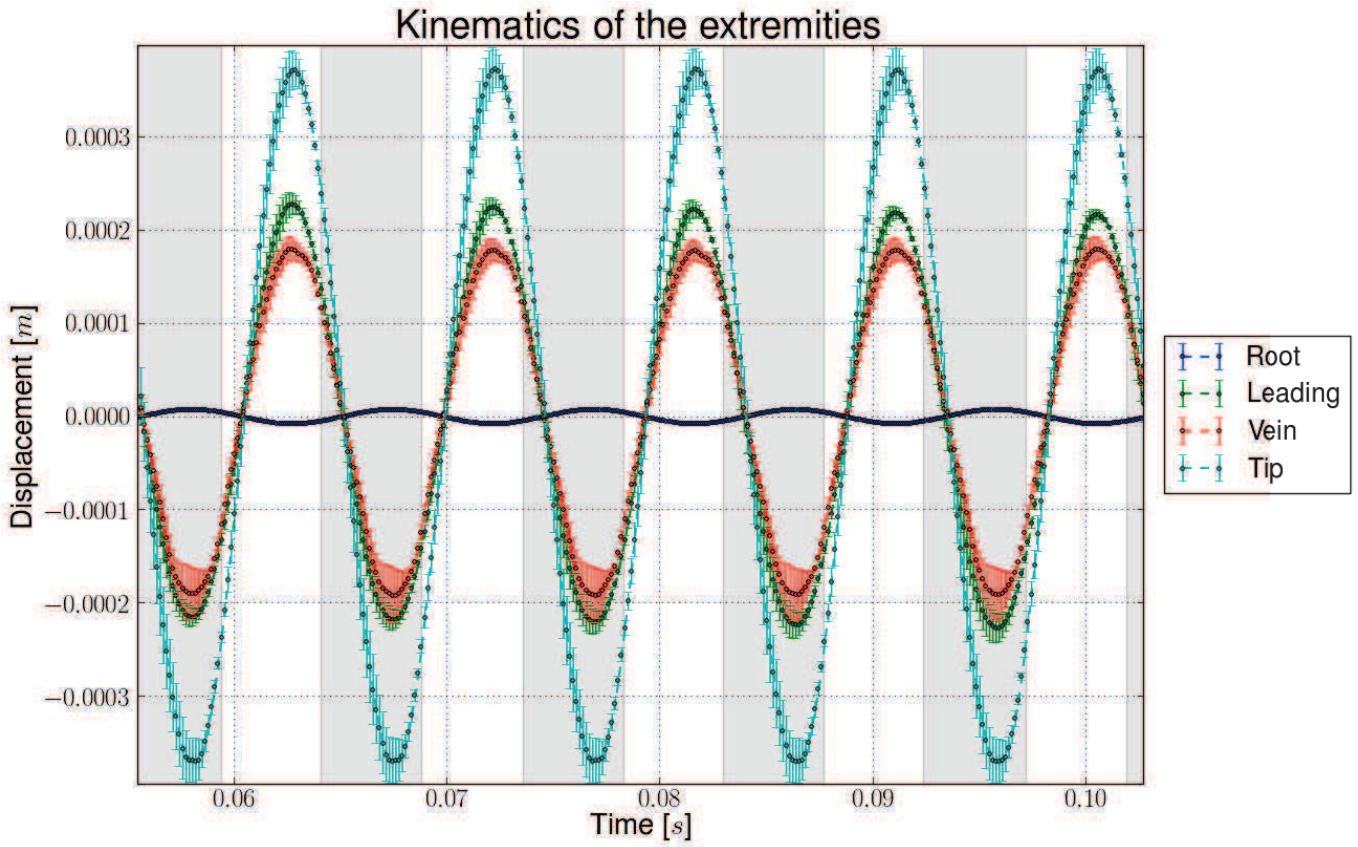

(a) Small actuation displacement

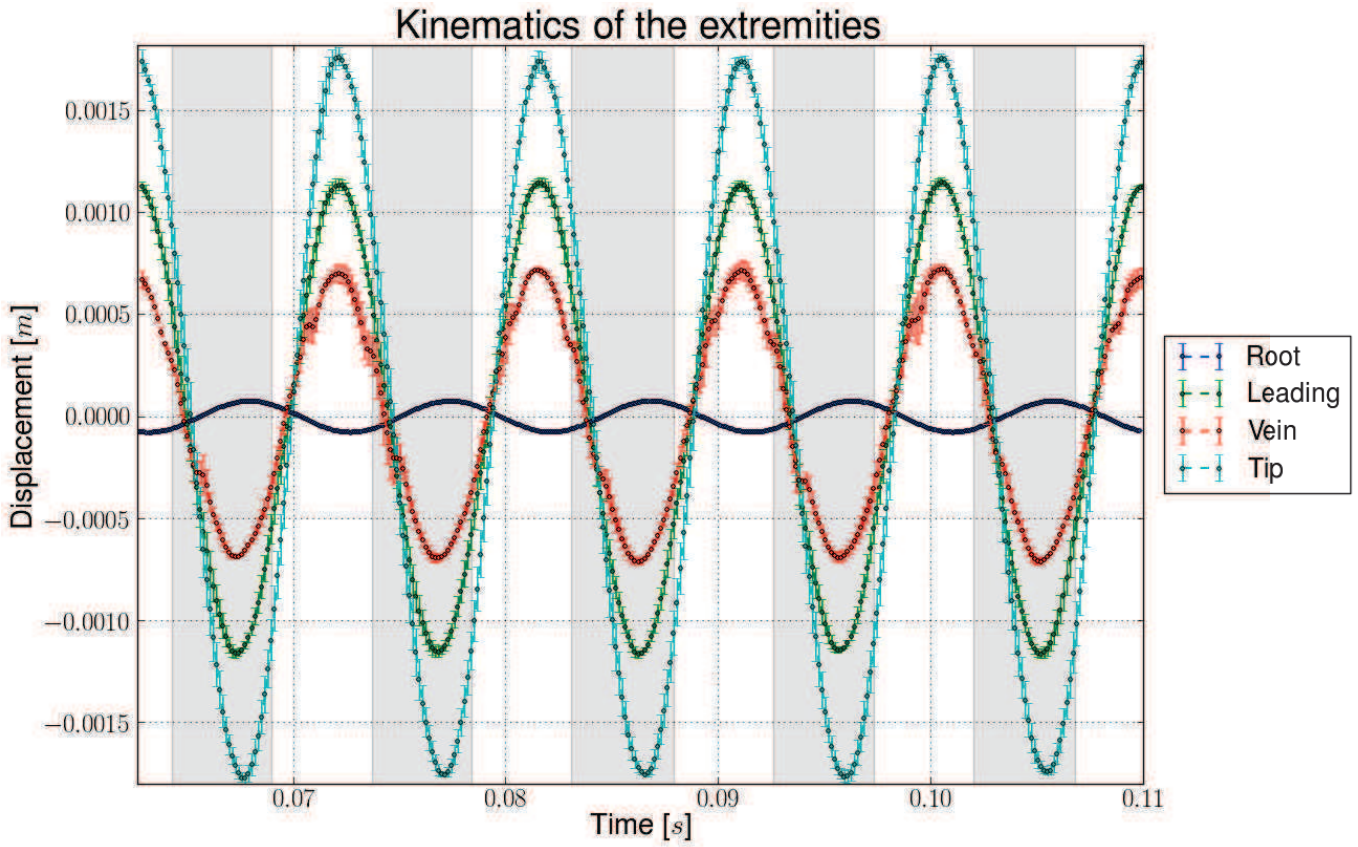

(b) Large actuation displacement

Figure E.12: Experimental data for the wing FM3 when actuated in air i.e. with aerodynamic coupling. More details about the experimental data are given in table E.4.

E.2.2 EM4

Table E.5: Summary of the experimental results for EM4 actuated at its air resonant frequency.

Medium		**Vacuum**		**Air**	
Exp. Pressure [*mbar*]		3.3e-3 to 4.1e-3		992	
Actuation type		SA	LA	SA	LA
Root	Mean Exp. Error μm]	0.1	1.5	0.2	0.6
	STD on Exp. Error [μm]	0.0	0.7	0.1	0.3
	Exp. Amp. [μm]	7.7	77.9	7.6	76.8
Leading-edge	Mean Exp. Error [μm]	3.4	67.8	7.3	19.5
	STD on Exp. Error [μm]	2.6	29.8	3.0	9.4
	Exp. Amp. [μm]	48.5	886.0	40.8	415.5
Vein 1	Mean Exp. Error [μm]	2.4	22.2	2.2	13.7
	STD on Exp. Error [μm]	0.9	10.3	1.3	7.7
	Exp. Amp. [μm]	24.1	321.8	13.8	121.3
Vein 2	Mean Exp. Error [μm]	3.9	60.5	4.3	21.9
	STD on Exp. Error [μm]	1.7	25.1	2.0	13.0
	Exp. Amp. [μm]	55.3	754.8	49.5	337.2
Tip	Mean Exp. Error [μm]	4.6	120.6	4.2	26.8
	STD on Exp. Error [μm]	2.3	59.2	3.1	14.5
	Exp. Amp. [μm]	103.3	1463.2	183.8	1359.0

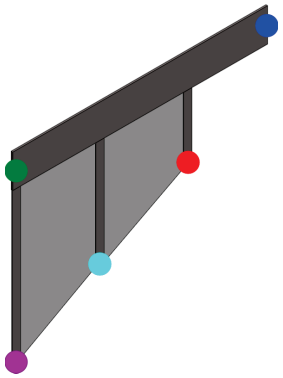

Figure E.13: CAD view of the EM4 wing with its extremity colored as in the figures E.14 and E.15.

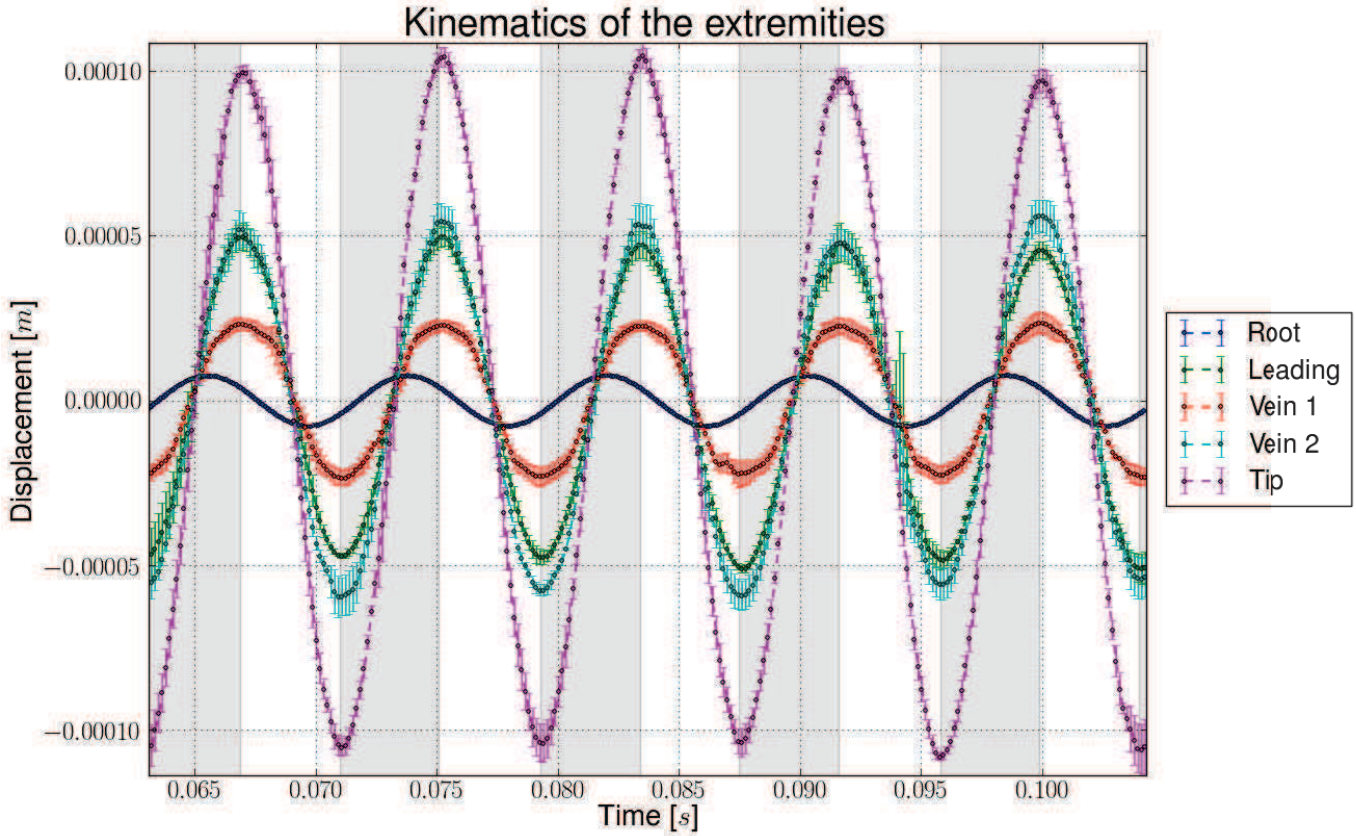

(a) Small actuation displacement

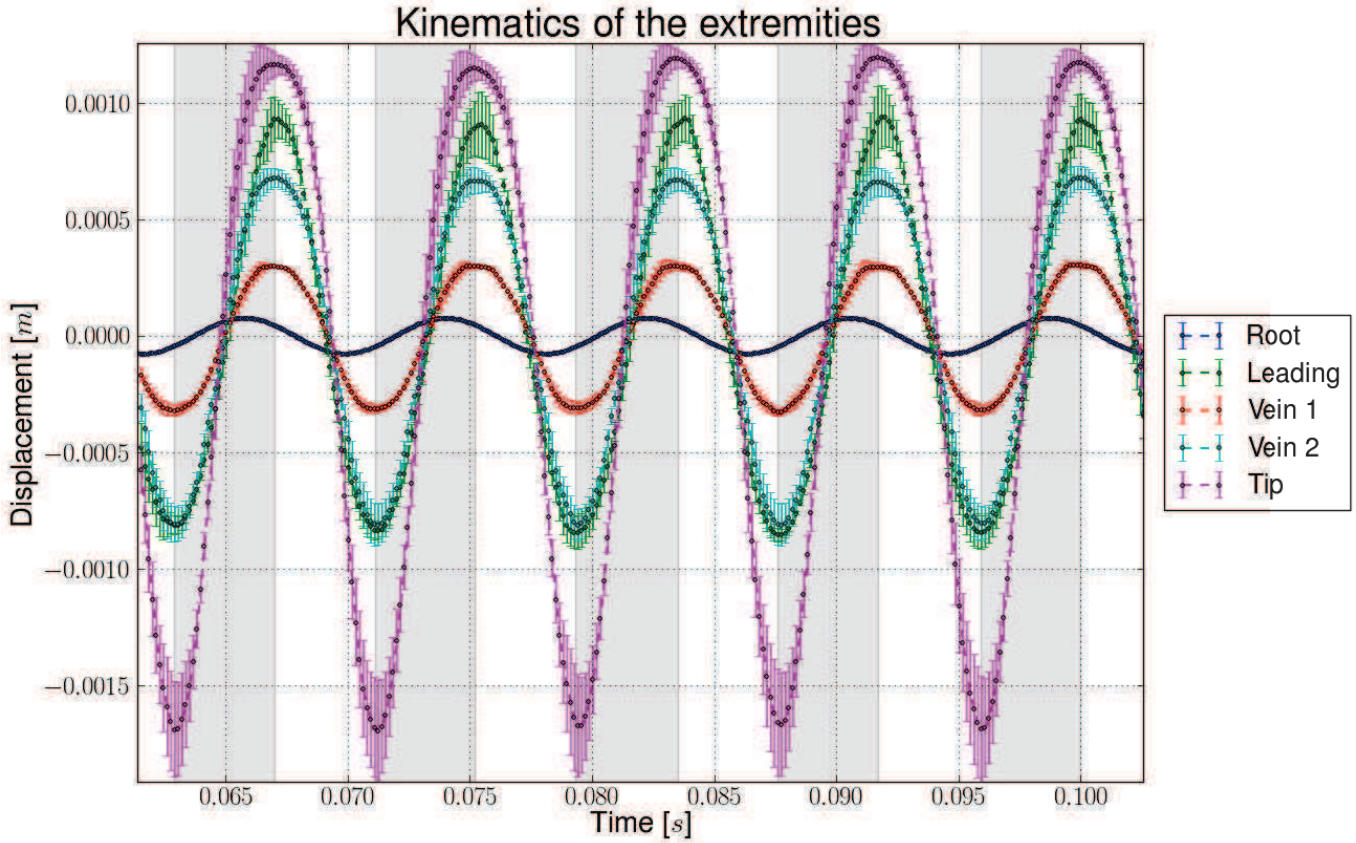

(b) Large actuation displacement

Figure E.14: Experimental data for the wing EM4 when actuated in vacuum i.e. without aerodynamic coupling. More details about the experimental data are given in table E.5.

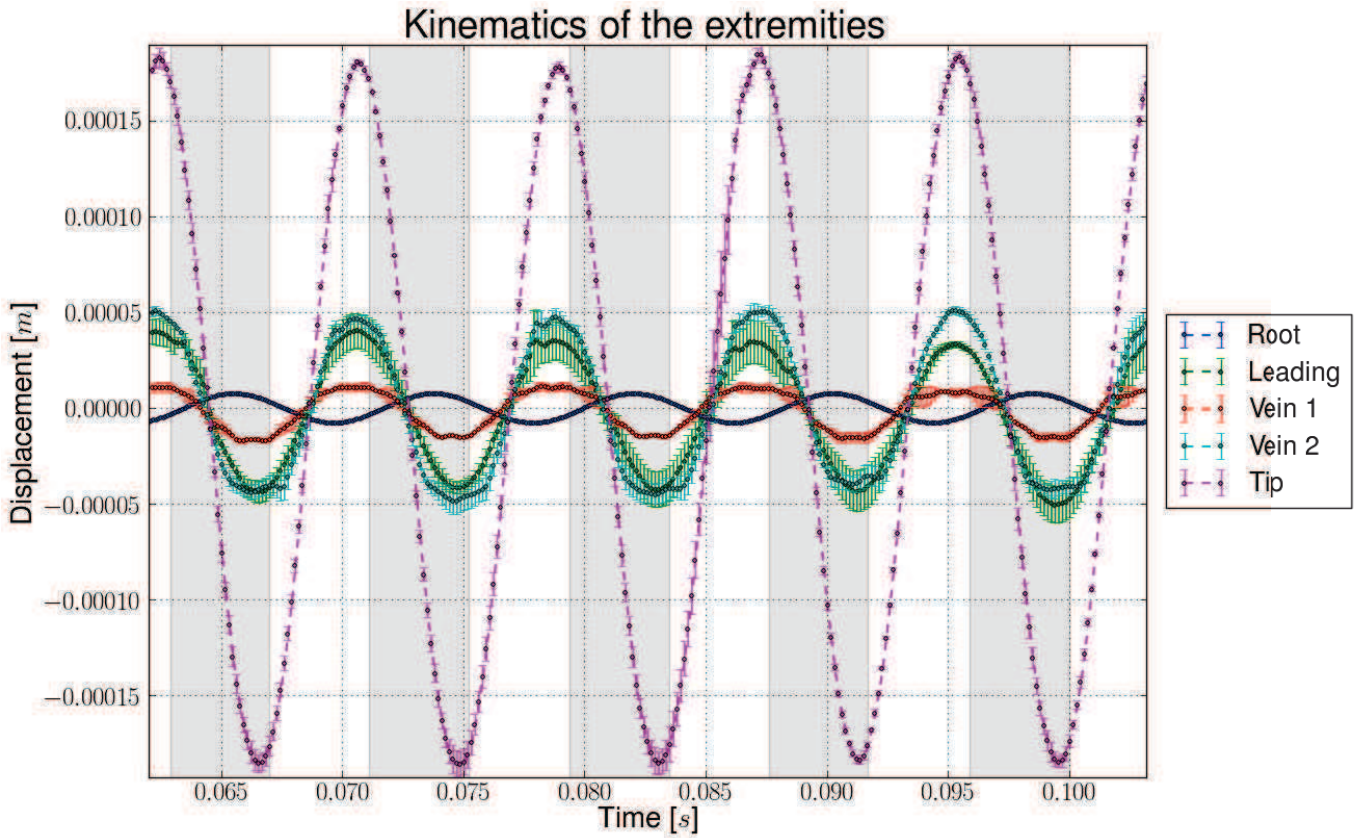

(a) Small actuation displacement

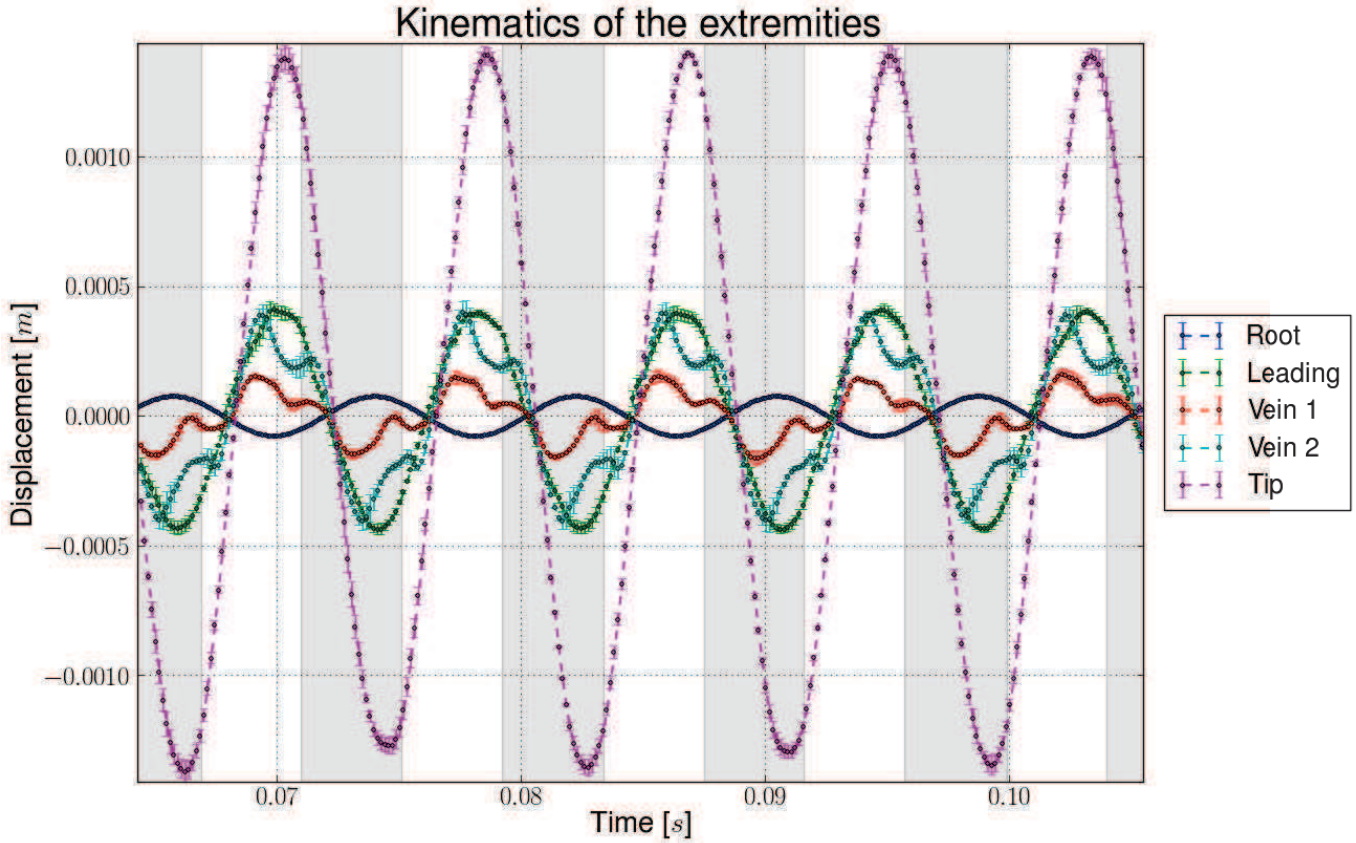

(b) Large actuation displacement

Figure E.15: Experimental data for the wing EM4 when actuated in air i.e. with aerodynamic coupling. More details about the experimental data are given in table E.5.

Appendix F

Description of commons optimization algorithms

Contents

The aims of this appendix is to introduce the various techniques at hand to solve optimization problems and is largely inspired by the introduction from Verstraete [2010], the web pages of Jakob [2013] and the appendix C of Bergmann [2004]. More technical details about optimization algorithms can be found in Schwefel [1995] and in Nocedal and Wright [2006].

Optimization problems are today being more and more used for multidisciplinary design tasks as a way to reduce the time and cost of a design process. Indeed until recently, such task was done mostly by refining a previous design using some know-how and a trial and error approach. With the advances in numerical modeling, the latter can be shortened by evaluating numerically the performance of the system. However to get ride of the iterative approach, a number of tools have been devised to assist the designer in finding autonomously the best compromise for its design regarding several objectives. Thus the designer's expertise is preserved and focused in analyzing the most promising solutions and not getting it by cumbersome and non-productive iterations. Various methods are thus now available to handle these optimization tasks efficiently depending on the nature of the problem, either one or several objectives to optimize, and of its characteristics.

Indeed and as seen in the figure F.1, each optimization problem has its own specificities with for example a design space containing some forbidden zones, not physical solutions for example (the white areas), or numerous sub-optima. For sake of completeness, an optimization problem with multiple sub-optima is referred as multi-modal and uni-modal otherwise. Typically, the search for a fitter design is done by altering iteratively a previous one, which can be seen mathematically as:

$$x_{i+1} = x_i + \alpha_i + S_i \tag{F.1}$$

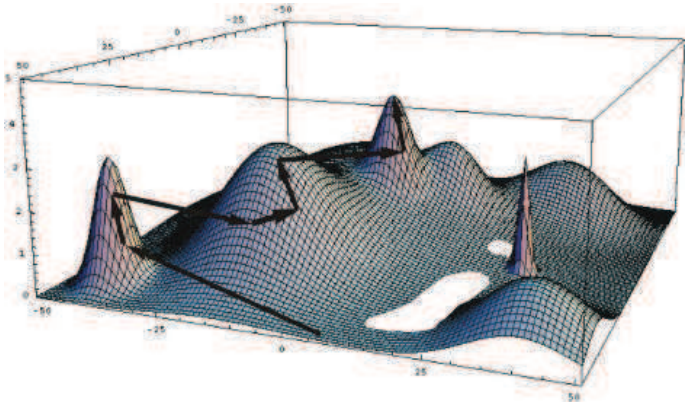

Figure F.1: Search space of a two-dimensional optimization problem (Source: Jakob [2013])

where x_{i+1} is the new guess for a fitter design and x_i the previous one, S_i is the search direction and α_i is a scalar defining the amplitude of the change in the S_i direction at the i-th iteration. This is better outlined in the figure F.1, by the various arrows.

Thus two family of optimization methods have emerged: the deterministic and the non-deterministic ones. The first ones are methods showing an identical behavior when starting from the same starting point and are more prone to single-modal problem. The second ones may return different results and are more suitable to multi-modal problem given their 'randomness' response. The difference is due to the way the search is conducted i.e. how the search direction S_i and the search length α_i are determined.

F.1 Deterministic procedures

The deterministic procedure are searching the optimal by iteratively setting a search direction towards the most promising slope. If the design space contains a sole optimum and the slope vary continuously smoothly, such procedures tend to be quite effective, but otherwise tends to be prone to local optimum problems and to a dependency to the starting points. Two groups are distinguished by the way of determining the search direction and length: the indirect procedures, requiring information on the partial derivation of the objective function, and the direct procedures, requiring only heuristic values of the objective function.

F.1.1 Indirect procedures

As outlined before, the indirect procedures are based on the knowledge of the partial derivatives of the objective function at least in the neighborhood of the current point of evaluation. Thus, the derivatives provide detailed trends on the slope of the objective function and enable the determination of the most promising search direction and length quite easily. Therefore, if the derivatives exists and vary sufficiently smoothly, the convergence rate of the optimization increases drastically using such procedures. However the computation of the derivatives is a computational intensive process, increasing with the order of the derivatives needed, which can be detrimental for the overall performance of the optimization.

Two categories are available depending on the order of the derivatives: the first order ones, based on the gradient or its approximation using finite differences, and the second order ones based on the Hessian. Both categories determine generally the search direction S_i while the search length α_i is determined by line search method.

F.1.1.1 Gradient based methods

Several gradient based methods exist in the literature. However the most familiar gradient based methods are the steepest descent, the quasi-Newton and the conjugate gradient. They are here briefly described.

a) The steepest descent method

As suggested by its name, this method proposes a new design in the direction where the objective function is decreasing the most, i.e. offering the steepest descent. The search direction $\vec{S_i}$ is thus opposed to the gradient of the objective function as:

$$S_i = -\nabla f(x_i) \tag{F.2}$$

The search length α_i is chosen small enough such that the method does not overshoot the descent of the objective function and can either be fixed or redefined at each iteration.

The main drawbacks of this methods are a relatively slow convergence rate near the optimum, a strong dependency to the starting points as well as to dead end on a local optima.

b) The quasi-Newton method

As suggested by its name, this method is derived from the Newton method, presented more lengthily in the section F.1.1.2, which required the costly determination of the Hessian $\mathbf{H}$ of the objective function. The idea is here to replace the costly computation by an approximation $\mathbf{B}$ which can be much more simple to compute as well as having some computing interesting properties, such as symmetry. The approximation is chosen so as to satisfy the following equation :

$$\Delta x = x_i - \mathbf{B}(f)(x_i)^{-1} \nabla f(x_i) \tag{F.3}$$

The various quasi-Newton methods differs in the way they establish the matrix $\mathbf{B}$. Among them, the most notorious are the Broyden-Fletcher-Goldfarb-Shano (BFGS), the Davidon-Fletcher-Powell (DFP) and the SR1 (Symmetric Rank One matrix) methods. By default in the above formulation, the search length α_i is 1. However to improve the convergence, α_i can be added explicitly to the search length and updated at each iterations using line search.

Given that the method uses an approximation of the matrix, it is quite efficient in finding optima at a moderate cost when compared to the full Newton method. This is why, the quasi-Newton is quite popular among the optimization applications.

c) The conjugate gradient

The method can be seen as a refinement of the steepest descent method, except that each search direction will be conjugate[1] to the gradient after the initial step ($i = 1$) taken, like in the steepest descent, as opposed to the gradient:

$$S_i = \begin{cases} -\nabla f(x_i) & \text{for } i = 1 \\ -\nabla f(x_i) + \beta_i S_{i-1} & \text{for } i > 1 \end{cases} \tag{F.5}$$

Various methods exists to determine the scalar β_i giving special properties to the algorithm. The Fletcher-Reeves, Polack-Ribière or the Hestenes-Stiefel methods are among the most notorious for such

[1] Two non-zero vectors u and v are conjugate with respect to $\mathbf{A}$ if:

$$u^T \mathbf{A} v = 0 \tag{F.4}$$

tasks. The search length is again determined by line search.

Main advantages of the conjugate gradient is its relative low computational load while being faster than the steepest descent method and being less demanding that the quasi-Newton methods.

F.1.1.2 Hessian based methods

Procedure based on the Hessian are more scare and derived directly from the Newton's method which is here described.

The Newton method try to construct a sequence of design point x_i using curvature information of the objective function. Considering a Taylor expansion of the objective function around the design point x_i:

$$f(x_i + \Delta x) = f(x_i) + \nabla f(x_i)^T \Delta x + \frac{1}{2}\Delta x^T \mathbf{H}(f)(x_i)\Delta x \tag{F.6}$$

where the local extremum of this approximation is outlined by computing its gradient versus Δx as :

$$\nabla f(x_i + \Delta x) = \nabla f(x_i) + \mathbf{H}(f)(x_i)\Delta x \tag{F.7}$$

By setting this gradient to zero, the next design point x_{i+1} can be determined as:

$$x_{i+1} = x_i + \Delta x = x_i - \mathbf{H}(f)(x_i)^{-1} \nabla f(x_i) \tag{F.8}$$

Assimilating this expression with the one given in equation F.1, the direction search S_i is the last term including the Hessian and the gradient operators. There the search length α_i is by default to 1. However for safety and smoother optimization, the method is often modified to include a smaller search length by stating explicitly α_i in the equation as:

$$x_{i+1} = x_i + \Delta x = x_i - \alpha_i \mathbf{H}(f)(x_i)^{-1} \nabla f(x_i) \tag{F.9}$$

The search length is again found and updated by line search.

The Newton method is very efficient for finding optima given its use of the curvature information. However, computing the inverse of the Hessian in high dimensions can be an expensive process especially if the objective function is not known analytically.

F.1.2 Direct procedures

In comparison to the indirect procedures, the direct ones complete an optimization without resorting to the derivation of the objective function and require just piece-wise consistency and can thus be used more widely. The main procedures are the ones based on pattern or on polyhedron.

F.1.2.1 Pattern strategies

The pattern strategies are searching iteratively for a fitter design x_{i+1} along orthogonal directions at a given search length α_i. Each candidate design draw thus around the current design x_i a frame, i.e. a cross. If a fitter design is found, the new design is directly selected and adopted as the center of new reference frame. If not, the search directions, through a rotation of the frame as in the Rosenbrock Procedure for example, or the search length, by shrinking or growing it, are modified so as to find a fitter design. The process iterates until no fitter design, within an margin or not, can be found whatever the search direction and the search length are. An example is given in the figure F.2.

A main advantage of such methods is its derivative-free aspect along with its relative simplicity. However its convergence speed might be affected by an oscillating behavior near the optimum making it less competitive than the steepest descent for example if the derivative of the objective function are available.

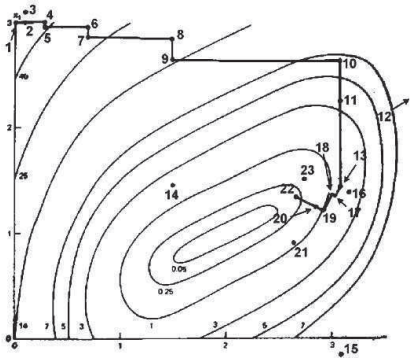

Figure F.2: Example of the Rosenbrock procedure using discrete steps (the number denotes the order in which the points are generated) (Source:`http://www.kniaz.net/software/RosNM.aspx`).)

F.1.3 Polyhedron strategies

In contrast to the above algorithms, polyhedron strategies are using simultaneously the information from several points in the search space, forming thus a polyhedron in space. The most notorious methods are the Nelder-Mead method, better known as the downhill simplex method and its constrained version the Complex. Below is only the simplex method briefly described.

The methods are based on the use of a simplex[2], which is a polytope[3] of $N + 1$ vertices in N dimension. Classical examples of simplices include a line segment on a line and a triangle on a plane. Starting form an initial simplex, iterative transformations of the simplex will occurred following some strategies so as to tends toward a better design at each iteration and ultimately towards the optimum. The possible transformations are the reflection, the expansion, the contraction and the shrinkage as shown in the figure F.3.

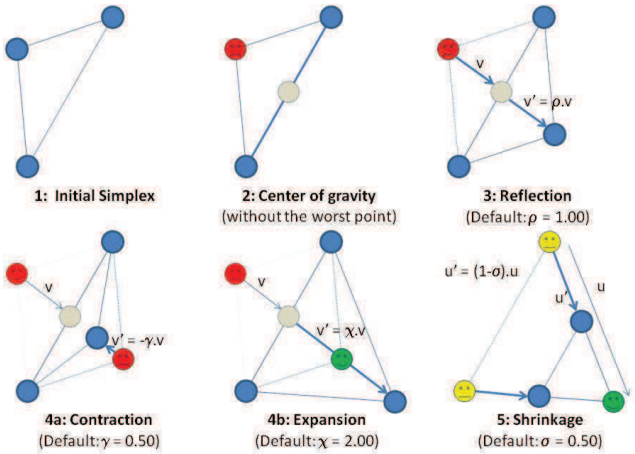

Figure F.3: Main steps of the simplex algorithm (Source: `http://capsis.cirad.fr/capsis/documentation/optimisation`).

As described in the figure F.3, the values of each vertex of the initial simplex are first evaluated. Then, the worst design point (vertex) is discarded and the center of gravity of the remaining simplex is evaluated. The discarded vertex is then reflected over the previously computed center of gravity and evaluated (steps

[2] A simplex is a generalization of the notion of a triangle or tetrahedron to arbitrary dimension Wikipedia [2013b].

[3] In elementary geometry, a polytope is a geometric object with flat sides, which exists in any general number of dimensions. A polygon is a polytope in two dimensions, a polyhedron in three dimensions, and so on in higher dimensions (such as a polychoron in four dimensions) Wikipedia [2013a].

2 and 3). Three cases are here available depending on the performance of the reflected design compared to the remaining designs of the simplex.

1. If the reflected design is the worst one, the contraction step occurs so as to step away from this worst design direction (step 4a). If the contracted design is better, a novel simplex is build by replacing the worst vertex by the new contracted one. If not, the shrinkage step occurs with the reflected simplex two worst vertices being shift towards the best vertex (step 5) and a novel iteration starts.

2. If the reflected design is the new best one, the expansion step occurs so as to run further into this interesting and juicy direction (step 4b). Once the expanded design evaluated an before starting a new iteration, a novel simplex is build by replacing the worst vertex by either the expanded design or the reflected design if the expanded design is worst than the reflected one.

3. If the reflected design is in the average of the others, a convergence check occurs before starting a new iteration if necessary.

The process iterates until the area of the simplex is below a certain value i.e. all the vertices within a certain margin from one another. The convergence checks occurs at the end of each iteration with each new and fitter simplex. An example of the process is given in the figure F.4.

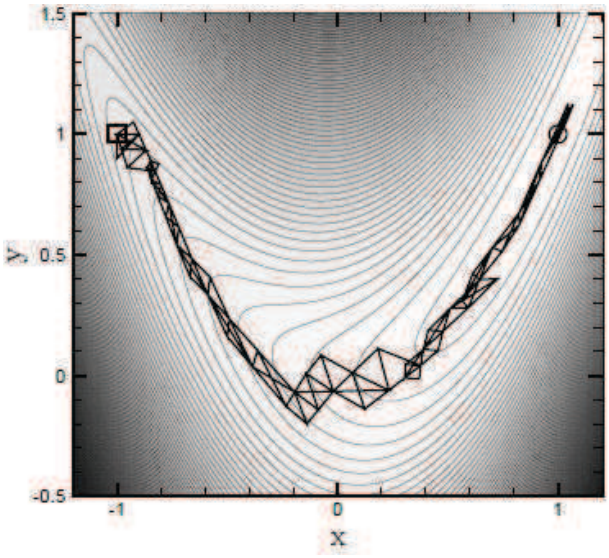

Figure F.4: Example of the Nelder-Mead method applied to the Rosenbrock function. The process starts with the simplex around the square and finish at the circle indicating the minima (Source: Bergmann [2004]).

The main advantages of the simplex method is its ease of implementation and of use, its efficiency on non-differentiable functions. However the methods tends to be prone to initialization problem and to an increasing computation cost when the dimension N increases.

F.2 Nondeterministic procedures

Unlike the deterministic procedures, the nondeterministic procedure are searching the design space by introducing some more randomness to accelerate the optimization. This randomness makes the procedures less sensitive to modeling errors and provides also a way to escape local optima. Thus, they are thus better fitted to multi-modal problems, problems with local optima, and less prone to starting points problems. Mains ideas behind the nondeterministic procedures are to find a sufficiently good approximation of the global optima by trading generally accuracy for speed.

Various methods have emerged taking generally inspiration from real world behavior and mathematically adapt it to optimization problems. The simulated annealing and the evolutionary algorithms are good examples of such inspiration and efficiency for non-linear multi-modal optimization problems. They are therefore here below shortly described. Other methods, inspired by nature, are available such as swarm algorithms or neuroevolution.

F.2.1 Simulated annealing

The simulated annealing is a generic probabilistic metaheuristic used for finding a good approximation of the global optimum of a given function in a large design space. The method is inspired by the annealing process in metallurgy, a technique where a material is heated up to a maximum temperature value at where all particles of the material randomly move, followed by a controlled cooling. During the cooling, all particles arrange themselves in the low energy ground state of the solid lattice, i.e. the most stable state, according to the energy level of each molecule and also the cooling temperature and rate. The aim is here to increase its ductility and to make it more workable by redistributing and destroying dislocations within the material.

Different simulated annealing methods exist but they are all using a common scheme. At each iteration, a random perturbation is applied to an existing design x_i and the resulting design is evaluated. If a fitter design is found, the previous design is discarded and the fitter is held back for the next iteration i.e perturbation. If not, the resulting design, although worse, can also be accepted depending on the stage of the cooling process, hence the analogy with the annealing process. The probability of such replacement is driven by the virtual temperature and the virtual energy. The latter one is equal to the difference in terms of performance between the two designs, while the former is a number, decreasing with the iteration steps, reducing the probability of accepting a worse design. Even if at first glance it might look weird, this acceptance of a new design is beneficial for the optimization as it increases the chance of finding a global optimum and shifting away from a local one.

The various simulated annealing methods differ in their way of perturbing each design iteration, in terms of variables and amplitudes, of computing the probability to accept a worse design and of setting the criterion reducing the virtual temperature. Main advantages of the simulated annealing is its efficiency to work around a design space and find a global optimum. However a large number of iterations are necessary increasing thus the computational cost of the optimization

F.2.2 Evolutionary algorithms

Evolutionary algorithms are based on Darwinian evolution and reproduce the evolution steps seen in species to evolve and adapt theirs characteristics by mechanisms such as mutation, reproduction, recombination and selection in response to specific environment constraints so as to be the fittest within theirs environmental niches and have better chance of surviving and/or reproducing.

Unlike other optimization methods, where at each iteration only one design is evaluated, the evolutionary algorithms are population based meaning that at each iteration a population of designs is generated and evaluated. Thus a design is referred as an individual, the objective function is named the fitness function.

Several evolution strategies exist, all inspired to some extent from nature. The most popular one is the genetic algorithm taking the analogy down to the gene level. Here the population consists of a fixed number of individuals, each having a set of properties, its genotype or chromosomes, which are encoded as binary string. This binary representation is essential for successful optimization as it allows a proper definition of

the reproduction mechanisms.

The evolution usually starts from a population of randomly generated individuals and tries to iteratively get a fitter population. The population in each iteration is referred as a generation. At each generation, the fitness of every individual is evaluated before the reproduction mechanisms come into plays to define the next generation using the performance of the current one. Two different individuals can thus mate and generate an offspring. The main reproduction mechanism is the cross-over where the genotype of the parents are recombined at a randomly chosen position to form two children and replace the parents in the upcoming generation.

The selection of parents is done via the selection mechanism, commonly either by the tournament or the roulette wheel selection method, which try to mate individuals with favorable characteristics. In the tournament selection, several tournaments, where the individuals are chosen at random from the population, are running and each winner, the fittest individual, is chosen as a parent. In the roulette wheel selection, the probability to be selected as a parent is proportional to the fitness of each individual with a larger area reserved on the wheel. The roulette wheel selection tends to be more elitist than the tournament selection, favoring the reproduction of only the fittest individuals, and thus tends to impoverish the genetic diversity of the population which might slow down the convergence as a more limited design space is explored.

After the cross-overs, a mutation mechanism might happened for the creation of the new generation by changing randomly a bit in the binary strings. It aims at increasing the genetic diversity of the population by exploring more broadly the design space and avoid the trap of a local minima. During the evolutionnary process, the creation of the new generation, it is possible that the best individuals might be lost and most genetic algorithms use the elitism strategy to breed it in the upcoming generation.

Once the new population is created, the evaluation process starts again and so on. Commonly, the algorithm terminates when either a maximum number of generations has been reached, or a satisfactory fitness level has been reached over the population.

Main advantages of the genetic algorithms is its efficiency to work around a multi-modal design space by avoiding initialization problems. The main drawback of genetic algorithms is its very high computational load as the population sized have to be sufficiently large so as to maximize the genetic diversity, i.e. to explore extensively the design space. If the evaluation of one individual is short and computationally non-intensive, it is satisfactory. If not, generally when the fitness function is a model of some sort, surrogate models might eventually be implemented, either using an off-line or an online database, to decrease the computational load. They approximate the behavior of the fitness function as closely as possible while being computationally cheaper. It might thus greatly increase the evaluation speed and the overall efficiency of the genetic algorithms.

Appendix G

List of publications and conferences

Journal

A. Bontemps, T. Vanneste, J.-B. Paquet, T. Dietsch, S. Grondel, and E. Cattan. Design and performance of an insect-inspired nano air vehicle. *Smart Materials and Structures*, 22(1):014008, Jan. 2013.

International conferences with lecture committee

X. Q. Bao, A. Bontemps, T. Vanneste, J.-B. Paquet, S. Grondel, and E. Cattan. Fabrication and actuation of flapping-wing robotic insect prototype using selected polymer. In *International Workshop on Bio-inspired Robots*, Nantes, France, 2011a.

X. Q. Bao, T. Vanneste, A. Bontemps, S. Grondel, J.-B. Paquet, and E. Cattan. Microfabrication of bio-inspired SU-8 wings and initial analyses of their aeroelastic behaviours for microrobotic insects. In *2011 IEEE International Conference on Robotics and Biomimetics (ROBIO2011)*, pages 1487–1494, Phuket, Thailand, 2011b. IEEE.

J.-B. Paquet, T. Vanneste, A. Bontemps, S. Grondel, and E. Cattan. Aerodynamic FMAV with vibrating wings at insect size. In *48th International Symposium of Applied Aerodynamics*, St Louis, France, 2013. AAAF.

T. Vanneste, J.-B. Paquet, X. Q. Bao, T. Dargent, S. Grondel, and E. Cattan. Conception of Resonant Wings on an Insect-Scale. In *International Micro Air Vehicle Conference and Flight Competition (IMAV2010)*, Braunschweig, Germany, 2010.

T. Vanneste, A. Bontemps, X. Q. Bao, J.-B. Paquet, S. Grondel, and E. Cattan. Polymer-based flapping-wing robotic insects: Progresses in wing fabrication, conception and simulation. In *International Mechanical Engineering Congress and Exposition 2011*, Denver, CO, USA, 2011. ASME.

T. Vanneste, J.-B. Paquet, S. Grondel, and E. Cattan. Design of a lift-optimized flapping-wing using a finite element aeroelastic framework of insect flight. In *53rd AIAA/ASME/ASCE/AHS/ASC Structures, Structural Dynamics and Materials Conference*, Honolulu, HI, USA, 2012a.

T. Vanneste, J.-B. Paquet, S. Grondel, and E. Cattan. Aeroelastic simulation of flexible flapping wing based on structural FEM and quasi steady aerodynamic model. In *28th International Congress of the Aeronautical Sciences*, Brisbane, Australia, 2012b.

International conferences without lecture committee

A. Bontemps, T. Vanneste, X. Q. Bao, J.-B. Paquet, S. Grondel, and E. Cattan. Prototyping of a like insect flapping wing object. In *Poster session of the International Workshop on Bio-inspired Robots*, Nantes, France, 2011a.

A. Bontemps, T. Vanneste, J.-B. Paquet, S. Grondel, and E. Cattan. Prototyping of an insect-like nano aerial vehicle. In *Poster session of the International Mechanical Engineering Congress and Exposition 2011*, Denver, CO, USA, 2011b.

National conference with lecture committee

T. Vanneste, J.-P. Bourez, J.-B. Paquet, S. Grondel, and E. Cattan. Visualisation de l'écoulement autour d'une aile d'insecte artificielle. In *14ème Congrès Français de Visualisation et de Traitement d'Images en Mécanique des Fluides*, Lille, France, 2011.

References

M. Abdulrahim, H. Garcia, G. F. Ivey, and R. Lind. Flight testing a micro air vehicle using morphing for aeroservoelastic control. In *45 th AIAA/ASME/ASCE/AHS/ASC Structures, Structural Dynamics and Materials Conference*, Palm Springs, CA, USA, 2004.

A. Agrawal and S. K. Agrawal. Design of Bio-inspired Flexible Wings for Flapping-Wing Micro-sized Air Vehicle Applications. *Advanced Robotics*, 23(7):979–1002, May 2009.

F. Albe, M. Bastide, Y. Lutz, J.-M. Desse, and J.-L. H. Tribillon. Color holography: Present state of the research activities at ISL. In *Holography 2000*, pages 128–136, St. Poelton, Austria, 2000.

S. Ansari, R. W. Zbikowski, and K. Knowles. Non-linear unsteady aerodynamic model for insect-like flapping wings in the hover. Part 1: Methodology and analysis. *Proceedings of the Institution of Mechanical Engineers, Part G: Journal of Aerospace Engineering*, 220(3):169–186, 2006a.

S. Ansari, R. W. Zbikowski, and K. Knowles. Non-linear unsteady aerodynamic model for insect-like flapping wings in the hover. Part 2: Implementation and validation. *Proceedings of the Institution of Mechanical Engineers, Part G: Journal of Aerospace Engineering*, 220(3):169–186, 2006b.

S. A. Ansari. *Nonlinear, Unsteady, aerodynamic model for insect-like flapping wings in the hover with micro air vehicle application.* PhD thesis, University of Cranfield, 2004.

S. A. Ansari, R. W. Zbikowski, and K. Knowles. Aerodynamic modelling of insect-like flapping flight for micro air vehicles. *Progress in Aerospace Sciences*, 42(2):129–172, 2006c.

S. A. Ansari, N. Phillips, G. Stabler, P. C. Wilkins, R. W. . Zbikowski, and K. Knowles. Experimental investigation of some aspects of insect-like flapping flight aerodynamics for application to micro air vehicles. *Experiments in Fluids*, 46(5):777–798, Apr. 2009.

Ansys Inc. *Release 11.0 Documentation for ANSYS.* Canonsburg, PA, USA, 2007.

H. Aono, C.-K. Kang, C. E. Cesnik, and W. Shyy. A Numerical Framework for Isotropic and Anisotropic Flexible Flapping Wing Aerodynamics and Aeroelasticity. In *28th AIAA Applied Aerodynamics Conference*, Chicago, Illinois, USA, 2010.

A. Azuma. *The biokinetics of flying and swimming.* AIAA, Berlin, 1992.

K. Azuma, H. Takahashi, T. Kan, K. Matsumoto, and I. Shimoyama. Triaxial force sensor with strain concentration notch beam for measurement of insect flight force. In *25th IEEE International Conference on Micro Electro Mechanical Systems (MEMS2012)*, pages 140–143, Paris, France, 2012.

X. Bao, T. Dargent, S. Grondel, J.-B. Paquet, and E. Cattan. Improved micromachining of all SU-8 3D structures for a biologically-inspired flying robot. *Microelectronic Engineering*, 88(8):2218–2224, Aug. 2011a.

X. Q. Bao and E. Cattan. Golden Ratio-Based and Tapered Diptera Inspired Wings: Their Design and Fabrication Using Standard MEMS Technology. *Journal of Bionic Engineering*, 8(2):174 – 180, 2011.

X. Q. Bao, T. Vanneste, A. Bontemps, S. Grondel, J.-B. Paquet, and E. Cattan. Microfabrication of bio-inspired SU-8 wings and initial analyses of their aeroelastic behaviours for microrobotic insects. In *2011 IEEE International Conference on Robotics and Biomimetics (ROBIO2011)*, pages 1487–1494, Phuket, Thailand, 2011b. IEEE.

A. Baritou. Synergies gagnantes autour d' un drone. *Air & Cosmos*, (2348):24, 2013.

P. S. Beran, G. H. Parker, R. D. Snyder, and M. Blair. Design Analysis Strategies for Flapping Wing Micro Air Vehicles. In *International Forum on Aeroelasticity and Structural Dynamics*, Stockholm, Sweden, 2007.

M. Bergmann. *Optimisation aérodynamique par réduction de modèle POD et contrôle optimal. Application au sillage laminaire d'un cylindre circulaire.* PhD thesis, Institut national polytechnique de Lorraine, 2004.

G. J. Berman and Z. J. Wang. Energy-minimizing kinematics in hovering insect flight. *Journal of Fluid Mechanics*, 582:153–168, 2007.

J. M. Birch and M. H. Dickinson. Spanwise flow and the attachment of the leading-edge vortex on insect wings. *Nature*, 412(6848):729–33, Aug. 2001.

J. M. Birch and M. H. Dickinson. The influence of wing-wake interactions on the production of aerodynamic forces in flapping flight. *The Journal of Experimental Biology*, 206(13):2257–2272, July 2003.

J. M. Birch, W. B. Dickson, and M. H. Dickinson. Force production and flow structure of the leading edge vortex on flapping wings at high and low Reynolds numbers. *The Journal of Experimental Biology*, 207 (7):1063–1072, 2004.

Bitcraze AB. About Bitcraze, 2012. URL `http://www.bitcraze.se/about/`.

M. Blair, G. H. Parker, P. S. Beran, and R. D. Snyder. A Computational Design Framework for Flapping Micro Air Vehicles. In *45th AIAA Aerospace Sciences Meeting and Exhibit*, Reno, NV, USA, 2007.

F. R. Blom, S. Bouwstra, M. Elwenspoek, and J. H. J. Fluitman. Dependence of the quality factor of micro-machined silicon beam resonators on pressure and geometry. *Journal of Vacuum Science and Technology B: Microelectronics, processing and phenomena*, 10(1):19–26, Jan. 1992.

F. Bohorquez, P. Samuel, J. Sirohi, D. Pines, L. Rudd, R. Perel, and C. Park. Design, Analysis and Hover Performance of a Rotary Wing Micro Air Vehicle. *Journal of the American Helicopter Society*, 48(2):11, 2003.

C. T. Bolsman, B. Palsson, J. F. L. Goosen, R. H. Munnig Schmidt, and F. van Keulen. The Use of Resonant Structures for Miniaturizing FMAVs. In *3rd US-European Competition and Workshop on Micro Air Vehicles (MAV07) and the 7th European Micro Air vehicle Conference and Flight Competition*, Toulouse, France, 2007.

C. T. Bolsman, J. F. L. Goosen, and F. van Keulen. Design Overview of a Resonant Wing Actuation Mechanism for Application in Flapping Wing MAVs. *International Journal of Micro Air Vehicles*, 1(4): 263–272, 2009.

A. Bontemps, T. Vanneste, J.-B. Paquet, T. Dietsch, S. Grondel, and E. Cattan. Design and performance of an insect-inspired nano air vehicle. *Smart Materials and Structures*, 22(1):014008, Jan. 2013.

F. M. Bos, D. Lentink, B. W. Van Oudheusden, and H. Bijl. Influence of wing kinematics on aerodynamic performance in hovering insect flight. *Journal of Fluid Mechanics*, 594(-1):341–368, Jan. 2008.

R. H. Buckholz. A two-component dynamic wind tunnel balance for mounted insects. *Journal of Physics E: Scientific Instruments*, 13(1):61–63, Jan. 1980.

R. H. Buckholz. Measurements of Unsteady Periodic Forces generated by the Blowfly Flying in a Wind Tunnel. *The Journal of Experimental Biology*, 90(1):163–173, Feb. 1981.

R. Carr, J.-M. Moschetta, C. Thipyopas, and G. Mehta. A tilt-body fixed-wing micro aerial vehicle for autonomous transition flight. In *International Micro Air Vehicle Conference and Flight Competition (IMAV2010)*, Braunschweig, Germany, 2010.

K. D. Chabak. *Conceptual study of rotary-wing microrobotics*. Master thesis, Air Force Institute of Technology, 2008.

S. Chang, J. Warren, and F.-P. Chiang. Mechanical testing of EPON SU-8 with SIEM. In *Microscale Systems: Mechanics and Measurements Symposium*, Orlando, FL, USA, 2000.

P. Chi, W. Zhang, W. Chen, H. Li, K. Meng, F. Cui, W. Liu, and X. Wu. Design and fabrication of an SU-8 biomimetic flapping-wing micro air vehicle by MEMS technology. *Jiqiren(Robot)*, 33(3):366–370, 2011.

S. K. Chimakurthi. *A computational aeroelasticity framework for analyzing flapping wings*. PhD thesis, University of Michigan, 2009.

I. Chowdhury and S. P. Dasgupta. Computation of Rayleigh damping coefficients for large systems. *The Electronic Journal of Geotechnical Engineering*, 8, 2003.

M. Cloupeau, J. F. Devillers, and D. Devezeaux. Direct Measurements of Instantaneous Lift in Desert Locust; Comparison with Jensen'S Experiments on Detached Wings. *The Journal of Experimental Biology*, 80(1): 1–15, June 1979.

N. R. Coleman. *Micro-Scale Flapping Wings for the Advancement of Flying MEMS*. Master thesis, Air Force Institute of Technology, Mar. 2009.

S. A. Combes and T. L. Daniel. Into thin air: contributions of aerodynamic and inertial-elastic forces to wing bending in the hawkmoth Manduca sexta. *The Journal of Experimental Biology*, 206(17):2999–3006, 2003a.

S. A. Combes and T. L. Daniel. Flexural stiffness in insect wings I. Scaling and the influence of wing venation. *The Journal of Experimental Biology*, 206(17):2979–2987, 2003b.

S. A. Combes and T. L. Daniel. Flexural stiffness in insect wings II. Spatial distribution and dynamic wing bending. *The Journal of Experimental Biology*, 206(17):2989–2997, 2003c.

T. Combes, A. Malik, and G. Bramesfeld. Fluid-Structure Interaction Simulation for the Design of Bio-Inspired Micro Air Vehicle Wings. In *30th AIAA Applied Aerodynamics Conference*, New Orleans, LA, USA, 2012.

P. Czekalowski, A. Gronczewski, and K. Sibilski. Water tunnel experimental investigation on the aerodynamic performance of flapping wings for nano air vehicles. In *29th AIAA Applied Aerodynamics Conference*, Honolulu, HI, USA, 2011.

S. Daily. Human Aging Gene Found In Flies, 2008. URL `http://www.sciencedaily.com/releases/2008/05/080511205328.htm`.

T. Dargent. *Vibrating wings microsystem: MEMS technologies for the fabrication of a bioinspired MEMS.* PhD thesis, Université Lille Nord-de-France, 2010.

T. Dargent, S. Grondel, J.-B. Paquet, E. Cattan, and C. Soyer. Vibrating wing analysis with passive torsion for micro flying robot. In *IEEE/RSJ International Conference on Intelligent Robots and Systems (IROS2008)*, pages 451–457, Nice, France, 2008.

T. Dargent, X. Bao, S. Grondel, G. Le Brun, J.-B. Paquet, C. Soyer, and E. Cattan. Micromachining of an SU-8 flapping-wing flying micro-electro-mechanical system. *Journal of Micromechanics and Microengineering*, 19(8):85028, 2009.

DARPA and DSO. BAA-06-06: Nano Air Vehicle (NAV) Program, 2005. URL `https://www.fbo.gov/index?s=opportunity&mode=form&id=e88cb2b0a71e6487c60283c05de48ceb&tab=core&_cview=1`.

J. C. Dawson, T. J. Smith, M. Elhindi, P. G. Huang, P. Beran, and G. Parker. Flapping Micro Air Vehicle: Wing Fabrication and Analysis. In *51st AIAA Aerospace Sciences Meeting including the New Horizons Forum and Aerospace Exposition*, number January, Grapevine, TX, USA, 2013.

G. C. H. E. de Croon, K. M. E. de Clercq, R. Ruijsink, B. Remes, and C. de Wagter. Design, aerodynamics, and vision-based control of the DelFly. *International Journal of Micro Air Vehicles*, 1(2):71–98, 2009.

J.-M. Desse, P. Picart, and P. Tankam. Digital color holography applied to fluid and structural mechanics. *Optics and Lasers in Engineering*, 50(1):18–28, Jan. 2012.

M. H. Dickinson. The effects of wing rotation on unsteady aerodynamics performance at low Reynolds numbers. *The Journal of Experimental Biology*, 192(1):179–206, 1994.

M. H. Dickinson and K. Gotz. Unsteady aerodynamic performance of model wings at low Reynolds numbers. *The Journal of Experimental Biology*, 174(1):45–64, 1993.

M. H. Dickinson, F.-O. Lehmann, and S. P. Sane. Wing Rotation and the Aerodynamic Basis of Insect Flight. *Science*, 284(5422):1954–1960, 1999.

W. B. Dickson and M. H. Dickinson. The effect of advance ratio on the aerodynamics of revolving wings. *The Journal of Experimental Biology*, 207(4):4269–81, Nov. 2004.

R. Dudley. *The biomechanics of insect flight: form, function, evolution.* Princeton Univ Press, 2002.

C. P. Ellington. The Aerodynamics of Hovering Insect Flight. I. The Quasi-Steady Analysis. *Philosophical Transactions of the Royal Society B: Biological Sciences*, 305(1122), 1984a.

C. P. Ellington. The Aerodynamics of Hovering Insect Flight. II. Morphological Parameters. 305(1122): 17–40, 1984b.

C. P. Ellington. The Aerodynamics of Hovering Insect Flight. III. Kinematics. *Philosophical Transactions of the Royal Society B: Biological Sciences*, 305(1122):41–78, 1984c.

C. P. Ellington. The Aerodynamics of Hovering Insect Flight. IV. Aeorodynamic Mechanisms. *Philosophical Transactions of the Royal Society B: Biological Sciences*, 305(1122):79–113, 1984d.

C. P. Ellington. The Aerodynamics of Hovering Insect Flight. V. A Vortex Theory. *Philosophical Transactions of the Royal Society B: Biological Sciences*, 305(1122):115–144, 1984e.

C. P. Ellington. The novel aerodynamics of insect flight: applications to micro-air vehicles. *The Journal of Experimental Biology*, 202(23):3439–3448, 1999.

C. P. Ellington, C. van den Berg, A. P. Willmott, and A. L. Thomas. Leading-edge vortices in insect flight. *Nature*, 384(6610):626–630, Dec. 1996.

A. R. Ennos. The kinematics and aerodynamics of the Free Flight of some Diptera. *The Journal of Experimental Biology*, 142(1):49–85, 1989.

R. Feng and R. J. Farris. The characterization of thermal and elastic constants for an epoxy photoresist SU8 coating. 37(22):4793–4799, Nov. 2002.

R. Feng and R. J. Farris. Influence of processing conditions on the thermal and mechanical properties of SU8 negative photoresist coatings. *Journal of Micromechanics and Microengineering*, 13(1):80, 2003.

R. Fotouhi. Dynamic analysis of very flexible beams. *Journal of Sound and Vibration*, 305:521–533, 2007.

R. Ganguli, S. Gorb, F.-O. Lehmann, and S. Mukherjee. An Experimental and Numerical Study of Calliphora Wing Structure. *Experimental Mechanics*, 50(8):1183–1197, Nov. 2009.

J. W. Gerdes, S. K. Gupta, and S. a. Wilkerson. A Review of Bird-Inspired Flapping Wing Miniature Air Vehicle Designs. *Journal of Mechanisms and Robotics*, 4(2):021003, 2012.

M. Ghommem, M. R. Hajj, B. K. Stanford, L. T. Watson, and P. S. Beran. Global and Local Optimization of Flapping Kinematics. In *53rd AIAA/ASME/ASCE/AHS/ASC Structures, Structural Dynamics and Materials Conference*, Honolulu, HI, USA, 2012.

A. Gogulapati. *Nonlinear Approximate Aeroelastic Analysis of Flapping Wings in Hover and Forward Flight*. PhD thesis, Univeristy of Michigan, 2011.

A. Gogulapati and P. P. Friedmann. Nonlinear Aeroelastic Effects in Flapping Wing Micro Air Vehicles. In *49th AIAA/ASME/ASCE/AHS/ASC Structures, Structural Dynamics, and Materials Conference*, Schaumburg, Illinois, USA, 2008.

A. Gogulapati, P. P. Friedmann, E. Kheng, and W. Shyy. Approximate Aeroelastic Modeling of Flapping Wings : Comparison with CFD and Experimental Data. In *51st AIAA/ASME/ASCE/AHS/ASC Structures, Structural Dynamics, and Materials Conference*, Orlando, Florida, USA, 2010.

P. Gopalakrishnan. *Unsteady Aerodynamic and Aeroelastic Analysis of Flapping Flight*. PhD thesis, Virginia Polytechnic Insitute and State University, 2008.

C. F. Graetzel, S. N. Fry, F. Beyeler, Y. Sun, and B. J. Nelson. Real-Time Microforce Sensors and High Speed Vision System for Insect Flight Control Analysis. In O. Khatib, V. Kumar, and D. Rus, editors, *Experimental Robotics*, volume 39 of *Springer Tracts in Advanced Robotics*, pages 451–460. Springer Berlin Heidelberg, Berlin, Heidelberg, 2008.

C. F. Graetzel, B. J. Nelson, and S. N. Fry. Frequency response of lift control in Drosophila. *Journal of the Royal Society, Interface / the Royal Society*, 7(52):1603–16, Nov. 2010.

J. M. Grasmeyer and M. T. Keennon. Development of the Black Widow Micro Air Vehicle. In *39th AIAA Aerospace Sciences Meeting and Exhibit*, volume 195, Reno, NV, USA, 2001.

W. E. Green and P. Y. Oh. A Hybrid MAV for Ingress and Egress of Urban Environments. *IEEE Transactions on Robotics*, 25(2):253–263, Apr. 2009.

M. Groen. *PIV and force measurements on the flapping-wing MAV DelFly II*. Master thesis, Delft University of Technology, 2010.

A. Guedama. Implémentation d'une base de données expérimentale pour validation d'un modèle numérique d'ailes biomimétiques. Technical report, Onera, Lille, France, 2010.

M. Hamamoto, Y. Ohta, K. Hara, and T. Hisada. Application of fluid-structure interaction analysis to flapping flight of insects with deformable wings. *Advanced Robotics*, 21(1), Jan. 2007.

J.-S. Han, J.-W. Chang, I.-M. Kang, and S.-T. Kim. Flow Visualization and Force Measurement of an Insect-Based Flapping Wing. In *48th AIAA Aerospace Sciences Meeting Including the New Horizons Forum and Aerospace Exposition*, Orlando, FL, USA, 2010.

Z. Hao, A. Erbil, and F. Ayazi. An analytical model for support loss in micromachined beam resonators with in-plane flexural vibrations. *Sensors and Actuators A: Physical*, 109(1-2):156–164, 2003.

S. Heathcote, I. Gursul, and D. Martin. Flexible Flapping Airfoil Propulsion at Zero Freestream Velocity. *AIAA Journal*, 42(11):2196–2204, 2004.

S. Heathcote, Z. J. Wang, and I. Gursul. Effect of spanwise flexibility on flapping wing propulsion. *Journal of Fluids and Structures*, 24(2):183–199, 2008.

R. Herbert, P. Young, C. Smith, R. J. Wootton, and K. Evans. The hind wing of the desert locust (Schistocerca gregaria Forskal). III. A finite element analysis of a deployable structure. *The Journal of Experimental Biology*, 203(19):2945–2955, 2000.

S. Ho, H. Nassef, N. Pornsin-Sirirak, Y.-C. Tai, and C.-M. Ho. Unsteady aerodynamics and flow control for flapping wing flyers. *Progress in Aerospace Sciences*, 39(8):635–681, Nov. 2003.

J. Hodara. Modélisation numérique des ailes battantes d'un micro-drone et optimisation du banc d'essai des prototypes. Technical report, Onera, Lille, France, 2011.

M. Hopcroft, T. Kramer, G. Kim, K. Takashima, Y. Higo, D. Moore, and J. Brugger. Micromechanical testing of SU-8 cantilevers. *Fatigue and Fracture of Engineering Materials and Structures*, 28(8):735–742, 2005.

H. Hosaka and K. Itao. Theoretical and Experimental Study on Airflow Damping of Vibrating Microcantilevers. *Journal of Vibration and Acoustics*, 121(1):64–69, 1999.

G. Huon. Flapping wing aerodynamics and low reynolds aerodynamics. Master, SUPAERO, Toulouse, France, 2007.

P. G. Ifju, D. A. Jenkins, S. Ettinger, Y. Lian, W. Shyy, and M. R. Waszak. Flexible-Wing-Based Micro Air Vehicles. In *40th AIAA Aerospace Sciences Meeting and Exhibit*, Reno, NV, USA, 2002.

K. Isogai, Y. Kamisawa, and H. Sato. Optimum Aeroelastic Design of Resonance Type Flapping Wing for Micro Air Vehicles. *Transactions of the Japan Society for Aeronautical and Space Sciences*, 52(178): 238–245, 2010.

W. Jakob. Optimisation, 2013. URL `http://www.iai.fzk.de/www-extern-kit/index.php?id=1949&L=1`.

B. Johnson, D. Claxton, B. K. Stanford, V. Jagdale, and P. G. Ifju. Development of a Composite Bendable-Wing Micro Air Vehicle. In *45th AIAA Aerospace Sciences Meeting*, pages 8–11, Reno, NV, USA, 2007.

K. D. Jones, S. Duggan, and M. F. Platzer. Flapping-wing propulsion for a micro air vehicle. In *39th AIAA Aerospace Sciences Meeting and Exhibit*, Reno, NV, USA, 2001.

C.-K. Kang, H. Aono, C. E. Cesnik, and W. Shyy. Effects of Flexibility on the Aerodynamic Performance of Flapping Wings. In *6th AIAA Theoretical Fluid Mechanics Conference*, Honolulu, HI, USA, 2011.

J. Katz and A. Plotkin. *Low-Speed Aerodynamics: From Wing Theory to Panel Methods*. McGraw-Hill, San Francisco, CA, USA, 1991.

M. T. Keennon. Tailless Flapping Wing Propulsion and Control Development for the Nano Hummingbird Micro Air Vehiclee. In *American Helicopter Society (AHS) International Future Vertical Lift Aircraft Design Conference*, San Francisco, CA, USA, 2012.

A. B. Kesel, U. Philippi, and W. Nachtigall. Biomechanical aspects of the insect wing: an analysis using the finite element method. *Computers in Biology and Medicine*, 28(4):423–437, 1998.

A. Khaldi, C. Plesse, C. Soyer, E. Cattan, F. Vidal, C. Chevrot, and D. Teyssié. Dry Etching Process on a Conducting Interpenetrating Polymer Network Actuator for a Flapping Fly Micro Robot. In *International Mechanical Engineering Congress and Exposition 2011*, pages 755–757, Denver, CO, USA, 2011. ASME.

Z. A. Khan and S. K. Agrawal. Optimal Hovering Kinematics of Flapping Wings for Micro Air Vehicles. *AIAA journal*, 49(2):257–268, 2011.

KMel Robotics LLC. Vehicles, 2012. URL `http://kmelrobotics.com/index.php?n=Main.Products`.

M. Kovac, A. Guignard, J.-D. Nicoud, J.-C. Zufferey, and D. Floreano. A 1 . 5g SMA-actuated Microglider looking for the Light. In *2007 IEEE International Conference on Robotics and Automation (ICRA2007)*, pages 367–372, Roma, Italy, 2007.

I. Kroo, F. Prinz, M. Shantz, P. Kunz, G. Fay, S. Cheng, T. Fabian, and C. Partridge. The Mesicopter : A Miniature Rotorcraft Concept Phase II Final Report. Technical report, Stanford University, Stanford, CA, USA, 2001.

L. Labarrere. Faisabilité d'une mesure de portance sur une aile résonante de nano-drone. Master, Onera, Lille, France, 2012.

M. Lalanne, P. Berthier, and J. Der Hagopian. *Mechanical Vibrations for Engineers*. Wiley-Interscience-Europe, 1984.

M. Lasek, J. Pietrucha, K. Sibilski, and M. Zlocka. The comparative evaluation of power requirements for fixed, rotary and flapping wings air vehicles. In *25th International Congress of the Aeronautical Sciences (ICAS2006)*, Hamburg, Germany, 2006.

F.-O. Lehmann and S. Pick. The aerodynamic benefit of wing-wing interaction depends on stroke trajectory in flapping insect wings. *The Journal of Experimental Biology*, 210(Pt 8):1362–77, Apr. 2007.

J. G. Leishman. *Principles of Helicopter Aerodynamics*. Cambridge University Press, 2006.

D. Lentink and M. H. Dickinson. Rotational accelerations stabilize leading edge vortices on revolving fly wings. *The Journal of Experimental Biology*, 212(16):2705–19, Aug. 2009.

D. Lentink, S. R. Jongerius, and N. L. Bradshaw. The Scalable Design of Flapping Micro-Air Vehicles Inspired by Insect Flight. In *Flying Insects and Robots*, chapter 14, pages 185–205. Springer Berlin Heidelberg, Berlin, Heidelberg, 2010.

J. K. Lindsey. File:Helophilus.pendulus.wing.detail.jpg - Wikimedia Commons, 2004. URL `http://commons.wikimedia.org/wiki/File:Helophilus.pendulus.wing.detail.jpg`.

H. Liu, T. Nakata, N. Gao, M. Maeda, H. Aono, and W. Shyy. Micro air vehicle-motivated computational biomechanics in bio-flights: aerodynamics, flight dynamics and maneuvering stability. *Acta Mechanica Sinica*, 26(6):863–879, Dec. 2010.

Z. Liu and J.-M. Moschetta. Rotary vs. Flapping-Wing Nano Air Vehicles: Comparing Hovering Power. In *European Micro Air Vehicle Conference and Flight Competition 2009 (EMAV2009)*, pages 21–27, Delft, the Netherlands, 2009.

H. Lorenz, M. Despont, N. Fahrni, N. LaBianca, P. Renaud, and P. Vettiger. SU-8: a low-cost negative resist for MEMS. *Journal of Micromechanics and Microengineering*, 7(3):121–124, Sept. 1997.

K. B. Lua, K. C. Lai, T. T. Lim, and K. S. Yeo. On the aerodynamic characteristics of hovering rigid and flexible hawkmoth-like wings. *Experiments in Fluids*, 49(6):1263–1291, Apr. 2010.

A. Luc-Bouhali. Progress of the REMANTA project on MAV. In *European Micro Air Vehicle Conference and Flight Competition (EMAV2006)*, Braunschweig, Germany, 2006.

J. M. McMichael and M. S. Francis. Micro Air Vehicles - Toward a New Dimension in Flight, 1997. URL `http://www.fas.org/irp/program/collect/docs/mav_auvsi.htm`.

K. Meng, W. Zhang, W. Chen, H. Li, P. Chi, C. Zou, X. Wu, F. Cui, W. Liu, and J. Chen. The design and micromachining of an electromagnetic MEMS flapping-wing micro air vehicle. *Microsystem Technologies*, 18(1):127–136, Dec. 2011.

N. Miki and I. Shimoyama. A micro-flight mechanism with rotational wings. In *IEEE 13th International Conference on Micro Electro Mechanical Systems (MEMS2000)*, pages 158–163, 2000.

F. O. Minotti. Unsteady two-dimensional theory of a flapping wing. *Physical Review E*, 66(5):51907, Nov. 2002.

J.-M. Moschetta, C. Thipyopas, and S. Shkarayev. On Fixed-Wing Micro-Air Vehicles with Hovering Capabilities. In *46th AIAA Aerospace Sciences Meeting and Exhibit*, Reno, NV, USA, 2008.

D. Mueller, H. Bruck, and S. Gupta. Measurement of Thrust and Lift Forces Associated With Drag of Compliant Flapping Wing for Micro Air Vehicles Using a New Test Stand Design. *Experimental Mechanics*, 50(6):725–735, 2010.

T. J. Mueller. *Fixed and flapping wing aerodynamics for micro air vehicle applications.* AIAA, 2001.

P. Muren. Picoflyer description, 2005. URL `http://www.proxflyer.com/pi_description.htm`.

H. Nagai and K. Isogai. Effects of Flapping Wing Kinematics on Hovering and Forward Flight Aerodynamics. *AIAA Journal*, 49(8):1750–1762, 2011.

H. Nagai, K. Isogai, M. Murozono, and T. Fujishiro. Investigation on structural and aerodynamic characteristics of resonant type elastic flapping wing. In *28th International Congress of the Aeronautical Sciences (ICAS2012)*, Brisbane, Australia, 2012.

M. Nasir, M. H. Dickinson, and D. Liepmann. Multidirectional force and torque sensor for insect flight research. In *13th International Conference on Solid-State Sensors, Actuators and Microsystems (TRANSDUCERS2005)*, volume 1, pages 555–558, Seoul, Korea, 2005. IEEE.

Q. V. Nguyen, Q. T. Truong, H. C. Park, N. S. Goo, and D. Byun. Measurement of Force Produced by an Insect-Mimicking Flapping-Wing System. *Journal of Bionic Engineering*, 7(Supplement 1):S94 – S102, 2010.

J. Nocedal and S. Wright. *Numerical Optimization.* Springer, 2nd edition, 2006.

M. Okamoto and A. Azuma. Experimental Study on Aerodynamic Characteristics of Unsteady Wings at Low Reynolds Number. *AIAA Journal*, 43(12):3–6, 2005.

T. Ono and M. Esashi. Energy dissipation in submicrometer thick single-crystal silicon cantilevers. *Journal of Microelectromechanical Systems*, 11(6):775–783, Dec. 2002. ISSN 1057-7157.

J.-J. Orteu. Mesure 3D de formes et de déformations par stéréovision, 2002.

M. F. M. Osborne. Aerodynamics of Flapping Flight with Application to Insects. *The Journal of Experimental Biology*, 28(2):221–245, 1951.

J.-B. Paquet and J.-P. Bourez. Experiments on oscillating wings at low Reynolds numbers. In *European Micro Air Vehicle Conference and Flight Competition (EMAV2006)*, Braunschweig, Germany, 2006.

C. B. Pedersen. *An indicial-Polhamus Model Of Aerodynamics of Insect-like Flapping Wings in Hober*. PhD thesis, Cranfield University, 2003.

C. S. Perone. *Pyevolve v0.6rc1 documentation*, 2010. URL `http://pyevolve.sourceforge.net/0_6rc1/`.

N. Phillips and K. Knowles. Effect of flapping kinematics on the mean lift of an insect-like flapping wing. *Proceedings of the Institution of Mechanical Engineers, Part G: Journal of Aerospace Engineering*, 225(7): 723–736, July 2011.

D. Pines and F. Bohorquez. Challenges Facing Future Micro-Air-Vehicle Development. *Journal of Aircraft*, 43(2):290–305, 2006.

E. C. Polhamus. A concept of the vortex lift of sharp-edge delta wings based on a leading-edge-suction analogy. *NASATND3767*, 1966.

N. Pornsin-Sirirak, Y.-C. Tai, H. Nassef, and C.-M. Ho. Titanium-alloy MEMS wing technology for a micro aerial vehicle application. *Sensors and Actuators A: Physical*, 89(1-2):95–103, 2001.

Prox Dynamics. PD-100 PRS, 2013. URL `http://www.proxdynamics.com/products/pd_100_prs/`.

D. I. Pullin and Z. J. Wang. Unsteady forces on an accelerating plate and application to hovering insect flight. *Journal of Fluid Mechanics*, 509, 2004.

M. Ramasamy, B. Johnson, and J. G. Leishman. Understanding the Aerodynamic Efficiency of a Hovering Micro-Rotor. *Journal of the American Helicopter Society*, 53(4):17, 2008.

J. V. Rayner. A vortex theory of animal flight. Part 1. The vortex wake of a hovering animal. *Journal of Fluid Mechanics*, 91(04):697–730, Apr. 1979.

E. Roussel, P. Gnemmi, and S. Changey. State of Progress of the Gun Launched Micro Air Vehicle. In *International Micro Air Vehicle Conference and Flight Competition 2012 (IMAV2012)*, Braunschweig, Germany, 2012.

D. Saharon and M. Luttges. Three-dimensional flow produced by a pitching-plunging model dragonfly wing. In *25th AIAA Aerospace Sciences Meeting*, Reno, NV, USA, 1987.

D. Saharon and M. Luttges. Visualization of unsteady separated flow produced by mechanically driven dragonfly wing kinematics model. In *26th AIAA Aerospace Sciences Meeting*, Reno, NV, USA, 1988.

E. Sällström, L. Ukeiley, P. Wu, and P. G. Ifju. Three-Dimensional Averaged Flow And Wing Deformation Around Flexible Flapping Wings. In *39th AIAA Fluid Dynamics Conference*, San Antonia, TX, USA, 2009.

P. Samuel, J. Sirohi, F. Bohorquez, and R. Couch. Design and testing of a rotary wing MAV with an active structure for stability and control. In *AHS 61st Annual Forum*, volume 61, page 1946, Grapevine, TX, USA, 2005.

S. P. Sane. The aerodynamics of insect flight. *The Journal of Experimental Biology*, 206(23):4191–4208, 2003.

S. P. Sane and M. H. Dickinson. The control of flight force by a flapping wing: lift and drag production. *The Journal of Experimental Biology*, 204(15):2607–2626, 2001.

S. P. Sane and M. H. Dickinson. The aerodynamic effects of wing rotation and a revised quasi-steady model of flapping flight. *The Journal of Experimental Biology*, 205(8):1087–1096, 2002.

S. Schmid and C. Hierold. Damping mechanisms of single-clamped and prestressed double-clamped resonant polymer microbeams. *Journal of Applied Physics*, 104(9):93516, 2008.

H.-P. P. Schwefel. *Evolution and Optimum Seeking*. Wiley-Interscience, 1995.

L. I. Sedov. *Two-dimensional problems in hydrodynamics and aerodynamics*. Interscience Publishers, 1965.

P. Seshadri, M. Benedict, and I. Chopra. A novel mechanism for emulating insect wing kinematics. *Bioinspiration & biomimetics*, 7(3):036017, Sept. 2012.

W. Shyy, H. Aono, S. K. Chimakurthi, P. Trizila, C.-K. Kang, C. E. Cesnik, and H. Liu. Recent progress in flapping wing aerodynamics and aeroelasticity. *Progress in Aerospace Sciences*, 46(7):284–327, 2010.

T. Sims, A. Palazotto, and A. Norris. A Structural Dynamic Analysis of a Manduca Sexta Forewing. *International Journal of Micro Air Vehicles*, 2(3):119–140, Sept. 2010.

B. Singh. *Dynamics and Aeroelasticity of Hover-Capable Flapping Wings: Experiments and Analysis*. PhD thesis, University of Maryland, 2006.

C. Smith, R. Herbert, R. J. Wootton, and K. Evans. The hind wing of the desert locust (Schistocerca gregaria Forskal). II. Mechanical properties and functioning of the membrane. *The Journal of Experimental Biology*, 203(19):2933–2943, 2000.

M. J. C. Smith. Simulating moth wing aerodynamics - Towards the development of flapping-wing technology. *AIAA Journal*, 34(7):1348–1355, 1996.

B. K. Stanford, P. S. Beran, and M. Kobayashi. Aeroelastic Optimization of Flapping Wing Venation: A Cellular Division Approach. *AIAA Journal*, 50(4):938–951, Apr. 2012a.

B. K. Stanford, P. S. Beran, and R. D. Snyder. Stability and Power Optimality in Time-Periodic Flapping Wing Structures. In *53rd AIAA/ASME/ASCE/AHS/ASC Structures, Structural Dynamics and Materials Conference*, Honolulu, HI, USA, 2012b.

E. Steltz, S. Avadhanula, and R. S. Fearing. High lift force with 275 Hz wing beat in MFI. In *2007 IEEE/RSJ International Conference on Intelligent Robots and Systems (IROS2007)*, pages 3987–3992, San Diego, CA, USA, 2007.

E. C. Stewart, M. J. Patil, R. A. Canfield, and R. D. Snyder. Parametric Representation and Shape Optimization of Flapping Micro Air Vehicle Wings. *International Journal of Micro Air Vehicles*, 4(3), 2012.

W. Su and C. E. Cesnik. Nonlinear Aeroelastic Simulations of a Flapping Wing Micro Air Vehicle Using Two Unsteady Aerodynamic Formulations. In *51st AIAA/ASME/ASCE/AHS/ASC Structures, Structural Dynamics, and Materials Conference*, Orlando, FL, USA, 2010.

Y. Sun, S. N. Fry, D. P. Potasek, D. J. Bell, and B. J. Nelson. Characterizing Fruit Fly Flight Behavior Using a Microforce Sensor With a New Comb-Drive Configuration. *Journal of Microelectromechanical Systems*, 14(1):4–11, 2005.

S. Sunada and C. P. Ellington. A new method for explaining the generation of aerodynamic forces in flapping flight. *Mathematical Methods in the Applied Sciences*, 24(17-18):1377–1386, 2001.

S. Sunada, D. Ong, X. Meng, H. Wang, L. Zeng, and K. KawachiI. Optical Measurement of the Deformation, Motion, and Generated Force of the Wings of a Moth, Mythimna Separata (Walker). *JSME International Journal Series B*, 45(4):836–842, 2002.

H. Taha, M. R. Hajj, and P. S. Beran. Unsteady Nonlinear Aerodynamics of Hovering MAVs/Insects. In *51st AIAA Aerospace Sciences Meeting including the New Horizons Forum and Aerospace Exposition*, Grapevine, TX, USA, 2013.

H. Takahashi, Y. Aoyama, K. Ohsawa, H. Tanaka, E. Iwase, K. Matsumoto, and I. Shimoyama. Differential pressure measurement using a free-flying insect-like ornithopter with an MEMS sensor. *Bioinspiration & Biomimetics*, 5(3):36005, 2010.

X. Tan, W. Zhang, X. Ke, W. Chen, C. Zou, W. Liu, F. Cui, X. Wu, and H. Li. Development of Flapping-wing Micro Air Vehicle in Asia. In *10th World Congress on Intelligent Control and Automation*, pages 3939–3942, Beijing, China, 2012. IEEE.

H. Tanaka and R. J. Wood. Fabrication of corrugated artificial insect wings using laser micromachined molds. *Journal of Micromechanics and Microengineering*, 20(7):075008, July 2010.

H. Tanaka, K. Matsumoto, and I. Shimoyama. Fabrication of a three-dimensional insect-wing model by micromolding of thermosetting resin with a thin elastmeric mold. *Journal of Micromechanics and Microengineering*, 17(12):2485–2490, Dec. 2007.

H. Tanaka, K. Matsumoto, and I. Shimoyama. Design and performance of micromolded plastic butterfly wings on butterfly ornithopter. In *2008 IEEE/RSJ International Conference on Intelligent Robots and Systems (IROS2008)*, pages 3095–3100, Nice, France, Sept. 2008. IEEE.

H. Tanaka, J. P. Whitney, and R. J. Wood. Effect of Flexural and Torsional Wing Flexibility on Lift Generation in Hoverfly Flight. *Integrative and comparative biology*, 51(1):142–150, May 2011.

J. Tang, D. Viieru, and W. Shyy. A Study of Aerodynamics of Low Reynolds Number Flexible Airfoils. In *37th AIAA Fluid Dynamics Conference and Exhibit*, Miami, FL, USA, 2007.

J. Tang, S. K. Chimakurthi, R. Palacios, C. E. Cesnik, and W. Shyy. Computational Fluid-Structure Interaction of a Deformable Flapping Wing for Micro Air Vehicle Applications. In *46th AIAA Aerospace Sciences Meeting and Exhibit*, Reno, NV, USA, 2008.

M. J. Tarascio, M. Ramasamy, I. Chopra, and J. G. Leishman. Flow Visualization of Micro Air Vehicle Scaled Insect-Based Flapping Wings. *Journal of Aircraft*, 42(2):385–390, Mar. 2005.

T. Theodorsen. General theory of aerodynamic instability and the mechanism of flutter. Technical report, NACA, 1935.

B. Thiria and R. Godoy-Diana. How wing compliance drives the efficiency of self-propelled flapping flyers. *Physical Review E*, 82(1):15303, 2010.

J. Toomey and J. D. Eldredge. Numerical and experimental study of the fluid dynamics of a flapping wing with low order flexibility. *Physics of Fluids*, 20(7):73603, 2008.

L. W. Traub. Analysis and Estimation of the Lift Components of Hovering Insects. *Journal of Aircraft*, 41 (2):284–289, 2004.

J. R. Usherwood and C. P. Ellington. The aerodynamics of revolving wings I. Model hawkmoth wings. *The Journal of Experimental Biology*, 205(11):1547–1564, 2002.

C. van den Berg and C. P. Ellington. The vortex wake of a 'hovering' model hawkmoth. *Philosophical Transactions of the Royal Society B: Biological Sciences*, 352(1351):317–328, Mar. 1997a.

C. van den Berg and C. P. Ellington. The three-dimensional leading-edge vortex of a 'hovering' model hawkmoth. *Philosophical Transactions of the Royal Society B: Biological Sciences*, 352(1351):329–340, Mar. 1997b.

T. Vanneste, J.-B. Paquet, X. Q. Bao, T. Dargent, S. Grondel, and E. Cattan. Conception of Resonant Wings on an Insect-Scale. In *International Micro Air Vehicle Conference and Flight Competition (IMAV2010)*, Braunschweig, Germany, 2010.

T. Vanneste, A. Bontemps, X. Q. Bao, J.-B. Paquet, S. Grondel, and E. Cattan. Polymer-based flapping-wing robotic insects: Progresses in wing fabrication, conception and simulation. In *International Mechanical Engineering Congress and Exposition 2011*, Denver, CO, USA, 2011a. ASME.

T. Vanneste, J.-P. Bourez, J.-B. Paquet, S. Grondel, and E. Cattan. Visualisation de l'écoulement autour d'une aile d'insecte artificielle. In *14ème Congrès Français de Visualisation et de Traitement d'Images en Mécanique des Fluides*, Lille, France, 2011b.

T. Verstraete. Introduction to Optimization and Multidisciplinary Design. In *VKI Lectures Series - Introduction to Optimization and Multidisciplinary Design in Aeronautics and Turbomachinery*, Rhode-Saint-Genèse, Belgium, 2010.

J. A. Walker and M. W. Westneat. Mechanical performance of aquatic rowing and flying. *Proceedings. Biological sciences / The Royal Society*, 267(1455):1875–81, 2000.

S. M. Walker, A. L. Thomas, and G. K. Taylor. Deformable wing kinematics in free-flying hoverflies. *Journal of The Royal Society Interface*, 7(42):131–142, May 2009.

Z. J. Wang. Dissecting Insect Flight. *Annual Review of Fluid Mechanics*, 37(1):183–210, Jan. 2005.

D. Watman and T. Furukawa. A parametric study of flapping wing performance using a robotic flapping wing. In *2009 IEEE International Conference on Robotics and Automation (ICRA2009)*, pages 3638–3643, Kobe, Japan, 2009.

U. G. K. Wegst and M. F. Ashby. The mechanical efficiency of natural materials. *Philosophical Magazine*, 84(21):2167–2186, 2004.

T. Weis-Fogh. Quick Estimates of Flight Fitness in Hovering Animals, Including Novel Mechanisms for Lift Production. *The Journal of Experimental Biology*, 59(1):169–230, 1973.

T. Weis-Fogh and M. Jensen. Biology and Physics of Locust Flight. I. Basic Principles in Insect Flight. A Critical Review. *Philosophical Transactions of the Royal Society B: Biological Sciences*, 239(667):415–458, July 1956.

Wikipedia. Polytope, 2013a. URL `http://en.wikipedia.org/wiki/Polytope`.

Wikipedia. Simplex, 2013b. URL `http://en.wikipedia.org/wiki/Simplex`.

P. J. Wilkin. The instantaneous force on a desert locust, Schistocerca gregaria (Orthoptera: Acrididae), flying in a wind tunnel. *Journal of the Kansas Entomological Society*, 63(2):316–328, 1990.

P. C. Wilkins. *Some Unsteady Aerodynamics Relevant to Insect-inspired Flapping-wing Micro Air Vehicles*. PhD thesis, Cranfield University, 2008.

A. P. Willmott, C. P. Ellington, and A. Thomas. Flow visualization and unsteady aerodynamics in the flight of the hawkmoth, Manduca sexta. *Philosophical Transactions of the Royal Society B: Biological Sciences*, 352(1351):303–316, Mar. 1997.

R. J. Wood. Design, fabrication, and analysis of a 3DOF, 3cm flapping-wing MAV. In *2007 IEEE/RSJ International Conference on Intelligent Robots and Systems (IROS2007)*, pages 1576–1581, San Diego, CA, USA, 2007a.

R. J. Wood. Liftoff of a 60mg flapping-wing MAV. In *2007 IEEE/RSJ International Conference on Intelligent Robots and Systems (IROS2007)*, pages 1889–1894, San Diego, CA, USA, 2007b.

R. J. Wood and R. S. Fearing. Flight force measurements for a micromechanical flying insect. In *2001 IEEE/RSJ International Conference on Intelligent Robots and Systems (IROS2001)*, volume 1, pages 355–362, Maui, HI, USA, 2001.

R. J. Wood, S. Avadhanula, E. Steltz, M. Seeman, J. Entwistle, A. Bachrach, G. Barrows, and R. S. Fearing. Design, fabrication and initial results of a 2g autonomous glider. In *2005 IEEE Industrial Electronics Society Meeting*, Raleigh, NC, USA, 2005.

R. J. Wood, K.-J. Cho, and K. Hoffman. A novel multi-axis force sensor for microrobotics applications. *Smart Materials and Structures*, 18(12):125002, Dec. 2009.

R. J. Wood, B. M. Finio, M. Karpelson, K. Y. Ma, P. S. Sreetharan, H. Tanaka, and J. P. Whitney. Progress on 'pico' air vehicles. *The International Journal of Robotics Research*, 31(11):1292–1302, Aug. 2012.

R. J. Wootton. Functional Morphology of Insect Wings. *Annual Review of Entomology*, 37(1):113–140, 1992.

R. J. Wootton, K. E. Evans, R. C. Herbert, and C. W. Smith. The hind wing of the desert locust (Schistocerca gregaria Forskal). I. Functional morphology and mode of operation. *The Journal of Experimental Biology*, 203(19):2921–2931, Oct. 2000.

R. J. Wootton, R. Herbert, P. Young, and K. Evans. Approaches to the structural modelling of insect wings. *Philosophical Transactions of the Royal Society B: Biological sciences*, 358(1437):1577–87, Sept. 2003.

P. Wu and P. G. Ifju. Micro Air Vehicle Flapping Wing Effectiveness, Efficiency and Aeroelasticity Relationships. In *48th AIAA Aerospace Sciences Meeting Including the New Horizons Forum and Aerospace Exposition*, Orlando, FL, USA, 2010.

P. Wu, B. K. Stanford, and P. G. Ifju. Structural Deformation Measurements of Anisotropic Flexible Flapping Wings for Micro Air Vehicles. In *49th AIAA/ASME/ASCE/AHS/ASC Structures, Structural Dynamics, and Materials Conference*, Schaumburg, IL, USA, 2008.

P. Wu, P. G. Ifju, B. K. Stanford, E. Sällström, L. Ukeiley, R. Love, and R. Lind. A Multidisciplinary Experimental Study of Flapping Wing Aeroelasticity in Thrust Production. In *50th AIAA/ASME/ASCE/AHS/ASC Structures, Structural Dynamics, and Materials Conference*, Palm Springs, CA, USA, 2009a.

P. Wu, B. K. Stanford, and P. G. Ifju. Passive Bending and Twisting Motion during the Flapping Stroke of a Micro Elastic Wing for Thrust Production. In *47th AIAA Aerospace Sciences Meeting Including The New Horizons Forum and Aerospace Exposition*, Orlando, FL, USA, 2009b.

P. Wu, B. K. Stanford, E. Sällström, L. Ukeiley, and P. G. Ifju. Structural dynamics and aerodynamics measurements of biologically inspired flexible flapping wings. *Bioinspiration & biomimetics*, 6(1):016009, Mar. 2011.

J. Yan. Wing Force Map Characterization and Simulation for the MicroMechanical Flying Robotic. In *Insect, IEEE Int. Conf. on Intelligent Robots and Systems, Oct 28-30, 2003, Las Vegas NV*, 2003.

Y. Yongliang, T. Binggang, and M. Huiyang. An analytic approach to theoretical modeling of highly unsteady viscous flow excited by wing flapping in small insects. *Acta Mechanica Sinica*, 19(6):508–516, 2003.

J. Young, S. M. Walker, R. J. Bomphrey, G. K. Taylor, and A. L. Thomas. Details of insect wing design and deformation enhance aerodynamic function and flight efficiency. *Science*, 325(5947):1549–52, Sept. 2009.

R. W. Zbikowski. On aerodynamic modelling of an insect-like flapping wing in hover for micro air vehicles. *Philosophical Transactions of the Royal Society A: Mathematical, Physical and Engineering Sciences*, 360 (1791):273–290, 2002.

L. Zhao, Q. Huang, X. Deng, and S. P. Sane. Aerodynamic effects of flexibility in flapping wings. *Journal of the Royal Society Interface*, 7(44):485–97, Mar. 2010.

J.-C. Zufferey, A. Klaptocz, A. Beyeler, J.-D. Nicoud, and D. Floreano. A 10-gram Microflyer for Vision-based Indoor Navigation. In *2006 IEEE/RSJ International Conference on Intelligent Robots and Systems (IROS2006)*, pages 3267–3272, Beijing, China, 2006.

Aeroelastic framework of insect-like flapping-wing applied to the design of a resonant nano air vehicle

Abstract: Developing insect-like flapping-wing drones from scratch is an ambitious and arduous task for designers due to a lack of well-established know-how. To speed up the development of such vehicles through the preliminary design stage, a framework modeling the aeroelastic phenomena encountered in insect flight is an asset and is the subject of this thesis.

Its kernel is a FEM based structural solver coupled in a blade-element approach to a quasi-steady aerodynamic model of insect flight accounting for the wing flexibility, both in the spanwise and in the chordwise direction, and for its large displacement. The complete framework is devised so as to maintain the computation load low while being modular enough for a wide range of applications.

To validate the overall aeroelastic framework, a two-steps process has been undertaken with in one hand numerical studies and in the other hand experimental ones acquired on a dedicated test bench. The framework computation agrees satisfactorily, capturing the damping due to the aerodynamic force, and thus paves the way for preliminary design applications of a flapping-wing vehicle.

To exhibit the capabilities of the framework as a preliminary design tool, two applications on a resonant nano air vehicle are performed: the definition of an efficient actuation strategy and the search of an aerodynamic potentially interesting wing geometry by plugging the framework to a genetic algorithm. The results are coherent with the ones found in nature and are under implementation on the nano air vehicle.

Keywords: Flapping-wing, aeroelastic framework, flexible wing, optimization, design tool

Développement d'un outil de modélisation aéroélastique du vol battu de l'insecte appliqué à la conception d'un nano-drone résonant

Résumé: Développer, à partir de zéro, un drone imitant le vol battu de l'insecte est une tâche ambitieuse et ardue pour un designer en raison du manque de savoir-faire en la matière. Pour en accélérer le développement pendant les phases de design préliminaires, un outil modélisant les phénomènes aéroélastiques du vol de l'insecte est un véritable atout pour le designer et est le sujet de cette thèse.

Le coeur de cet outil est un solveur éléments finis 'structure' couplé, en utilisant une approche par tranche, à un modèle aérodynamique quasi-statique du vol de l'insecte prenant en compte la flexibilité de l'aile, à la fois selon l'envergure et la corde, mais aussi ses grands déplacements. L'ensemble est conçu de manière à contenir le coût de calcul tout en étant assez modulaire pour s'adapter à un large panel d'applications.

Afin de valider l'intégralité de cet outil, un processus en deux étapes a été entrepris avec d'abord une approche numérique et ensuite une validation expérimentale grâce à un banc de caractérisation dédié. Les résultats du modèle concordent de manière satisfaisante dans les deux cas, capturant l'amortissement dû aux forces aérodynamiques, et ouvrent ainsi la voie à son utilisation pour le design de drones à ailes battantes.

Pour démontrer l'intérêt de cette approche lors des phases de design préliminaires, deux applications sur un nano-drone résonant sont réalisées: la définition d'une stratégie d'actionnement efficace et la recherche d'une géométrie d'aile potentiellement intéressante d'un point de vue aérodynamique, en couplant l'outil de modélisation à un algorithme génétique. Les résultats obtenus sont cohérents avec ceux trouvés dans la nature et sont en cours d'implémentation sur le drone.

Mots clés: Aile battante, modèle aéroelastique, aile souple, optimisation, outil de dimensionnement

This work has been financially supported by the Agence Nationale pour la Recherche and by the Fondation d'Entreprise EADS and accomplished at the Onera - The French Aerospace Lab, F-59045 Lille, France.